Particle Physics Research Centre

Queen Mary, University of London

School of Physics and Astronomy

Measurement of the Drell–Yan triple-differential cross-section in pp collisions at $\sqrt{s} = 8\,\mathrm{TeV}$ with the ATLAS detector

Lewis James Armitage

Submitted in partial fulfilment of the requirements of the Degree of Doctor of Philosophy

STATEMENT OF ORIGINALITY

I, Lewis James Armitage, confirm that the research included within this thesis is my own work or that where it has been carried out in collaboration with, or supported by others, that this is duly acknowledged below and my contribution indicated. Previously published material is also acknowledged below.

I attest that I have exercised reasonable care to ensure that the work is original, and does not to the best of my knowledge break any UK law, infringe any third party's copyright or other Intellectual Property Right, or contain any confidential material.

I accept that the College has the right to use plagiarism detection software to check the electronic version of the thesis.

I confirm that this thesis has not been previously submitted for the award of a degree by this or any other university.

Signature:

Date: March 22, 2017

ABSTRACT

This thesis presents the measurement and results of the $Z/\gamma^* \rightarrow \mu^+\mu^-$ Drell–Yan triple-differential cross-section, using $20.24\,\text{fb}^{-1}$of ATLAS data recorded in 2012 at a centre-of-mass energy of $\sqrt{s} = 8\,\text{TeV}$. The triple-differential cross-section is measured as a function of dimuon invariant mass, $m_{\mu\mu}$, dimuon rapidity, $y_{\mu\mu}$, and lepton decay angle in the Collins-Soper frame, $\cos\theta^*$. These dimensions provide sensitivity to the parton composition of the proton through the parton density functions, PDFs, and the weak effective mixing angle, $\sin^2\theta_W^{\text{eff}\cdot}$, via the forward-backward asymmetry, A_{FB}. The measurement is performed on and around the Z-boson's invariant mass peak, $46 < m_{\mu\mu} < 200\,\text{GeV}$, in a kinematic fiducial volume of muon transverse momentum, $p_T > 20$ GeV, and muon pseudo-rapidity $|\eta| \leq 2.4$. The results are unfolded from the detector level to the Born, bare and dressed levels, where a precision of $< 0.6\%$ is reported in the central bins. The data is combined with an electron channel measurement resulting in a combined result with reduced total uncertainty. The combined result is shown to constrain PDF uncertainties and achieve the most constrained $\sin^2\theta_W^{\text{eff}\cdot}$ uncertainty yet reported at the LHC.

ACKNOWLEDGEMENTS

During my time as a PhD student I feel that I have achieved and experienced many things that, when growing-up, I never thought possible. These things would not have happened without the patience, guidance and encouragement from many others. I would like to thank my supervisor, Eram Rizvi, for his support and wisdom. He always listened when I had any problems and offered sage advice when I had questions. I would like to thank the other academics in the PPRC group for the many interesting and useful conversations. I also thank the students (PhD, intern and otherwise!) for the friendships we have shared during our time together. I would also like to thank the support staff of the department for their invaluable work.

As the majority of my PhD was spent in Geneva, many thanks are made to the UKLO at CERN for organising the technicalities of my stay and the many academics that I met and answered numerous questions I had. I wish to thank both the students on LTA and the interns of the UN for the unforgettable memories we enjoyed together.

The full analysis would not have come to fruition without the dedicated work from Tony Kwan, Richard Keeler, Alexandre Glazov and Elena Yatsenko; and without doubt, the rest of the ATLAS Collaboration. I recognise support from the STFC in funding the PhD allowing me to conduct this research.

I would like to extend special thanks to my good friend Edouard Joly for keeping me sane during these years; to my loving parents, Marian and Alastair, for their absolute support and faith in me; and finally to my two brothers, Andrew and Tim, who, among their many other accomplishments, have instilled in me happiness and self-worth.

CONTENTS

PREFACE

In modern high energy particle physics the proton is both a fundamental tool for the advancement of the science and an example of our limited description of it. Where once thought fundamental, the proton is a composite of quarks (fermionic particles) and gluons (gauge bosons of the strong nuclear force). Hadronic particle accelerators rely on the stability and mass of the proton to achieve the highest energy man-made particle interactions. The large hadron collider (LHC), based in Geneva, Switzerland, is currently the highest energy particle accelerator on earth. During its first set of data-taking operations (Run-1) the LHC collided protons with centre-of-mass energies of 7 TeV in 2010 and 8 TeV in 2012. Recently in 2015 the LHC has re-started collisions at 13 TeV for 'Run-2', the highest centre-of-mass energies ever recorded in a collider. In this thesis the full $\sqrt{s} = 8\,\text{TeV}$ ATLAS data set is used, which is currently the largest recorded ATLAS data set.

Precise knowledge about the structure of the proton is vital as both a fundamental test of quantum chromo dynamics (QCD) and a route to improve future simulations of hadronic interactions. These points can be achieved by extracting the parton distribution functions (PDFs) from data recorded by the ATLAS detector on the LHC. Furthermore, measurements of fundamental physical constants that are limited by PDF precision can be improved by such data, such as $\sin^2\theta_W^{\text{eff}\cdot}$. Section 1 summarises the origin of $\sin^2\theta_W^{\text{eff}\cdot}$, and the parton distribution functions. Also discussed in this section is the Drell–Yan process and how its measurement can be made sensitive to these parameters. Sections 2 and 3 summarise the operation of the LHC, the ATLAS detector and event reconstruction. These descriptions focus on details relevant to a muon channel measurement of the Drell–Yan process. Monte Carlo event simulation is described in Section 4.

Sections 5-10 describe the measurement in detail, documenting the data sets used, the event selection criteria, Monte Carlo (MC) corrections and the agreement between data and predictions in control distributions. Systematic and statistical uncertainties contributing to the final cross-section measurement are discussed and detailed in Section 11. The final muon channel measurement results are presented in Section 12.

Sections 13-15 demonstrates the potential of the performed measurement. In these sections the thesis measurement, which is performed in the muon channel, is combined with an externally performed (i.e. not the thesis author's own work) electron channel measurement. The combined muon and electron channel data are shown to have reduced uncertainties compared to muon channel only data. A preliminary PDF extraction and $\sin^2\theta_W^{\text{eff}\cdot}$ sensitivity study using externally calculated MCFM theory predictions is also presented. Section 16 summarises the measurement conclusions.

Modern particle physics experiments require large collaborations of people to design, operate and characterise the experimental apparatus as well as fulfil the computing, software and data analysis needs. The ATLAS collaboration, consisting of over 3000 members, is a prime example

of this and as such all analyses are considered to be authored by the collaboration. The Monte Carlo simulation and all data and Monte Carlo corrections are produced by other members of the ATLAS collaboration as well as the tools for the integrated luminosity measurement. The electron channel measurements used for the combination (Section 14) was produced by ATLAS member Tony Kwan. The combination procedure and the combined profiling extraction of the PDFs and $\sin^2\theta_W^{\text{eff}\cdot}$ were performed by ATLAS member Alexandre Glazov. All other work presented in this thesis was produced by the thesis author unless explicitly stated or referenced. This also applies to the figures and tables where it is stated in the caption.

Along with the measurement in this thesis, a number of other studies and measurements were performed throughout the PhD. However, they are not included in this document as they were not deemed directly relevant to the triple-differential cross-section measurement. The non-presented material that the thesis author has worked on includes studies and data for the 8 TeV high mass Drell–Yan analysis (ATLAS paper [10.1007/JHEP08(2016)009][1], ATLAS internal note [ATL-COM-PHYS-2015-1381][2]) and studies of electron trigger bandwidth limitations between the ATLAS trigger modules and the level-1 topological processors for the future ATLAS 'phase-2' upgrade. The author of this thesis has also contributed to the Drell–Yan triple-differential cross-section ATLAS internal note [ATL-COM-PHYS-2015-1575][3].

1. THE THEORY OF THE STANDARD MODEL

A. The fundamental particles

Everything observed in the universe is found to be composed of a few basic building blocks known as fundamental particles, and governed by four fundamental forces. The Standard Model of particle physics is currently the most rigorously tested theory of how these particles and three of the four forces entwine. Its success has been gauged on its predictive power[4–8] and its description of almost all experimental results[9].

Of the fundamental particles the Standard Model comprises twelve fermions, spin 1/2 particles, which form two categories: leptons and quarks. Each category is further subdivided into three generations, as shown in Table 1. Each of these fermionic particles has an associated anti-fermion associated by charge conjugation.

Fermions			$U(1)$ Charge	T_3	Colour
Leptons					
e^-	μ^-	τ^-	-1	$-1/2$	-
ν_e	ν_μ	ν_τ	0	1/2	-
Quarks					
u	c	t	2/3	1/2	(r,g,b)
d	s	b	$-1/3$	$-1/2$	(r,g,b)
I	II	III	Generation		

TABLE 1: The fermion families of the Standard Model and their associated properties: the electromagnetic charge, in units of electron charge; the third component of the isospin T_3; and the $SU(3)_C$ colour charge.

The interactions between the fermions are mediated by the gauge/goldstone bosons. The bosons attributed to the electromagnetic and weak forces are the γ, Z and $W^\pm$. In the Standard Model the γ couples to electric ($U(1)$) charge and the Z and the $W^\pm$ couple to all fermions. The recently discovered H arises through symmetry breaking of the $SU(2)_L$ interaction and has a coupling proportional to mass. Additionally, there are eight gluons of different 'colour' charges that couple to the corresponding colour charges of themselves and of the quarks. The colours are conventionally denoted *red*, *green* or *blue*.

Due to the divergent and non-perturbative nature of the strong force, quarks are not observed as free particles. Instead they bind together to form hadronic states of integer unit charge, commonly consisting of either a quark anti-quark pair, called a meson; a three (anti-)quark state, called a

baryon; or even a five (anti-)quark state, termed a pentaquark, as has recently been discovered at the LHC[10].

The force of gravity, although described classically by Einstein's theory of General Relativity, is not described in the Standard Model. Attempts have been made to formulate frameworks of quantum-gravity[11,12], however no evidence has yet been observed to support such formalisms.

The Standard Model is constructed mathematically by the use of group theory, requiring that the Lagrangian is invariant under gauge transformations. For example, the electromagnetic field can be constructed as a unitary group, $U(1)$, by considering its gauge symmetry of the electric charge. When the global symmetry is required to be a local symmetry and gauge field is quantised, the resulting quanta are massless gauge bosons. In total, the Standard Model is a non-commutative (non-Abelian) gauge theory with the symmetry groups $SU(3)_C \times SU(2)_L \times U(1)_Y$[13–15].

$SU(3)_C$ encompasses quantum chromo dynamics (QCD) and describes the interaction between the quarks and gluons via the colour charge. The adjoint representation of $SU(3)_C$ gives rise to eight colour states, known as the colour octet, formed from combinations of colour and anti-colour. As gluons themselves carry components of the colour charge they not only mediate, but also participate in QCD interactions. The electromagnetic and weak interactions are unified through the $SU(2)_L \times U(1)_Y$ gauge group, forming the electro-weak (EW) part of the theory. As already mentioned, $U(1)$ represents electromagnetism and its associated gauge boson, the photon (γ). $SU(2)_L$ describes the rest of electroweak theory through weak isospin and is responsible for the massless W^0, W^1 and W^2 gauge bosons. When the $SU(2)$ symmetry is broken however, with what is now known as the Brout-Englert-Higgs (BEH) mechanism[16–18], four components of the Goldstone boson arise from the spontaneous symmetry breaking. Of these four components, three are absorbed as longitudinal terms by the W^0, W^1 and W^2 to form the now massive Z, W^+ and W^- bosons respectively and the remaining component is the spin-0 Higgs boson.

Confirmation of the spin-1 nature of the gluon along with demonstration of gluon radiation (bremsstrahlung) was observed at PLUTO and PETRA (DESY)[19]. Observations of neutral current interactions were reported at Gargamelle, at CERN[20] with the discovery and first measurements of the $W^{\pm}$ and the Z occurring at UA1 and UA2 at the SPS (CERN)[21–24].

The following sections will focus on the origins of the weak mixing angle, θ_W, its relation to the masses of the $W^{\pm}$ and Z and the form of the parton distribution functions.

B. The electro-weak interaction

In the Glashow-Weinberg-Salam Model of $SU(2)_L \times U(1)_Y$ a weak isospin doublet containing a lepton and associated neutrino is defined, along with its adjoint, as:

$$\chi_L = \begin{pmatrix} \nu_L \\ e_L \end{pmatrix} , \qquad \bar{\chi} = \begin{pmatrix} \bar{\nu}_L & \bar{e}_L \end{pmatrix} . \tag{1}$$

The doublet is introduced with a weak isospin quantum number T, for which the doublet has $T = \frac{1}{2}$, with the upper and lower members of the doublet having $T_3 = \pm\frac{1}{2}$, respectively. These are acted on by isospin generators, τ^i, which take the form of 2×2 Pauli matrices that satisfy the Lie Algebra in the form of cyclic-commutation.

The combined weak and electromagnetic theory is formed from the triplet of weak currents and the electromagnetic current:

$$J^i_\mu = \bar{\chi}_L \gamma_\mu \tfrac{1}{2} \tau^i \chi_L \, , \tag{2}$$

$$J^{em}_\mu = Q \left(\bar{e}_L \gamma_\mu e_L + \bar{e}_R \gamma_\mu e_R \right) , \tag{3}$$

where γ are the standard gamma-matrices recognised from Lorentz algebra and Q denotes the charge of the particle. The raising and lowering operators for the charges can be written as:

$$\tau^\pm = \tfrac{1}{2} \left(\tau^1 \pm \tau^2 \right) , \tag{4}$$

$$J^\pm_\mu = \bar{\chi}_L \gamma_\mu \tau^\pm \chi_L = J^1_\mu \pm i J^2_\mu \, . \tag{5}$$

Due to the difference in chirality between the neutral current parts (i.e J^3_μ and J^{em}_μ) an additional current, J^Y_μ, must be added to maintain the gauge theory. This leads to the following, which also defines the relationship between electric charge, Q, the third component of weak isospin, T_3 and weak hypercharge, Y_W;

$$J^{em}_\mu = J^3_\mu + \tfrac{1}{2} J^3_\mu \, , \tag{6}$$

$$Q = T_3 + \tfrac{1}{2} Y_W \, , \tag{7}$$

which is readily seen in Table 1.

The theory is required to be invariant under local gauge transformations, and so vector fields are added to couple to the currents. Fortunately, the Lagrangian, $\mathcal{L}$, can be constructed in separate terms. The $SU(2)_L$ symmetry is gauged by the introduction of an isotriplet of vector gauge bosons W^i_μ, $(i = 1, 2, 3)$ with coupling, g. The $U(1)_Y$ symmetry is gauged through the vector boson, B_μ with coupling, $\frac{1}{2}g'$. The interaction of the vector fields with the currents take the form, $-g J^{i\mu} W^i_\mu - \frac{1}{2} g' J^{Y\mu} B_\mu$, resulting in lepton-gauge boson terms:

$$\mathcal{L}(l) = \bar{\chi}_L \gamma^\mu [i\partial_\mu - \frac{1}{2} g \vec{\tau} . \vec{W}_\mu + \frac{1}{2} g' B_\mu] \chi_L + \bar{e}_R \gamma^\mu [i\partial_\mu + g' B_\mu] e_R \, . \tag{8}$$

The interaction pieces of $\mathcal{L}(l)$ can be separated into charged current (CC), $\mathcal{L}_{CC}$, and neutral current (NC), $\mathcal{L}_{NC}$, terms corresponding to exchange of electrically charged $W^{\pm}$ or electrically neutral Z^0. Notably, when considering the full $\vec{\tau}.\vec{W}_\mu$ term and defining the charged vector fields $W^{\pm} = \frac{1}{\sqrt{2}}(W^1 \mp iW^2)$, they can be written as:

$$\mathcal{L}_{CC} = -\tfrac{1}{2}g[J^+_\mu W^{+\mu} + J^-_\mu W^{-\mu}]\,, \tag{9}$$

$$\mathcal{L}_{NC} = -gJ^3_\mu W^{3\mu} - \tfrac{1}{2}g' J^Y_\mu B^\mu\,, \tag{10}$$

which shows that the charged raising and lowering currents couple to the charged $W^{\pm}$ fields.

The vector fields W^3_μ and B_μ will appear in nature as an entwined mix. Therefore, the physical neutral vector fields Z_μ and A_μ are defined accordingly:

$$\begin{pmatrix} \gamma \\ Z \end{pmatrix} = \begin{pmatrix} \cos\theta_W & \sin\theta_W \\ -\sin\theta_W & \cos\theta_W \end{pmatrix} \begin{pmatrix} B^0 \\ W^0 \end{pmatrix}\,, \tag{11}$$

where θ_W is the weak mixing angle. From requirements of A_μ the couplings can be shown to have useful relations such as, $g\sin\theta_W = g'\cos\theta_W = e$. By the use of these relations, and after manipulation, the interaction pieces of the Lagrangian may be written:

$$\mathcal{L}_{CC} + \mathcal{L}_{NC} = -\frac{g}{\sqrt{2}}[J^+_\mu W^{+\mu} + J^-_\mu W^{-\mu}] - eJ^{em}_\mu A^\mu - \frac{g}{\cos\theta_W}[J^3_\mu - \sin^2\theta_W J^{em}_\mu]Z^\mu\,. \tag{12}$$

This currently does not include the gauge invariant kinetic energy terms for the vector boson fields W^i_μ and B_μ. These are included in the following form:

$$\mathcal{L}_W = -\tfrac{1}{4}\vec{W}_{\mu\nu}\vec{W}^{\mu\nu}\,, \tag{13}$$

$$\mathcal{L}_B = -\tfrac{1}{4}B_{\mu\nu}B^{\mu\nu}\,, \tag{14}$$

where, $\vec{W}_{\mu\nu} = \partial_\mu\vec{W}_\nu - \partial_\nu\vec{W}_\mu - g\vec{W}_\mu \times \vec{W}_\nu$, and the Abelian field strength tensor $B_{\mu\nu} = \partial_\mu B_\nu - \partial_\nu B_\mu$. From this, one can pick-out the $(\partial_\mu V)VV$ and $VVVV$ terms which encompass the three- and four-point self-interactions.

C. The Brout-Englert-Higgs Mechanism

For the scope of this thesis the BEH Mechanism does not need to be covered in extensive detail, so a brief description shall be provided here. It is clear from the Lagrangian terms in the previous section that there are no parameters for the mass. They are formulated by introducing an $SU(2)_L$ doublet of complex scalar Higgs fields with similar quantum number assignment as the isospin doublet and adding a scalar contribution to the Glashow Model Lagrangian:

$$\Phi_L = \begin{pmatrix} \phi^+ \\ \phi^0 \end{pmatrix}\,, \tag{15}$$

$$\mathcal{L}_\Phi = (D_\mu\Phi)^\dagger D^\mu\Phi - V(\Phi)\,, \tag{16}$$

where D_μ is the $SU(2)_L \times U(1)_Y$ covariant derivative involving the vector fields $\vec{W}_\mu$ and B_μ, and $V(\Phi)$ is an invariant and renormalisable scalar potential:

$$D_\mu = \partial_\mu + \tfrac{i}{2} g \vec{\tau}.\vec{W}_\mu + i g' \tfrac{1}{2} Y B_\mu \,, \tag{17}$$

$$V(\Phi) = \mu^2(\Phi^\dagger \Phi) - \lambda(\Phi^\dagger \Phi)^2 \,. \tag{18}$$

By constraining μ and λ appropriately a manifold of minima below $V(\Phi) = 0$ is obtained that is invariant in $SU(2)_L \times U(1)_Y$, commonly known as the "wine bottle" potential. The Φ doublet can be written in terms of real scalar fields $\phi^+ = \frac{1}{\sqrt{2}}(\phi_1 + i\phi_2)$ and $\phi^0 = \frac{1}{\sqrt{2}}(\phi_3 + i\phi_4)$ and as such the $SU(2)_L \times U(1)_Y$ symmetry may be spontaneously broken by picking vacuum expectation values for $\phi_{1\ldots4}$. In order for the photon to remain massless the non-zero vacuum expectation value is assigned to the ϕ_3 neutral field, $\langle 0|\phi_3|0\rangle^2 = v^2 = \mu^2/\lambda$. By defining the scalar Higgs field through the relation, $\phi_3 = H + v$, a unitary gauge is chosen so that ϕ_1, ϕ_2, ϕ_4 can be eliminated. The Lagrangian, $\mathcal{L}_\Phi$, can then be evaluated in unitary gauge;

$$\Phi = \frac{1}{\sqrt{2}} \begin{pmatrix} 0 \\ H + v \end{pmatrix} \,, \tag{19}$$

$$\begin{aligned} \mathcal{L}_\Phi &= \frac{1}{2}\partial_\mu H \partial^\mu H + \frac{1}{4} g^2 (H^2 + 2vH + v^2) W_\mu^+ W^{-\mu} \\ &+ \frac{1}{8}(g^2 + g^{'2})(H^2 + 2vH + v^2) Z_\mu Z^\mu \\ &+ \mu^2 H^2 + \frac{\lambda}{4}(H^4 + 4vH^3) \,. \end{aligned} \tag{20}$$

From the earlier relations of θ_W to g and g', and identifying the $m_W^2 W_\mu^+ W^{-\mu}$ and $\frac{1}{2} m_Z^2 Z_\mu Z^\mu$ terms, the weak mixing angle is shown to have the following relation to the W and Z boson masses:

$$\frac{m_W}{m_Z} = \cos\theta_W \,. \tag{21}$$

However, the relation is commonly expressed in terms of the squared sine of the weak mixing angle:

$$\sin^2\theta_W = 1 - \frac{m_W^2}{m_Z^2} \,. \tag{22}$$

The lepton masses are generated by adding the Yukawa term using the same unitary gauge, Φ, and Yukawa coupling parameter, G_e;

$$\mathcal{L}_Y(e) = -G_e[\chi_L \Phi e_R + \bar{e}_R \Phi^\dagger \chi_L] \,. \tag{23}$$

D. The structure of the proton and PDFs

The most precise measurements of proton structure have been obtained through Deep(ly) Inelastic Scattering (DIS) experiments. In such experiments the proton is probed by a lepton via the exchange

of an electroweak boson, γ^*/Z or $W^\pm$. The Feynman diagram for the DIS process is shown in Figure 1.

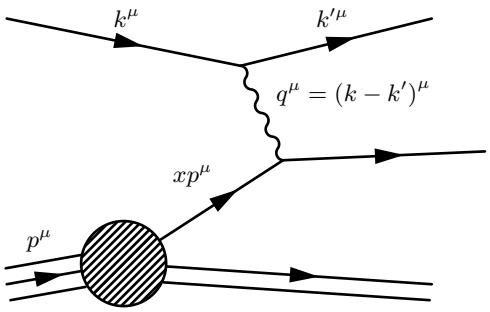

FIG. 1: Deep inelastic scattering Feynman diagram and kinematics.

The struck parton carries a fraction x, typically called the Bjorken momentum fraction, of the incoming hadron's four-momentum. The virtuality, or energy transferred in the hard scatter, is denoted $Q^2 = -q^2$ and the mass of the outgoing hadronic system is W^2. DIS is considered "deep" when $Q^2 \gg M_p^2$, implying a large momentum transfer, and "inelastic" for $W^2 \gg M_p^2$, where M_p is the mass of the proton.

To account for the unknown form of the propagator at any particular interaction, the DIS cross-sections are parametrised with a series of structure functions. These structure functions carry the information from the hadronic tensors and take different forms depending on whether the interaction is neutral current (NC) or charged current (CC), and additionally whether the initial states are polarised or not. The form of the unpolarised NC cross-section utilises the following generalised structure functions[25], $\tilde{F}$:

$$\sigma^{\pm}_{r,NC} = \frac{d^2\sigma^{e^\pm P}_{NC}}{dx\,dQ^2} \cdot \frac{Q^4 x}{2 \pm \alpha^2 Y_+} = \tilde{F}_2 \mp \frac{Y_-}{Y_+} x\tilde{F}_3 - \frac{y^2}{Y_+}\tilde{F}_L \,. \tag{24}$$

where the reduced cross-section, $\sigma^{\pm}_{r,NC}$, absorbs a helicity factor, the photon propagator and the electromagnetic coupling constant, α. The inelasticity parameter is related to the fractional energy transfer, y, through $Y_\pm = 1 \pm (1-y)^2$. The structure functions can be written in terms of pure photon exchange, pure Z boson exchange and from the γ/Z interference:

$$\begin{aligned}
\tilde{F}_2 &= F_2^\gamma - \kappa_Z v_e \cdot F_2^{\gamma Z} + \kappa_Z^2 (v_e^2 + a_e^2) \cdot F_2^Z \,, \\
\tilde{F}_L &= F_L^\gamma - \kappa_Z v_e \cdot F_L^{\gamma Z} + \kappa_Z^2 (v_e^2 + a_e^2) \cdot F_L^Z \,, \\
x\tilde{F}_3 &= \kappa_Z a_e \cdot xF_3^{\gamma Z} - \kappa_Z^2 \cdot 2 v_e a_e \cdot xF_3^Z \,,
\end{aligned} \tag{25}$$

where v_e and a_e are the vector and axial-vector weak couplings of the lepton to the Z boson respectively, and where κ_Z reveals the structure functions' dependence on the weak mixing angle:

$$\kappa_Z(Q) = \frac{Q^2}{Q^2 + m_Z^2} \cdot \frac{1}{4\sin^2\theta_W \cos^2\theta_W} \,. \tag{26}$$

A prediction that arises from the quark-proton model is the scaling of the structure functions, $F_i(x, Q^2) \to F_i(x)$, for fixed x and in the Bjorken limit $Q^2 \to \infty$ and $v/Q^2 =$ fixed. In this limit it is assumed that the transverse momentum of the partons is small, however this is contradicted by QCD in which hard gluon radiation from the quarks scales logarithmically, which can be particularly large at small x. Gluon radiation results in the evolution of the structure functions. Notably as Q^2 increases, gluon radiation increases, which may subsequently split into $q\bar{q}$ pairs. Conceptually these pairs are called the quark sea and it is through this process that the different quark flavour contributions can be probed. At high Q^2 and low x this leads to a softening of the valence quark momentum distributions and the enhancement of the gluon density and the $q\bar{q}$ sea[26].

The partonic contribution to the structure functions can be expressed in terms of the probability density, $f(x, Q^2)$, of encountering a parton between x and $x + dx$ in a frame in which the proton's momentum is large. These probability densities are commonly called the parton distribution functions (PDFs) and are related to the structure functions by:

$$\begin{aligned} F_2^{\gamma} &= x \sum_{i=q,\bar{q}} Q_i^2 [f_i(x, Q^2)] \,, \\ F_2^{\gamma Z} &= x \sum_{i=q,\bar{q}} 2 Q_i v_i [f_i(x, Q^2)] \,, \\ F_2^{Z} &= x \sum_{i=q,\bar{q}} (v_i^2 + a_i^2) [f_i(x, Q^2)] \,, \end{aligned} \tag{27}$$

which are dependent on singlet quark densities only. The F_3 functions are dependent on the difference between the quark and antiquark momentum distributions:

$$\begin{aligned} F_3^{\gamma Z} &= \sum_{q} 2 Q_q v_q [f_q(x, Q^2) - f_{\bar{q}}(x, Q^2)] \,, \\ F_3^{Z} &= \sum_{q} 2 a_q^2 v_q^2 [f_q(x, Q^2) - f_{\bar{q}}(x, Q^2)] \,. \end{aligned} \tag{28}$$

These probability densities are determined experimentally by extracting from collider data. PDF extraction is further described in Section 15. Figure 2 shows example individual parton contributions to the parton distribution functions.

Although the PDFs themselves are not directly calculable under perturbative QCD their evolution with scale, μ_F, is. They must be measured at an initial scale, μ_0, before QCD predictions can be compared to the data at other scales. PDF evolution is governed by the Dokshitzer-Gribov-Lipatov-Altarelli-Parisi (DGLAP) evolution equations[27,28], as shown in Equation 29 in which $P_{i \leftarrow j}$ are the Altarelli-Parisi splitting functions[29] that give the probability of parton j producing parton i. The splitting functions have been calculated at next-to-leading order (NLO) and at next-to-next-to-leading order (NNLO) in perturbative orders of $(\alpha_s \log \mu_F^2)^n$;

$$\frac{\partial f_i(x, \mu_F^2)}{\partial \log \mu_F^2} = \frac{\alpha_s}{2\pi} \sum_j \int_x^1 \frac{dz}{z} P_{i \leftarrow j}^{(1)}(z) f_i \left(\frac{x}{z}, \mu_F^2 \right) \,. \tag{29}$$

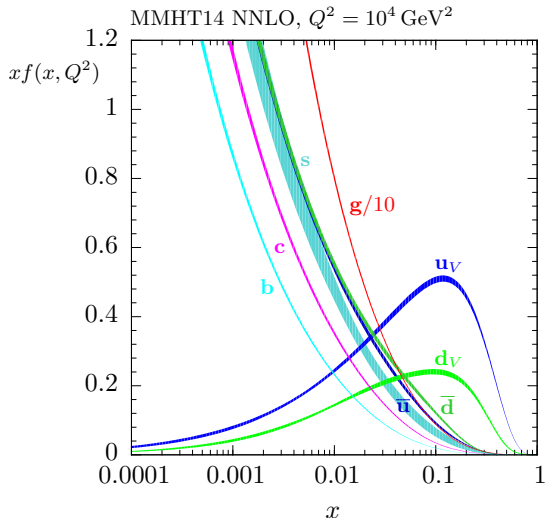

FIG. 2: Parton distribution functions produced by the MMHT group[26] at $Q^2 = 10000\,\mathrm{GeV}^2$.

E. Cross-sections in hadron collisions

In general a cross-section involving hadrons in the initial state is not directly calculable in perturbation theory for QCD[30]. Where the short-distance interactions of the hard process may be derived to various degrees of leading orders in EW and QCD, the long-range hadronic parts, e.g PDFs, are not. Factorisation theorems allow the prediction of such cross-sections by separating (factorising) the short-distance part from the long-distance part. Factorisation also allows for the universal application of the PDFs regardless of process they were dependently derived from.

For this analysis factorisation allows the measurement of the Drell–Yan process to use and impact the parton distribution functions. The factorisation theorem for the Drell–Yan process measured differentially in Q^2 takes the following form:

$$\frac{d\sigma}{dQ^2} = \sum_a \int_{x_A}^1 d\xi_A \int_{x_B}^1 d\xi_B \left[f_{a/A}(\xi_A) f_{b/B}(\xi_B) + (A \leftrightarrow B)_{a \neq b} \right] \hat{\sigma}(Q^2)\,, \tag{30}$$

where $f_{a/A}(\xi_A)$ is a PDF of encountering a parton a in a hadron A with fractional momentum ξ_A, and where $\hat{\sigma}(Q^2, y, \cos\theta^*)$ is the cross-section of the hard (short-distance) interaction.

F. The Drell–Yan process

The neutral current Drell–Yan process[31] is defined at leading order as the the s-channel production of a virtual gauge boson from two incoming hadrons with associated initial state quarks and a subsequent decay to two final state leptons. The mediating bosons are a virtual γ^*, a virtual Z and

an interference of the two. The initial state quarks are of the same flavour and as such one may originate from the valence and one from the quark-sea; or both from the quark-sea. Figure 3 shows the Feynman diagram representation of the Drell–Yan process. It is the dominant form of Z boson

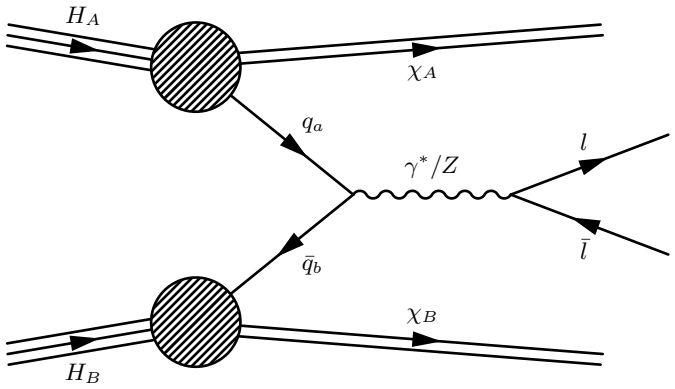

FIG. 3: Feynman diagram of the Drell–Yan process.

production at hadron-hadron colliders and both the neutral and charged current processes have been studied extensively at the LHC by the ATLAS[32–34], CMS[35–38] and LHCb[39–43] collaborations.

The Drell–Yan cross-section may be measured differentially to achieve sensitivity to the underlying physics distributions, namely the PDFs and EW constants. The triple-differential Drell–Yan cross-section at leading order (LO) may be written[31,44,45],

$$\begin{aligned}\frac{d^3\sigma}{dm\,dy\,d\cos\theta^*} &= \frac{\pi\alpha^2}{3sm}\sum_q \left[f_q(x_a,Q^2)f_{\bar{q}}(x_b,Q^2)+(q\leftrightarrow\bar{q})\right] \\ &\cdot \left(P_q^{\gamma}+P_q^{\gamma Z}\frac{2m^2(m^2-m_Z^2)}{(m^2-m_Z^2)^2+\Gamma_Z^2m_Z^2}+P_q^{Z}\frac{m^4}{(m^2-m_Z^2)^2+\Gamma_Z^2m_Z^2}\right), \end{aligned} \tag{31}$$

where m is the invariant mass of the hard scatter, m_Z is the Z-mass[46] and the following bosonic and interference terms have been isolated:

$$P_q^{\gamma} = Q_l^2Q_q^2(1+\cos^2\theta^*)\,, \tag{32}$$

$$P_q^{\gamma Z} = \frac{Q_lQ_q}{\sin^2\theta_W\cos^2\theta_W}\left[v_lv_q(1+\cos^2\theta^*)+2a_la_q\cos\theta^*\right], \tag{33}$$

$$P_q^{Z} = \frac{1}{\sin^4\theta_W\cos^4\theta_W}\left[(v_l^2+a_l^2)(v_q^2+a_q^2)+8v_la_lv_qa_q\cos\theta^*\right]. \tag{34}$$

The differential observables of the Drell–Yan process m, y and $\cos\theta^*$ are defined below.

The measurable parameters of the interaction are defined in terms of the incoming hadrons, the quarks involved in the hard scatter or the dilepton pair. The centre-of-mass energy of a hadron-hadron collision, $\sqrt{s}$, may be written in terms of the four momenta of the incoming hadrons, H_A

and H_B,

$$\sqrt{s} = \sqrt{(p_A + p_B)^2}\,. \tag{35}$$

The momentum transfer, Q^2, may be written in terms of the fractional momentum the quarks carry,

$$Q^2 = (x_a p_A + x_b p_B)^2\,, \tag{36}$$

which in the limit of small quark masses, may be written,

$$Q^2 = x_a x_b s = \hat{s}\,. \tag{37}$$

In high energy physics colliders, such as the LHC, colliding particles typically meet head-on along a predefined beam-axis, z, to maximise interaction energies. Angular quantities that are not defined perpendicular to this axis suffer from being susceptible to reference-frame boosts and as such are not invariant quantities. A 'pseudo-angular' quantity, rapidity, can be defined for the γ/Z boson that is invariant to Lorentz-boosts along the beam axis,

$$y = \frac{1}{2}\ln\left(\frac{E + p_z}{E - p_z}\right)\,. \tag{38}$$

For interactions with a centre-of-mass energy of $\sqrt{s} = 8\,\text{TeV}$ the maximum rapidity is given by $|y^{max}| = \ln(\sqrt{s}/m_Z) = 4.47$. The invariant mass of a pair of massless particles is defined as,

$$m_{ab} = \sqrt{2(E_a E_b - \mathbf{p}_a \cdot \mathbf{p}_b)}\,. \tag{39}$$

The centre-of-mass energy, rapidity and invariant mass are related to the momentum transfer through the simple relation,

$$x_{a,b} = \frac{m_{ab} e^{\pm y}}{\sqrt{s}}\,. \tag{40}$$

Figure 4 shows the different contributions to Drell–Yan cross-section arising from the photon, Z and interference terms as a function of lepton-pair invariant mass[47]. The photonic part, P_q^γ, provides the dominant contribution at low and very high masses. The Z part provides the large Z-mass resonance through the $(M^2 - m_Z^2)^{-1}$ massive propagator term in Equation 31. The interference term provides an underlying contribution at low masses and a significant contribution directly either side of the Z-peak. The sign of the interference term changes from negative to positive about m_Z.

At leading order when the γ/Z decays the lepton-pair will be produced 'back-to-back' in the dilepton rest frame. When considering higher order electroweak corrections, the angle between the leptons gain a functional dependence due to final state radiation (FSR). However, care must be taken as the kinematics of the event also depends on the initial state quarks. The partons originating from

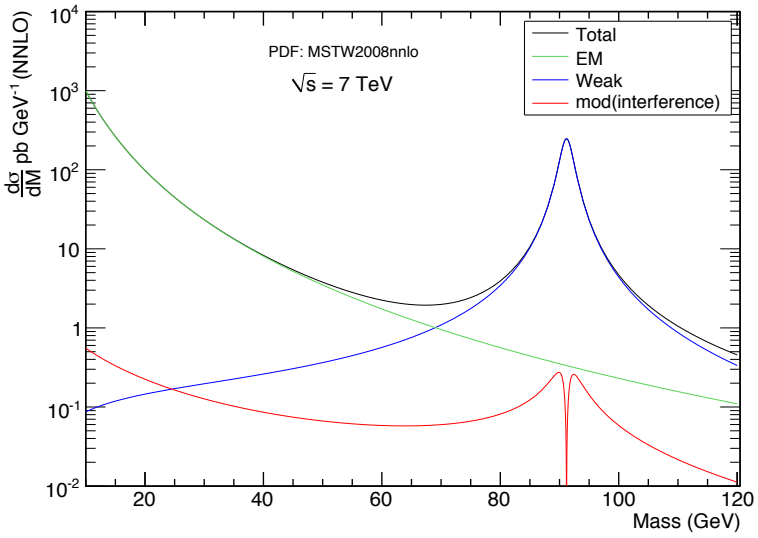

FIG. 4: The Drell–Yan cross-section as function of invariant mass plotted at $\sqrt{s} = 7\,\text{TeV}$ showing the different contributions of the γ^*, Z and interference terms[47].

the hadrons may collide with a non-zero value of momentum transverse to the proton's direction. Also, higher order QCD gluon initial state radiation (ISR) must be considered. This renders a simple dilepton decay angle insufficient. A quantity is therefore defined in the Collins-Soper frame[48] that defines the angle between the momentum vector of the incoming partons and outgoing lepton. Figure 5 shows the Collins-Soper angle, θ^*, in the rest frame of the dilepton system. The angle is defined with respect to the momentum vectors of the outgoing leptons and a longitudinal axis bisecting the momentum vectors of the incoming partons. The cosine of the Collins-Soper angle can be written in terms of laboratory frame quantities:

$$\cos\theta^* = \frac{p_z^{ll}}{|p_z^{ll}|} \frac{2(p_1^+ p_2^- - p_1^- p_2^+)}{m_{ll}\sqrt{m_{ll}^2 + (p_T^{ll})^2}}\,, \tag{41}$$

where

$$p_i^\pm = E_i \pm p_{z,i} \tag{42}$$

and $i = 1, 2$ correspond to the negatively charged lepton and positively charged anti-lepton respectively and p_z and p_T are the longitudinal and transverse components of the four-momentum respectively.

Through the $\cos\theta^*$ variable Drell–Yan events can be classified into two categories: forward and backward. Forward events are defined as having a negatively charged lepton produced in the same direction as an incoming valence quark, $\cos\theta^* > 0$. Backward events are defined with the positively

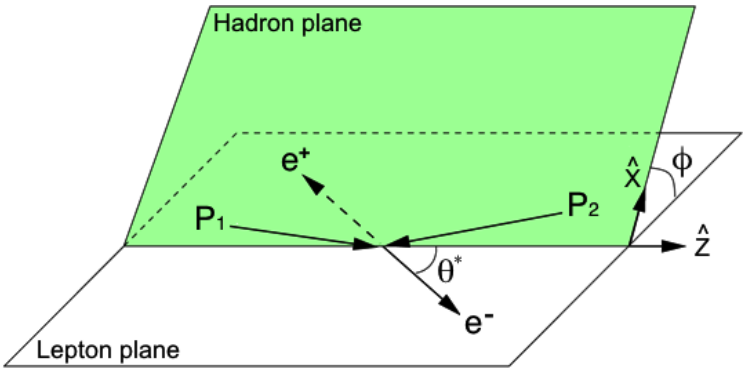

FIG. 5: The Collins-Soper frame for parton-parton interactions producing a lepton-antilepton pair. The longitudinal axis, $\hat{z}$, bisects the momentum vectors on the incoming partons $\mathbf{P_1}$ and $-\mathbf{P_2}$. The Collins-Soper angle is defined as the angle between $\hat{z}$ and the lepton momentum vector, $\mathbf{e}^-$.

charged anti-lepton produced in the same direction as the valence quark, $\cos\theta^* < 0$. The two definitions allow the forward-backward asymmetry to be defined; the difference between forward, σ_F, and backward, σ_B, cross-sections divided by the total:

$$A_{FB} = \frac{\sigma_F - \sigma_B}{\sigma_F + \sigma_B}\,. \tag{43}$$

Higher order corrections to the leading order Drell–Yan process can be seen in Figures 6 and 7. They may include virtual corrections of gluons and photons; real emission of photons, gluons and quarks; and quark scattering processes, where a gluon or photon originates from the parent hadron. Further higher order corrections include additional vertices and self-energy corrections and as such the number of possible Feynman diagrams increases exponentially. The computation of cross-sections at these higher orders requires considerable computing power.

Higher order corrections may be factored into the leading order definition of the weak mixing angle of Equation 22. This redefinition is commonly called the effective weak mixing angle,

$$\sin^2\theta_W^{\text{eff}} = \kappa_f \sin^2\theta_W\,, \tag{44}$$

where κ_f is a fermion dependent form factor absorbing the radiative higher order electroweak effects.

The kinematics of the Drell–Yan process can be simulated on the event level at next-to-leading (NLO) order and then corrected post-simulation to obtain a NNLO prediction. This can be achieved by applying K-factors to simulation. In the case just mentioned this would appears as,

$$K_{NNLO} = \frac{\sigma_{NNLO}(m^2, y)}{\sigma_{NLO}(m^2, y)}\,. \tag{45}$$

The measurement parameters of dilepton invariant mass, m_{ll}, rapidity, y_{ll}, and lepton decay angle, $\cos\theta^*$, have been chosen to achieve sensitivity to the physics underlying the interaction. The

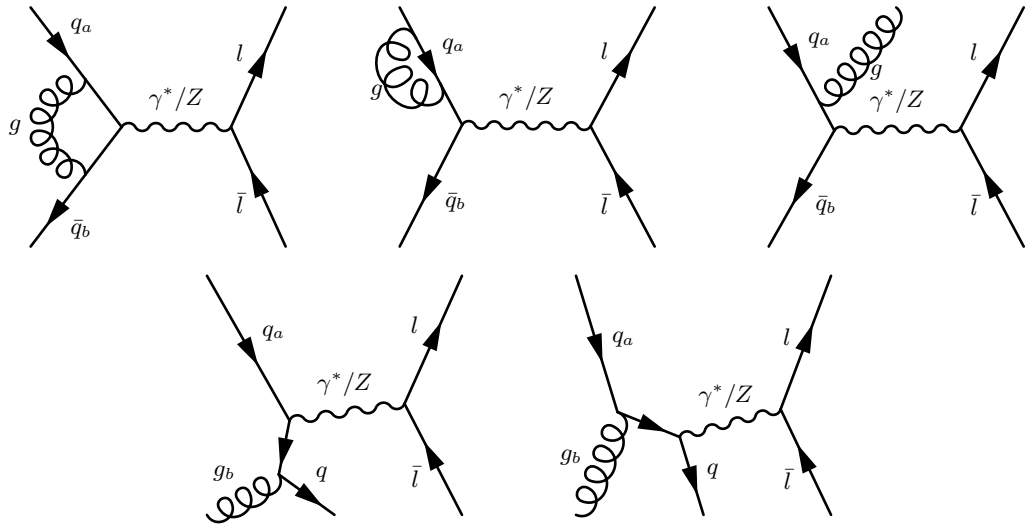

FIG. 6: Example higher order QCD corrections to the Drell–Yan process.

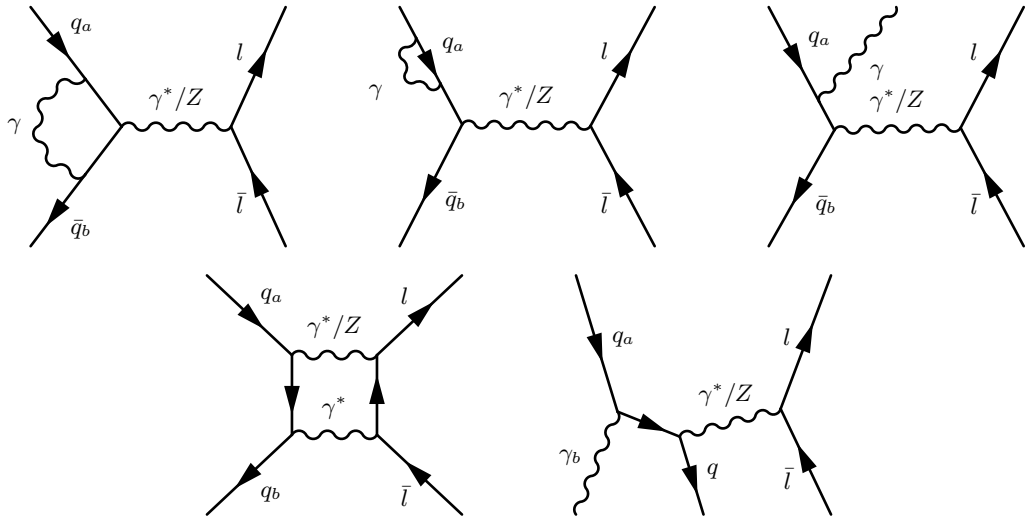

FIG. 7: Example higher order EW corrections to the Drell–Yan process.

dominant couplings of the partons to the mediating boson change with mass as was seen in Figure 4. At low mass the interaction is dominated by the electromagnetic couplings to the virtual photon and on the Z-peak they are dominated by the vector and axial-vector couplings; the different charge dependence allows the u and d PDF contributions to be resolved. The different quark contributions from the quark-sea can be probed through the evolution of the momentum transfer, x, by measuring boosted interactions of the boson rapidity; flavour sensitivity as a function of rapidity can be seen

in Figure 8. The lepton decay angle, $\cos\theta^*$, can be used to measure PDFs[49] through the frames' dependence on initial quark momentum; the $u\bar{u}$ and $d\bar{d}$ give different contributions as can be seen in Figure 9. Additionally, the effective weak mixing angle can be simultaneously extracted from the forward-backward asymmetry alongside the PDFs - an effort that has not been reported in the literature.

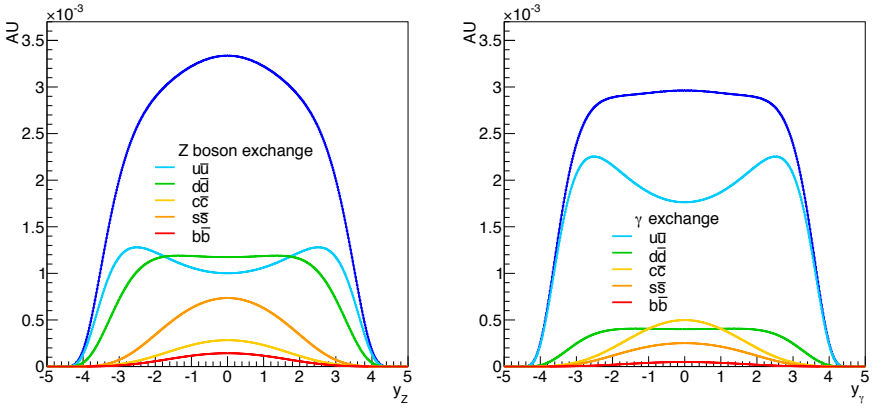

FIG. 8: The quark flavour decomposition for the neutral-current Drell–Yan process at $\sqrt{s} = 8\,\text{TeV}$ as a function of boson rapidity[45]. In these plots the y-axis has been scaled to arbitrary units (AU).

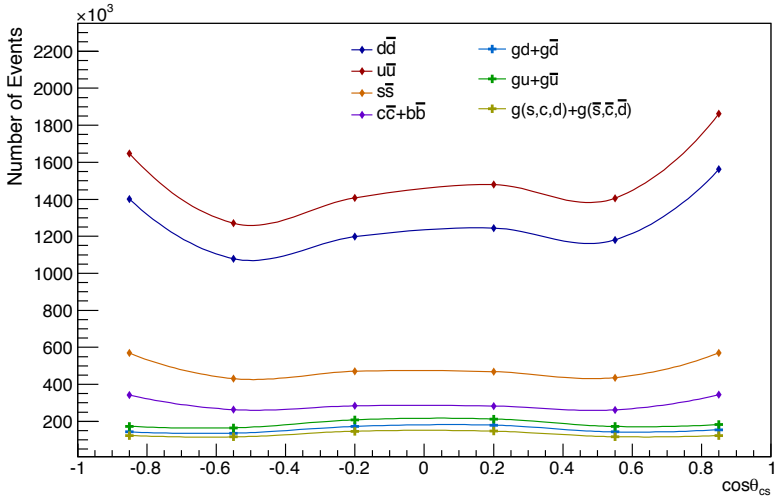

FIG. 9: The quark flavour decomposition at NLO for the neutral-current Drell–Yan process at $\sqrt{s} = 8\,\text{TeV}$ as a function of lepton decay angle using the Herwig MC generator.

2. THE ATLAS EXPERIMENT AT CERN

A. CERN & Accelerator Facilities

The European Organization for Nuclear Research (CERN) is a European research organisation that provides particle accelerators and additional infrastructure for high-energy physics research. The primary laboratory site sits astride the Franco-Swiss boarder in the Canton of Geneva, Switzerland, and, due to its geographical centrality, plays host to a wide area network hub for large-scale distributed computing. The laboratory and infrastructure is maintained by CERN and over 600 associated institutes and universities around the world[50].

A schematic of the accelerator facilities may be seen in Figure 10, and a list of the current accelerators is summarised in Table 2.

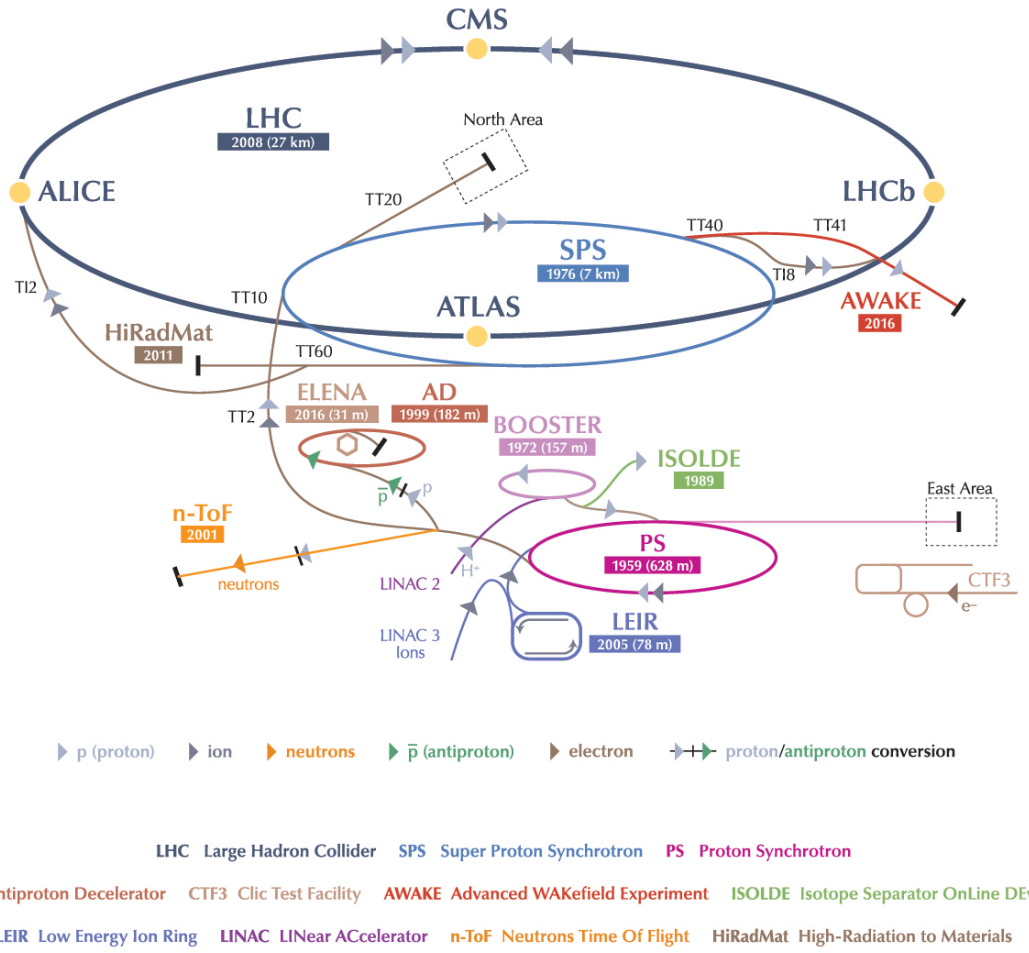

FIG. 10: The accelerator complex at the European Organization for Nuclear Research[51].

The physics programmes at CERN demand a variety of colliding payloads with each collider optimised for its consignment. In the past CERN has operated proton-antiproton (Sp$\bar{\text{p}}$S) and electron-positron (LEP) colliders. Currently the highest energy interactions at CERN are achieved by colliding either protons ("pp" collisions) or lead nuclei ("Pb" collisions) together in the LHC. Electron colliders give smaller backgrounds for physics analyses however suffer from synchrotron-radiation losses, limiting maximum obtainable centre-of-mass energy and luminosity. Conversely, proton colliders have relatively low synchrotron-radiation losses but large backgrounds from the interacting proton remnants. Heavy-ion collisions provide insights into quark-gluon plasmas.

The particle beams used at CERN are generated using simple processes. The protons used for acceleration are produced by using a strong electric field to strip away electrons from a hydrogen gas. Heavy (lead) ions are produced by vaporising a purified lead sample and ionising the vapour with an electric current. Charged states are refined by repeatedly passing the ions through carbon foils[52] fully stripping the ions down to Pb^{82+}.

The bare nucleons are accelerated rapidly by the use of radio-frequency cavities. Each part of the accelerator chain successively increases the energy of the proton/heavy-ion beam. Super-conducting magnets collimate the beams and guide them around the paths of the accelerators. The average spread of particle position and momenta within the beam affects the efficiency of beam operations and the luminosities observed at the interaction points (IPs). This profile of the position and momentum densities is characterised by the value of emittance within the beam pipe. An individual particle's emittance in relation to the emittance value of the beam may be calculated so that beam corrections can be applied to reduce the average spread of position and momentum; this is called stochastic cooling and is achieved with a feedback-loop system of beam-monitors and Klystron cavities, or fast "kicker" magnets.

Name	Energy	Consignment	Details
Linac2	50 MeV	protons	Linear accelerator for injection into the Proton Synchrotron Booster.
Linac3	4.2 MeV/u	heavy ions	Linear accelerator for injection into the Low Energy Ion Ring.
Proton Synchrotron Booster (PBS)	1.4 GeV	protons	Provides beams for the On-Line Isotope Mass Separator and increases proton energy for injection into the Proton Synchrotron.
On-Line Isotope Mass Separator (ISOLDE)	1.4 GeV	protons	Produces radioactive nuclei for numerous nuclear-physics, biophysics and astrophysics experiments.
Low Energy Ion Ring (LEIR)	72 MeV/u	heavy ions	Increases heavy ion energy for injection into the Proton Synchrotron.
Proton Synchrotron (PS)	28 GeV	protons & heavy ions	Increases energies for injection into the Super Proton Synchrotron and the Antiproton Decelerator.
Neutron Time-of-Flight (n-ToF)	MeV $\rightarrow$ GeV	neutrons	Produces a wide energy spectrum neutron beam for precision neutron experiments.
Super Proton Synchrotron (SPS)	450 GeV	protons & heavy ions	Provides beams for fixed target experiments such as COMPAS, NA61, NA62 and CNGS. It also injects into the Large Hadron Collider.
High-Radiation to Materials (HiRadMat)	440 GeV	protons & heavy ions	Provides high-intensity pulsed beams for experiments on materials or accelerator components.
Antiproton Decelerator (AD)	26.0 $\rightarrow$ 0.1 GeV	antiprotons	Provides stochastically cooled antiprotons for fixed antimatter experiments and further cooling.
Extra Low Energy Antiproton (ELENA)	5.3 $\rightarrow$ 0.1 MeV	antiprotons	Provides further cooling of beams from the Antiproton Decelerator and simultaneous delivery to antiproton experiments.
Large Hadron Collider (LHC)	6.5 TeV	protons & heavy ions	Provides interaction points of counter-circulating beams for high energy particle physics experiments.

TABLE 2: List of accelerator facilities at CERN.

B. The Large Hadron Collider

The Large Hadron Collider is a particle accelerator of 26.659 km circumference. It first operated at an initial energy of 3.5 TeV per beam (7 TeV total) in 2010, 4.0 TeV per beam (8 TeV total - of which the data in this thesis is based) in 2012 and 6.5 TeV per beam (13 TeV total) in 2015. It is considered to be the largest, most complex experimental facility ever built[52,53].

The Large Hadron Collider is structurally divided into eight arcs and eight insertion sections. Each arc contains 154 dipole magnets for steering the beam and each insertion comprises a long straight section for either physics (beam collisions), injection, beam dumping or beam cleaning.

The LHC has three vacuum systems, two provide insulation for the cryomagnets and the helium distribution line; the third to evacuate the beam pipe to reduce beam-gas losses. Each magnet in the LHC contributes to optimising the trajectory of the beams. There are 1232 dipole magnets in total and 392 quadrupole magnets to focus the beam for the collision points.

Quantity	Number
Circumference	26.569 km
Dipole operating temperature	1.9 K
Number of RF cavities	8 per beam
Peak magnetic dipole field	8.33 T
RMS transverse beam size	18.8 μm
RMS bunch length	9.4 cm
Full crossing angle, 2α	290 μrad
Bunch spacing	50 ns
No. bunches per proton beam	1380
Average pileup, μ	37
Peak luminosity	$7700 \times 10^{30}\,\mathrm{cm}^{-2}\mathrm{s}^{-1}$
Typical luminosity decay time	6 h

TABLE 3: Operational parameters for the Large Hadron Collider[52,54,55] operating at $\sqrt{s} = 8\,\mathrm{TeV}$.

The superconducting cavities allow for 2808 tightly formed (low emittance) proton bunches to be accelerated simultaneously. Tightly formed bunches yield higher luminosities at the physics interaction points and consistency in the number of interactions per bunch crossing. Operation parameters of the large hadron collider are given in Table 3.

The physics experiments are housed on the interaction points of the LHC. The two general purpose detectors, ATLAS and CMS, are optimised for high luminosity discovery physics and occupy diametrically opposed IP's: IP1 and IP5. The heavy-ion and B-physics experiments, ALICE and LHCb respectively, are installed at IPs 2 and 8 and operate at lower luminosities than ATLAS and

CMS. Two smaller experiments exist on the same interactions points as ATLAS and CMS: LHCf, which measures very forward neutral particles for cosmic-ray physics and is located either side of IP1; and TOTEM, which is dedicated to diffractive physics and elastic/total cross-sections and shares IP5 with CMS[55].

C. Luminosity Measurement

The pre-accelerator chain of the LHC requires a "bunched mode" operation of the beam. The two counter rotating beams are each composed of a string of short bunches, focused to a small transverse profile and brought into collision at one or more of the interaction points of the collider. The bunch luminosity is dependent on the time- and position-dependent beam density functions, $\rho_{1,2}(x, y, z, t)$, and total number of protons in the colliding bunches, $n_{1,2}$:

$$\mathcal{L}_b = f_r n_1 n_2 K \int \rho_1(x, y, z, t)\rho_2(x, y, z, t)dx\, dy\, dz\, dt\,, \tag{46}$$

where f_r is the revolution frequency and K is the kinematic factor,

$$K = \sqrt{(\vec{v}_1 - \vec{v}_2)^2 - \frac{(\vec{v}_1 \times \vec{v}_2)^2}{c^2}}\,, \tag{47}$$

with the beam velocity vectors, $\vec{v}_{1,2}$. The instantaneous luminosity is given by,

$$\mathcal{L} = \sum_b \mathcal{L}_b\,. \tag{48}$$

The bunch luminosity at an interaction point can be expressed as,

$$\mathcal{L}_b = \frac{R_{\text{ref}}}{\sigma_{\text{ref}}} \Rightarrow \frac{\mu_{\text{vis}} f_r}{\sigma_{\text{vis}}}\,, \tag{49}$$

where R_{ref} is the rate of a reference collision process and σ_{ref} is the corresponding cross-section. The process may be arbitrarily chosen, for example in the case of inelastic pp collisions μ is the average number of interactions per bunch crossing. Luminometers used at the different experiments at the LHC are given in Table 4. The methods, as described in Table 5, can by employed by luminometers to compute the visible μ for a luminosity determination.

Most luminometers provide bunch-by-bunch ("bbb") luminosity measurements. This is essential for the LHC because of the non-linearity between intrinsic ($\mu \leq 1$) and high pile-up ($\mu \gg 1$) operation and it assists with precise bunch-by-bunch corrections which may require μ-dependent corrections of the calorimeter response. However, some luminometers may operate in a bunch-averaged ("ba") mode, which can additionally provide independent methods to cross check against computed results[55].

Experiment/Source	Luminometer type	Integration	Acronym	Algorithm
ALICE	Scintillator array	bbb	V0	Event_AND
ATLAS	pCVD-diamond pads	bbb	BCM	Event_OR, Event_AND
	Gas/quartz Cherenkov tubes	bbb	LUCID	Event_OR, Event_AND, Hit counting
	Si strip+pixel tracker: No. vertices	bbb	"Vtx"	Vtx counting
	Si strip+pixel tracker: No. tracks	bbb	"Trks"	Trk counting
	Forward calorimeter: gap currents	ba	FCal	Particle flux
	TILE calorimeter: PMT currents	ba	TILE	Particle flux
CMS	Pixel tracker: No. clusters	bbb	"Pixel"	Hit counting
	Si strip+pixel tracker: No. vertices	bbb	"Vtx"	Vtx counting
	Forward Fe/quartz calorimeter	bbb	HF	Hit counting
LHCb	VELO vertex tracker: ≥ 2 tracks	bbb	"Tracks"	Event_OR
	VELO vertex tracker: ≥ 1 vertex	bbb	"Vertex"	Event_OR
LHC diagnostics	Ar-N_2 ionisation chamber	bbb	BRAN	Event_OR

TABLE 4: Luminometers employed at the LHC. Table modified from reference[55]. The algorithms are detailed in Table 5.

Van der Meer scans are used to deduce the absolute luminosity scale of the IPs in the LHC by comparing the peak of the van de Meer (vdM) scan to the visible interaction rate[56], μ_{vis}, through the relation:

$$\sigma_{\text{vis}} = \mu_{\text{vis}}^{\text{max}} \frac{2\pi \Sigma_x \Sigma_y}{n_1 n_2}\,, \tag{50}$$

where $\Sigma_{x,y}$ are the luminosity curve integrals, which are dependent on beam operation and x-y correlation and can be found in the literature[57,58].

For this thesis the ATLAS online luminosity calculation (lumiCalc) tool was used to compute the integrated luminosity for the 2012 data set using the best determination from the luminometer data and accounting for run-quality (GRL) and trigger scale-factors. The cumulative luminosity is shown in Figure 11. The delivered luminosity to the ATLAS detector is defined as the luminosity delivered from the start of stable beams until the LHC requests ATLAS to put the detector in a safe standby mode to allow a beam dump or beam studies. Inefficiency in the data acquisition and the 'warm start' inefficiency is reflected by the recorded luminosity. A warm start involves ramping the high-voltage of the tracking detectors and turning on the pixel system's preamplifiers.

The total integrated luminosity for this analysis is computed to be $20.2 \pm 0.4\,\text{fb}^{-1}$. This contributes as one of the largest sources of uncertainty in the analysis.

Method	Algorithm	Description
Event counting	Inclusive (Event_OR)	If a hit was made in either the forward or backward parts of the detector Poisson statistics can be used to determine μ based on zero event occurrence.
	Coincidence (Event_AND)	Similar to the Event_OR case, however requiring the "AND" condition introduces an extra efficiency factor, which alters the determination response.
Hit counting	Hit counting	Assuming a Poisson distribution for No. events per bunch crossing and a binomial distribution for the No. hits, μ can be determined from the probability to have a hit per bunch crossing.
Particle counting	Track algorithm	Track counting is conceptually similar to hit counting but utilises low-level triggering which allows for a full readout of the tracking detectors; this gives a larger S/B.
	Vertex algorithm	By requiring low-level triggers and counting the reconstructed vertices in each bunch crossing, the inclusive process can be counted; the determination is linear at low μ however vertex masking and fake vertices give non-linear effects at larger μ.
Particle flux	Particle flux	The rate of particles entering the detector may be measured by the ionisation current flowing through LAr calorimeter cells or current drawn by PMTs of a hadronic calorimeter. The behaviour is linear in μ and is independent from counting techniques.

TABLE 5: Luminosity determination methods at the LHC. Luminometers utilising these methods are listed in Table 4.

D. The ATLAS Detector

The ATLAS ("A toroidal LHC apparatus") detector is a general-purpose detector designed to measure the myriad decays involved in Standard Model and new physics processes. The final state products yield individual particle-detector interactions within the different components of the detector. These interactions leave hits throughout the detector and subsequently may be reconstructed as particle tracks. Different particles may be identified due to the nature of their interactions within the detector.

The short lifetime of the heavier fermions and bosons, in addition to the principles of confinement that quarks and gluons must obey, determines the set of particles that can be observed with

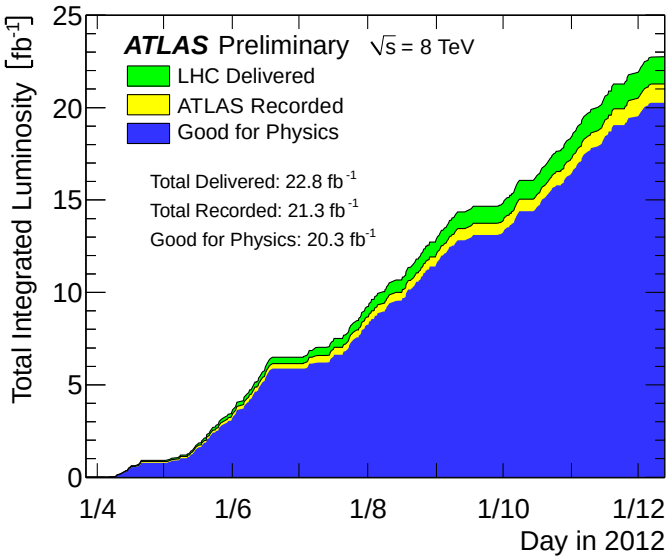

FIG. 11: Cumulative luminosity versus time delivered to (green), recorded by ATLAS (yellow), and certified to be good quality data (blue) during stable beams and for pp collisions at 8 TeV centre-of-mass energy in 2012. The luminosity shown represents the preliminary 8 TeV luminosity calibration. The All Good efficiency is determined from data quality assessed after reprocessing.[59].

conventional methods. The particles that can be directly detected are the following: photons, electrons, muons, protons, neutrons and long-lived mesons such as pions and kaons. Neutrinos are not detected because of their weak interaction with matter, for which large volumes of detector material are needed. Tau particles and b-mesons may traverse a short distance away from the beamline and can be indirectly detected from their displaced vertices of their decay products.

The ATLAS detector layout is shown in Figures 12 and 13. ATLAS uses a right-handed coordinate system with the origin located at the interaction point. The z-axis is defined along the beam-axis with positive $\hat{z}$ taken to be the clockwise direction around the LHC ring. The x-y plane, perpendicular to $\hat{z}$, takes the x-axis pointing towards the centre of the LHC ring and the y-axis pointing upwards. The azimuthal angle, ϕ, is measured clockwise around $\hat{z}$, with $\phi = 0$ corresponding to the x-axis (a diagram is provided in the appendix, Figure 92). The polar angle, θ, is measured from $\hat{z}$ but is usually expressed in terms of rapidity (Equation 38). In the approximation of negligible particle masses, the pseudo-rapidity can be defined:

$$\eta = -\ln\left(\tan\left(\frac{\theta}{2}\right)\right) . \tag{51}$$

The transverse momentum of a particle, p_T, is defined as the magnitude of its momentum vector projected onto the transverse ($\hat{x}$-$\hat{y}$) plane. This additionally allows for the definition of the transverse

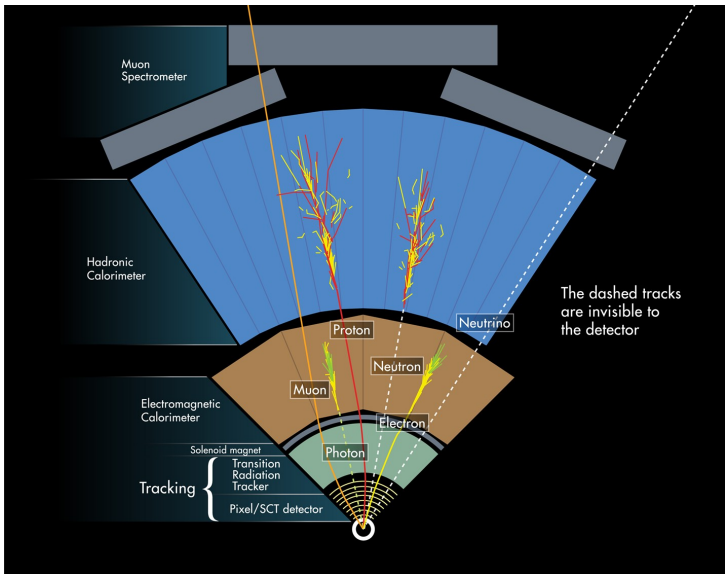

FIG. 12: Methods of particle detection in the ATLAS detector[60]. The different coloured regions in the diagram correspond to different sub-detector systems.

energy of a particle, i, and the total measured missing-energy of an event, respectively:

$$E_T^2 = m^2 + p_T^2\,, \tag{52}$$

$$\not{E}_T = -\sum_i E_T^i\,, \tag{53}$$

where the summation occurs over all reconstructed particles in the event. The azimuthal-polar separation unit ('separation distance'), ΔR, used in clustering algorithms and object overlap definitions is defined as:

$$\Delta R = \sqrt{(\Delta\eta)^2 + (\Delta\phi)^2}\,. \tag{54}$$

The Inner Detector

The inner detector (ID) is the closest detector to the interaction point. It covers the pseudo-rapidity range of $|\eta| \leq 2.5$ and is designed to track charged-particle trajectories and locate interaction vertices. The curvature of charged tracks due to the externally applied 2 T magnetic field allows for a transverse momentum resolution of $\sigma_{p_T}/p_T = 0.05\%\, p_T\,\text{GeV}$[62]. Three components comprise the ID, which, in order of proximity to the IP, are: the silicon pixel detector, semiconductor tracker (SCT) and the transition radiation tracker (TRT)[62]. Figure 14 shows the layout of the ID subsystems.

The silicon pixel detector is made up of three separate cylindrical layers in the barrel and three disks in either end-cap perpendicular to the beam-axis. When a charged particle passes through a

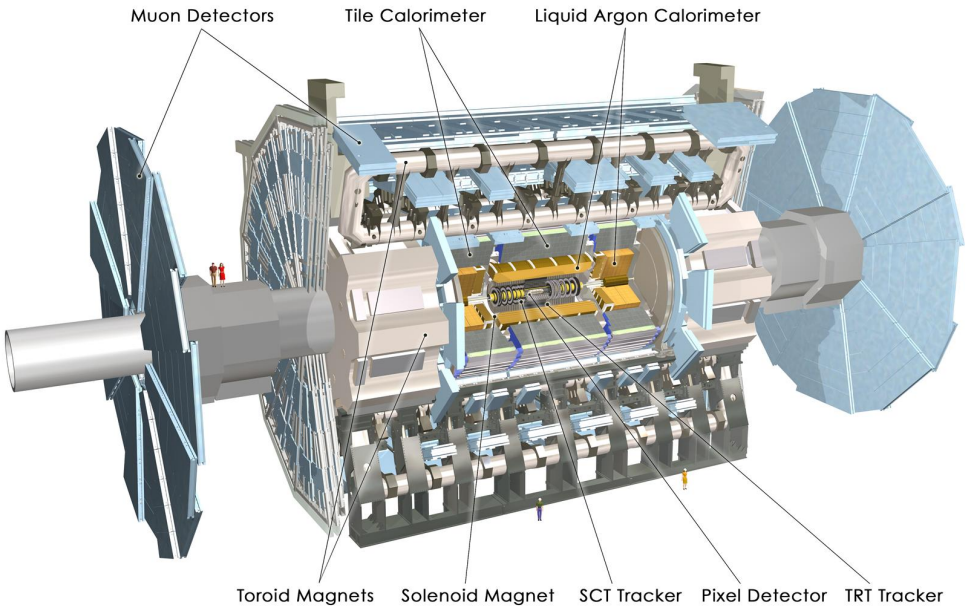

FIG. 13: Computer generated image of the ATLAS detector layout identifying the the sub-detector components[61].

silicon layer a swath of electrons are liberated. The electron/hole charge is collected by an applied bias voltage over the hit pixel. Readout chips on the front-end of the units collect and buffer the charge pulses for the trigger system. Particles typically pass though three layers of silicon (typical pixel dimensions: $50 \times 400\,\mu^2$m) allowing a r-ϕ resolution of $10\,\mu$m and $115\,\mu$m in z[62]. Due to the proximity to the beam-line and to reduce noise, radiation-hard materials are used and the system is kept at an operating temperature between $-5\,^\circ$C and $-10\,^\circ$C.

The semiconductor tracker surrounds the silicon pixel detector with four layers of silicon strips in the barrel region, covering the $|\eta| < 1.4$ region, and nine SCT disks in either end-cap extending the coverage to $1.4 < |\eta| < 2.5$. The SCT is similar to the pixel detector in using charged-track-ionisation for detection. Due to the design specification for hermetic coverage the modules are non-trivially arranged and in places overlap. The silicon strips are tilted at a tangential angle of 40 mrad to the SCT circumference to allow overlaps and separated at a distance of $80\,\mu$m. Determining exact spacial coordinates of each strip is a difficult task and is further discussed in the muon ID alignment section (Section 3 D) due to its impact through applied sagitta corrections, discussed in Section 8. The resolutions in the barrel and end-caps are $17\,\mu$m and $580\,\mu$m in r-ϕ and z, respectively[62].

The transition radiation tracker surrounds the pixel detector and the SCT with straw gas-tube trackers interleaved with transition radiation material. Each gas-tube is 4 mm in diameter and filled

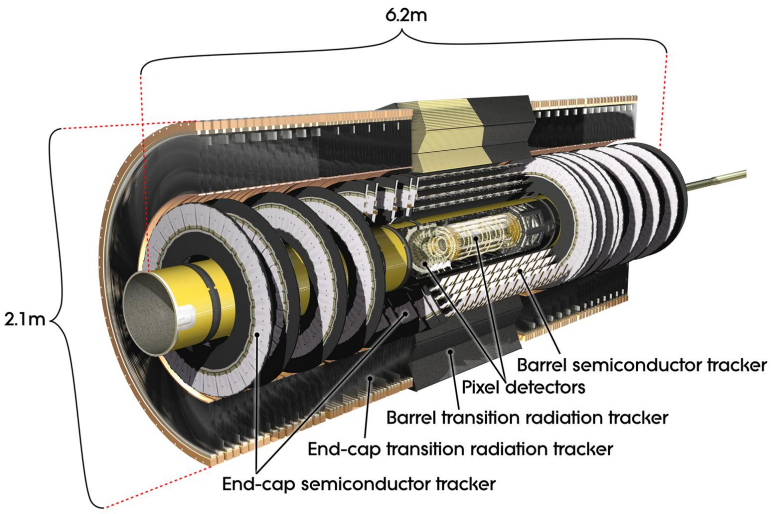

FIG. 14: ATLAS schematic of the inner detector subsystems[63].

with a gas mixture of 70% Xe, 27% CO_2 and 3% O_2; Xe is the ionisation medium, O_2 increases the charge drift velocity and CO_2 stabilises the mixture. A wire passing through the centre of the tube acts as an anode to collect drifting charge. The transition material between tubes is formed from polypropylene, a material with widely varying refractive indices. When charged particles pass through the transition material the change in refractive index causes both transition radiation and subsequent pair-production from the transition radiation. These lower energy charged particles ionises the gas mixture in the tube. The amount of transition radiation depends on mass, therefore providing a method of particle identification. The gas-tubes are arranged perpendicular to the beam-axis in the barrel region and radially outward in the end-caps.

The Calorimetric Systems

Calorimetry within the ATLAS detector is provided by the electromagnetic (ECAL) and hadronic (HCAL) calorimeter sub-detectors. Calorimeter modules are located in the barrel, the end-caps, the extended-barrel and the forward calorimeter (FCal). The arrangement of the calometeric system is shown in Figure 15 and covers the pseudo-rapidity range, $|\eta| < 4.9$.

Sampling calorimeters are used, in which the ionisation energy is measured between alternating layers of passive absorption material and active detection material. As a high energy charged particle passes through the absorption material it causes a cascade of electrons and photons, known as an EM shower. Similarly, a strongly interacting particle will induce hadronic showers passing through

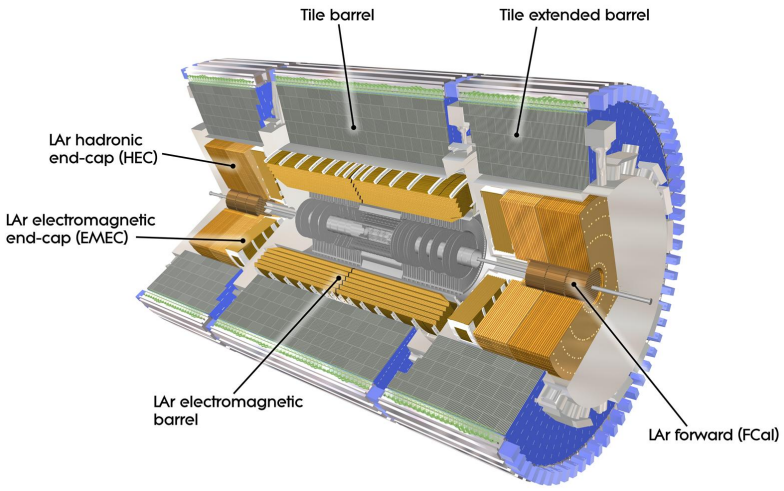

FIG. 15: ATLAS schematic of the electromagnetic and hadronic colorimetry subsystems surrounding the greyed-out inner detector[64].

a highly dense absorption material. The depth of electromagnetic and hadronic calorimeters is such that electromagnetic and hadronic showers are contained within the calorimetry and limit punch-through to the muon spectrometers. Electromagnetic shower depth is measured in terms of bremsstrahlung radiation lengths, X_0: the mean distance an electron traverses before its energy is reduced by $1/e$. Hadronic shower depth is measured in terms of mean-free-path or interaction lengths, λ: the mean distance a relativistic particle traverses without undergoing a quasi-elastic (diffractive) interaction. The ATLAS calorimeter depths are $> 22X_0$ and $> 11\lambda$ respectively.

The electromagnetic calorimeter consists of a barrel part (EMB) and two end-caps (EMEC). Lead absorber plates and the stainless steel structure form the passive material for the production of bremsstrahlung and photon production of e^+e^- pairs. The resulting electromagnetic cascade ionises the active layer, liquid argon (LAr) gas, where the charge is collected by copper readout electrodes. Due to the presence of the ID and the magnetic solenoids, electrons and photons lose energy before entering the ECAL. Therefore an active detection (pre-sampler) layer is deployed in front of the first passive layer to provide measurements and corrections for showers originating in the ID. The ECAL has an energy resolution of $\frac{\sigma_E}{E} = \frac{10\%}{\sqrt{E}} \oplus 0.7\%$; dependent on stochastic effects of the shower development and non-uniformity of the overall response[65].

The hadronic calorimeter occupies the region $|\eta| < 3.2$, and is formed from the hadronic tile calorimeter (TileCal) in the barrel and end-cap (HEC) units. The tile calorimeter uses plastic tile scintillator plates for fast luminescence from interactions with hadronic showers. The hadronic

showers originate from hadron-nucleon interactions within the preceding absorption material; this may be the steel absorbers in the HCAL or the earlier lead absorbers in the ECAL. The scintillated photons are collected by wavelength shifting fibres to photomultipliers outside the calorimeter. The hadronic end-cap uses LAr sampling colorimetry with copper absorbers to measure particle showers in the end-cap; LAr is utilised for its radiation hardness particularly encountered in the forward regions. The HECs each contain two wheel units (Front, Back) formed around the forward colorimetry. The coverage for hadronic showers provided by the TileCal and HEC is $|\eta| < 1.7$ and $1.5 < |\eta| < 3.2$ respectively, with an energy resolution across the HCAL of $\frac{\sigma_E}{E} = \frac{50\%}{\sqrt{E}} \oplus 3\%$[62].

The forward calorimeter (FCAL) covers the forward detection region, $3.1 < |\eta| < 4.9$, and is integrated into the end-cap cryostats to achieve this. Additionally, due to the high radiation levels of the forward region and neutron back-scattering off the ID, the FCAL is recessed by 1.2 m from the EMB. The compact design of the FCAL covers 10λ for which a schematic is shown in Figure 16. The FCAL consists of three layers. The primary layer closest to the interaction point (FCAL1) is an electromagnetic colorimetry layer and two successive layers (FCAL2, FCAL3) of hadronic colorimetry. FCAL1 uses regularly spaced copper plates perpendicular to the beam-pipe with a hexagonal matrix of electrodes: a copper rod surrounded by a copper tube with active LAr gas suspended between the two, providing $28X_0$. FCAL2 and FCAL3 are similar, however deploy tungsten rods instead of copper and fill the matrix gaps with tungsten-alloy slugs to limit transverse hadronic spread.

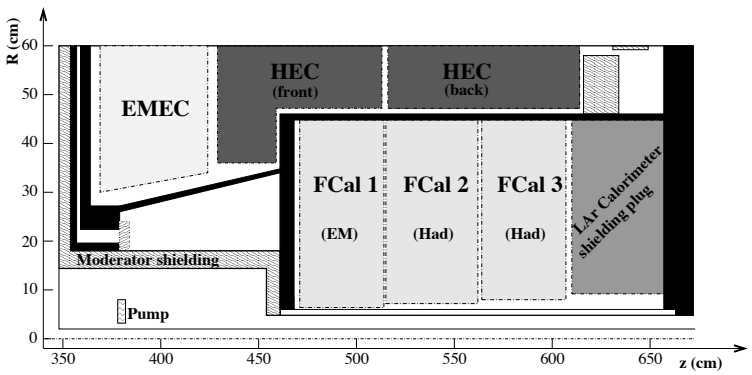

FIG. 16: ATLAS schematic of the forward calorimeter with labelled electromagnetic and hadronic subsystems[62].

The Magnet System

Trajectories of charged particles are bent by the Lorentz force when passing through the magnetic fields generated by the ATLAS magnet system. A hybrid system of four large superconducting magnets provide a stable complex magnetic field with a minimum of 50 mT over a volume of approximately 12,000 m^3. A solenoid that is aligned with the beam axis generates a 2 T axial magnetic field through the inner detector, providing an (r-ϕ) bending plane. It is made from NbTi, which achieves strong fields per degree of thickness, while the flux is returned by the steel of the HCAL and the girder structure. The barrel toroid of eight symmetrically positioned NbTiCu coils produces a 0.5 T magnetic field for the cylindrical volume enclosing the ECAL and HCAL. Charged particles moving through the toroid magnetic field are bent in the (r-η) plane. The two end-cap toroids are composed of eight flat NbTiCu square coil units in a structure reinforced by eight keystone wedges to withstand internal Lorentz forces generated when producing the 1 T field to cover the end-caps.

Internal measurement of the magnetic field within the ID is provided by permanent nuclear magnetic resonance (NMR) probes, each with an accuracy of 0.01 in $|\mathbf{B}|$. Internal measurements of the magnetic field within the muon system is provided by 3D-Hall cards mounted on the muon chambers, each with an accuracy of 0.2 T in $|\mathbf{B}|$. The ATLAS magnetic field was additionally mapped in the commissioning process using a Hall card array[66]. The magnet system can be seen in Figures 13 and 17.

The Muon System

Muons traverse through the ID, ECAL and HCAL leaving ionisation tracks but losing little of their energy in the process. Therefore muon kinematics must be determined from precise hit measurements of the curvature of the muon tracks. The muon spectrometers (MS), encapsulating the ATLAS detector volume, provide high precision tracking for high transverse muon-momentum measurements $p_T > 200$ GeV where muon tracks become increasingly linear. The layout of the muon system is shown in Figure 17 highlighting the four muon detector technologies used: monitored drift tube chambers, cathode strip chambers, resistive plate trigger-chambers and thin gap trigger-chambers.

Monitored drift tube (MDT) chambers cover the pseudo-rapidity regions in the barrel and the end-caps of $|\eta| < 1.0$ and $1.0 < |\eta| < 2.7$ respectively. The chambers are composed of at least six layers of aluminium drift tubes, each filled with a mixture of 93% Ar, 7% CO_2 and trace water for high voltage stability between the drift tube wall and a centrally suspended gold-plated tungsten anode wire. Muons traversing the drift tube induce electron-ion pairs that cascade creating further pairs in the high voltage field with an avalanche effect. The resolution of a single chamber is

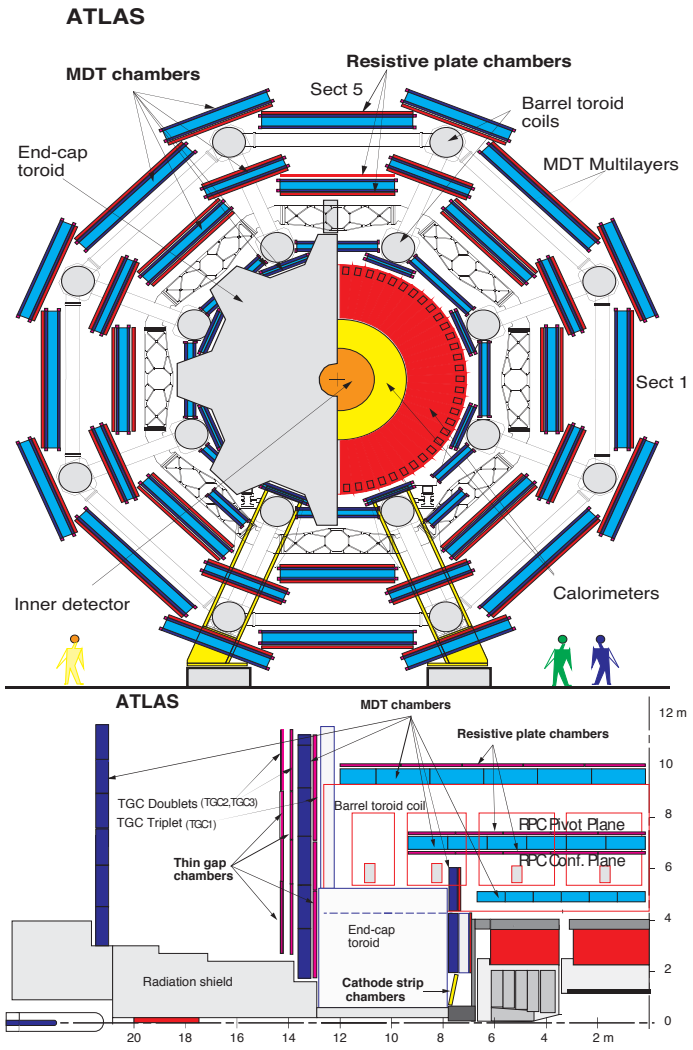

FIG. 17: ATLAS schematic showing the muon detection system and the toroid barrel and end-cap magnets in the x-y plane and along the length of the beam axis[67].

35 μm. Due to the construction requirements of ATLAS and the need for cables and services to the calorimeters and ID, full MDT coverage is not observed at $\eta \simeq 0$.

Cathode strip chambers (CSC) operate in the forward end-cap region $2.0 < |\eta| < 2.7$ where the particle flux is greater. The CSCs are multiwire proportional chambers with a 93% Ar, 7% CO_2 gas mix where the anode wires and cathode strips are aligned radially from the IP. Cascading electron-ion hits across a chamber translate to a resolution of 45 μm.

Resistive plate chambers (RPC) are required to provide readout information for the trigger system

because of the large 700 ns charge drift time in the MDTs and CSCs. The resistive plate chamber units are made from two parallel plates of Bakelite, a resistive material, containing an active gas, 97% $C_2H_2F_4$ and 3% C_4H_{10}. Metallic strips are placed across the back of each plate with each plate aligned orthogonal to the other, allowing the drifted charge to provide a 2D coordinate. The time resolution is 1.5 ns with typical signal width of 5 ns; additionally, this allows accurate bunch crossing identification.

Thin gap chambers (TGC) are higher granularity end-cap chambers, which counteracts a larger 4 ns time resolution with higher rate capability. One set is of TGCs are placed before end-cap toroid aiding the CSCs and three behind complementing the MDTs. The TGCs are multi-wire proportional chambers using graphite cathodes and a highly quenching gas mixture of CO_2 and $n - C_5H_2$ allowing operation in a quasi-saturated mode.

The alignment of the ATLAS MS was found to heavily impact the muon transverse momentum determinations in this thesis. The MS alignment is further discussed in Section 3 C and a detailed study given in Section 8.

E. Trigger and Data Aquisition

The design bunch separation of 25 ns gives a maximum bunch crossing rate of 40 MHz at the IPs. ATLAS can only record events at an average rate of 200 Hz to data storage for analysis, therefore an event triggering system is used. The triggering system filters events by using a three-level process; the level 1 trigger is hardware based, the level 2 trigger and the event filter are software based.

The level 1 (L1) trigger uses reduced-granularity energy deposit information from the calorimeters and the fast muon triggers to make a fast trigger decision. The trigger looks for tau seeded energy deposits in the calorimeters, jet energy deposits in the HCAL, EM energy clusters in the ECAL and proximate muon trigger-chamber hits. This reduces the input rate to a maximum of 75 kHz for the next trigger level in the sequence, with a decision latency of 2 μm[62]. The L1 trigger also forms regions of interest (RoI) from energy or track clusters in the sub-detectors; the higher trigger levels uses these regions in their trigger decisions.

The level 2 (L2) trigger has more time to make a trigger decision so it has access to the full granularity of all sub detectors within the RoI. The rate out of the L2 trigger is 3 kHz with a processing latency of 10 ms.

The event filter (EF) collects the buffered information from the L2 system for a final store/reject decision. The EF gets a relatively long decision time on the order of one second, allowing offline reconstruction algorithms and basic calibrations to be applied in the decision. The rate out of the EF is 200 Hz, which is written to data tape-storage at the CERN Tier-0 computing centre.

Throughout the triggering process the different levels have access to a "menu" of predetermined kinematic requirements. This allows for different signatures of events to be triggered upon. In some cases a particular set of kinematic requirements from an item on the trigger menu will result in the design rates of the subsequent level to be exceeded. In this case the trigger will be pre-scaled: a programmed fraction of such events will be automatically rejected to reduce the trigger item rate.

In this analysis, accepted events originating from three separate muon triggers are analysed. The triggers are:

- EF_mu18_tight_EFFS_mu18
- EF_mu24i_tight
- EF_mu36_tight

The notation format is the following: the "EF_" denotes that the last trigger level involved in the trigger decision was the event filter; the object is then listed ("mu"= muon); then the kinematic cut value, for muons this is in values of transverse momentum (GeV); isolation "i" is listed if an isolation requirement was imposed on the triggered object; the object quality requirement of either "_tight"/"_medium"/"_loose" is listed also. In some cases the event filter applies a scan of the detector for other potential trigger objects for the trigger decision, denoted by "EFFS_".

The algorithms employed by the triggering system can never be perfect in their operation and so induces trigger efficiencies in analyses and associated uncertainties. This is further discussed in Section 7.

3. MUON RECONSTRUCTION IN ATLAS

A. Muon Reconstruction Algorithms

Energy deposits and hit information recorded by the ATLAS detector are reconstructed into physics objects (electrons, muons, photons, etc.) in offline processing after the data has been recorded. Although reconstruction also occurs in the event filter of HLT, more accurate calibration and alignment information is used. The reconstruction algorithms have full access to the full granularity sub-detector read-out information across the ATLAS detector. There are many different approaches that can be taken when writing a reconstruction algorithm, which has lead to a range of different algorithms being applied to the data. The "author" of any given reconstructed physics object is the algorithm that produced it and, during offline reconstruction, different algorithms may author slightly different objects from the same hit information. Each author will have its own associated reconstruction efficiency and uncertainty; Section 7 discusses this further.

Muons in ATLAS are reconstructed using four different sources of hit information to calculate the trajectory, producing different "types" of muons: stand-alone, combined, segment-tagged and calorimeter-tagged[68].

- Stand-alone (SA) muons take their trajectories exclusively from the MS. Impact parameters are determined by extrapolating the track through the calorimeters, taking into account energy losses, back to the closest point of approach to the beamline. This method allows for extended coverage of the MS up to $2.5 < |\eta| < 2.7$.

- Combined (CB) muons track reconstruction is performed independently in the ID and MS. A successful combination forms a combined track spanning the ID and MS which can be used for determining kinematics. CB muons are the most commonly used type of muons due to their high purity.

- Segment-tagged (ST) muons are formed when a track in the ID can be extrapolated to at least one track segment in an MDT or CSC chamber. This can extend coverage to low p_T muons or in regions of limited MS coverage.

- Calorimeter-tagged (CaloTag) muons matches an extrapolation of an ID track to energy deposits in the calorimeters compatible with a minimally-ionising particle. CaloTag muons provide additional acceptance for uninstrumented MS regions such as $|\eta| \simeq 0.0$, however suffer from low purity.

Muon reconstruction algorithms are organised into different "chains". Each chain contains its own sub-structure of reconstruction algorithms that manage the reconstruction of the SA, CB, ST

or CaloTag muon-object definitions.

The first chain is the statistical combination (STACO) chain which statistically combines tracks using the ID and MS track vector's covariance matrices, and extrapolates iteratively adding track segments in the direction of the extrapolation. The second chain is the muon identification (MuID) chain which performs global refits of ID and MS segments to combine tracks and extrapolates using weighted track covariance matrices. The MuID chain also implements a separate strategy of extrapolating ID hits outward towards MDT and CSC segments via a Hough transform, which are named "MuGirl" muons. The third chain (third-chain) is the unified muon chain that ranks the quality of the authored muons from all other chains and records the highest available quality muon candidates. This analysis uses third-chain muons with additional muon quality requirements as recommended by the ATLAS muon combined performance (MCP) group. Of the third-chain muons used in this analysis, 99.21% are authored by MuID, 0.68% by MuGirl and 0.11% by STACO.

B. The Momentum Measurement

As a muon traverses the ATLAS detector its path will be bent according to the magnetic field vectors it passes through. The degree of curvature depends on the momentum vector of the muon through the Lorentz force, $\vec{F} = Q\vec{v} \times \vec{B}$. Therefore, the curvature of tracks within the ATLAS detector can be used to experimentally determine a muon's momentum.

In a simplified case of a homogeneous magnetic field, B, traversed by a charged particle with versine angle, 2θ, the momentum may be calculated by a measurement of the sagitta of the particle's arc through the magnetic field. The sagitta of the arc is related to the radius by, $s = r(1 - \cos\theta)$ as shown in Figure 18.

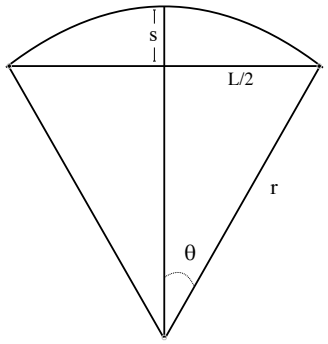

FIG. 18: Diagram showing an arc of length L, radius of curvature r and sagitta s.

By equating the acceleration of the Lorentz force with the centripetal acceleration, the helical

radius, r, will be given by,

$$r = \frac{p_T \sin\theta}{QB} \,. \tag{55}$$

High momentum particles will have large arcs relative to the detector with a correspondingly small sagitta. The particle's momentum can then be determined assuming large value r and small value θ, through geometric relations,

$$p_T = \frac{L^2 QB}{8s} \,. \tag{56}$$

The inverse dependence on the sagitta measurement results in the fractional uncertainty of the momentum being proportional to the momentum itself. The arc's curvature is determined by reconstructing hits and track segments, as described earlier. The muon reconstruction algorithms take into account the different magnetic field profiles, and thus the different bending planes acting in the ID and MS volumes.

C. ATLAS Muon Spectrometer Alignment

The barrel of the muon spectrometer, MDT chambers and CSC chambers are aligned using optical alignment sensors. However, because of the "projective configuration"[62] used in the alignment some specific geometrical distortions cannot be captured. Track-based alignment algorithms are therefore used in combination with the optical system to achieve positioning accuracy. Additionally, the cryostat vessels of the toroid magnets interrupt the light-path between the inner and middle layers of the end-cap muon system requiring a system of optical-lines, high-precision rulers (alignment bars) and proximity sensors.

If a systematic mis-alignment occurs in the muon chamber positions then a non-symmetric disparity in track positions can be created between muons and anti-muons due to their different curvature in the magnetic field, as can be seen in Figure 19. As this will cause a difference in the sagitta measurement the transverse momentum determination will also be affected. The transverse momentum may be mis-measured at a higher value for one charge, and lower for an opposite charge case. The magnitude of this effect depends on where in the detector the hits are being reconstructed and the momentum (scale) of the muon.

Conventionally, physics analyses of the ATLAS reconstructed data integrate over charge-dependent muon momentum scale effects across the detector, however the triple-differential measurement presented in this thesis is susceptible to these effects because of the rapidity and dilepton decay angle differentials; y is sensitive to (η-ϕ) or detector region, and $\cos\theta^*$ is sensitive to charge dependent momentum scale. The regional impact of the MS alignment on the charge dependent momentum

scale is seen in Section 8, where it is concluded that only ID hit information should be used in the determination of the muon transverse momentum for this analysis.

D. ATLAS Inner Detector Alignment

Each track recorded by ATLAS induces an average of 36 hits across the inner detector. For the location of these hits to be accurately determined and reconstructed into ID tracks, the actual positions in space of the silicon modules (pixel and SCT) and the straws (TRT) should be known. This gives six degrees of freedom per module if treated as a rigid body. In total, considering components in the ID, there are almost 36,000 degrees of freedom to be constrained.

ID component positions are known from surveys before data-taking and precision installation; the SCT positioning also uses laser interferometric monitoring. Additionally, low-rate tracks from well-known sources provide alignment constraints by minimisation of track residuals. Such sources include muons from cosmic-ray interactions in the upper atmosphere, beam-halo tracks, IP + vertex events, J/Ψ track pairs and overlap-region tracks. Figure 20 shows where overlap-regions exist in pseudo-rapidity and relative positions of the sub-detector modules.

Certain degrees of freedom are not constrained well by the data and may even hide global distortions of the geometry, such as cylindrical torsion; these are termed "weak modes". Repeated cycling between $-20\,\mathrm{C}^\circ$ and $+20\,\mathrm{C}^\circ$ of the inner components can also cause distortions over short and long

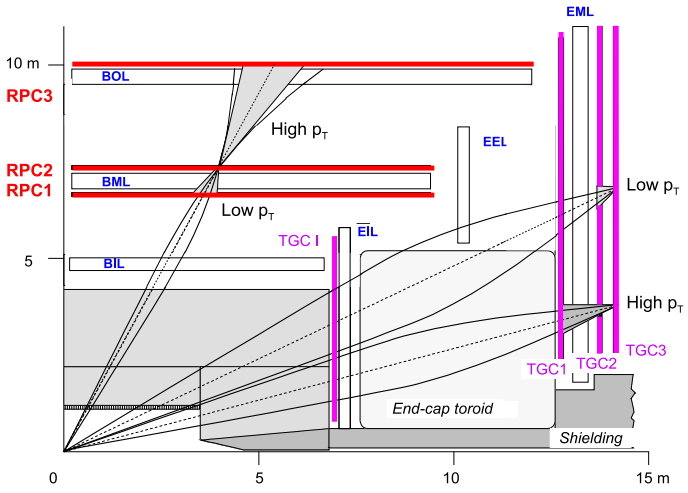

FIG. 19: Schematic of the ATLAS muon system showing different curvature trajectories of muons traversing the subsystems[62]. The dashed lines show straight-line trajectories through the detector subsystems and the curved lines either side show the paths of charged muons.

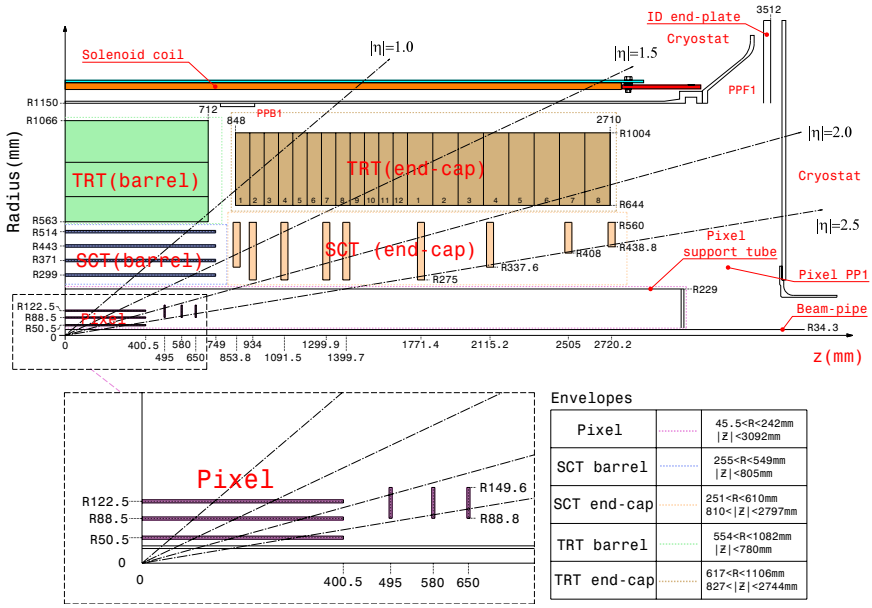

FIG. 20: Schematic of the ATLAS inner detector showing pseudo-rapidity isobars through the different ID components[62].

term operation.

Since the final data reprocessing of the 2012 ATLAS $\sqrt{s} = 8\,\text{TeV}$ data, additional regional ID distortions were discovered which affected the charge-dependent momentum scale. To account for this, additional sagitta corrections are applied in this analysis. The effects of the sagitta corrections are discussed in Section 8.

4. MONTE-CARLO SIMULATION

A. Monte Carlo in High Energy Physics

For the physics analysis presented in this thesis the response of the detector must be known so that physics parameters extracted from the data set are generalised and not unique to the detector setup. Furthermore, it is not possible to apply kinematic selection criteria that provide a 100% pure (background free) signal sample in data. It is therefore important to produce theoretical predictions of both the signal and background processes that yield final state dimuon responses in the ATLAS detector.

Theoretical predictions cannot be simply generated by convolving the probability flux of a physics process with an analytical response of the ATLAS detector. This is because the ATLAS detector is too complex; an analytical form of the response cannot be derived. It is complex because there are many degrees of freedom from the components of the sub-detectors as well as the degrees of freedom of the physics process itself, and due to the binary nature of the ATLAS trigger system, which itself is dependent on event-level kinematics. Event level theoretical predictions must therefore be used to compare against the data.

The Monte Carlo (MC) method is used to generate event-level theoretical predictions. As well as being a tool for numerical integration, the MC method can be used to simulate on an event-by-event basis. Monte Carlo simulation in high-energy physics involves random number generation to determine the kinematic properties of individual events according to normalised multi-differential kinematic cross-sections. Once the kinematics of the event has been determined the event final states can be "convolved" with the detector through MC hit simulation according to multiple scattering probabilities and pixel/cell/drift-tube responses. Event generation is repeated many times to form a Monte Carlo sample, so that a high statistical significance of the process is achieved.

B. Monte Carlo for ATLAS Analyses

In ATLAS the MC simulation of different physics processes are organised into 'samples' of events. The process and relevant parameters used in the event generation are documented in databases along with the simulation version at each stage. Generation of events kinematics and decays involves several steps:

1. Matrix elements are calculated to a defined order of strong and electroweak coupling, α_{s} and α_{EW} respectively.

2. Radiation of gluons and gluon splitting for parton showers are calculated for the initial and

final states from the scale of the interaction down to a cut-off scale typically of the order 1 GeV.

3. Interactions between the remnants of the incoming protons are calculated, based on phenomenological models, to form the "underlying event".

4. Hadronisation of remaining coloured partons into colourless hadrons, which may subsequently follow decay chains to longer lived particles that traverse the detector.

5. Final state radiation is added to final state charged leptons in the event.

Six different Monte Carlo generators are used directly in this analysis along with a precision tool for photon corrections. They are called POWHEG, Pythia8, MC@NLO, LPair, Herwig++ and Photos.

- Pythia8 is a general purpose MC event generator that operates at LO. It has an extensive library of hard processes, parton shower models, beam remnant simulation, hadronisation and particle decays. Hadronisation in Pythia8 follows the Lund string model[69,70].

- MC@NLO is an NLO generator which interfaces into a hadronisation model, however as hadronisation models typically contain some NLO corrections a method is applied to avoid double-counting. Monte Carlo generator event weights are used to book the NLO phase-space with ± 1 integer values[71].

- POWHEG is an NLO generator that uses a hardest-radiation-first (Powheg) method of merging parton showers with NLO calculations. It interfaces into p_T ordered parton-shower hadronisation models[72–74].

- LPair is a MC event generator dedicated to electromagnetic production of lepton pairs in lepton-lepton, lepton-hadron or hadron-hadron interactions via a two-photon process. By reformulating the matrix element it is able to avoid difficult gauge calculations and produce numerically stable results[75,76].

- Herwig++ is a general purpose MC event generator. Hadronisation in Herwig++ is an angular ordered cluster hadronisation model[77–80].

- Photos is a precision radiative-correction modelling tool for final state charged leptons. It is able to add Bremsstrahlung radiation to events from a parent MC generator[81].

The effects of in-time pile-up, where more than one event occurs at each bunch crossing leave additional tracks in the detector, are included by adding separately generated minimum bias events.

Minimum bias interactions are pp events that constitute the vast majority of the pp inelastic cross-section, that are recorded with a highly-prescaled low-rate trigger; such events typically consist of simple gg and gq scattering. In simulation, minimum bias interactions and the underlying event are generated using the parameter set from the AU2 tune to the ATLAS data[82].

The generated final state particles are simulated through the ATLAS detector material with the GEANT4 package[83]. Although the ATLAS description in GEANT4 is highly detailed, alignments within the detector, imperfect knowledge of the magnetic field volume and incomplete rendering of the cables and services within the detector lead to differences in resolutions between data and simulation. The detector simulation outputs digitised hits in the simulated components of ATLAS. This allows for the same reconstruction methods to be applied to MC simulation as is applied to data, thereby minimising reconstruction method biases.

Each step in the event reconstruction chain of the data and MC simulation is completed using the ATLAS Athena framework and stored on disk in analysis formats such as "analysis data objects" (AODs) or as nTuples as required by different physics working groups within the ATLAS experiment. These formats are accessed using the object oriented ROOT analysis libraries provided by CERN[84].

For the efficiency of the various analyses, the data is filtered at the trigger level into analysis streams. The streams are based around events containing, for example, trigger electrons or trigger muons, known as the `muons stream` and the `electrons stream`, respectively. Furthermore, most analyses don't require all the detector readout information so file sizes and computing requirements can be reduced by including only commonly used event information. The data is recorded to disk or tape at each processing stage and the provenance, a string identifying the file's processing history, is recorded in the file's name and in an online database.

5. DATA SETS FOR THE DRELL–YAN MEASUREMENT

A. The ATLAS Data Set

The data set used for this analysis was collected in 2012 and corresponds to an integrated luminosity of $20.24\,\mathrm{fb}^{-1}$. The centre-of-mass energy is $\sqrt{s} = 8\,\mathrm{TeV}$ with a bunch separation of 50 ns. ATLAS data and MC simulation is accessed through Standard Model working group "`NTUP_COMMON`" nTuples, processed with a final provenance tag of "`_p1575`". Data events are selected using the SM Good Run List (GRL) which corresponds to periods of stable LHC collisions and operations of the relevant ATLAS detector components. The GRL is computed by the ATLAS luminosity calculator using the tag "`OflLumi-8TeV-003`". The data periods used by the analyses and their corresponding integrated luminosities are shown in Table 6.

Period	No. Events	$\mathcal{L}\,[\mathrm{fb}^{-1}]$
A	43,651,420	0.78536
B	163,532,962	5.04721
C	80,935,368	1.39750
D	112,738,915	3.27501
E	81,667,914	2.52552
G	41,182,058	1.27851
H	49,412,952	1.45242
I	34,765,048	1.02154
J	88,410,196	2.60988
L	29,040,147	0.84631
Total		20.2392

GRL: `data12_8TeV.periodAllYear_DetStatus-v61-pro14-02_DetStatus-v61-pro14-02_DQDefects-00-01-00_PHYS_StandardGRL_All_Good.xml`

TABLE 6: The ATLAS data periods used in the analysis displaying the total number of recorded events with at least one activated muon trigger and corresponding integrated luminosities associated to the SM good runs list (GRL).

B. Monte Carlo Simulation Samples

Simulated Drell–Yan Processes

The Drell–Yan process is simulated with `powheg` matched to `pythia8` for simulation of parton showers. The PDF set used by the Drell–Yan simulations is CT10[85]. In this thesis, Drell–Yan Monte Carlo samples will be henceforth referred to as signal Monte Carlo or signal MC.

Signature	$M_{\mu\bar{\mu}}$ [GeV]	ATLAS MC Run No.	σ [pb]	K-factor	ϵ^{filter} [%]	N_{evt} [k]	$\mathcal{L}$ [fb^{-1}]
$Z \to \mu\bar{\mu}$ (dm)	8-20	129520	1879.8	$k(m_{\mu\bar{\mu}})$	0.68	2970	2
$Z \to \mu\bar{\mu}$	20-60	129521	789.36	$k(m_{\mu\bar{\mu}})$	100.00	5000	6
$Z \to \mu\bar{\mu}$ (dm)	20-60	129522	373.63	$k(m_{\mu\bar{\mu}})$	26.65	9888	99
$Z \to \mu\bar{\mu}$ (dm)	> 60	129681	1109.9	$k(m_{\mu\bar{\mu}})$	56.61	50000	81
$Z \to \mu\bar{\mu}$ (sm)	> 60	129686	1109.9	$k(m_{\mu\bar{\mu}})$	30.93	14996	57
$Z \to \mu\bar{\mu}$ (zm)	> 60	129697	1109.9	$k(m_{\mu\bar{\mu}})$	12.46	2994	21
$Z \to \mu\bar{\mu}$	120-180	129524	9.8445	$k(m_{\mu\bar{\mu}})$	100.00	4999	508
$Z \to \mu\bar{\mu}$	180-250	129525	1.5710	$k(m_{\mu\bar{\mu}})$	100.00	1000	637
$Z \to \mu\bar{\mu}$	250-400	129526	0.5492	$k(m_{\mu\bar{\mu}})$	100.00	5999	1092
$Z \to \mu\bar{\mu}$	400-600	129527	0.0897	$k(m_{\mu\bar{\mu}})$	100.00	3947	4402

TABLE 7: Table of the Drell–Yan `powheg-pythia8` Monte Carlo samples used in the analysis. The CT10 PDF set is used with the AU2 tune. The first column gives the signature of the process being simulated followed by the mass range in which the events were generated, internal ATLAS MC run numbers and the production cross-section. The next columns are the K-factor and the efficiency ϵ^{filter} with which the sample was filtered with [$|\eta_\mu| < 2.7$, leading $p_T > 15\,\text{GeV}$ and sub-leading $p_T > 10\,\text{GeV}$] for either di-, single- or zero-muon filtered final states; (dm), (sm), (zm) respectively. Lastly, the number N_{evt} of generated events, and the integrated luminosity of each sample is given. The NNLO K-factor is a function of invariant mass and is further discussed in Section 7

.

The signal MC samples are given in Table 7. From the table it is seen that multiple signal MC samples cover the same invariant mass range. These are required to cover the full kinematic phase space of the process. The three signal samples generated with invariant masses of $m_{ll} > 60\,\text{GeV}$ are produced with different filter requirements on lepton p_T and η. It is possible for both final state muons to pass these filter requirements in which case they are classified as "dm" events, otherwise only one muon will pass, classified as "sm", or no muons will pass the filter, classified as "zm". The sum of the three samples equates to an unfiltered signal sample. The filter requirements are:

$|\eta_\mu| < 2.7$, leading $p_T > 15\,\text{GeV}$ and sub-leading $p_T > 10\,\text{GeV}$.

In order to simulate events with masses between $20 < m_{ll} < 60\,\text{GeV}$, a high-statistics signal MC sample is used. Similar to the $m_{ll} > 60\,\text{GeV}$ (`129681`) sample, the sample is filtered to keep only events with leptons that are generated, before reconstruction, in the central part of the detector. Unlike the $m_{ll} > 60\,\text{GeV}$ samples, no dedicated sample exists to cover the missing "sm" or "zm" phase space. To include all the kinematic phase space, a separate low-statistics sample without requirements on the leptons is used to form a "recovery" sample. Inverted filter requirements are placed on the low-statistics sample to only accept events from the missing phase space: events are required to be generated anywhere but the central region of the detector.

Additional signal MC samples generated with high and low invariant masses are used to ensure high statistical precision in these regions and to accurately account for migration of events into the analysis fiducial volume. The fiducial volume is given in Section 6 B. To avoid double counting of the event generation phase space within invariant mass regions, a requirement of $m_{ll} < 120\,\text{GeV}$ is applied to the three filtered $m_{ll} > 60\,\text{GeV}$ samples.

The K-factors applied to the Drell–Yan signal MC is further discussed in Section 7.

Simulated Background Processes

By definition, real collisions that occur within the ATLAS detector are integrated over all physics processes. Therefore, while the ATLAS data will include the Drell–Yan events that this analysis aims to measure, background processes that have a similar final state or that can mimic the final state through mis-identified objects will be present in the analysis. Example processes that are expected to have a non-negligible contribution to the analysis are shown in Figure 21. These given processes are simulated in MC, for which the details of the data sets are given in the following subsections. Multijet production will also contribute as a background, however typically only heavy-flavour components are simulated in MC and although the production cross-section is large the high-energy dimuon branching ratio is small. This leads to inefficient simulation of the heavy flavour multijet components. Therefore QCD background contributions in this thesis are estimated directly from data; this is discussed in Section 9.

In this analysis, although $Z/\gamma^* \to \tau\bar{\tau}$ is a Drell–Yan process, the decays of the taus will contaminate the muon channel measurement and is therefore treated as a background. The $Z/\gamma^* \to \tau\bar{\tau}$ background is simulated with the same generator and parameters as the signal MC samples and its details are listed in Table 8.

Photon-induced processes are sub-categorised according to the origin of the initial state photons. Double-dissociative (dd) processes, where both photons originate from photon component of the

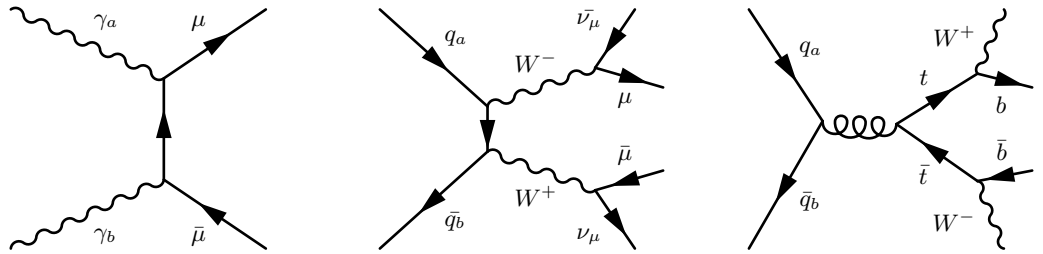

(a) Photon-induced dimuon production.

(b) WW diboson production.

(c) $t\bar{t}$ production with leptonic decays.

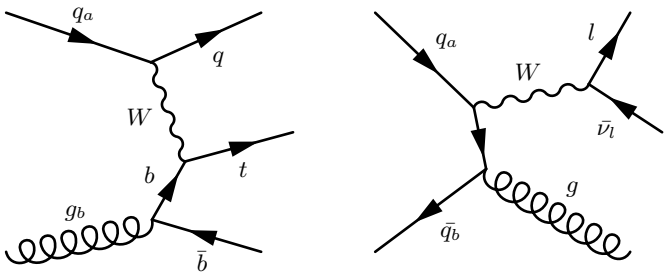

(d) t-channel single-top production.

(e) $W \to l\bar{\nu}_l$ production.

FIG. 21: Example background processes to the measurement of the dimuon channel Drell–Yan process. Other processes include WZ and ZZ production, which are included in the more general "diboson" definition, and $Z \to \tau\bar{\tau}$ and multijet production.

PDFs, are simulated using `pythia8`. Single-dissociative (sd) processes, where one photon originates as part of the photon PDF and the other originates from the proton charge itself, are simulated using `herwig`. Exclusive (ex) processes, where both photons originate from the proton charge, are simulated using `lpair`. The `MRST2004QED` PDF set was used for the PDF of the photon and the samples are listed in Table 9.

The diboson (WW, WZ, ZZ) MC samples are generated with `herwig` using the `CTEQ6L1` PDF set. An extra normalisation scaling is applied to the WW component due to a detailed background study provided by the ATLAS $H \to WW^*$ production measurement[89]. The associated uncertainty from the background study is applied when using the WW samples with the scaling. Information on the diboson samples can be seen in Table 10.

The $t\bar{t}$ (ttbar) background MC is simulated by `powheg` to generate matrix elements and `pythia6` to describe the underlying event and parton showers. Decays from single-top process are simulated using `powheg-pythia6`. Table 11 lists the top samples used in the analysis.

The $W \to l\nu$ background is simulated separately for $W^\pm \to \mu\nu$, and $W^\pm \to \tau\nu$ using `sherpa`

Signature	$m_{\tau\bar{\tau}}$ [GeV]	MC Run No.	σ^{NLO} [pb]	K-factor	ϵ^{filter} [%]	N_{evt} [k]	Uncertainty [%]
$Z \to \tau\bar{\tau}$	> 60	147808	1109.9	$k(m_{\tau\bar{\tau}})$	100.0	5000	5
$Z \to \tau\bar{\tau}$	180-250	158731	1.2485	$k(m_{\tau\bar{\tau}})$	100.0	150	5
$Z \to \tau\bar{\tau}$	250-400	158732	0.4361	$k(m_{\tau\bar{\tau}})$	100.0	150	5
$Z \to \tau\bar{\tau}$	400-600	158733	0.0718	$k(m_{\tau\bar{\tau}})$	100.0	150	5
$Z \to \tau\bar{\tau}$	600-800	158734	0.0180	$k(m_{\tau\bar{\tau}})$	100.0	150	5

TABLE 8: Background Drell–Yan `powheg-pythia8` Monte Carlo sample used in the analysis. The first column is the signature simulated followed by the internal ATLAS run number corresponding to each sample. Next are the `powheg-pythia8` NLO cross-section, K-factor, filter efficiency ϵ^{filter}, and the number of events. The K-factor is at NNLO including NLO EW effects and is provided as a function of $m_{\ell\ell}$ and is also used for the signal $Z \to \mu\bar{\mu}$ samples. Finally, the systematic uncertainty on the normalisation of the samples is also given[86].

with the CT10 PDFs. The samples are listed in Table 12.

Signature	$m_{\mu\bar{\mu}}$ [GeV]	MC run No.	σ^{LO} [pb]	K-factor	ϵ^{filter} [%]	N_{evt} [k]	Uncertainty [%]
$\gamma\gamma\,(dd) \to \mu\bar{\mu}$	7-20	129660	149.89	0.70	24.16	500	40
$\gamma\gamma\,(dd) \to \mu\bar{\mu}$	20-60	129661	26.600	0.70	33.01	500	40
$\gamma\gamma\,(dd) \to \mu\bar{\mu}$	60-200	129662	2.6931	0.70	100.0	500	40
$\gamma\gamma\,(dd) \to \mu\bar{\mu}$	200-600	129663	0.12164	0.70	100.0	200	40
$\gamma\gamma\,(sd) \to \mu\bar{\mu}$	60-200	185346	5.0420	0.70	100.0	500	40
$\gamma\gamma\,(sd) \to \mu\bar{\mu}$	200-600	185347	0.8730	0.70	100.0	200	40
$\gamma\gamma\,(sd) \to \mu\bar{\mu}$	600-1500	185348	0.0400	0.70	100.0	100	40
$\gamma\gamma\,(ex) \to \mu\bar{\mu}$	20-60	185337	26.600	0.70	9.595	500	40
$\gamma\gamma\,(ex) \to \mu\bar{\mu}$	60-200	185338	26.600	0.70	26.31	200	40
$\gamma\gamma\,(ex) \to \mu\bar{\mu}$	> 200	185339	26.600	0.70	37.71	100	40

TABLE 9: Photon-induced Monte Carlo samples used in the analysis, listing the double-dissociative (dd) process generated by `pythia8`, the single-dissociative (sd) process generated by `lpair` and the exclusive (ex) process generated by `herwig`. The first column is the signature simulated followed by the generated invariant mass and the internal ATLAS run number corresponding to each sample. Next are the LO cross-sections determined using the MRST2004QED PDF set and NLO K-factors. The filter efficiency ϵ^{filter} for selecting [$|\eta_\mu| < 2.7$, leading $p_T > 15\,\text{GeV}$ and sub-leading $p_T > 10\,\text{GeV}$] dimuon final states on the "ex" samples and "dd" samples between 7-60 GeV. Finally, the number of events and the normalisation uncertainty is given[87,88].

Signature	MC Run No.	$\sigma\,\text{Br}$ [pb]		K-factor	ϵ^{filter} [%]	N_{evt} [k]	Extra Scale	Uncertainty [%]
		`herwig`	NLO					
$WW \to \ell X$	105985	32.501	58.7	1.8060	38.21	2500	1.20	10.0
$ZZ \to \ell X$	105986	4.6914	7.2	1.5347	21.17	245	–	4.2
$WZ \to \ell X$	105987	12.009	20.3	1.6904	30.55	1000	–	4.0

TABLE 10: Diboson `herwig` Monte Carlo samples used in the analysis. The first column is the signature simulated followed by the internal ATLAS run number corresponding to each sample. Next are the `herwig` LO cross-section, the NLO cross-section calculated using MCFM, the LO→NLO K-factor, filter efficiency ϵ^{filter} representing the branching ratio for the final state, and the number of events. An extra scale factor used for the WW process[89] is also shown and the uncertainty assigned to the background normalisation is also given[90–92].

Signature	MC Run No.	σ Br[pb]		K-factor	ϵ^{filter} [%]	N_{evt} [k]	Uncertainty [%]
		`powheg`	NNLO				
$t\bar{t} \to \ell X$	110404	210.84	252.89	1.1994	54.30	50000	6
$t\bar{t} \to XX$	105204	210.84	252.89	1.1994	45.70	9905	6
Single Top t-channel	110090	17.520	–	1.0500	100.00	5000	6
Single Anti-top t-channel	110091	9.3932	–	1.0616	100.00	1000	6
Single Top s-channel	110119	1.6424	–	1.1067	100.00	6000	6
$Wt \to X$	110140	20.461	22.37	1.0933	100.00	1000	6

TABLE 11: Top `powheg-pythia6` Monte Carlo samples used in the analysis. The first column is the signature simulated followed by the internal ATLAS run number corresponding to each sample. Next are the `powheg-pythia6` NLO cross-section, the NNLO cross-section calculated using `TOP2.0`, the NLO→NNLO K-factor, filter efficiency ϵ^{filter} representing the final state branching ratio, and the number of events. Finally, the normalisation uncertainty is also given for the NNLO cross-section[93–99].

Signature	MC Run No.	σ Br [pb]		K-factor	N_{evt}	Uncertainty [%]
		`powheg`	NNLO			
$W^+ \to \mu\nu$	147801	6891.0	7104.6	1.03	22972	5
$W^- \to \mu\nu$	147804	4790.2	4919.5	1.03	16854	5
$W^+ \to \tau\nu$	147802	6890.0	7103.6	1.03	29949	5
$W^- \to \tau\nu$	147805	4790.9	4920.3	1.03	5000	5

TABLE 12: Background W boson `powheg-pythia8` Monte Carlo sample used in the analysis. The first column is the signature simulated followed by the internal ATLAS run number corresponding to each sample. Next are the `powheg-pythia8` NLO cross-section, K-factor at NNLO, and the number of events. Finally, the normalisation uncertainty is also given[100,101].

6. THE MEASUREMENT PHASE SPACE

A. Event Selection Criteria

The Drell–Yan signal is discriminated from background processes by placing kinematic requirements on events. Additional requirements are used to reject reconstructed muons in the event that appear to be either poorly reconstructed, non-prompt or fake muons. Muons that originate from the hard scatter of an interaction are defined as prompt muons. Muons that originate from secondary decays, i.e. away from the $\hat{z}$-axis, are defined as non-prompt muons. Non-muon particles that are reconstructed as muons are called "fake" muons. The contribution of fake muons to this analysis is negligible due to the large number of hadronic interaction lengths of the HCAL whereas the contribution from non-prompt muons is significant.

The selection criteria for $Z \to \mu\bar{\mu}$ candidates are defined below. Details of the criteria are provided in the subsections.

- Event passes the ATLAS data quality good runs list (GRL: Table 6).
- Event rejected if the LAr Error is present.
- Event has ≥ 2 tracks associated to the primary vertex.
- Event passed one of the following trigger requirements based on highest p_T^μ muon:
  - $p_T^\mu < 25\,\text{GeV}$ and `EF_mu18_tight_mu8_effs`.
  - $p_T^\mu > 25\,\text{GeV}$ and either `EF_mu24i_tight` or `EF_mu36_tight`.
- Event contains at least one muon that is triggered-matched to an activated trigger.
- Event has ≥ 2 combined third-chain algorithm muons passing the following selections.
  - Muon passes muon combined performance (MCP) quality criteria.
  - Muon passes `medium+` reconstruction definition.
  - $p_T^\mu > 20\,\text{GeV}$
  - $|\eta_\mu| < 2.4$
  - $|z_{PV}| < 10\,\text{mm}$
  - Isolation requirement, $I_\mu = \sum p_T^{(\Delta R=0.2)}/p_T^\mu < 0.1$
- Event does not have ≥ 3 muons after all previous selection criteria.
- Event contains two muons after all previous selection criteria, which are of opposite sign electric charge.

where the individual muon momenta, p_T^μ, is determined from the ID only. The individual selection criteria are further described below:

ATLAS Data Quality GRL & LAr Flags

Dimuon events are taken from good data runs with no error flags arising from liquid argon (LAr) components in the ATLAS detector. LAr noise bursts can occur during detector-operations, therefore an error flag is recorded so these events can be removed.

Tracks associated to the Primary Vertex

Tracks of an event are reconstructed back to a central vertex and are only recorded if the associated transverse momentum satisfies $p_T^{\mathrm{Trk}} > 400\,\mathrm{MeV}$. The primary vertex is defined as the vertex with the highest value $\sum \left(p_T^{\mathrm{Trk}}\right)^2$ where the sum incudes all tracks associated to the vertex. A requirement of three or more tracks to the primary vertex, in addition to the impact parameter requirement, removes muon signatures originating from cosmic ray interactions in the upper atmosphere.

Trigger Requirements

As previously described in Section 2 E, this analysis uses three different muon triggers. This allows a greater acceptance of muon momenta at low value p_T^{μ} and higher efficiency of individual muons at high value p_T^{μ}. In addition, at least one reconstructed muon in the event is required to have equivalent values of p_T^{μ}, η_{μ} and ϕ_{μ} to the object that passed the trigger; this muon is considered to be "trigger-matched".

MCP Quality Criteria

A set of criteria is recommended by the Muon Combined Performance (MCP) group within ATLAS for removing poorly reconstructed muons[68]. The inner detector must have a certain number of hits with respect to dead sensors, holes in acceptance or outlying TRT hits. Also, the ID tracks must have a successful TRT extension if the track lies within the TRT acceptance. An unsuccessful TRT extension is defined as either no recorded TRT hits or a set of TRT hits associated as outliers. The requirements are:

- Number of pixel hits + number of crossed dead pixel sensors > 0.
- Number of SCT hits + number of crossed dead SCT sensors > 4.
- Number of pixel holes + number of SCT holes < 3.
- A successful TRT extension in the η_{μ} acceptance of the TRT:
  - For $0.1 < |\eta_{\mu}| < 1.9$, require $n > 5$ and $n_{\mathrm{TRT}}^{outliers} < 0.9n$

where $n_{\text{TRT}}^{\text{hits}}$ denotes the number of TRT hits of the muon track, $n_{\text{TRT}}^{\text{outliers}}$ the number of TRT outliers of the muon track and $n = n_{\text{TRT}}^{\text{hits}} + n_{\text{TRT}}^{\text{outliers}}$.

The MCP group also recommends a restriction on the significance of the muon momentum balance to improve reconstruction quality for MuID and MuGirl muons. This limits the number of muons originating from decays in-flight. This criteria is included in the MCP group's definition of a reconstructed `medium+` muon.

- For MuID muons: muon momentum balance significance < 4.
- For MuGirl muons: muon momentum balance significance < 4 and is a combined muon.

Detector Acceptance

Due to the coverage of detector components, only muons within $|\eta_\mu| < 2.5$ are accurately reconstructed in ATLAS. Furthermore, limitations imposed by corrections to muon trigger efficiencies reduce the acceptance range to $|\eta_\mu| < 2.4$. The trigger requirements also impose a lower value p_T^μ threshold for accurate muon reconstruction. This is further described in Section 6 B.

Impact parameter

Muons from secondary decays of long-lived particles are rejected by an impact parameter, $|z_{PV}|$, criterion. The impact parameter, z_{PV}, is defined as the $\hat{z}$ offset closest point of approach of a muon track to the primary vertex. The data distribution of z_{PV} is shown in Figure 22a, where the shaded regions show muons accepted and rejected by the impact parameter. The criterion is shown to act on the tail of the distribution where the cross-section has fallen by 2.7 orders of magnitude. The criterion also rejects muon signatures originating from cosmic ray interactions in the upper atmosphere. The rejection of these signatures is shown in Figure 22b. The plot shows that when such muons traverse the beamline they mimic a non-boosted back-to-back dimuon event, as shown in the central part of the $\eta_\mu^1 + \eta_\mu^2$ spectrum.

Isolation Requirement

The isolation requirement discriminates against semileptonic decays of heavy quarks[1]. The isolation parameter, I_μ, is defined as the scalar sum of transverse momenta of additional objects within a cone of ΔR about the muon track divided by the muon transverse momentum: $\sum p_T^{(\Delta R=0.2)}/p_T^\mu$. The isolation distributions are used in the determination of the dimuon multijet background for which distributions are shown in Section 9.

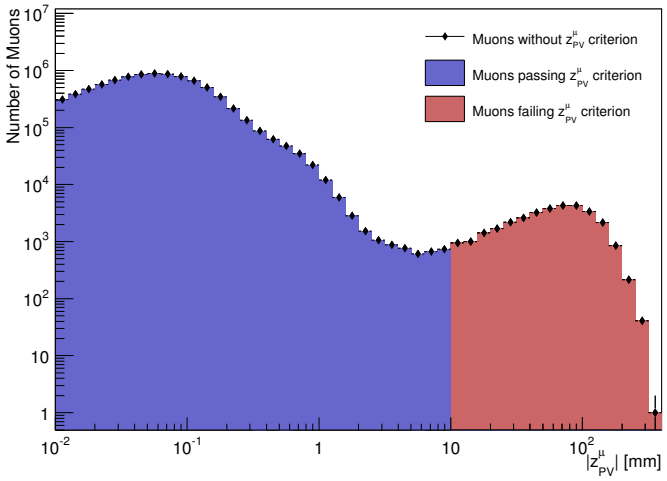

(a) The impact parameter distribution of muons in data with and without the z_{PV} criterion.

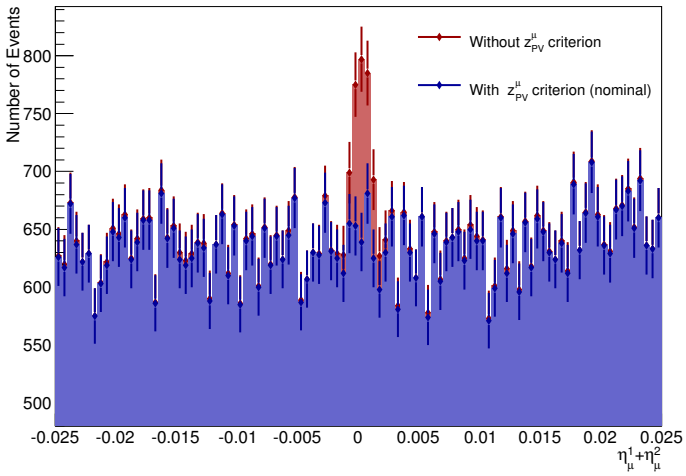

(b) The data distribution of leading, η^1_μ, and sub-leading, η^2_μ, addition of muon pseudo-rapidities.

FIG. 22: The impact parameter criterion applied to data distributions. The shaded regions under the data points show the regions where the muons are accepted (blue) and rejected (red) by the criterion. The $\eta^1_\mu + \eta^2_\mu$-axis has been focused in on the central part of the distribution where the contribution of muon signatures originating from cosmic ray interactions in the upper atmosphere is seen in the red shaded region (without z^{μ}_{PV} criterion) above the nominally selected data.

Drell–Yan Signature

Drell–Yan events are expected to have two high-energy final state leptons of opposite sign electric charge. Therefore, a veto of events containing ≥ 3 muons and an opposite sign criterion are required.

In Section 10 A the number of events passing each criterion for data and MC is presented, where the events have applied weights and corrections as described in Section 7.

B. The Kinematic Fiducial Volume

A prerequisite for the production of theory calculations is to have a well defined kinematic phase space for which the calculations are to be performed. This is because theory calculations would otherwise integrate inclusively over all kinematics leading to large theory extrapolation uncertainties when compared against the data. In this analysis the kinematic phase space is defined to be close to the experimental acceptance.

Due to the coverage provided by the inner detector and the muon spectrometer, as well as limitations imposed by muon trigger requirements, muons are only accurately measured in a pseudo-rapidity range of $-2.4 < \eta_\mu < 2.4$. In addition to this, trigger limitations define a minimum transverse muon-momentum, p_T^μ, for which muons are recorded. The lowest p_T^μ muon trigger used in this analysis has its threshold at 18 GeV. To measure in a region away from threshold effects the fiducial transverse muon-momentum region is $p_T > 20\,\text{GeV}$. This also indirectly places a lower limit on the value of dimuon invariant mass that can be measured: the lower limit for $m_{\mu\mu}$ is taken to be $m_{\mu\mu} > 46\,\text{GeV}$. An upper limit of $m_{\mu\mu} < 200\,\text{GeV}$ is required. These three regions in η_μ, p_T^μ and $m_{\mu\mu}$ define the kinematic "fiducial volume".

As well as these requirements manifesting themselves in the experimental selection criteria for reconstructed events, they are applied as fiducial selection criteria for the generated truth MC particles. Truth MC definitions are discussed in the unfolding section (Section 6 D). The fiducial volume is summarised below, where the kinematics are taken at either the Born, bare or dressed truth-levels defining the unfolding:

- $|\eta_\mu| < 2.4$
- $p_T^\mu > 20\,\text{GeV}$
- $46 < m_{\mu\mu} < 200\,\text{GeV}$

C. Three-Dimensional Binning

The locations of the bin edges are chosen to maximise the physics sensitivity whilst limiting the effects of sparsely populated bins. The bin edges are motivated as follows: The sign change of the forward-backward asymmetry, A_{FB}, about the Z-boson mass peak is measured with bins directly either side of m_Z. The mass binning continues in coarse mass bins, to mitigate migrations. Migrations in mass are due to effects of final state radiation and p_T^μ reconstruction effects. The upper mass bin edge was chosen so that the full width of the Z is covered, high values of A_{FB} are measured and a high statistical precision is achieved. Fine binning in rapidity, $|y_{\mu\mu}|$, was chosen for the PDF variation and an even number of bins in $\cos\theta^*$ allows for the A_{FB} determination (Equation 43) as well as sensitivity to gq contributions from the PDFs (Figure 9).

The high $m_{\mu\mu}$ bin edges align with the binning scheme of the 2011 W/Z measurement[32] and the 2012 high mass Drell–Yan precision measurement[1]. The low $m_{\mu\mu}$ bin edges away from the mass peak align with the 2011 low mass Drell–Yan measurement[102].

The final binning scheme that is used across the three dimensions in the analysis is:

- $m_{\mu\mu}$: (46, 66, 80, 91, 102, 116, 150, 200) GeV
  - 7 bins.
- $|y_{\mu\mu}|$: (0.0, 0.2, 0.4, 0.6, 0.8, 1.0, 1.2, 1.4, 1.6, 1.8, 2.0, 2.2, 2.4)
  - 12 bins.
- $\cos\theta^*$: (-1.0, -0.7, -0.4, 0.0, 0.4, 0.7, 1.0)
  - 6 bins.
- Total Number of Bins: $7 \times 12 \times 6 = 504$

In the rapidity and $\cos\theta^*$ dimensions migrations are minimal due to accurate muon η_μ and ϕ_μ measurements, shown in the sampling resolution plots in Figures 23-26. The sampling resolution, $\mathcal{R}$, is the standard deviation of a variable, x:

$$\mathcal{R}(x) = \sigma\left[x_{\text{rec}} - x_{\text{gen}}\right] . \tag{57}$$

where x_{gen} is the generated "true" value from truth MC and x_{rec} is the reconstructed (measured) value. Figures 23 and 24 show for each mass bin a $y_{\mu\mu}$ and $\cos\theta^*$ plane with a point in each bin with the location corresponding to the mean value, $\langle x_{\text{rec}}\rangle$, of events falling within that bin and error bars corresponding to the sampling resolution as measured in that bin. The background colour gradient shows the magnitude of the two dimensional sampling resolution normalised to the bin widths:

$$\tilde{\mathcal{R}}(x,y) = \sqrt{\sigma^2\left[\frac{x_{\text{rec}} - x_{\text{gen}}}{\delta_x}\right] + \sigma^2\left[\frac{y_{\text{rec}} - y_{\text{gen}}}{\delta_y}\right]} . \tag{58}$$

where y is the variable of the second dimension and $\delta_{x,y}$ are the bins widths. Figures 25 and 26 show the sampling resolutions in $m_{\mu\mu}$ and $y_{\mu\mu}$ for constant $\cos\theta^*$.

The sampling resolution of the three dimensions show highly accurate $y_{\mu\mu}$ and $\cos\theta^*$ measurements on and above the Z-peak. The exceptions to this are on the edges of the $y_{\mu\mu}$-$\cos\theta^*$ phase space where the concentration of events towards the bin edges and significant resolutions indicate migrations into neighbouring bins. The $m_{\mu\mu}$ and $y_{\mu\mu}$ sampling resolution planes show limited values of resolution in the $m_{\mu\mu}$ dimension directly below the Z-peak, expected due to migrations from FSR contaminating the low $m_{\mu\mu}$ bins. This occurs because FSR absorbs a fraction of the original muon momentum reducing the observed invariant mass of the final state dimuon pair. The much larger cross-section of the Z-peak ($80 < m_{\mu\mu} < 102\,\text{GeV}$) compared to lower masses ($66 < m_{\mu\mu} < 80\,\text{GeV}$) causes the FSR effect to dominate the resolution in this region. The resolution in $m_{\mu\mu}$ is also seen to degrade with increasing $y_{\mu\mu}$.

To aide with displaying the binning in tables a linearised representation is adopted. A unique bin number is assigned to each bin when iterating over $m_{\mu\mu}$, $|y_{\mu\mu}|$ and $\cos\theta^*$ respectively. An equation for the transposition is provided and an example is shown in Table 13:

$$\left(m_{\mu\mu}^{(i)}, |y_{\mu\mu}^{(j)}|, \cos\theta^{*(k)}\right) \rightarrow \mathcal{B} = 72(i-1) + 6(j-1) + (k-1) + 1\,, \tag{59}$$

where,

$$i = 1, 2 \ldots 7\,,$$
$$j = 1, 2 \ldots 12\,,$$
$$k = 1, 2 \ldots 6\,.$$

Analysis bin, $\mathcal{B}$	Bin edges		
1	$46 < m_{\mu\mu} < 66\,\text{GeV}$	$0.0 < \lvert y_{\mu\mu}\rvert < 0.2$	$-1.0 < \cos\theta^* < -0.7$
2	$46 < m_{\mu\mu} < 66\,\text{GeV}$	$0.0 < \lvert y_{\mu\mu}\rvert < 0.2$	$-0.7 < \cos\theta^* < -0.4$
3	$46 < m_{\mu\mu} < 66\,\text{GeV}$	$0.0 < \lvert y_{\mu\mu}\rvert < 0.2$	$-0.4 < \cos\theta^* < 0.0$
4	$46 < m_{\mu\mu} < 66\,\text{GeV}$	$0.0 < \lvert y_{\mu\mu}\rvert < 0.2$	$0.0 < \cos\theta^* < 0.4$
5	$46 < m_{\mu\mu} < 66\,\text{GeV}$	$0.0 < \lvert y_{\mu\mu}\rvert < 0.2$	$0.4 < \cos\theta^* < 0.7$
6	$46 < m_{\mu\mu} < 66\,\text{GeV}$	$0.0 < \lvert y_{\mu\mu}\rvert < 0.2$	$0.7 < \cos\theta^* < 1.0$
7	$46 < m_{\mu\mu} < 66\,\text{GeV}$	$0.2 < \lvert y_{\mu\mu}\rvert < 0.4$	$-1.0 < \cos\theta^* < -0.7$
⋮	⋮	⋮	⋮
499	$150 < m_{\mu\mu} < 200\,\text{GeV}$	$2.0 < \lvert y_{\mu\mu}\rvert < 2.4$	$-1.0 < \cos\theta^* < -0.7$
500	$150 < m_{\mu\mu} < 200\,\text{GeV}$	$2.0 < \lvert y_{\mu\mu}\rvert < 2.4$	$-0.7 < \cos\theta^* < -0.4$
501	$150 < m_{\mu\mu} < 200\,\text{GeV}$	$2.0 < \lvert y_{\mu\mu}\rvert < 2.4$	$-0.4 < \cos\theta^* < 0.0$
502	$150 < m_{\mu\mu} < 200\,\text{GeV}$	$2.0 < \lvert y_{\mu\mu}\rvert < 2.4$	$0.0 < \cos\theta^* < 0.4$
503	$150 < m_{\mu\mu} < 200\,\text{GeV}$	$2.0 < \lvert y_{\mu\mu}\rvert < 2.4$	$0.4 < \cos\theta^* < 0.7$
504	$150 < m_{\mu\mu} < 200\,\text{GeV}$	$2.0 < \lvert y_{\mu\mu}\rvert < 2.4$	$0.7 < \cos\theta^* < 1.0$

TABLE 13: Example of the linearised analysis binning used in the analysis. In this formalism bins of $m_{\mu\mu}$ and $|y_{\mu\mu}|$ are fixed while the $\cos\theta^*$ dimension is iterated over. Once a cycle of $\cos\theta^*$ is completed the $|y_{\mu\mu}|$ dimension is incremented and $\cos\theta^*$ re-iterated over. This continues until a full cycle of $|y_{\mu\mu}|$ is complete at which point $m_{\mu\mu}$ is incremented, and the process repeats, providing each bin a unique bin number.

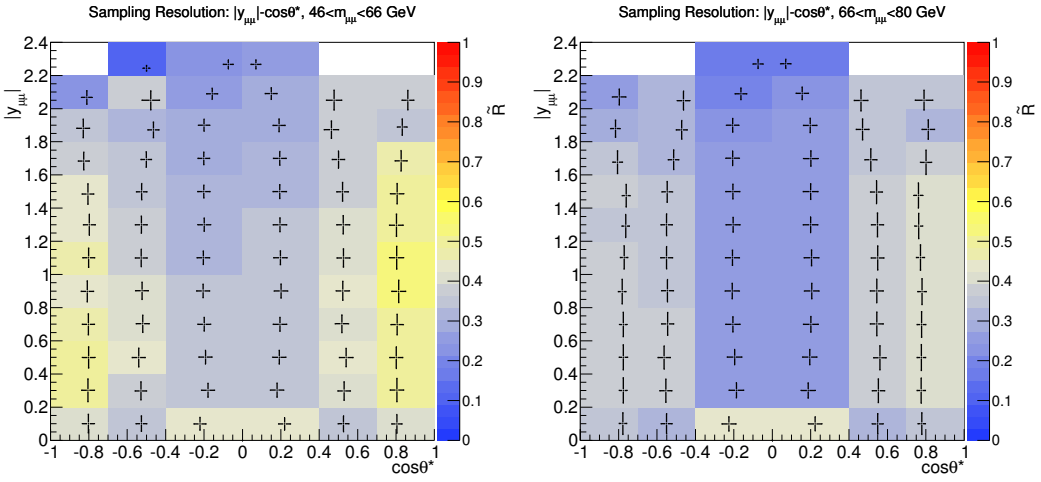

(a) Drell-Yan signal MC sampling resolution in the $46 < m_{\mu\mu} < 66\,\text{GeV}$ mass window.

(b) Drell-Yan signal MC sampling resolution in the $66 < m_{\mu\mu} < 80\,\text{GeV}$ mass window.

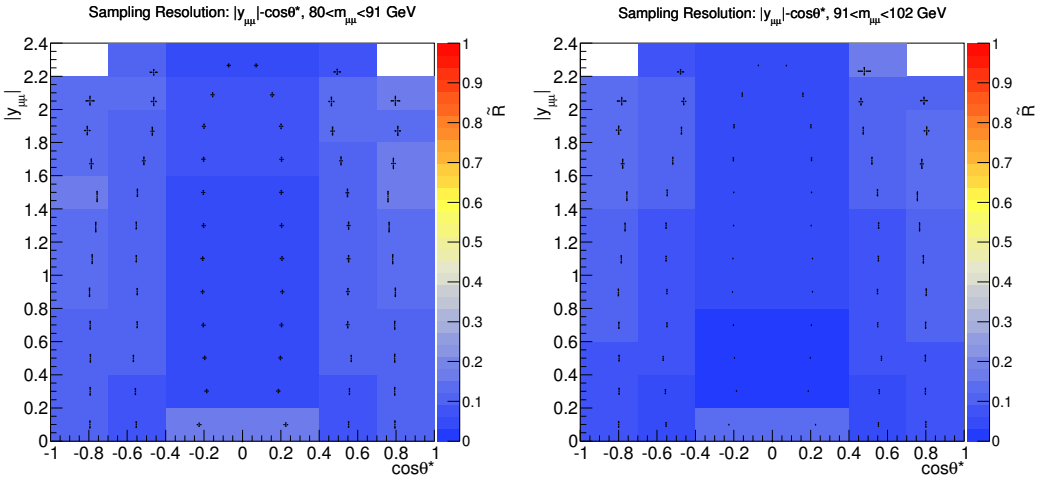

(c) Drell-Yan signal MC sampling resolution in the $80 < m_{\mu\mu} < 91\,\text{GeV}$ mass window.

(d) Drell-Yan signal MC sampling resolution in the $91 < m_{\mu\mu} < 102\,\text{GeV}$ mass window.

FIG. 23: Two dimensional ($|y_{\mu\mu}|$, $\cos\theta^*$) plots of the dimuon sampling resolution, $\mathcal{R}$, (points) and the normalised sampling resolution, $\tilde{\mathcal{R}}$, (colour gradient) in the first four invariant mass windows of the measurement. Final state muons before FSR (the Born truth-level) are used as the truth comparator in the resolution definitions for these figures.

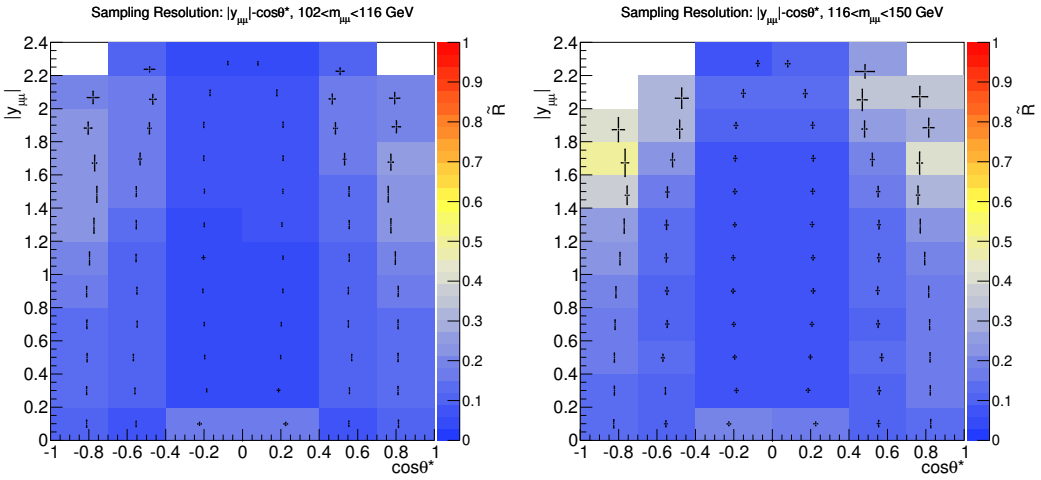

(a) Drell-Yan signal MC sampling resolution in the $102 < m_{\mu\mu} < 116\,\text{GeV}$ mass window.

(b) Drell-Yan signal MC sampling resolution in the $116 < m_{\mu\mu} < 150\,\text{GeV}$ mass window.

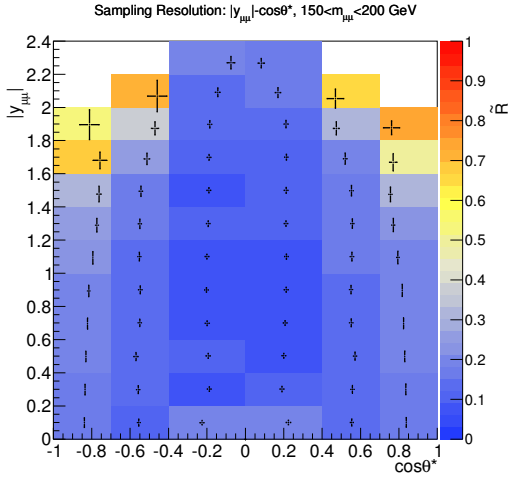

(c) Drell-Yan signal MC sampling resolution in the $150 < m_{\mu\mu} < 200\,\text{GeV}$ mass window.

FIG. 24: Two dimensional ($|y_{\mu\mu}|$, $\cos\theta^*$) plots of the dimuon sampling resolution, $\mathcal{R}$, (points) and the normalised sampling resolution, $\tilde{\mathcal{R}}$, (colour gradient) in the last three invariant mass windows of the measurement. Final state muons before FSR (the Born truth-level) are used as the comparator in the resolution definitions for these figures.

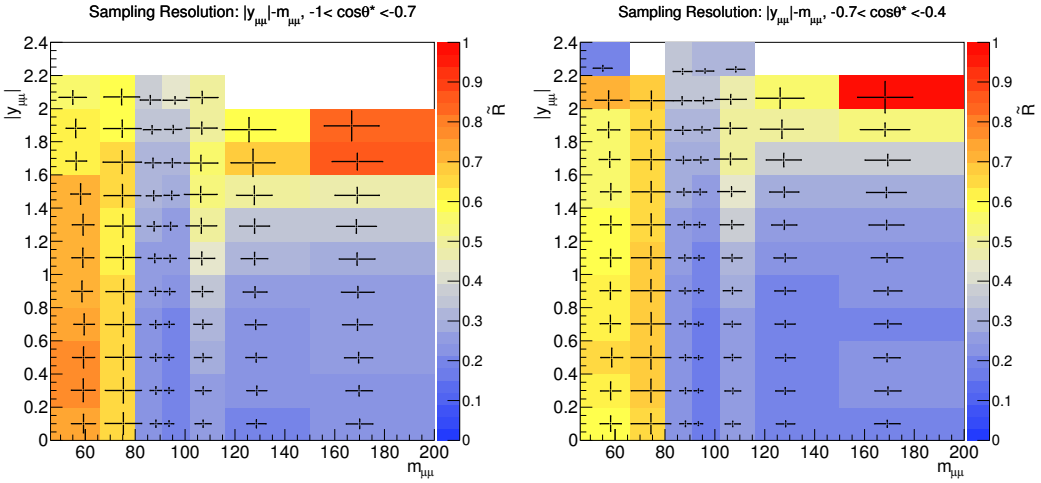

(a) Drell-Yan signal MC sampling resolution in the $-1.0 < \cos\theta^* < -0.7$ region.

(b) Drell-Yan signal MC sampling resolution in the $-0.7 < \cos\theta^* < -0.4$ region.

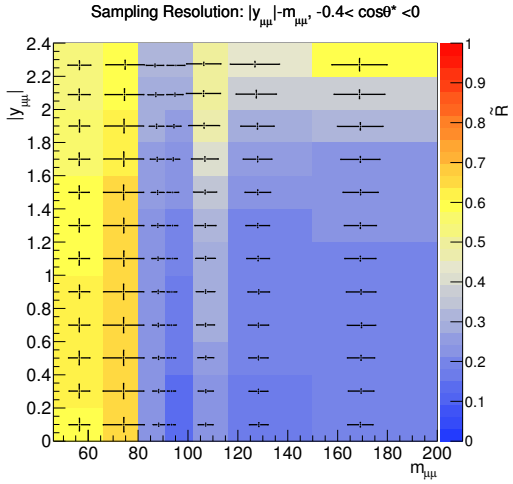

(c) Drell-Yan signal MC sampling resolution in the $-0.4 < \cos\theta^* < 0.0$ region.

FIG. 25: Two dimensional ($|y_{\mu\mu}|$-$m_{\mu\mu}$) plots of the dimuon sampling resolution, $\mathcal{R}$, (points) and the normalised sampling resolution, $\tilde{\mathcal{R}}$, (colour gradient) in the first three dimuon decay angle regions of the measurement. Final state muons before FSR (the Born truth-level) are used as the comparator in the resolution definitions for these figures.

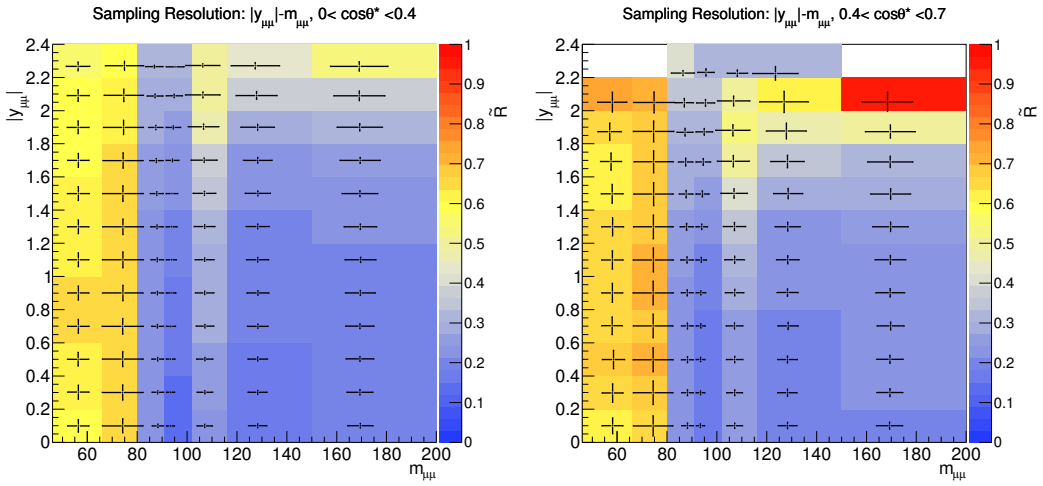

(a) Drell-Yan signal MC sampling resolution in the $0.0 < \cos\theta^* < 0.4$ region.

(b) Drell-Yan signal MC sampling resolution in the $0.4 < \cos\theta^* < 0.7$ region.

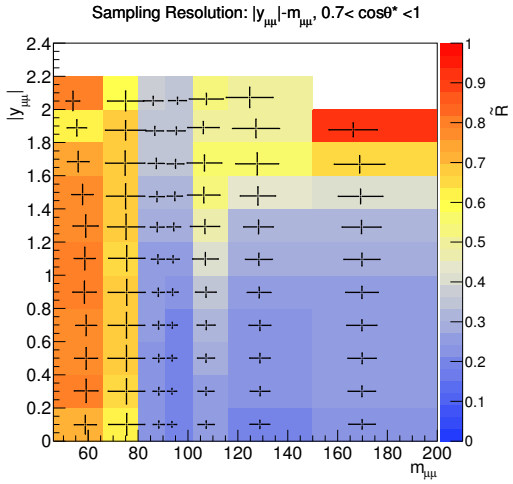

(c) Drell-Yan signal MC sampling resolution in the $0.7 < \cos\theta^* < 1.0$ region.

FIG. 26: Two dimensional ($|y_{\mu\mu}|$-$m_{\mu\mu}$) plots of the dimuon sampling resolution, $\mathcal{R}$, (points) and the normalised sampling resolution, $\tilde{\mathcal{R}}$, (colour gradient) in the last three dimuon decay angle regions of the measurement. Final state muons before FSR (the Born truth-level) are used as the comparator in the resolution definitions for these figures.

D. Cross-section Unfolding

As shown in Figures 23-26, observables are affected by the geometrical acceptance, detection efficiency, and finite resolution of the measuring device. In general, the true value of a physical observable is different from the measurement because of such physical limitations and algorithm biases. These effects are considered to be "folded" into reconstructed distributions. To produce a generalised result the reconstructed distributions are "unfolded" back to a MC generator-level definition[103]. This allows theorists to make predictions without knowledge of the ATLAS detector.

For a distribution of true values, $\vec{x}$, and measured values, $\vec{y}$, the transformation between the two is given by

$$\mathbf{R}\ \vec{x} = \vec{y}\,, \tag{60}$$

where $\mathbf{R}$ is known as the response matrix. The matrix elements, R^{ij}, define the probability that true value x^i is measured as value y^j. The response matrix is produced using Monte Carlo simulation which includes both the physics of each event before reconstruction and the simulation of particles interacting with the detector.

The inversion of the response matrix unfolds the reconstructed distributions, $\vec{y}$, giving the true distributions, $\vec{x}$;

$$\vec{x} = \mathbf{R}^{-1}\ \vec{y}\,. \tag{61}$$

True distributions are independent of the measuring device. This allows unfolded measured results to be comparable to not only results from other experiments, but to theoretical predictions as well. This also results in a choice of how to define the truth-level. For the Drell–Yan process an ambiguity arises from the treatment of final state radiation (FSR). Three levels are commonly defined[104]:

- Born: Event kinematics determined from leptons before QED FSR.
- Bare: Event kinematics determined from leptons after QED FSR.
- Dressed: A hybrid, where 4-vectors of the bare leptons are recombined with radiated photons within a cone of $\Delta R < 0.1$.

The Born truth-level is defined to be the same as the leading order in QED Drell–Yan process resulting in a full QED correction through the unfolding. The bare truth-level is defined to be similar to reconstructed quantities so that no QED correction is performed through unfolding. The dressed truth-level is also defined to be similar to reconstructed parameters, however it accounts for the inability of EM calorimeters to resolve electron FSR deposits in the case of collinear photon emission. In this analysis reconstructed results are unfolded to all Born, bare and dressed truth-levels

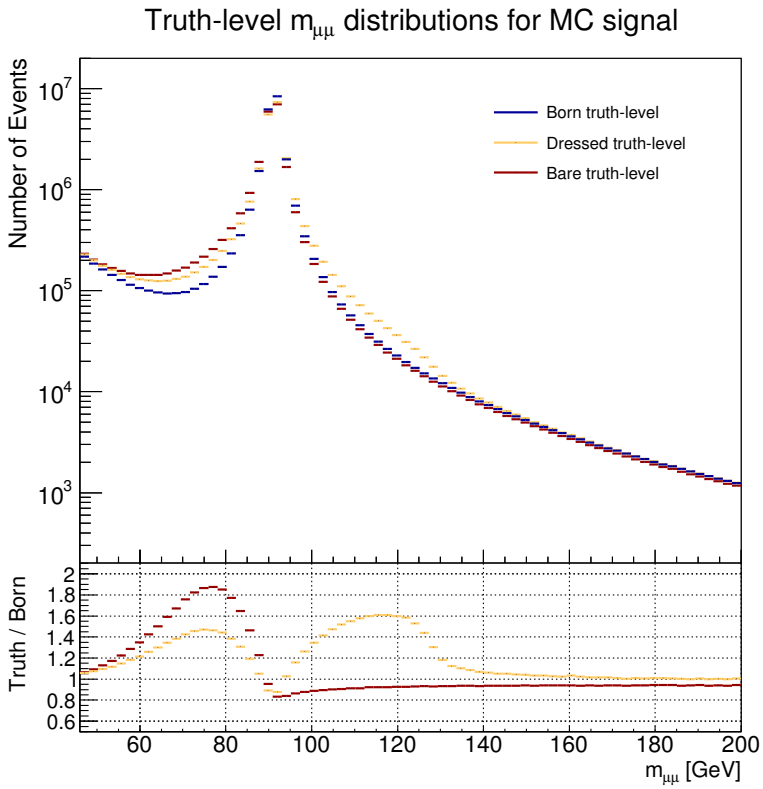

FIG. 27: Invariant mass differences between the Born, bare and dressed truth-levels. The distributions are taken from the Drell–Yan signal MC at $\sqrt{s} = 8\,\text{TeV}$.

within the kinematic fiducial volume. A combination is performed with unfolded electron channel results at the Born truth-level, detailed in Section 14. Although muons do not suffer from the same FSR resolution problem, unfolding to the dressed truth-level could allow for a more accurate future combination of both the muon and electron channel data. For this reason results are presented at all three truth-levels.

The difference in the truth-levels as a function of invariant mass is shown is Figure 27. The bare truth-level shows the large effect of FSR in migrating events to lower values of $m_{\mu\mu}$. Although the effect is dominant on and below the Z-peak, a significant effect is seen above the Z-peak. The dressed truth-level shows similar downward migrations as seen with the bare truth-level, however inclusion of ISR and photons from the underlying event cause large upward migrations which are further enhanced by the rapidly falling cross-section.

Due to the effect of significant migrations observed from the sampling resolution plots of Section 6 C the unfolding method of choice is the iterative Bayesian unfolding procedure. Bayesian

unfolding is based on Bayes' theorem[103,105]:

$$P(x^i|y^j) = \frac{P(y^j|x^i)P(x^i)}{P(y^j)}\,, \tag{62}$$

where $P(x^i|y^j)$ is the conditional probability of true value x^i having observed y^i, and is dependant on the conditional probability $P(y^j|x^i)$ of measuring y^j after generating x^i. The probability $P(x^i)$ is also called the "prior" and is defined as the probability of having a true spectrum x^i. The response matrix is defined as $P(y^j|x^i)$ and is estimated as the ratio of the number of measured events, y^j, and the number of true events, x^i;

$$R^{ji} = P(y^j|x^i) = \frac{y^j}{x^i}\,, \tag{63}$$

The inverted response matrix, $(R^{-1})^{ij}$, of Equation 61 is given by:

$$(R^{-1})^{ij} = P(x^i|y^j)\,. \tag{64}$$

In Equation 62, Monte Carlo simulation is used to calculate $P(x^i)$ and $P(y^j)$;

$$P(x^i) = \frac{x^i}{\sum_{i=0}^{m} x^i}, \qquad P(y^j) = \frac{y^j}{\sum_{j=0}^{n} y^j}\,. \tag{65}$$

A difficulty is recognised in that the choice of prior, $P(x^i)$, can bias the unfolded measurement of the data, x'^i. The bias can be reduced by replacing the prior with the probability $P(x'^i)$ of having an unfolded data spectrum x'^i. When this technique is applied iteratively this method is known as iterative Bayesian unfolding[106],

$$P(x'^i) = \frac{x'^i}{\sum_{i=0}^{m} x'^i}\,. \tag{66}$$

The initial prior is taken from Monte Carlo simulation. By iterating, the unfolded distribution appears less like the Monte Carlo truth and more like the data. However, this causes uncertainties on the unfolded distribution to increase with the number of iterations, because the unfolding trains to artefacts in the data. This effect is shown in Section 11 C. The full cross-section calculation, which includes the unfolding of the reconstructed data, is given and discussed in Section 12. The nominal number of Bayesian unfolding iterations used in this analysis is $n_{\text{iter.}} = 1$.

E. Acceptance, Purity and Stability

The acceptance, purity and stability quantify the effects and behaviour of event migrations. For large bins or high resolution the acceptance can be interpreted as the reconstruction efficiency. The

purity indicates how many of the reconstructed events were originally generated in a given bin. The stability shows the outward migration of events from a given bin.

The acceptance ($\mathcal{A}$), purity ($\mathcal{P}$) and stability ($\mathcal{S}$) for a given bin are defined in Equations 67, 68 and 69 respectively. Note that in this case the definition of acceptance is identically equal to the elements of the unfolding response matrix, $\mathbf{R}$. The acceptance, purity and stability are calculated from the truth and reconstruction information of MC signal events:

$$\mathcal{A} = \frac{N_{tot}^{rec}}{N_{tot}^{gen}}\,, \tag{67}$$

$$\mathcal{P} = \frac{N_{stay}^{gen}}{N_{tot}^{rec}}\,, \tag{68}$$

$$\mathcal{S} = \frac{N_{stay}^{gen}}{N_{tot}^{gen}}\,, \tag{69}$$

where N_{tot}^{rec} is the total number of reconstructed events measured in the given bin and N_{tot}^{gen} is the total number of generated events produced in the given bin. N_{stay}^{gen} is the total number of generated events in the given bin that were explicitly reconstructed in the same given bin[107].

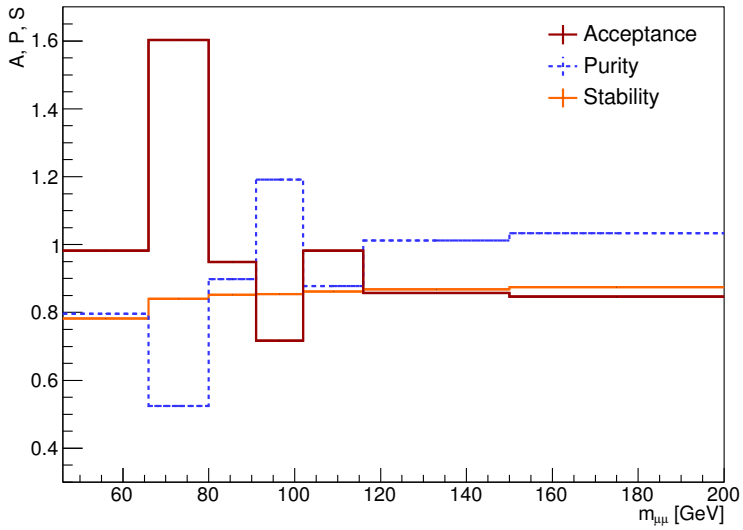

FIG. 28: The Drell–Yan signal acceptance ($\mathcal{A}$), purity ($\mathcal{P}$) and stability ($\mathcal{S}$) in the invariant mass bins of the 3D measurement. Generated events are defined at the Born truth-level. Uncertainties on the values show statistical uncertainties only.

The acceptance, purity and stability defined at the Born truth-level is shown as a function of invariant mass in Figure 28. The plot is generated exclusively from Drell–Yan signal Monte Carlo

where each event has the relevant reconstruction- and generator-level corrections and weights. The applied corrections and weights are discussed in the forthcoming sections. The figure shows a high acceptance in the $66 < m_{ll} < 80\,\text{GeV}$ invariant mass bin due to large migrations off the Z-peak where the cross-section is high, as a result of final state radiation. This is in part a similar effect to that shown in Figure 27. The purity follows an opposite behaviour to the acceptance. The purity is largest above the Z-peak ($91 < m_{ll} < 102\,\text{GeV}$) where the relative number of migrating events into the mass bin, compared to the cross-section, is smallest. The stability is shown to slightly increase over the invariant mass range.

The acceptance, purity and stability are also shown in $|y_{\mu\mu}|$ and $\cos\theta^*$ for each invariant mass bin in Figures 29-34. Large acceptance values are observed in low statistics regions (high value $|y_{\mu\mu}|$, high value $|\cos\theta^*|$). The low statistics regions have bins that do not capture any events, therefore such bins do not have a value and appear blank in the 2D plots. Large upward migrations are seen in the high rapidity regions for $102 < m_{\mu\mu} < 150\,\text{GeV}$ from detector resolution of the transverse muon-momentum. This is mitigated in the higher mass bins due to the large mass bin widths.

The purity plots confirm the conclusions of the acceptance plots: large upward migrations in large $m_{\mu\mu}$ and large $|y_{\mu\mu}|$ bins, and large migrations downward off the Z-peak due to FSR. Additionally, the dilution of the forward-backward asymmetry is observed in the $66 < m_{\mu\mu} < 80\,\text{GeV}$ mass bin. The dilution occurs from Z-peak events generated with a high cross-section at low value $|A_{FB}|$ migrating downwards due to FSR contaminating the lower mass bins where events are generated with high $|A_{FB}|$.

The stability plots show that the migrations originate from the Z-peak, $80 < m_{\mu\mu} < 102\,\text{GeV}$.

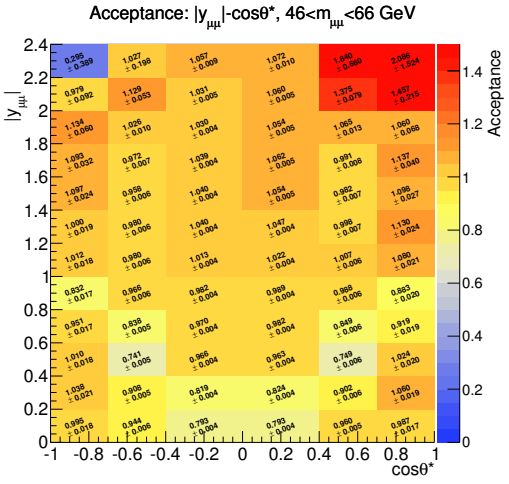

(a) Drell–Yan signal MC acceptance, $\mathcal{A}$, in the $46 < m_{\mu\mu} < 66\,\text{GeV}$ mass window.

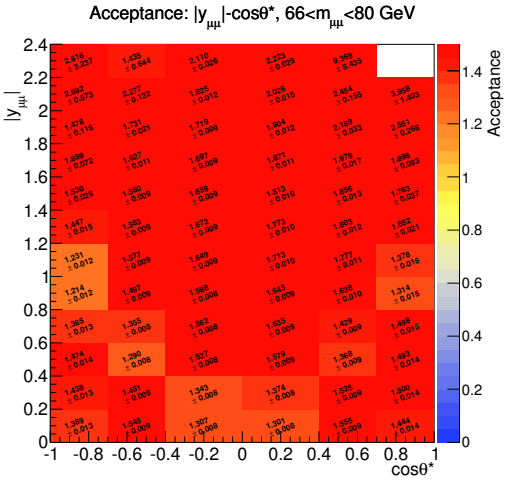

(b) Drell–Yan signal MC acceptance, $\mathcal{A}$, in the $66 < m_{\mu\mu} < 80\,\text{GeV}$ mass window.

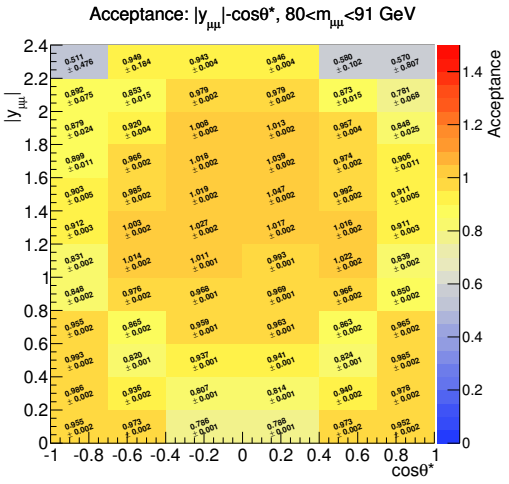

(c) Drell–Yan signal MC acceptance, $\mathcal{A}$, in the $80 < m_{\mu\mu} < 91\,\text{GeV}$ mass window.

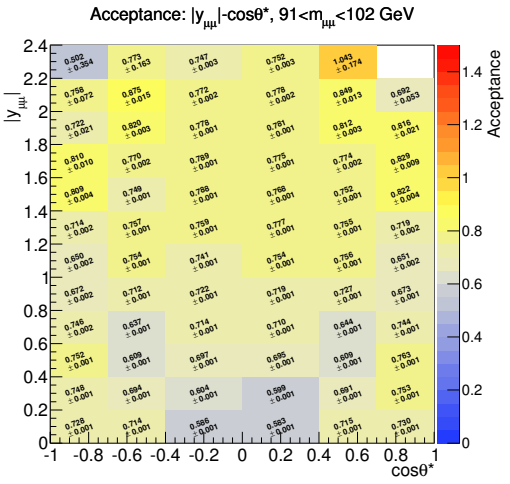

(d) Drell–Yan signal MC acceptance, $\mathcal{A}$, in the $91 < m_{\mu\mu} < 102\,\text{GeV}$ mass window.

FIG. 29: Two dimensional ($|y_{\mu\mu}|$, $\cos\theta^*$) plots of the Drell–Yan signal acceptance in the first four invariant mass windows of the measurement. Uncertainties on the values show statistical uncertainties only.

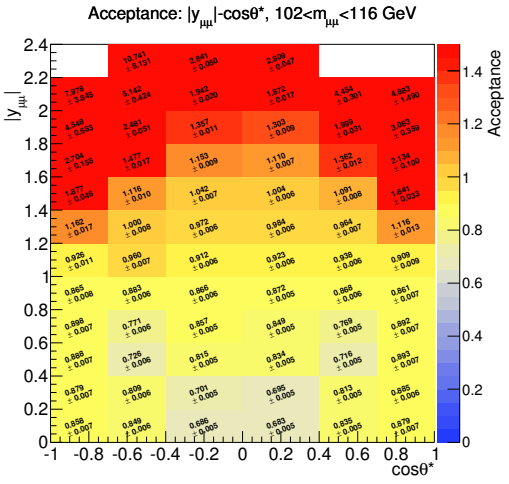

(a) Drell–Yan signal MC acceptance, $\mathcal{A}$, in the $102 < m_{\mu\mu} < 116\,\text{GeV}$ mass window.

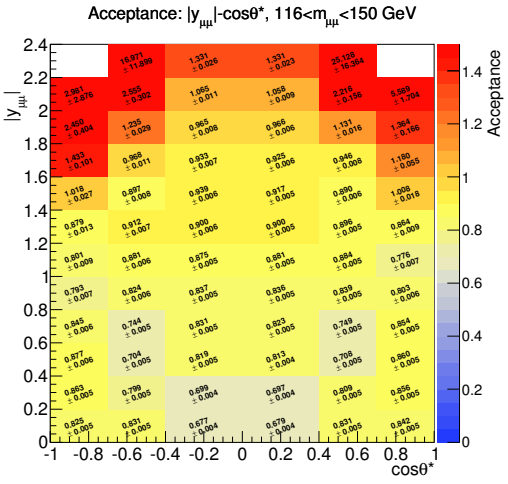

(b) Drell–Yan signal MC acceptance, $\mathcal{A}$, in the $116 < m_{\mu\mu} < 150\,\text{GeV}$ mass window.

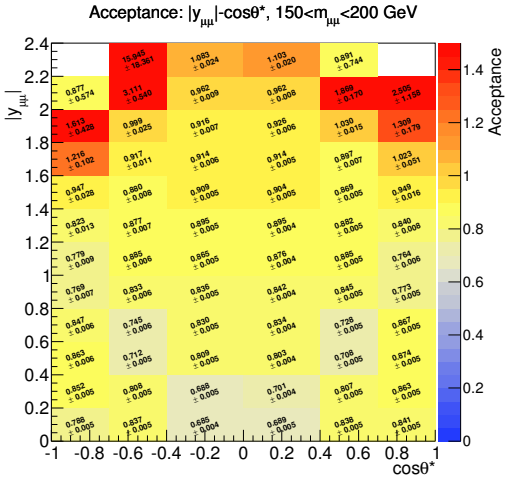

(c) Drell–Yan signal MC acceptance, $\mathcal{A}$, in the $150 < m_{\mu\mu} < 200\,\text{GeV}$ mass window.

FIG. 30: Two dimensional ($|y_{\mu\mu}|$, $\cos\theta^*$) plots of the Drell–Yan signal acceptance in the last three invariant mass windows of the measurement. Uncertainties on the values show statistical uncertainties only.

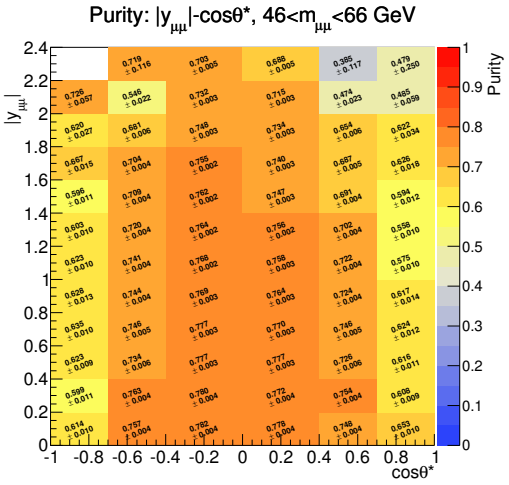

(a) Drell–Yan signal MC purity, $\mathcal{P}$, in the $46 < m_{\mu\mu} < 66\,\text{GeV}$ mass window.

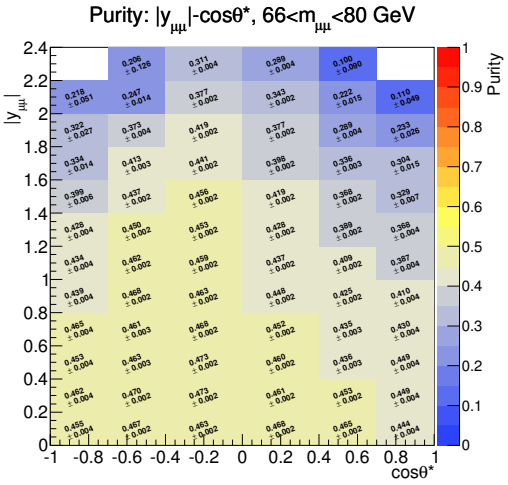

(b) Drell–Yan signal MC purity, $\mathcal{P}$, in the $66 < m_{\mu\mu} < 80\,\text{GeV}$ mass window.

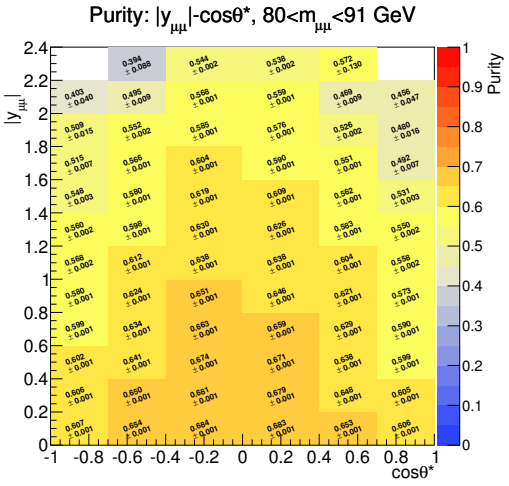

(c) Drell–Yan signal MC purity, $\mathcal{P}$, in the $80 < m_{\mu\mu} < 91\,\text{GeV}$ mass window.

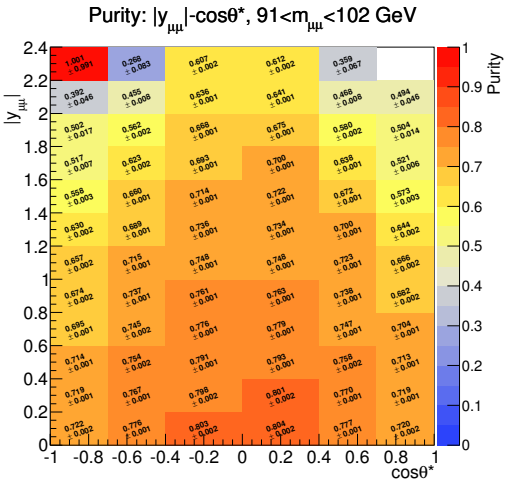

(d) Drell–Yan signal MC purity, $\mathcal{P}$, in the $91 < m_{\mu\mu} < 102\,\text{GeV}$ mass window.

FIG. 31: Two dimensional ($|y_{\mu\mu}|$, $\cos\theta^*$) plots of the Drell–Yan signal purity in the first four invariant mass windows of the measurement. Uncertainties on the values show statistical uncertainties only.

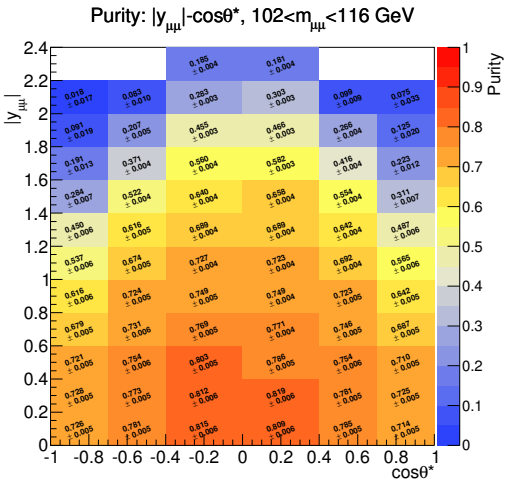

(a) Drell–Yan signal MC purity, $\mathcal{P}$, in the $102 < m_{\mu\mu} < 116\,\text{GeV}$ mass window.

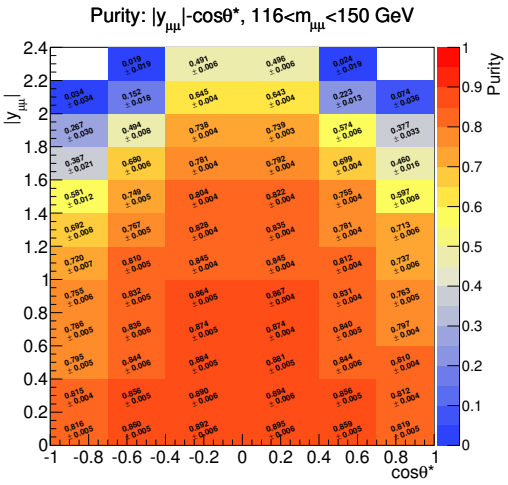

(b) Drell–Yan signal MC purity, $\mathcal{P}$, in the $116 < m_{\mu\mu} < 150\,\text{GeV}$ mass window.

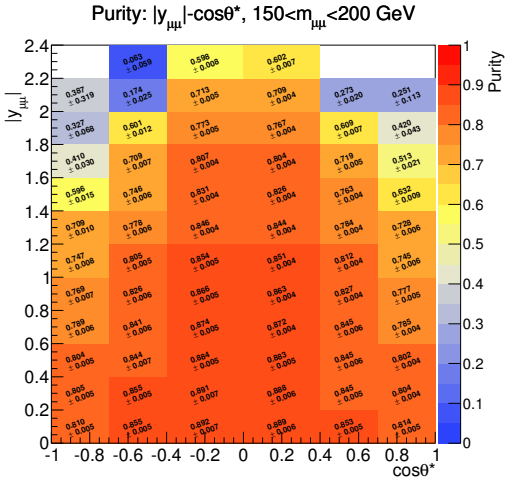

(c) Drell–Yan signal MC purity, $\mathcal{P}$, in the $150 < m_{\mu\mu} < 200\,\text{GeV}$ mass window.

FIG. 32: Two dimensional ($|y_{\mu\mu}|$, $\cos\theta^*$) plots of the Drell–Yan signal purity in the last three invariant mass windows of the measurement. Uncertainties on the values show statistical uncertainties only.

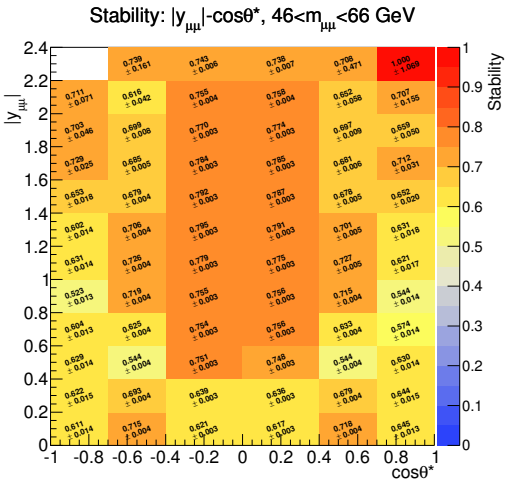

(a) Drell–Yan signal MC stability, $\mathcal{S}$, in the $46 < m_{\mu\mu} < 66\,\text{GeV}$ mass window.

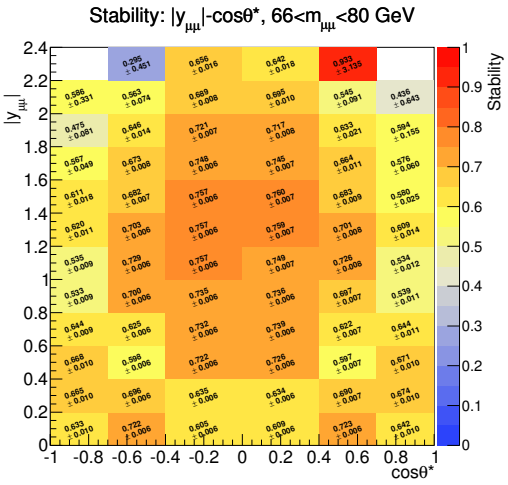

(b) Drell–Yan signal MC stability, $\mathcal{S}$, in the $66 < m_{\mu\mu} < 80\,\text{GeV}$ mass window.

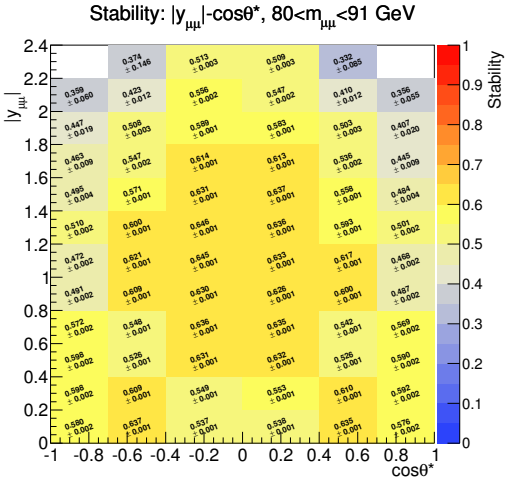

(c) Drell–Yan signal MC stability, $\mathcal{S}$, in the $80 < m_{\mu\mu} < 91\,\text{GeV}$ mass window.

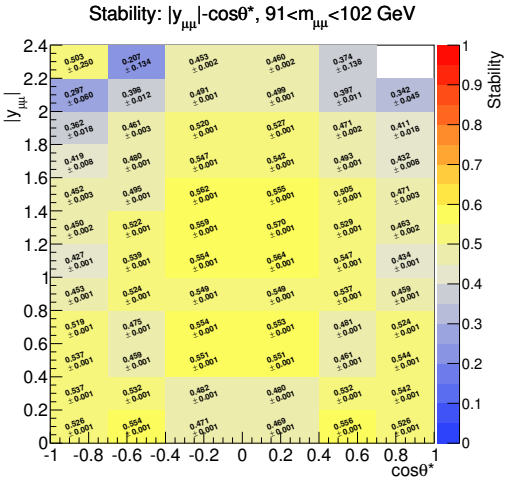

(d) Drell–Yan signal MC stability, $\mathcal{S}$, in the $91 < m_{\mu\mu} < 102\,\text{GeV}$ mass window.

FIG. 33: Two dimensional ($|y_{\mu\mu}|$, $\cos\theta^*$) plots of the Drell–Yan signal stability in the first four invariant mass windows of the measurement. Uncertainties on the values show statistical uncertainties only.

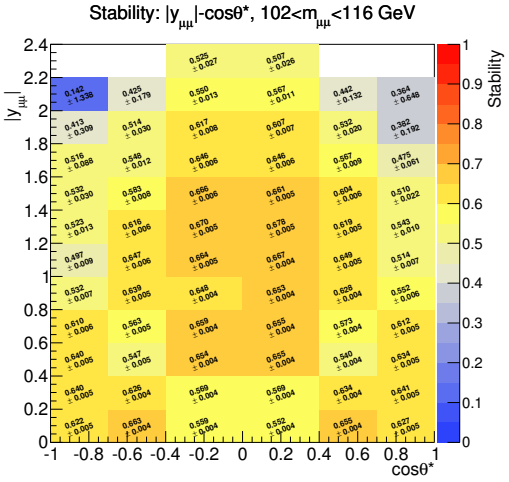

(a) Drell–Yan signal MC stability, $\mathcal{S}$, in the $102 < m_{\mu\mu} < 116\,\text{GeV}$ mass window.

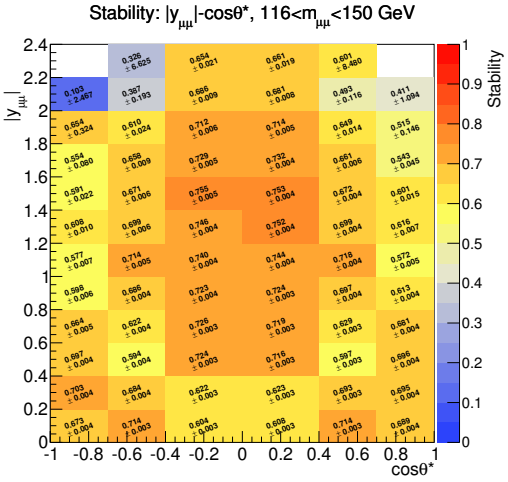

(b) Drell–Yan signal MC stability, $\mathcal{S}$, in the $116 < m_{\mu\mu} < 150\,\text{GeV}$ mass window.

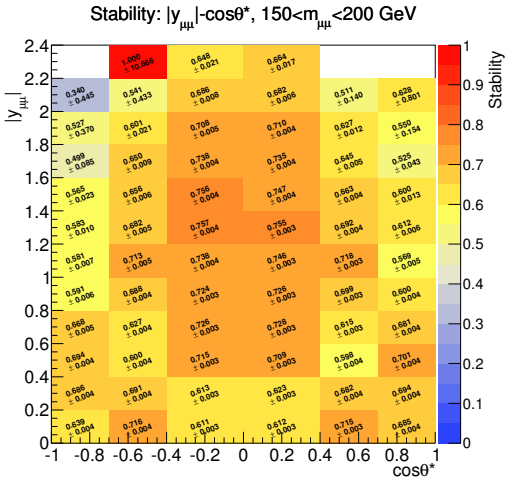

(c) Drell–Yan signal MC stability, $\mathcal{S}$, in the $150 < m_{\mu\mu} < 200\,\text{GeV}$ mass window.

FIG. 34: Two dimensional ($|y_{\mu\mu}|$, $\cos\theta^*$) plots of the Drell–Yan signal stability in the last three invariant mass windows of the measurement. Uncertainties on the values show statistical uncertainties only.

7. MONTE CARLO CORRECTIONS

To achieve the most accurate unfolding all resolutions and efficiencies in MC should be the same as in data. MC is therefore corrected to match data. Additional corrections are applied to MC for underlying physics effects and data-taking conditions.

A. Generator-Level Weights

To be compared to data, each MC simulation sample must be normalised to the luminosity and the underlying physics. This is achieved by assigning weights to each event for every MC sample. The following sections define the individual weights applied in this analysis.

Weights applied to generator-level quantities are defined as the generator-level weights. Where an approved Standard Model Working Group (SMWG) package has been used its name is given along with the package version.

Monte Carlo Generator Weights

Next-to-leading order in QCD MC generators use dedicated generator weights, g_{mc}, to avoid double-counting of NLO effects in the hadronisation model. Next-to-leading order in QCD MC samples used in this thesis have generator weights of $g_{\text{mc}} = \pm 1$ for each event. Leading order in QCD MC samples used in this thesis have generator weights of $g_{\text{mc}} = 1$ for each event.

Luminosity Normalisation

Monte Carlo samples must be normalised to the integrated luminosity of the data. The luminosity normalisation of a MC sample is dependent on the sample cross-section, σ; the sum of generator event weights in the sample, $\sum g_{\text{mc}}$; the filter efficiency of the sample, ϵ^{filter}; and the integrated luminosity of the data it is to be normalised against, $\mathcal{L}_{\text{data}}$. The luminosity weighting of each sample is given by:

$$w_{\mathcal{L}} = \frac{\mathcal{L}_{\text{data}}}{\mathcal{L}_{\text{MC}}} = \frac{\sigma \epsilon^{\text{filter}}}{\sum g_{\text{mc}}} \mathcal{L}_{\text{data}} \,. \tag{70}$$

Figure 35a shows the effect of luminosity weighting upon DY signal MC events. The top panel shows the unweighted MC sample mass distributions in stacked histograms revealing the difference in numbers of events in each MC sample. The bottom panel shows the luminosity weighted samples in histogram stacks, where the total sum shows continuity across MC sample edges for all except the lowest mass sample.

The dimuon filtered signal MC sample in the $8 < m_{\mu\mu} < 20\,\text{GeV}$ region is included to quantify upward migration of reconstructed events into the fiducial volume from low values of $m_{\mu\mu}$. 6.89 ± 0.78 reconstructed events pass the selection criteria, which is not significant. Therefore the production of single- and zero-muon signal MC samples in that region was not deemed necessary.

Monte Carlo K-factors

Monte Carlo K-factors improve the generated cross-section prediction of a sample by reweighting to a more precise prediction. The K-factors applied to the Drell–Yan MC are calculated as a ratio of the best available theory calculation over the MC generator cross-sections. The theoretical calculations are performed at NNLO in perturbative QCD including additive missing higher-order (HO) EW corrections using the `FEWZ-3.1.b2` program package[108–110]. The missing HO EW corrections include weak loop effects, QED initial state radiation and interference terms arising from ISR and FSR. The corrections are adapted to MC that simulates QED ISR and FSR via `PHOTOS`[81]. The NNLO PDF set used is `MSTW2008NNLO`[111].

A K-factor scaling of 0.7 is applied to the photon-induced (PI) process to match NLO calculations of `SANC`[87,88]. The theoretical part of the $t\bar{t}$ K-factor is obtained from `Top++2.0` NNLO in QCD calculations using a top-quark mass of 172.5 GeV and including resummation of next-to-next-to-leading logarithmic soft-gluon terms[93–98]. The single top-quark K-factor was produced with included soft-gluon resummation at next-to-next-to-leading logarithm accuracy[99]. Diboson cross-section calculations were performed at NLO with `MCFM`[90,91] using the CT10 PDF. Finally, $W \to \ell\bar{\nu}$ production theory calculations are performed with `FEWZ-NNLO`.

The MC K-factors are applied as generator-level weights to each event in the MC samples. The mass dependent DY MC K-factors used in the analysis is shown in Figure 35b. They are shown to deviate from unity by 4.0%-2.0% across the $m_{\mu\mu}$ range.

Z Mass Lineshape Corrections

The Powheg-Pythia simulation is reweighted to improve the Born-level description of the lineshape. The Z lineshape is described in the nominal signal MC with a fixed width following the modified minimal subtraction ($\overline{MS}$) scheme[112–114], whereas an improved description is achieved using a running width, based on renormalisation group evolution equations (RGEs)[115–117]. The ATLAS SMWG provides the lineshape reweighting tool for this purpose. The lineshape tool used is listed in Table 38. The effect of the lineshape correction is shown in Figure 36a.

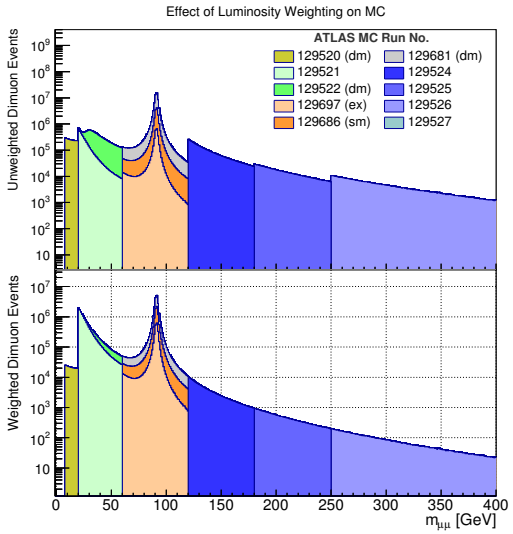

(a) The effect of luminosity weighting upon the invariant mass, $m_{\mu\mu}$, binned DY signal MC samples. The top panel shows the unweighted $m_{\mu\mu}$ distributions and the bottom panel shows the luminosity weighted samples.

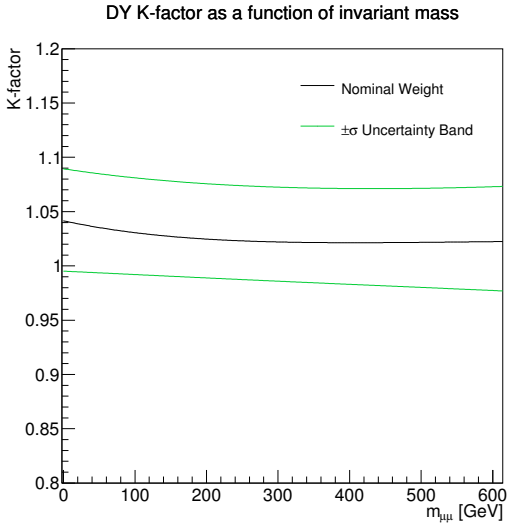

(b) The functional form of the invariant mass, $m_{\mu\mu}$, dependent K-factors applied to the Drell–Yan MC. The green curves show the ± 1 standard deviation band associated to the uncertainty on the determination of K-factors.

FIG. 35: Luminosity weighting and K-factor cross-section correction applied at the truth-level to MC simulation. Histogram error bars are statistical.

Event Primary Vertex Corrections

Monte Carlo simulation of event primary vertices has a mis-modelling with respect to the z-axial displacement. To bring the primary vertex z-axial displacement (z_{PV}) distribution of the Drell–Yan MC in-line with observed data, truth-level primary vertex corrections are applied. These corrections come in the form of a per-event reweighting of the truth z_{PV} distribution to on-peak $Z \to e\bar{e}$ data samples. A tool for the reweighting was provided by the ATLAS SMWG group and is listed in Table 38. The effect of this correction is shown in Figure 36b.

Pile-up Corrections

A correction is made to the MC to account for the increased level of in-time pile-up observed during data taking in the ATLAS detector. A tool was used to correct the average number of interactions per bunch crossing, $\langle\mu\rangle$, in MC by reweighting to the data. However, to maintain an accurate description of the number of event interaction vertices a global $\langle\mu\rangle$ scaling of 1.09 is applied,

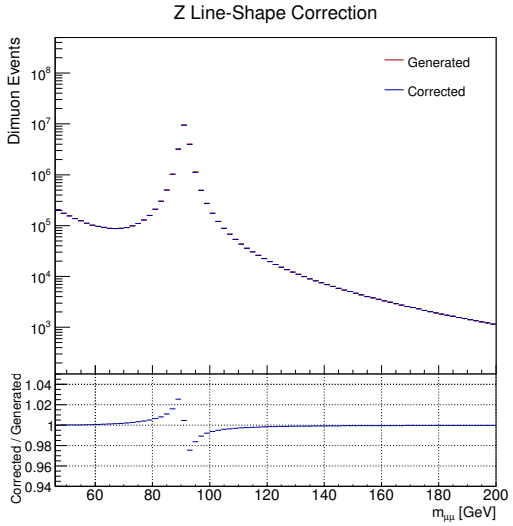

(a) The invariant mass, $m_{\mu\mu}$, dependent lineshape correction for the Z-boson modelling applied to the Drell–Yan signal MC. The top panel shows the nominal lineshape generated in MC and the corrected running-width lineshape. The bottom panel shows the ratio of the corrected and generated lineshapes.

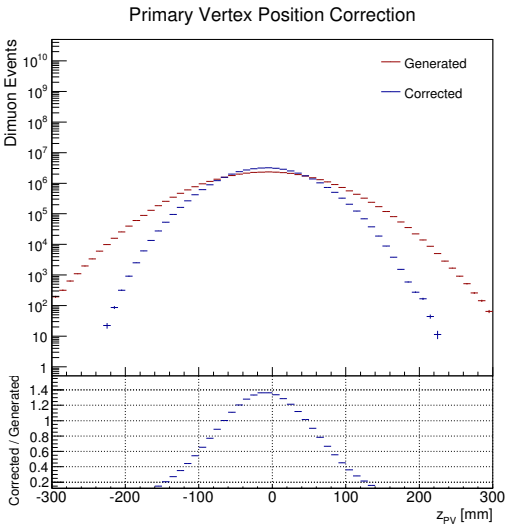

(b) The Z-boson vertex position correction applied to the Drell–Yan signal MC. The top panel shows the generated vertex positions generated in MC and the corrected vertex positions. The bottom panel shows the ratio of the generated and the corrected vertex positions.

FIG. 36: Lineshape and vertex position corrections applied at the truth-level to MC simulation. Histogram error bars are statistical.

as recommended by the SMWG. The effect of this correction is shown in Figures 37a and 37b. Here, the description of the low tail-end of the $\langle\mu\rangle$ distribution is shown to improve along with the lower and central regions of the number of vertices per bunch crossing, N_{Vtx}, distribution.

B. Reconstruction Level Corrections

Updated geometry data sets and calibration analyses performed after data taking result in an improved description of the ATLAS detector. This information is used to improve the simulated detector response in MC.

Corrections to reconstructed quantities are applied at the reconstruction-level only. The following sections define the reconstruction-level weights applied in this analysis.

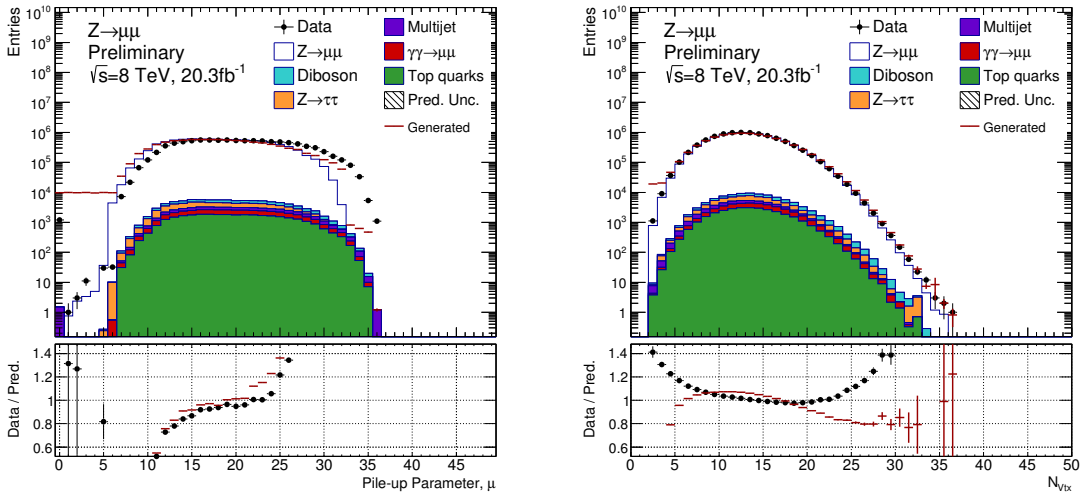

(a) Effect of pile-up weighting upon the reconstructed MC description of the average number of interactions per bunch crossing, $\langle\mu\rangle$.

(b) Effect of pile-up weighting upon the reconstructed MC description of the number of vertices per bunch crossing, N_{Vtx}.

FIG. 37: Reconstruction effects of the pile-up reweighting correction and global $\langle\mu\rangle$ scaling applied at the truth-level to MC simulation. Reconstructed MC and data are shown after applying the full event selection criteria. The uncorrected MC is given by the red line while the corrected is given by the stacked MC histograms and data points are in black. Histogram error bars in the figures include statistical uncertainties only. The bottom panels show the agreements between data and MC with uncorrected and corrected MC.

Muon Combined Performance Corrections

Corrections are applied to the MC at reconstruction level to account for imperfect modelling of muon reconstruction, muon momentum resolution and muon momentum scale. The muon reconstruction efficiencies were determined by the muon combined performance (MCP) group using tag-and-probe methods[68]. The MCP group packages used by the measurement are listed in Table 38.

The tag-and-probe method uses two muons from the decay of the same particle (tupically the Z or the J/ψ) to determine the efficiency of a set of selection criteria. One muon is defined as the "tag", which follows tight selections to ensure the purity of the sample, and the other as the "probe" to test the individual muon efficiency. Both muons are tested for being the tag and the probe to avoid systematic biases. The tag-and-probe method is performed on both data and MC allowing a scale-factor to be determined from their ratio. The scale-factor can then be used as a correction weight.

The effect of muon momentum corrections is shown in Figures 38a and 38b. The corrected muon momenta show an average increase in the number of high-p_T^μ muons found. This affects the resolution of the reconstructed Z-peak, where a better agreement between data and MC is seen for the broader, corrected MC distribution. The average reconstruction efficiency correction is shown for leading muon p_T^μ in Figure 39a. The average reconstruction correction is shown to be $< 0.1\%$ across the p_T^μ range. The shaded region shows the systematic uncertainty band of the reconstruction efficiency corrections. The last bin shows a large systematic uncertainty, however the contribution to the final cross-section is deemed small, as < 10 events occupy this bin.

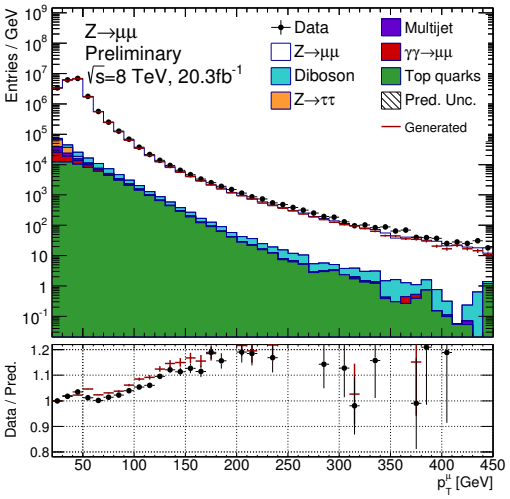

(a) The effect of muon momentum smearing upon the reconstructed MC description of the muon p_T^μ. The uncorrected muon p_T^μ in MC is given by the red line, corrected by the stacked MC histograms and data points in black.

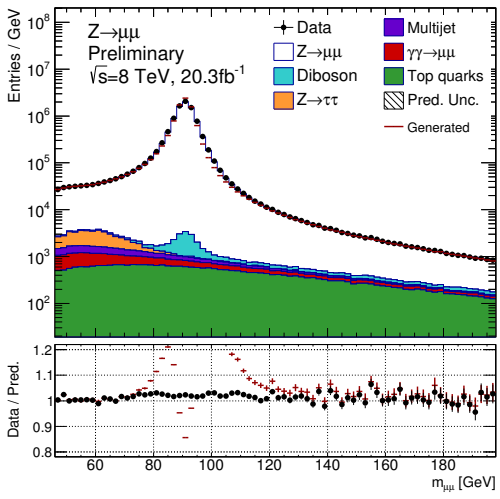

(b) The effect of muon momentum smearing upon the reconstructed MC description of the invariant mass, $m_{\mu\mu}$. The uncorrected $m_{\mu\mu}$ in MC is given by the red line, corrected by the stacked MC histograms and data points in black.

FIG. 38: Reconstruction-level effects of applying the muon momentum smearing to ID muon p_T^μ. Reconstructed MC and data are shown after applying the full event selection criteria. Histogram error bars in the figures include statistical uncertainties only. The bottom panels show the agreement between data and MC for uncorrected MC (blue) and corrected MC (red).

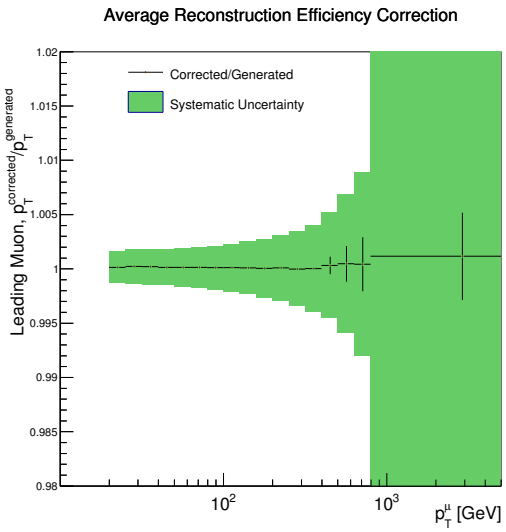

(a) The average leading-muon reconstruction efficiency correction as a function of leading-muon transverse momentum.

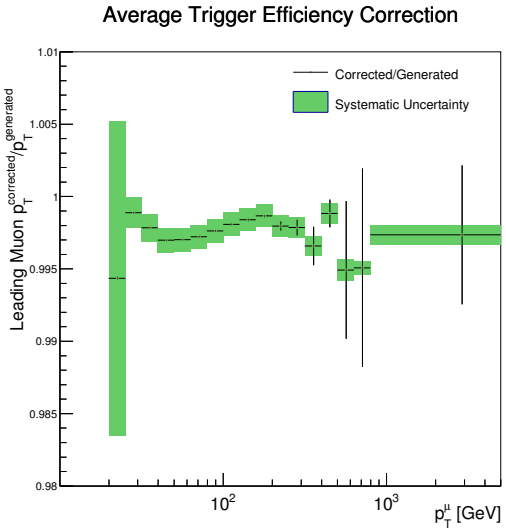

(b) The average muon trigger efficiency correction as a function of leading-muon transverse momentum.

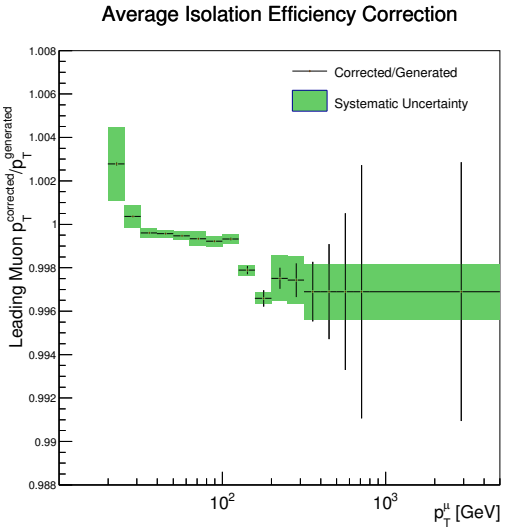

(c) The average leading-muon isolation efficiency correction as a function of leading-muon transverse momentum.

FIG. 39: The average reconstruction, isolation and trigger efficiency corrections used in the analysis as a function of Drell–Yan signal MC leading muon p_T^{μ}. The average correction is shown as a ratio of the corrected leading-muon p_T^{μ} spectra to the generated (uncorrected) spectra. Error bars on the data points show the DY MC statistical uncertainties only. The green uncertainty band shows the $\pm\sigma$ shifted correlated uncertainties of the corrections.

Trigger Efficiency Corrections

Two sets of trigger efficiency corrections are used in this analysis: a high precision set determined in the measurement of the high mass Drell–Yan cross-section[33] and a set that extends the trigger efficiency coverage to the low mass regime. The low mass muon trigger efficiencies were determined by the muon trigger signature (MTS) group through tag-and-probe methods and is well documented[68,118]. The high precision trigger efficiencies were produced as a dedicated and precise set of efficiencies that do not rely on calibration associated to the J/ψ resonances.

For the ease of error propagation the two sets are used in independent p_T^μ regions: muons with $p_T^\mu < 25\,\text{GeV}$ receive trigger efficiency corrections according to the MTS efficiency set; muons with $p_T^\mu > 25\,\text{GeV}$ receive trigger efficiency corrections according to the high precision set.

A brief description of the method used to determine the high precision trigger efficiency corrections follows below for quick reference.. The full description with associated efficiency plots, maps and studies can be found in an ATLAS thesis documenting a measurement of the High Mass Drell–Yan cross-section, by Robert Hickling[119] The following work was not produced by this thesis' author.

The independent set was determined via tag-and-probe using the following conditions for the tag:

- MCP `medium+` defined third-chain muon
- $p_T^\mu > 25\,\text{GeV}$
- $|z_{PV}| < 3\,\text{mm}$
- $I_\mu < 0.1$
- MCP quality criteria
- ΔR match between tag muon and trigger muon from either `EF_mu24i_tight` or `EF_mu36_tight`

For the probe:

- MCP `medium+` defined third-chain muon
- $p_T^\mu > 20\,\text{GeV}$
- $I_\mu < 0.1$
- MCP quality criteria

For the combined tag-and-probe system:

- $|\Delta d_{PV}\,(\text{tag, probe})| < 10\,\text{mm}$
- $|\Delta z_{PV}\,(\text{tag, probe})| < 20\,\text{mm}$
- $\Delta m_Z = |m_Z - m(\text{tag, probe})| < 10\,\text{GeV}$

where d_{PV} is the radial displacement of the closest point of approach of the muon track from the primary vertex location and the PDG value of the Z boson mass[46] is $m_Z = 91.1876 \pm 0.0021\,\text{GeV}$.

Drell–Yan signal MC was compared to background subtracted data where the background was determined from MC and a QCD multijet component estimated from the modified ABCD method, similar to that described in Section 9. Due to the varying subsystem performance in the ATLAS detector the efficiency set was parametrised in η and ϕ with an additional parameter accounting for a residual p_T^μ dependence. An additional muon charge dependence was included due to gaps in specific η-ϕ regions because of faulty and/or non-installed chambers and effects from the toroidal magnetic field towards the edges of the muon η acceptance.

The systematic uncertainties were derived from three components, a background contamination systematic, an event topology systematic and a residual p_T^μ dependence systematic. The background contamination systematic was calculated by shifting the requirements on the tag muon p_T^μ by $\pm 10\%$, the tag and probe muon isolation by $\pm 10\%$ and the tag and probe Δm_Z by $\pm 50\%$. The topological systematic was derived from the effect of placing a constraint upon the absolute difference in ϕ between the tag and probe of $||\Delta\phi| - \pi| > 0.1$. The p_T^μ dependence systematic was taken from the p_T^μ deviation after re-applying the generated trigger efficiencies back to the probe muon. The high precision muon trigger efficiencies were approved for use by the MTS group.

The low mass muon trigger efficiency corrections have an average precision of 0.5% in the $46 < m_{\mu\mu} < 66\,\text{GeV}$ region. The high precision set have an average precision of 0.1% in the $66 < m_{\mu\mu} < 200\,\text{GeV}$ region.

The average trigger efficiency correction as a function of leading muon p_T^μ is shown in Figure 39b. The average correction is below unity showing that the trigger efficiencies are higher in the generated MC than observed in data. The largest correction is seen at $p_T^\mu \simeq 20\,\text{GeV}$, the p_T^μ region of the dimuon trigger. The low p_T^μ region of the dimuon trigger was previously observed to require larger efficiency corrections than the single muon triggers and was also reported to have small residual dependencies on p_T^μ and the number of pile-up events in the end-cap region[118].

Isolation and Impact Parameter Efficiency Corrections

In this analysis isolation and impact parameter criteria are used to suppress both the QCD multijet background and backgrounds with muons originating from quark decays. This necessitates an accurate description of the isolation and impact parameter selection criteria efficiencies. Isolation and impact parameter efficiency corrections were previously determined in the muon channel for the ATLAS high mass Drell–Yan analysis[33]. A detailed description of the efficiency correction derivation can be found in an ATLAS thesis documenting a measurement of the High Mass Drell–Yan cross-section, by Robert Hickling[119]. A brief description is provided below for quick reference. The following work was not produced by this thesis' author.

The isolation and impact parameter efficiency corrections were determined via the tag-and-probe method. The loose impact parameter criterion was included in the isolation definition to provide a single, simple set of efficiencies.

The tag-and-probe was performed using the following conditions for the tag:

- MCP `medium+` defined third-chain muon
- $p_T^\mu > 25\,\text{GeV}$
- $|z_{PV}| < 3\,\text{mm}$
- $I_\mu < 0.1$
- MCP quality criteria

For the probe muon:

- MCP `medium+` defined third-chain muon
- $p_T^\mu > 20\,\text{GeV}$
- MCP quality criteria

For the combined tag-and-probe system:

- $\Delta m_Z = |m_Z - m(\text{tag}, \text{probe})| < 10\,\text{GeV}$

where m_Z is the PDG value of the Z boson[46]. Signal Drell–Yan MC was compared to background subtracted data where the background was determined from MC and a QCD multijet component estimated with the modified ABCD method, similar to that described in Section 9. The efficiency corrections were parametrised in p_T^μ due the strong efficiency dependence with p_T^μ. Although a limited dependence in η was observed a systematic uncertainty of 0.017% was assigned to cover this dependence.

The background contamination systematic uncertainty was evaluated by modifying the tag-and-probe conditions and taking the difference:

- Tag $I_\mu < 0.26$
- Tag $p_T^\mu > 40\,\text{GeV}$
- Combined $\Delta m_Z = |m_Z - m(\text{tag}, \text{probe})| < 15\,\text{GeV}$

The topological systematic was evaluated in the same manner by restricting the acoplanarity of the tag-and-probe system by $||\Delta\phi| - \pi| < 2.0$. The weak η dependence was factored in as a systematic

uncertainty by calculating the average efficiency correction across the η range and averaging the deviation in each bin with respect to the average efficiency correction.

The average isolation efficiency corrections are shown in Figure 39c. The average correction is shown to be very close to unity. The non-isolated dimuon trigger is clearly seen in the first and second data-points due to their deviation and larger systematic uncertainty bands.

List of Official Packages

A list of software packages used in this analysis is provided in the appendix in Table 38. The ID muon sagitta corrections are detailed in the next section.

8. INNER DETECTOR SAGITTA CORRECTIONS

A. Combined Muons and Explicit Use of Inner Detector p_T^μ

Combined Muon p_T^μ

In this measurement third-chain authored muons are used and studied, as previously discussed in Section 3. The standard recommendation from the ATLAS muon combined performance (MCP) group is to use the combined (MS & ID) third-chain muon kinematics.

The MCP group gives additional recommendations for selecting muons of good quality (`medium+` and MCP quality criteria in Section 6 A). However, it was observed that when applying the full selection and using combined muons the data description of the forward-backward asymmetry was poorly described. Figure 40 shows the observed discrepancy between data and MC.

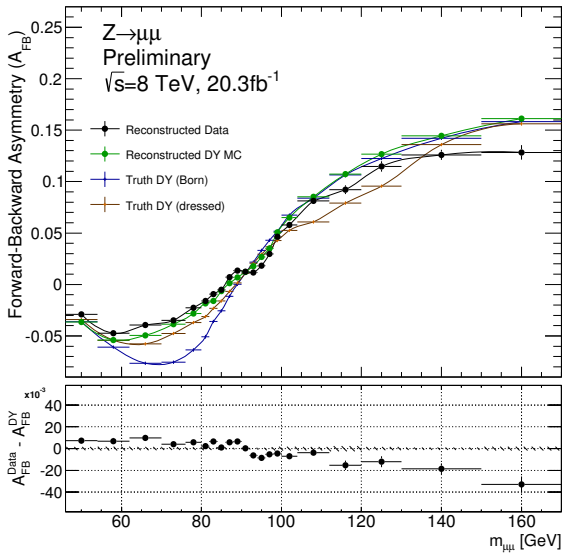

FIG. 40: Forward-backward asymmetry as a function of $m_{\mu\mu}$ for the predictions of two truth-levels (Born and dressed) calculated from the signal MC, and non-unfolded results from reconstructed signal MC and background-subtracted data. The bottom panel displays the difference between reconstructed MC DY signal, $A_{FB}^{\rm DY}$, and reconstructed background-subtracted data, $A_{FB}^{\rm data}$. A smooth curve is displayed between points for clarity. Error bars show statistical uncertainties only.

In Figure 40 Born and dressed truth-level events pass fiducial volume criteria, and reconstructed DY and data pass the event selection criteria while using combined muon p_T^μ. Events are corrected as discussed in the previous section. The bottom panel shows the difference between the distributions

of the background-subtracted data and Drell–Yan MC: $A_{FB}^{\text{data}} - A_{FB}^{\text{DY}}$. The figure shows A_{FB} dilution at low invariant mass values in the dressed truth-level and reconstruction-level distributions when compared to the Born truth-level. The dilution is caused by FSR migrating events off the Z-peak, where they are generated with low $|A_{FB}|$ values, into regions where events are generated with higher $|A_{FB}|$ values. This effect is enhanced by the rapidly falling cross-section either side of the Z-peak. Clearly observed in the data trace (black) is the asymmetric inflection about the Z-peak, not consistent with the truth-level A_{FB} predictions.

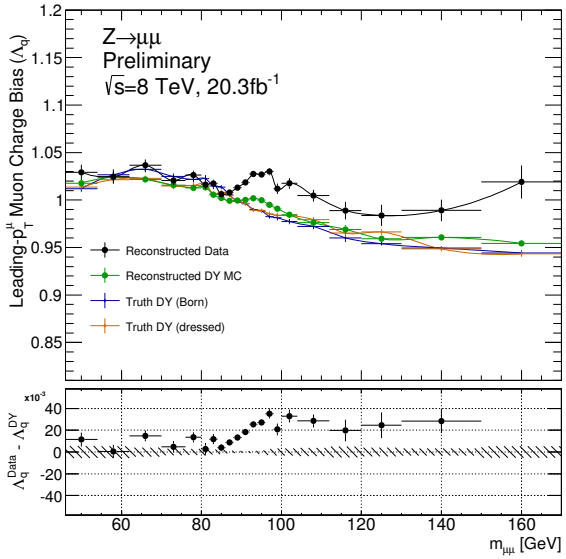

FIG. 41: The leading-p_T^μ muon charge bias as a function of $m_{\mu\mu}$ for the predictions of two truth-levels (Born and dressed) calculated from the signal MC, and non-unfolded results from reconstructed DY signal MC and background-subtracted data. The bottom panel displays the difference between reconstructed MC DY signal Λ_q^{DY} and reconstructed background-subtracted data Λ_q^{data}. A smooth curve is displayed between points for clarity. Error bars show statistical uncertainties only.

The measurement of A_{FB} has a strong dependence on muon transverse momentum and charge through the definition of $\cos\theta^*$. A new variable was introduced to test the charge-dependent muon momentum scale measured in the ATLAS detector. The leading-p_T^μ muon charge bias, Λ_q, is defined:

$$\Lambda_q = \frac{N(p_T^+ > p_T^-)}{N(p_T^- > p_T^+)}\,. \tag{71}$$

where $N(p_T^+ > p_T^-)$ is the number of events satisfying the requirement that the muon with highest p_T^μ in the event is of positive charge, and $N(p_T^- > p_T^+)$ the number of events satisfying the requirement that the muon with highest p_T^μ in the event is of negative charge. In Drell–Yan events this

quantity directly gives information on whether muons of a particular charge are more likely to be reconstructed with a higher momentum.

The leading-p_T^μ muon charge-bias was found to be poorly described. Figure 41 shows the Λ_q distributions. The MC truth-level distributions show the underlying influence of A_{FB} as a function of $m_{\mu\mu}$ in their deviation from unity either side of the Z-peak. The reconstruction-level MC shows a small percent-level deviation about the Z-peak, however a much larger background-subtracted data deviation continues up to high $m_{\mu\mu}$ values. These deviations occur at similar $m_{\mu\mu}$ values to the A_{FB} inflection, and directly show that positively-charged muons are more likely to be reconstructed with a higher transverse momentum than negatively-charged muons.

The poor A_{FB} and Λ_q descriptions were found to be amplified when looking at specific regions within the ATLAS detector when requiring both muons to be within a given pseudo-rapidity region. When decomposed in detector component η-regions, i.e. barrel and end-caps, the most notable charge dependent discrepancies were observed in the negative η hemisphere end-cap, shown in Figure 42a and 42b. In this region positively charged muons are much more likely to be reconstructed with a higher p_T^μ than negatively charged muons. This results in the distortion of the A_{FB} distributions. This effect is not accounted for in the reconstruction simulation of the Drell–Yan MC.

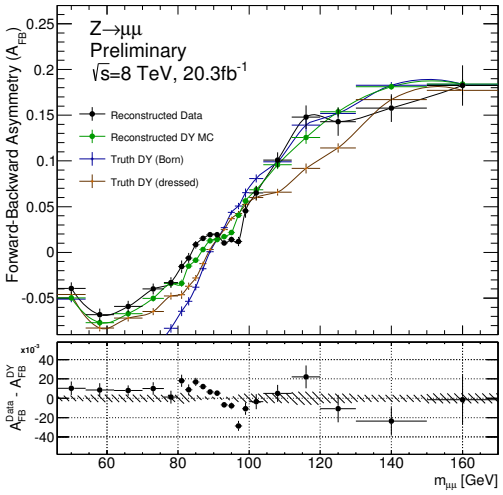

(a) A_{FB} distributions, in the -η hemisphere end-cap, $-2.4 < \eta < -1.05$, using combined muon (ID & MS) p_T^{μ}.

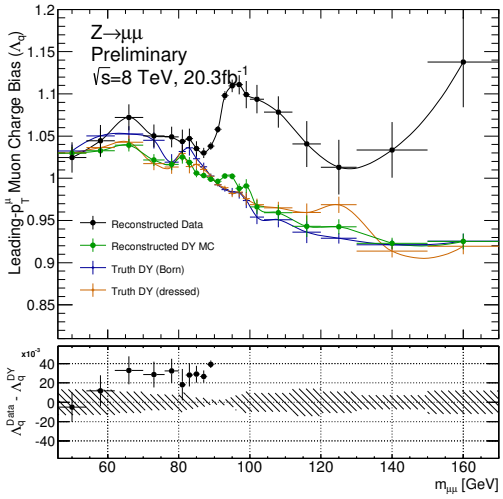

(b) Λ_q distributions, in the -η hemisphere end-cap, $-2.4 < \eta < -1.05$, using combined muon (ID & MS) p_T^{μ}.

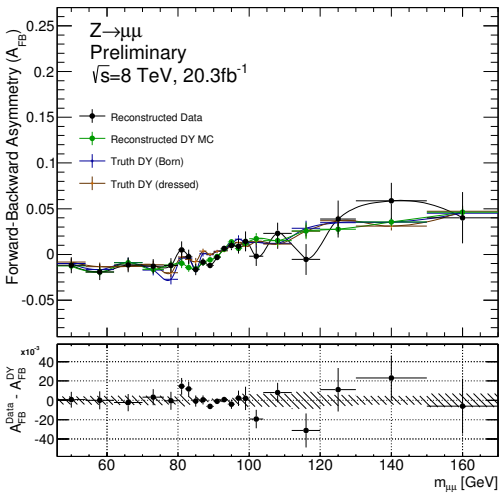

(c) A_{FB} distributions, in the -η barrel hemisphere, $-1.05 < \eta < 0.0$, using combined muon (ID & MS) p_T^{μ}.

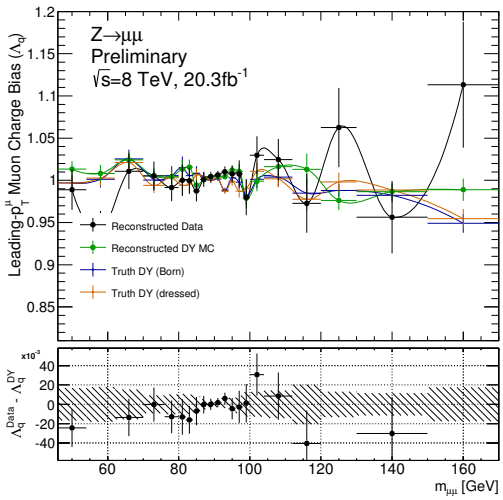

(d) Λ_q distributions, in the -η barrel hemisphere, $-1.05 < \eta < 0.0$, using combined muon (ID & MS) p_T^{μ}.

FIG. 42: Plots of the forward-backward asymmetry and the leading-p_T^{μ} muon charge bias decomposed into different regions of the ATLAS detector. Both muons are required to pass the η condition and the muon kinematics are derived from the combined (ID & MS) information. The bottom panels display the difference between reconstructed MC DY signal and reconstructed background-subtracted data. A smooth curve is displayed between points for clarity. Error bars show statistical uncertainties only.

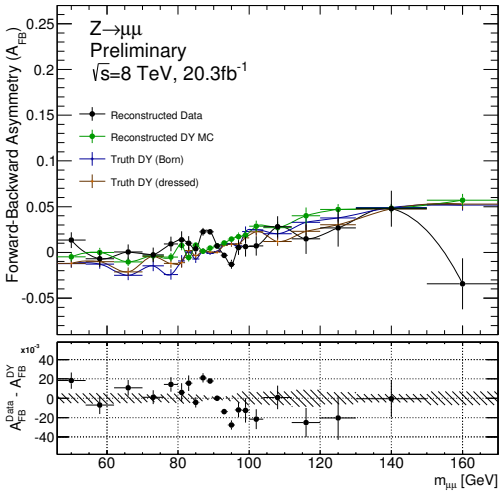

(a) A_{FB} distributions, in the $+\eta$ barrel hemisphere, $0.0 < \eta < 1.05$, using combined muon (ID & MS) p_T^{μ}.

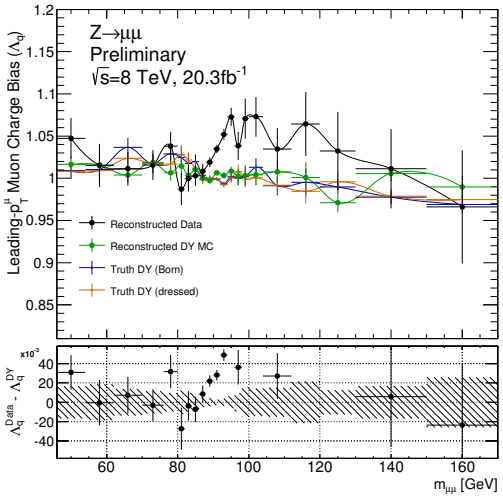

(b) Λ_q distributions, in the $+\eta$ barrel hemisphere, $0.0 < \eta < 1.05$, using combined muon (ID & MS) p_T^{μ}.

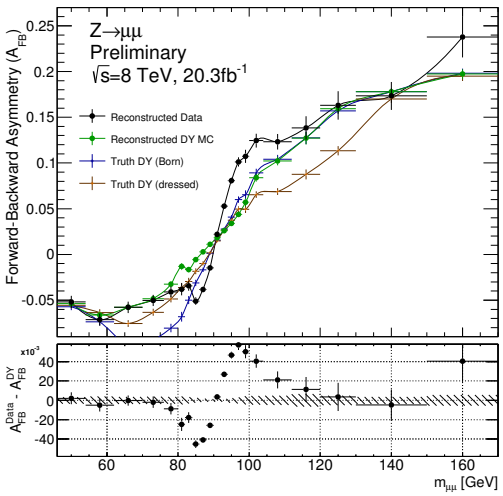

(c) A_{FB} distributions, in the $+\eta$ hemisphere end-cap, $1.05 < \eta < 2.4$, using combined muon (ID & MS) p_T^{μ}.

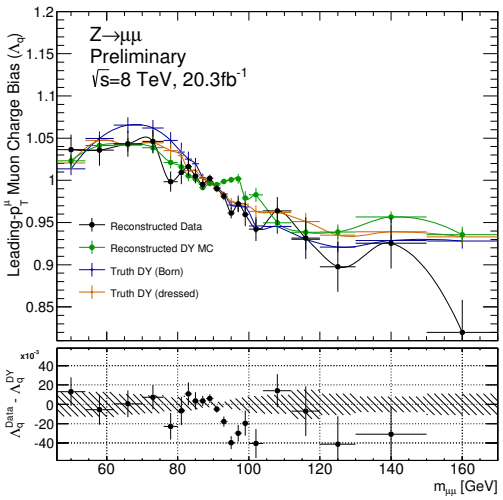

(d) Λ_q distributions, in the $+\eta$ hemisphere end-cap, $1.05 < \eta < 2.4$, using combined muon (ID & MS) p_T^{μ}.

FIG. 43: Plots of the forward-backward asymmetry and the leading-p_T^{μ} muon charge bias decomposed into different regions of the ATLAS detector. Both muons are required to pass the η condition and the muon kinematics are derived from the combined (ID & MS) information. The bottom panels display the difference between reconstructed MC DY signal and reconstructed background-subtracted data. A smooth curve is displayed between points for clarity. Error bars show statistical uncertainties only.

Inner Detector Based p_T^μ

The poor A_{FB} agreement seen in Figure 40 has been observed in ATLAS $\sqrt{s} = 7\,\text{TeV}$ analyses of Z-boson transverse momentum distributions[120] and precision measurements of the W-mass[121]. The inflection observed in the ratio of Figure 43c is of an opposite sign to the inflection observed in Figure 42a. This anti-symmetry is consistent with a global mis-alignment of the muon spectrometer position with respect to the inner detector resulting in charge dependent p_T^μ reconstruction discrepancies. The MS mis-alignment effects are overcome by using only the inner detector component of the combined muon transverse momentum for both ATLAS data and reconstructed MC. All other combined muon information (η_μ, ϕ_μ, θ_μ, etc.) are still used, but quantities dependent on p_T^μ, such as the dimuon invariant mass, are recalculated for ID based p_T^μ.

The effect of exclusively using inner detector based p_T^μ is shown in the A_{FB} and Λ_q distributions of Figures 44 and 45 decomposed in detector component η-regions. The -η hemisphere end-cap shows an improvement in the data Λ_q distribution from the 12% deviation between data and MC observed in Figure 42b to 5% observed in Figure 44b. Also seen is an induced deviation away from the truth-level predictions of the reconstructed MC in this region. Additionally, Figure 44a shows the reconstructed MC deviates significantly in the forward-backward asymmetry about 90 GeV. This reconstruction effect is discussed in the next subsection. The A_{FB} data agrees well with the truth predictions. The barrel region shows improved reconstructed agreement between data and MC in both $\pm\eta$ hemispheres. Notably the data inflections about the Z-peak in Figures 43a and 43c are removed when using ID based p_T^μ as shown in Figures 45a and 45c. Although ID based p_T^μ generally shows significant improvements, the inconsistencies in A_{FB} and Λ_q highlight further discrepancies between reconstruction in data and MC.

Inner detector transverse momenta are more susceptible to charge dependent momentum effects from inner detector displacements. Such displacements may occur from curl distortion of ID modules, linear twisting of the ID structure and global ID $\hat{z}$-axial offset. The test of a systematic ID $\hat{z}$-axial offset is performed by measuring the central value and RMS-width of the Z-peak for reconstruction-level events. The data is divided into leading-p_T^μ muons of positive charge and negative charge, and also into different radial ϕ sectors of the ATLAS detector. The central value and RMS-width are measured for each sub-set of the data and plotted as a function of ϕ. Figures 46a and 46b show the plotted sub-sets of data and MC. The ratio in the bottom panel shows the difference between data and MC normalised to the measured sub-set RMS-width in data, for both positively- and negatively-charged leading-p_T^μ muons. The anti-symmetric sinusoidal difference seen between positively- and negatively-charged leading-p_T^μ muons is consistent with a systematic $\hat{z}$-axial offset in data.

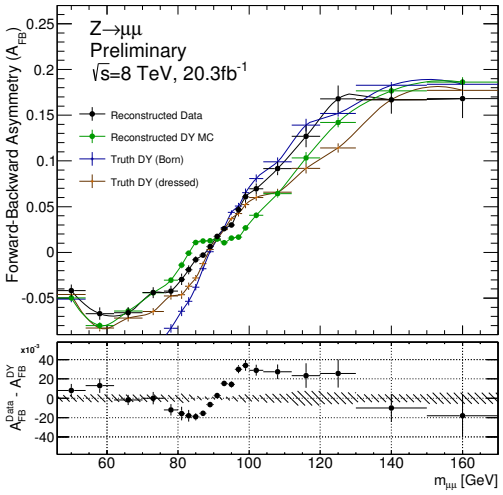

(a) A_{FB} distributions, in the -η hemisphere end-cap, $-2.4 < \eta < -1.05$, using inner detector (ID) based p_T^{μ}.

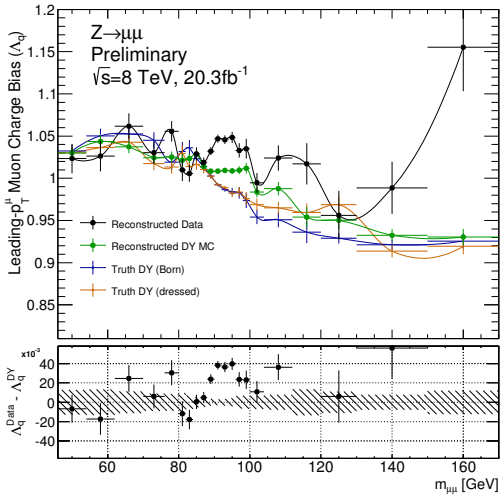

(b) Λ_q distributions, in the -η hemisphere end-cap, $-2.4 < \eta < -1.05$, using inner detector (ID) based p_T^{μ}.

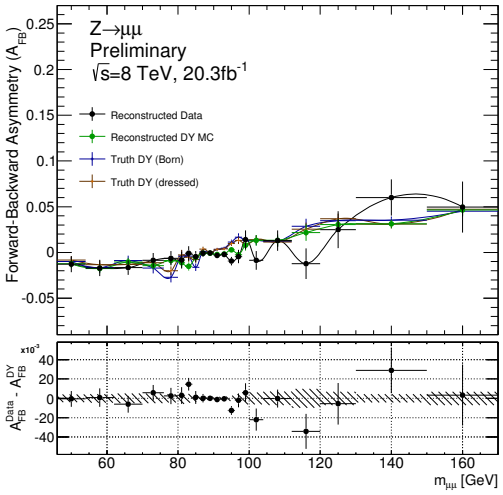

(c) A_{FB} distributions, in the -η barrel hemisphere, $-1.05 < \eta < 0.0$, using inner detector (ID) based p_T^{μ}.

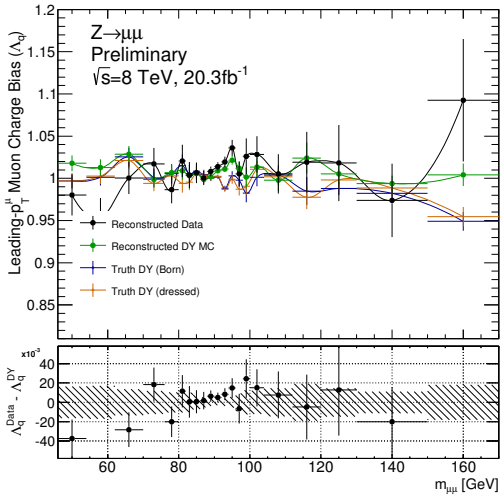

(d) Λ_q distributions, in the -η barrel hemisphere, $-1.05 < \eta < 0.0$, using inner detector (ID) based p_T^{μ}.

FIG. 44: Plots of the forward-backward asymmetry and the leading-p_T^{μ} muon charge bias decomposed into different regions of the ATLAS detector. Both muons are required to pass the η condition and the muon kinematics are derived from the ID information. The bottom panels display the difference between reconstructed MC DY signal and reconstructed background-subtracted data. A smooth curve is displayed between points for clarity. Error bars show statistical uncertainties only.

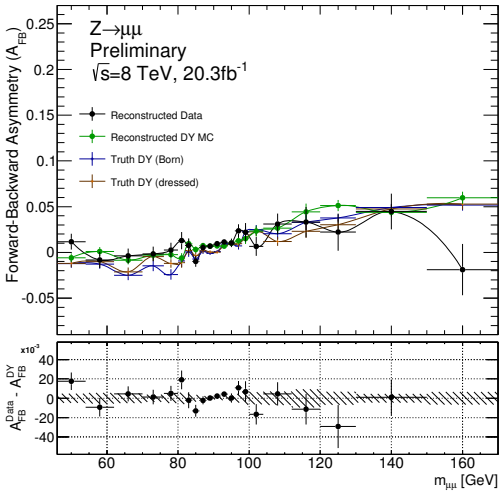

(a) A_{FB} distributions, in the $+\eta$ barrel hemisphere, $0.0 < \eta < 1.05$, using inner detector (ID) based p_T^μ.

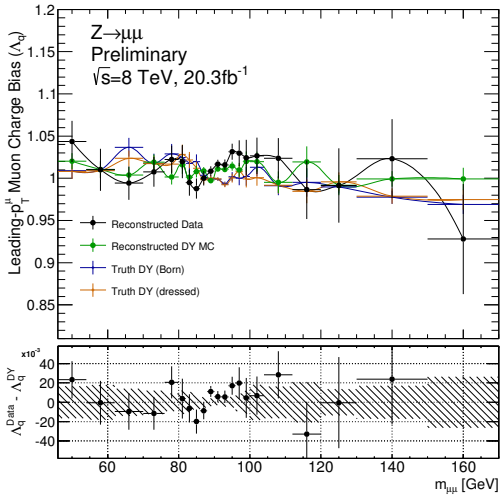

(b) Λ_q distributions, in the $+\eta$ barrel hemisphere, $0.0 < \eta < 1.05$, using inner detector (ID) based p_T^μ.

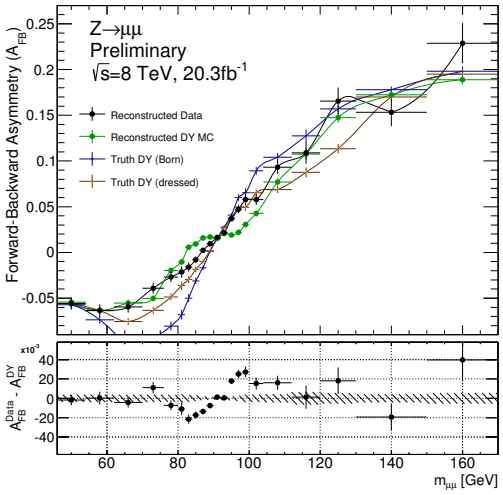

(c) A_{FB} distributions, in the $+\eta$ hemisphere end-cap, $1.05 < \eta < 2.4$, using inner detector (ID) based p_T^μ.

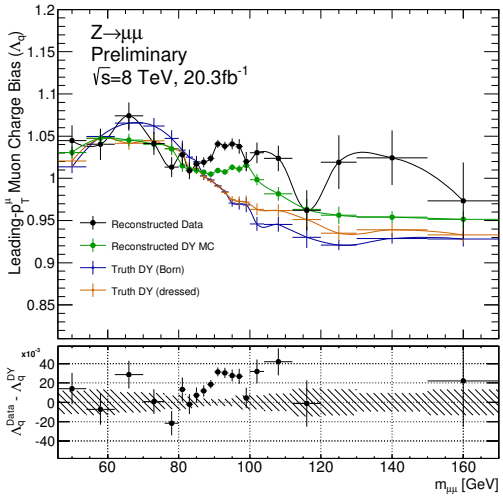

(d) Λ_q distributions, in the $+\eta$ hemisphere end-cap, $1.05 < \eta < 2.4$, using inner detector (ID) based p_T^μ.

FIG. 45: Plots of the forward-backward asymmetry and the leading-p_T^μ muon charge bias decomposed into different regions of the ATLAS detector. Both muons are required to pass the η condition and the muon kinematics are derived from the ID information. The bottom panels display the difference between reconstructed MC DY signal and reconstructed background-subtracted data. A smooth curve is displayed between points for clarity. Error bars show statistical uncertainties only.

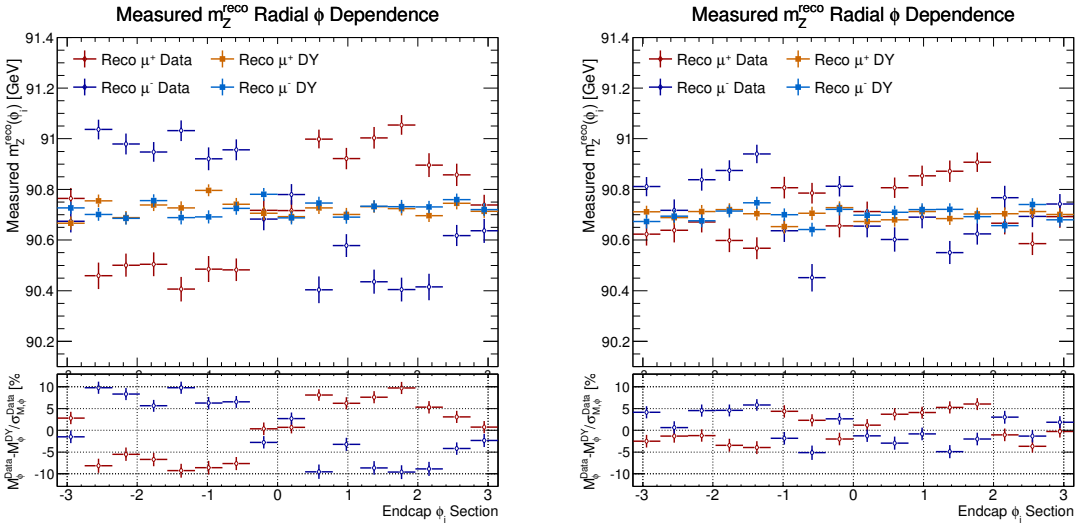

(a) Z-peak position as a function of radial ϕ sectors of the ATLAS detector in the -η hemisphere end-cap, $-2.4 < \eta < -1.05$, using inner detector (ID) based p_T^μ.

(b) Z-peak position as a function of radial ϕ sectors of the ATLAS detector in the +η hemisphere end-cap, $1.05 < \eta < 2.4$, using inner detector (ID) based p_T^μ.

FIG. 46: The leading-p_T^μ radial ϕ dependence of the Z-peak position reconstructed in the ATLAS ID end-caps. The reconstructed DY signal MC prediction (μ^+ leading-muons in orange, μ^- leading-muons in light-blue) is shown along with the measured data (μ^+ leading-muons in red, μ^- leading-muons in dark-blue). The bottom panels show the relative positively- and negatively-charged leading-p_T^μ muon agreement between data and MC. The agreement is shown as a percentage of the measured Z-peak width in data. Error bars show statistical uncertainties only.

B. Sagitta Bias Corrections

Inner Detector Sagitta Bias Corrected p_T^{μ}

Deformations of the inner detector result in incorrect measurements of the sagitta of muon tracks. This makes the effects of deformations not only region dependent but also charge dependent. In this analysis these effects are accounted for through "sagitta bias" corrections. The following equation describes these corrections:

$$p_T^{\text{sag}} = \frac{p_T^{\text{data}}}{\left(1+\alpha(\eta)\right)\left(1+q\,\delta_{\text{sag}}(\eta,\phi)\,p_T^{\text{data}}\right)}\,, \tag{72}$$

where p_T^{data} is the nominally reconstructed inner detector muon transverse momentum in data, q is the (anti-)muon charge, $\delta_{\text{sag}}(\eta,\phi)$ is the sagitta bias correction, determined as a function of muon η and ϕ, and p_T^{sag} is the corrected momentum in data, taking into account the detector sagitta bias effects. Additionally factored in are radial corrections of the form $p_T^{\text{data}} = p_T^{\text{corr}}(1+\alpha(\eta))$ where p_T^{corr} is a corrected momentum accounting for imperfect knowledge of magnetic field and material distribution, as a function of muon η. The sagitta bias was independently determined in the inclusive W-mass measurement. The full determination is described in the corresponding support note[121], however a short description is provided. The work in the following description was not performed by the author.

The Z mass peak positions were determined for a sample of $Z \to \mu\bar{\mu}$ events passing a dimuon requirement of: ≥ 2 combined muons; MCP criteria, impact parameter and isolation criteria (same as defined in Section 6 A); `EF_mu18` trigger, opposite charge muons and $p_T^{\mu} > 22\,\text{GeV}$. The events were binned two-dimensionally in 50 bins of η for both the μ and $\bar{\mu}$ (resulting in 2500 total bins). This was performed for both data and MC and the ratio of the two data sets was input to a χ^2 minimisation of the radial and sagitta biases to simultaneously determine the radial and sagitta biases. Bin occupancy limits of 50 events were imposed to ensure enough data for a mass peak determination.

As a complement to the above, the ratio of energy deposited in the calorimeter (E) to the momentum as measured by the inner detector (p) was compared for electrons and positrons. Under the assumption that the calorimeter response is independent of the charge of the measured particle, the sagitta bias may be extracted from the differences in the mean value. This method is called the E/p method. The E/p method measures the global bias, which benefits from increased statistics of $W \to e\nu$ events and cancellation of material effects and momentum resolution.

$$\delta_{\text{sag}} = \frac{\langle E/p\rangle^{+} - \langle E/p\rangle^{-}}{2\,\langle E_T\rangle}\,. \tag{73}$$

The two results were combined using a weighted average. The sagitta biases were found to

manifest radial curls and twists of the inner detector, the variation of which were found to be broad compared to the binning size.

The sagitta corrections are applied to all reconstructed data in the analysis using Equation 72. The radial ϕ Z-peak positions for sagitta corrected data is shown in Figures 47a and 47b for the ATLAS end-caps. The distribution of the Z-peak position in the different ϕ sectors show a large reduction in the spread of measured m_{Z_ϕ} values and a reduction of the sinusoidal variation. This has the effect of narrowing the reconstructed Z mass width in the full analysis.

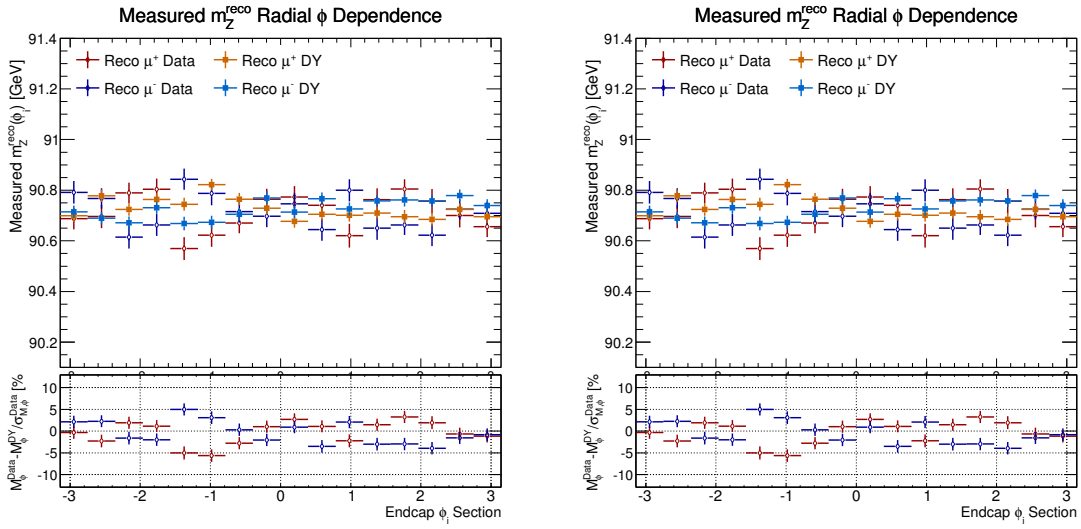

(a) Z-peak position as a function of radial ϕ sectors of the ATLAS detector in the -η hemisphere end-cap, $-2.4 < \eta < -1.05$, using inner detector (ID) sagitta bias corrected p_T^μ.

(b) Z-peak position as a function of radial ϕ sectors of the ATLAS detector in the +η hemisphere end-cap, $1.05 < \eta < 2.4$, using inner detector (ID) sagitta bias corrected p_T^μ.

FIG. 47: The leading-p_T^μ radial ϕ dependence of the Z-peak position reconstructed in the ATLAS ID end-caps. The reconstructed DY signal MC prediction (μ^+ leading-muons in orange, μ^- leading-muons in light-blue) is shown along with the measured data (μ^+ leading-muons in red, μ^- leading-muons in dark-blue). The bottom panels show the relative positively- and negatively-charged leading-p_T^μ muon agreement between data and MC. The agreement is shown as a percentage of the measured Z-peak width in data. Error bars show statistical uncertainties only.

The improved agreement between data and MC of the forward-backward asymmetry and leading-p_T^μ muon charge bias is shown in Figures 48 and 49. When using the sagitta corrected ID p_T^μ the data adheres closer to reconstructed MC predictions of A_{FB} and Λ_q by a factor of 2 about the Z-peak. The residual reconstructed MC Λ_q offset above the Z-peak is also described in data in Figure 49d. Residual effects are expected as not all inner detector distortions can be accounted for

or fully simulated in MC. The effect of inflections and "kinks" are significantly reduced by using this procedure, which provides a better agreement between data and MC. As a result, the unfolding of the data is more accurate.

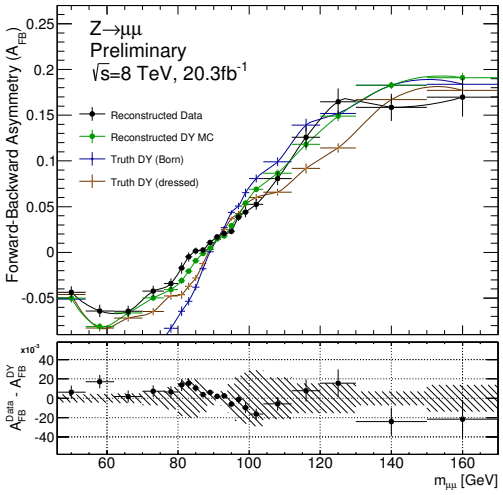

(a) A_{FB} distributions, in the -η hemisphere end-cap, $-2.4 < \eta < -1.05$, using inner detector (ID) sagitta bias corrected p_T^{μ}.

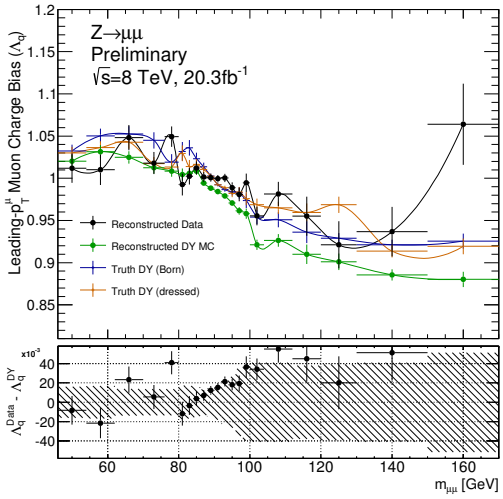

(b) Λ_q distributions, in the -η hemisphere end-cap, $-2.4 < \eta < -1.05$, using inner detector (ID) sagitta bias corrected p_T^{μ}.

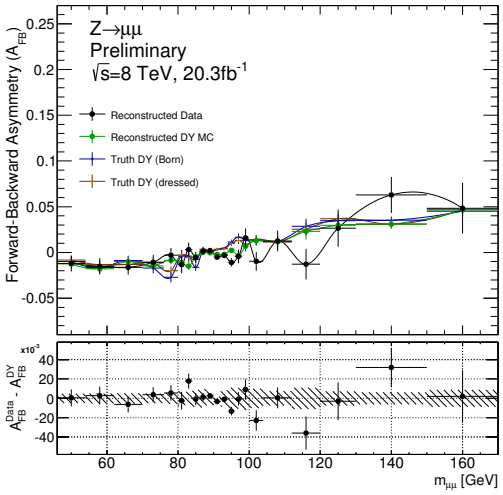

(c) A_{FB} distributions, in the -η barrel hemisphere, $-1.05 < \eta < 0.0$, using inner detector (ID) sagitta bias corrected p_T^{μ}.

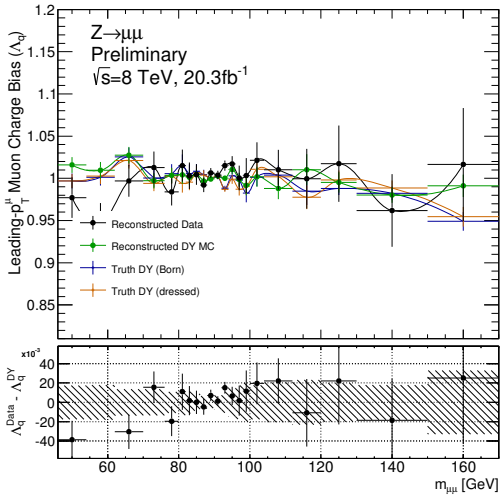

(d) Λ_q distributions, in the -η barrel hemisphere, $-1.05 < \eta < 0.0$, using inner detector (ID) sagitta bias corrected p_T^{μ}.

FIG. 48: Plots of the forward-backward asymmetry and the leading-p_T^{μ} muon charge bias decomposed into different regions of the ATLAS detector. Both muons are required to pass the η condition where ID sagitta bias corrected p_T^{μ} information is used. The bottom panels display the difference between reconstructed MC DY signal and reconstructed background-subtracted data. A smooth curve is displayed between points for clarity. Error bars show statistical uncertainties only.

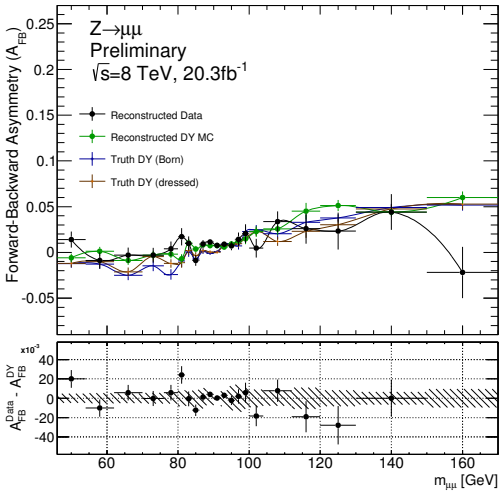

(a) A_{FB} distributions, in the $+\eta$ barrel hemisphere, $0.0 < \eta < 1.05$, using inner detector (ID) sagitta bias corrected p_T^{μ}.

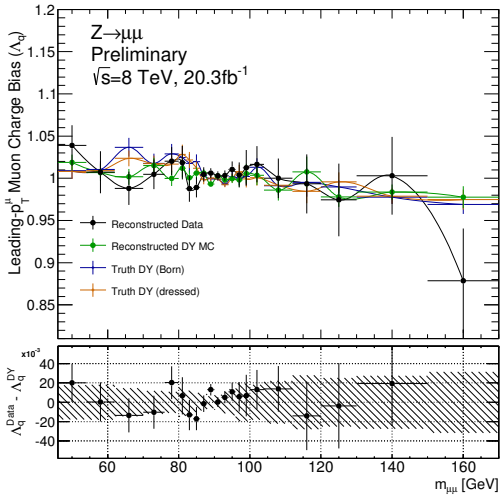

(b) Λ_q distributions, in the $+\eta$ barrel hemisphere, $0.0 < \eta < 1.05$, using inner detector (ID) sagitta bias corrected p_T^{μ}.

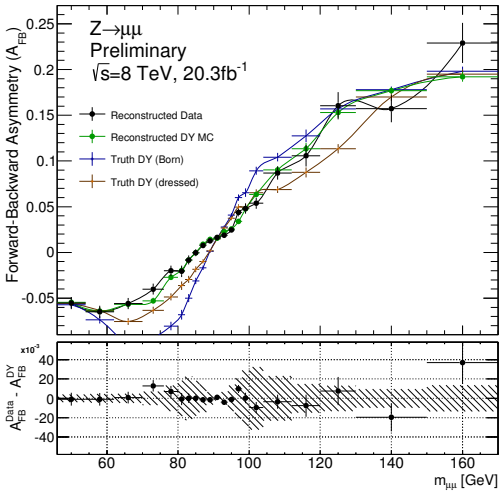

(c) A_{FB} distributions, in the $+\eta$ hemisphere end-cap, $1.05 < \eta < 2.4$, using inner detector (ID) sagitta bias corrected p_T^{μ}.

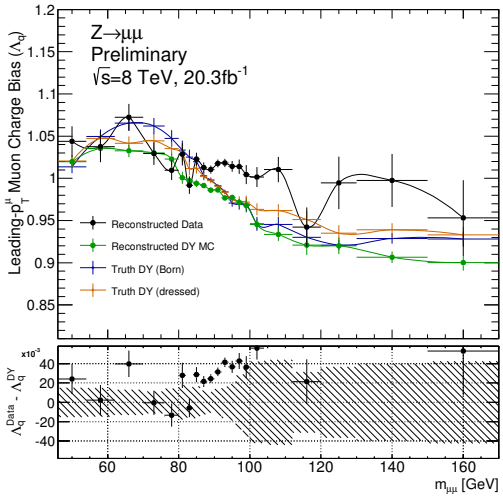

(d) Λ_q distributions, in the $+\eta$ hemisphere end-cap, $1.05 < \eta < 2.4$, using inner detector (ID) sagitta bias corrected p_T^{μ}.

FIG. 49: Plots of the forward-backward asymmetry and the leading-p_T^{μ} muon charge bias decomposed into different regions of the ATLAS detector. Both muons are required to pass the η condition where ID sagitta bias corrected p_T^{μ} information is used. The bottom panels display the difference between reconstructed MC DY signal and reconstructed background-subtracted data. A smooth curve is displayed between points for clarity. Error bars show statistical uncertainties only.

9. QCD MULTIJET BACKGROUND ESTIMATION

The QCD multijet background is not accurately described in Monte Carlo and the efficiency of the selection criteria result in low statistical precision of such samples. To achieve an accurate determination of the multijet background a "data driven" method is used. This means deriving a multijet estimate directly from the available reconstructed data.

A. QCD Multijet Normalisation

A statistically independent QCD multijet estimation can be made by extrapolating from multijet enriched samples of the data. The multijet enriched samples are created by inverting the isolation requirement of the selection criteria used to reject muons originating from hadronic decays (Section 6 A), and also by inverting the opposite-sign charge requirement. By splitting the dimuon isolation spectra into opposite-sign (OS) and same-sign (SS) components, the isolation spectra is better able to be decomposed into light and heavy flavour components. The shape of the light flavour component is expected to be independent of dimuon charge asymmetry and thus provide a similar isolation shape in OS and SS dimuon events. This forms the basis of the extrapolation where it is assumed that the ratio of isolated OS and isolated SS events is equal to the ratio of anti-isolated OS and anti-isolated SS events. Such a relation has the following form:

$$\frac{N^{\mathrm{OS}}_{\mathrm{isolated}}}{N^{\mathrm{SS}}_{\mathrm{isolated}}} = \frac{N^{\mathrm{OS}}_{\mathrm{anti-isolated}}}{N^{\mathrm{SS}}_{\mathrm{anti-isolated}}} \,. \tag{74}$$

This procedure is commonly known as the ABCD method, where the ABCD regions are defined as shown in Figure 50.

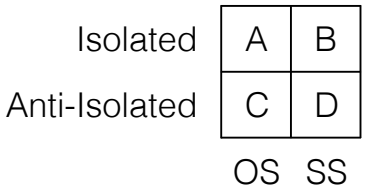

FIG. 50: Conceptual diagram of the different "ABCD" regions used in the ABCD method. Region 'A' is also called the signal region.

Using Equation 74 the number of multijet events in the signal-dominated isolated OS region can be trivially solved for,

$$N^{\mathrm{OS}}_{\mathrm{isolated}} = N^{\mathrm{SS}}_{\mathrm{isolated}} \cdot \frac{N^{\mathrm{OS}}_{\mathrm{anti-isolated}}}{N^{\mathrm{SS}}_{\mathrm{anti-isolated}}} \,. \tag{75}$$

The assumption on the OS and SS shape similarity is naïve however, as the heavy flavour component is expected to give more OS events due to decays of $c\bar{c}$ and $b\bar{b}$. This changes the shape of the OS isolation spectra, and therefore the $N^{\text{OS}}_{\text{anti-isolated}}/N^{\text{SS}}_{\text{anti-isolated}}$ ratio will gain an isolation, I_μ, dependence.

The heavy flavour contribution to the OS isolation spectra in addition to the light flavour component is accounted for by fitting the isolation ratio. This achieves a required I_μ dependence. Equation 74 is modified to account for this:

$$\frac{N^{\text{OS}}_{\text{isolated}}}{N^{\text{SS}}_{\text{isolated}}} = F_{abcd}(I_\mu)\big|_{I_\mu=0.05}\,, \tag{76}$$

where $F_{abcd}(I_\mu)\big|_{I_\mu=0.05}$ is a fit as a function of isolation, to the $N^{\text{OS}}_{\text{anti-isolated}}/N^{\text{SS}}_{\text{anti-isolated}}$ ratio, evaluated in the centre of the isolation region, $I_\mu < 0.1$. Equation 76 is a more general form of 74 and can be shown to be equivalent when F_{abcd} is a 0^{th}-order polynomial. Table 14 lists the percentage differences between data and MC showing the multijet enrichment of the statistically independent regions. The isolated same-sign region is shown to have high multijet enrichment ($> 75\%$) and the anti-isolated regions have very high enrichment ($> 99\%$).

Region	$m_{\mu\mu}$	Data	Total MC	Difference
Isolated same-sign (B)	$46 < m_{\mu\mu} < 66\,\text{GeV}$	2549	342.6	86.56%
	$46 < m_{\mu\mu} < 200\,\text{GeV}$	5862	1394.2	76.22%
Anti-isolated opposite-sign (C)	$46 < m_{\mu\mu} < 66\,\text{GeV}$	178378	1061.6	99.40%
	$46 < m_{\mu\mu} < 200\,\text{GeV}$	390774	2936.0	99.25%
Anti-isolated same-sign (D)	$46 < m_{\mu\mu} < 66\,\text{GeV}$	87070	727.5	99.16%
	$46 < m_{\mu\mu} < 200\,\text{GeV}$	197214	1730.5	99.12%

TABLE 14: Summary of the number of reconstructed events found in the different multijet-enriched regions. Values are provided for the full fiducial mass range and the lowest mass bin where the relative multijet background is expected to be highest. The Total MC column lists the sum of simulated MC processes as described in Section 5 B. The percentage difference between data and MC shows the scale of multiject enrichment.

The fit is performed in a limited region of the anti-isolation spectra where the heavy flavour component is significant. The isolation spectra for OS and SS events is shown in Figure 51 where the isolation spectra have been normalised to unity. The figure shows the ratio of the isolation spectra in the bottom panel where a strong I_μ dependence is observed for low values of I_μ. The nominal 1^{st}-order polynomial fit applied to the ratio is displayed in red with the fit parameters displayed on the plot. The fit is performed close to the isolation region, $I_\mu < 0.1$, and restricted to a region of linearity.

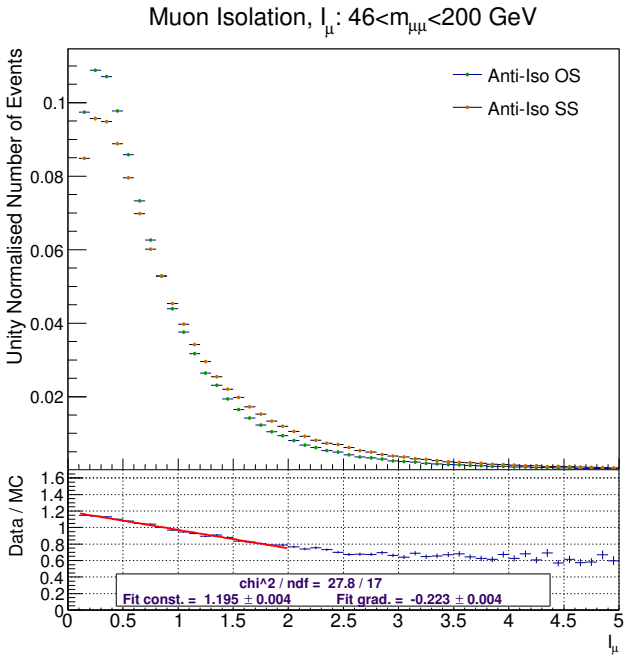

FIG. 51: The dimuon anti-isolation spectra of OS and SS events with the applied extrapolation fit to the ratio. The fit gradient and constant term is displayed on the plot along with the χ^2 and number of degrees of freedom. Error bars show statistical uncertainties only.

If the extrapolation is performed in terms of normalised ABCD regions, such as shown in Figure 51, then the extrapolation factor, $F_{abcd}(I_\mu)\big|_{I_\mu}$, must be replaced with the normalised extrapolation factor $f_{abcd}(I_\mu)\big|_{I_\mu}$ with the appropriate scaling:

$$F_{abcd}(I_\mu)\big|_{I_\mu=0.05} = \frac{N^{\mathrm{OS}}_{\mathrm{anti-isolated}}}{N^{\mathrm{SS}}_{\mathrm{anti-isolated}}} \cdot f_{abcd}(I_\mu)\big|_{I_\mu=0.05}\,. \tag{77}$$

Although the extrapolation is restricted in anti-isolation to a region of linearity ($0.1 < I_\mu < 2.0$), the normalisations are determined for all I_μ. Inserting the normalised extrapolation factor into Equation 76 gives:

$$\frac{N^{\mathrm{OS}}_{\mathrm{isolated}}}{N^{\mathrm{SS}}_{\mathrm{isolated}}} = \frac{N^{\mathrm{OS}}_{\mathrm{anti-isolated}}}{N^{\mathrm{SS}}_{\mathrm{anti-isolated}}} \cdot f_{abcd}(I_\mu)\big|_{I_\mu=0.05}\,. \tag{78}$$

For ease of labelling, the different regions are defined:

- Region A: $N^A_{\mathrm{QCD}} = N^{\mathrm{OS}}_{\mathrm{isolated}}$
- Region B: $N^B_{\mathrm{QCD}} = N^{\mathrm{SS}}_{\mathrm{isolated}}$
- Region C: $N^C_{\mathrm{QCD}} = N^{\mathrm{OS}}_{\mathrm{anti-isolated}}$

- Region D: $N^{D}_{\mathrm{QCD}} = N^{\mathrm{SS}}_{\mathrm{anti-isolated}}$

Outside the measurement region the number of multijet events is substituted with the estimation from the data after subtracting simulated MC predictions (Section 5 B): $N_{\mathrm{QCD}} = N_{\mathrm{Data}} - N_{\mathrm{MC}}$. The extrapolated fit, $f_{abcd}(I_\mu)$, observes good linear approximation in the neighbouring region of anti-isolation: $0.1 < \mathrm{I}_\mu < 2.0$. The fit is determined numerically from the ratios of regions C & D and the evaluation limit, $\big|_{I_\mu}$, is defined to be the value of the fit evaluated at the mid-point of the isolated signal region, $I_\mu = 0.05$. The final form of the QCD multijet background estimation in the measurement region, N^{A}_{QCD}, is the following:

$$N^{A}_{\mathrm{QCD}} = \frac{(N^{B}_{\mathrm{Data}} - N^{B}_{\mathrm{MC}})(N^{C}_{\mathrm{Data}} - N^{C}_{\mathrm{MC}})}{(N^{D}_{\mathrm{Data}} - N^{D}_{\mathrm{MC}})} \cdot f_{abcd}(I_\mu)\big|_{I_\mu=0.05}\,. \tag{79}$$

This data driven QCD multijet background estimation method is otherwise known as the ABCD modified method[119].

B. QCD Multijet Shape Templates

The ABCD method is used to determine the multijet normalisation for each mass region in the measurement binning. This provides seven different mass region normalisations. To determine the number of multijet events in each individual $|y_{\mu\mu}|$ and $\cos\theta^*$ bin within the seven mass regions, the shape of the multijet in $|y_{\mu\mu}|$ and $\cos\theta^*$ is derived from the data. Anti-isolated data events after subtracting simulated MC processes are used to estimate the shape of the multijet QCD. The anti-isolated data events are binned in $|y_{\mu\mu}|$ and $|\cos\theta^*|$. The $|y_{\mu\mu}|$ bin boundaries are the same as the measurement binning, and the $|\cos\theta^*|$ boundaries are equivalent to the $\cos\theta^* > 0$ binning. The moduli are used due to the assumed invariance to the sign of the rapidity and invariance in lepton decay angle. The $y_{\mu\mu}$ and $\cos\theta^*$ invariance is shown in Figure 52. Here, the inverted data points are equivalent to the nominal but with inverted sign of $y_{\mu\mu}$ or $\cos\theta^*$. The modulus of $\cos\theta^*$ achieves greater statistical precision in the shape template, which is vital for the extremities of the binning phase space.

Once a shape template has been determined for each mass region it is normalised according to each region's ABCD multijet normalisation. This gives the initial estimation of the QCD multijet background.

C. QCD Multijet MC Bias Corrections

The QCD multijet estimation can become biased to MC predictions of the isolation distributions and Drell–Yan signal cross-section normalisation. Therefore the QCD multijet determination is

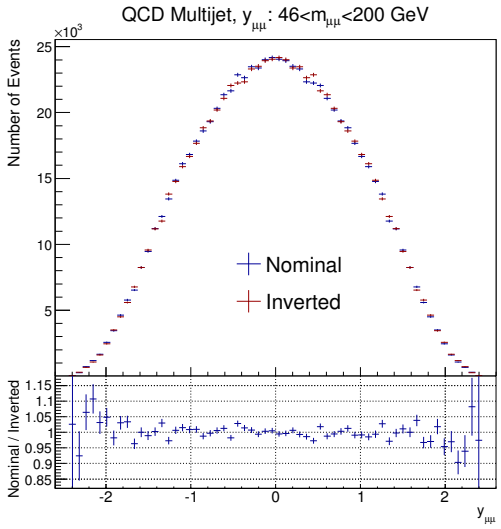

(a) Anti-isolated data $y_{\mu\mu}$ distribution integrated in $\cos\theta^*$. The sign invariance is shown by the inverted distribution.

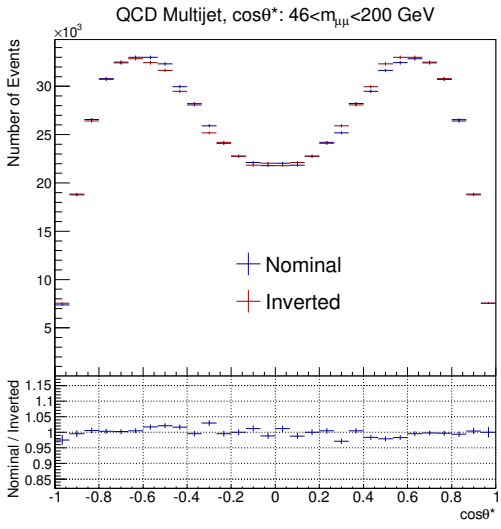

(b) Anti-isolated data $\cos\theta^*$ distribution integrated in $y_{\mu\mu}$. The sign invariance is shown by the inverted distribution.

FIG. 52: QCD multijet invariance to the $y_{\mu\mu}$ and $\cos\theta^*$ dimensions. The nominal multijet shapes are shown alongside the shape with inverted sign, effectively mirroring the $y_{\mu\mu}$ and $\cos\theta^*$ distributions about $y_{\mu\mu} = 0$ and $\cos\theta^* = 0$ respectively. Error bars show statistical uncertainties only.

iterated upon, where within each iteration the DY signal is scaled by the remaining difference between background-subtracted data and DY signal. The applied scaling directly alters the multijet normalisations for each mass region and the 2D multijet $|y_{\mu\mu}|$-$\cos\theta^*$ template shape. The new multijet determination is then used to calculate the new difference between background-subtracted data and nominal DY signal for the next iteration step. The process is iterated until a stable multijet DY scaling factor (ratio of background-subtracted data and DY signal) is obtained. The multijet DY scaling factors for each mass region as a function of iteration number are listed in Table 15.

The final QCD multijet estimation in each mass region is the 2D $|y_{\mu\mu}|$-$\cos\theta^*$ template normalised to the ABCD mass region with stable multijet DY scaling factors.

Two systematic uncertainties are assigned to the dimuon QCD multijet estimation: an isolation uncertainty, which affects the $|y_{\mu\mu}|$-$\cos\theta^*$ template shape; and an extrapolation uncertainty affecting the mass region normalisation. This is discussed further in Section 11. The final QCD multijet estimation is shown in Figures 53 and 54. The QCD multijet contributes ~ 150 events per bin in the $46 < m_{\mu\mu} < 66\,\text{GeV}$ mass window, which decreases to ~ 15 and ~ 7 events on the Z-peak ($80 < m_{\mu\mu} < 91\,\text{GeV}$) and above the Z-peak ($102 < m_{\mu\mu} < 116\,\text{GeV}$), respectively.

$m_{\mu\mu}$ Region [GeV]	Multijet MC Bias Iteration			
	0^{th}	1^{st}	2^{nd}	3^{rd}
$46 < m_{\mu\mu} < 66$	1.0	1.0026	1.0026	1.0026
$66 < m_{\mu\mu} < 80$	1.0	1.0199	1.0198	1.0198
$80 < m_{\mu\mu} < 91$	1.0	1.0199	1.0199	1.0199
$91 < m_{\mu\mu} < 102$	1.0	1.0197	1.0197	1.0197
$102 < m_{\mu\mu} < 116$	1.0	1.0231	1.0231	1.0231
$116 < m_{\mu\mu} < 150$	1.0	1.0120	1.0119	1.0119
$150 < m_{\mu\mu} < 200$	1.0	1.0130	1.0129	1.0129

TABLE 15: QCD multijet $m_{\mu\mu}$ DY scaling factors for each iteration step. The 0^{th}-order iteration represents the nominal ABCD method multijet estimation. The scaling factors are shown to converge after three iterations.

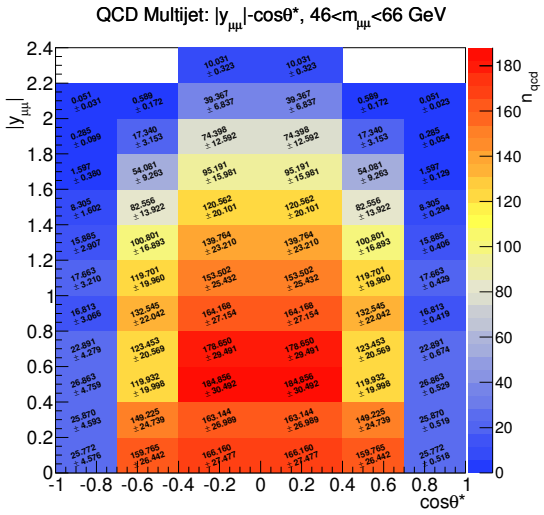

(a) Multijet estimation in the $46 < m_{\mu\mu} < 66$ mass window.

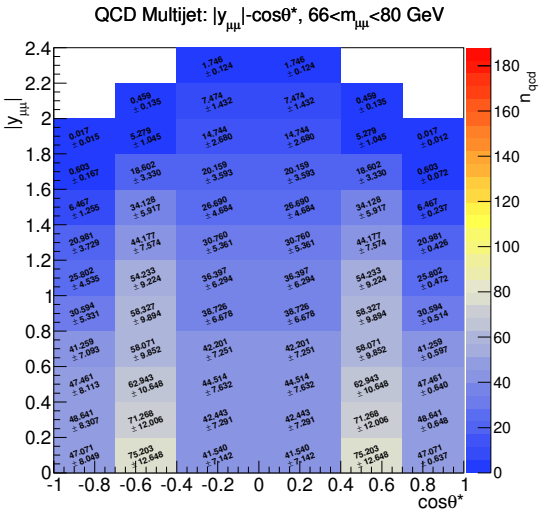

(b) Multijet estimation in the $66 < m_{\mu\mu} < 80$ mass window.

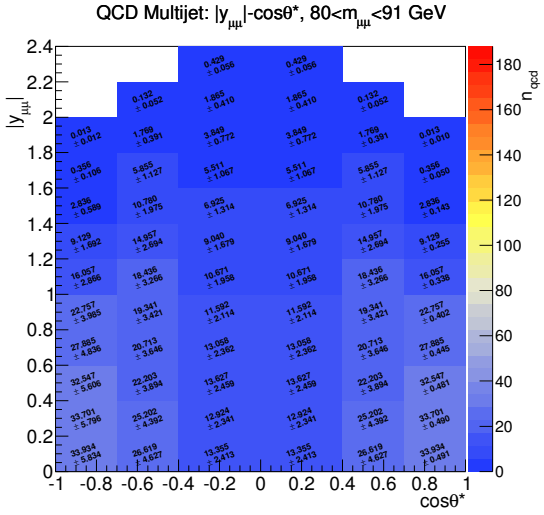

(c) Multijet estimation in the $80 < m_{\mu\mu} < 91$ mass window.

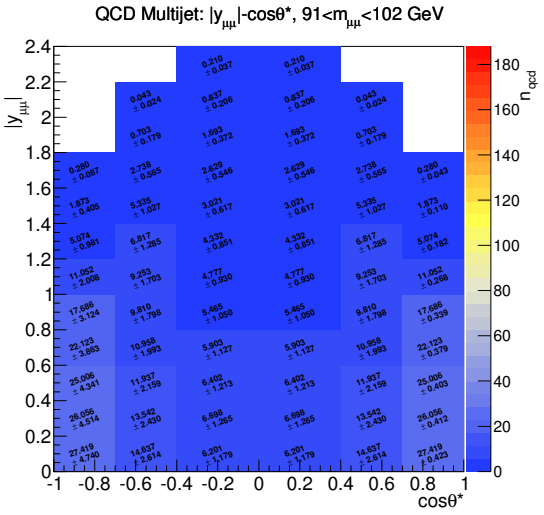

(d) Multijet estimation in the $91 < m_{\mu\mu} < 102$ mass window.

FIG. 53: Two dimensional (y-$\cos\theta^*$) plots of the dimuon QCD multijet background estimation in the first four invariant mass windows of the measurement. Uncertainties on the values include multijet systematic uncertainties, as described in Section 11, only.

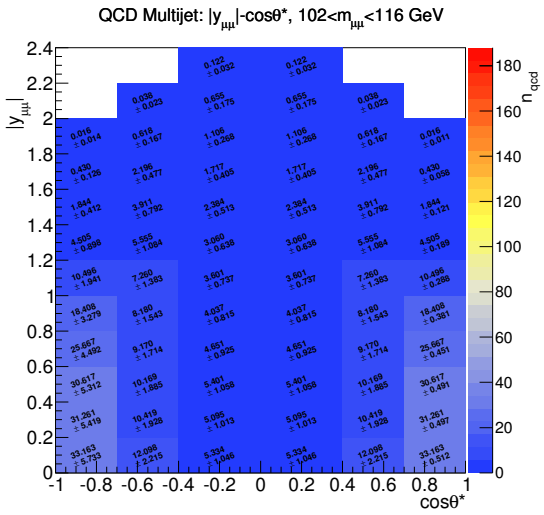

(a) Multijet estimation in the $102 < m_{\mu\mu} < 116$ mass window.

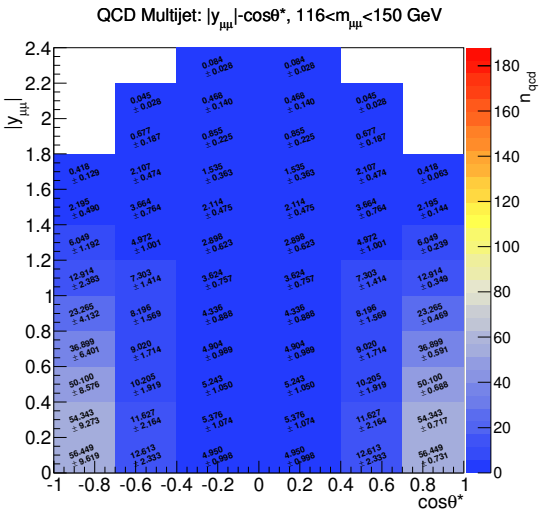

(b) Multijet estimation in the $116 < m_{\mu\mu} < 150$ mass window.

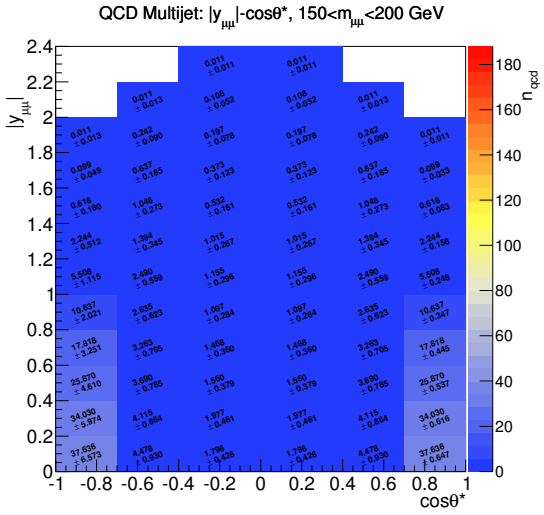

(c) Multijet estimation in the $116 < m_{\mu\mu} < 150$ mass window.

FIG. 54: Two dimensional (y-$\cos\theta^*$) plots of the dimuon QCD multijet background estimation in the last three invariant mass windows of the measurement. Uncertainties on the values include multijet systematic uncertainties, as described in Section 11, only.

10. CUTFLOW AND CONTROL DISTRIBUTIONS

A. Selection Criteria Cutflow

Events are required to satisfy the event selection criteria (Section 6 A). The number of events that pass each criterion are recorded and used to quantify the efficiency of each criterion and the degree of background rejection. Additionally, it can serve as a method of validation of the analysis code when cross-checking against analyses using equivalent selection criteria. The selection criteria cutflow is shown in Table 16.

The cutflow shows that the requirement on the number of muons greatly reduces the diboson and W backgrounds. The impact parameter criterion on z_{PV} further efficiently reduces the W backgrounds. The muon p_T^{μ} requirements greatly suppresses the $Z \to \tau\bar{\tau}$ and $t\bar{t}$ backgrounds. Through the selection criteria the backgrounds are reduced in most cases by three orders of magnitude, whereas the Drell–Yan signal is only reduced by a factor of 0.504.

B. Analysis Control Distributions

The agreement between ATLAS $\sqrt{s} = 8\,\text{TeV}$ data and the MC simulation is shown in the standard set of control distributions in Figures 55-57. The total weighted contributions from each MC simulation sample is summed and stacked along with the estimated data-driven QCD multijet background. The ratio panels show the ratio between the data and the summed MC+QCD sources.

Figures 55 and 56 show sub-selections for $|y| < 1$ and $|y| > 1$ respectively, in three selected $m_{\mu\mu}$ bins. The different regions show the behaviour of the control distributions in separate parts of the measurement phase space. Figure 57 shows plots inclusive in $|y|$ and invariant mass distributions decomposed in the $|y|$ regions. Good agreement is observed between data and MC, except in p_T related distributions. The poor modelling in MC is therefore accounted for with a Drell-Yan Z-p_T modelling systematic, discussed further in Section 11 B. The overall offset between data and MC of 1.7% is consistent with other analyses[2,122,123] and, although not shown on the plots, is within the luminosity uncertainty of ±1.9%.

Selection	Data	$Z \to \mu\bar{\mu}$	$Z \to \tau\bar{\tau}$	$\gamma\gamma \to \mu\bar{\mu}$	$WW\|WZ\|ZZ$	$t\bar{t}$	$t\|\bar{t}$	$W \to \mu\bar{\nu_\mu}$	$W \to \tau\bar{\nu_\tau}$	Total MC
Lepton filter	147149783.0	18621458.3	1647956.7	323127.2	236836.2	1390153.1	119067.3	41934857.8	4473087.3	68746543.9
Primary vertex & tracks	146797679.0	18454122.6	1638395.3	279435.4	236055.0	1389953.8	119039.0	41677505.9	4451347.6	68245854.6
Event triggers	128759244.0	14611302.0	524381.5	65474.3	171134.4	713761.2	66498.1	30809804.8	1273249.8	48235606.2
Number of muons ≥ 2	57793890.0	13626753.9	167678.8	58416.7	58859.0	382696.5	31196.5	5883576.9	249005.4	20458183.6
MCP `medium+`	45038739.0	13346366.0	138682.8	56677.2	47849.7	330012.2	26230.4	3507045.2	148758.9	17601622.3
Trigger matching	44845692.0	13345491.3	138650.4	56669.9	47838.4	329802.6	26213.1	3505907.0	148701.2	17599273.9
Passes MCP criteria	42090399.0	12591839.4	129964.5	54561.5	44225.0	316134.0	24874.4	3006209.2	128205.5	16296013.6
$\|z^{\mu}_{PV}\| < 10.0\,\text{mm}$	42090399.0	12591839.4	129964.5	54561.5	44225.0	316134.0	24874.4	3006209.2	128205.5	16296013.6
$\|\eta_\mu\| < 2.4$	35221277.0	11721482.0	101867.9	46105.0	34291.3	284474.4	21651.1	746612.7	39738.8	12996223.2
$p^{\mu}_T > 20.0\,\text{GeV}$	11592958.0	9654966.2	24968.1	17058.8	21656.0	81907.0	6341.6	15695.1	1641.4	9824234.1
$I_\mu < 0.1$	9931282.0	9510238.5	24193.2	16802.3	20853.5	38359.6	3517.4	2231.0	206.6	9616402.1
3rd muon veto	9929806.0	9509925.6	24193.2	16802.1	20146.0	38269.1	3511.9	2231.0	206.6	9615285.4
Opposite sign	9922316.0	9509763.3	24177.7	16799.6	19839.9	37388.9	3443.9	1875.1	206.6	9613495.1
$m_{\mu\mu} > 46\,\text{GeV}$	9742781.0	9410357.0	22112.4	13960.5	18727.9	32367.4	2975.9	1633.6	206.6	9502341.3
$46 < m_{\mu\mu} < 200\,\text{GeV}$	9719611.0	9392947.3	22091.5	13331.4	17750.3	28724.8	2621.4	1606.0	206.6	9479279.3

TABLE 16: Muon channel cutflow of fully weighted events passing the analysis selection criteria, as described in section 6 A. The 'Lepton filter' is a pre-selection criterion that is defined as: two or more leptons, ℓ, with $p^{\ell}_T > 10\,\text{GeV}$. The criterion is looser than the 'Number of muons' and 'p^{μ}_T' requirements and exists for the purpose of computing efficiency. The Total MC column does not include the QCD multijet background estimation.

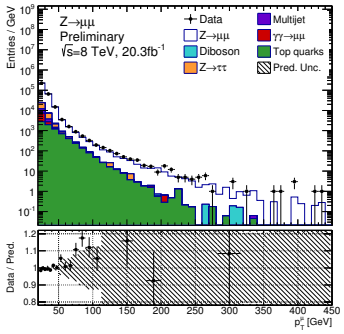

(a) Muon p_T^{μ} for $|y_{\mu\mu}| < 1.0$ and $46 < m_{\mu\mu} < 66\,\text{GeV}$.

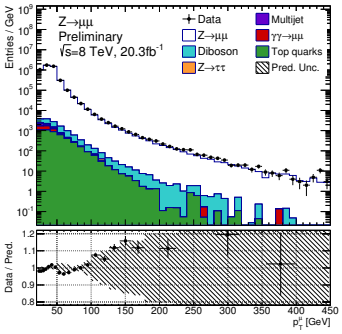

(b) Muon p_T^{μ} for $|y_{\mu\mu}| < 1.0$ and $80 < m_{\mu\mu} < 91\,\text{GeV}$.

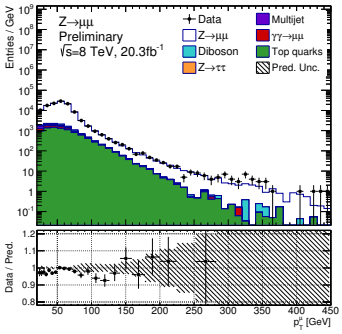

(c) Muon p_T^{μ} for $|y_{\mu\mu}| < 1.0$ and $116 < m_{\mu\mu} < 150\,\text{GeV}$.

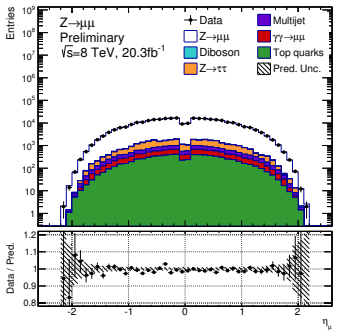

(d) Muon η_{μ} for $|y_{\mu\mu}| < 1.0$ and $46 < m_{\mu\mu} < 66\,\text{GeV}$.

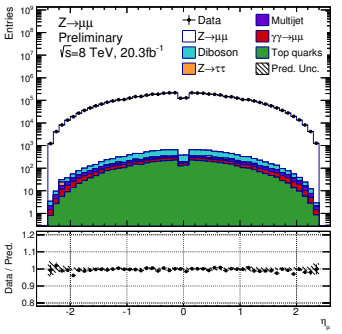

(e) Muon η_{μ} for $|y_{\mu\mu}| < 1.0$ and $80 < m_{\mu\mu} < 91\,\text{GeV}$.

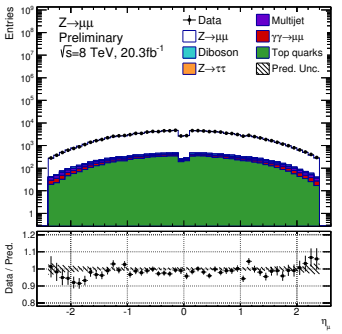

(f) Muon η_{μ} for $|y_{\mu\mu}| < 1.0$ and $116 < m_{\mu\mu} < 150\,\text{GeV}$.

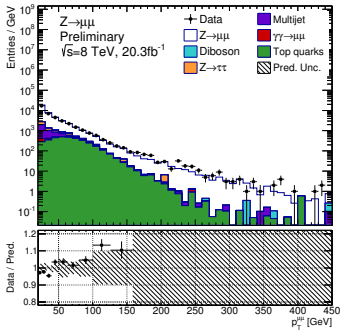

(g) Dimuon p_T for $|y_{\mu\mu}| < 1.0$ and $46 < m_{\mu\mu} < 66\,\text{GeV}$.

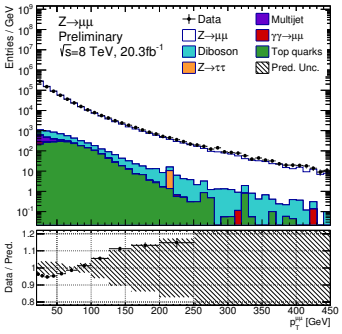

(h) Dimuon p_T for $|y_{\mu\mu}| < 1.0$ and $80 < m_{\mu\mu} < 91\,\text{GeV}$.

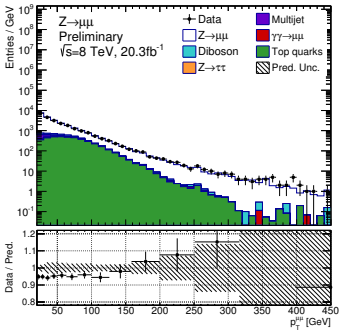

(i) Dimuon p_T for $|y_{\mu\mu}| < 1.0$ and $116 < m_{\mu\mu} < 150\,\text{GeV}$.

FIG. 55: Control distributions of muon and dimuon kinematic variables in different regions of the measurement phase space. All plots contained in this figure fulfil the requirement $|y_{\mu\mu}| < 1.0$. The error bars show statistical uncertainties only.

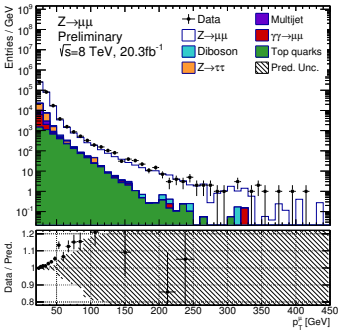

(a) Muon p_T^{μ} for $|y_{\mu\mu}| > 1.0$ and $46 < m_{\mu\mu} < 66\,\text{GeV}$.

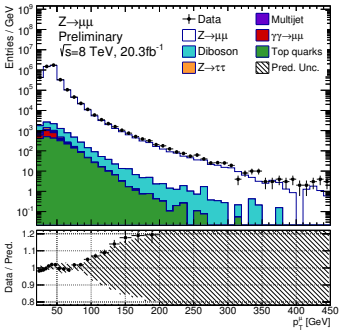

(b) Muon p_T^{μ} for $|y_{\mu\mu}| > 1.0$ and $80 < m_{\mu\mu} < 91\,\text{GeV}$.

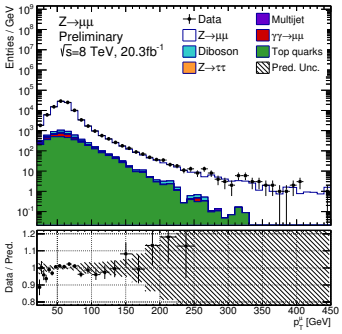

(c) Muon p_T^{μ} for $|y_{\mu\mu}| > 1.0$ and $116 < m_{\mu\mu} < 150\,\text{GeV}$.

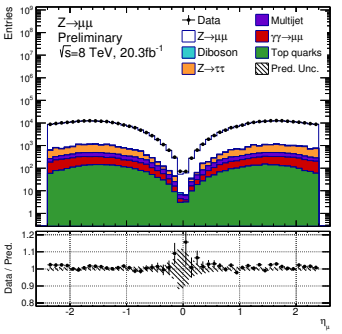

(d) Muon η_{μ} for $|y_{\mu\mu}| > 1.0$ and $46 < m_{\mu\mu} < 66\,\text{GeV}$.

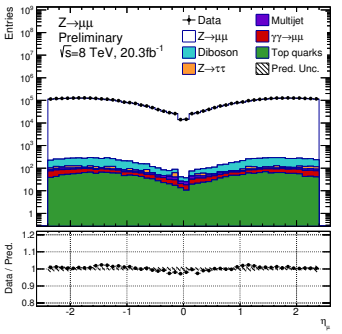

(e) Muon η_{μ} for $|y_{\mu\mu}| > 1.0$ and $80 < m_{\mu\mu} < 91\,\text{GeV}$.

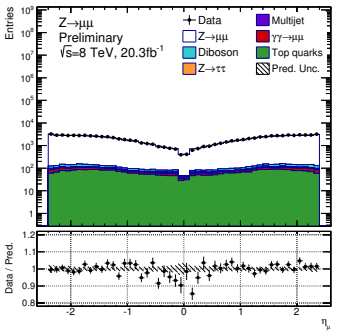

(f) Muon η_{μ} for $|y_{\mu\mu}| > 1.0$ and $116 < m_{\mu\mu} < 150\,\text{GeV}$.

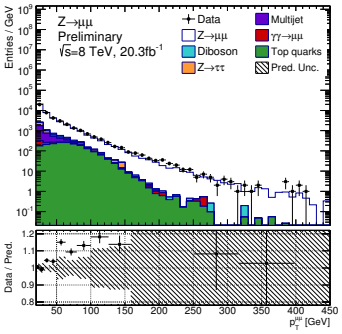

(g) Dimuon p_T for $|y_{\mu\mu}| > 1.0$ and $46 < m_{\mu\mu} < 66\,\text{GeV}$.

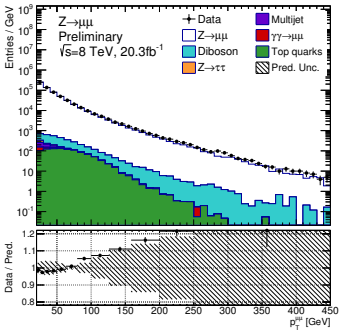

(h) Dimuon p_T for $|y_{\mu\mu}| > 1.0$ and $80 < m_{\mu\mu} < 91\,\text{GeV}$.

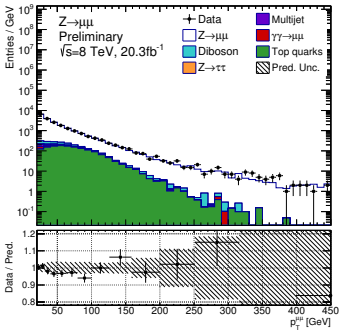

(i) Dimuon p_T for $|y_{\mu\mu}| > 1.0$ and $116 < m_{\mu\mu} < 150\,\text{GeV}$.

FIG. 56: Control distributions of muon and dimuon kinematic variables in different regions of the measurement phase space. All plots contained in this figure fulfil the requirement $|y_{\mu\mu}| < 1.0$. The error bars show statistical uncertainties only.

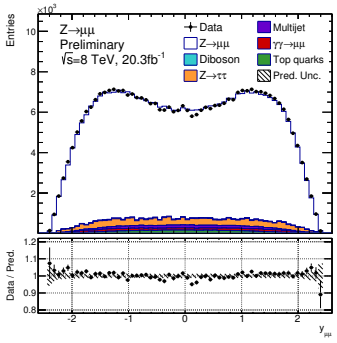

(a) Dimuon $y_{\mu\mu}$ for all $|y_{\mu\mu}|$ and $46 < m_{\mu\mu} < 66\,\text{GeV}$.

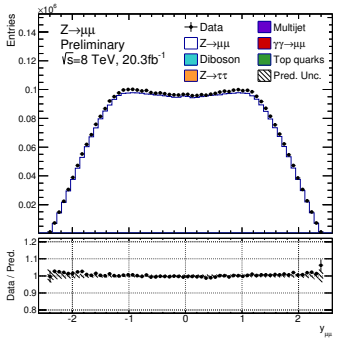

(b) Dimuon $y_{\mu\mu}$ for all $|y_{\mu\mu}|$ and $80 < m_{\mu\mu} < 91\,\text{GeV}$.

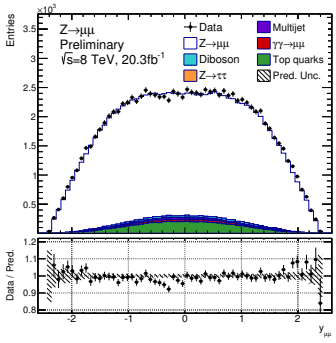

(c) Dimuon $y_{\mu\mu}$ for all $|y_{\mu\mu}|$ and $116 < m_{\mu\mu} < 150\,\text{GeV}$.

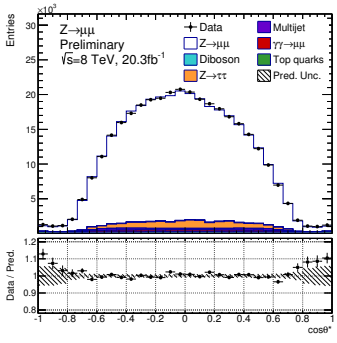

(d) Dimuon $\cos\theta^*$ for all $|y_{\mu\mu}|$ and $46 < m_{\mu\mu} < 66\,\text{GeV}$.

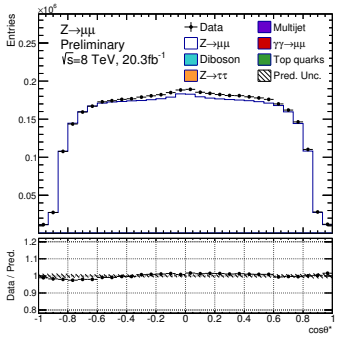

(e) Dimuon $\cos\theta^*$ for all $|y_{\mu\mu}|$ and $80 < m_{\mu\mu} < 91\,\text{GeV}$.

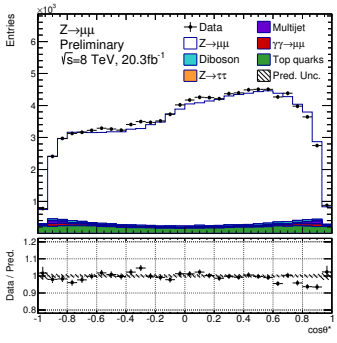

(f) Dimuon $\cos\theta^*$ for all $|y_{\mu\mu}|$ and $116 < m_{\mu\mu} < 150\,\text{GeV}$.

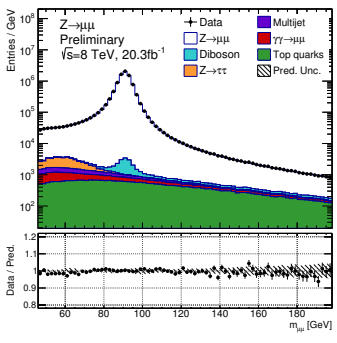

(g) Dimuon $m_{\mu\mu}$ for all $|y_{\mu\mu}|$.

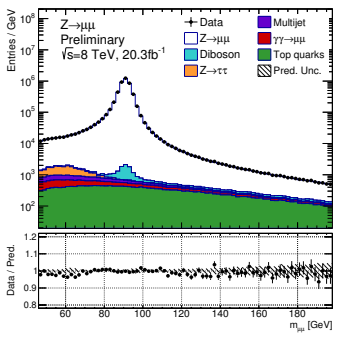

(h) Dimuon $m_{\mu\mu}$ for $|y_{\mu\mu}| < 1.0$.

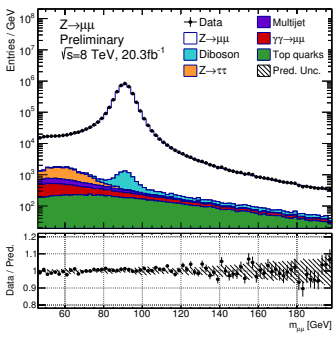

(i) Dimuon $m_{\mu\mu}$ for $|y_{\mu\mu}| > 1.0$.

FIG. 57: Control distributions of the dimuon differential variables used in different regions of the measurement phase space. The error bars show statistical uncertainties only.

11. SYSTEMATIC UNCERTAINTIES

The cross-section measurements are subject to experimental and theoretical uncertainties. Each source of uncertainty is classified as correlated or uncorrelated between measurement bins. The uncertainties on each source are propagated to the cross-section and A_{FB} measurements using a variety of well known methods.

The offset method is used to determine correlated uncertainties and estimate template uncertainties. Toy MC uncertainty propagation is used to estimate uncorrelated uncertainty components where the uncorrelated component is non-Poissonian. The bootstrap resampling technique is used to estimate statistical or statistically decomposed uncorrelated Poissonian components.

A. Uncertainty Propagation

The nominal set of measured cross-section values presented in the forthcoming results sections (Sections 12-14) list the measured central values and the statistical and systematic uncertainties. Practically, the determination of each uncertainty component involves repeating the cross-section calculation many times according to the propagation method. The term "nominal" explicitly refers to the calculation of the central values including the associated unfolding response matrices. Each variation of the cross-section calculation is performed "in isolation", meaning that it uses its own determination of multijet background and unfolding response matrices.

The Offset Method

The offset method is used to estimate bin-to-bin correlated uncertainties, in most cases symmetrising the propagated uncertainty about the central value. The cross-section calculation is repeated twice each time the offset method is implemented, once varying the source up and another varying the source down by one standard deviation of the uncertainty. This yields cross-section values of σ^+ and σ^- respectively. The difference between the varied cross-section value, $\sigma^\pm$, and the nominal σ is the propagated uncertainty to the cross-section:

$$\Delta^\pm = \sigma^\pm - \sigma\,. \tag{80}$$

where Δ is the propagated uncertainty. The sign convention is important for determining how the cross-section changes for a given upwards or downwards offset. In the data tables provided in the results section, only the upwards offset is summarised for correlated uncertainties. The total uncertainty however, is calculated from the symmetrised offset from the nominal, i.e. $(|\Delta^+|+|\Delta^-|)/2$.

The offset method's advantage is its relative simplicity, however its drawback is that systematic uncertainties may be over-estimated when the bin-to-bin correlation model is oversimplified.

The Toy Monte Carlo Method

The toy MC method estimates propagated uncorrelated uncertainties by using a set of pseudo-experiments (toys) generated by varying the source central value according to a Gaussian distribution with standard deviation equal to the source uncertainty value. Practically, this is achieved by using a random number generator in association with the Gaussian distribution to determine the varied source central values, and hence why it is considered a MC method. Each toy/variation yields its own unique final cross-section values. The distribution of toy MC cross-section values about the nominal set is used to determine the propagated source uncertainty, Δ^{toys}:

$$\Delta^{\text{toys}} = \sqrt{\frac{1}{N}\sum_{i=1}^{N}\left(\sigma_i^{\text{toy}} - \bar{\sigma}^{\text{toy}}\right)^2}, \tag{81}$$

where,

$$\bar{\sigma}^{\text{toy}} = \frac{1}{N}\sum_{i=1}^{N}\sigma_i^{\text{toy}}, \tag{82}$$

and N is the number of MC toys used, σ_i^{toy} are the i^{th} toy cross-section values and $\bar{\sigma}^{\text{toy}}$ is the mean of the toy cross-section values. The Toy MC method achieves greater numerical stability compared to the offset method, however is more computationally intensive. The number of toys required typically needs to be greater than the number of measurement bins for good statistical precision.

The Bootstrap Method

The bootstrap method is used to estimate the statistical uncertainties due to the finite size of the $\sqrt{s} = 8\,\text{TeV}$ ATLAS data set and the statistical precision of the MC samples. The sample to be assessed (data or MC) is statistically re-sampled to form statistical replicas of the nominal. By generating many replicas the propagated statistical uncertainty is estimated from the distribution of cross-sections about the nominal.

Let $\mathbf{X}$ be a finite sample of n measurements,

$$\mathbf{X} = \{X_1, X_2, X_3, \ldots, X_{n-1}, X_n\}, \tag{83}$$

where X_i is the i^{th} measurement of $\mathbf{X}$. Re-sampling of $\mathbf{X}$ may be performed when assuming that the occurrence of each measurement follows a Poisson distribution, P, with a mean of $\mu_p = 1$.

A random number generator can be used to distribute, according to $P(\mu_p)$, individual Poisson weights for each measurement. For example,

$$\mathbf{P} = \{2, 0, 1, \ldots, 1, 0\}\,, \tag{84}$$

which results in the following re-sampled set, $\mathbf{X}'$:

$$\begin{aligned} \mathbf{X}' &= \mathbf{P} \cdot \mathbf{X} \\ &= \{2, 0, 1, \ldots, 1, 0\} \cdot \{X_1, X_2, X_3, \ldots, X_{n-1}, X_n\} \\ &= \{X_1, X_1, X_3, \ldots, X_{n-1}\}\,. \end{aligned} \tag{85}$$

The resulting re-sampled set is then used in-place of the nominal sample for that bootstrap replica. Cross-section values for each replica are calculated and the RMS variance of the replica values about the nominal defines the propagated statistical uncertainty. Like the toy MC method, many bootstrap replicas are required to achieve a high degree of precision of the estimation.

For N bootstrap replicas, the statistical uncertainty on the sample is taken to be the standard deviation of replica values:

$$\Delta^{\text{replicas}} = \sqrt{\frac{1}{N}\sum_{i=1}^{N}\left(\sigma_i^{\text{replica}} - \bar{\sigma}^{\text{replica}}\right)^2}\,, \tag{86}$$

where,

$$\bar{\sigma}^{\text{replica}} = \frac{1}{N}\sum_{i=1}^{N}\sigma_i^{\text{replica}}\,, \tag{87}$$

where $\sigma_i^{\text{replica}}$ are the i^{th} replica cross-section values and $\bar{\sigma}^{\text{replica}}$ is the mean of the replica cross-section values.

Covariance and Correlation Matrices

Bin-to-bin correlations for each toy MC or bootstrap source are automatically encoded in covariance matrices calculated from the sets of toy or replica variations. The covariance between two bins, l and m, of the cross-section measurement is defined as:

$$\text{cov}(\sigma^{(l)}, \sigma^{(m)}) = \frac{1}{N}\sum_{i=1}^{N}\left(\sigma_i^{(l)} - \bar{\sigma}^{(l)}\right)\left(\sigma_i^{(m)} - \bar{\sigma}^{(m)}\right)\,, \tag{88}$$

where σ_i is the i^{th} toy or replica of the uncertainty source, and

$$\bar{\sigma}^{(l)} = \frac{1}{N}\sum_{i=1}^{N}\sigma_i^{(l)}\,. \tag{89}$$

This representation also allows for the uncertainty source to be decomposed into a nuisance parameter representation, further discussed in Section 14. The correlation between two bins may be calculated from their covariance using the relation:

$$\text{corr}(\sigma^{(l)}, \sigma^{(m)}) = \frac{\text{cov}(\sigma^{(l)}, \sigma^{(m)})}{\text{cov}(\sigma^{(l)}, \sigma^{(l)}) \cdot \text{cov}(\sigma^{(m)}, \sigma^{(m)})} \,. \tag{90}$$

B. Sources of Uncertainty

Data Statistics

The $\sqrt{s} = 8\,\text{TeV}$ data set recorded by the ATLAS detector has limited statistics which lead to a statistical uncertainty on the final unfolded differential cross-section measurement. The data uncertainty is quantified using the bootstrap resampling method using 1000 replica re-sampled distributions. The propagated uncertainty is $\sim 1.2\%$ of the cross-section below the Z-peak in $m_{\mu\mu}$, $\sim 0.3\%$ on the Z-peak and $\sim 4\%$ above the Z-peak.

Luminosity Uncertainty

A constant uncertainty of $\pm 1.9\%$ is assigned to the integrated luminosity (calculated using luminosity tag `OflLumi-8TeV-004`) systematic uncertainty[124].

Monte Carlo Statistics

Each MC sample has a finite number of events which leads to a statistical uncertainty on the final cross-section values. The bootstrap re-sampling method is used with 1000 bootstrap replicas for each MC process to estimate the propagated uncertainty. The uncertainty is $\sim 1\%$ of the cross-section below the Z-peak ($m_{\mu\mu} < 66\,\text{GeV}$), $\sim 0.2\%$ on and about the Z-peak and $\sim 1.2\%$ above the Z-peak ($m_{\mu\mu} > 150\,\text{GeV}$).

Monte Carlo Cross-Section and K-factors

A generated MC sample is normalised according to its physics process cross-section. The uncertainty on the cross-section value is propagated using the offset method due to its correlation across events. Up and down variations of the cross-section also include uncertainties on the K-factor. Table 17 summarises the MC cross-section uncertainties. The combined uncertainty is $\sim 1\%$ of

the cross-section away from the Z-peak ($m_{\mu\mu} < 66\,\text{GeV}$ and $m_{\mu\mu} < 150\,\text{GeV}$) and $\sim 0.2\%$ on the Z-peak.

Process	$\delta\sigma$ [%]	Process	$\delta\sigma$ [%]
$\gamma\gamma \to \mu\bar{\mu}$	40.0	$Z \to \tau\bar{\tau}$	5.0
$t\bar{t}$	6.0	WW	10.0
$t\|\bar{t}$	6.0	ZZ	4.2
$W \to \mu\bar{\nu}$	5.0	WZ	4.0
$W \to \tau\bar{\nu}$	5.0	–	–

TABLE 17: Correlated systematic uncertainties of the different MC processes, before propagation, used in the analysis. The correlated uncertainties are propagated using the offset method.

Parton Distribution Function Systematics

The signal MC used in the analysis is generated using the CT10 central PDF[85,125]. In addition to the central set, the CT10 group provides 52 error sets for which a PDF fitting parameter was varied either positively or negatively by its uncertainty. The offset method is therefore used for the PDF uncertainties. Following the recommended CT10 prescription[85], the following equation is used to quantify the effect on the unfolded cross-section:

$$\Delta^{\pm} = \sqrt{\sum_{i=1}^{26} \left[\max\left(\sigma_i^{(\pm)} - \sigma, \sigma_i^{(\mp)} - \sigma\right)\right]^2}, \tag{91}$$

where σ is the nominal set of cross-section values, $\sigma_i^{(\pm)}$ is the upward or downward variation and the summation is performed over the varied PDF parameters. The uncertainty is largest at low $m_{\mu\mu}$ values where the effect is $\sim 1\%$ of the cross-section and falls gradually to $\sim 0.1\%$ at high $m_{\mu\mu}$ values.

Unfolding Method

Bayesian unfolding is used in this analysis because of statistical dilution, due to large number of bins, and the low bin purity arising from migrations off the Z-mass peak. The unfolding uncertainty follows the ATLAS Standard Model working group recommendation[126]. The unfolding uncertainty is determined from a data-driven closure test where the nominal signal MC is reweighted as a function of $m_{\mu\mu}$, $|y_{\mu\mu}|$ and $\cos\theta^*$. The weights are applied at the dressed truth-level producing a "pseudo-data" sample that has an improved agreement to real data at reconstruction-level. The

pseudo-data sample is unfolded with the nominal response matrix and the difference between the unfolded pseudo-data and the pseudo-data truth is the test of the closure and the estimate of unfolding uncertainty. The reweight w is defined as

$$w_{ijk} = \frac{N_{ijk}^{\text{data}} - N_{ijk}^{\text{bkg}}}{N_{ijk}^{\text{sig}}}, \tag{92}$$

where i, j, and k are the measurement bin indices; N^{data} is the number of selected reconstructed data events; N^{bkg} the number of selected reconstructed background events; and N^{sig} is the number of selected reconstructed DY signal events. The uncertainty is largest in the regions where the acceptance (Equation 67, Figures 29 and 30) is large. It is further discussed in the next subsection.

Muon Reconstruction Efficiency Corrections

The recommended procedure[127] for propagating the systematic uncertainties of the muon reconstruction efficiency corrections is to use the offset method for the correlated components and the toy MC method for the uncorrelated components.

For the offset method the muon reconstruction efficiency tool is used to provide weights offset by one standard deviation of the correlated component. This method is applied as a function of muon charge, p_T^{μ}, η_{μ} and ϕ_{μ} to every reconstructed MC muon and the effect is propagated fully to the cross section level. The difference with respect to the nominal is the propagated correlated uncertainty.

Toy MC is used to treat the uncorrelated part by randomly varying each muon's reconstruction efficiency weighting according to a gaussian with width equal to the uncorrelated systematic uncertainty. For each MC toy this is applied to every reconstructed MC event and the effect is propagated fully to the cross section. 1000 MC toys are used. The distribution about the nominal provides the estimate of the uncertainty. The scale of the combined uncertainty is $\sim 0.4\%$ of the cross-section across the measurement binning.

Muon Trigger Efficiency Corrections

The uncertainties for the high precision and MTS group sets of muon trigger efficiency corrections are able to be propagated simultaneously due to their separate muon p_T^{μ} regimes. Both sets of correlated systematic components are propagated using the offset method where the muon trigger efficiency correction is varied up and down by one standard deviation. Both sets of statistical components are propagated using the toy MC method where 1000 MC toys are used. The combined uncertainty is $\sim 0.1\%$ of the cross-section on and above the Z-peak and $\sim 0.3\%$ for $m_{\mu\mu} < 66\,\text{GeV}$.

Isolation and Impact Parameter Efficiencies

Muon isolation and impact parameter corrections also have correlated and uncorrelated uncertainty components. The offset method propagates one standard deviation shifted variations of the correlated component to the cross-section level. The toy MC method propagates the uncorrelated uncertainties using 1000 MC toys. The combined uncertainty is $\sim 0.3\%$ of the cross-section across the measurement binning.

QCD Multijet Background

The QCD multijet estimation has two associated systematic error components associated with the ABCD multijet method. The first is the isolation choice which affects the y-$\cos\theta^*$ template shape and the signal contamination in the anti-isolated regions. The second is the choice of fit parameters applied for the f_{abcd} extrapolation into the signal region. The statistical uncertainty is implicit in the data and MC statistical uncertainties and therefore is already accounted for with the determination of their uncertainties via the bootstrap resampling method.

The isolation choice uncertainty component is determined by varying the isolation requirement for the anti-isolated signal region. The nominal anti-isolation requirement for each muon is $I_\mu > 0.1$. Table 18 lists the variations of the isolation region and percentage change in the total multijet estimation.

Isolation Variation	DY Signal Contamination	Change in Multijet
$0.1 < I_\mu$ (nominal)	3.4%	–
$0.1 < I_\mu < 0.3$	5.1%	+3.9%
$0.3 < I_\mu < 0.5$	3.3%	+20.1%
$0.5 < I_\mu < 1.0$	3.3%	+3.6%
$1.0 < I_\mu < 2.0$	3.3%	-15.3%

TABLE 18: The isolation, I_μ, variations used to estimate the uncertainty in the determination of the QCD multijet background. The percentage of signal contamination present in each sub-region is listed along with the percentage change in total multijet background. The presented values are taken from the $46 < m_{\mu\mu} < 200\,\text{GeV}$ region.

Each anti-isolation region is statistically independent and provides a variation on the template for the y-$\cos\theta^*$ shape estimation. The template shapes in the $46 < m_{\mu\mu} < 66\,\text{GeV}$ mass window of the nominal and the two largest variations, $0.3 < I_\mu < 0.5$ and $1.0 < I_\mu < 2.0$ are shown in Figure 58. The $0.3 < I_\mu < 0.5$ variation shows a smaller fraction of events occurring at low $y_{\mu\mu}$ values and a

greater fraction of events at high $y_{\mu\mu}$ values. The opposite is true for the $1.0 < I_\mu < 2.0$ variation where a greater fraction of events are found at low $y_{\mu\mu}$ values. The shape in $\cos\theta^*$ is stable across isolation variations. The effect of varying the specific anti-isolation regions is propagated to cross-section values. The QCD multijet isolation component is the standard deviation of the cross-section differences about the nominal.

The extrapolation fit parameter uncertainty is determined from the standard deviation of four different fit constraints. Table 19 lists the variations of the f_{abcd} fitting range.

f_{abcd} Fit Range	f_{abcd} Value	Change in Multijet
$0.1 < I_\mu^{\text{Fit}} < 2.0$ (nominal)	1.18	–
$0.1 < I_\mu^{\text{Fit}} < 0.5$	1.17	-1.4%
$0.5 < I_\mu^{\text{Fit}} < 1.0$	1.21	+2.5%
$1.0 < I_\mu^{\text{Fit}} < 2.0$	1.14	-4.0%
$2.0 < I_\mu^{\text{Fit}} < 3.0$	1.00	-1.6%

TABLE 19: The f_{abcd} fit range variations, I_μ^{Fit}, used in the estimation of the fit parameter uncertainty on the multijet estimation. The f_{abcd} value is shown along with the change in total multijet background. The presented values are taken from the $46 < m_{\mu\mu} < 200\,\text{GeV}$ region.

The set of variations does not affect the template shapes but does affect the mass-window multijet normalisations. The different variations on the fitting range are propagated to cross-section values and the propagated uncertainty is calculated from the standard deviation.

In principle, the f_{abcd} fit can be any n^{th}-order polynomial. A 1^{st}-order polynomial was chosen due to model simplicity. Variations of higher orders are not included as this would effectively double-count the extrapolation fit parameter uncertainty. The combined uncertainty is $\sim 0.1\%$ of the cross-section on and above the Z-peak and $\sim 0.4\%$ for $m_{\mu\mu} < 66\,\text{GeV}$ where the multijet background is most prominent.

Muon Momentum Corrections

The uncertainties of the muon momentum resolution and momentum scale corrections are propagated using the offset method. The muon combined performance group provides a tool for varying each muon momentum correction by ± 1 standard deviation. However, for the purposes of achieving an accurate bin-to-bin correlation model for the combination of electron- and muon-channel results (Section 14) the muon momentum resolution is decomposed into different η_μ regions of the detector.

Table 20 lists the different η_μ regions of the decomposition. For each region both the ± 1 standard deviation variations are propagated. Muons that are reconstructed within the decomposition region

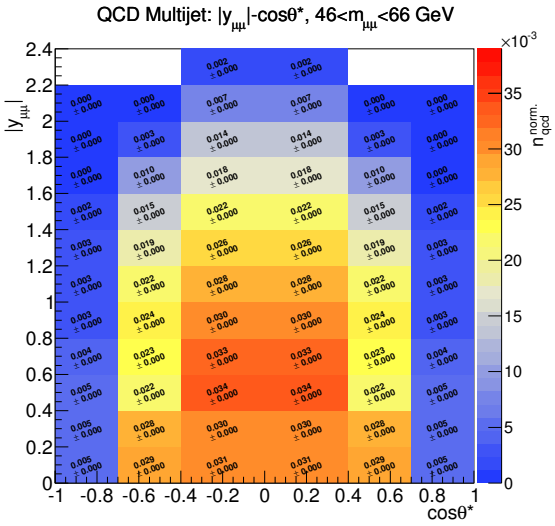

(a) The unit normalised nominal multijet background template in the $46 < m_{\mu\mu} < 66\,\text{GeV}$ mass window.

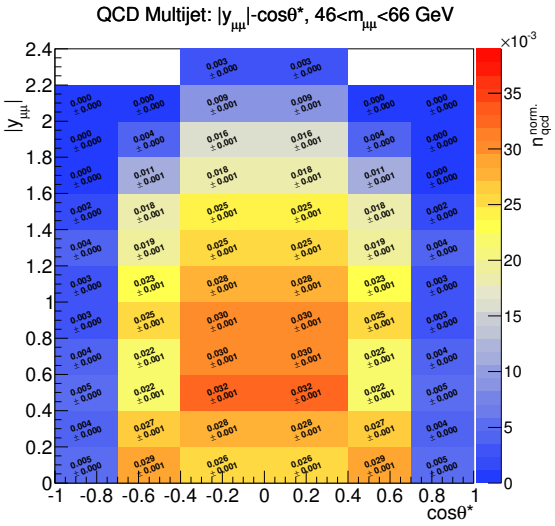

(b) The unit normalised $0.3 < I_\mu < 0.5$ isolation variation of the multijet background template in the $46 < m_{\mu\mu} < 66\,\text{GeV}$ mass window.

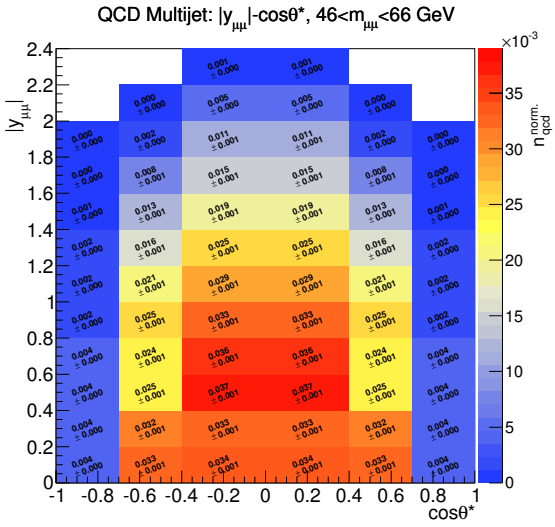

(c) The unit normalised $1.0 < I_\mu < 2.0$ isolation variation of the multijet background template in the $46 < m_{\mu\mu} < 66\,\text{GeV}$ mass window.

FIG. 58: Two dimensional ($|y_{\mu\mu}|$, $\cos\theta^*$) plots of the QCD multijet template shape in the first mass window of the measurement. The templates are shown before normalisation to the ABCD multijet mass region estimate. Uncertainties of the values show statistical uncertainties only.

are corrected with the offset variation and muons outside the region receive the nominal correction. The decompositions are propagated through to the cross-section level with the offset definition of the uncertainty. The quadratic sum of the decomposed uncertainties were found to be consistent with the non-decomposed uncertainty propagation.

-η Decompositions	+η Decompositions
$-2.4 < \eta_\mu < -2.0$	$0.0 < \eta_\mu < 0.4$
$-2.0 < \eta_\mu < -1.6$	$0.4 < \eta_\mu < 0.8$
$-1.6 < \eta_\mu < -1.2$	$0.8 < \eta_\mu < 1.2$
$-1.2 < \eta_\mu < -0.8$	$1.2 < \eta_\mu < 1.6$
$-0.8 < \eta_\mu < -0.4$	$1.6 < \eta_\mu < 2.0$
$-0.4 < \eta_\mu < 0.0$	$2.0 < \eta_\mu < 2.4$

TABLE 20: The -η and +η hemisphere inner detector muon momentum correction uncertainty decompositions.

The momentum scale uncertainty increases with $m_{\mu\mu}$: the effect is $\sim 0.4\%$ of the cross-section on the Z-peak and $\sim 0.5\%$ above the Z-peak, $m_{\mu\mu} > 116\,\text{GeV}$. The resolution uncertainty is smallest on the Z-peak and at low $|y_{\mu\mu}|$ values at $\sim 0.1\%$ of the cross-section, and largest at high $|y_{\mu\mu}|$ and $m_{\mu\mu}$ values at $\sim 1\%$.

Z-boson p_T Modelling

The control distributions of Figures 55-57 highlighted the inaccurate modelling of the dimuon transverse momentum, $p_T^{\mu\mu}$, in MC. The uncertainty attributed to this is accounted for by correcting the Z-boson p_T distributions at the truth level and observing the effect on the cross-section values.

The correction is a reweighting to the nominal reconstructed difference between data and signal MC (Equation 92) as a function of $p_T^{\mu\mu}$. The Z-p_T corrections are determined separately in each of the different mass windows of the cross-section binning to achieve a Z-p_T $m_{\mu\mu}$ dependence. The corrections are applied as a function of Z-p_T and $m_{\mu\mu}$ at the bare truth-level and propagated through to cross-section values. The normalisation of the MC is preserved through the corrections. Figure 59 shows the $p_T^{\mu\mu}$ and p_T^{μ} control distributions before and after the corrections. The difference between the nominal and the Z-p_T reweighted cross-sections is taken as the Z-boson p_T modelling uncertainty. The uncertainty is $\sim 0.2\%$ of the cross-section on the Z-peak and $< 0.1\%$ either side of the Z-peak.

C. Analysis of Uncertainty Contributions

The largest contributing uncertainties (excluding the 1.9% luminosity uncertainty) for the triple-differential cross-sections unfolded using Born truth-level response matrices are shown as a function of $\cos\theta^*$ in Figures 60-66. The figures show statistical uncertainties (data and MC) to be largest either side of the Z-peak where the statistical precision is diluted across the large number of bins. In these regions the statistical uncertainties are of a similar magnitude to the systematic uncertainties below the Z-peak, whereas statistical uncertainties are slightly larger above the Z-peak. The MC systematic uncertainties are shown to give a percentage-level contribution in the low $m_{\mu\mu} < 66\,\text{GeV}$ region due to the relatively large $\gamma\gamma \to \mu\bar{\mu}$ and $Z \to \tau\bar{\tau}$ backgrounds that are seen in the control distributions in Figure 10 B. The PDF uncertainty also gives percentage-level contributions below the peak. On the Z-peak the unfolding and muon momentum scale uncertainties are the dominant sources. The unfolding uncertainty shows complex shapes in the three-dimensional phase space because of the limited accuracy of the response matrix in describing event migrations. The unfolding uncertainty is further discussed below. Above the Z-peak data and MC statistical uncertainties dominate alongside the unfolding systematic uncertainty.

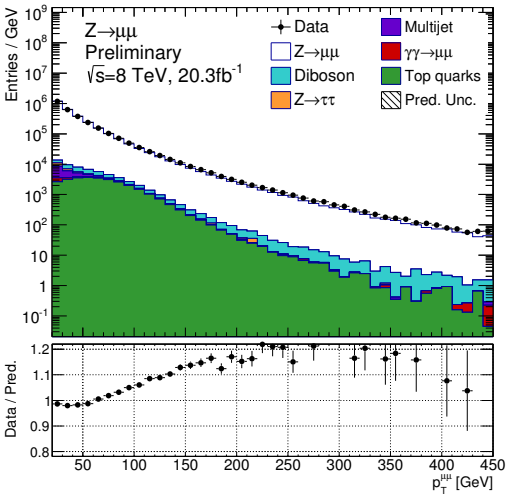

(a) Nominal reconstructed dimuon $p_T^{\mu\mu}$.

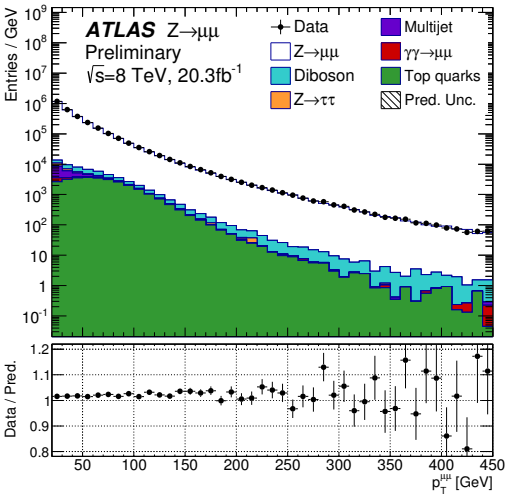

(b) Z-p_T corrected dimuon $p_T^{\mu\mu}$.

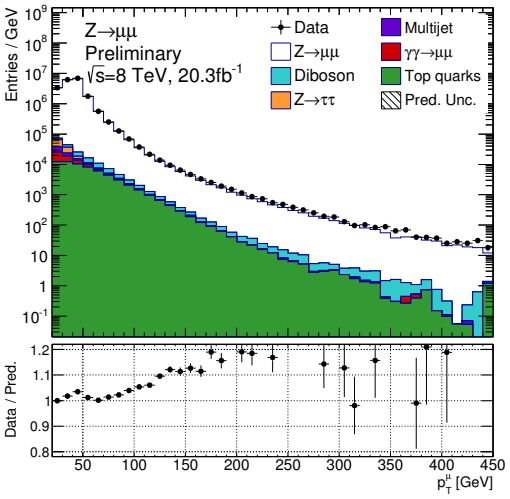

(c) Nominal reconstructed muon p_T^{μ}.

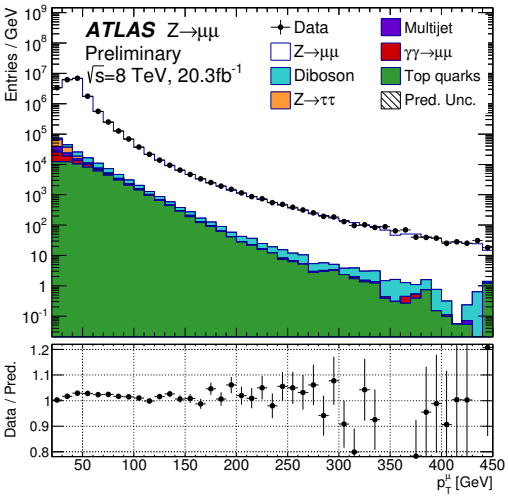

(d) Z-p_T corrected muon p_T^{μ}.

FIG. 59: Effect of the Z-boson p_T modelling corrections used in the determination of the modelling uncertainty upon the muon and dimuon transverse momentum distributions. The distributions are inclusive in $46 < m_{\mu\mu} < 200\,\text{GeV}$. The error bars show statistical uncertainties only.

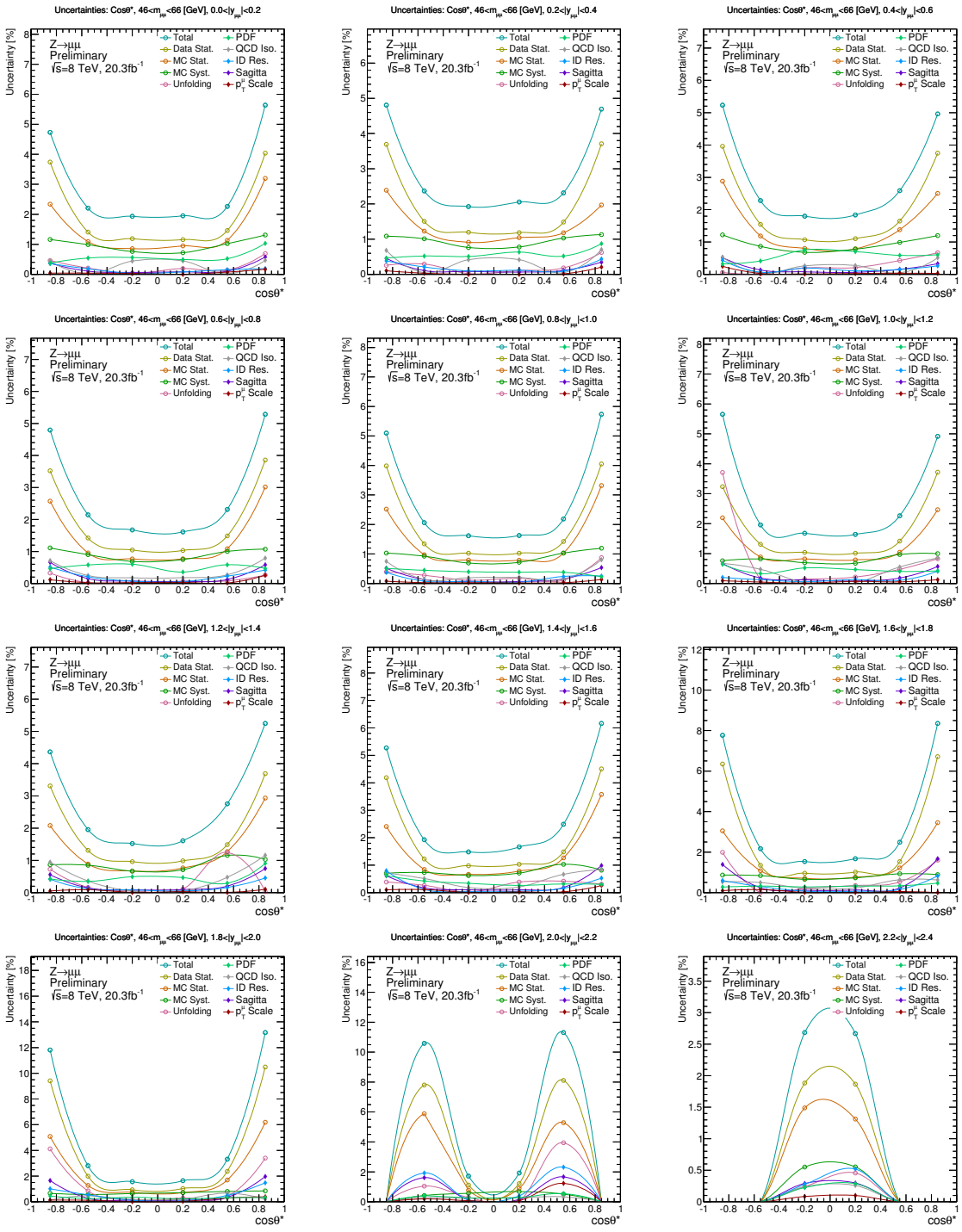

FIG. 60: Largest sources of uncertainty across each rapidity bin within the $46 < m_{ll} < 66\,\text{GeV}$ mass regime.

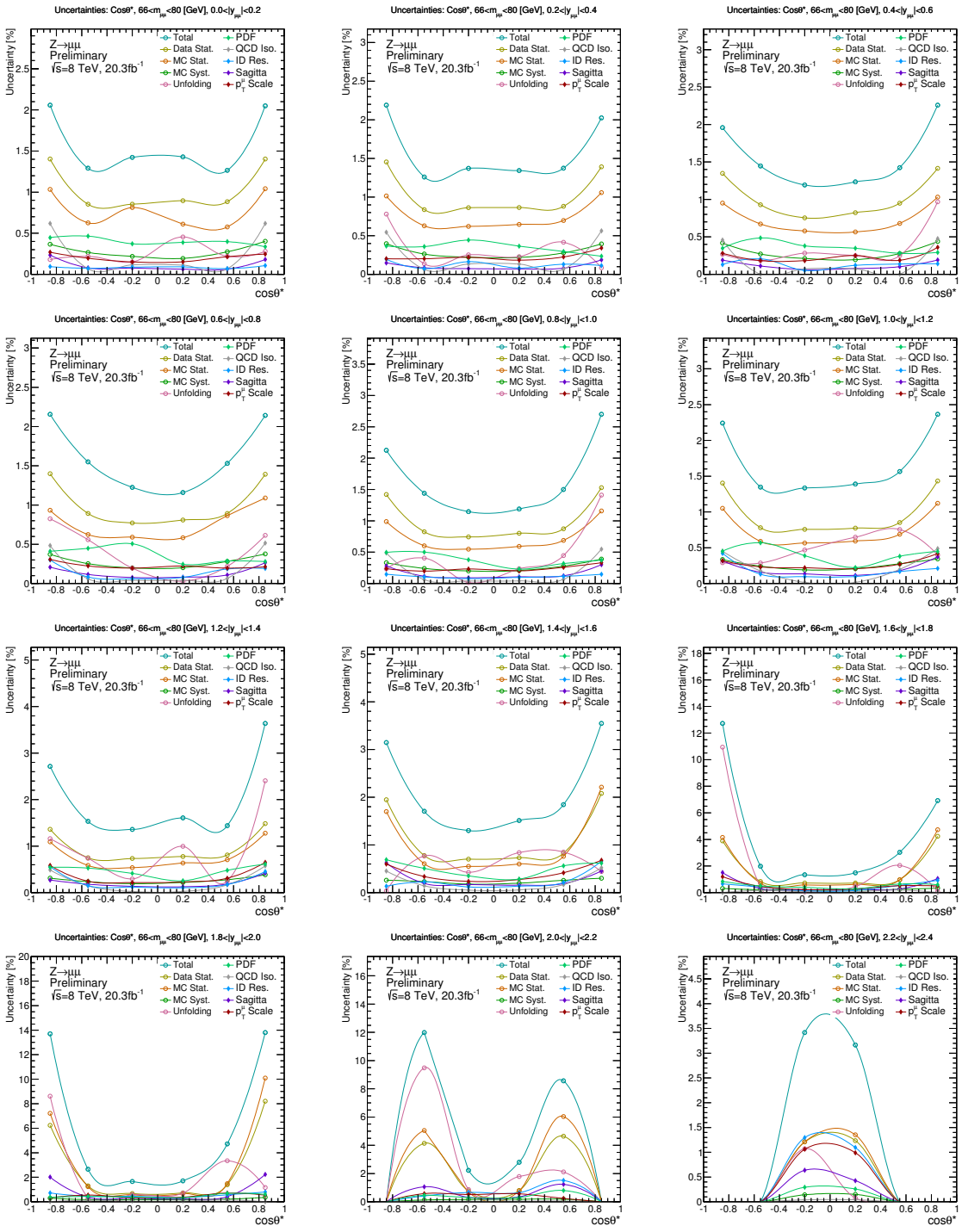

FIG. 61: Largest sources of uncertainty across each rapidity bin within the $66 < m_{ll} < 80\,\text{GeV}$ mass regime.

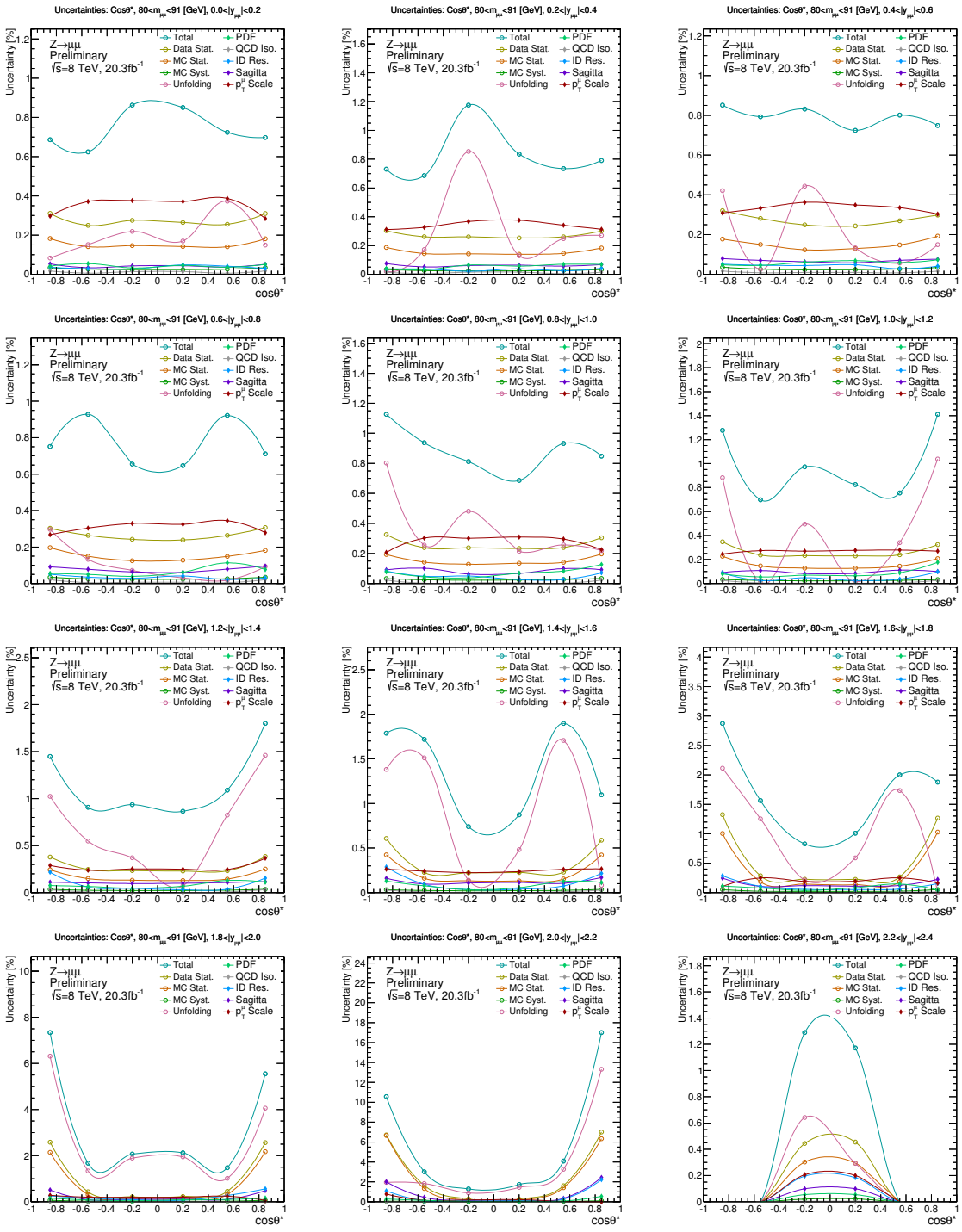

FIG. 62: Largest sources of uncertainty across each rapidity bin within the $80 < m_{ll} < 91\,\text{GeV}$ mass regime.

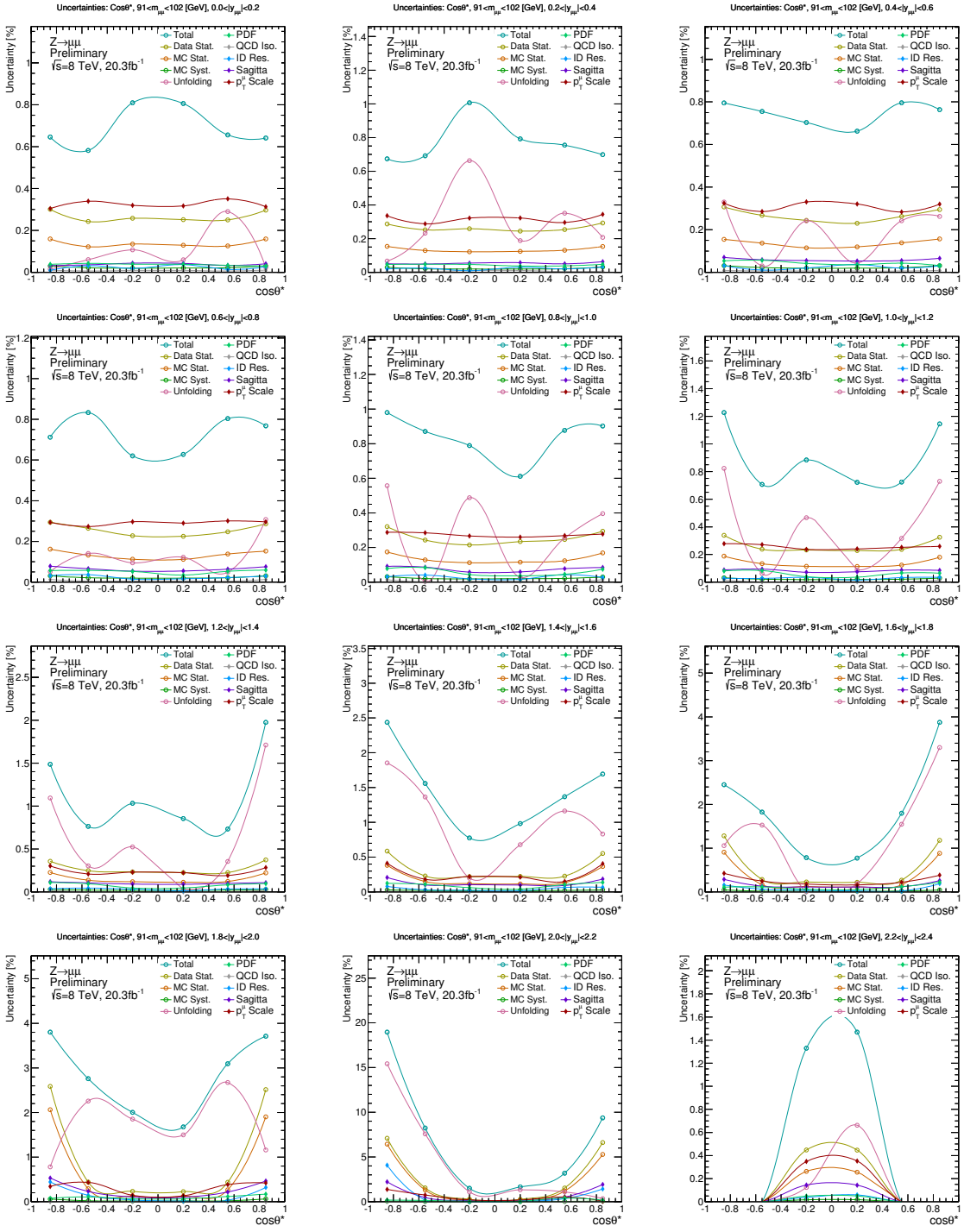

FIG. 63: Largest sources of uncertainty across each rapidity bin within the $91 < m_{ll} < 102\,\text{GeV}$ mass regime.

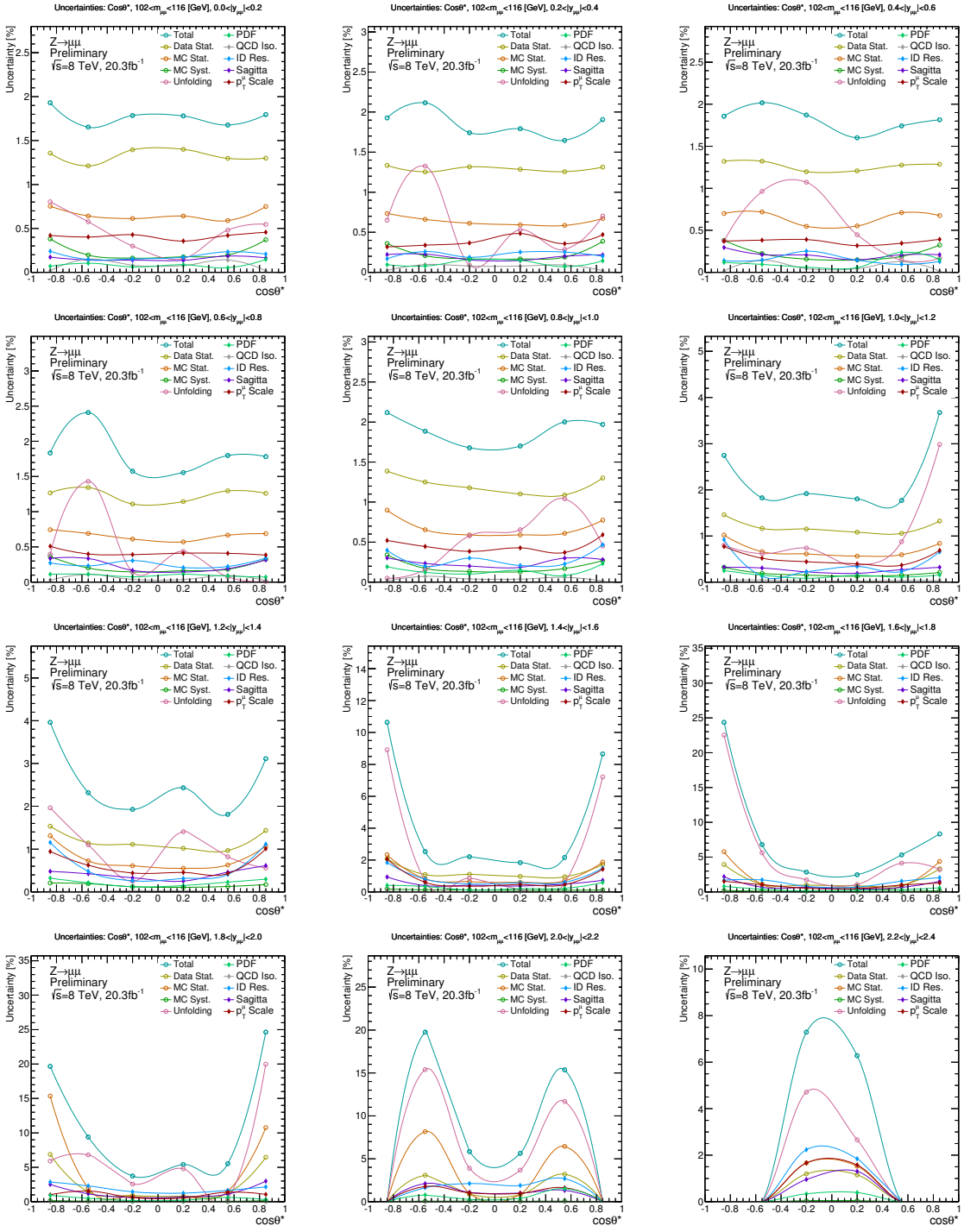

FIG. 64: Largest sources of uncertainty across each rapidity bin within the $102 < m_{ll} < 116\,\text{GeV}$ mass regime.

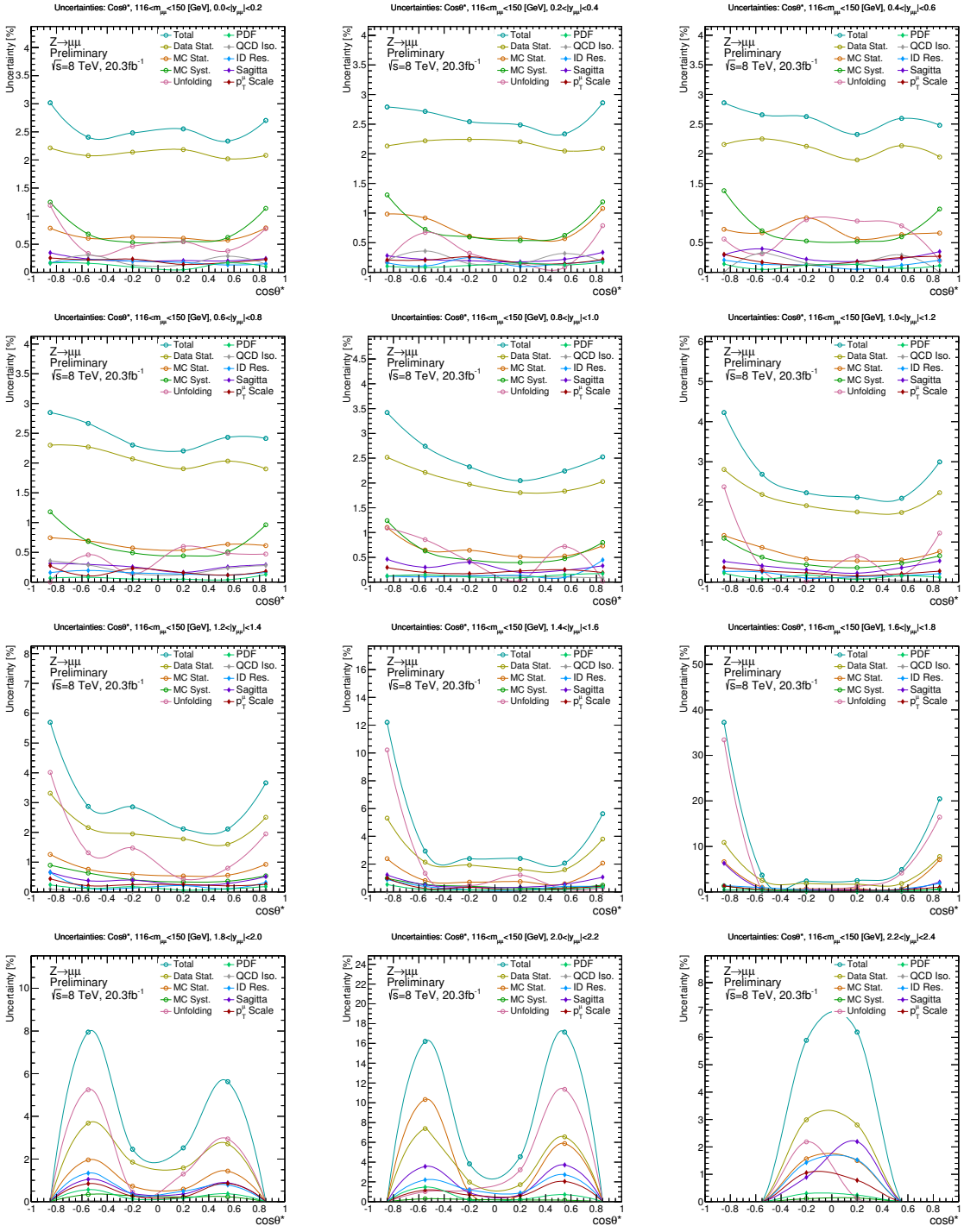

FIG. 65: Largest sources of uncertainty across each rapidity bin within the $116 < m_{ll} < 150\,\text{GeV}$ mass regime.

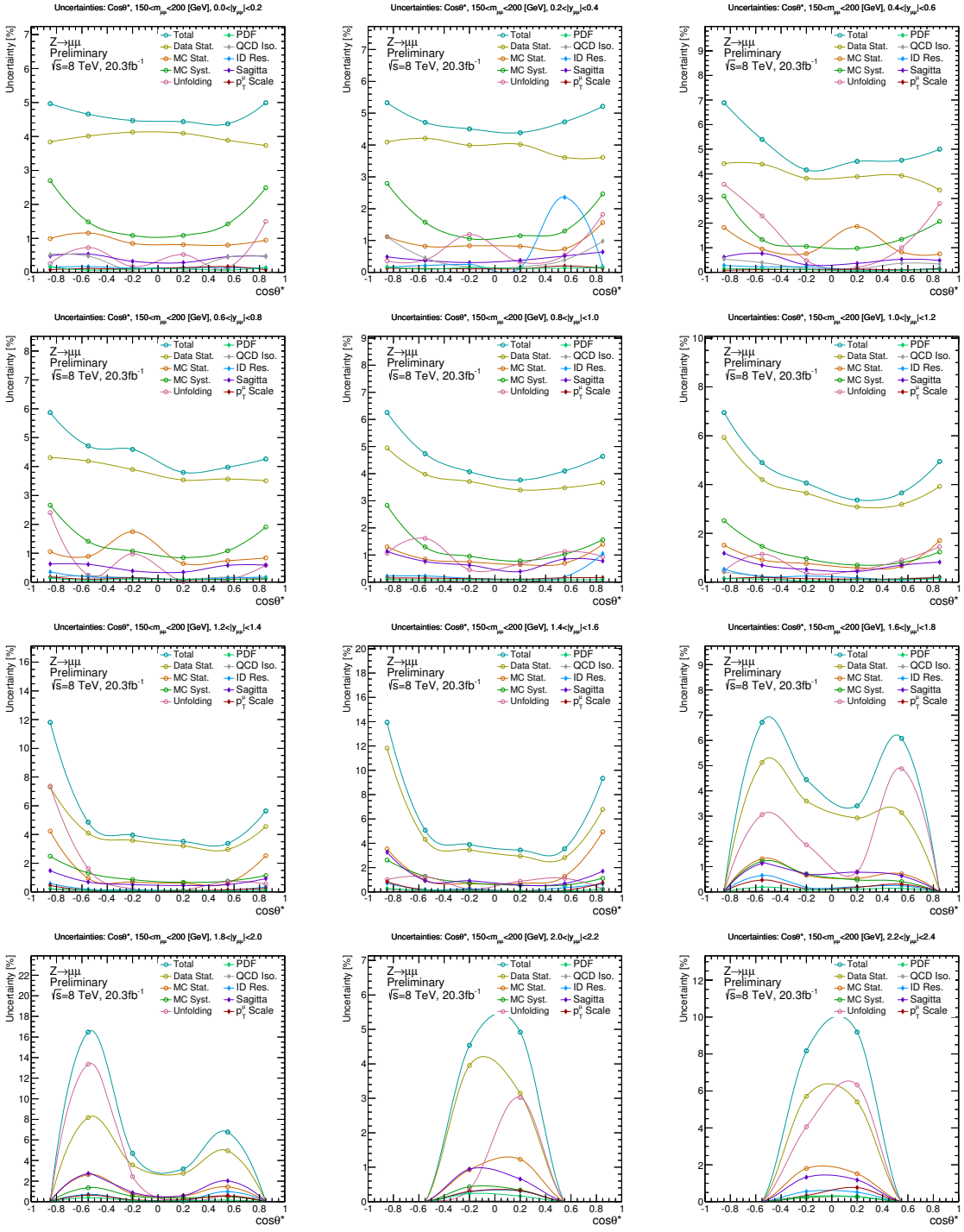

FIG. 66: Largest sources of uncertainty across each rapidity bin within the $150 < m_{ll} < 200\,\text{GeV}$ mass regime.

A prominent feature of the largest contributing uncertainty plots of Figures 60-66 are the shapes induced by the the unfolding uncertainty. The largest contribution of the unfolding to the total uncertainty is seen in the peak regions, $80 < m_{\ell\ell} < 91\,\text{GeV}$ and $91 < m_{\ell\ell} < 102\,\text{GeV}$. A test of the behaviour of the unfolding uncertainty was performed to ensure that a reduction and smoothing of the unfolding uncertainty occurs with an increase in the number of Bayesian unfolding iterations. Figure 67 shows the leading muon channel uncertainties for an example set of bins for different numbers of Bayesian iterations. The unfolding systematic shows a reduction when increasing the number of iterations along with increased statistical and p_T^μ-scale uncertainties due to the unfolding training to the new p_T^μ-scale, as expected by the iterative Bayesian method.

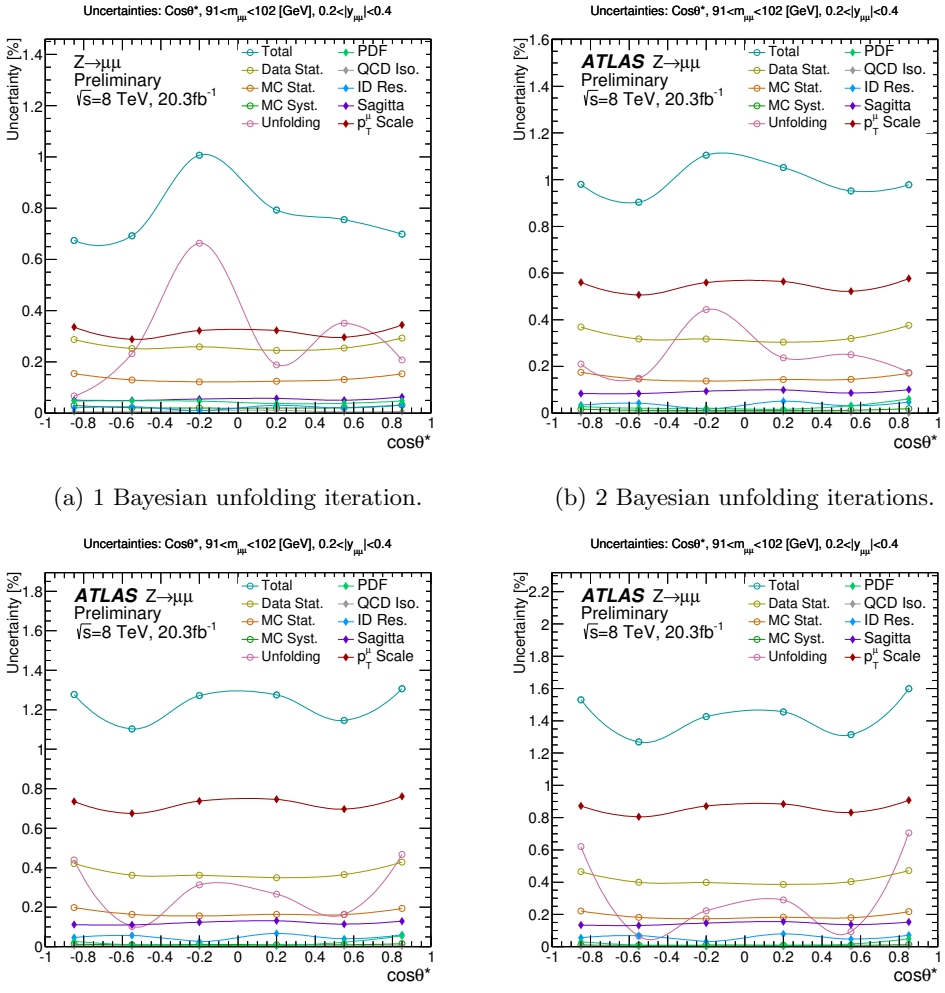

(a) 1 Bayesian unfolding iteration.

(b) 2 Bayesian unfolding iterations.

(c) 3 Bayesian unfolding iterations.

(d) 4 Bayesian unfolding iterations.

FIG. 67: Leading muon channel uncertainties for the $91 < m_{\mu\mu} < 102\,\text{GeV}$ and $0.2 < |y_{\mu\mu}| < 0.4$ cross-section bin for different numbers of Bayesian unfolding iterations.

To gauge the relative importance of the different uncertainty contributions across the triple-differential 504 cross-section bins, a new type of uncertainty plot has been developed. The uncertainty frequency plots show the number of bins in the measurement that contribute within a range of relative uncertainty. The figures allow for the identification of the largest systematic sources and for checks of anomalies. On the y-axis the names of the sources are listed. The z-axis (coloured) shows the cumulative number of bins that have values of uncertainty within the ranges given on the x-axis. The x-axis shows the ranges of relative uncertainty (uncertainty divided by cross-section value) in which the bins are accumulated. The uncertainty frequency plot for cross-sections unfolded using Born truth-level response matrices is shown in Figure 68. This shows the full 504 bins of the measurement (46 of which are vetoed due to limited data statistics, as discussed in the next subsection). Equivalent figures for dressed and bare unfolded results are provided in the appendix (Figures 94 and 95). Table 21 is provided for the y-axis row aliases used in these figures.

Additional uncertainty frequency plots are shown for three different mass regions of the data: below, on and above the Z-peak, Figures 69-71 respectively. The muon channel achieves an overall systematic precision similar to that of the statistical uncertainty of the ATLAS data. The largest sources are the unfolding systematic, the muon momentum scale and the MC DY signal statistical uncertainty. Below the Z-peak, Figure 69 shows the relatively large ($\sim 1\%$) MC systematic uncertainties of $\gamma\gamma \to \mu\bar{\mu}$ ("EW_PI") and $Z \to \tau\bar{\tau}$ ("BS_Ztautau"). Figure 70 shows the dominant uncertainties ($\sim 0.4\%$) of unfolding, muon momentum scale, muon reconstruction efficiency and muon isolation (not previously shown in Figures 60-66). Above the Z-peak Figure 71 shows the now large ($\sim 1\%$) $t\bar{t}$ systematic uncertainty ("EW_ttbar") as it is a more prominent background in the high mass region. The ID resolution uncertainties are also shown to increase in the $m_{\mu\mu} > 102\,\text{GeV}$ region because of the smaller measurable sagitta of muons with high p_T^{μ}.

Comparisons of the uncertainty frequency plots in the appendix show that the most precise cross-section values are obtained when unfolding using dressed truth-level MC response matrices. The smaller uncertainties are due to a small reduction of the unfolding uncertainty and data statistic uncertainty. A further discussion of the dressed- and bare-results is given in the appendix (Section 17).

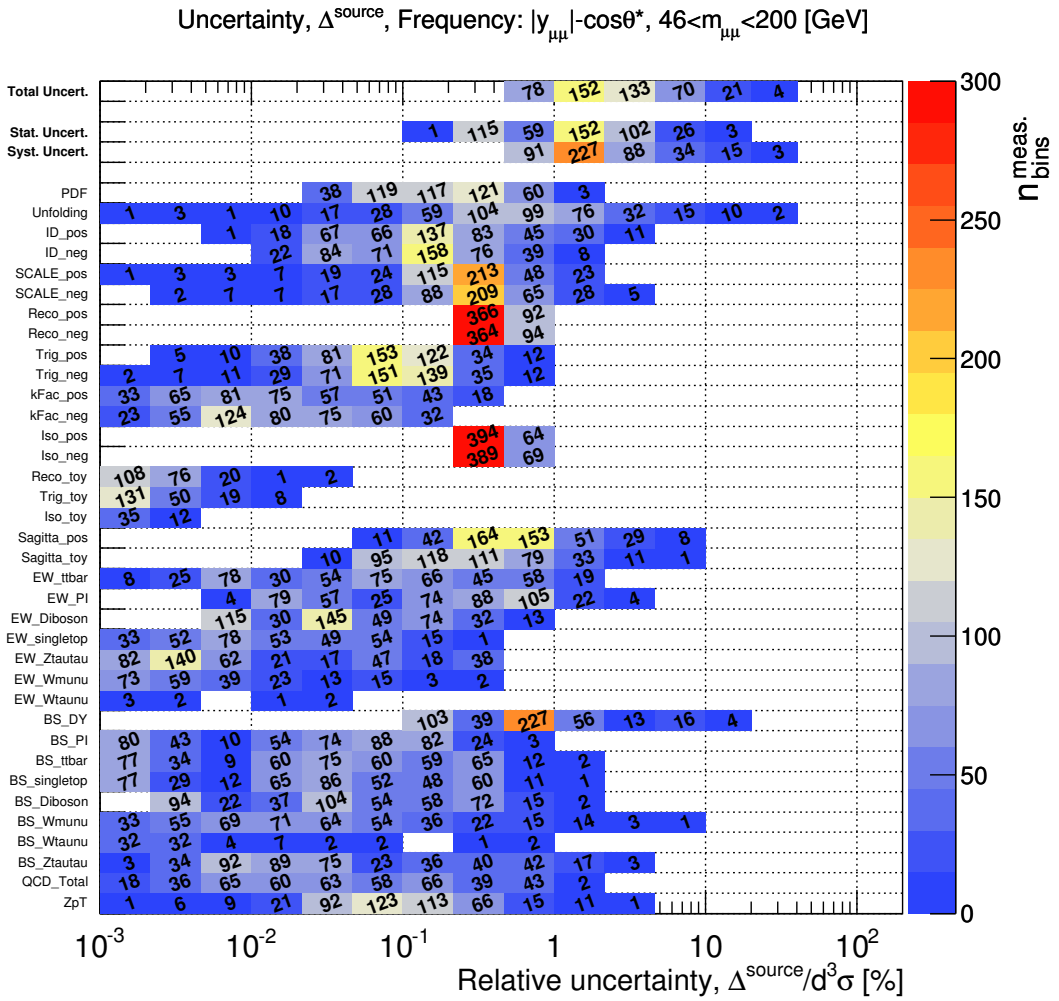

FIG. 68: Systematic and statistical uncertainty frequency distributions for the Born truth-level cross-sections. The first row is the total uncertainty, which is composed of the two rows directly below named "Stat. Uncert." and "Syst. Uncert." summed quadratically. The "Syst. Uncert." row is the quadratic sum of all of the remaining rows below. Table 21 summarises the y-axis aliases of the uncertainty sources. The phase space includes 504 measurement bins, 46 of which are vetoed because of low expected statistical precision.

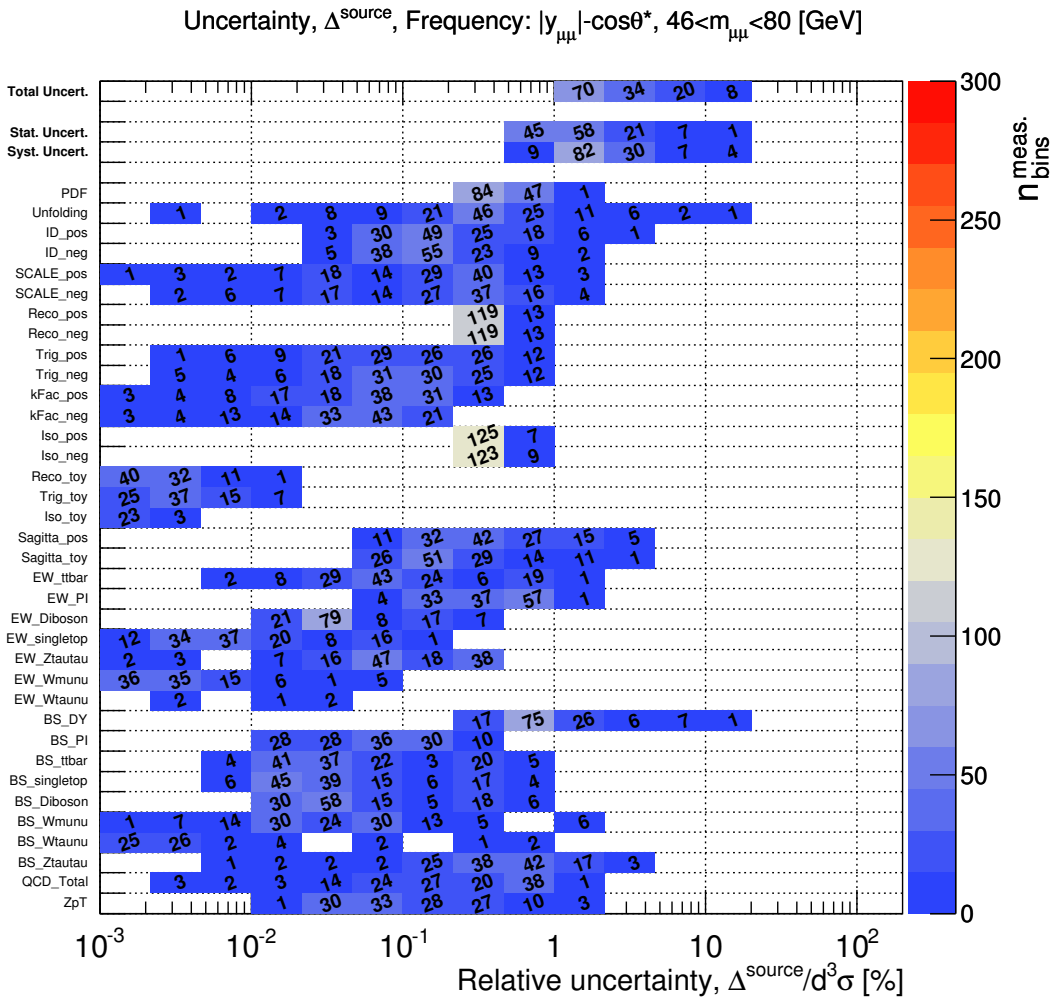

FIG. 69: Systematic and statistical uncertainty frequency distributions for the born cross-sections in the first two mass regions of the measurement. The first row is the total uncertainty, which is composed of the two rows directly below named "Stat. Uncert." and "Syst. Uncert." summed quadratically. The "Syst. Uncert." row is the quadratic sum of all of the remaining rows below. Table 21 summarises the y-axis aliases of the uncertainty sources. The phase space includes 144 measurement bins, 12 of which are vetoed because of low expected statistical precision.

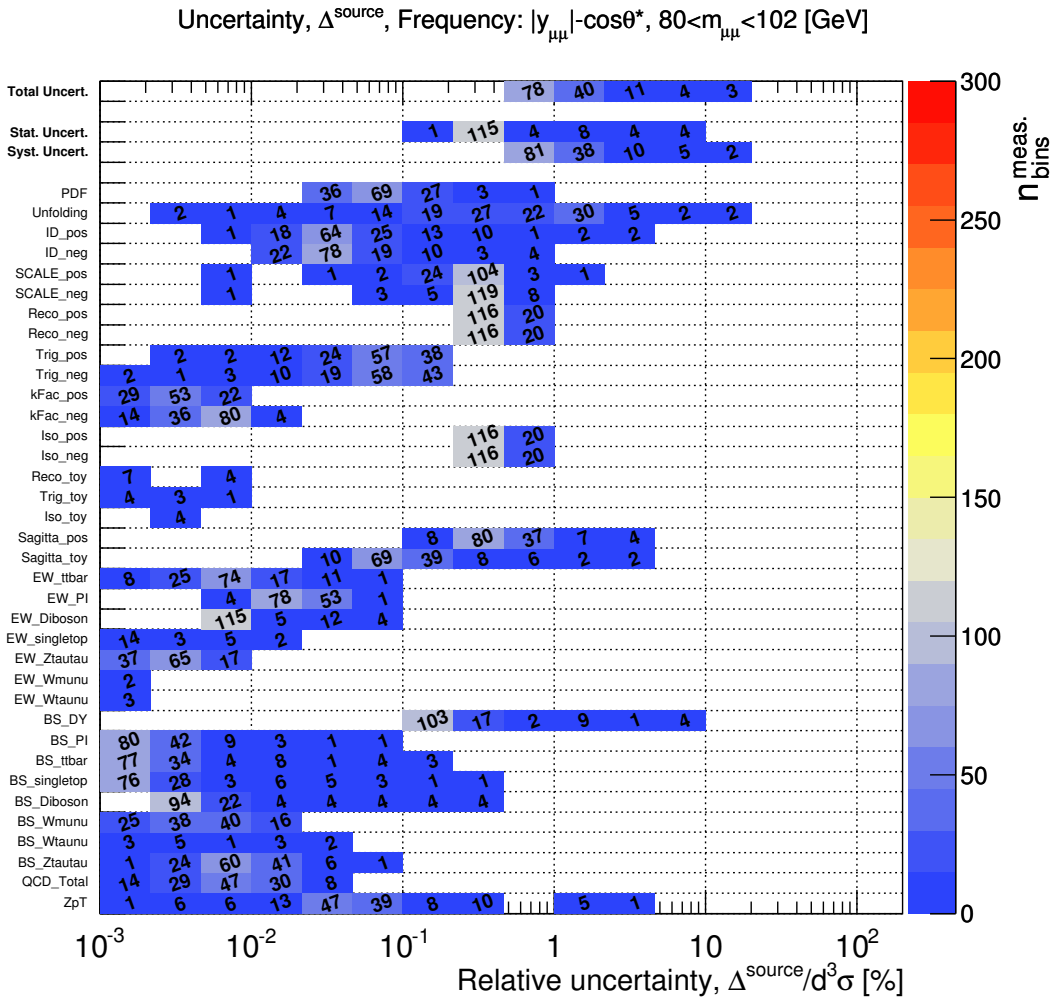

FIG. 70: Systematic and statistical uncertainty frequency distributions for the born cross-sections in the two mass regions about the Z-peak. The first row is the total uncertainty, which is composed of the two rows directly below named "Stat. Uncert." and "Syst. Uncert." summed quadratically. The "Syst. Uncert." row is the quadratic sum of all of the remaining rows below. Table 21 summarises the y-axis aliases of the uncertainty sources. The phase space includes 144 measurement bins, 8 of which are vetoed because of low expected statistical precision.

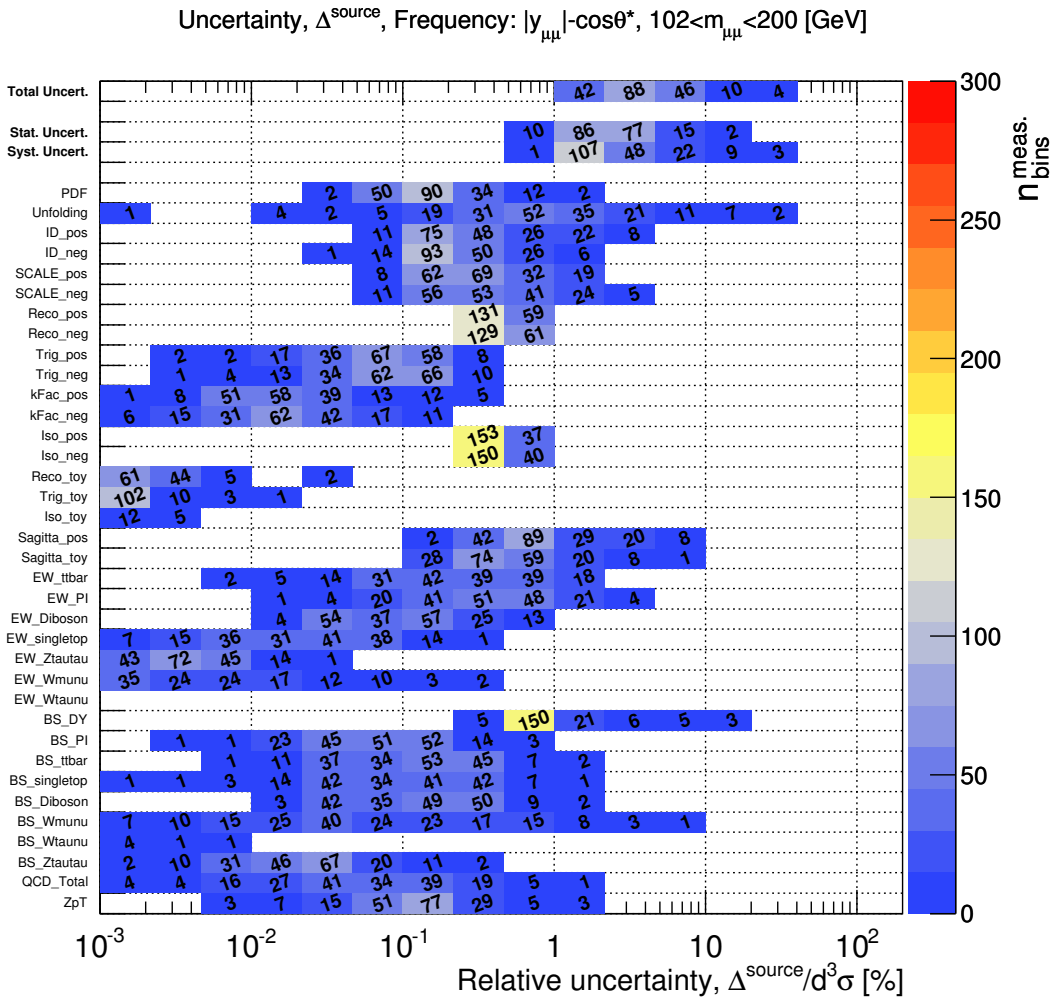

FIG. 71: Systematic and statistical uncertainty frequency distributions for the born cross-sections in the last three mass region of the measurement. The first row is the total uncertainty, which is composed of the two rows directly below named "Stat. Uncert." and "Syst. Uncert." summed quadratically. The "Syst. Uncert." row is the quadratic sum of all of the remaining rows below. Table 21 summarises the y-axis aliases of the uncertainty sources. The phase space includes 216 measurement bins, 26 of which are vetoed because of low expected statistical precision.

Alias	Error description	Alias	Error description
Total Uncert.	The total uncertainty on the cross section	Sagitta_toy	Sagitta uncorrelated uncertainties
Stat. Uncert.	The statistical error from 8 TeV data	EW_ttbar	ttbar correlated cross-section uncertainty
Syst. Uncert.	The quadrature sum of all systematic errors	EW_PI	PI correlated cross-section uncertainty
PDF	The systematic errors from PDF eigenvectors	EW_Diboson	Diboson correlated cross-section uncertainty
Unfolding	The systematic error due to MC unfolding	EW_singletop	singletop correlated cross-section uncertainty
ID_pos	Momentum smearing ID upward variation	EW_Ztautau	Ztautau correlated cross-section uncertainty
ID_neg	Momentum smearing ID downward variation	EW_Wmunu	Wmunu correlated cross-section uncertainty
Scale_pos	Momentum smearing Scale upward variation	EW_Wtaunu	Wtaunu correlated cross-section uncertainty
Scale_neg	Momentum smearing Scale downward variation	BS_Data	Data uncorrelated statistical uncertainty
Reco_pos	Reconstruction efficiency correlated upward variation	BS_DY	DY signal uncorrelated statistical uncertainty
Reco_neg	Reconstruction efficiency correlated downward variation	BS_PI	PI uncorrelated statistical uncertainty
Trig_pos	Trigger efficiency correlated upward variation	BS_ttbar	ttbar uncorrelated statistical uncertainty
Trig_neg	Trigger efficiency correlated downward variation	BS_singletop	singletop uncorrelated statistical uncertainty
kFac_pos	DY k-Factor correlated upward variation	BS_Dibson	Diboson uncorrelated statistical uncertainty
kFac_neg	DY k-Factor correlated downward variation	BS_Wmunu	Wmunu uncorrelated statistical uncertainty
Iso_pos	Isolation efficiency correlated upward variation	BS_Wtaunu	Wtaunu uncorrelated statistical uncertainty
Iso_neg	Isolation efficiency correlated downward variation	BS_Ztautau	Ztautau uncorrelated statistical uncertainty
Reco_toy	Reconstruction efficiency uncorrelated component	QCD_Tot	QCD multijet background total uncertainty
Trig_toy	Trigger efficiency uncorrelated component	ZpT	Z-boson p_T correction systematic uncertainty
Iso_toy	Isolation efficiency uncorrelated component		

TABLE 21: Description of the aliases used on the y-axis of the uncertainty frequency plots (Figures 68-71 and 94-95).

D. Low Statistics Bin Vetoing

In the extremities of the binning phase-space (high value $|y_{\mu\mu}|$ and $|\cos\theta^*|$) the expected number of reconstructed DY signal events is small. This is shown in the Drell–Yan signal expectation plots of Figures 72 and 73. The low cross-section in these bins is due to detector kinematic acceptance in η_μ and p_T^μ.

To ensure cross-section results with well-understood systematic and statistical uncertainties, bins with fewer than 25 reconstructed DY signal events are vetoed from the cross-section measurements. The vetoing of analysis bins occurs after the iterative Bayesian unfolding and is based on the nominal cross-section results only. Systematic or statistical replicas of the nominal (e.g. toy MC, bootstrap, etc.) cannot cause an analysis bin to be vetoed by a downward replica fluctuation.

Figures 72 and 73 show the bins that pass the low statistics bin vetoing requirement in the muon channel. Bins coloured in blue are bins that have passed the requirement whereas bins that are light brown are bins that have failed the requirement. Blank bins have zero reconstructed MC events in, which also fail the requirement.

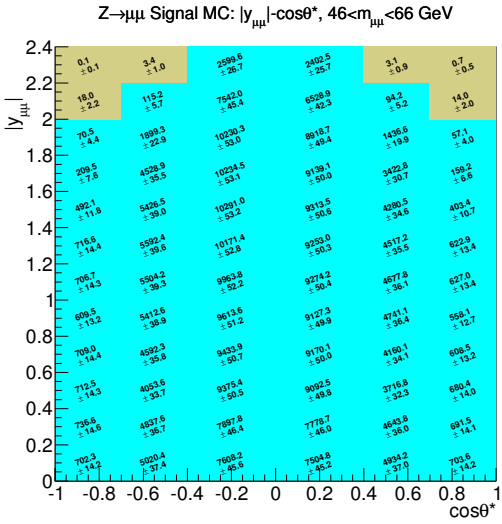

(a) Drell–Yan signal MC expectation in the $46 < m_{\mu\mu} < 66\,\text{GeV}$ mass window.

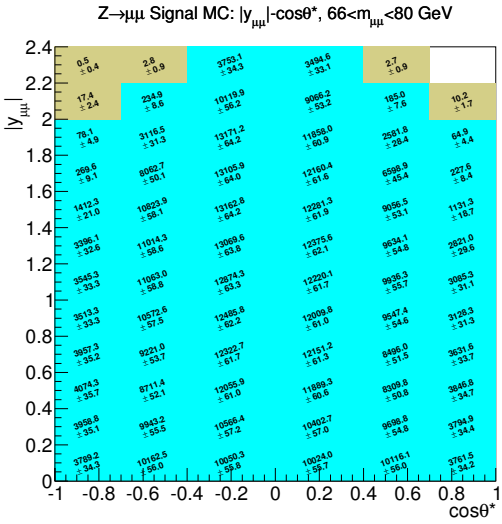

(b) Drell–Yan signal MC expectation in the $66 < m_{\mu\mu} < 80\,\text{GeV}$ mass window.

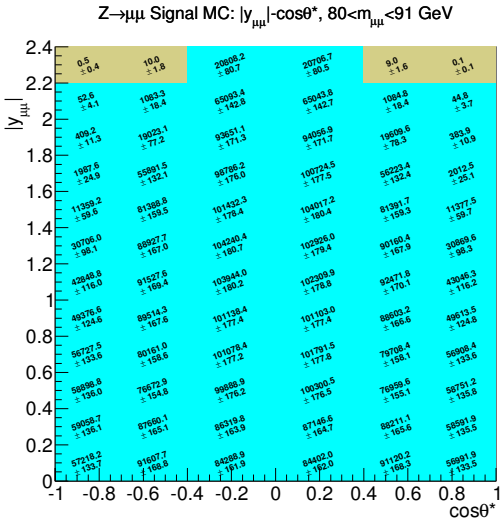

(c) Drell–Yan signal MC expectation in the $80 < m_{\mu\mu} < 91\,\text{GeV}$ mass window.

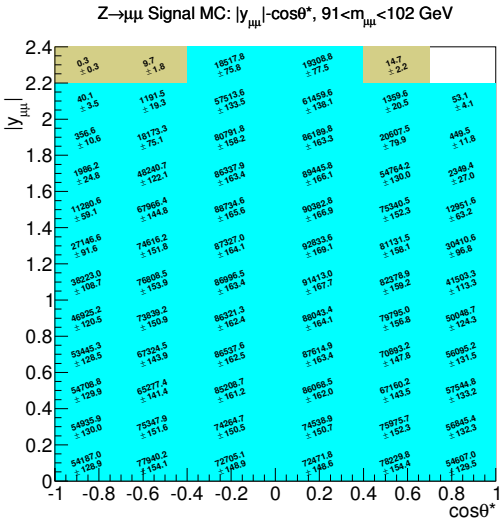

(d) Drell–Yan signal MC expectation in the $91 < m_{\mu\mu} < 102\,\text{GeV}$ mass window.

FIG. 72: Two dimensional ($|y_{\mu\mu}|$, $\cos\theta^*$) plots of the reconstructed DY signal expectation in the first four invariant mass windows of the measurement. Bins that are shown in blue pass the low statistics bin vetoing, bins in light brown are vetoed by the requirement and blank bins without a value are also vetoed. Only statistical uncertainties are shown on the values in each bin.

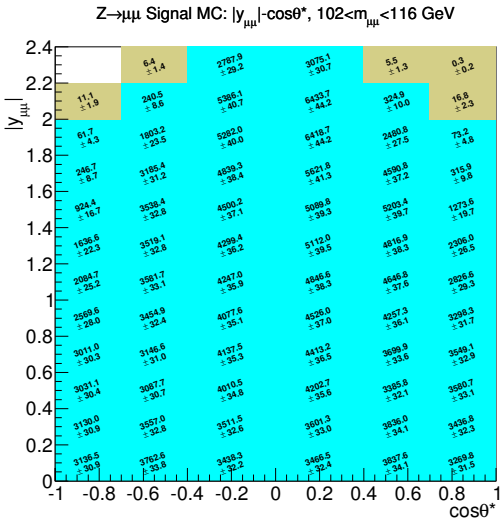

(a) Drell–Yan signal MC expectation in the $102 < m_{\mu\mu} < 116\,\text{GeV}$ mass window.

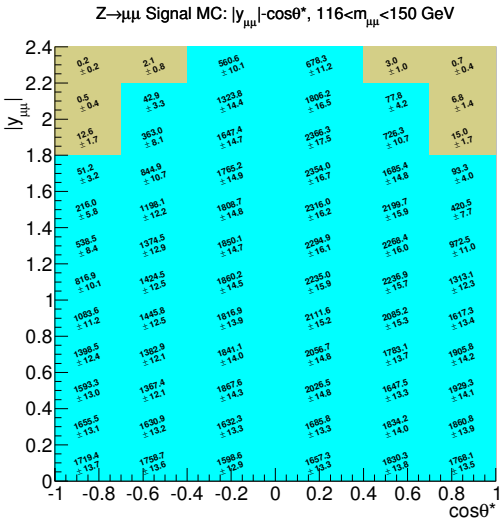

(b) Drell–Yan signal MC expectation in the $116 < m_{\mu\mu} < 150\,\text{GeV}$ mass window.

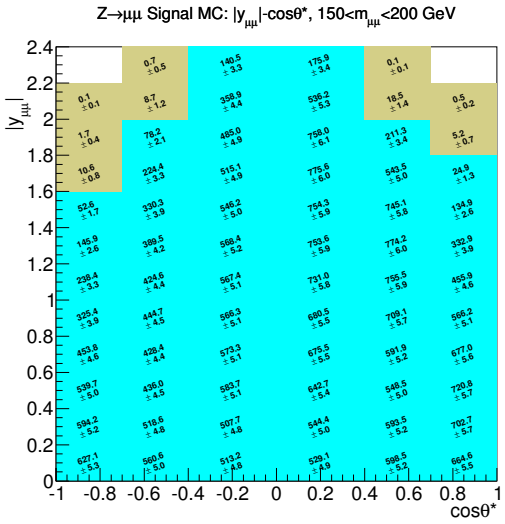

(c) Drell–Yan signal MC expectation in the $150 < m_{\mu\mu} < 200\,\text{GeV}$ mass window.

FIG. 73: Two dimensional ($|y_{\mu\mu}|$, $\cos\theta^*$) plots of the reconstructed DY signal expectation in the last three invariant mass windows of the measurement. Bins that are shown in blue pass the low statistics bin vetoing, bins in light brown are vetoed by the requirement and blank bins without a value are also vetoed. Only statistical uncertainties are shown on the values in each bin.

12. MEASUREMENT RESULTS

A. Triple-Differential Cross-sections

The triple-differential Drell–Yan cross-section (Equation 31) is measured using the following relationship between ATLAS data, MC and the unfolding response matrix:

$$\left(\frac{d^3\sigma}{dm_{\mu\mu}\, d|y_{\mu\mu}|\, d\cos\theta^*}\right)_{uvw} = \frac{M^{ijk}_{uvw}\,(N^{\text{sig}}_{ijk} - N^{bkg}_{ijk})}{\mathcal{L}\,(\delta m_{\mu\mu})_u\,(\delta|y_{\mu\mu}|)_v\,(\delta\cos\theta^*)_w}\,, \tag{93}$$

$$i, j, k, u, v, w = 1, 2, 3, \ldots \tag{94}$$

where N^{sig} and N^{bkg} are the number of ATLAS data and estimated background events that pass the selection criteria respectively; M is the iterated inverted response matrix of the Bayesian unfolding method; $\mathcal{L}$ is the integrated luminosity of the data set; $\delta m_{\mu\mu}$, $\delta|y_{\mu\mu}|$, and $\delta\cos\theta^*$ are the bin widths; i, j, and k are the bin indices corresponding to reconstructed-level quantities; and u, v, and w are the bin indices corresponding to truth-level quantities. The fiducial volume of the measurement has been defined in Section 6 B.

Cross-section measurement results are typically reported in the literature at one truth-level only and correction factors (C-factors) are provided to scale the reported result to a different truth-level. The Born, dressed and bare truth-levels have been defined in Section 6 D. These scale factors are determined directly from truth-level MC distributions. For example, the C-factors to scale away from the Born truth-level to the dressed or bare truth-levels are defined as:

$$C^{\text{dres.}}_{uvw} = \frac{d^3\sigma^{\text{dres.}}_{uvw}}{d^3\sigma^{\text{Born}}_{uvw}}\,, \qquad C^{\text{bare}}_{uvw} = \frac{d^3\sigma^{\text{bare}}_{uvw}}{d^3\sigma^{\text{Born}}_{uvw}}\,, \tag{95}$$

where u, v and w are indices of the measurement binning and σ_{uvw} is the cross-section generated at the Born, dressed or bare truth-level in the bin.

The following terms are defined when referring to the different unfolded cross-section results:

- Born-results: Measured cross-section values unfolded using Born truth-level MC response matrices.
- Dressed-results: Measured cross-section values unfolded using dressed truth-level MC response matrices.
- Bare-results: Measured cross-section values unfolded using Bare truth-level MC response matrices.

The ATLAS $\sqrt{s} = 8\,\text{TeV}$ measured triple-differential Born-results are presented in Tables 22-32. The tables summarises the bin edges of each measurement bin, the measured cross-section values and the associated statistical and systematic uncertainty. Also listed is a decomposition of the

systematic uncertainty sources and C-factors to scale to effective dressed- or bare-results. Directly unfolded Born-, dressed- and bare-results are presented in Tables 39-45 in the appendix, showing total uncertainties and the corresponding truth-level `powheg-pythia8` prediction. Born-results are shown as a function of $\cos\theta^*$ in Figures 74-80. The measured central values are shown with a ± 1 standard deviation uncertainty band. The data statistical uncertainty is displayed along with the systematic contribution of all other uncertainties added in quadrature, excluding luminosity uncertainty. Born truth-level MC predictions with the MC statistical uncertainties, as summarised in the appendix, are shown in these figures for reference.

Figures 74-80 show expected behaviour of cross-section over the $m_{\mu\mu}$ dimension: the cross-section increases by 1.5 orders of magnitude from the low $m_{\mu\mu}$ region to the Z-peak region, and decreases by 2.8 orders of magnitude from the Z-peak region to the highest mass bin; systematic uncertainties are shown to be slightly larger than the statistical uncertainties below the Z-peak and slightly smaller than the statistical uncertainties above the Z-peak, as shown in the uncertainty frequency plots of Figures 69 and 71; and the Z-peak region shows systematically dominated uncertainties in the central bins ($|y_{\mu\mu}| < 1.6$ and $|\cos\theta^*| < 0.7$) of $< 0.7\%$. The $|y_{\mu\mu}|$ dimension shows an increase in the $\cos\theta^*$ asymmetry with increasing $|y_{\mu\mu}|$ up until $|y_{\mu\mu}| < 2.0$ where the asymmetry decreases due to the kinematic constraints of the fiducial volume criteria. The $\cos\theta^*$ asymmetry is shown to invert about the Z-peak $m_{\mu\mu} = 91\,\text{GeV}$ bin edge. Also in this region the asymmetry is seen to be smallest due to A_{FB} changing sign about zero. The forward-backward asymmetries are shown in the next subsection. The data agrees well with the MC theory prediction but shows a known modelling discrepancy in the $\cos\theta^*$ dimension on the Z-peak[128].

				Triple Differential Cross-section Values																								
$\mathcal{B}$	$m_{\mu\mu}$ [GeV]	$\lvert y_{\mu\mu}\rvert$	$\cos\theta^*$	$d^3\sigma^{\text{Born}}_{\text{meas.}}$ [pb/GeV]	$\Delta^{\text{Stat.}}_{\text{meas.}}$ [%]	$\Delta^{\text{Syst.}}_{\text{meas.}}$ [%]	Δ^{Trigger} [%]		$\Delta^{\text{Reconst.}}$ [%]		Δ^{ID} [%]	Δ^{Sagitta} [%]	Δ^{Scale} [%]	$\Delta^{Z-p\text{T}}$ [%]	$\Delta^{\text{Isolation}}$ [%]		Δ^{QCD} [%]	$\Delta^{\text{MC Bkg.}}$ [%]		$\Delta^{\text{MC Signal}}$ [%]		Δ^{PDF} [%]	$\Delta^{\text{Unfd.}}$ [%]	$C_{\text{Dres.}}$	C_{Bare}
							uncor.	corr.	uncor.	corr.					uncor.	corr.		uncor.	corr.	uncor.	corr.				
1	46 – 66	0.0 – 0.2	-1.0 – -0.7	0.0143	±3.74	±2.94	0.01	−0.57	0.00	−0.28	0.23	0.37	0.08	0.29	0.00	−0.26	0.46	1.651	−1.157	1.73	−0.03	0.63	0.34	1.17	1.25
2	46 – 66	0.0 – 0.2	-0.7 – -0.4	0.1042	±1.41	±1.82	0.00	−0.36	0.00	−0.24	0.12	0.11	0.07	0.16	0.00	−0.24	0.04	0.915	−0.990	0.58	−0.16	0.90	−0.15	1.08	1.12
3	46 – 66	0.0 – 0.2	-0.4 – 0.0	0.1439	±1.19	±1.70	0.00	−0.02	0.00	−0.44	0.05	0.07	0.02	0.28	0.00	−0.42	0.44	0.702	−0.761	0.49	−0.17	0.93	−0.05	1.10	1.16
4	46 – 66	0.0 – 0.2	0.0 – 0.4	0.1423	±1.16	±1.69	0.00	−0.01	0.00	−0.46	0.10	0.09	0.02	0.32	0.00	−0.43	0.45	0.818	−0.720	0.47	−0.20	0.81	−0.19	1.10	1.16
5	46 – 66	0.0 – 0.2	0.4 – 0.7	0.1006	±1.46	±1.87	0.00	−0.38	0.00	−0.25	0.10	0.10	0.03	0.17	0.00	−0.25	0.04	1.000	−1.020	0.56	−0.15	0.86	−0.22	1.08	1.13
6	46 – 66	0.0 – 0.2	0.7 – 1.0	0.0140	±4.04	±4.10	0.02	−0.59	0.00	−0.29	0.13	0.58	0.07	0.24	0.00	−0.26	0.47	2.772	−1.311	1.63	−0.18	1.66	−0.83	1.14	1.20
7	46 – 66	0.2 – 0.4	-1.0 – -0.7	0.0146	±3.69	±3.07	0.01	−0.68	0.00	−0.30	0.40	0.45	0.02	0.70	0.00	−0.28	0.69	1.327	−1.089	1.96	0.07	0.75	0.25	1.15	1.21
8	46 – 66	0.2 – 0.4	-0.7 – -0.4	0.1032	±1.51	±1.96	0.00	−0.36	0.00	−0.31	0.20	0.11	0.01	0.16	0.00	−0.30	0.05	1.085	−1.008	0.57	−0.18	0.85	−0.31	1.08	1.12
9	46 – 66	0.2 – 0.4	-0.4 – 0.0	0.1447	±1.20	±1.64	0.00	−0.00	0.00	−0.39	0.09	0.08	0.00	0.21	0.00	−0.37	0.42	0.771	−0.763	0.48	−0.22	0.84	−0.00	1.09	1.15
10	46 – 66	0.2 – 0.4	0.0 – 0.4	0.1438	±1.18	±1.87	0.00	−0.00	0.00	−0.41	0.12	0.07	−0.01	0.24	0.00	−0.39	0.42	0.935	−0.781	0.46	−0.32	1.04	−0.11	1.09	1.16
11	46 – 66	0.2 – 0.4	0.4 – 0.7	0.1000	±1.48	±1.90	0.01	−0.34	0.00	−0.32	0.09	0.11	−0.01	0.07	0.00	−0.31	0.06	1.012	−1.033	0.65	−0.14	0.86	−0.13	1.08	1.12
12	46 – 66	0.2 – 0.4	0.7 – 1.0	0.0140	±3.70	±3.05	0.01	−0.67	0.00	−0.30	0.23	0.35	−0.22	0.48	0.00	−0.27	0.71	0.954	−1.128	1.72	0.08	1.41	0.68	1.20	1.27
13	46 – 66	0.4 – 0.6	-1.0 – -0.7	0.0140	±3.95	±3.40	0.01	−0.67	0.01	−0.36	0.31	0.52	−0.00	0.07	0.00	−0.31	0.54	2.354	−1.225	1.67	−0.07	0.53	−0.24	1.15	1.22
14	46 – 66	0.4 – 0.6	-0.7 – -0.4	0.1077	±1.54	±1.76	0.00	−0.30	0.00	−0.39	0.07	0.13	0.11	0.11	0.00	−0.37	0.05	0.952	−0.868	0.73	−0.11	0.69	−0.06	1.07	1.12
15	46 – 66	0.4 – 0.6	-0.4 – 0.0	0.1458	±1.07	±1.74	0.00	−0.03	0.00	−0.29	0.19	0.08	0.02	0.20	0.00	−0.28	0.27	0.687	−0.682	0.41	−0.20	1.24	−0.17	1.10	1.16
16	46 – 66	0.4 – 0.6	0.0 – 0.4	0.1416	±1.11	±1.73	0.00	−0.04	0.00	−0.30	0.13	0.06	0.00	0.23	0.00	−0.30	0.27	0.679	−0.781	0.40	−0.22	1.16	−0.19	1.10	1.16
17	46 – 66	0.4 – 0.6	0.4 – 0.7	0.0962	±1.65	±2.11	0.00	−0.29	0.00	−0.41	0.21	0.15	0.08	0.09	0.00	−0.39	0.06	1.171	−0.990	0.70	−0.17	0.97	−0.40	1.08	1.13
18	46 – 66	0.4 – 0.6	0.7 – 1.0	0.0144	±3.76	±3.29	0.01	−0.70	0.00	−0.34	0.29	0.33	0.19	0.65	0.00	−0.31	0.52	1.637	−1.207	1.87	0.10	0.98	0.76	1.14	1.21
19	46 – 66	0.6 – 0.8	-1.0 – -0.7	0.0153	±3.52	±3.22	0.01	−0.55	0.01	−0.41	0.44	0.66	−0.03	0.23	0.00	−0.37	0.72	1.931	−1.107	1.71	−0.03	0.78	0.16	1.13	1.20
20	46 – 66	0.6 – 0.8	-0.7 – -0.4	0.1085	±1.42	±1.76	0.00	−0.23	0.00	−0.37	0.21	0.15	0.01	0.02	0.00	−0.37	0.25	0.716	−0.898	0.63	−0.04	0.96	−0.09	1.07	1.11
21	46 – 66	0.6 – 0.8	-0.4 – 0.0	0.1483	±1.05	±1.51	0.00	−0.05	0.00	−0.24	0.07	0.08	−0.08	0.26	0.00	−0.24	0.18	0.625	−0.687	0.43	−0.18	0.99	−0.03	1.09	1.15
22	46 – 66	0.6 – 0.8	0.0 – 0.4	0.1433	±1.03	±1.33	0.00	−0.05	0.00	−0.24	0.07	0.06	−0.02	0.20	0.00	−0.24	0.18	0.659	−0.748	0.42	−0.19	0.59	−0.08	1.10	1.16
23	46 – 66	0.6 – 0.8	0.4 – 0.7	0.0982	±1.49	±1.91	0.00	−0.32	0.00	−0.39	0.18	0.12	−0.01	0.06	0.00	−0.38	0.27	0.858	−1.004	0.66	−0.12	0.96	−0.10	1.08	1.13
24	46 – 66	0.6 – 0.8	0.7 – 1.0	0.0139	±3.86	±3.65	0.01	−0.68	0.01	−0.42	0.36	0.59	−0.46	0.40	0.00	−0.38	0.80	2.332	−1.079	1.94	−0.01	0.81	0.19	1.13	1.20
25	46 – 66	0.8 – 1.0	-1.0 – -0.7	0.0150	±3.98	±3.24	0.01	−0.32	0.01	−0.44	0.50	0.52	−0.07	−0.40	0.00	−0.40	0.76	1.728	−1.028	1.93	−0.01	0.87	−0.43	1.13	1.18
26	46 – 66	0.8 – 1.0	-0.7 – -0.4	0.1088	±1.34	±1.67	0.00	−0.24	0.00	−0.30	0.09	0.13	−0.18	0.05	0.00	−0.29	0.14	0.791	−0.929	0.54	−0.12	0.73	−0.40	1.07	1.12
27	46 – 66	0.8 – 1.0	-0.4 – 0.0	0.1475	±1.03	±1.36	0.00	0.00	0.00	−0.25	0.07	0.06	−0.02	0.25	0.00	−0.25	0.20	0.686	−0.693	0.40	−0.21	0.66	−0.14	1.08	1.15
28	46 – 66	0.8 – 1.0	0.0 – 0.4	0.1400	±1.03	±1.35	0.00	−0.03	0.00	−0.24	0.05	0.07	−0.00	0.26	0.00	−0.24	0.21	0.671	−0.719	0.41	−0.18	0.63	−0.13	1.09	1.16
29	46 – 66	0.8 – 1.0	0.4 – 0.7	0.0976	±1.42	±1.72	0.00	−0.34	0.00	−0.30	0.18	0.16	0.15	0.10	0.00	−0.30	0.15	0.845	−1.034	0.60	−0.11	0.63	−0.02	1.09	1.14
30	46 – 66	0.8 – 1.0	0.7 – 1.0	0.0132	±4.05	±4.01	0.01	−0.51	0.01	−0.48	0.70	0.54	0.02	−0.25	0.00	−0.43	0.81	2.473	−1.198	2.15	−0.13	0.44	0.49	1.14	1.21
31	46 – 66	1.0 – 1.2	-1.0 – -0.7	0.0169	±3.23	±4.47	0.01	−0.48	0.00	−0.39	0.28	0.67	−0.15	0.06	0.00	−0.37	0.68	1.402	−0.750	1.71	−0.02	1.04	3.45	1.13	1.17
32	46 – 66	1.0 – 1.2	-0.7 – -0.4	0.1139	±1.31	±1.50	0.00	−0.23	0.00	−0.27	0.13	0.18	−0.02	0.04	0.00	−0.27	0.48	0.668	−0.823	0.58	−0.08	0.54	0.09	1.06	1.10
33	46 – 66	1.0 – 1.2	-0.4 – 0.0	0.1481	±1.04	±1.49	0.00	0.09	0.00	−0.26	0.06	0.12	−0.00	0.20	0.00	−0.26	0.03	0.735	−0.696	0.38	−0.24	0.85	−0.24	1.09	1.14
34	46 – 66	1.0 – 1.2	0.0 – 0.4	0.1382	±1.01	±1.41	0.00	−0.03	0.00	−0.25	0.15	0.08	0.04	0.27	0.00	−0.25	0.03	0.684	−0.681	0.41	−0.24	0.76	−0.15	1.09	1.16
35	46 – 66	1.0 – 1.2	0.4 – 0.7	0.0956	±1.42	±1.84	0.00	−0.38	0.00	−0.27	0.18	0.18	−0.05	0.03	0.00	−0.27	0.55	0.867	−0.968	0.59	−0.14	0.67	0.46	1.09	1.14
36	46 – 66	1.0 – 1.2	0.7 – 1.0	0.0125	±3.72	±3.16	0.01	−0.54	0.01	−0.41	0.44	0.57	0.09	0.28	0.00	−0.38	0.86	1.420	−0.990	1.93	−0.02	0.68	0.90	1.19	1.27
37	46 – 66	1.2 – 1.4	-1.0 – -0.7	0.0158	±3.29	±2.82	0.01	−0.46	0.00	−0.37	0.49	0.56	−0.17	0.13	0.00	−0.34	0.95	0.982	−0.866	1.83	−0.00	0.67	0.66	1.13	1.18
38	46 – 66	1.2 – 1.4	-0.7 – -0.4	0.1177	±1.31	±1.50	0.00	−0.23	0.00	−0.29	0.12	0.15	−0.01	0.04	0.00	−0.29	0.36	0.655	−0.848	0.58	−0.10	0.58	−0.06	1.06	1.10
39	46 – 66	1.2 – 1.4	-0.4 – 0.0	0.1518	±0.96	±1.34	0.00	0.10	0.00	−0.27	0.07	0.09	0.06	0.19	0.00	−0.26	0.05	0.559	−0.668	0.38	−0.16	0.81	−0.09	1.09	1.14
40	46 – 66	1.2 – 1.4	0.0 – 0.4	0.1391	±0.99	±1.41	0.00	−0.01	0.00	−0.27	0.06	0.10	0.04	0.23	0.00	−0.26	0.05	0.658	−0.709	0.41	−0.24	0.77	0.13	1.10	1.16
41	46 – 66	1.2 – 1.4	0.4 – 0.7	0.0863	±1.49	±2.28	0.00	−0.38	0.00	−0.30	0.23	0.20	0.09	0.08	0.00	−0.29	0.48	1.092	−1.156	0.66	−0.27	0.49	−1.13	1.08	1.13
42	46 – 66	1.2 – 1.4	0.7 – 1.0	0.0114	±3.70	±3.91	0.01	−0.61	0.00	−0.38	0.35	0.75	−0.16	0.48	0.00	−0.36	1.17	2.121	−1.037	2.07	−0.09	1.51	−0.21	1.18	1.26
43	46 – 66	1.4 – 1.6	-1.0 – -0.7	0.0099	±4.18	±3.11	0.01	−0.21	0.00	−0.40	0.80	0.61	−0.09	0.39	0.00	−0.37	0.72	1.262	−0.698	2.03	−0.01	1.05	0.57	1.16	1.21
44	46 – 66	1.4 – 1.6	-0.7 – -0.4	0.1162	±1.22	±1.52	0.00	−0.22	0.00	−0.32	0.13	0.17	0.03	0.10	0.00	−0.31	0.52	0.617	−0.728	0.57	−0.10	0.69	0.01	1.06	1.09
45	46 – 66	1.4 – 1.6	-0.4 – 0.0	0.1547	±0.98	±1.19	0.00	0.06	0.00	−0.29	0.05	0.10	0.01	0.14	0.00	−0.28	0.19	0.524	−0.619	0.38	−0.17	0.55	−0.04	1.08	1.13
46	46 – 66	1.4 – 1.6	0.0 – 0.4	0.1352	±1.03	±1.34	0.00	0.01	0.00	−0.30	0.07	0.10	0.02	0.24	0.00	−0.29	0.21	0.652	−0.709	0.42	−0.24	0.43	−0.38	1.09	1.15
47	46 – 66	1.4 – 1.6	0.4 – 0.7	0.0868	±1.49	±2.00	0.00	−0.38	0.00	−0.33	0.13	0.19	0.05	0.10	0.00	−0.32	0.67	1.086	−1.035	0.68	−0.24	0.53	−0.22	1.09	1.13
48	46 – 66	1.4 – 1.6	0.7 – 1.0	0.0084	±4.52	±4.18	0.01	−0.42	0.00	−0.41	0.88	0.99	0.11	0.48	0.00	−0.38	0.84	2.712	−0.823	2.31	−0.19	0.53	0.61	1.17	1.23

TABLE 22: Measured cross-section values unfolded to the Born truth-level in the 1$^{\text{st}}$ 48 bins of the measurement. The luminosity uncertainty of 1.9% is not included.

$\mathcal{B}$	$m_{\mu\mu}$ [GeV]	$\lvert y_{\mu\mu}\rvert$	$\cos\theta^*$	Triple Differential Cross-section Values																							
				$d^3\sigma^{\text{Born}}_{\text{meas.}}$ [pb/GeV]	$\Delta^{\text{Stat.}}_{\text{meas.}}$ [%]	$\Delta^{\text{Syst.}}_{\text{meas.}}$ [%]	Δ^{Trigger} [%]		$\Delta^{\text{Reconst.}}$ [%]		Δ^{ID} [%]	Δ^{Sagitta} [%]	Δ^{Scale} [%]	$\Delta^{Z-p\text{T}}$ [%]	$\Delta^{\text{Isolation}}$ [%]		Δ^{QCD} [%]	$\Delta^{\text{MC Bkg.}}$ [%]		$\Delta^{\text{MC Signal}}$ [%]		Δ^{PDF} [%]	$\Delta^{\text{Unfd.}}$ [%]	$C_{\text{Dres.}}$	C_{Bare}
							uncor.	corr.	uncor.	corr.					uncor.	corr.		uncor.	corr.	uncor.	corr.				
49	46 – 66	1.6 – 1.8	-1.0 – -0.7	0.0044	±6.36	±4.54	0.00	0.13	0.00	−0.45	0.91	1.40	0.03	0.86	0.00	−0.40	0.53	0.943	−0.867	2.83	0.01	0.47	−2.55	1.10	1.12
50	46 – 66	1.6 – 1.8	-0.7 – -0.4	0.0946	±1.35	±1.74	0.00	−0.21	0.00	−0.37	0.20	0.24	0.20	0.03	0.00	−0.36	0.50	0.843	−0.837	0.66	−0.19	0.55	−0.38	1.06	1.08
51	46 – 66	1.6 – 1.8	-0.4 – 0.0	0.1509	±0.96	±1.25	0.00	0.02	0.00	−0.32	0.11	0.12	0.02	0.11	0.00	−0.31	0.21	0.589	−0.656	0.40	−0.21	0.47	−0.26	1.07	1.13
52	46 – 66	1.6 – 1.8	0.0 – 0.4	0.1324	±1.01	±1.39	0.00	0.04	0.00	−0.33	0.15	0.13	0.08	0.21	0.00	−0.32	0.23	0.637	−0.738	0.42	−0.26	0.55	−0.30	1.09	1.16
53	46 – 66	1.6 – 1.8	0.4 – 0.7	0.0716	±1.54	±2.02	0.00	−0.32	0.00	−0.38	0.18	0.23	0.01	0.08	0.00	−0.36	0.64	0.944	−0.931	0.78	−0.20	0.54	0.70	1.08	1.12
54	46 – 66	1.6 – 1.8	0.7 – 1.0	0.0036	±6.72	±4.65	0.00	−0.02	0.00	−0.45	0.62	1.67	−0.23	0.90	0.00	−0.40	0.63	0.988	−0.892	3.25	0.00	0.77	1.95	1.19	1.22
55	46 – 66	1.8 – 2.0	-1.0 – -0.7	0.0018	±9.26	±7.21	0.01	0.12	0.01	−0.51	1.12	1.62	−0.17	0.48	0.00	−0.46	0.12	1.345	−0.642	5.07	−0.00	0.69	4.23	1.10	1.15
56	46 – 66	1.8 – 2.0	-0.7 – -0.4	0.0396	±1.99	±1.96	0.00	−0.16	0.00	−0.40	0.23	0.27	−0.08	0.05	0.00	−0.39	0.48	0.871	−0.565	0.98	−0.12	0.40	0.82	1.07	1.10
57	46 – 66	1.8 – 2.0	-0.4 – 0.0	0.1520	±0.94	±1.35	0.00	0.01	0.00	−0.37	0.20	0.11	0.04	0.14	0.00	−0.36	0.18	0.605	−0.640	0.41	−0.23	0.56	−0.35	1.07	1.12
58	46 – 66	1.8 – 2.0	0.0 – 0.4	0.1313	±1.04	±1.27	0.00	0.04	0.00	−0.37	0.07	0.13	0.00	0.17	0.00	−0.36	0.21	0.572	−0.709	0.43	−0.21	0.38	−0.14	1.09	1.15
59	46 – 66	1.8 – 2.0	0.4 – 0.7	0.0274	±2.38	±2.30	0.00	−0.20	0.00	−0.41	0.42	0.35	−0.22	0.14	0.00	−0.40	0.67	1.265	−0.812	1.17	−0.14	0.53	−0.41	1.13	1.17
60	46 – 66	1.8 – 2.0	0.7 – 1.0	0.0014	±10.47	±7.65	0.01	0.05	0.01	−0.53	1.34	1.96	0.13	0.60	0.00	−0.47	0.19	1.597	−0.850	5.83	−0.00	0.57	3.76	1.15	1.15
61	46 – 66	2.0 – 2.2	-1.0 – -0.7	–	–	–	–	–	–	–	–	–	–	–	–	–	–	–	–	–	–	–	–	–	–
62	46 – 66	2.0 – 2.2	-0.7 – -0.4	0.0024	±7.81	±6.66	0.00	0.07	0.01	−0.50	1.62	1.61	0.45	1.96	0.00	−0.46	0.27	3.883	−0.420	4.29	−0.19	0.76	0.28	1.17	1.23
63	46 – 66	2.0 – 2.2	-0.4 – 0.0	0.1155	±1.12	±1.27	0.00	0.04	0.00	−0.44	0.13	0.13	0.01	0.10	0.00	−0.42	0.25	0.595	−0.571	0.48	−0.20	0.42	0.09	1.07	1.12
64	46 – 66	2.0 – 2.2	0.0 – 0.4	0.0967	±1.22	±1.51	0.00	0.05	0.00	−0.44	0.44	0.16	0.02	0.17	0.00	−0.42	0.29	0.739	−0.679	0.51	−0.27	0.46	0.07	1.10	1.16
65	46 – 66	2.0 – 2.2	0.4 – 0.7	0.0016	±8.32	±7.59	0.00	0.07	0.01	−0.49	1.81	1.71	0.57	1.61	0.00	−0.45	0.34	1.013	−0.522	5.26	−0.02	0.84	4.28	1.27	1.40
66	46 – 66	2.0 – 2.2	0.7 – 1.0	–	–	–	–	–	–	–	–	–	–	–	–	–	–	–	–	–	–	–	–	–	–
67	46 – 66	2.2 – 2.4	-1.0 – -0.7	–	–	–	–	–	–	–	–	–	–	–	–	–	–	–	–	–	–	–	–	–	–
68	46 – 66	2.2 – 2.4	-0.7 – -0.4	–	–	–	–	–	–	–	–	–	–	–	–	–	–	–	–	–	–	–	–	–	–
69	46 – 66	2.2 – 2.4	-0.4 – 0.0	0.0386	±1.88	±1.87	0.00	0.04	0.00	−0.53	0.26	0.29	0.09	0.11	0.00	−0.50	0.24	1.241	−0.550	0.82	−0.26	0.37	0.16	1.08	1.14
70	46 – 66	2.2 – 2.4	0.0 – 0.4	0.0350	±1.87	±1.93	0.00	0.02	0.00	−0.52	0.72	0.30	0.00	0.05	0.00	−0.50	0.26	0.962	−0.546	0.90	−0.19	0.48	−0.46	1.09	1.15
71	46 – 66	2.2 – 2.4	0.4 – 0.7	–	–	–	–	–	–	–	–	–	–	–	–	–	–	–	–	–	–	–	–	–	–
72	46 – 66	2.2 – 2.4	0.7 – 1.0	–	–	–	–	–	–	–	–	–	–	–	–	–	–	–	–	–	–	–	–	–	–
73	66 – 80	0.0 – 0.2	-1.0 – -0.7	0.0784	±1.40	±1.57	0.00	−0.25	0.00	−0.24	0.12	0.23	0.19	−0.14	0.00	−0.24	0.62	0.437	−0.369	0.93	0.01	0.72	0.04	1.35	1.66
74	66 – 80	0.0 – 0.2	-0.7 – -0.4	0.1952	±0.85	±1.12	0.00	−0.01	0.00	−0.24	0.08	0.08	0.15	−0.04	0.00	−0.23	0.07	0.220	−0.267	0.59	−0.03	0.76	0.20	1.40	1.79
75	66 – 80	0.0 – 0.2	-0.4 – 0.0	0.1702	±0.85	±1.22	0.00	0.06	0.00	−0.43	0.10	0.08	0.14	0.03	0.00	−0.42	0.12	0.566	−0.219	0.55	−0.07	0.61	−0.10	1.44	1.88
76	66 – 80	0.0 – 0.2	0.0 – 0.4	0.1765	±0.90	±1.23	0.00	0.07	0.00	−0.43	0.07	0.06	0.17	0.04	0.00	−0.42	0.11	0.281	−0.194	0.59	−0.05	0.65	0.44	1.44	1.87
77	66 – 80	0.0 – 0.2	0.4 – 0.7	0.1936	±0.88	±1.04	0.00	−0.01	0.00	−0.24	0.08	0.06	0.20	−0.03	0.00	−0.24	0.07	0.143	−0.274	0.59	−0.01	0.64	0.23	1.42	1.81
78	66 – 80	0.0 – 0.2	0.7 – 1.0	0.0762	±1.40	±1.53	0.00	−0.26	0.00	−0.24	0.16	0.18	0.29	−0.18	0.00	−0.23	0.62	0.342	−0.402	0.94	0.01	0.56	0.26	1.36	1.68
79	66 – 80	0.2 – 0.4	-1.0 – -0.7	0.0812	±1.45	±1.57	0.00	−0.18	0.00	−0.25	0.14	0.15	0.28	−0.14	0.00	−0.25	0.54	0.382	−0.395	0.93	−0.01	0.60	0.59	1.33	1.63
80	66 – 80	0.2 – 0.4	-0.7 – -0.4	0.1977	±0.84	±1.03	0.00	0.02	0.00	−0.28	0.10	0.09	0.23	−0.05	0.00	−0.28	0.06	0.238	−0.263	0.57	−0.03	0.59	0.11	1.41	1.79
81	66 – 80	0.2 – 0.4	-0.4 – 0.0	0.1725	±0.86	±1.19	0.00	0.05	0.00	−0.37	0.16	0.07	0.24	0.06	0.00	−0.37	0.13	0.299	−0.223	0.55	−0.07	0.73	−0.18	1.43	1.86
82	66 – 80	0.2 – 0.4	0.0 – 0.4	0.1718	±0.87	±1.10	0.00	0.05	0.00	−0.39	0.07	0.07	0.20	0.04	0.00	−0.38	0.13	0.260	−0.218	0.56	−0.06	0.60	0.18	1.44	1.88
83	66 – 80	0.2 – 0.4	0.4 – 0.7	0.1852	±0.88	±1.08	0.00	0.03	0.00	−0.30	0.10	0.08	0.13	−0.06	0.00	−0.29	0.07	0.337	−0.278	0.60	−0.05	0.48	−0.36	1.44	1.85
84	66 – 80	0.2 – 0.4	0.7 – 1.0	0.0745	±1.39	±1.46	0.00	−0.26	0.00	−0.24	0.12	0.19	0.35	−0.05	0.00	−0.24	0.56	0.424	−0.395	0.94	0.01	0.38	0.31	1.36	1.67
85	66 – 80	0.4 – 0.6	-1.0 – -0.7	0.0785	±1.35	±1.57	0.00	−0.16	0.00	−0.26	0.16	0.19	0.30	−0.10	0.00	−0.26	0.46	0.299	−0.418	0.94	0.00	0.57	−0.67	1.35	1.64
86	66 – 80	0.4 – 0.6	-0.7 – -0.4	0.1980	±0.93	±1.23	0.00	0.09	0.00	−0.36	0.17	0.11	0.17	−0.02	0.00	−0.35	0.00	0.256	−0.271	0.61	−0.03	0.79	0.01	1.39	1.76
87	66 – 80	0.4 – 0.6	-0.4 – 0.0	0.1780	±0.75	±1.03	0.00	0.03	0.00	−0.29	0.06	0.06	0.20	0.04	0.00	−0.28	0.07	0.244	−0.212	0.52	−0.06	0.62	0.29	1.42	1.84
88	66 – 80	0.4 – 0.6	0.0 – 0.4	0.1700	±0.82	±1.01	0.00	0.03	0.00	−0.30	0.10	0.08	0.25	0.05	0.00	−0.30	0.07	0.165	−0.196	0.56	−0.03	0.58	0.19	1.45	1.90
89	66 – 80	0.4 – 0.6	0.4 – 0.7	0.1808	±0.95	±1.14	0.00	0.06	0.00	−0.37	0.11	0.10	0.30	−0.04	0.00	−0.37	0.00	0.279	−0.278	0.62	−0.04	0.46	0.35	1.45	1.88
90	66 – 80	0.4 – 0.6	0.7 – 1.0	0.0736	±1.42	±1.56	0.00	−0.27	0.00	−0.26	0.16	0.19	0.35	−0.12	0.00	−0.26	0.48	0.344	−0.438	0.97	0.00	0.49	−0.53	1.37	1.67
91	66 – 80	0.6 – 0.8	-1.0 – -0.7	0.0836	±1.40	±1.65	0.00	−0.14	0.00	−0.32	0.22	0.21	0.28	−0.22	0.00	−0.32	0.48	0.166	−0.372	0.95	0.02	0.67	0.71	1.32	1.59
92	66 – 80	0.6 – 0.8	-0.7 – -0.4	0.2012	±0.89	±1.20	0.00	0.15	0.00	−0.37	0.10	0.12	0.15	−0.04	0.00	−0.37	0.06	0.153	−0.254	0.60	−0.01	0.74	0.21	1.39	1.76
93	66 – 80	0.6 – 0.8	-0.4 – 0.0	0.1751	±0.77	±1.15	0.00	0.02	0.00	−0.25	0.04	0.08	0.18	0.06	0.00	−0.24	0.04	0.272	−0.198	0.53	−0.07	0.84	−0.24	1.41	1.83
94	66 – 80	0.6 – 0.8	0.0 – 0.4	0.1671	±0.81	±0.86	0.00	0.02	0.00	−0.25	0.09	0.08	0.19	0.04	0.00	−0.24	0.04	0.269	−0.201	0.52	−0.06	0.41	0.04	1.45	1.90
95	66 – 80	0.6 – 0.8	0.4 – 0.7	0.1765	±0.89	±1.21	0.00	0.06	0.00	−0.39	0.16	0.11	0.23	−0.04	0.00	−0.38	0.06	0.586	−0.282	0.64	−0.04	0.47	0.07	1.46	1.88
96	66 – 80	0.6 – 0.8	0.7 – 1.0	0.0716	±1.39	±1.71	0.00	−0.25	0.00	−0.33	0.14	0.27	0.22	−0.20	0.00	−0.33	0.52	0.445	−0.377	1.01	−0.02	0.46	0.79	1.39	1.72

TABLE 23: Measured cross-section values unfolded to the Born truth-level in the 2$^{\text{nd}}$ 48 bins of the measurement. The luminosity uncertainty of 1.9% is not included.

$\mathcal{B}$	$m_{\mu\mu}$ [GeV]	$\lvert y_{\mu\mu}\rvert$	$\cos\theta^{\star}$	Triple Differential Cross-section Values																							
				$d^3\sigma^{\text{Born}}_{\text{meas.}}$ [pb/GeV]	$\Delta^{\text{Stat.}}_{\text{meas.}}$ [%]	$\Delta^{\text{Syst.}}_{\text{meas.}}$ [%]	Δ^{Trigger} [%]		$\Delta^{\text{Reconst.}}$ [%]		Δ^{ID} [%]	Δ^{Sagitta} [%]	Δ^{Scale} [%]	$\Delta^{Z-\text{pT}}$ [%]	$\Delta^{\text{Isolation}}$ [%]		Δ^{QCD} [%]	$\Delta^{\text{MC Bkg.}}$ [%]		$\Delta^{\text{MC Signal}}$ [%]		Δ^{PDF} [%]	$\Delta^{\text{Unfd.}}$ [%]	$C_{\text{Dres.}}$	C_{Bare}
							uncor.	corr.	uncor.	corr.					uncor.	corr.		uncor.	corr.	uncor.	corr.				
97	66 – 80	0.8 – 1.0	-1.0 – -0.7	0.0830	±1.42	±1.71	0.00	−0.13	0.00	−0.41	0.12	0.28	0.29	−0.25	0.00	−0.40	0.49	0.210	−0.328	0.98	0.01	0.82	−0.47	1.32	1.59
98	66 – 80	0.8 – 1.0	-0.7 – -0.4	0.2068	±0.83	±1.18	0.00	0.16	0.00	−0.31	0.08	0.12	0.22	−0.07	0.00	−0.31	0.06	0.186	−0.241	0.55	−0.02	0.83	0.06	1.36	1.72
99	66 – 80	0.8 – 1.0	-0.4 – 0.0	0.1756	±0.74	±0.99	0.00	0.09	0.00	−0.25	0.08	0.09	0.22	0.05	0.00	−0.25	0.04	0.186	−0.200	0.53	−0.04	0.62	−0.14	1.40	1.83
100	66 – 80	0.8 – 1.0	0.0 – 0.4	0.1630	±0.80	±0.86	0.00	0.04	0.00	−0.24	0.08	0.11	0.25	0.06	0.00	−0.24	0.04	0.215	−0.207	0.55	−0.05	0.38	−0.10	1.44	1.90
101	66 – 80	0.8 – 1.0	0.4 – 0.7	0.1716	±0.87	±1.07	0.00	0.03	0.00	−0.32	0.13	0.12	0.18	−0.08	0.00	−0.32	0.07	0.267	−0.278	0.64	−0.06	0.53	−0.17	1.47	1.91
102	66 – 80	0.8 – 1.0	0.7 – 1.0	0.0672	±1.53	±2.09	0.00	−0.24	0.00	−0.43	0.12	0.30	0.17	−0.28	0.00	−0.42	0.55	0.363	−0.391	1.08	−0.02	0.61	−1.24	1.39	1.73
103	66 – 80	1.0 – 1.2	-1.0 – -0.7	0.0835	±1.40	±1.84	0.00	−0.05	0.00	−0.43	0.44	0.32	0.38	−0.28	0.00	−0.42	0.45	0.290	−0.336	0.97	−0.01	0.71	−0.71	1.30	1.55
104	66 – 80	1.0 – 1.2	-0.7 – -0.4	0.2053	±0.78	±1.33	0.00	0.17	0.00	−0.28	0.14	0.16	0.21	−0.03	0.00	−0.28	0.18	0.214	−0.241	0.55	−0.03	0.94	−0.41	1.37	1.71
105	66 – 80	1.0 – 1.2	-0.4 – 0.0	0.1756	±0.76	±1.01	0.00	0.16	0.00	−0.26	0.11	0.13	0.24	0.04	0.00	−0.26	0.02	0.175	−0.189	0.53	−0.05	0.64	0.05	1.40	1.82
106	66 – 80	1.0 – 1.2	0.0 – 0.4	0.1591	±0.77	±0.91	0.00	0.05	0.00	−0.25	0.12	0.11	0.18	0.08	0.00	−0.25	0.02	0.239	−0.207	0.55	−0.06	0.37	−0.25	1.45	1.92
107	66 – 80	1.0 – 1.2	0.4 – 0.7	0.1631	±0.85	±1.27	0.00	0.02	0.00	−0.29	0.19	0.18	0.28	−0.05	0.00	−0.28	0.20	0.270	−0.275	0.64	−0.06	0.63	−0.55	1.49	1.94
108	66 – 80	1.0 – 1.2	0.7 – 1.0	0.0666	±1.43	±2.32	0.00	−0.17	0.00	−0.45	0.21	0.37	0.51	−0.19	0.00	−0.44	0.49	0.263	−0.340	1.06	0.00	0.74	1.50	1.42	1.76
109	66 – 80	1.2 – 1.4	-1.0 – -0.7	0.0695	±1.36	±1.91	0.00	−0.01	0.00	−0.39	0.46	0.27	0.55	−0.22	0.00	−0.38	0.48	0.388	−0.309	1.02	−0.02	0.89	−0.07	1.26	1.53
110	66 – 80	1.2 – 1.4	-0.7 – -0.4	0.2115	±0.75	±1.28	0.00	0.16	0.00	−0.30	0.10	0.18	0.28	−0.04	0.00	−0.30	0.15	0.212	−0.233	0.55	−0.05	0.87	0.34	1.35	1.69
111	66 – 80	1.2 – 1.4	-0.4 – 0.0	0.1764	±0.73	±1.04	0.00	0.17	0.00	−0.27	0.11	0.14	0.24	0.06	0.00	−0.27	0.03	0.192	−0.192	0.49	−0.05	0.68	−0.04	1.39	1.81
112	66 – 80	1.2 – 1.4	0.0 – 0.4	0.1550	±0.78	±1.14	0.00	0.05	0.00	−0.28	0.09	0.13	0.24	0.04	0.00	−0.27	0.03	0.304	−0.220	0.54	−0.10	0.42	−0.67	1.45	1.94
113	66 – 80	1.2 – 1.4	0.4 – 0.7	0.1584	±0.81	±1.46	0.00	0.01	0.00	−0.30	0.20	0.19	0.25	−0.03	0.00	−0.29	0.17	0.219	−0.279	0.67	−0.04	0.79	0.72	1.51	1.97
114	66 – 80	1.2 – 1.4	0.7 – 1.0	0.0490	±1.49	±2.31	0.00	−0.13	0.00	−0.40	0.42	0.42	0.70	−0.24	0.00	−0.39	0.58	0.291	−0.385	1.21	−0.02	1.02	−0.89	1.42	1.77
115	66 – 80	1.4 – 1.6	-1.0 – -0.7	0.0277	±1.94	±2.90	0.00	0.08	0.00	−0.39	0.36	0.62	0.59	−0.22	0.00	−0.38	0.45	0.338	−0.259	1.68	−0.01	1.16	−1.51	1.30	1.57
116	66 – 80	1.4 – 1.6	-0.7 – -0.4	0.2058	±0.78	±1.34	0.00	0.14	0.00	−0.33	0.28	0.19	0.36	−0.08	0.00	−0.33	0.14	0.170	−0.229	0.58	−0.03	0.81	−0.26	1.32	1.64
117	66 – 80	1.4 – 1.6	-0.4 – 0.0	0.1786	±0.70	±1.01	0.00	0.13	0.00	−0.29	0.15	0.17	0.17	0.04	0.00	−0.29	0.05	0.214	−0.180	0.51	−0.07	0.58	−0.15	1.37	1.78
118	66 – 80	1.4 – 1.6	0.0 – 0.4	0.1550	±0.73	±1.09	0.00	0.08	0.00	−0.30	0.14	0.16	0.23	0.05	0.00	−0.30	0.06	0.222	−0.197	0.56	−0.07	0.47	0.48	1.45	1.94
119	66 – 80	1.4 – 1.6	0.4 – 0.7	0.1435	±0.83	±1.49	0.00	−0.01	0.00	−0.33	0.10	0.19	0.38	−0.05	0.00	−0.33	0.17	0.223	−0.263	0.72	−0.06	0.93	0.29	1.50	1.98
120	66 – 80	1.4 – 1.6	0.7 – 1.0	0.0198	±2.09	±3.48	0.00	−0.08	0.00	−0.39	0.61	0.46	0.66	−0.16	0.00	−0.38	0.53	0.903	−0.308	2.02	−0.07	1.02	2.06	1.45	1.86
121	66 – 80	1.6 – 1.8	-1.0 – -0.7	0.0058	±3.89	±9.97	0.00	0.13	0.00	−0.43	0.85	1.50	−0.01	−0.00	0.00	−0.41	0.00	0.319	−0.306	4.06	−0.01	1.35	8.76	1.27	1.65
122	66 – 80	1.6 – 1.8	-0.7 – -0.4	0.1461	±0.84	±1.66	0.00	0.10	0.00	−0.37	0.33	0.30	0.45	−0.03	0.00	−0.37	0.16	0.238	−0.218	0.69	−0.05	0.84	−0.68	1.32	1.64
123	66 – 80	1.6 – 1.8	-0.4 – 0.0	0.1746	±0.73	±1.08	0.00	0.09	0.00	−0.33	0.14	0.21	0.24	0.04	0.00	−0.32	0.07	0.225	−0.190	0.53	−0.07	0.65	−0.02	1.37	1.78
124	66 – 80	1.6 – 1.8	0.0 – 0.4	0.1479	±0.72	±1.12	0.00	0.10	0.00	−0.33	0.15	0.26	0.22	0.06	0.00	−0.33	0.07	0.202	−0.188	0.59	−0.06	0.48	0.43	1.47	1.96
125	66 – 80	1.6 – 1.8	0.4 – 0.7	0.0973	±0.97	±1.96	0.00	0.00	0.00	−0.38	0.57	0.28	0.55	−0.04	0.00	−0.37	0.20	0.344	−0.250	0.89	−0.09	1.06	−0.59	1.53	2.03
126	66 – 80	1.6 – 1.8	0.7 – 1.0	0.0040	±4.24	±5.78	0.00	−0.01	0.00	−0.44	0.80	1.06	0.82	0.29	0.00	−0.41	0.01	0.441	−0.337	4.70	−0.02	0.97	2.61	1.49	1.96
127	66 – 80	1.8 – 2.0	-1.0 – -0.7	0.0020	±6.29	±9.23	0.00	0.12	0.00	−0.51	2.07	2.00	0.04	−1.55	0.00	−0.49	0.01	0.536	−0.281	7.23	−0.01	0.53	4.56	1.09	1.36
128	66 – 80	1.8 – 2.0	-0.7 – -0.4	0.0540	±1.30	±2.17	0.00	0.08	0.00	−0.41	0.31	0.37	0.60	0.04	0.00	−0.41	0.12	0.406	−0.169	1.14	−0.04	0.72	−1.21	1.34	1.69
129	66 – 80	1.8 – 2.0	-0.4 – 0.0	0.1727	±0.67	±1.27	0.00	0.08	0.00	−0.38	0.36	0.28	0.33	0.02	0.00	−0.38	0.05	0.190	−0.168	0.53	−0.06	0.61	−0.34	1.36	1.74
130	66 – 80	1.8 – 2.0	0.0 – 0.4	0.1404	±0.73	±1.31	0.00	0.10	0.00	−0.38	0.49	0.23	0.37	0.07	0.00	−0.38	0.06	0.194	−0.184	0.62	−0.06	0.54	0.29	1.46	1.93
131	66 – 80	1.8 – 2.0	0.4 – 0.7	0.0340	±1.39	±3.03	0.00	0.04	0.00	−0.42	0.49	0.42	0.80	0.10	0.00	−0.41	0.15	0.386	−0.220	1.46	−0.06	1.12	−2.01	1.60	2.17
132	66 – 80	1.8 – 2.0	0.7 – 1.0	0.0009	±8.18	±11.09	0.00	0.04	0.01	−0.51	2.19	2.22	0.56	0.37	0.00	−0.49	0.01	0.641	−0.365	10.08	−0.02	0.92	2.80	1.40	1.82
133	66 – 80	2.0 – 2.2	-1.0 – -0.7	–	–	–	–	–	–	–	–	–	–	–	–	–	–	–	–	–	–	–	–	–	–
134	66 – 80	2.0 – 2.2	-0.7 – -0.4	0.0035	±4.19	±9.97	0.00	0.08	0.00	−0.47	0.18	1.07	0.58	0.81	0.00	−0.46	0.03	0.356	−0.130	5.04	−0.03	0.76	8.38	1.45	1.95
135	66 – 80	2.0 – 2.2	-0.4 – 0.0	0.1254	±0.77	±1.47	0.00	0.08	0.00	−0.45	0.62	0.32	0.54	0.03	0.00	−0.44	0.04	0.156	−0.158	0.64	−0.05	0.49	−0.32	1.36	1.75
136	66 – 80	2.0 – 2.2	0.0 – 0.4	0.1000	±0.80	±1.70	0.00	0.09	0.00	−0.45	0.66	0.35	0.53	0.03	0.00	−0.44	0.05	0.290	−0.184	0.72	−0.09	0.51	−0.54	1.47	1.95
137	66 – 80	2.0 – 2.2	0.4 – 0.7	0.0024	±4.64	±7.70	0.00	0.08	0.00	−0.47	1.37	1.24	0.69	0.64	0.00	−0.46	0.06	0.280	−0.190	5.92	−0.02	1.27	4.22	1.63	2.32
138	66 – 80	2.0 – 2.2	0.7 – 1.0	–	–	–	–	–	–	–	–	–	–	–	–	–	–	–	–	–	–	–	–	–	–
139	66 – 80	2.2 – 2.4	-1.0 – -0.7	–	–	–	–	–	–	–	–	–	–	–	–	–	–	–	–	–	–	–	–	–	–
140	66 – 80	2.2 – 2.4	-0.7 – -0.4	–	–	–	–	–	–	–	–	–	–	–	–	–	–	–	–	–	–	–	–	–	–
141	66 – 80	2.2 – 2.4	-0.4 – 0.0	0.0394	±1.21	±3.11	0.00	0.07	0.00	−0.54	1.39	0.64	1.05	−0.07	0.00	−0.53	0.04	0.295	−0.140	1.14	−0.07	0.49	−1.76	1.39	1.77
142	66 – 80	2.2 – 2.4	0.0 – 0.4	0.0363	±1.24	±2.62	0.00	0.06	0.00	−0.54	0.96	0.43	1.06	0.07	0.00	−0.53	0.04	0.385	−0.148	1.28	−0.07	0.42	0.61	1.42	1.89
143	66 – 80	2.2 – 2.4	0.4 – 0.7	–	–	–	–	–	–	–	–	–	–	–	–	–	–	–	–	–	–	–	–	–	–
144	66 – 80	2.2 – 2.4	0.7 – 1.0	–	–	–	–	–	–	–	–	–	–	–	–	–	–	–	–	–	–	–	–	–	–

TABLE 24: Measured cross-section values unfolded to the Born truth-level in the 3$^{\text{rd}}$ 48 bins of the measurement. The luminosity uncertainty of 1.9% is not included.

$\mathcal{B}$	$m_{\mu\mu}$ [GeV]	$\lvert y_{\mu\mu}\rvert$	$\cos\theta^{\star}$	Triple Differential Cross-section Values																						
				$d^3\sigma^{\text{Born}}_{\text{meas.}}$ [pb/GeV]	$\Delta^{\text{Stat.}}_{\text{meas.}}$ [%]	$\Delta^{\text{Syst.}}_{\text{meas.}}$ [%]	Δ^{Trigger} [%]		$\Delta^{\text{Reconst.}}$ [%]		Δ^{ID} [%]	Δ^{Sagitta} [%]	Δ^{Scale} [%]	$\Delta^{Z-\text{pT}}$ [%]	$\Delta^{\text{Isolation}}$ [%]		Δ^{QCD} [%]	$\Delta^{\text{MC Bkg.}}$ [%]		$\Delta^{\text{MC Signal}}$ [%]		Δ^{PDF} [%]	$\Delta^{\text{Unfd.}}$ [%]	$C_{\text{Dres.}}$	C_{Bare}
							uncor.	corr.	uncor.	corr.					uncor.	corr.		uncor.	corr.	uncor.	corr.				
145	80 – 91	0.0 – 0.2	-1.0 – -0.7	2.2379	±0.31	±0.63	0.00	−0.06	0.00	−0.24	0.04	0.05	0.29	−0.03	0.00	−0.24	0.02	0.012	−0.034	0.19	0.00	0.07	−0.24	0.96	1.06
146	80 – 91	0.0 – 0.2	-0.7 – -0.4	3.5689	±0.25	±0.56	0.00	0.02	0.00	−0.24	0.03	0.03	0.37	−0.04	0.00	−0.24	0.01	0.018	−0.027	0.14	−0.00	0.09	−0.16	0.98	1.07
147	80 – 91	0.0 – 0.2	-0.4 – 0.0	3.0719	±0.28	±0.73	0.00	0.06	0.00	−0.42	0.02	0.04	0.37	−0.02	0.00	−0.42	0.01	0.022	−0.024	0.14	−0.00	0.05	−0.13	0.98	1.07
148	80 – 91	0.0 – 0.2	0.0 – 0.4	3.0748	±0.26	±0.79	0.00	0.07	0.00	−0.43	0.05	0.04	0.38	−0.01	0.00	−0.43	0.01	0.015	−0.024	0.14	−0.00	0.08	−0.26	0.98	1.07
149	80 – 91	0.0 – 0.2	0.4 – 0.7	3.5641	±0.26	±0.66	0.00	0.01	0.00	−0.24	0.03	0.04	0.38	−0.03	0.00	−0.24	0.01	0.010	−0.027	0.14	−0.00	0.06	−0.37	0.98	1.07
150	80 – 91	0.0 – 0.2	0.7 – 1.0	2.2575	±0.31	±0.66	0.00	−0.10	0.00	−0.23	0.06	0.05	0.29	−0.05	0.00	−0.23	0.02	0.014	−0.034	0.18	0.00	0.08	0.33	0.96	1.06
151	80 – 91	0.2 – 0.4	-1.0 – -0.7	2.2473	±0.30	±0.64	0.00	0.02	0.00	−0.25	0.03	0.08	0.30	−0.04	0.00	−0.25	0.02	0.011	−0.033	0.19	0.00	0.07	−0.35	0.96	1.06
152	80 – 91	0.2 – 0.4	-0.7 – -0.4	3.5357	±0.26	±0.57	0.00	0.04	0.00	−0.28	0.04	0.05	0.35	−0.06	0.00	−0.28	0.01	0.012	−0.026	0.14	−0.00	0.05	0.13	0.97	1.07
153	80 – 91	0.2 – 0.4	-0.4 – 0.0	3.0562	±0.26	±1.00	0.00	0.05	0.00	−0.37	0.02	0.06	0.38	0.01	0.00	−0.37	0.02	0.013	−0.024	0.14	−0.00	0.11	−0.74	0.98	1.07
154	80 – 91	0.2 – 0.4	0.0 – 0.4	3.0770	±0.25	±0.70	0.00	0.05	0.00	−0.39	0.04	0.06	0.38	0.02	0.00	−0.39	0.02	0.013	−0.024	0.14	−0.00	0.09	0.02	0.98	1.07
155	80 – 91	0.2 – 0.4	0.4 – 0.7	3.5745	±0.26	±0.66	0.00	0.04	0.00	−0.29	0.03	0.06	0.35	−0.07	0.00	−0.29	0.01	0.012	−0.027	0.14	−0.00	0.12	0.30	0.97	1.07
156	80 – 91	0.2 – 0.4	0.7 – 1.0	2.2615	±0.30	±0.83	0.00	−0.08	0.00	−0.24	0.04	0.07	0.30	−0.04	0.00	−0.24	0.02	0.017	−0.034	0.18	0.00	0.12	0.64	0.96	1.06
157	80 – 91	0.4 – 0.6	-1.0 – -0.7	2.2311	±0.32	±0.55	0.00	0.04	0.00	−0.26	0.03	0.08	0.32	−0.03	0.00	−0.26	0.02	0.018	−0.036	0.18	0.00	0.08	0.10	0.96	1.06
158	80 – 91	0.4 – 0.6	-0.7 – -0.4	3.5180	±0.28	±0.71	0.00	0.11	0.00	−0.36	0.04	0.07	0.33	−0.04	0.00	−0.36	0.01	0.011	−0.026	0.15	−0.00	0.07	−0.24	0.97	1.07
159	80 – 91	0.4 – 0.6	-0.4 – 0.0	3.0479	±0.25	±0.72	0.00	0.03	0.00	−0.29	0.04	0.06	0.35	−0.02	0.00	−0.29	0.01	0.015	−0.023	0.13	−0.00	0.10	−0.43	0.98	1.07
160	80 – 91	0.4 – 0.6	0.0 – 0.4	3.0647	±0.24	±0.61	0.00	0.03	0.00	−0.30	0.04	0.06	0.35	−0.03	0.00	−0.30	0.01	0.019	−0.024	0.13	−0.00	0.12	−0.15	0.98	1.07
161	80 – 91	0.4 – 0.6	0.4 – 0.7	3.5473	±0.27	±0.73	0.00	0.08	0.00	−0.37	0.02	0.07	0.32	−0.04	0.00	−0.37	0.01	0.012	−0.027	0.16	−0.00	0.10	0.24	0.97	1.07
162	80 – 91	0.4 – 0.6	0.7 – 1.0	2.2428	±0.30	±0.58	0.00	−0.09	0.00	−0.26	0.04	0.08	0.33	−0.04	0.00	−0.26	0.02	0.010	−0.035	0.19	0.00	0.12	0.17	0.96	1.06
163	80 – 91	0.6 – 0.8	-1.0 – -0.7	2.2134	±0.30	±0.72	0.00	0.05	0.00	−0.31	0.04	0.09	0.27	−0.09	0.00	−0.31	0.02	0.008	−0.034	0.20	0.00	0.09	−0.43	0.96	1.05
164	80 – 91	0.6 – 0.8	-0.7 – -0.4	3.5049	±0.26	±0.86	0.00	0.17	0.00	−0.37	0.04	0.08	0.31	−0.01	0.00	−0.37	0.01	0.014	−0.025	0.15	−0.00	0.08	−0.53	0.97	1.07
165	80 – 91	0.6 – 0.8	-0.4 – 0.0	3.0424	±0.24	±0.51	0.00	0.02	0.00	−0.25	0.03	0.06	0.32	−0.00	0.00	−0.25	0.01	0.012	−0.023	0.13	−0.00	0.07	0.04	0.97	1.07
166	80 – 91	0.6 – 0.8	0.0 – 0.4	3.0453	±0.24	±0.52	0.00	0.03	0.00	−0.25	0.04	0.06	0.32	0.00	0.00	−0.25	0.01	0.018	−0.024	0.13	−0.00	0.10	0.07	0.97	1.07
167	80 – 91	0.6 – 0.8	0.4 – 0.7	3.5218	±0.26	±0.81	0.00	0.08	0.00	−0.39	0.02	0.08	0.34	−0.01	0.00	−0.39	0.00	0.019	−0.026	0.15	−0.00	0.18	0.40	0.97	1.08
168	80 – 91	0.6 – 0.8	0.7 – 1.0	2.2279	±0.31	±0.60	0.00	−0.08	0.00	−0.32	0.04	0.10	0.28	−0.09	0.00	−0.32	0.02	0.011	−0.034	0.18	0.00	0.13	0.09	0.97	1.06
169	80 – 91	0.8 – 1.0	-1.0 – -0.7	2.1907	±0.33	±0.84	0.00	0.05	0.00	−0.39	0.10	0.09	0.21	−0.06	0.00	−0.39	0.02	0.018	−0.033	0.20	−0.00	0.13	0.50	0.96	1.05
170	80 – 91	0.8 – 1.0	-0.7 – -0.4	3.4648	±0.24	±0.94	0.00	0.18	0.00	−0.32	0.04	0.10	0.30	−0.05	0.00	−0.32	0.00	0.013	−0.025	0.14	−0.00	0.07	−0.71	0.97	1.07
171	80 – 91	0.8 – 1.0	-0.4 – 0.0	3.0237	±0.24	±0.60	0.00	0.09	0.00	−0.26	0.05	0.06	0.30	0.00	0.00	−0.25	0.01	0.010	−0.022	0.13	−0.00	0.06	0.28	0.96	1.07
172	80 – 91	0.8 – 1.0	0.0 – 0.4	3.0125	±0.23	±0.54	0.00	0.04	0.00	−0.25	0.03	0.07	0.31	−0.00	0.00	−0.25	0.01	0.014	−0.024	0.13	−0.00	0.11	−0.00	0.96	1.08
173	80 – 91	0.8 – 1.0	0.4 – 0.7	3.4956	±0.24	±0.96	0.00	0.05	0.00	−0.33	0.05	0.10	0.30	−0.06	0.00	−0.33	0.00	0.013	−0.027	0.14	−0.00	0.14	0.74	0.97	1.08
174	80 – 91	0.8 – 1.0	0.7 – 1.0	2.2070	±0.31	±0.75	0.00	−0.08	0.00	−0.40	0.08	0.09	0.25	−0.05	0.00	−0.40	0.02	0.012	−0.034	0.20	−0.00	0.21	0.18	0.97	1.06
175	80 – 91	1.0 – 1.2	-1.0 – -0.7	1.9416	±0.35	±0.83	0.00	0.12	0.00	−0.44	0.08	0.09	0.24	−0.02	0.00	−0.44	0.03	0.023	−0.034	0.23	−0.00	0.13	0.28	0.97	1.06
176	80 – 91	1.0 – 1.2	-0.7 – -0.4	3.4388	±0.24	±0.60	0.00	0.18	0.00	−0.29	0.02	0.11	0.27	−0.07	0.00	−0.29	0.01	0.011	−0.026	0.15	−0.00	0.09	−0.19	0.97	1.07
177	80 – 91	1.0 – 1.2	-0.4 – 0.0	2.9757	±0.23	±0.57	0.00	0.16	0.00	−0.27	0.04	0.08	0.28	−0.01	0.00	−0.27	0.00	0.009	−0.022	0.13	−0.00	0.12	−0.01	0.96	1.07
178	80 – 91	1.0 – 1.2	0.0 – 0.4	2.9896	±0.23	±0.73	0.00	0.05	0.00	−0.26	0.03	0.09	0.27	−0.01	0.00	−0.26	0.00	0.015	−0.023	0.13	−0.00	0.11	0.50	0.96	1.07
179	80 – 91	1.0 – 1.2	0.4 – 0.7	3.4426	±0.24	±0.59	0.00	0.04	0.00	−0.29	0.03	0.11	0.28	−0.08	0.00	−0.29	0.01	0.011	−0.026	0.14	−0.00	0.15	−0.16	0.97	1.08
180	80 – 91	1.0 – 1.2	0.7 – 1.0	1.9292	±0.32	±0.94	0.00	−0.01	0.00	−0.45	0.09	0.10	0.25	−0.04	0.00	−0.45	0.03	0.020	−0.033	0.21	−0.00	0.29	−0.40	0.97	1.07
181	80 – 91	1.2 – 1.4	-1.0 – -0.7	1.2781	±0.38	±0.88	0.00	0.14	0.00	−0.41	0.17	0.11	0.29	−0.08	0.00	−0.41	0.03	0.025	−0.035	0.26	−0.00	0.12	0.37	0.97	1.06
182	80 – 91	1.2 – 1.4	-0.7 – -0.4	3.3831	±0.25	±0.62	0.00	0.19	0.00	−0.31	0.05	0.10	0.24	−0.07	0.00	−0.31	0.01	0.013	−0.025	0.15	−0.00	0.11	0.12	0.96	1.07
183	80 – 91	1.2 – 1.4	-0.4 – 0.0	2.9439	±0.23	±0.57	0.00	0.17	0.00	−0.28	0.02	0.10	0.26	−0.02	0.00	−0.28	0.00	0.013	−0.023	0.13	−0.00	0.08	−0.02	0.95	1.07
184	80 – 91	1.2 – 1.4	0.0 – 0.4	2.9419	±0.23	±0.74	0.00	0.06	0.00	−0.28	0.03	0.10	0.25	−0.02	0.00	−0.28	0.00	0.016	−0.022	0.13	−0.01	0.12	0.48	0.95	1.08
185	80 – 91	1.2 – 1.4	0.4 – 0.7	3.3634	±0.23	±0.71	0.00	0.03	0.00	−0.30	0.03	0.11	0.24	−0.07	0.00	−0.30	0.01	0.015	−0.026	0.15	−0.00	0.21	−0.38	0.97	1.08
186	80 – 91	1.2 – 1.4	0.7 – 1.0	1.2716	±0.38	±1.12	0.00	−0.00	0.00	−0.42	0.14	0.12	0.33	−0.07	0.00	−0.42	0.03	0.014	−0.036	0.26	−0.00	0.19	−0.75	0.97	1.07
187	80 – 91	1.4 – 1.6	-1.0 – -0.7	0.4838	±0.61	±1.28	0.00	0.13	0.00	−0.40	0.22	0.16	0.20	−0.06	0.00	−0.40	0.03	0.021	−0.033	0.42	−0.00	0.21	0.97	0.96	1.06
188	80 – 91	1.4 – 1.6	-0.7 – -0.4	3.1512	±0.23	±1.03	0.00	0.16	0.00	−0.34	0.05	0.10	0.24	−0.05	0.00	−0.34	0.01	0.010	−0.024	0.16	−0.00	0.12	0.79	0.96	1.07
189	80 – 91	1.4 – 1.6	-0.4 – 0.0	2.8767	±0.22	±0.58	0.00	0.13	0.00	−0.30	0.05	0.11	0.23	−0.02	0.00	−0.30	0.00	0.013	−0.021	0.13	−0.01	0.05	0.15	0.95	1.07
190	80 – 91	1.4 – 1.6	0.0 – 0.4	2.8817	±0.23	±0.60	0.00	0.08	0.00	−0.31	0.04	0.11	0.25	−0.02	0.00	−0.31	0.00	0.012	−0.022	0.13	−0.01	0.09	0.17	0.95	1.08
191	80 – 91	1.4 – 1.6	0.4 – 0.7	3.1030	±0.23	±1.16	0.00	0.02	0.00	−0.34	0.09	0.11	0.26	−0.04	0.00	−0.34	0.01	0.015	−0.026	0.16	−0.00	0.21	−0.94	0.96	1.08
192	80 – 91	1.4 – 1.6	0.7 – 1.0	0.4749	±0.59	±0.96	0.00	−0.01	0.00	−0.40	0.25	0.17	0.28	−0.04	0.00	−0.40	0.03	0.036	−0.036	0.42	−0.00	0.19	0.45	0.97	1.07

TABLE 25: Measured cross-section values unfolded to the Born truth-level in the 4^{th} 48 bins of the measurement. The luminosity uncertainty of 1.9% is not included.

$\mathcal{B}$	$m_{\mu\mu}$ [GeV]	$\lvert y_{\mu\mu}\rvert$	$\cos\theta^{\star}$	Triple Differential Cross-section Values																						
				$d^3\sigma^{\text{Born}}_{\text{meas.}}$ [pb/GeV]	$\Delta^{\text{Stat.}}_{\text{meas.}}$ [%]	$\Delta^{\text{Syst.}}_{\text{meas.}}$ [%]	Δ^{Trigger} [%]		$\Delta^{\text{Reconst.}}$ [%]		Δ^{ID} [%]	Δ^{Sagitta} [%]	Δ^{Scale} [%]	$\Delta^{Z-\text{pT}}$ [%]	$\Delta^{\text{Isolation}}$ [%]		Δ^{QCD} [%]	$\Delta^{\text{MC Bkg.}}$ [%]		$\Delta^{\text{MC Signal}}$ [%]		Δ^{PDF} [%]	$\Delta^{\text{Unfd.}}$ [%]	$C_{\text{Dres.}}$	C_{Bare}
							uncor.	corr.	uncor.	corr.					uncor.	corr.		uncor.	corr.	uncor.	corr.				
193	80 – 91	1.6 – 1.8	-1.0 – -0.7	0.0900	±1.33	±2.26	0.00	0.14	0.00	−0.43	0.36	0.25	0.09	0.38	0.00	−0.42	0.01	0.055	−0.050	1.00	−0.00	0.19	1.82	0.96	1.06
194	80 – 91	1.6 – 1.8	-0.7 – -0.4	2.2120	±0.29	±0.95	0.00	0.13	0.00	−0.38	0.09	0.11	0.22	−0.05	0.00	−0.38	0.01	0.013	−0.024	0.19	−0.00	0.13	0.63	0.95	1.06
195	80 – 91	1.6 – 1.8	-0.4 – 0.0	2.8230	±0.23	±0.63	0.00	0.10	0.00	−0.34	0.05	0.12	0.20	−0.02	0.00	−0.34	0.00	0.032	−0.021	0.14	−0.01	0.06	0.22	0.95	1.07
196	80 – 91	1.6 – 1.8	0.0 – 0.4	2.8078	±0.23	±0.85	0.00	0.10	0.00	−0.34	0.06	0.11	0.19	−0.02	0.00	−0.34	0.00	0.011	−0.022	0.14	−0.01	0.14	−0.58	0.96	1.08
197	80 – 91	1.6 – 1.8	0.4 – 0.7	2.1911	±0.27	±1.26	0.00	0.03	0.00	−0.39	0.11	0.12	0.27	−0.05	0.00	−0.39	0.01	0.017	−0.025	0.19	−0.01	0.24	−0.99	0.96	1.08
198	80 – 91	1.6 – 1.8	0.7 – 1.0	0.0892	±1.27	±1.45	0.00	−0.01	0.00	−0.43	0.10	0.23	0.20	0.45	0.00	−0.42	0.01	0.060	−0.053	1.02	−0.00	0.07	0.60	0.96	1.08
199	80 – 91	1.8 – 2.0	-1.0 – -0.7	0.0209	±2.59	±5.80	0.00	0.13	0.00	−0.51	0.29	0.50	0.18	1.07	0.00	−0.51	0.00	0.142	−0.066	2.15	−0.00	0.29	5.17	0.95	1.04
200	80 – 91	1.8 – 2.0	-0.7 – -0.4	0.8019	±0.44	±1.64	0.00	0.10	0.00	−0.42	0.22	0.09	0.20	−0.05	0.00	−0.42	0.01	0.025	−0.025	0.30	−0.00	0.13	1.44	0.95	1.06
201	80 – 91	1.8 – 2.0	-0.4 – 0.0	2.7056	±0.22	±1.50	0.00	0.09	0.00	−0.40	0.08	0.11	0.19	−0.02	0.00	−0.40	0.00	0.013	−0.021	0.14	−0.01	0.07	1.34	0.95	1.07
202	80 – 91	1.8 – 2.0	0.0 – 0.4	2.6807	±0.23	±1.53	0.00	0.11	0.00	−0.40	0.09	0.11	0.21	−0.04	0.00	−0.40	0.00	0.014	−0.022	0.14	−0.01	0.15	−1.36	0.95	1.08
203	80 – 91	1.8 – 2.0	0.4 – 0.7	0.7840	±0.45	±1.30	0.00	0.07	0.00	−0.43	0.24	0.11	0.23	−0.02	0.00	−0.43	0.01	0.029	−0.026	0.33	−0.01	0.17	−1.00	0.96	1.08
204	80 – 91	1.8 – 2.0	0.7 – 1.0	0.0192	±2.54	±5.02	0.00	0.01	0.00	−0.50	0.39	0.47	0.06	1.26	0.00	−0.50	0.00	0.123	−0.067	2.20	−0.00	0.28	4.21	0.92	1.06
205	80 – 91	2.0 – 2.2	-1.0 – -0.7	0.0025	±6.91	±8.00	0.00	0.11	0.01	−0.62	1.22	2.08	−0.72	2.62	0.00	−0.61	0.00	0.336	−0.069	6.86	−0.00	0.40	−1.41	0.89	1.01
206	80 – 91	2.0 – 2.2	-0.7 – -0.4	0.0487	±1.66	±3.16	0.00	0.09	0.00	−0.49	0.13	0.46	0.10	0.24	0.00	−0.48	0.00	0.065	−0.039	1.34	−0.00	0.22	2.70	0.96	1.08
207	80 – 91	2.0 – 2.2	-0.4 – 0.0	1.9323	±0.28	±0.88	0.00	0.08	0.00	−0.47	0.15	0.12	0.19	−0.03	0.00	−0.47	0.00	0.012	−0.021	0.17	−0.00	0.06	0.42	0.95	1.07
208	80 – 91	2.0 – 2.2	0.0 – 0.4	1.9236	±0.27	±1.23	0.00	0.09	0.00	−0.46	0.17	0.14	0.20	−0.03	0.00	−0.46	0.00	0.023	−0.023	0.17	−0.01	0.09	−0.93	0.95	1.08
209	80 – 91	2.0 – 2.2	0.4 – 0.7	0.0490	±1.61	±3.16	0.00	0.08	0.00	−0.49	0.18	0.34	0.01	0.27	0.00	−0.48	0.00	0.071	−0.039	1.36	−0.00	0.13	2.72	0.95	1.09
210	80 – 91	2.0 – 2.2	0.7 – 1.0	0.0026	±7.04	±15.79	0.00	0.05	0.00	−0.62	1.38	2.49	0.64	1.83	0.00	−0.61	0.00	0.481	−0.099	6.29	−0.00	0.86	14.00	0.93	1.03
211	80 – 91	2.2 – 2.4	-1.0 – -0.7	–	–	–	–	–	–	–	–	–	–	–	–	–	–	–	–	–	–	–	–	–	–
212	80 – 91	2.2 – 2.4	-0.7 – -0.4	–	–	–	–	–	–	–	–	–	–	–	–	–	–	–	–	–	–	–	–	–	–
213	80 – 91	2.2 – 2.4	-0.4 – 0.0	0.6426	±0.44	±1.10	0.00	0.07	0.00	−0.56	0.19	0.10	0.23	−0.00	0.00	−0.56	0.00	0.047	−0.021	0.30	−0.01	0.09	−0.55	0.95	1.07
214	80 – 91	2.2 – 2.4	0.0 – 0.4	0.6441	±0.45	±0.98	0.00	0.06	0.00	−0.55	0.17	0.10	0.20	−0.02	0.00	−0.55	0.00	0.038	−0.023	0.29	−0.01	0.09	0.23	0.95	1.07
215	80 – 91	2.2 – 2.4	0.4 – 0.7	–	–	–	–	–	–	–	–	–	–	–	–	–	–	–	–	–	–	–	–	–	–
216	80 – 91	2.2 – 2.4	0.7 – 1.0	–	–	–	–	–	–	–	–	–	–	–	–	–	–	–	–	–	–	–	–	–	–
217	91 – 102	0.0 – 0.2	-1.0 – -0.7	2.7900	±0.30	±0.57	0.00	−0.04	0.00	−0.24	0.03	0.03	−0.31	−0.06	0.00	−0.24	0.01	0.013	−0.031	0.16	0.00	0.06	0.12	0.95	0.84
218	91 – 102	0.0 – 0.2	-0.7 – -0.4	4.1437	±0.24	±0.51	0.00	0.02	0.00	−0.24	0.03	0.04	−0.34	−0.02	0.00	−0.24	0.01	0.012	−0.022	0.12	0.00	0.07	0.06	0.95	0.84
219	91 – 102	0.0 – 0.2	-0.4 – 0.0	3.5585	±0.26	±0.70	0.00	0.06	0.00	−0.42	0.02	0.04	−0.31	−0.04	0.00	−0.42	0.01	0.015	−0.020	0.13	0.00	0.06	0.02	0.95	0.84
220	91 – 102	0.0 – 0.2	0.0 – 0.4	3.5763	±0.25	±0.73	0.00	0.07	0.00	−0.43	0.05	0.04	−0.33	−0.05	0.00	−0.43	0.01	0.009	−0.021	0.13	0.00	0.06	0.14	0.95	0.84
221	91 – 102	0.0 – 0.2	0.4 – 0.7	4.1856	±0.25	±0.58	0.00	0.02	0.00	−0.24	0.02	0.03	−0.35	−0.03	0.00	−0.24	0.01	0.011	−0.022	0.12	0.00	0.06	0.27	0.94	0.84
222	91 – 102	0.0 – 0.2	0.7 – 1.0	2.8131	±0.30	±0.56	0.00	−0.09	0.00	−0.24	0.03	0.04	−0.32	−0.05	0.00	−0.24	0.01	0.010	−0.031	0.16	0.00	0.05	−0.10	0.95	0.84
223	91 – 102	0.2 – 0.4	-1.0 – -0.7	2.7689	±0.29	±0.62	0.00	0.03	0.00	−0.25	0.01	0.05	−0.35	−0.06	0.00	−0.25	0.01	0.008	−0.030	0.15	0.00	0.08	0.30	0.95	0.84
224	91 – 102	0.2 – 0.4	-0.7 – -0.4	4.0894	±0.25	±0.60	0.00	0.04	0.00	−0.28	0.03	0.05	−0.31	−0.07	0.00	−0.28	0.01	0.007	−0.021	0.12	0.00	0.08	−0.25	0.95	0.84
225	91 – 102	0.2 – 0.4	-0.4 – 0.0	3.5570	±0.26	±0.86	0.00	0.05	0.00	−0.37	0.02	0.05	−0.33	0.00	0.00	−0.37	0.01	0.008	−0.020	0.12	0.00	0.08	0.56	0.95	0.84
226	91 – 102	0.2 – 0.4	0.0 – 0.4	3.5707	±0.25	±0.67	0.00	0.06	0.00	−0.39	0.03	0.06	−0.33	−0.00	0.00	−0.39	0.01	0.008	−0.020	0.12	0.00	0.06	−0.09	0.95	0.84
227	91 – 102	0.2 – 0.4	0.4 – 0.7	4.1693	±0.25	±0.65	0.00	0.04	0.00	−0.30	0.02	0.05	−0.31	−0.06	0.00	−0.29	0.01	0.007	−0.021	0.13	0.00	0.06	−0.35	0.95	0.84
228	91 – 102	0.2 – 0.4	0.7 – 1.0	2.8272	±0.29	±0.70	0.00	−0.08	0.00	−0.24	0.01	0.06	−0.33	−0.07	0.00	−0.24	0.01	0.009	−0.032	0.15	0.00	0.08	−0.46	0.94	0.84
229	91 – 102	0.4 – 0.6	-1.0 – -0.7	2.7406	±0.31	±0.54	0.00	0.05	0.00	−0.26	0.04	0.07	−0.33	−0.05	0.00	−0.26	0.01	0.012	−0.031	0.16	0.00	0.09	0.02	0.95	0.84
230	91 – 102	0.4 – 0.6	-0.7 – -0.4	4.0419	±0.27	±0.65	0.00	0.11	0.00	−0.36	0.02	0.06	−0.28	−0.04	0.00	−0.36	0.01	0.008	−0.022	0.13	0.00	0.09	0.08	0.95	0.84
231	91 – 102	0.4 – 0.6	-0.4 – 0.0	3.5178	±0.24	±0.59	0.00	0.03	0.00	−0.29	0.01	0.06	−0.32	−0.03	0.00	−0.29	0.01	0.010	−0.020	0.12	0.00	0.07	0.23	0.95	0.84
232	91 – 102	0.4 – 0.6	0.0 – 0.4	3.5697	±0.23	±0.56	0.00	0.03	0.00	−0.31	0.04	0.05	−0.31	−0.04	0.00	−0.31	0.01	0.011	−0.020	0.12	0.00	0.06	0.04	0.95	0.84
233	91 – 102	0.4 – 0.6	0.4 – 0.7	4.1720	±0.26	±0.71	0.00	0.08	0.00	−0.37	0.02	0.06	−0.27	−0.04	0.00	−0.37	0.01	0.015	−0.022	0.14	0.00	0.07	−0.29	0.95	0.84
234	91 – 102	0.4 – 0.6	0.7 – 1.0	2.8291	±0.29	±0.54	0.00	−0.08	0.00	−0.26	0.02	0.07	−0.32	−0.04	0.00	−0.26	0.01	0.011	−0.031	0.15	0.00	0.05	−0.07	0.94	0.84
235	91 – 102	0.6 – 0.8	-1.0 – -0.7	2.6847	±0.29	±0.67	0.00	0.05	0.00	−0.31	0.04	0.08	−0.30	−0.11	0.00	−0.31	0.01	0.007	−0.031	0.17	0.00	0.09	0.30	0.94	0.84
236	91 – 102	0.6 – 0.8	-0.7 – -0.4	4.0262	±0.26	±0.80	0.00	0.17	0.00	−0.38	0.03	0.07	−0.28	−0.01	0.00	−0.38	0.00	0.012	−0.022	0.13	0.00	0.09	0.43	0.95	0.84
237	91 – 102	0.6 – 0.8	-0.4 – 0.0	3.4967	±0.23	±0.49	0.00	0.02	0.00	−0.25	0.03	0.05	−0.29	−0.02	0.00	−0.25	0.01	0.008	−0.020	0.11	0.00	0.09	−0.11	0.95	0.84
238	91 – 102	0.6 – 0.8	0.0 – 0.4	3.5509	±0.23	±0.49	0.00	0.03	0.00	−0.25	0.03	0.05	−0.28	−0.01	0.00	−0.25	0.01	0.009	−0.020	0.11	0.00	0.06	−0.13	0.95	0.84
239	91 – 102	0.6 – 0.8	0.4 – 0.7	4.1673	±0.25	±0.75	0.00	0.08	0.00	−0.39	0.02	0.06	−0.30	−0.01	0.00	−0.39	0.00	0.027	−0.022	0.14	0.00	0.08	−0.33	0.95	0.84
240	91 – 102	0.6 – 0.8	0.7 – 1.0	2.8455	±0.29	±0.60	0.00	−0.08	0.00	−0.31	0.03	0.08	−0.29	−0.12	0.00	−0.31	0.01	0.007	−0.031	0.15	0.00	0.10	0.04	0.94	0.84

TABLE 26: Measured cross-section values unfolded to the Born truth-level in the 5^{th} 48 bins of the measurement. The luminosity uncertainty of 1.9% is not included.

$\mathcal{B}$	$m_{\mu\mu}$ [GeV]	$\lvert y_{\mu\mu}\rvert$	$\cos\theta^{\star}$	Triple Differential Cross-section Values																							
				$d^3\sigma^{\text{Born}}_{\text{meas.}}$ [pb/GeV]	$\Delta^{\text{Stat.}}_{\text{meas.}}$ [%]	$\Delta^{\text{Syst.}}_{\text{meas.}}$ [%]	Δ^{Trigger} [%]		$\Delta^{\text{Reconst.}}$ [%]		Δ^{ID} [%]	Δ^{Sagitta} [%]	Δ^{Scale} [%]	$\Delta^{Z-\text{pT}}$ [%]	$\Delta^{\text{Isolation}}$ [%]		Δ^{QCD} [%]	$\Delta^{\text{MC Bkg.}}$ [%]		$\Delta^{\text{MC Signal}}$ [%]		Δ^{PDF} [%]	$\Delta^{\text{Unfd.}}$ [%]	$C_{\text{Dres.}}$	C_{Bare}
							uncor.	corr.	uncor.	corr.					uncor.	corr.		uncor.	corr.	uncor.	corr.				
241	91 – 102	0.8 – 1.0	-1.0 – -0.7	2.6156	±0.32	±0.75	0.00	0.06	0.00	−0.38	0.04	0.09	−0.29	−0.08	0.00	−0.38	0.01	0.010	−0.032	0.17	0.00	0.13	−0.25	0.94	0.84
242	91 – 102	0.8 – 1.0	-0.7 – -0.4	3.9560	±0.24	±0.79	0.00	0.18	0.00	−0.32	0.04	0.09	−0.29	−0.05	0.00	−0.32	0.00	0.007	−0.021	0.12	0.00	0.14	0.50	0.95	0.84
243	91 – 102	0.8 – 1.0	-0.4 – 0.0	3.4496	±0.22	±0.63	0.00	0.09	0.00	−0.26	0.01	0.06	−0.27	−0.02	0.00	−0.26	0.00	0.006	−0.019	0.11	0.00	0.07	−0.37	0.96	0.84
244	91 – 102	0.8 – 1.0	0.0 – 0.4	3.5368	±0.23	±0.50	0.00	0.04	0.00	−0.25	0.01	0.06	−0.26	−0.02	0.00	−0.25	0.00	0.010	−0.020	0.11	0.00	0.06	−0.08	0.95	0.84
245	91 – 102	0.8 – 1.0	0.4 – 0.7	4.1417	±0.25	±0.95	0.00	0.05	0.00	−0.33	0.05	0.08	−0.28	−0.05	0.00	−0.33	0.00	0.010	−0.022	0.12	0.00	0.07	−0.75	0.95	0.84
246	91 – 102	0.8 – 1.0	0.7 – 1.0	2.8144	±0.29	±0.72	0.00	−0.07	0.00	−0.40	0.02	0.08	−0.29	−0.07	0.00	−0.40	0.01	0.012	−0.030	0.17	0.00	0.12	0.08	0.94	0.84
247	91 – 102	1.0 – 1.2	-1.0 – -0.7	2.2094	±0.34	±0.84	0.00	0.14	0.00	−0.44	0.05	0.09	−0.30	−0.06	0.00	−0.44	0.01	0.019	−0.031	0.20	0.00	0.13	−0.29	0.94	0.84
248	91 – 102	1.0 – 1.2	-0.7 – -0.4	3.8914	±0.24	±0.59	0.00	0.19	0.00	−0.30	0.02	0.09	−0.25	−0.07	0.00	−0.30	0.00	0.006	−0.022	0.13	0.00	0.14	0.15	0.95	0.84
249	91 – 102	1.0 – 1.2	-0.4 – 0.0	3.3978	±0.23	±0.55	0.00	0.16	0.00	−0.27	0.02	0.07	−0.24	−0.02	0.00	−0.27	0.00	0.006	−0.018	0.11	0.00	0.07	−0.09	0.96	0.84
250	91 – 102	1.0 – 1.2	0.0 – 0.4	3.4979	±0.23	±0.70	0.00	0.05	0.00	−0.26	0.01	0.07	−0.23	−0.02	0.00	−0.26	0.00	0.013	−0.019	0.11	0.00	0.06	−0.49	0.96	0.84
251	91 – 102	1.0 – 1.2	0.4 – 0.7	4.1530	±0.24	±0.55	0.00	0.04	0.00	−0.30	0.04	0.09	−0.25	−0.07	0.00	−0.30	0.00	0.008	−0.021	0.12	0.00	0.11	0.14	0.95	0.84
252	91 – 102	1.0 – 1.2	0.7 – 1.0	2.4072	±0.32	±0.82	0.00	−0.00	0.00	−0.45	0.04	0.08	−0.23	−0.06	0.00	−0.45	0.02	0.015	−0.029	0.18	0.00	0.11	0.26	0.94	0.84
253	91 – 102	1.2 – 1.4	-1.0 – -0.7	1.4392	±0.36	±0.87	0.00	0.14	0.00	−0.41	0.03	0.12	−0.29	−0.13	0.00	−0.41	0.02	0.013	−0.030	0.22	0.00	0.19	−0.21	0.95	0.84
254	91 – 102	1.2 – 1.4	-0.7 – -0.4	3.7577	±0.25	±0.61	0.00	0.19	0.00	−0.31	0.04	0.11	−0.22	−0.05	0.00	−0.31	0.00	0.007	−0.022	0.14	0.00	0.16	−0.15	0.95	0.84
255	91 – 102	1.2 – 1.4	-0.4 – 0.0	3.3348	±0.23	±0.57	0.00	0.17	0.00	−0.28	0.02	0.09	−0.24	−0.03	0.00	−0.28	0.00	0.007	−0.018	0.11	0.00	0.08	−0.06	0.96	0.84
256	91 – 102	1.2 – 1.4	0.0 – 0.4	3.4547	±0.23	±0.70	0.00	0.06	0.00	−0.28	0.01	0.09	−0.22	−0.03	0.00	−0.28	0.00	0.010	−0.018	0.11	−0.00	0.08	−0.47	0.96	0.84
257	91 – 102	1.2 – 1.4	0.4 – 0.7	4.0877	±0.23	±0.57	0.00	0.04	0.00	−0.31	0.04	0.10	−0.19	−0.05	0.00	−0.31	0.00	0.010	−0.021	0.12	0.00	0.14	0.22	0.95	0.84
258	91 – 102	1.2 – 1.4	0.7 – 1.0	1.5982	±0.37	±1.18	0.00	0.00	0.00	−0.42	0.03	0.11	−0.27	−0.14	0.00	−0.42	0.02	0.015	−0.028	0.21	0.00	0.16	0.87	0.94	0.84
259	91 – 102	1.4 – 1.6	-1.0 – -0.7	0.5311	±0.59	±1.10	0.00	0.13	0.00	−0.40	0.05	0.21	−0.43	−0.23	0.00	−0.40	0.01	0.016	−0.030	0.38	0.00	0.21	−0.43	0.95	0.83
260	91 – 102	1.4 – 1.6	-0.7 – -0.4	3.4349	±0.23	±1.07	0.00	0.16	0.00	−0.34	0.03	0.10	−0.18	−0.03	0.00	−0.34	0.01	0.006	−0.021	0.15	0.00	0.18	−0.85	0.95	0.84
261	91 – 102	1.4 – 1.6	-0.4 – 0.0	3.2494	±0.22	±0.59	0.00	0.13	0.00	−0.31	0.03	0.10	−0.22	−0.03	0.00	−0.31	0.00	0.007	−0.018	0.12	0.00	0.10	−0.21	0.96	0.84
262	91 – 102	1.4 – 1.6	0.0 – 0.4	3.4032	±0.22	±0.60	0.00	0.08	0.00	−0.31	0.02	0.10	−0.22	−0.03	0.00	−0.31	0.00	0.008	−0.018	0.11	0.00	0.07	−0.27	0.96	0.84
263	91 – 102	1.4 – 1.6	0.4 – 0.7	3.8184	±0.23	±0.91	0.00	0.02	0.00	−0.34	0.04	0.09	−0.14	−0.04	0.00	−0.34	0.01	0.015	−0.021	0.13	0.00	0.17	0.68	0.95	0.84
264	91 – 102	1.4 – 1.6	0.7 – 1.0	0.5968	±0.55	±1.06	0.00	−0.01	0.00	−0.40	0.08	0.18	−0.38	−0.25	0.00	−0.40	0.01	0.019	−0.029	0.37	0.00	0.22	−0.45	0.95	0.85
265	91 – 102	1.6 – 1.8	-1.0 – -0.7	0.0979	±1.28	±1.50	0.00	0.14	0.00	−0.43	0.15	0.29	−0.40	−0.33	0.00	−0.43	0.01	0.053	−0.046	0.90	0.00	0.17	0.64	0.96	0.83
266	91 – 102	1.6 – 1.8	-0.7 – -0.4	2.3828	±0.29	±0.98	0.00	0.13	0.00	−0.39	0.03	0.13	−0.27	−0.05	0.00	−0.39	0.00	0.006	−0.019	0.16	0.00	0.19	−0.61	0.95	0.84
267	91 – 102	1.6 – 1.8	-0.4 – 0.0	3.1739	±0.23	±0.60	0.00	0.10	0.00	−0.34	0.02	0.11	−0.18	−0.04	0.00	−0.34	0.00	0.017	−0.018	0.13	0.00	0.11	−0.15	0.96	0.84
268	91 – 102	1.6 – 1.8	0.0 – 0.4	3.3587	±0.22	±0.67	0.00	0.10	0.00	−0.35	0.02	0.11	−0.17	−0.04	0.00	−0.35	0.00	0.008	−0.017	0.11	0.00	0.09	0.36	0.95	0.84
269	91 – 102	1.6 – 1.8	0.4 – 0.7	2.7083	±0.27	±1.02	0.00	0.03	0.00	−0.39	0.03	0.12	−0.23	−0.05	0.00	−0.39	0.01	0.010	−0.020	0.16	0.00	0.20	0.69	0.95	0.84
270	91 – 102	1.6 – 1.8	0.7 – 1.0	0.1134	±1.18	±2.25	0.00	−0.01	0.00	−0.43	0.18	0.26	−0.34	−0.29	0.00	−0.43	0.01	0.047	−0.043	0.88	0.00	0.36	1.81	0.96	0.84
271	91 – 102	1.8 – 2.0	-1.0 – -0.7	0.0216	±2.57	±2.25	0.00	0.13	0.00	−0.51	0.23	0.53	−0.22	0.16	0.00	−0.51	0.00	0.136	−0.062	2.01	0.00	0.13	0.05	0.95	0.83
272	91 – 102	1.8 – 2.0	-0.7 – -0.4	0.8529	±0.44	±1.18	0.00	0.10	0.00	−0.43	0.06	0.23	−0.42	−0.11	0.00	−0.43	0.00	0.012	−0.021	0.29	0.00	0.18	−0.71	0.96	0.84
273	91 – 102	1.8 – 2.0	-0.4 – 0.0	2.9905	±0.23	±1.44	0.00	0.09	0.00	−0.40	0.04	0.11	−0.15	−0.03	0.00	−0.40	0.00	0.007	−0.017	0.13	0.00	0.11	−1.28	0.95	0.84
274	91 – 102	1.8 – 2.0	0.0 – 0.4	3.2230	±0.23	±1.14	0.00	0.11	0.00	−0.40	0.02	0.10	−0.12	−0.03	0.00	−0.40	0.00	0.008	−0.017	0.12	0.00	0.11	0.93	0.95	0.84
275	91 – 102	1.8 – 2.0	0.4 – 0.7	0.9773	±0.44	±1.52	0.00	0.07	0.00	−0.43	0.05	0.21	−0.37	−0.13	0.00	−0.43	0.00	0.018	−0.020	0.27	0.00	0.19	1.24	0.96	0.84
276	91 – 102	1.8 – 2.0	0.7 – 1.0	0.0231	±2.50	±3.51	0.00	0.01	0.00	−0.51	0.21	0.46	−0.35	0.42	0.00	−0.50	0.00	0.120	−0.061	1.89	0.00	0.28	−2.75	0.99	0.85
277	91 – 102	2.0 – 2.2	-1.0 – -0.7	0.0022	±7.06	±14.20	0.00	0.11	0.01	−0.63	1.16	2.05	−0.81	1.28	0.00	−0.62	0.00	0.347	−0.070	6.65	0.01	0.34	−12.19	1.02	0.83
278	91 – 102	2.0 – 2.2	-0.7 – -0.4	0.0509	±1.56	±5.17	0.00	0.09	0.00	−0.49	0.19	0.48	−0.55	−0.24	0.00	−0.49	0.00	0.062	−0.036	1.31	0.00	0.25	−4.87	0.98	0.84
279	91 – 102	2.0 – 2.2	-0.4 – 0.0	2.1576	±0.28	±0.90	0.00	0.08	0.00	−0.47	0.02	0.13	−0.21	−0.04	0.00	−0.47	0.00	0.010	−0.017	0.15	0.00	0.10	−0.42	0.96	0.84
280	91 – 102	2.0 – 2.2	0.0 – 0.4	2.3021	±0.26	±1.04	0.00	0.09	0.00	−0.47	0.04	0.13	−0.19	−0.03	0.00	−0.47	0.00	0.011	−0.017	0.15	−0.00	0.08	0.68	0.95	0.84
281	91 – 102	2.0 – 2.2	0.4 – 0.7	0.0626	±1.52	±2.36	0.00	0.08	0.00	−0.49	0.33	0.51	−0.54	−0.19	0.00	−0.49	0.00	0.057	−0.033	1.19	0.00	0.67	−1.57	0.97	0.84
282	91 – 102	2.0 – 2.2	0.7 – 1.0	0.0034	±6.67	±7.14	0.00	0.05	0.00	−0.64	2.20	1.95	−0.39	0.85	0.00	−0.62	0.00	0.456	−0.079	5.37	0.00	0.28	−3.30	0.95	0.85
283	91 – 102	2.2 – 2.4	-1.0 – -0.7	–	–	–	–	–	–	–	–	–	–	–	–	–	–	–	–	–	–	–	–	–	–
284	91 – 102	2.2 – 2.4	-0.7 – -0.4	–	–	–	–	–	–	–	–	–	–	–	–	–	–	–	–	–	–	–	–	–	–
285	91 – 102	2.2 – 2.4	-0.4 – 0.0	0.7239	±0.45	±1.16	0.00	0.07	0.00	−0.56	0.09	0.15	−0.34	−0.02	0.00	−0.56	0.00	0.029	−0.017	0.26	−0.00	0.08	0.60	0.96	0.84
286	91 – 102	2.2 – 2.4	0.0 – 0.4	0.7517	±0.45	±0.98	0.00	0.06	0.00	−0.56	0.05	0.14	−0.34	−0.02	0.00	−0.56	0.00	0.017	−0.017	0.26	0.00	0.08	−0.02	0.96	0.84
287	91 – 102	2.2 – 2.4	0.4 – 0.7	–	–	–	–	–	–	–	–	–	–	–	–	–	–	–	–	–	–	–	–	–	–
288	91 – 102	2.2 – 2.4	0.7 – 1.0	–	–	–	–	–	–	–	–	–	–	–	–	–	–	–	–	–	–	–	–	–	–

TABLE 27: Measured cross-section values unfolded to the Born truth-level in the 6$^{\text{th}}$ 48 bins of the measurement. The luminosity uncertainty of 1.9% is not included.

Triple Differential Cross-section Values																														
$\mathcal{B}$	$m_{\mu\mu}$ [GeV]	$\lvert y_{\mu\mu}\rvert$	$\cos\theta^{\star}$	$d^3\sigma^{\text{Born}}_{\text{meas.}}$ [pb/GeV]	$\Delta^{\text{Stat.}}_{\text{meas.}}$ [%]	$\Delta^{\text{Syst.}}_{\text{meas.}}$ [%]	Δ^{Trigger} [%]		$\Delta^{\text{Reconst.}}$ [%]		Δ^{ID} [%]	Δ^{Sagitta} [%]	Δ^{Scale} [%]	$\Delta^{Z-\text{pT}}$ [%]	$\Delta^{\text{Isolation}}$ [%]		Δ^{QCD} [%]	$\Delta^{\text{MC Bkg.}}$ [%]		$\Delta^{\text{MC Signal}}$ [%]		Δ^{PDF} [%]	$\Delta^{\text{Unfd.}}$ [%]	$C_{\text{Dres.}}$	C_{Bare}
							uncor.	corr.	uncor.	corr.					uncor.	corr.		uncor.	corr.	uncor.	corr.				
289	102 – 116	0.0 – 0.2	-1.0 – -0.7	0.1079	±1.36	±1.39	0.00	0.02	0.00	−0.25	0.16	0.17	−0.41	0.04	0.00	−0.25	0.05	0.170	−0.380	0.72	0.05	0.10	0.92	1.35	0.90
290	102 – 116	0.0 – 0.2	-0.7 – -0.4	0.1297	±1.21	±1.11	0.00	0.02	0.00	−0.25	0.16	0.14	−0.40	0.05	0.00	−0.25	0.15	0.267	−0.196	0.59	0.01	0.17	−0.62	1.30	0.91
291	102 – 116	0.0 – 0.2	-0.4 – 0.0	0.1117	±1.39	±1.10	0.00	0.06	0.00	−0.44	0.15	0.14	−0.38	0.06	0.00	−0.43	0.08	0.079	−0.162	0.60	0.01	0.11	−0.44	1.26	0.90
292	102 – 116	0.0 – 0.2	0.0 – 0.4	0.1151	±1.40	±1.07	0.00	0.07	0.00	−0.45	0.15	0.14	−0.40	0.05	0.00	−0.43	0.08	0.219	−0.178	0.58	−0.00	0.15	0.29	1.25	0.91
293	102 – 116	0.0 – 0.2	0.4 – 0.7	0.1392	±1.30	±1.00	0.00	0.02	0.00	−0.25	0.22	0.19	−0.40	0.04	0.00	−0.25	0.14	0.100	−0.196	0.56	0.01	0.09	0.49	1.28	0.91
294	102 – 116	0.0 – 0.2	0.7 – 1.0	0.1082	±1.30	±1.22	0.00	−0.03	0.00	−0.25	0.24	0.16	−0.39	0.03	0.00	−0.25	0.05	0.226	−0.370	0.69	0.05	0.25	−0.56	1.34	0.91
295	102 – 116	0.2 – 0.4	-1.0 – -0.7	0.1045	±1.34	±1.14	0.00	0.08	0.00	−0.26	0.16	0.22	−0.33	0.04	0.00	−0.26	0.05	0.230	−0.360	0.69	0.04	0.16	−0.26	1.35	0.91
296	102 – 116	0.2 – 0.4	-0.7 – -0.4	0.1339	±1.25	±1.68	0.00	0.05	0.00	−0.30	0.29	0.23	−0.31	0.05	0.00	−0.29	0.10	0.226	−0.207	0.61	0.01	0.13	1.38	1.32	0.90
297	102 – 116	0.2 – 0.4	-0.4 – 0.0	0.1138	±1.32	±1.01	0.00	0.05	0.00	−0.39	0.18	0.15	−0.41	0.08	0.00	−0.38	0.08	0.081	−0.168	0.60	0.01	0.26	−0.04	1.26	0.90
298	102 – 116	0.2 – 0.4	0.0 – 0.4	0.1151	±1.29	±1.09	0.00	0.06	0.00	−0.41	0.17	0.15	−0.45	0.10	0.00	−0.40	0.08	0.085	−0.166	0.60	0.01	0.25	−0.33	1.26	0.90
299	102 – 116	0.2 – 0.4	0.4 – 0.7	0.1414	±1.26	±0.97	0.00	0.04	0.00	−0.31	0.19	0.20	−0.37	0.01	0.00	−0.30	0.09	0.084	−0.191	0.59	0.01	0.12	0.34	1.30	0.91
300	102 – 116	0.2 – 0.4	0.7 – 1.0	0.1130	±1.31	±1.09	0.00	−0.03	0.00	−0.25	0.20	0.22	−0.51	0.05	0.00	−0.25	0.05	0.223	−0.387	0.64	0.03	0.26	0.21	1.32	0.90
301	102 – 116	0.4 – 0.6	-1.0 – -0.7	0.1022	±1.32	±1.37	0.00	0.11	0.00	−0.28	0.19	0.30	−0.48	0.08	0.00	−0.27	0.05	0.115	−0.381	0.71	0.05	0.18	0.80	1.36	0.91
302	102 – 116	0.4 – 0.6	-0.7 – -0.4	0.1244	±1.32	±1.40	0.00	0.12	0.00	−0.37	0.17	0.21	−0.40	0.05	0.00	−0.36	0.14	0.250	−0.225	0.68	0.02	0.16	−0.87	1.37	0.91
303	102 – 116	0.4 – 0.6	-0.4 – 0.0	0.1141	±1.20	±1.37	0.00	0.03	0.00	−0.30	0.22	0.21	−0.43	0.05	0.00	−0.30	0.04	0.073	−0.157	0.55	0.01	0.10	1.04	1.32	0.90
304	102 – 116	0.4 – 0.6	0.0 – 0.4	0.1142	±1.21	±0.96	0.00	0.03	0.00	−0.32	0.20	0.15	−0.41	0.05	0.00	−0.31	0.04	0.071	−0.148	0.54	0.01	0.09	0.39	1.31	0.92
305	102 – 116	0.4 – 0.6	0.4 – 0.7	0.1396	±1.28	±1.08	0.00	0.08	0.00	−0.38	0.16	0.21	−0.33	0.04	0.00	−0.37	0.13	0.191	−0.190	0.66	0.01	0.38	0.12	1.33	0.91
306	102 – 116	0.4 – 0.6	0.7 – 1.0	0.1156	±1.28	±1.15	0.00	−0.03	0.00	−0.27	0.21	0.21	−0.49	0.04	0.00	−0.27	0.04	0.104	−0.321	0.64	0.04	0.26	−0.50	1.29	0.91
307	102 – 116	0.6 – 0.8	-1.0 – -0.7	0.1006	±1.27	±1.42	0.00	0.10	0.00	−0.33	0.23	0.34	−0.41	−0.01	0.00	−0.32	0.05	0.110	−0.368	0.72	0.04	0.18	0.81	1.32	0.90
308	102 – 116	0.6 – 0.8	-0.7 – -0.4	0.1211	±1.35	±1.36	0.00	0.18	0.00	−0.39	0.22	0.34	−0.30	0.07	0.00	−0.38	0.11	0.086	−0.201	0.70	0.02	0.19	−0.64	1.40	0.90
309	102 – 116	0.6 – 0.8	-0.4 – 0.0	0.1098	±1.11	±0.93	0.00	0.02	0.00	−0.26	0.25	0.17	−0.45	0.08	0.00	−0.26	0.04	0.107	−0.144	0.60	0.01	0.12	0.14	1.38	0.91
310	102 – 116	0.6 – 0.8	0.0 – 0.4	0.1168	±1.14	±0.98	0.00	0.03	0.00	−0.26	0.16	0.14	−0.36	0.05	0.00	−0.26	0.04	0.110	−0.162	0.58	0.01	0.18	−0.46	1.37	0.91
311	102 – 116	0.6 – 0.8	0.4 – 0.7	0.1406	±1.29	±1.29	0.00	0.08	0.00	−0.40	0.16	0.19	−0.34	0.06	0.00	−0.40	0.10	0.252	−0.180	0.64	0.00	0.14	−0.65	1.35	0.91
312	102 – 116	0.6 – 0.8	0.7 – 1.0	0.1153	±1.26	±1.18	0.00	−0.04	0.00	−0.33	0.27	0.32	−0.48	0.01	0.00	−0.32	0.04	0.152	−0.324	0.67	0.04	0.12	−0.41	1.28	0.91
313	102 – 116	0.8 – 1.0	-1.0 – -0.7	0.0880	±1.39	±1.57	0.00	0.13	0.00	−0.40	0.42	0.30	−0.52	0.05	0.00	−0.39	0.03	0.244	−0.344	0.87	0.04	0.31	0.63	1.35	0.90
314	102 – 116	0.8 – 1.0	-0.7 – -0.4	0.1200	±1.25	±1.30	0.00	0.19	0.00	−0.34	0.24	0.23	−0.39	0.04	0.00	−0.33	0.07	0.071	−0.171	0.66	0.01	0.20	0.79	1.43	0.91
315	102 – 116	0.8 – 1.0	-0.4 – 0.0	0.1088	±1.18	±1.22	0.00	0.09	0.00	−0.27	0.23	0.20	−0.35	0.06	0.00	−0.27	0.04	0.066	−0.134	0.59	0.01	0.16	0.82	1.48	0.90
316	102 – 116	0.8 – 1.0	0.0 – 0.4	0.1188	±1.10	±1.03	0.00	0.04	0.00	−0.26	0.17	0.18	−0.44	0.07	0.00	−0.26	0.04	0.230	−0.128	0.54	0.01	0.24	0.43	1.43	0.91
317	102 – 116	0.8 – 1.0	0.4 – 0.7	0.1469	±1.09	±1.10	0.00	0.05	0.00	−0.35	0.16	0.30	−0.34	0.04	0.00	−0.34	0.06	0.168	−0.168	0.59	0.01	0.14	0.53	1.34	0.91
318	102 – 116	0.8 – 1.0	0.7 – 1.0	0.1101	±1.30	±1.72	0.00	−0.02	0.00	−0.41	0.35	0.28	−0.52	0.05	0.00	−0.40	0.03	0.258	−0.265	0.73	0.03	0.37	−1.13	1.28	0.91
319	102 – 116	1.0 – 1.2	-1.0 – -0.7	0.0666	±1.47	±1.97	0.00	0.17	0.00	−0.45	1.02	0.32	−0.56	0.07	0.00	−0.44	0.05	0.116	−0.330	0.96	0.03	0.41	0.53	1.38	0.89
320	102 – 116	1.0 – 1.2	-0.7 – -0.4	0.1144	±1.17	±1.38	0.00	0.19	0.00	−0.31	0.34	0.31	−0.49	0.04	0.00	−0.31	0.05	0.069	−0.191	0.66	0.01	0.25	0.82	1.48	0.91
321	102 – 116	1.0 – 1.2	-0.4 – 0.0	0.1061	±1.16	±0.98	0.00	0.17	0.00	−0.29	0.26	0.22	−0.47	0.11	0.00	−0.28	0.03	0.171	−0.153	0.58	0.01	0.13	−0.06	1.54	0.91
322	102 – 116	1.0 – 1.2	0.0 – 0.4	0.1177	±1.08	±1.10	0.00	0.05	0.00	−0.27	0.40	0.19	−0.39	0.10	0.00	−0.27	0.03	0.154	−0.126	0.55	0.01	0.26	−0.49	1.50	0.91
323	102 – 116	1.0 – 1.2	0.4 – 0.7	0.1492	±1.05	±1.05	0.00	0.04	0.00	−0.31	0.28	0.27	−0.41	0.01	0.00	−0.31	0.04	0.057	−0.151	0.60	0.01	0.18	0.42	1.36	0.91
324	102 – 116	1.0 – 1.2	0.7 – 1.0	0.0927	±1.32	±2.30	0.00	0.02	0.00	−0.46	0.67	0.32	−0.67	0.10	0.00	−0.46	0.04	0.077	−0.204	0.83	0.02	0.25	1.67	1.30	0.90
325	102 – 116	1.2 – 1.4	-1.0 – -0.7	0.0422	±1.55	±2.51	0.00	0.15	0.00	−0.44	1.19	0.48	−1.16	0.01	0.00	−0.43	0.02	0.088	−0.214	1.28	0.02	0.52	0.65	1.48	0.91
326	102 – 116	1.2 – 1.4	-0.7 – -0.4	0.1083	±1.15	±2.18	0.00	0.19	0.00	−0.33	0.44	0.42	−0.47	0.06	0.00	−0.32	0.01	0.062	−0.190	0.74	0.01	0.35	1.75	1.53	0.90
327	102 – 116	1.2 – 1.4	-0.4 – 0.0	0.1023	±1.11	±1.54	0.00	0.17	0.00	−0.30	0.43	0.33	−0.55	0.07	0.00	−0.29	0.03	0.065	−0.122	0.60	0.01	0.20	1.06	1.60	0.90
328	102 – 116	1.2 – 1.4	0.0 – 0.4	0.1191	±1.02	±1.19	0.00	0.06	0.00	−0.30	0.23	0.25	−0.44	0.07	0.00	−0.29	0.03	0.043	−0.107	0.54	0.01	0.23	0.51	1.52	0.91
329	102 – 116	1.2 – 1.4	0.4 – 0.7	0.1503	±0.97	±1.18	0.00	0.04	0.00	−0.32	0.37	0.46	−0.37	0.06	0.00	−0.32	0.01	0.147	−0.127	0.62	−0.00	0.37	0.27	1.39	0.91
330	102 – 116	1.2 – 1.4	0.7 – 1.0	0.0598	±1.44	±2.89	0.00	0.00	0.00	−0.45	1.08	0.61	−1.03	0.05	0.00	−0.45	0.02	0.091	−0.171	1.06	0.02	0.47	−1.95	1.32	0.91
331	102 – 116	1.4 – 1.6	-1.0 – -0.7	0.0138	±2.10	±5.67	0.00	0.15	0.00	−0.44	1.63	0.96	−1.60	−0.33	0.00	−0.43	0.05	0.115	−0.198	2.37	0.02	0.69	−4.09	1.67	0.90
332	102 – 116	1.4 – 1.6	-0.7 – -0.4	0.0955	±1.09	±2.14	0.00	0.16	0.00	−0.36	0.85	0.40	−0.54	0.15	0.00	−0.36	0.01	0.055	−0.138	0.83	0.01	0.56	1.22	1.58	0.90
333	102 – 116	1.4 – 1.6	-0.4 – 0.0	0.0977	±1.10	±1.19	0.00	0.13	0.00	−0.33	0.47	0.41	−0.37	0.10	0.00	−0.32	0.01	0.055	−0.125	0.64	0.01	0.19	0.01	1.63	0.91
334	102 – 116	1.4 – 1.6	0.0 – 0.4	0.1170	±0.98	±1.54	0.00	0.08	0.00	−0.33	0.51	0.37	−0.44	0.09	0.00	−0.33	0.01	0.054	−0.098	0.59	0.01	0.34	0.99	1.53	0.91
335	102 – 116	1.4 – 1.6	0.4 – 0.7	0.1408	±0.94	±1.95	0.00	0.02	0.00	−0.36	0.57	0.48	−0.58	0.11	0.00	−0.36	0.01	0.213	−0.105	0.67	−0.00	0.38	−1.22	1.40	0.91
336	102 – 116	1.4 – 1.6	0.7 – 1.0	0.0231	±1.71	±4.24	0.00	−0.01	0.00	−0.44	1.84	0.73	−1.44	−0.22	0.00	−0.43	0.04	0.252	−0.118	1.75	0.01	0.93	2.56	1.46	0.91

TABLE 28: Measured cross-section values unfolded to the Born truth-level in the 7$^{\text{th}}$ 48 bins of the measurement. The luminosity uncertainty of 1.9% is not included.

$\mathcal{B}$	$m_{\mu\mu}$ [GeV]	$\lvert y_{\mu\mu}\rvert$	$\cos\theta^{\star}$	Triple Differential Cross-section Values																						
				$d^3\sigma^{\text{Born}}_{\text{meas.}}$ [pb/GeV]	$\Delta^{\text{Stat.}}_{\text{meas.}}$ [%]	$\Delta^{\text{Syst.}}_{\text{meas.}}$ [%]	Δ^{Trigger} [%]		$\Delta^{\text{Reconst.}}$ [%]		Δ^{ID} [%]	Δ^{Sagitta} [%]	Δ^{Scale} [%]	$\Delta^{Z-\text{pT}}$ [%]	$\Delta^{\text{Isolation}}$ [%]		Δ^{QCD} [%]	$\Delta^{\text{MC Bkg.}}$ [%]		$\Delta^{\text{MC Signal}}$ [%]		Δ^{PDF} [%]	$\Delta^{\text{Unfd.}}$ [%]	$C_{\text{Dres.}}$	C_{Bare}
							uncor.	corr.	uncor.	corr.					uncor.	corr.		uncor.	corr.	uncor.	corr.				
337	102 – 116	1.6 – 1.8	-1.0 – -0.7	0.0024	±3.91	±18.71	0.00	0.14	0.00	−0.48	2.55	2.19	−1.58	−0.20	0.00	−0.46	0.02	0.403	−0.224	5.80	0.02	1.46	−17.22	1.88	0.93
338	102 – 116	1.6 – 1.8	-0.7 – -0.4	0.0630	±1.10	±3.43	0.00	0.14	0.00	−0.41	1.51	0.67	−0.98	0.10	0.00	−0.41	0.00	0.052	−0.120	1.08	0.01	0.64	−2.05	1.65	0.90
339	102 – 116	1.6 – 1.8	-0.4 – 0.0	0.0926	±0.98	±2.50	0.00	0.10	0.00	−0.37	0.68	0.63	−0.58	0.10	0.00	−0.36	0.01	0.045	−0.105	0.70	0.01	0.22	−2.05	1.60	0.91
340	102 – 116	1.6 – 1.8	0.0 – 0.4	0.1178	±0.88	±1.78	0.00	0.11	0.00	−0.37	0.67	0.41	−0.45	0.14	0.00	−0.36	0.01	0.047	−0.087	0.64	0.01	0.41	1.13	1.52	0.91
341	102 – 116	1.6 – 1.8	0.4 – 0.7	0.1031	±0.95	±2.60	0.00	0.02	0.00	−0.41	1.57	0.66	−0.95	0.08	0.00	−0.41	0.00	0.040	−0.085	0.80	0.01	0.52	0.84	1.45	0.91
342	102 – 116	1.6 – 1.8	0.7 – 1.0	0.0043	±3.33	±6.33	0.00	−0.01	0.00	−0.47	2.22	1.53	−1.56	−0.51	0.00	−0.46	0.02	0.729	−0.152	4.23	0.02	0.90	−3.01	1.60	0.90
343	102 – 116	1.8 – 2.0	-1.0 – -0.7	0.0004	±6.93	±16.11	0.01	0.14	0.01	−0.56	3.86	2.53	−0.84	0.22	0.00	−0.54	0.00	0.694	−0.179	15.24	0.02	1.77	−0.51	2.46	0.77
344	102 – 116	1.8 – 2.0	-0.7 – -0.4	0.0213	±1.45	±4.54	0.00	0.11	0.00	−0.46	2.35	1.16	−1.54	0.01	0.00	−0.45	0.00	0.062	−0.091	1.99	0.02	0.82	−2.16	1.80	0.90
345	102 – 116	1.8 – 2.0	-0.4 – 0.0	0.0879	±0.90	±2.04	0.00	0.09	0.00	−0.43	1.30	0.61	−0.58	0.14	0.00	−0.42	0.01	0.033	−0.078	0.74	0.01	0.31	−0.12	1.62	0.90
346	102 – 116	1.8 – 2.0	0.0 – 0.4	0.1175	±0.80	±3.20	0.00	0.11	0.00	−0.43	1.20	0.69	−0.57	0.18	0.00	−0.42	0.01	0.030	−0.071	0.68	0.01	0.36	2.53	1.50	0.91
347	102 – 116	1.8 – 2.0	0.4 – 0.7	0.0365	±1.22	±5.49	0.00	0.06	0.00	−0.46	1.76	1.10	−1.40	−0.01	0.00	−0.45	0.00	0.102	−0.064	1.49	0.01	0.98	−4.28	1.50	0.91
348	102 – 116	1.8 – 2.0	0.7 – 1.0	0.0008	±6.56	±16.95	0.00	0.01	0.00	−0.55	2.25	3.52	−2.11	−0.32	0.00	−0.54	0.01	0.346	−0.129	10.61	0.02	0.52	12.32	1.69	0.93
349	102 – 116	2.0 – 2.2	-1.0 – -0.7	–	–	–	–	–	–	–	–	–	–	–	–	–	–	–	–	–	–	–	–	–	–
350	102 – 116	2.0 – 2.2	-0.7 – -0.4	0.0013	±3.11	±12.56	0.00	0.10	0.00	−0.52	1.47	2.12	−1.59	−0.65	0.00	−0.52	0.01	0.152	−0.072	8.25	0.02	1.32	−8.75	2.34	0.92
351	102 – 116	2.0 – 2.2	-0.4 – 0.0	0.0627	±0.87	±3.22	0.00	0.09	0.00	−0.50	2.09	1.09	−1.06	0.23	0.00	−0.50	0.00	0.118	−0.065	0.98	0.01	0.44	−0.76	1.66	0.91
352	102 – 116	2.0 – 2.2	0.0 – 0.4	0.0798	±0.82	±2.98	0.00	0.09	0.00	−0.50	1.89	1.01	−0.92	0.24	0.00	−0.50	0.00	0.046	−0.054	0.86	0.01	0.66	0.33	1.55	0.91
353	102 – 116	2.0 – 2.2	0.4 – 0.7	0.0023	±3.18	±8.87	0.00	0.07	0.00	−0.53	2.43	1.33	−2.02	0.03	0.00	−0.52	0.01	0.144	−0.059	6.36	0.02	2.59	4.38	1.98	0.92
354	102 – 116	2.0 – 2.2	0.7 – 1.0	–	–	–	–	–	–	–	–	–	–	–	–	–	–	–	–	–	–	–	–	–	–
355	102 – 116	2.2 – 2.4	-1.0 – -0.7	–	–	–	–	–	–	–	–	–	–	–	–	–	–	–	–	–	–	–	–	–	–
356	102 – 116	2.2 – 2.4	-0.7 – -0.4	–	–	–	–	–	–	–	–	–	–	–	–	–	–	–	–	–	–	–	–	–	–
357	102 – 116	2.2 – 2.4	-0.4 – 0.0	0.0223	±1.21	±4.66	0.00	0.07	0.00	−0.60	2.31	0.96	−1.81	0.23	0.00	−0.60	0.01	0.034	−0.044	1.65	0.01	0.55	−2.34	1.64	0.90
358	102 – 116	2.2 – 2.4	0.0 – 0.4	0.0241	±1.15	±6.39	0.00	0.06	0.00	−0.60	1.72	1.30	−1.50	0.34	0.00	−0.60	0.01	0.040	−0.043	1.52	0.01	0.65	−5.24	1.55	0.91
359	102 – 116	2.2 – 2.4	0.4 – 0.7	–	–	–	–	–	–	–	–	–	–	–	–	–	–	–	–	–	–	–	–	–	–
360	102 – 116	2.2 – 2.4	0.7 – 1.0	–	–	–	–	–	–	–	–	–	–	–	–	–	–	–	–	–	–	–	–	–	–
361	116 – 150	0.0 – 0.2	-1.0 – -0.7	0.0237	±2.22	±1.99	0.00	0.07	0.00	−0.29	0.13	0.35	−0.12	−0.12	0.00	−0.27	0.16	0.529	−1.247	0.60	0.16	0.30	−1.10	1.15	0.93
362	116 – 150	0.0 – 0.2	-0.7 – -0.4	0.0250	±2.08	±1.19	0.00	0.02	0.00	−0.28	0.24	0.24	−0.15	−0.11	0.00	−0.26	0.31	0.243	−0.683	0.56	0.03	0.27	−0.31	1.17	0.93
363	116 – 150	0.0 – 0.2	-0.4 – 0.0	0.0222	±2.14	±1.21	0.00	0.07	0.00	−0.48	0.11	0.20	−0.23	−0.13	0.00	−0.44	0.13	0.247	−0.532	0.57	0.01	0.14	0.46	1.16	0.93
364	116 – 150	0.0 – 0.2	0.0 – 0.4	0.0218	±2.18	±1.27	0.00	0.07	0.00	−0.48	0.07	0.21	−0.17	−0.15	0.00	−0.45	0.14	0.221	−0.549	0.56	0.01	0.07	−0.60	1.16	0.93
365	116 – 150	0.0 – 0.2	0.4 – 0.7	0.0265	±2.02	±1.12	0.00	0.02	0.00	−0.28	0.23	0.20	−0.14	−0.13	0.00	−0.26	0.30	0.225	−0.622	0.52	0.03	0.28	−0.31	1.16	0.93
366	116 – 150	0.0 – 0.2	0.7 – 1.0	0.0256	±2.08	±1.69	0.00	0.02	0.00	−0.28	0.16	0.25	−0.19	−0.13	0.00	−0.27	0.15	0.590	−1.140	0.53	0.15	0.16	0.74	1.15	0.93
367	116 – 150	0.2 – 0.4	-1.0 – -0.7	0.0226	±2.13	±1.77	0.00	0.13	0.00	−0.30	0.09	0.28	−0.17	−0.16	0.00	−0.28	0.21	0.804	−1.309	0.57	0.15	0.17	−0.05	1.16	0.94
368	116 – 150	0.2 – 0.4	-0.7 – -0.4	0.0244	±2.22	±1.56	0.00	0.06	0.00	−0.33	0.16	0.22	−0.25	−0.14	0.00	−0.30	0.37	0.716	−0.727	0.56	0.03	0.15	−0.74	1.19	0.93
369	116 – 150	0.2 – 0.4	-0.4 – 0.0	0.0214	±2.24	±1.19	0.00	0.05	0.00	−0.42	0.26	0.20	−0.22	−0.07	0.00	−0.39	0.15	0.229	−0.595	0.55	0.01	0.19	−0.37	1.17	0.93
370	116 – 150	0.2 – 0.4	0.0 – 0.4	0.0218	±2.20	±1.10	0.00	0.06	0.00	−0.44	0.06	0.18	−0.13	−0.07	0.00	−0.41	0.15	0.221	−0.537	0.53	0.01	0.26	−0.10	1.17	0.93
371	116 – 150	0.2 – 0.4	0.4 – 0.7	0.0274	±2.05	±1.10	0.00	0.05	0.00	−0.34	0.12	0.22	−0.11	−0.13	0.00	−0.32	0.33	0.223	−0.623	0.52	0.03	0.21	−0.08	1.16	0.93
372	116 – 150	0.2 – 0.4	0.7 – 1.0	0.0251	±2.09	±2.01	0.00	0.01	0.00	−0.29	0.10	0.34	−0.27	−0.15	0.00	−0.27	0.19	0.936	−1.182	0.52	0.14	0.30	−0.97	1.14	0.93
373	116 – 150	0.4 – 0.6	-1.0 – -0.7	0.0216	±2.16	±1.72	0.00	0.15	0.00	−0.32	0.18	0.29	−0.19	−0.15	0.00	−0.29	0.02	0.371	−1.377	0.60	0.14	0.21	−0.27	1.17	0.93
374	116 – 150	0.4 – 0.6	-0.7 – -0.4	0.0240	±2.25	±1.30	0.00	0.13	0.00	−0.41	0.20	0.40	−0.17	−0.13	0.00	−0.38	0.34	0.274	−0.703	0.61	0.03	0.08	0.20	1.22	0.93
375	116 – 150	0.4 – 0.6	-0.4 – 0.0	0.0204	±2.12	±1.57	0.00	0.04	0.00	−0.34	0.14	0.22	−0.21	−0.15	0.00	−0.31	0.16	0.743	−0.527	0.55	0.01	0.20	−0.96	1.20	0.94
376	116 – 150	0.4 – 0.6	0.0 – 0.4	0.0221	±1.90	±1.31	0.00	0.03	0.00	−0.35	0.08	0.18	−0.22	−0.13	0.00	−0.33	0.14	0.232	−0.517	0.49	0.01	0.21	−0.87	1.20	0.94
377	116 – 150	0.4 – 0.6	0.4 – 0.7	0.0272	±2.14	±1.37	0.00	0.09	0.00	−0.42	0.11	0.24	−0.16	−0.10	0.00	−0.39	0.30	0.222	−0.600	0.60	0.03	0.13	−0.68	1.18	0.93
378	116 – 150	0.4 – 0.6	0.7 – 1.0	0.0267	±1.94	±1.44	0.00	0.00	0.00	−0.31	0.13	0.35	−0.24	−0.18	0.00	−0.29	0.02	0.390	−1.069	0.54	0.12	0.19	0.05	1.13	0.93
379	116 – 150	0.6 – 0.8	-1.0 – -0.7	0.0203	±2.31	±1.68	0.00	0.17	0.00	−0.37	0.21	0.32	−0.20	−0.26	0.00	−0.34	0.37	0.312	−1.192	0.68	0.12	0.12	0.35	1.17	0.93
380	116 – 150	0.6 – 0.8	-0.7 – -0.4	0.0234	±2.27	±1.32	0.00	0.19	0.00	−0.43	0.18	0.30	−0.23	−0.08	0.00	−0.40	0.30	0.270	−0.684	0.63	0.03	0.13	0.36	1.25	0.93
381	116 – 150	0.6 – 0.8	-0.4 – 0.0	0.0204	±2.07	±0.96	0.00	0.03	0.00	−0.29	0.15	0.26	−0.23	−0.12	0.00	−0.27	0.15	0.197	−0.492	0.54	0.01	0.09	0.06	1.25	0.93
382	116 – 150	0.6 – 0.8	0.0 – 0.4	0.0238	±1.90	±1.05	0.00	0.03	0.00	−0.29	0.15	0.16	−0.22	−0.13	0.00	−0.27	0.13	0.181	−0.442	0.50	0.01	0.08	0.58	1.21	0.93
383	116 – 150	0.6 – 0.8	0.4 – 0.7	0.0289	±2.03	±1.14	0.00	0.08	0.00	−0.44	0.14	0.26	−0.16	−0.08	0.00	−0.41	0.24	0.268	−0.508	0.58	0.02	0.07	0.27	1.20	0.94
384	116 – 150	0.6 – 0.8	0.7 – 1.0	0.0265	±1.90	±1.38	0.00	0.02	0.00	−0.36	0.13	0.29	−0.20	−0.20	0.00	−0.34	0.29	0.238	−0.963	0.54	0.09	0.20	0.23	1.13	0.93

TABLE 29: Measured cross-section values unfolded to the Born truth-level in the 8$^{\text{th}}$ 48 bins of the measurement. The luminosity uncertainty of 1.9% is not included.

$\mathcal{B}$	$m_{\mu\mu}$ [GeV]	$\lvert y_{\mu\mu}\rvert$	$\cos\theta^{\star}$	Triple Differential Cross-section Values																							
				$d^3\sigma^{\text{Born}}_{\text{meas.}}$ [pb/GeV]	$\Delta^{\text{Stat.}}_{\text{meas.}}$ [%]	$\Delta^{\text{Syst.}}_{\text{meas.}}$ [%]	Δ^{Trigger} [%]		$\Delta^{\text{Reconst.}}$ [%]		Δ^{ID} [%]	Δ^{Sagitta} [%]	Δ^{Scale} [%]	$\Delta^{Z-\text{pT}}$ [%]	$\Delta^{\text{Isolation}}$ [%]		Δ^{QCD} [%]	$\Delta^{\text{MC Bkg.}}$ [%]		$\Delta^{\text{MC Signal}}$ [%]		Δ^{PDF} [%]	$\Delta^{\text{Unfd.}}$ [%]	$C_{\text{Dres.}}$	C_{Bare}
							uncor.	corr.	uncor.	corr.					uncor.	corr.		uncor.	corr.	uncor.	corr.				
385	116 – 150	0.8 – 1.0	-1.0 – -0.7	0.0163	±2.53	±2.05	0.00	0.20	0.00	−0.44	0.20	0.46	−0.26	−0.18	0.00	−0.40	0.12	0.767	−1.244	0.84	0.10	0.23	−0.56	1.20	0.92
386	116 – 150	0.8 – 1.0	-0.7 – -0.4	0.0220	±2.22	±1.25	0.00	0.20	0.00	−0.37	0.14	0.30	−0.24	−0.12	0.00	−0.35	0.14	0.235	−0.635	0.63	0.03	0.25	−0.38	1.28	0.92
387	116 – 150	0.8 – 1.0	-0.4 – 0.0	0.0203	±1.97	±1.10	0.00	0.10	0.00	−0.30	0.09	0.40	−0.18	−0.13	0.00	−0.28	0.14	0.309	−0.449	0.58	0.01	0.19	−0.29	1.30	0.93
388	116 – 150	0.8 – 1.0	0.0 – 0.4	0.0236	±1.80	±0.87	0.00	0.05	0.00	−0.29	0.12	0.20	−0.19	−0.13	0.00	−0.27	0.12	0.179	−0.395	0.49	0.01	0.15	−0.12	1.26	0.93
389	116 – 150	0.8 – 1.0	0.4 – 0.7	0.0305	±1.83	±1.04	0.00	0.06	0.00	−0.38	0.10	0.24	−0.15	−0.13	0.00	−0.36	0.10	0.173	−0.470	0.49	0.02	0.24	0.36	1.20	0.93
390	116 – 150	0.8 – 1.0	0.7 – 1.0	0.0233	±2.03	±1.42	0.00	0.03	0.00	−0.44	0.12	0.33	−0.23	−0.16	0.00	−0.41	0.09	0.368	−0.802	0.61	0.07	0.29	−0.25	1.14	0.94
391	116 – 150	1.0 – 1.2	-1.0 – -0.7	0.0121	±2.82	±2.49	0.00	0.19	0.00	−0.50	0.27	0.52	−0.09	−0.19	0.00	−0.46	0.02	0.650	−1.093	0.97	0.08	0.38	−1.52	1.23	0.93
392	116 – 150	1.0 – 1.2	-0.7 – -0.4	0.0202	±2.19	±1.38	0.00	0.20	0.00	−0.35	0.24	0.41	−0.29	−0.17	0.00	−0.33	0.07	0.598	−0.629	0.66	0.03	0.14	0.02	1.32	0.93
393	116 – 150	1.0 – 1.2	-0.4 – 0.0	0.0201	±1.91	±1.05	0.00	0.17	0.00	−0.31	0.13	0.31	−0.25	−0.16	0.00	−0.30	0.11	0.177	−0.438	0.55	0.01	0.28	0.27	1.36	0.93
394	116 – 150	1.0 – 1.2	0.0 – 0.4	0.0237	±1.74	±0.90	0.00	0.06	0.00	−0.30	0.11	0.22	−0.19	−0.14	0.00	−0.29	0.10	0.150	−0.358	0.50	0.01	0.09	0.23	1.32	0.94
395	116 – 150	1.0 – 1.2	0.4 – 0.7	0.0306	±1.73	±1.15	0.00	0.04	0.00	−0.34	0.27	0.36	−0.28	−0.17	0.00	−0.33	0.05	0.168	−0.471	0.50	0.01	0.26	−0.47	1.22	0.93
396	116 – 150	1.0 – 1.2	0.7 – 1.0	0.0194	±2.22	±2.45	0.00	0.03	0.00	−0.50	0.41	0.53	−0.28	−0.16	0.00	−0.47	0.02	0.242	−0.653	0.74	0.05	0.19	−1.94	1.14	0.93
397	116 – 150	1.2 – 1.4	-1.0 – -0.7	0.0080	±3.35	±6.03	0.00	0.17	0.00	−0.50	0.54	0.67	−0.54	−0.28	0.00	−0.45	0.10	0.422	−0.917	1.23	0.05	0.38	5.65	1.34	0.93
398	116 – 150	1.2 – 1.4	-0.7 – -0.4	0.0185	±2.16	±1.74	0.00	0.20	0.00	−0.37	0.23	0.38	−0.19	−0.23	0.00	−0.34	0.02	0.237	−0.634	0.73	0.02	0.19	−1.15	1.39	0.93
399	116 – 150	1.2 – 1.4	-0.4 – 0.0	0.0187	±1.96	±1.54	0.00	0.17	0.00	−0.33	0.12	0.40	−0.17	−0.17	0.00	−0.31	0.01	0.165	−0.409	0.57	0.01	0.28	−1.11	1.40	0.93
400	116 – 150	1.2 – 1.4	0.0 – 0.4	0.0239	±1.77	±0.88	0.00	0.06	0.00	−0.33	0.15	0.23	−0.25	−0.12	0.00	−0.31	0.01	0.141	−0.332	0.52	0.01	0.09	−0.09	1.34	0.93
401	116 – 150	1.2 – 1.4	0.4 – 0.7	0.0315	±1.60	±1.17	0.00	0.04	0.00	−0.35	0.12	0.28	−0.16	−0.18	0.00	−0.34	0.01	0.139	−0.355	0.54	0.01	0.16	0.67	1.23	0.94
402	116 – 150	1.2 – 1.4	0.7 – 1.0	0.0133	±2.49	±1.63	0.00	0.01	0.00	−0.49	0.24	0.51	−0.32	−0.29	0.00	−0.46	0.06	0.289	−0.536	0.86	0.03	0.28	0.58	1.18	0.93
403	116 – 150	1.4 – 1.6	-1.0 – -0.7	0.0023	±5.35	±8.31	0.00	0.17	0.00	−0.53	0.57	1.24	−1.29	−0.57	0.00	−0.47	0.03	0.705	−1.007	2.31	0.06	0.94	−7.53	1.60	0.93
404	116 – 150	1.4 – 1.6	-0.7 – -0.4	0.0164	±2.15	±1.46	0.00	0.17	0.00	−0.40	0.31	0.51	−0.30	−0.18	0.00	−0.38	0.04	0.223	−0.538	0.78	0.02	0.26	−0.23	1.38	0.93
405	116 – 150	1.4 – 1.6	-0.4 – 0.0	0.0178	±1.93	±1.18	0.00	0.13	0.00	−0.36	0.27	0.34	−0.33	−0.24	0.00	−0.34	0.03	0.323	−0.401	0.62	−0.01	0.24	−0.22	1.44	0.93
406	116 – 150	1.4 – 1.6	0.0 – 0.4	0.0234	±1.62	±1.36	0.00	0.08	0.00	−0.37	0.19	0.33	−0.24	−0.18	0.00	−0.35	0.02	0.546	−0.281	0.51	0.01	0.28	−0.80	1.36	0.93
407	116 – 150	1.4 – 1.6	0.4 – 0.7	0.0299	±1.59	±1.31	0.00	0.02	0.00	−0.39	0.26	0.56	−0.26	−0.17	0.00	−0.38	0.02	0.137	−0.291	0.55	0.01	0.26	−0.67	1.22	0.93
408	116 – 150	1.4 – 1.6	0.7 – 1.0	0.0048	±3.75	±4.06	0.00	−0.01	0.00	−0.51	0.22	1.06	−0.73	−0.55	0.00	−0.47	0.01	1.383	−0.467	1.53	0.03	0.55	−2.93	1.34	0.94
409	116 – 150	1.6 – 1.8	-1.0 – -0.7	0.0003	±11.18	±31.29	0.01	0.19	0.01	−0.64	1.59	6.39	−1.83	−1.10	0.00	−0.52	0.20	1.957	−1.443	6.38	0.06	0.80	−29.72	2.13	0.92
410	116 – 150	1.6 – 1.8	-0.7 – -0.4	0.0109	±2.56	±3.02	0.00	0.14	0.00	−0.45	1.05	0.64	−0.50	−0.28	0.00	−0.43	0.03	0.269	−0.518	1.00	0.02	0.55	2.19	1.51	0.92
411	116 – 150	1.6 – 1.8	-0.4 – 0.0	0.0175	±1.87	±1.25	0.00	0.10	0.00	−0.40	0.47	0.40	−0.36	−0.16	0.00	−0.39	0.01	0.218	−0.349	0.67	0.01	0.20	0.21	1.46	0.92
412	116 – 150	1.6 – 1.8	0.0 – 0.4	0.0235	±1.68	±1.52	0.00	0.11	0.00	−0.40	0.21	0.44	−0.19	−0.21	0.00	−0.39	0.01	0.457	−0.285	0.53	−0.02	0.14	−0.99	1.35	0.93
413	116 – 150	1.6 – 1.8	0.4 – 0.7	0.0231	±1.83	±2.55	0.00	0.03	0.00	−0.44	0.75	0.37	−0.49	−0.22	0.00	−0.43	0.02	0.125	−0.228	0.69	0.01	0.38	2.05	1.26	0.94
414	116 – 150	1.6 – 1.8	0.7 – 1.0	0.0008	±7.69	±21.33	0.01	−0.02	0.03	−0.59	2.06	2.14	−0.84	−0.82	0.00	−0.50	0.11	5.806	−0.632	3.98	0.03	0.71	−19.84	1.47	0.93
415	116 – 150	1.8 – 2.0	-1.0 – -0.7	–	–	–	–	–	–	–	–	–	–	–	–	–	–	–	–	–	–	–	–	–	–	–
416	116 – 150	1.8 – 2.0	-0.7 – -0.4	0.0035	±3.74	±3.55	0.00	0.12	0.00	−0.50	1.30	1.06	−0.78	−0.37	0.00	−0.48	0.05	0.301	−0.352	1.94	0.02	0.96	−1.32	1.68	0.90
417	116 – 150	1.8 – 2.0	-0.4 – 0.0	0.0164	±1.87	±2.04	0.00	0.09	0.00	−0.47	0.32	0.39	−0.31	−0.26	0.00	−0.45	0.02	0.148	−0.282	0.71	0.01	0.21	1.61	1.45	0.93
418	116 – 150	1.8 – 2.0	0.0 – 0.4	0.0238	±1.57	±1.21	0.00	0.11	0.00	−0.47	0.49	0.36	−0.26	−0.24	0.00	−0.46	0.01	0.147	−0.216	0.57	0.00	0.27	0.13	1.34	0.93
419	116 – 150	1.8 – 2.0	0.4 – 0.7	0.0079	±2.68	±2.49	0.00	0.06	0.00	−0.50	0.93	0.88	−0.81	−0.36	0.00	−0.48	0.02	0.734	−0.225	1.25	0.01	0.59	−0.41	1.35	0.95
420	116 – 150	1.8 – 2.0	0.7 – 1.0	–	–	–	–	–	–	–	–	–	–	–	–	–	–	–	–	–	–	–	–	–	–	–
421	116 – 150	2.0 – 2.2	-1.0 – -0.7	–	–	–	–	–	–	–	–	–	–	–	–	–	–	–	–	–	–	–	–	–	–	–
422	116 – 150	2.0 – 2.2	-0.7 – -0.4	0.0002	±7.84	±13.80	0.00	0.09	0.00	−0.60	2.28	3.77	−2.49	−2.07	0.00	−0.57	0.05	0.775	−0.306	10.36	0.03	2.47	6.77	2.78	0.84
423	116 – 150	2.0 – 2.2	-0.4 – 0.0	0.0118	±2.00	±2.31	0.00	0.09	0.00	−0.55	1.25	0.91	−0.49	−0.33	0.00	−0.54	0.02	0.131	−0.231	0.92	0.01	0.28	0.67	1.49	0.93
424	116 – 150	2.0 – 2.2	0.0 – 0.4	0.0167	±1.70	±2.25	0.00	0.09	0.00	−0.54	1.06	0.72	−0.66	−0.29	0.00	−0.53	0.02	0.128	−0.178	0.76	0.01	0.38	0.95	1.38	0.93
425	116 – 150	2.0 – 2.2	0.4 – 0.7	0.0005	±6.51	±9.71	0.00	0.07	0.00	−0.56	1.45	3.64	−1.26	−1.25	0.00	−0.55	0.04	0.407	−0.150	5.91	0.02	1.21	5.95	1.92	0.97
426	116 – 150	2.0 – 2.2	0.7 – 1.0	–	–	–	–	–	–	–	–	–	–	–	–	–	–	–	–	–	–	–	–	–	–	–
427	116 – 150	2.2 – 2.4	-1.0 – -0.7	–	–	–	–	–	–	–	–	–	–	–	–	–	–	–	–	–	–	–	–	–	–	–
428	116 – 150	2.2 – 2.4	-0.7 – -0.4	–	–	–	–	–	–	–	–	–	–	–	–	–	–	–	–	–	–	–	–	–	–	–
429	116 – 150	2.2 – 2.4	-0.4 – 0.0	0.0040	±3.01	±3.03	0.00	0.07	0.00	−0.65	1.23	0.90	−1.38	−0.44	0.00	−0.65	0.04	0.130	−0.113	1.55	0.02	0.51	0.43	1.51	0.93
430	116 – 150	2.2 – 2.4	0.0 – 0.4	0.0047	±2.79	±4.36	0.00	0.06	0.00	−0.65	1.61	2.20	−0.87	−0.44	0.00	−0.64	0.03	0.146	−0.136	1.46	0.01	0.38	−2.51	1.44	0.94
431	116 – 150	2.2 – 2.4	0.4 – 0.7	–	–	–	–	–	–	–	–	–	–	–	–	–	–	–	–	–	–	–	–	–	–	–
432	116 – 150	2.2 – 2.4	0.7 – 1.0	–	–	–	–	–	–	–	–	–	–	–	–	–	–	–	–	–	–	–	–	–	–	–

TABLE 30: Measured cross-section values unfolded to the Born truth-level in the 9$^{\text{th}}$ 48 bins of the measurement. The luminosity uncertainty of 1.9% is not included.

$\mathcal{B}$	$m_{\mu\mu}$ [GeV]	$\lvert y_{\mu\mu}\rvert$	$\cos\theta^{\star}$	Triple Differential Cross-section Values																							
				$d^3\sigma^{\text{Born}}_{\text{meas.}}$ [pb/GeV]	$\Delta^{\text{Stat.}}_{\text{meas.}}$ [%]	$\Delta^{\text{Syst.}}_{\text{meas.}}$ [%]	Δ^{Trigger} [%]		$\Delta^{\text{Reconst.}}$ [%]		Δ^{ID} [%]	Δ^{Sagitta} [%]	Δ^{Scale} [%]	$\Delta^{Z-\text{pT}}$ [%]	$\Delta^{\text{Isolation}}$ [%]		Δ^{QCD} [%]	$\Delta^{\text{MC Bkg.}}$ [%]		$\Delta^{\text{MC Signal}}$ [%]		Δ^{PDF} [%]	$\Delta^{\text{Unfd.}}$ [%]	$C_{\text{Dres.}}$	C_{Bare}
							uncor.	corr.	uncor.	corr.					uncor.	corr.		uncor.	corr.	uncor.	corr.				
433	150 – 200	0.0 – 0.2	-1.0 – -0.7	0.0061	±3.84	±3.05	0.00	0.12	0.00	−0.37	0.16	0.48	−0.09	0.14	0.00	−0.31	0.57	0.839	−2.703	0.53	0.27	0.25	−0.12	0.99	0.94
434	150 – 200	0.0 – 0.2	-0.7 – -0.4	0.0053	±4.01	±2.18	0.00	0.03	0.00	−0.34	0.21	0.54	−0.12	0.10	0.00	−0.28	0.48	1.038	−1.487	0.51	0.03	0.11	−0.62	0.99	0.94
435	150 – 200	0.0 – 0.2	-0.4 – 0.0	0.0047	±4.12	±1.62	0.00	0.07	0.00	−0.54	0.07	0.33	−0.10	0.02	0.00	−0.46	0.03	0.616	−1.084	0.57	0.02	0.17	−0.25	0.99	0.94
436	150 – 200	0.0 – 0.2	0.0 – 0.4	0.0047	±4.10	±1.70	0.00	0.08	0.00	−0.55	0.14	0.29	−0.15	0.11	0.00	−0.47	0.03	0.586	−1.085	0.57	0.01	0.16	0.57	0.99	0.94
437	150 – 200	0.0 – 0.2	0.4 – 0.7	0.0057	±3.89	±1.85	0.00	0.02	0.00	−0.34	0.10	0.46	−0.16	0.13	0.00	−0.29	0.45	0.634	−1.429	0.51	0.03	0.11	−0.13	0.99	0.94
438	150 – 200	0.0 – 0.2	0.7 – 1.0	0.0068	±3.74	±3.17	0.00	0.07	0.00	−0.36	0.18	0.47	−0.09	0.10	0.00	−0.30	0.51	0.814	−2.486	0.48	0.24	0.23	1.45	0.99	0.94
439	150 – 200	0.2 – 0.4	-1.0 – -0.7	0.0056	±4.10	±3.43	0.00	0.18	0.00	−0.39	0.19	0.49	−0.13	0.08	0.00	−0.32	1.16	0.989	−2.796	0.54	0.26	0.28	0.75	0.99	0.94
440	150 – 200	0.2 – 0.4	-0.7 – -0.4	0.0052	±4.20	±2.05	0.00	0.06	0.00	−0.40	0.13	0.37	−0.18	0.02	0.00	−0.33	0.46	0.629	−1.572	0.54	0.04	0.16	−0.57	1.00	0.94
441	150 – 200	0.2 – 0.4	-0.4 – 0.0	0.0048	±3.99	±1.98	0.00	0.06	0.00	−0.49	0.26	0.31	−0.11	0.10	0.00	−0.42	0.17	0.605	−1.061	0.55	0.01	0.25	1.19	0.99	0.94
442	150 – 200	0.2 – 0.4	0.0 – 0.4	0.0048	±4.02	±1.67	0.00	0.06	0.00	−0.51	0.11	0.38	−0.12	0.11	0.00	−0.44	0.17	0.598	−1.150	0.56	0.02	0.20	−0.26	1.00	0.94
443	150 – 200	0.2 – 0.4	0.4 – 0.7	0.0060	±3.61	±2.52	0.00	0.05	0.00	−0.40	1.72	0.51	−0.20	0.05	0.00	−0.34	0.39	0.530	−1.300	0.52	0.03	0.22	0.58	1.00	0.94
444	150 – 200	0.2 – 0.4	0.7 – 1.0	0.0065	±3.62	±3.70	0.00	0.06	0.00	−0.37	0.25	0.64	−0.10	0.10	0.00	−0.31	1.01	1.485	−2.465	0.50	0.22	0.26	−1.80	1.00	0.94
445	150 – 200	0.4 – 0.6	-1.0 – -0.7	0.0045	±4.42	±5.18	0.00	0.23	0.00	−0.43	0.19	0.62	−0.27	0.07	0.00	−0.34	0.57	1.726	−3.090	0.60	0.24	0.26	−3.55	1.00	0.94
446	150 – 200	0.4 – 0.6	-0.7 – -0.4	0.0056	±4.40	±3.10	0.00	0.14	0.00	−0.48	0.26	0.77	−0.11	0.11	0.00	−0.40	0.40	0.717	−1.336	0.62	0.04	0.24	2.36	1.00	0.94
447	150 – 200	0.4 – 0.6	-0.4 – 0.0	0.0043	±3.82	±1.55	0.00	0.04	0.00	−0.39	0.24	0.31	−0.21	−0.11	0.00	−0.34	0.15	0.572	−1.052	0.49	0.01	0.19	0.43	1.00	0.94
448	150 – 200	0.4 – 0.6	0.0 – 0.4	0.0049	±3.89	±2.24	0.00	0.04	0.00	−0.41	0.09	0.37	−0.17	0.07	0.00	−0.35	0.14	1.804	−0.978	0.47	0.01	0.10	0.23	1.00	0.94
449	150 – 200	0.4 – 0.6	0.4 – 0.7	0.0060	±3.93	±2.05	0.00	0.10	0.00	−0.49	0.18	0.53	−0.09	0.11	0.00	−0.42	0.37	0.597	−1.336	0.58	0.03	0.14	−0.90	1.00	0.95
450	150 – 200	0.4 – 0.6	0.7 – 1.0	0.0072	±3.35	±3.50	0.00	0.05	0.00	−0.38	0.19	0.48	−0.19	0.07	0.00	−0.32	0.37	0.579	−2.070	0.47	0.15	0.18	2.58	0.98	0.94
451	150 – 200	0.6 – 0.8	-1.0 – -0.7	0.0045	±4.32	±4.01	0.00	0.24	0.00	−0.47	0.23	0.63	−0.14	0.03	0.00	−0.37	0.21	0.879	−2.655	0.58	0.17	0.23	2.63	0.99	0.94
452	150 – 200	0.6 – 0.8	-0.7 – -0.4	0.0050	±4.19	±1.97	0.00	0.21	0.00	−0.51	0.18	0.61	−0.14	0.17	0.00	−0.43	0.22	0.624	−1.406	0.64	0.03	0.11	0.31	1.01	0.94
453	150 – 200	0.6 – 0.8	-0.4 – 0.0	0.0041	±3.90	±2.40	0.00	0.03	0.00	−0.35	0.17	0.39	−0.16	0.07	0.00	−0.30	0.13	1.668	−1.076	0.51	0.01	0.18	−1.04	1.01	0.95
454	150 – 200	0.6 – 0.8	0.0 – 0.4	0.0052	±3.53	±1.24	0.00	0.03	0.00	−0.34	0.14	0.35	−0.09	0.07	0.00	−0.30	0.10	0.450	−0.846	0.46	0.01	0.16	−0.03	1.00	0.94
455	150 – 200	0.6 – 0.8	0.4 – 0.7	0.0066	±3.57	±1.64	0.00	0.09	0.00	−0.51	0.21	0.58	−0.06	0.15	0.00	−0.44	0.18	0.520	−1.088	0.54	0.02	0.14	0.14	1.00	0.94
456	150 – 200	0.6 – 0.8	0.7 – 1.0	0.0063	±3.50	±2.43	0.00	0.04	0.00	−0.44	0.17	0.58	−0.06	0.05	0.00	−0.37	0.15	0.639	−1.912	0.55	0.12	0.22	−0.85	0.99	0.94
457	150 – 200	0.8 – 1.0	-1.0 – -0.7	0.0034	±4.96	±3.57	0.00	0.25	0.00	−0.57	0.40	1.14	−0.17	0.13	0.00	−0.44	0.13	1.056	−2.875	0.81	0.15	0.20	−0.66	0.99	0.93
458	150 – 200	0.8 – 1.0	-0.7 – -0.4	0.0049	±3.98	±2.70	0.00	0.22	0.00	−0.45	0.14	0.76	−0.27	0.05	0.00	−0.38	0.02	0.594	−1.293	0.60	0.03	0.13	1.94	0.99	0.94
459	150 – 200	0.8 – 1.0	-0.4 – 0.0	0.0043	±3.72	±1.58	0.00	0.10	0.00	−0.35	0.14	0.62	−0.12	0.12	0.00	−0.31	0.07	0.558	−0.955	0.50	0.01	0.14	0.53	1.02	0.94
460	150 – 200	0.8 – 1.0	0.0 – 0.4	0.0051	±3.39	±1.39	0.00	0.05	0.00	−0.34	0.13	0.39	−0.11	0.12	0.00	−0.30	0.06	0.470	−0.779	0.45	0.00	0.14	−0.68	1.01	0.95
461	150 – 200	0.8 – 1.0	0.4 – 0.7	0.0065	±3.47	±2.14	0.00	0.06	0.00	−0.44	0.13	0.85	−0.14	0.09	0.00	−0.39	0.02	0.485	−1.020	0.50	0.01	0.13	−1.38	1.00	0.95
462	150 – 200	0.8 – 1.0	0.7 – 1.0	0.0056	±3.66	±2.58	0.00	0.04	0.00	−0.53	0.23	0.78	−0.09	0.18	0.00	−0.44	0.08	1.269	−1.559	0.58	0.09	0.17	−0.99	0.99	0.94
463	150 – 200	1.0 – 1.2	-1.0 – -0.7	0.0024	±5.94	±3.37	0.00	0.24	0.00	−0.64	0.38	1.18	−0.01	0.19	0.00	−0.50	0.42	1.206	−2.508	0.92	0.11	0.24	0.24	1.01	0.95
464	150 – 200	1.0 – 1.2	-0.7 – -0.4	0.0040	±4.22	±2.20	0.00	0.22	0.00	−0.43	0.20	0.70	−0.12	0.05	0.00	−0.36	0.24	0.640	−1.474	0.66	0.03	0.19	−0.91	1.01	0.94
465	150 – 200	1.0 – 1.2	-0.4 – 0.0	0.0042	±3.65	±1.48	0.00	0.19	0.00	−0.38	0.20	0.52	−0.21	0.09	0.00	−0.33	0.01	0.576	−0.964	0.51	0.01	0.09	−0.09	1.02	0.94
466	150 – 200	1.0 – 1.2	0.0 – 0.4	0.0053	±3.08	±1.18	0.00	0.06	0.00	−0.35	0.17	0.44	−0.20	0.12	0.00	−0.32	0.01	0.386	−0.697	0.44	0.00	0.16	0.18	1.02	0.94
467	150 – 200	1.0 – 1.2	0.4 – 0.7	0.0067	±3.18	±1.76	0.00	0.05	0.00	−0.40	0.14	0.69	−0.17	0.05	0.00	−0.36	0.14	0.462	−0.797	0.47	0.01	0.16	−1.07	1.00	0.94
468	150 – 200	1.0 – 1.2	0.7 – 1.0	0.0048	±3.91	±2.61	0.00	0.03	0.00	−0.58	0.25	0.82	−0.24	0.19	0.00	−0.50	0.22	1.556	−1.215	0.67	0.06	0.22	0.96	0.99	0.94
469	150 – 200	1.2 – 1.4	-1.0 – -0.7	0.0013	±7.44	±7.98	0.01	0.22	0.02	−0.70	1.15	1.51	−0.54	0.11	0.00	−0.50	0.18	4.116	−2.573	1.32	0.08	0.37	−5.75	1.00	0.93
470	150 – 200	1.2 – 1.4	-0.7 – -0.4	0.0038	±4.09	±2.53	0.00	0.22	0.00	−0.45	0.16	0.69	−0.10	0.12	0.00	−0.38	0.05	0.648	−1.326	0.68	0.02	0.19	1.66	1.01	0.94
471	150 – 200	1.2 – 1.4	-0.4 – 0.0	0.0040	±3.59	±1.47	0.00	0.19	0.00	−0.39	0.12	0.51	−0.12	0.11	0.00	−0.35	0.07	0.474	−0.867	0.50	0.01	0.10	0.51	1.03	0.95
472	150 – 200	1.2 – 1.4	0.0 – 0.4	0.0053	±3.20	±1.20	0.00	0.06	0.00	−0.38	0.15	0.44	−0.09	0.08	0.00	−0.35	0.06	0.364	−0.666	0.46	0.01	0.21	−0.29	1.01	0.94
473	150 – 200	1.2 – 1.4	0.4 – 0.7	0.0072	±2.96	±1.44	0.00	0.04	0.00	−0.41	0.09	0.51	−0.15	0.10	0.00	−0.38	0.03	0.372	−0.745	0.48	0.01	0.11	0.70	1.00	0.94
474	150 – 200	1.2 – 1.4	0.7 – 1.0	0.0031	±4.52	±3.13	0.00	0.01	0.00	−0.59	0.34	0.92	−0.26	0.14	0.00	−0.51	0.08	2.370	−1.137	0.79	0.03	0.22	−0.70	1.00	0.94
475	150 – 200	1.4 – 1.6	-1.0 – -0.7	0.0004	±12.08	±6.61	0.00	0.21	0.01	−0.75	0.67	3.34	−1.04	−0.24	0.00	−0.53	0.18	2.581	−2.746	2.55	0.07	0.60	2.82	1.04	0.94
476	150 – 200	1.4 – 1.6	-0.7 – -0.4	0.0031	±4.34	±2.15	0.00	0.19	0.00	−0.48	0.23	0.93	−0.10	0.14	0.00	−0.43	0.08	0.578	−1.295	0.78	0.02	0.23	−0.71	1.02	0.94
477	150 – 200	1.4 – 1.6	-0.4 – 0.0	0.0038	±3.44	±1.53	0.00	0.14	0.00	−0.42	0.18	0.92	−0.17	0.11	0.00	−0.39	0.08	0.404	−0.742	0.54	0.00	0.20	−0.15	1.02	0.94
478	150 – 200	1.4 – 1.6	0.0 – 0.4	0.0055	±2.94	±1.72	0.00	0.09	0.00	−0.42	0.14	0.54	−0.09	0.14	0.00	−0.39	0.06	0.549	−0.549	0.45	−0.00	0.10	1.19	1.01	0.94
479	150 – 200	1.4 – 1.6	0.4 – 0.7	0.0068	±2.81	±2.34	0.00	0.02	0.00	−0.46	0.34	0.69	−0.12	0.22	0.00	−0.42	0.04	1.169	−0.568	0.50	0.01	0.11	−1.56	1.00	0.94
480	150 – 200	1.4 – 1.6	0.7 – 1.0	0.0011	±6.69	±6.18	0.00	−0.01	0.01	−0.63	0.75	1.68	−0.57	−0.37	0.00	−0.52	0.08	4.661	−1.087	1.49	0.02	0.40	−2.75	1.00	0.95

TABLE 31: Measured cross-section values unfolded to the Born truth-level in the 10^{th} 48 bins of the measurement. The luminosity uncertainty of 1.9% is not included.

				Triple Differential Cross-section Values																										
$\mathcal{B}$	$m_{\mu\mu}$ [GeV]	$\lvert y_{\mu\mu}\rvert$	$\cos\theta^*$	$d^3\sigma^{\text{Born}}_{\text{meas.}}$ [pb/GeV]	$\Delta^{\text{Stat.}}_{\text{meas.}}$ [%]	$\Delta^{\text{Syst.}}_{\text{meas.}}$ [%]	Δ^{Trigger} [%]		$\Delta^{\text{Reconst.}}$ [%]		Δ^{ID} [%]	Δ^{Sagitta} [%]	Δ^{Scale} [%]	$\Delta^{Z-\text{pT}}$ [%]	$\Delta^{\text{Isolation}}$ [%]		Δ^{QCD} [%]	$\Delta^{\text{MC Bkg.}}$ [%]		$\Delta^{\text{MC Signal}}$ [%]		Δ^{PDF} [%]	$\Delta^{\text{Unfd.}}$ [%]	$C_{\text{Dres.}}$	C_{Bare}
							uncor.	corr.	uncor.	corr.					uncor.	corr.		uncor.	corr.	uncor.	corr.				
481	150 – 200	1.6 – 1.8	-1.0 – -0.7	–	–	–	–	–	–	–	–	–	–	–	–	–	–	–	–	–	–	–	–	–	–
482	150 – 200	1.6 – 1.8	-0.7 – -0.4	0.0020	±5.18	±2.78	0.00	0.16	0.00	−0.55	0.43	1.14	−0.19	0.14	0.00	−0.49	0.06	0.764	−1.235	1.07	0.02	0.33	−1.41	1.04	0.94
483	150 – 200	1.6 – 1.8	-0.4 – 0.0	0.0037	±3.59	±2.16	0.00	0.11	0.00	−0.47	0.12	0.70	−0.11	0.11	0.00	−0.44	0.02	0.356	−0.706	0.55	0.00	0.13	1.66	1.02	0.94
484	150 – 200	1.6 – 1.8	0.0 – 0.4	0.0052	±2.94	±1.43	0.00	0.11	0.00	−0.46	0.19	0.78	−0.12	0.19	0.00	−0.44	0.01	0.247	−0.479	0.49	−0.00	0.19	−0.56	1.02	0.95
485	150 – 200	1.6 – 1.8	0.4 – 0.7	0.0054	±3.12	±3.53	0.00	0.03	0.00	−0.51	0.32	0.63	−0.18	0.19	0.00	−0.48	0.02	0.295	−0.408	0.63	0.01	0.24	3.25	1.00	0.94
486	150 – 200	1.6 – 1.8	0.7 – 1.0	–	–	–	–	–	–	–	–	–	–	–	–	–	–	–	–	–	–	–	–	–	–
487	150 – 200	1.8 – 2.0	-1.0 – -0.7	–	–	–	–	–	–	–	–	–	–	–	–	–	–	–	–	–	–	–	–	–	–
488	150 – 200	1.8 – 2.0	-0.7 – -0.4	0.0006	±8.25	±10.81	0.00	0.13	0.00	−0.63	0.88	2.78	−0.71	−0.02	0.00	−0.55	0.02	1.435	−1.369	2.17	0.02	0.65	−9.89	1.03	0.94
489	150 – 200	1.8 – 2.0	-0.4 – 0.0	0.0033	±3.58	±2.36	0.00	0.09	0.00	−0.54	0.08	0.89	−0.18	0.21	0.00	−0.52	0.03	0.329	−0.552	0.67	0.01	0.19	−1.77	1.02	0.94
490	150 – 200	1.8 – 2.0	0.0 – 0.4	0.0051	±2.75	±1.53	0.00	0.11	0.00	−0.54	0.07	0.60	−0.12	0.19	0.00	−0.52	0.02	0.222	−0.370	0.51	0.00	0.15	−0.86	1.01	0.94
491	150 – 200	1.8 – 2.0	0.4 – 0.7	0.0017	±4.89	±4.34	0.00	0.06	0.00	−0.58	0.78	2.01	−0.33	0.02	0.00	−0.54	0.01	0.606	−0.463	1.26	0.01	0.25	−3.23	1.04	0.95
492	150 – 200	1.8 – 2.0	0.7 – 1.0	–	–	–	–	–	–	–	–	–	–	–	–	–	–	–	–	–	–	–	–	–	–
493	150 – 200	2.0 – 2.2	-1.0 – -0.7	–	–	–	–	–	–	–	–	–	–	–	–	–	–	–	–	–	–	–	–	–	–
494	150 – 200	2.0 – 2.2	-0.7 – -0.4	–	–	–	–	–	–	–	–	–	–	–	–	–	–	–	–	–	–	–	–	–	–
495	150 – 200	2.0 – 2.2	-0.4 – 0.0	0.0024	±3.98	±2.00	0.00	0.09	0.00	−0.64	0.28	0.95	−0.37	0.19	0.00	−0.61	0.03	0.335	−0.431	0.88	0.01	0.43	0.79	1.02	0.93
496	150 – 200	2.0 – 2.2	0.0 – 0.4	0.0038	±3.12	±2.24	0.00	0.10	0.00	−0.63	0.17	0.65	−0.31	0.23	0.00	−0.61	0.02	1.014	−0.328	0.70	0.01	0.28	1.31	1.01	0.94
497	150 – 200	2.0 – 2.2	0.4 – 0.7	–	–	–	–	–	–	–	–	–	–	–	–	–	–	–	–	–	–	–	–	–	–
498	150 – 200	2.0 – 2.2	0.7 – 1.0	–	–	–	–	–	–	–	–	–	–	–	–	–	–	–	–	–	–	–	–	–	–
499	150 – 200	2.2 – 2.4	-1.0 – -0.7	–	–	–	–	–	–	–	–	–	–	–	–	–	–	–	–	–	–	–	–	–	–
500	150 – 200	2.2 – 2.4	-0.7 – -0.4	–	–	–	–	–	–	–	–	–	–	–	–	–	–	–	–	–	–	–	–	–	–
501	150 – 200	2.2 – 2.4	-0.4 – 0.0	0.0009	±5.77	±5.80	0.00	0.07	0.00	−0.79	1.02	1.34	−0.56	0.32	0.00	−0.78	0.00	0.331	−0.228	1.76	0.02	0.48	5.03	1.01	0.94
502	150 – 200	2.2 – 2.4	0.0 – 0.4	0.0011	±5.34	±4.94	0.00	0.06	0.00	−0.86	0.92	1.16	−0.58	0.31	0.00	−0.84	0.00	0.293	−0.262	1.46	0.01	0.47	4.19	1.03	0.94
503	150 – 200	2.2 – 2.4	0.4 – 0.7	–	–	–	–	–	–	–	–	–	–	–	–	–	–	–	–	–	–	–	–	–	–
504	150 – 200	2.2 – 2.4	0.7 – 1.0	–	–	–	–	–	–	–	–	–	–	–	–	–	–	–	–	–	–	–	–	–	–

TABLE 32: Measured cross-section values unfolded to the Born truth-level in the last 24 bins of the measurement. The luminosity uncertainty of 1.9% is not included.

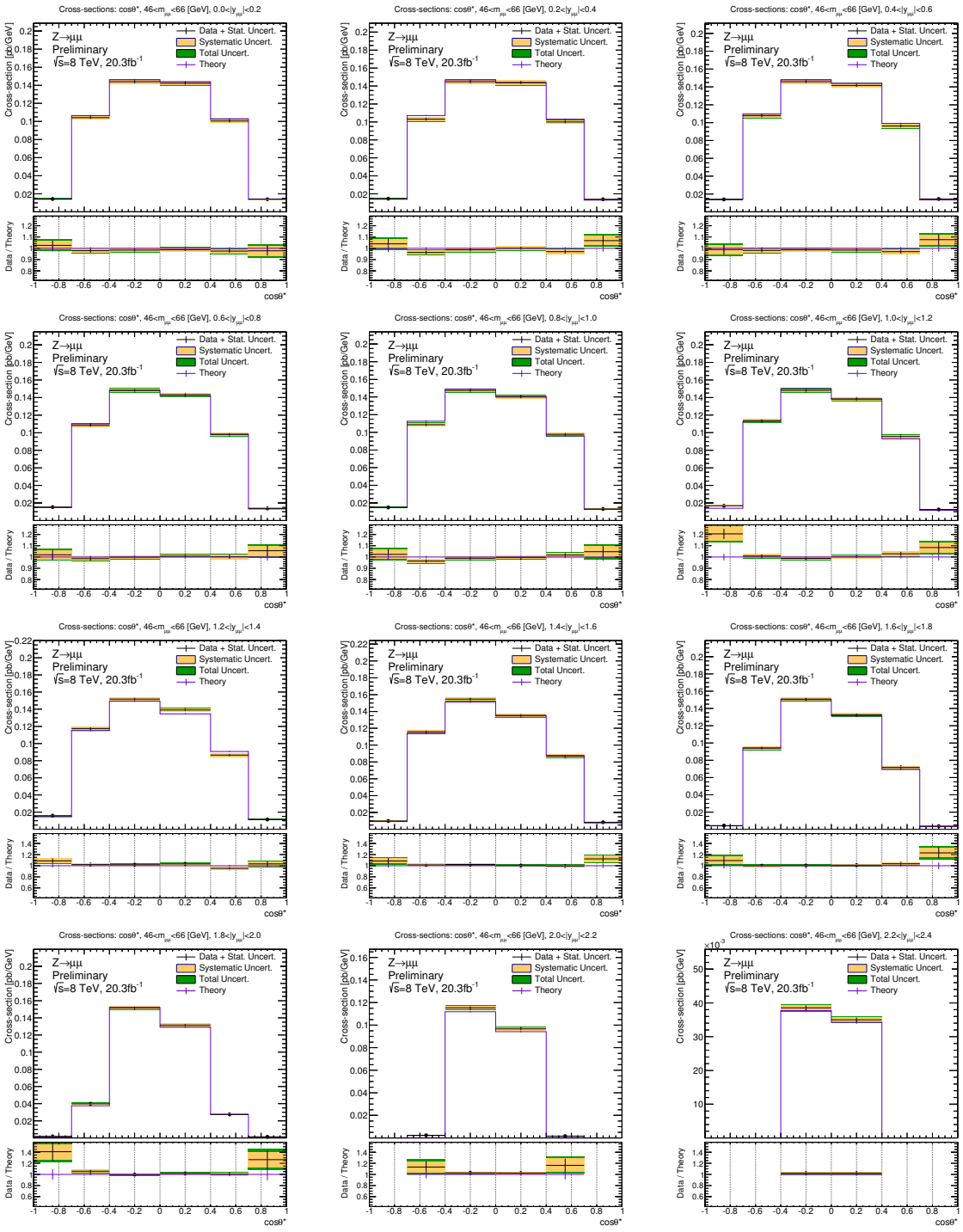

FIG. 74: Cross-section central values and uncertainty bands across each rapidity bin within the $46 < m_{ll} < 66\,\text{GeV}$ mass regime unfolded to the Born truth-level with one Bayesian iteration. Theory predictions are taken from `powheg-pythia8` Drell–Yan MC. The luminosity uncertainty of 1.9% is not included.

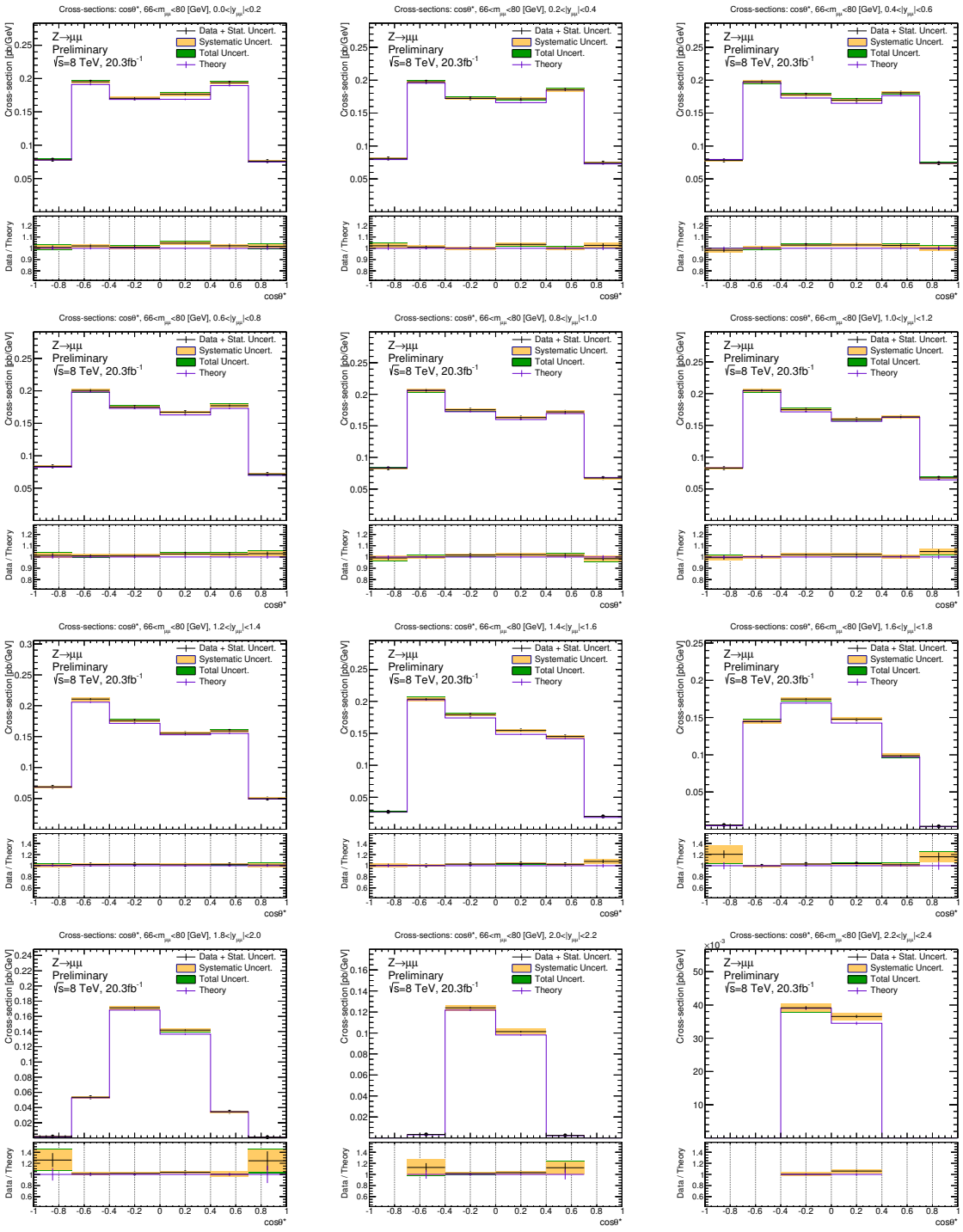

FIG. 75: Cross-section central values and uncertainty bands across each rapidity bin within the $66 < m_{ll} < 80\,\text{GeV}$ mass regime unfolded to the Born truth-level with one Bayesian iteration. Theory predictions are taken from `powheg-pythia8` Drell–Yan MC. The luminosity uncertainty of 1.9% is not included.

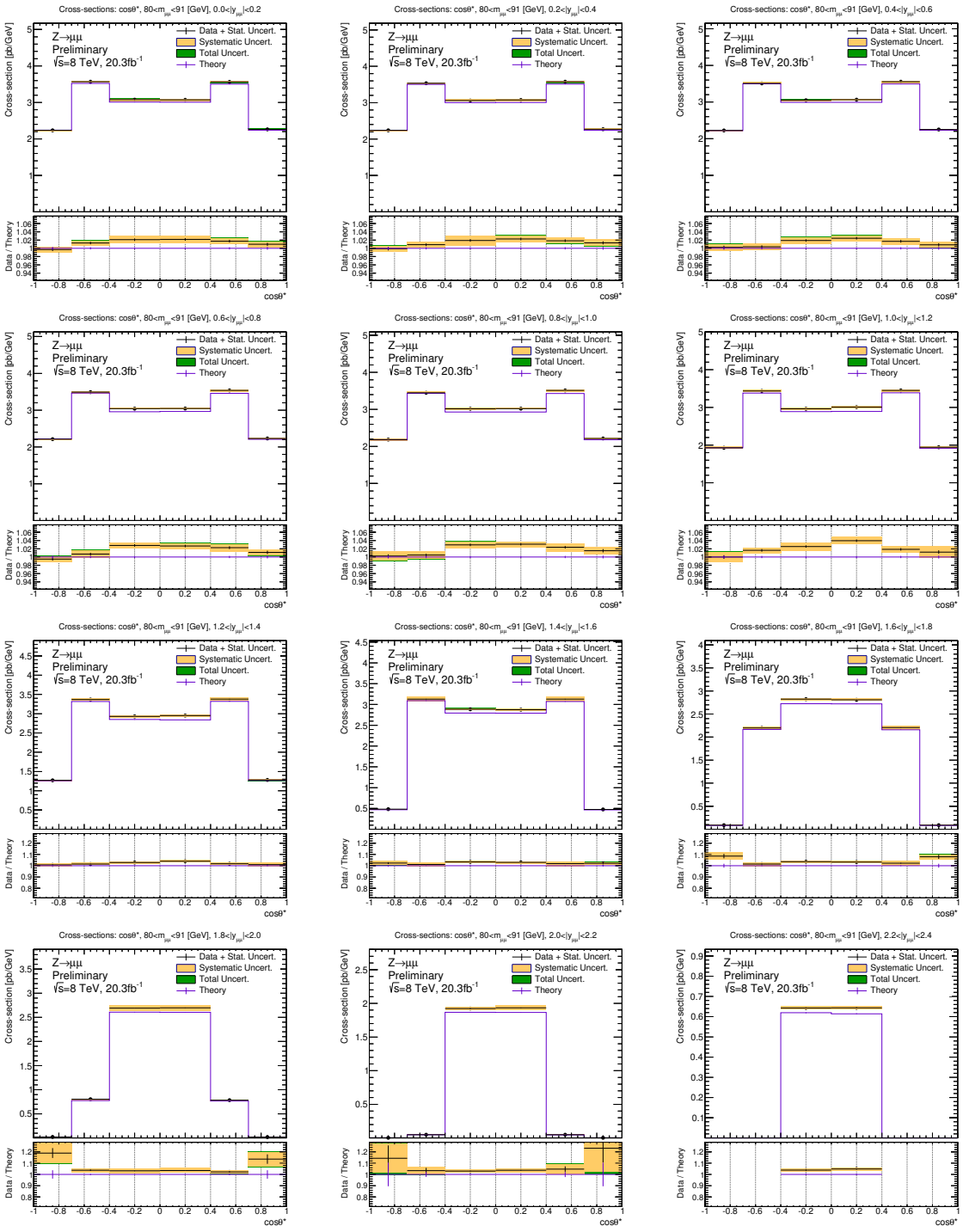

FIG. 76: Cross-section central values and uncertainty bands across each rapidity bin within the $80 < m_{ll} < 91\,\text{GeV}$ mass regime unfolded to the Born truth-level with one Bayesian iteration. Theory predictions are taken from `powheg-pythia8` Drell–Yan MC. The luminosity uncertainty of 1.9% is not included.

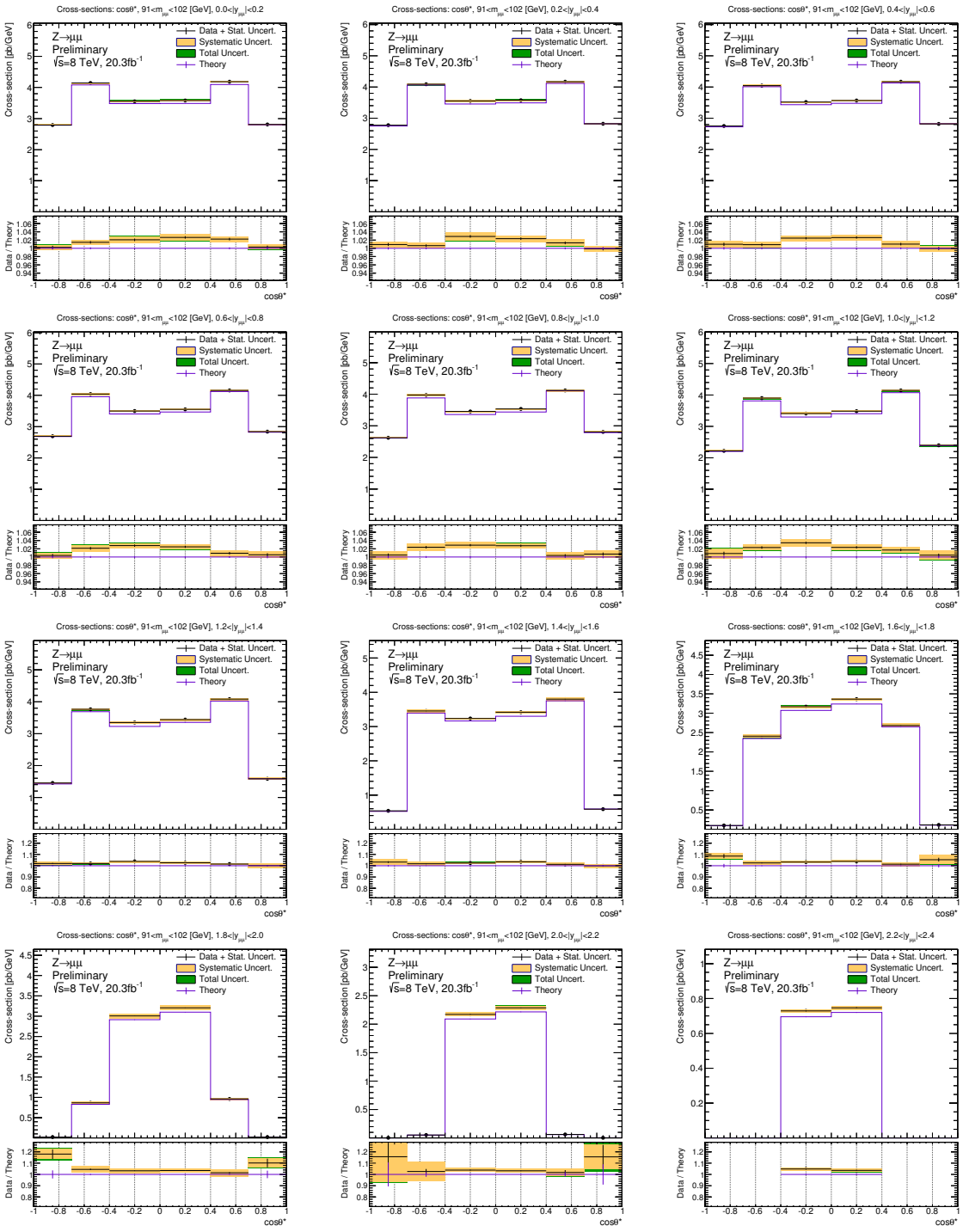

FIG. 77: Cross-section central values and uncertainty bands across each rapidity bin within the $91 < m_{ll} < 102\,\text{GeV}$ mass regime unfolded to the Born truth-level with one Bayesian iteration. Theory predictions are taken from `powheg-pythia8` Drell–Yan MC. The luminosity uncertainty of 1.9% is not included.

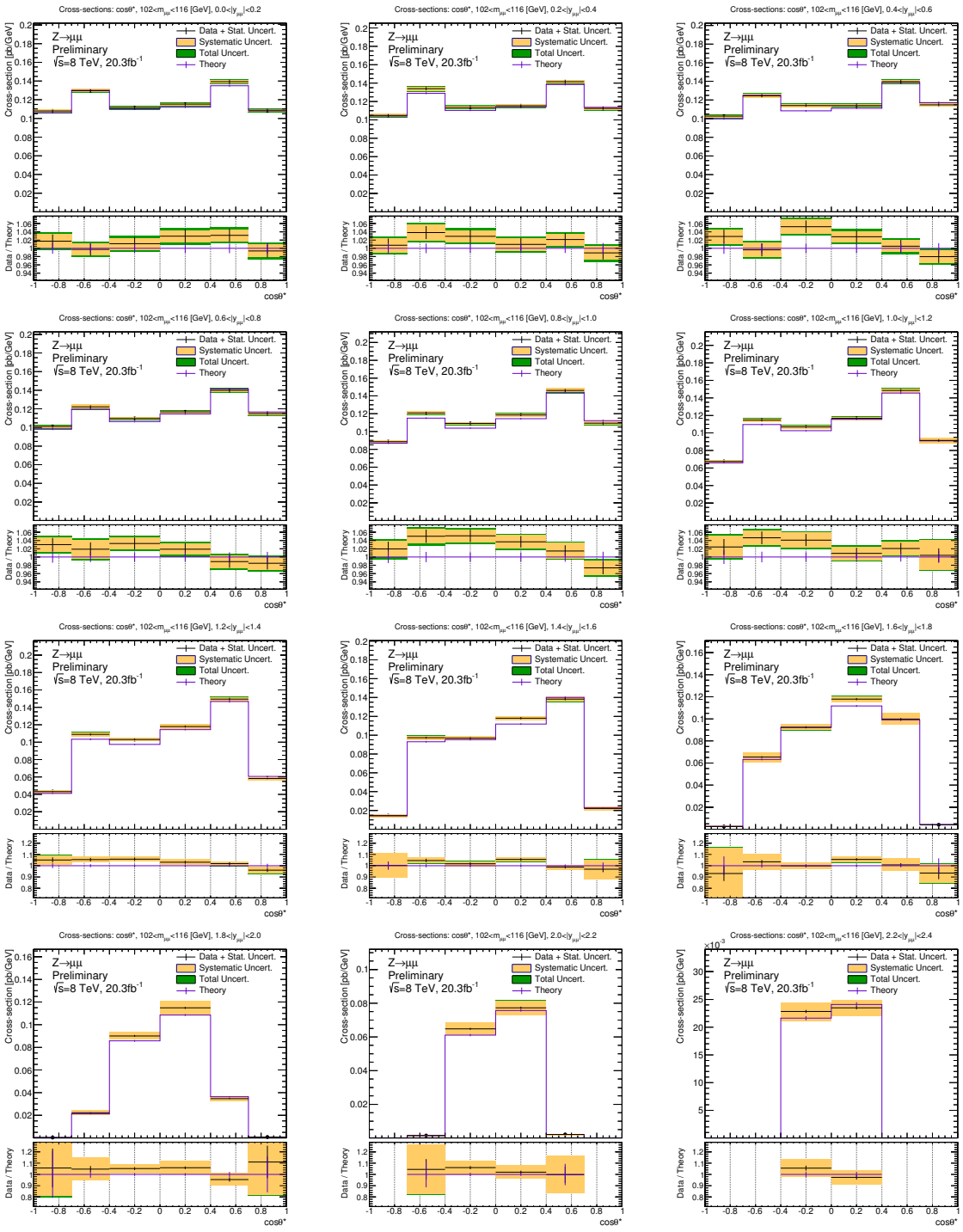

FIG. 78: Cross-section central values and uncertainty bands across each rapidity bin within the $102 < m_{ll} < 116\,\text{GeV}$ mass regime unfolded to the Born truth-level with one Bayesian iteration. Theory predictions are taken from `powheg-pythia8` Drell–Yan MC. The luminosity uncertainty of 1.9% is not included.

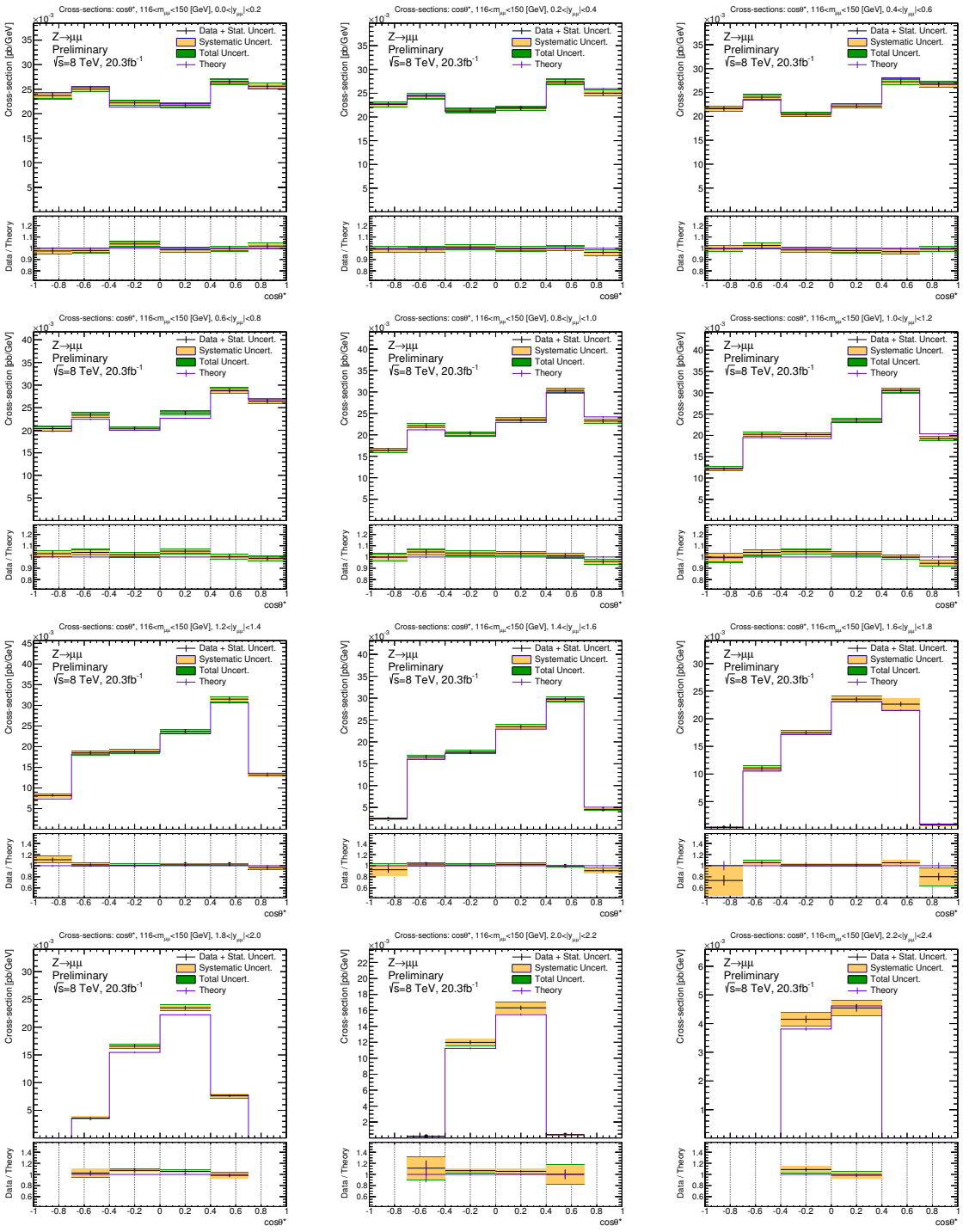

FIG. 79: Cross-section central values and uncertainty bands across each rapidity bin within the $116 < m_{ll} < 150\,\text{GeV}$ mass regime unfolded to the Born truth-level with one Bayesian iteration. Theory predictions are taken from `powheg-pythia8` Drell–Yan MC. The luminosity uncertainty of 1.9% is not included.

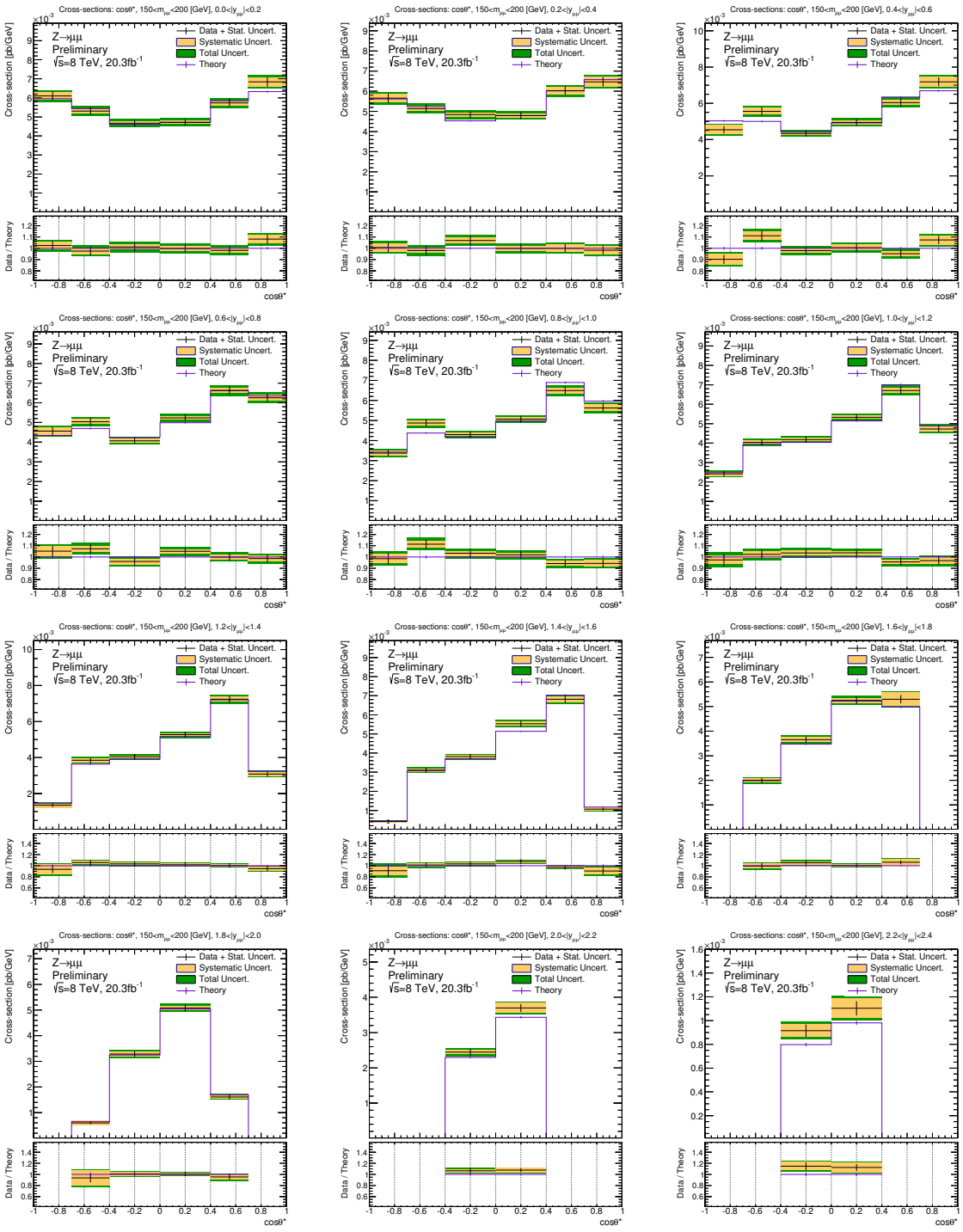

FIG. 80: Cross-section central values and uncertainty bands across each rapidity bin within the $150 < m_{ll} < 200\,\text{GeV}$ mass regime unfolded to the Born truth-level with one Bayesian iteration. Theory predictions are taken from `powheg-pythia8` Drell–Yan MC. The luminosity uncertainty of 1.9% is not included.

B. Integrated Cross-sections

The triple-differential Born-results are integrated to have only two bins in $\cos\theta^*$ from which A_{FB} values are calculated through Equation 43. The forward-backward asymmetries are shown as a function of $m_{\mu\mu}$ for each $|y_{\mu\mu}|$ bin in Figure 81. Additional distributions are made by inclusively integrating over two of the triple-differential measurement dimensions. The one dimensional cross-sections are shown in Figure 82.

The forward-backward asymmetry plots of Figure 81 are shown as a function of $m_{\mu\mu}$ for each separate bin of $|y_{\mu\mu}|$. The largest A_{FB} values are shown to increase as a function of $|y_{\mu\mu}|$ matching the MC theory prediction. The largest A_{FB} values are also shown to be statistically limited, where the statistical limitation is due to the low event yield in the highest $|\cos\theta^*| > 0.7$ bins. The one dimensional cross-sections show the Z-peak measured with a precision of $< 1\%$, with $< 2\%$ precision off-peak either side. One dimensional $|y_{\mu\mu}|$ and $\cos\theta^*$ are dominated by the large Z cross-section and highlight systematic percentage-level Z-boson mis-modelling. The 1D invariant mass cross-sections are in agreement with results published from the CMS collaboration[38] achieving similar total uncertanties.

This concludes the triple-differential Drell–Yan muon channel measurement. The following sections describe the scope of the work in a larger context of a combined result.

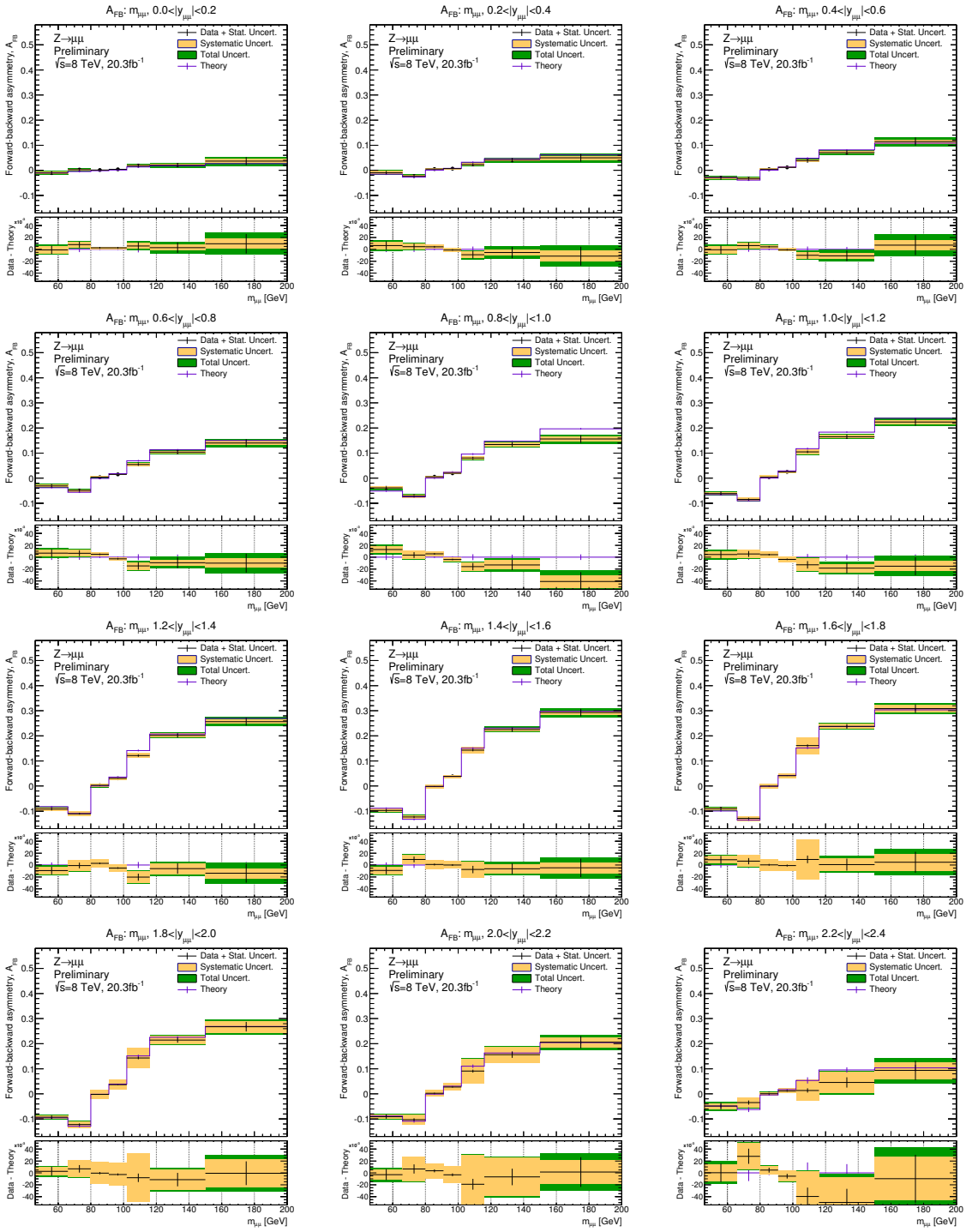

FIG. 81: A_{FB} central values and uncertainty bands for each rapidity region unfolded to the Born truth-level with one Bayesian iteration. Theory predictions are taken from `powheg-pythia8` Drell–Yan MC. The luminosity uncertainty of 1.9% is not included.

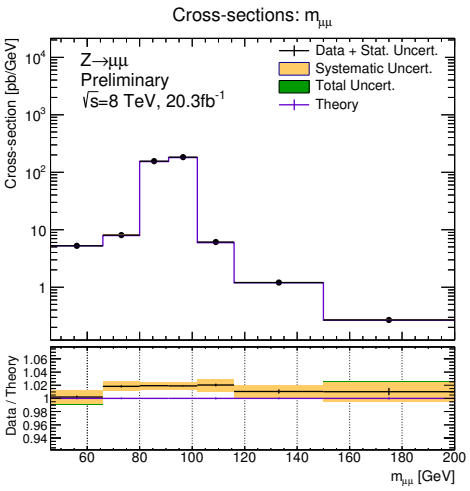

(a) Measured Drell–Yan cross-section as a function of dimuon invariant mass, $m_{\mu\mu}$.

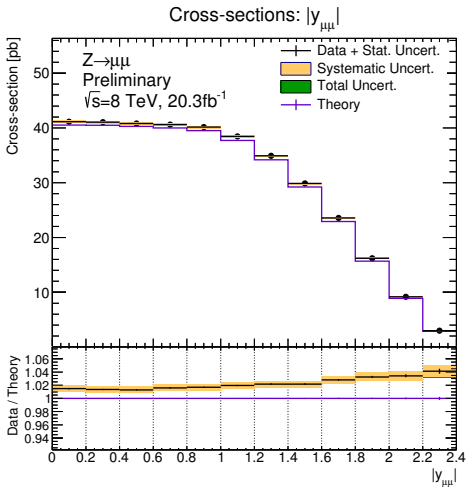

(b) Measured Drell–Yan cross-section as a function of absolute dimuon rapidity, $|y_{\mu\mu}|$.

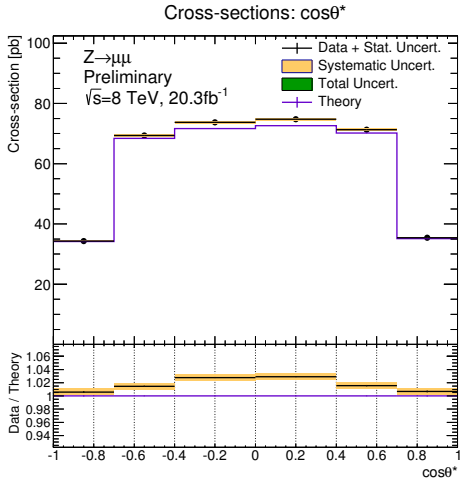

(c) Measured Drell–Yan cross-section as a function of dimuon decay angle in the Collin-Soper frame, $\cos\theta^*$.

FIG. 82: Triple-differential cross-section results integrated over two dimensions to form one-dimensional distributions. The cross-sections are unfolded to the Born truth-level with one Bayesian iteration. Theory predictions are taken from `powheg-pythia8` Drell–Yan MC. The luminosity uncertainty of 1.9% is not included.

13. ELECTRON CHANNEL MEASUREMENTS

Two separate electron channel triple-differential Drell–Yan cross-section measurements have been performed in tandem with the muon channel measurement. The electron channel measurements are optimised for two different electron reconstruction η regions of the ATLAS detector. The measurements are performed so that a combination of the two electron channels and the muon channel can be made, resulting in a single measurement with reduced total uncertainties. The electron channel measurements were not performed by the author of this thesis and nor are they described in full detail in this document, however brief summaries of the channels are provided. Detailed descriptions are found in the references[3]. The cross-section results of the electron channels are not yet finalised and are considered "work in progress" by the ATLAS collaboration.

A. The Electron CC and CF Channels

The CC channel is defined with both leptons being reconstructed in the central part of the detector, $|\eta| < 2.4$. The electron central-central (CC) channel is analogous to the muon channel presented in this thesis, which itself can also be considered a central-central channel. The measurement fiducial volume is defined to be equivalent so that a direct combination of the electron CC and muon channels can be performed. The kinematic selection criteria on the electrons are also unified, for this reason. Table 33 lists the fiducial volume criteria for the different channels, where p_T^e is the electron transverse momentum, η_e is the electron pseudo-rapidity and m_{ee} is the dielectron pair invariant mass.

Criteria		Muon (CC) channel	Electron CC channel	Electron CF channel	
				Central electron	Forward electron
Fiducial	p_T^ℓ	$p_T^\mu > 20\,\text{GeV}$	$p_T^e > 20\,\text{GeV}$	$p_T^e > 20\,\text{GeV}$	$p_T^e > 25\,\text{GeV}$
	$\lvert\eta^\ell\rvert$	$\lvert\eta^\mu\rvert < 2.4$	$\lvert\eta_e\rvert < 2.4$	$\lvert\eta_e\rvert < 2.4$	$2.5 < \lvert\eta_e\rvert < 4.9$
	$m_{\ell\ell}$	$m_{\mu\mu} > 46\,\text{GeV}$	$m_{ee} > 46\,\text{GeV}$	$66 < m_{ee} < 150\,\text{GeV}$	

TABLE 33: Fiducial volume selection criteria used in the different measurement channels.

The electron central-forward (CF) channel provides an extension to the CC measurement phase space coverage. The CF channel is defined with one electron being reconstructed in the central part of the detector and one electron being reconstructed in the forward parts of the detector, $2.5 < |\eta| < 4.9$. This increases the measurable Z-boson rapidity range, y_{ee}, and consequently allows higher values of A_{FB} to be measured. Due to measurement limitations of the forward parts

of the detector the same unified fiducial volume is not maintained. The data therefore requires extrapolation factors back to the CC fiducial volume to be used in the cross-section combinations.

In both electron channels, Drell–Yan signal events are selected from data and MC following a selection criteria method similar to the muon channel measurement. Corrections are applied to account for generator- and reconstruction-level mis-modelling effects. The same MC samples are used for consistency and the multijet background estimation is determined using a data-driven method. The data is unfolded using MC response matrices using the iterative Bayesian unfolding method where the nominal cross-section values are determined. Sources of uncertainty are propagated using the same techniques as described in Section 11 and correlation matrices are provided for nuisance parameter representation.

14. COMBINATION WITH THE ELECTRON CHANNEL

The combination of the muon and electron channel triple-differential cross-section measurements is performed using a method developed at HERA[129,130] A detailed description of the combination procedure can be found in the references[3,131]. The current combination procedure and the cross-section results from the electron channels are not finalised and are considered "work in progress" by the ATLAS collaboration. The combination procedure minimises the differences between two or more measurements of the same cross-section to give an averaged result with reduced total uncertainty. The procedure uses the bin-to-bin correlation information for each channel to account for correlated systematic uncertainties between the multiple channels. The HERA combination method uses a nuisance parameter representation of bin-to-bin correlations. Each cross-section measurement, e, is described as a χ^2_e function for which the average cross-section value, m_i, is to be determined:

$$\chi^2_e(m,b) = \sum_i^{N_{\mathcal{B}}} \left(\frac{m_i - (\mu_{i,e} + \sum_l^{N_{\text{corr.}}} \Gamma^{li}_e b_l)}{\Delta^{\text{uncor.}}_{i,e}} \right)^2 + \sum_l^{N_{\text{corr.}}} b_l^2 \,, \tag{96}$$

where $\mu_{i,e}$ are the measured cross section values and $N_{\mathcal{B}}$ is the total number of measurement bins; $N_{\text{corr.}}$ is the number of correlated uncertainty sources, Γ^{li}_e are the eigenvectors of the correlation matrices of the correlated source, l, and b_l are the nuisance parameters corresponding to the correlated uncertainty source; finally, $\Delta^{\text{uncor.}}_{i,e}$ are the total statistical bin-to-bin uncorrelated systematic uncertainties. For several measurements, the combined χ^2 function is given by the sum of the χ^2_e functions:

$$\chi^2_{tot}(m,b) = \chi^2_{\text{CC}ee}(m,b) + \chi^2_{\text{CF}ee}(m,b) + \chi^2_{\text{CC}\mu\mu}(m,b)\,. \tag{97}$$

where CCee is the electron CC measurement, CFee is the electron CF measurement and CC$\mu\mu$ is the muon (CC) measurement. For the minimisation of the $\chi^2_{tot}(m,b)$ function, Γ^{li}_e and b_l are allowed freedom to transform from the nuisance-parameter basis to better describe systematic correlations of the averaged result. The results of the combination are presented in Section 14 C. The thesis author did not produce the final set of combined Born-results.

The muon and electron channels both use covariance matrix representation of correlations. The combination procedure requires a transformation to a nuisance parameters representation which is discussed in the next subsection.

A. Transformation from Covariance Matrix to Nuisance Parameters

In the muon and electron channels, bin-to-bin correlations for several sources are determined using covariance matrices from the toy MC and bootstrap resampling techniques. To transform a

covariance matrix, C, into the nuisance parameter representation, as required for the χ^2 function used for the combination, it is decomposed using eigenvector decomposition. In practice when computing the eigenvectors, Γ, several eigenvalues of C may be close to zero and fluctuate below zero because of limited statistical precision. This is relevant for toy MC or bootstrap resampling methods if the number of toys/replicas is small compared to the number of measurement bins. To mitigate this problem, eigenvectors are sorted according to the magnitude of the eigenvalues so that an ordered sum over the eigenvalues can be calculated. When the sum exceeds a predefined fraction of its own nominal total, the correlation information for the remaining eigenvectors is ignored. The unused eigenvectors are added in quadrature to form a diagonal uncorrelated uncertainty matrix U.

$$C = \Gamma^T \Gamma \,, \tag{98}$$

$$C_{ij} \approx C'_{ij} = \sum_{l=1}^{N_c} \Gamma_{li} \Gamma_{lj} + \delta_{ij} U_i \,, \tag{99}$$

where N_c is the number of nuisance parameters required to describe C' and Γ_{li} are the contributing eigenvectors to C'. U_i are added to the uncorrelated uncertainty $\Delta_{i,e}^{\text{uncor.}}$ in Equation 96 in quadrature. The method preserves the total uncertainty by construction and, as an additional benefit, allows a reduction of the required number of nuisance parameters, N_c, describing C.

B. Combination χ^2 and the Unfolding Method

The optimal number of Bayesian iterations to use in the unfolding procedure is not a defined parameter. To determine an optimum number of iterations, a comparison of the combined unfolded CC results for Bayesian unfolding with a different number of iterations is performed. For consistency, the two measurement channels use the same number of iterations. The total χ^2/dof for the combination is used as the measure of this comparison.

Table 34 shows χ^2/dof for the combination using bin-by-bin and Bayesian unfolding methods. For each evaluation all systematic uncertainties are consistently determined using the corresponding unfolding method. Both statistical and total systematic uncertainties increase as the number of iterations increases, as has been discussed in Section 12. The table shows that the optimal χ^2/dof is obtained for one iteration of Bayesian unfolding.

C. Combined Results

The combination of the muon and electron CC data yields the total $\chi^2/dof = 474.9/451$. Combinations of the integrated cross-sections, shown in Table 35, show consistent χ^2/dof with other

Unfolding Method		χ^2/dof
Bin-by-bin		543.5/451
Bayesian	$n_{\text{itr.}} = 1$	474.9/451
	$n_{\text{itr.}} = 2$	532.2/451
	$n_{\text{itr.}} = 3$	545.7/451
	$n_{\text{itr.}} = 4$	550.2/451
	$n_{\text{itr.}} = 5$	552.5/451

TABLE 34: χ^2/dof for the combination of the muon and electron channel CC measurements for the bin-by-bin method and Bayesian method with different number of Bayesian iterations, $n_{\text{itr.}}$. $n_{\text{itr.}} = 1$ is the nominal number of Bayesian iterations used in the combination.

analyses[1,128,132]. This consistency is expected because the same data sets are used. The combined cross-section results are shown in Figures 83-89. The figures show the combined cross-section results in each invariant mass bin as a function of rapidity. The combined cross-section values from each $\cos\theta^*$ bin are shown on the same plot to compare shape differences. The forward-backward asymmetry dependence on $|y_{\ell\ell}|$ is clearly observed in the divergence of the cross-section in the opposite $\cos\theta^*$ bins. The conclusions drawn from the shapes of the results are the same as discussed in Section 12. The combination of the measurements provides a reduced total uncertainty: the smallest uncertainties of the muon channel Born-results are $< 0.6\%$ whereas the equivalent combined results achieve $< 0.3\%$; the largest uncertainties of the muon channel Born-results are $\sim 15\%$ which are reduced to $\sim 8\%$ for the combined result.

Integrated cross section type	χ^2/dof
Nominal $3D$ combination	474.9/451
1D in $\cos\theta^*$	2.6/6
1D in in $y_{\ell\ell}$	7.0/12
1D in $m_{\ell\ell}$	12.8/7
2D in ($m_{\ell\ell}$, $y_{\ell\ell}$)	103.4/84
2D in ($m_{\ell\ell}$, $\cos\theta^*$)	39.2/42
2D in ($y_{\ell\ell}$, $\cos\theta^*$)	62.6/68
3D, two bins in $\cos\theta^*$: (-1.0, 0.0, 1.0)	167.0/168
$46 < m_{\ell\ell} < 80\,\text{GeV}$	122.6/132
$80 < m_{\ell\ell} < 102\,\text{GeV}$	134.1/135
$102 < m_{\ell\ell} < 200\,\text{GeV}$	188.7/184

TABLE 35: χ^2 values and number of degrees of freedom for the standard combination and combination of $1D$, $2D$, and $3D$-differential cross sections, determined from the integration of the $3D$-tables, together with a 1D combination of low, peak and high $m_{\ell\ell}$ regions.

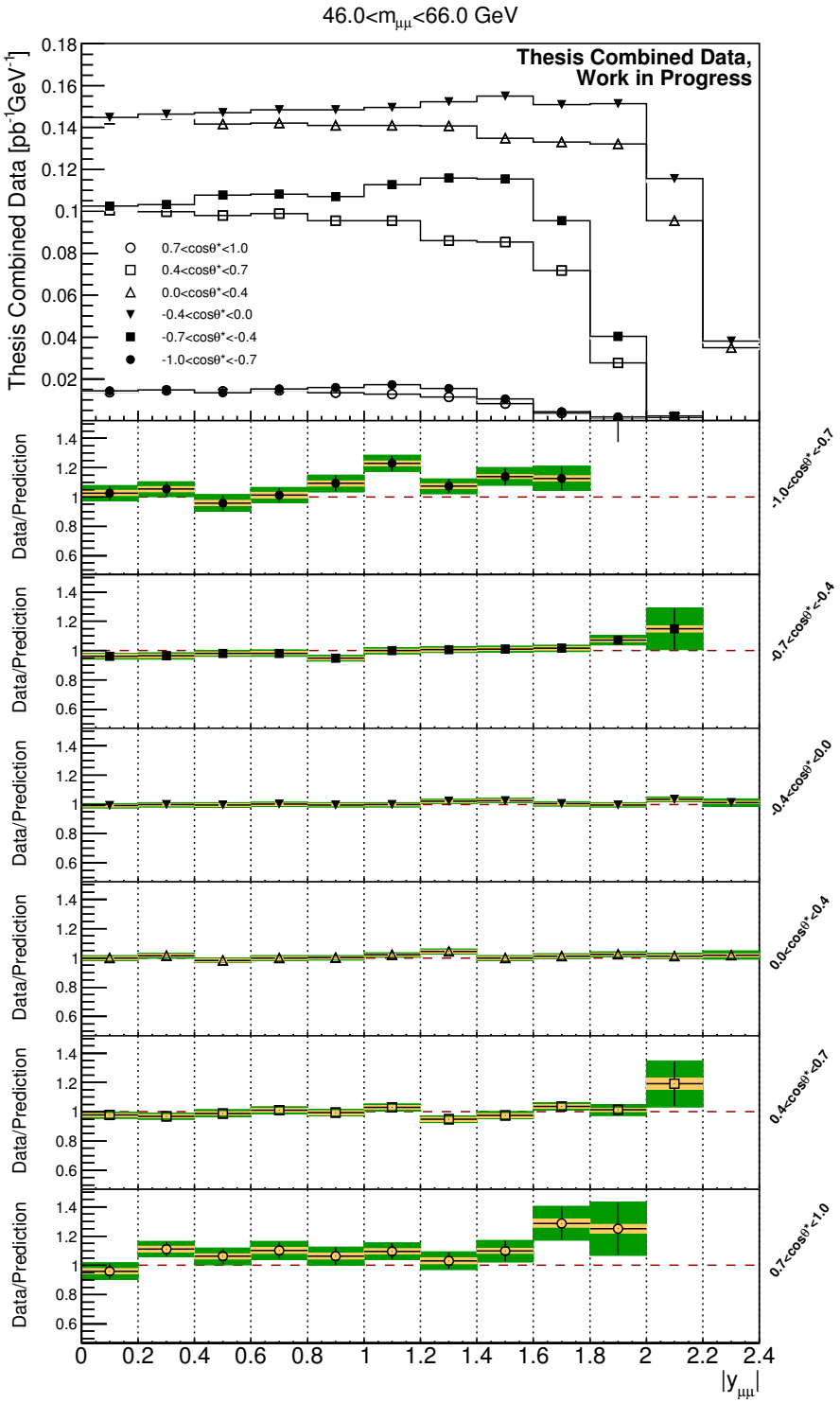

FIG. 83: Combined cross-section central values and uncertainty bands as a function of rapidity within the $46 < m_{ll} < 66\,\text{GeV}$ mass regime. Each set of points corresponds to a different $\cos\theta^*$ bin in the measurement. The ratios of data and MC predictions for each $\cos\theta^*$ bin are provided in the sub-panels. The luminosity uncertainty of 1.9% is not included.

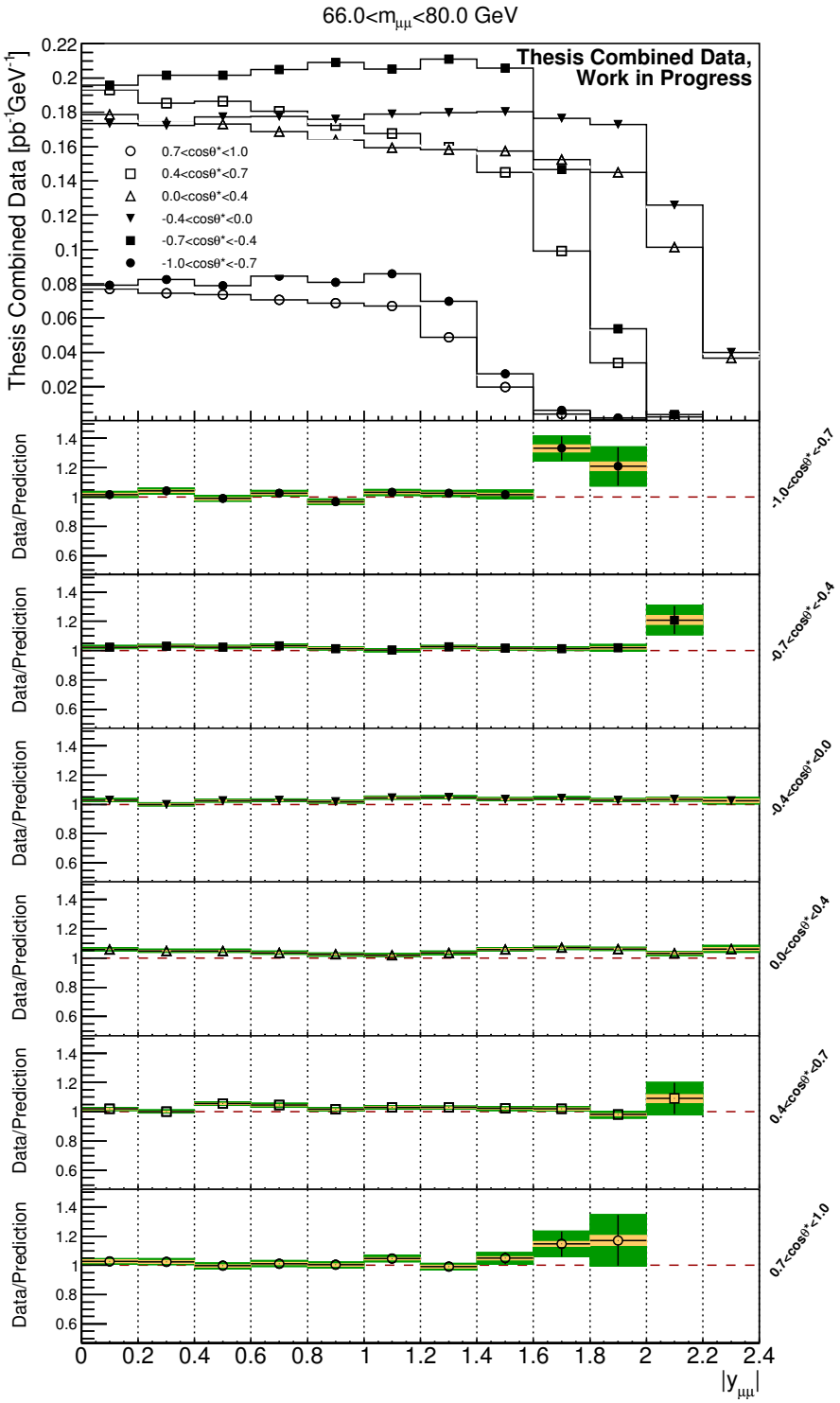

FIG. 84: Combined cross-section central values and uncertainty bands as a function of rapidity within the $66 < m_{ll} < 80\,\text{GeV}$ mass regime. Each set of points corresponds to a different $\cos\theta^*$ bin in the measurement. The ratios of data and MC predictions for each $\cos\theta^*$ bin are provided in the sub-panels. The luminosity uncertainty of 1.9% is not included.

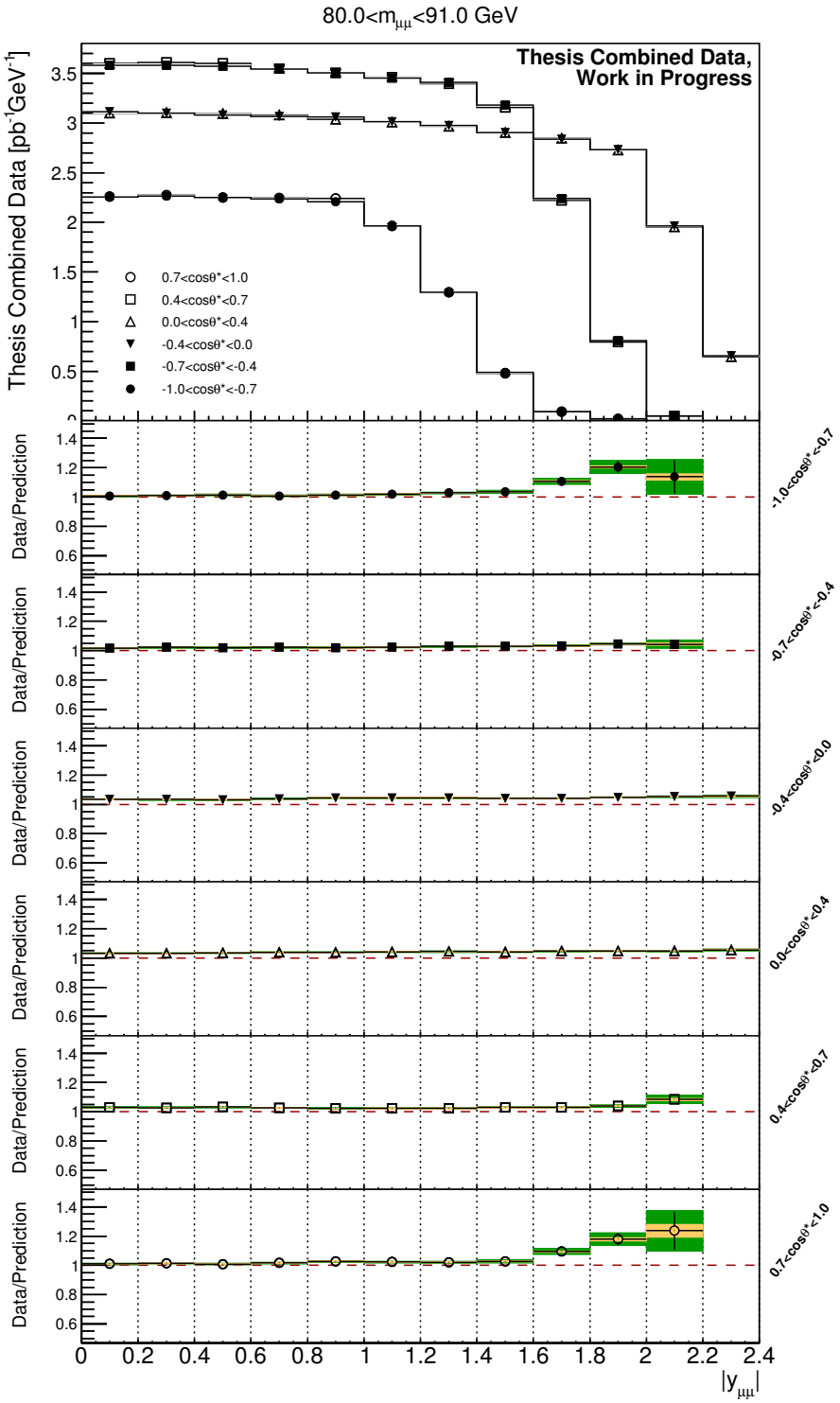

FIG. 85: Combined cross-section central values and uncertainty bands as a function of rapidity within the $80 < m_{ll} < 91\,\text{GeV}$ mass regime. Each set of points corresponds to a different $\cos\theta^*$ bin in the measurement. The ratios of data and MC predictions for each $\cos\theta^*$ bin are provided in the sub-panels. The luminosity uncertainty of 1.9% is not included.

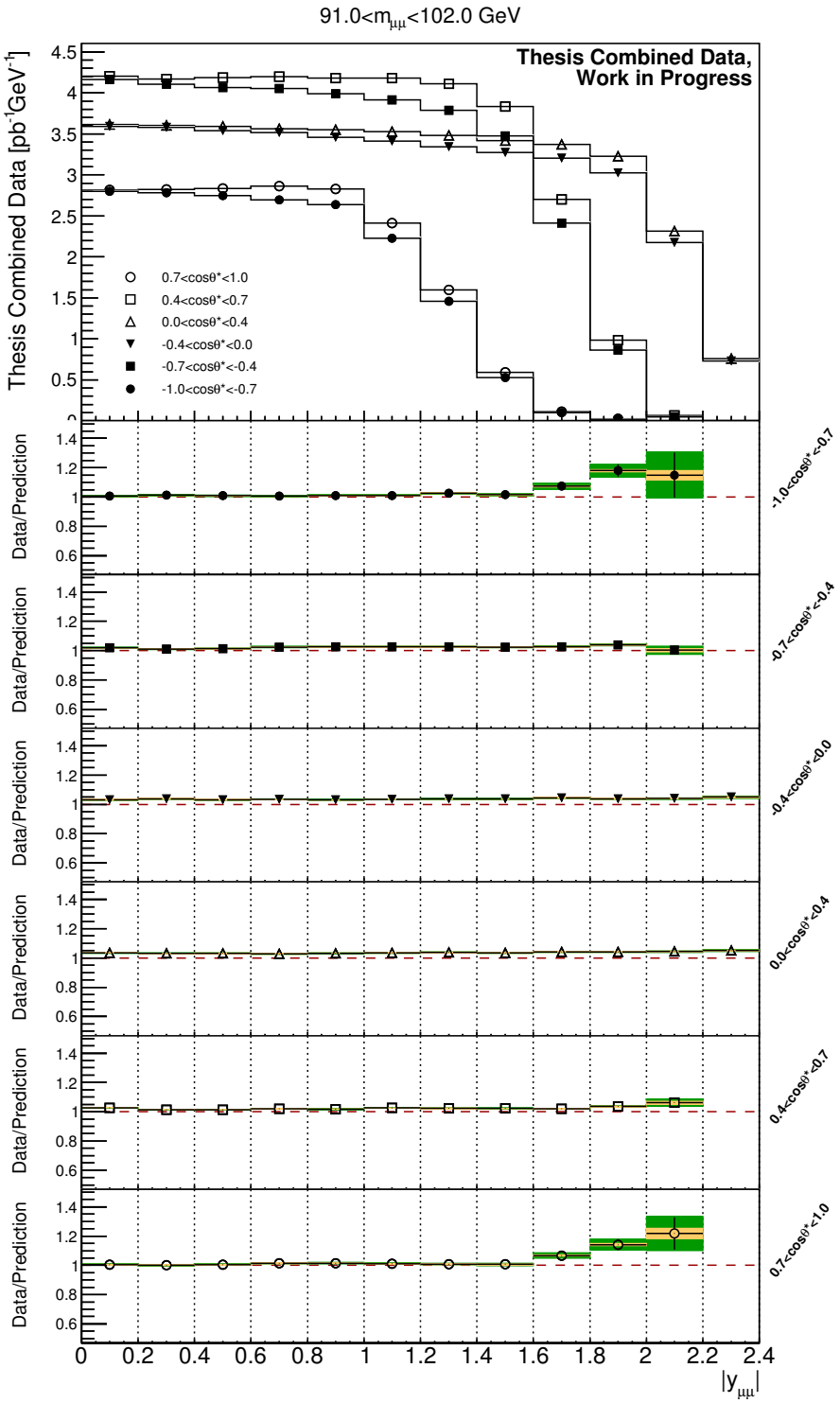

FIG. 86: Combined cross-section central values and uncertainty bands as a function of rapidity within the $91 < m_{ll} < 102\,\text{GeV}$ mass regime. Each set of points corresponds to a different $\cos\theta^*$ bin in the measurement. The ratios of data and MC predictions for each $\cos\theta^*$ bin are provided in the sub-panels. The luminosity uncertainty of 1.9% is not included.

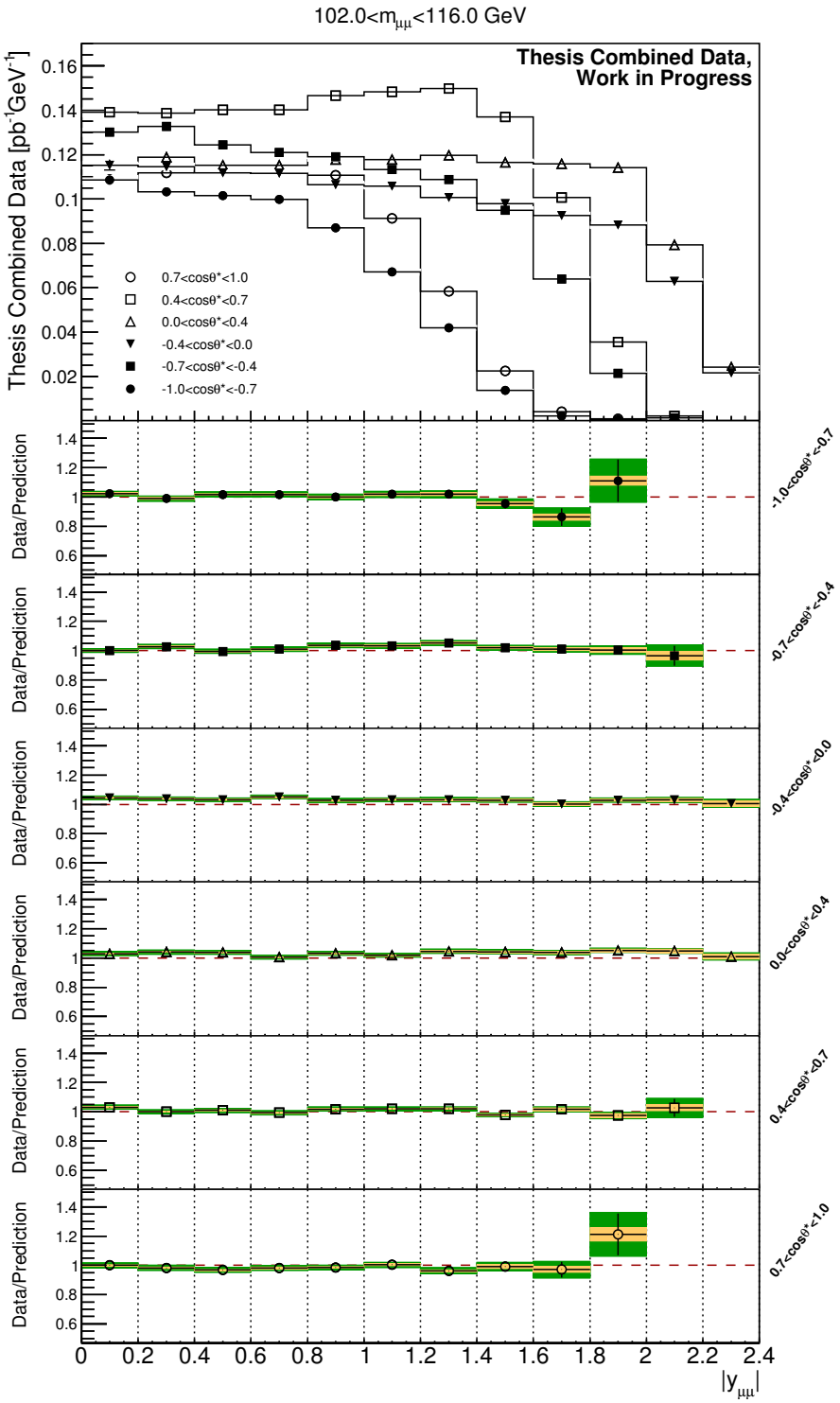

FIG. 87: Combined cross-section central values and uncertainty bands as a function of rapidity within the $102 < m_{ll} < 116\,\text{GeV}$ mass regime. Each set of points corresponds to a different $\cos\theta^*$ bin in the measurement. The ratios of data and MC predictions for each $\cos\theta^*$ bin are provided in the sub-panels. The luminosity uncertainty of 1.9% is not included.

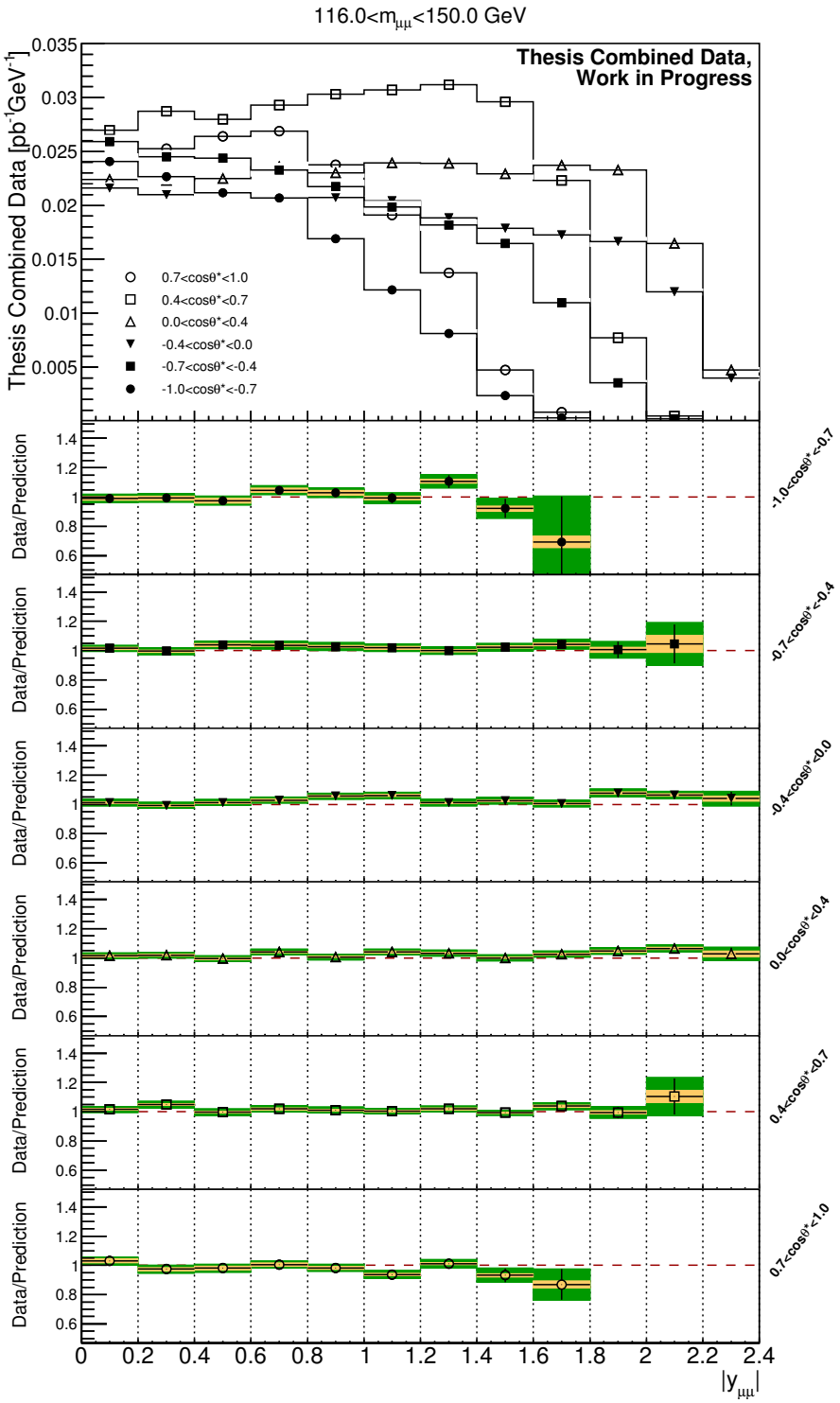

FIG. 88: Combined cross-section central values and uncertainty bands as a function of rapidity within the $116 < m_{ll} < 150\,\text{GeV}$ mass regime. Each set of points corresponds to a different $\cos\theta^*$ bin in the measurement. The ratios of data and MC predictions for each $\cos\theta^*$ bin are provided in the sub-panels. The luminosity uncertainty of 1.9% is not included.

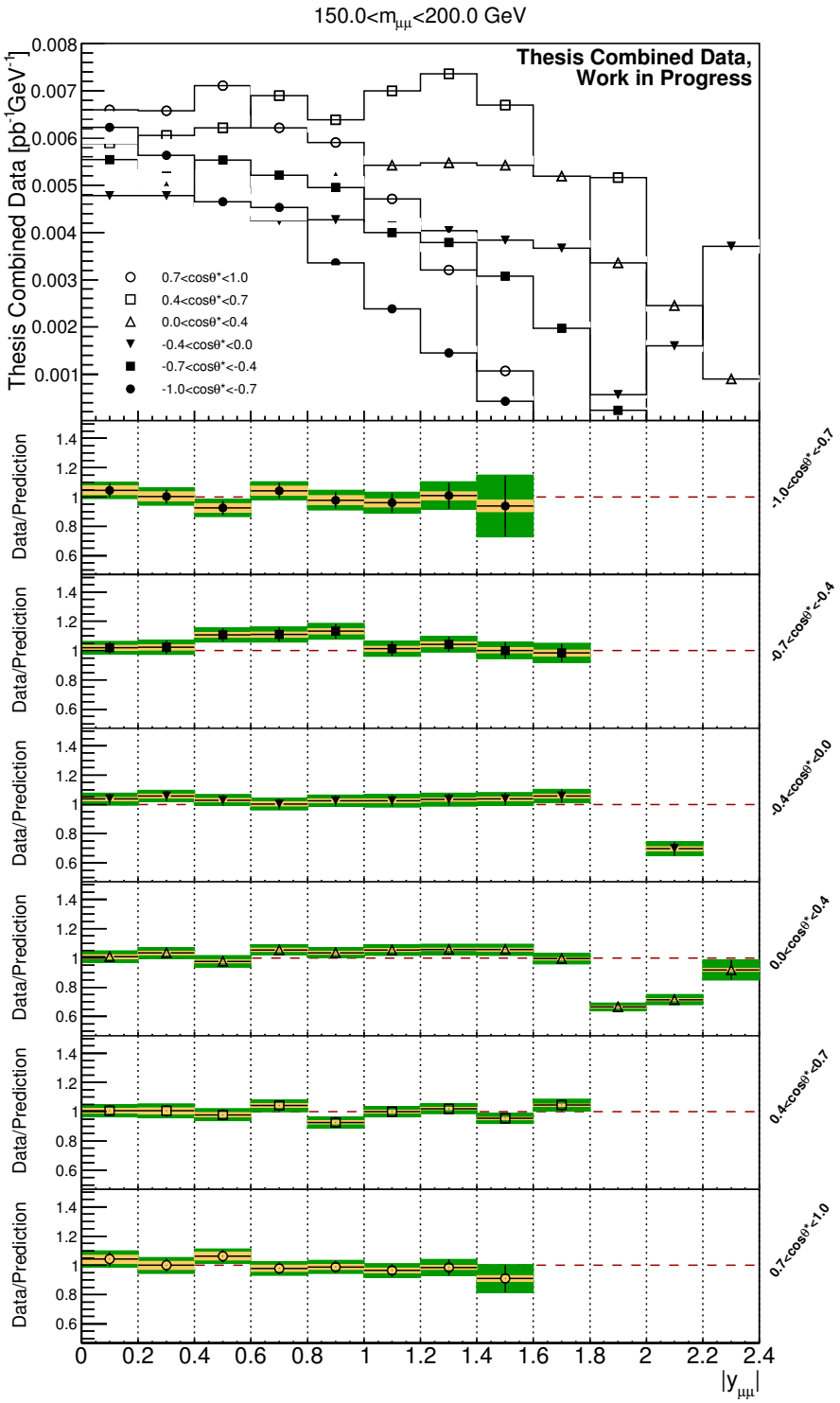

FIG. 89: Combined cross-section central values and uncertainty bands as a function of rapidity within the $150 < m_{ll} < 200\,\text{GeV}$ mass regime. Each set of points corresponds to a different $\cos\theta^*$ bin in the measurement. The ratios of data and MC predictions for each $\cos\theta^*$ bin are provided in the sub-panels. The luminosity uncertainty of 1.9% is not included.

15. PDF & WEAK MIXING ANGLE EXTRACTION

A (very) preliminary extraction is performed on the data to assess the sensitivity to the weak mixing angle, $\sin^2\theta_W^{\text{eff}\cdot}$ and the PDFs. The weak mixing angle is not directly extracted in this thesis because the theoretical predictions and framework for the extraction has not yet been set-up. Typically, such a direct extraction requires generating many predictions with slightly different values of $\sin^2\theta_W^{\text{eff}\cdot}$. A χ^2 scan is performed between the agreement of data and theory which is then fitted to as a function of $\sin^2\theta_W^{\text{eff}\cdot}$ for which the low inflection point in the χ^2 scan yields the extraction result. The method below reports a PDF extraction where $\sin^2\theta_W^{\text{eff}\cdot}$ is provided an optional degree of freedom in the extraction. The following theory predictions and electron channel data (from the subset of the combined data) are not the author's work. The following work does not bear affiliation to the ATLAS or X-fitter collaborations because the method and results are considered "work in progress". Figures 90 and 91 were produced by the thesis author. A detailed description of the procedure is found in the references[3].

A. MCFM Predictions and Electroweak Corrections

Rudimentary fixed-order predictions are calculated using `MCFM`[90,133] interfaced to the `APPLGRID`[134] program. The predictions are at LO and NLO QCD for any choice of PDF and renormalisation and factorisation scale. The G_μ electroweak parameter scheme is used in the calculations, where large higher-order corrections are absorbed into the precisely measured muon decay constant G_μ[135,136]. This parameterisation reduces the magnitude of electroweak corrections.

The settings of the `MCFM` program are summarised in Table 36. The `mcfm-bridge` package is used to help set the measurement binning in the `APPLGRID` program. The `APPLGRIDs` are generated using the `CT14nnlo` PDF set[85,125]. The source code locations of the analysis programs are listed in the table.

The `APPLGRIDs` are generated in sets of 2000 runs with 5×10^5 events generated in each run. This ensures $< 0.2\%$ statistical accuracy for most of the bins with some outliers having up to 2% accuracy. QED FSR effects are simulated with Photos[81]. Additional higher order electroweak corrections are performed using Fewz[137] to account for the effects of pure weak vertex and self-energy corrections, double boson exchange, initial state radiation, and the interference between ISR and FSR[138]. The Fewz corrections exclude FSR to avoid double-counting with Photos.

The Fewz predictions are calculated using the `Ct10nnlo`[85] PDF set. The renormalisation and factorisation scales are defined: $\mu_R = \mu_F = m_{\ell\ell}$. The contribution from photon induced processes is estimated using the `MRST2004QED` PDF set[139]. The photon induced corrections contribute $2-3\%$ of the theoretical predictions. The higher order electroweak corrections are applied to the theoretical

MCFM version	6.8
MCFM git	https://stash.desy.de/scm/sg/mcfm-zpol.git (branch Z)
APPLGRID bridge version	mcfm-bridge-0.0.35
APPLGRID bridge git	https://stash.desy.de/scm/sg/mcfm_bridge.git (branch Z3D)
APPLGRID version	applgrid-1.4.70
Renormalisation and factorisation scales	dynamic, $\mu_R = \mu_F = \sqrt{m_{\ell\ell}}$
Grid dimensions	$\lvert y_{\ell\ell}\rvert - \cos\theta^*$, in analysis mass bins

TABLE 36: Program versions and settings used by the MCFM program and APPLGRID interface. The locations of the current versions of the code are also provided.

predictions and give corrections of up to 5%.

B. Sensitivity to the Weak Mixing Angle

To perform the $\sin^2\theta_W^{\text{eff}\cdot}$ sensitivity study, the measured cross-section values are replaced by the central theory predictions. The data uncertainties and the bin-to-bin correlation model are preserved for the central values. The PDF uncertainties are approximated using the MMHT2014nnlo eigenvector set with nuisance parameters attributed to each eigenvector. The X-fitter program[140,141] is used to perform three profiling tests:

- Fixed $\sin^2\theta_W^{\text{eff}\cdot}$ and PDF nuisance parameters free.
- Free $\sin^2\theta_W^{\text{eff}\cdot}$ and PDF nuisance parameters fixed.
- Free $\sin^2\theta_W^{\text{eff}\cdot}$ and PDF nuisance parameters free.

The impact of the combined muon and electron channel data on PDF uncertainties is shown in Figure 90. The combined $\sin^2\theta_W^{\text{eff}\cdot}$ and PDF profiling compared to PDF-only profiling have very similar uncertainty bands. Visible improvements to the valence quark distributions are seen, attributed to forward-backward asymmetry sensitivity. The strange distribution is constrained by the $|y_{\ell\ell}|$ and $m_{\ell\ell}$ binned measurements. Figure 8 in Section 1 F shows the origin of this $m_{\mu\mu}$ and $y_{\ell\ell}$ quark decomposition sensitivity due to the differences in γ^* and Z couplings. The gluon component is improved, in part, from the $\cos\theta^*$ differential, which is also seen in Section 1 F in Figure 9.

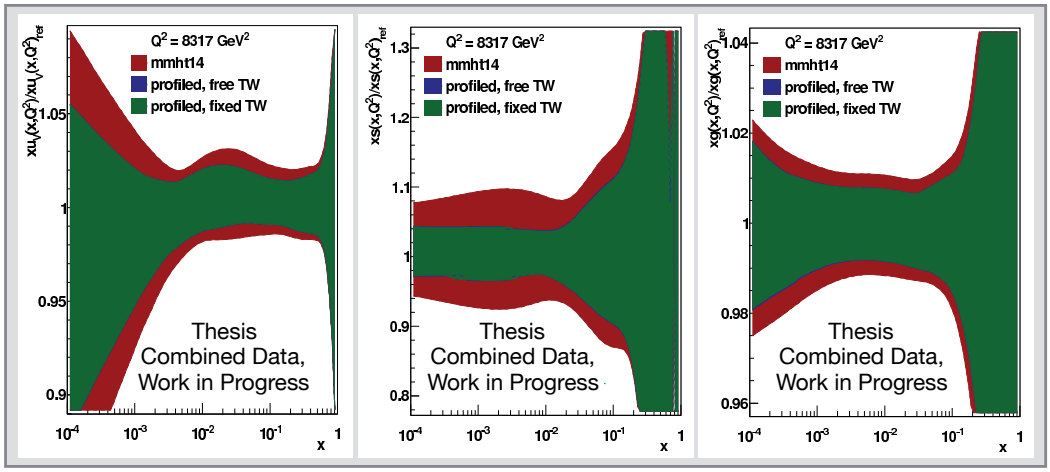

FIG. 90: Uncertainty bands for different PDF components at $Q^2 = m_Z^2 = 8317\,\mathrm{GeV}^2$ as a function of x. The displayed uncertainty bands are `MMHT2014nnlo` (outer red band), profiled `MMHT2014nnlo` with free $\sin^2\theta_W^{\mathrm{eff}\cdot}$ (blue middle band), and profiled `MMHT2014nnlo` with fixed $\sin^2\theta_W^{\mathrm{eff}\cdot}$ (inner green band). The PDF components (left to right) are: xu_v (u-valence); xs (strange); xg (gluon);

Table 37 lists resulting uncertainties for $\sin^2\theta_W^{\mathrm{eff}\cdot}$ when X-fitter profiling is performed including and excluding PDF uncertainties. From the difference of the uncertainties in quadrature, the estimated PDF uncertainty is 0.0004, which is significant however small compared to the experimental errors. The constrained uncertainty on $\sin^2\theta_W^{\mathrm{eff}\cdot}$ through the combined profiling method can be compared to state of the art and direct measurements. Figure 91 shows the constrained result in context with other measurements. The reported $\sin^2\theta_W^{\mathrm{eff}\cdot}$ sensitivity is shown to be competitive to the current best measurement reported at a hadron-hadron collider (D0). Furthermore, the constrained uncertainty is smaller than all other $\sin^2\theta_W^{\mathrm{eff}\cdot}$ measurements reported at the LHC.

	$\Delta\sin^2\theta_W^{\mathrm{eff}\cdot}$
With PDF uncertainties	0.00068
Without PDF uncertainties	0.00052

TABLE 37: Uncertainty on $\sin^2\theta_W^{\mathrm{eff}\cdot}$ from the profiled fit described in the text including or excluding PDF uncertainties from `MMHT2014nnlo` PDF set.

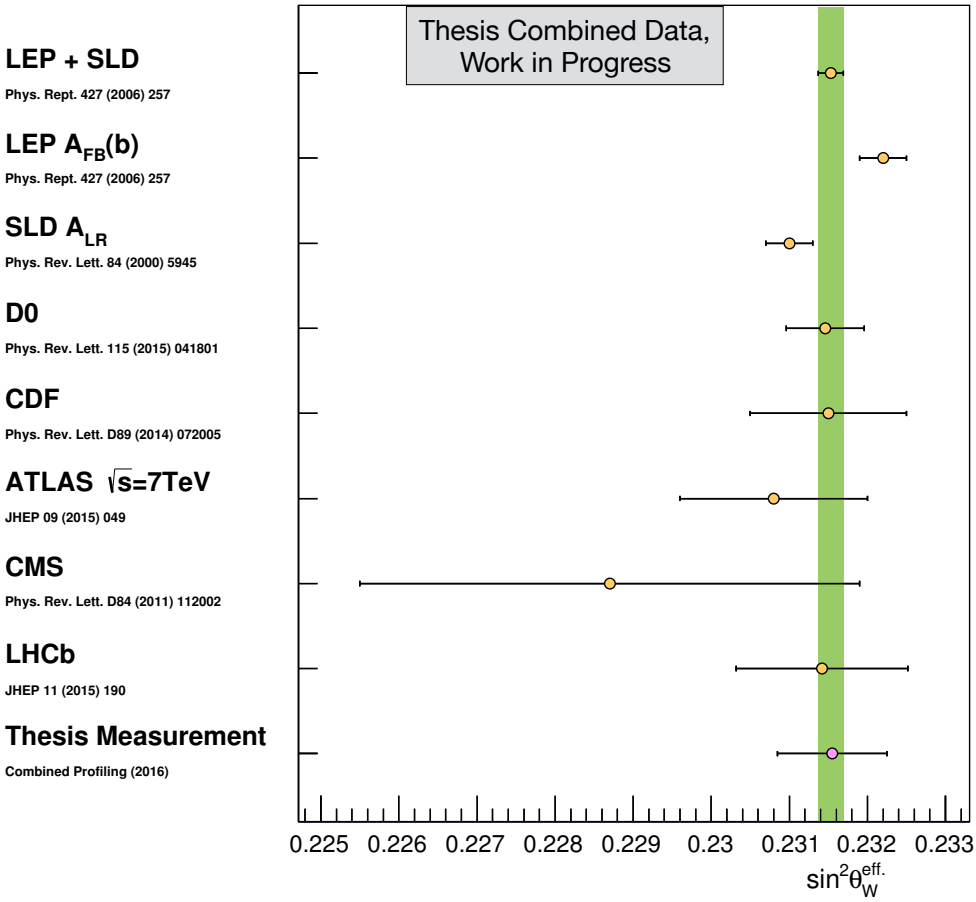

FIG. 91: Recent and most precise measurements of $\sin^2\theta_W^{\text{eff.}}$ performed at collider facilities[142–148]. The result from the combined LEP+SLD data is given by the vertical green line. The combined profiling data point is coloured magenta to distinguish that it is not a direct measurement and the central value is the $\sin^2\theta_W^{\text{eff.}}$ PDG global average[136].

16. MEASUREMENT CONCLUSIONS

The triple-differential Drell–Yan cross-section has been measured at $\sqrt{s} = 8\,\text{TeV}$ using a total integrated luminosity of $\mathcal{L} = 20.24\,\text{fb}^{-1}$ in the muon channel with the ATLAS detector. The measurement achieves a precision of up to 0.5% in the systematically limited central bins and percentage-level precision elsewhere due to statistical limitation. The forward-backward asymmetry was also calculated and found to increase with higher value $|y_{\mu\mu}|$ up to the kinematic acceptance limit set by the fiducial volume cuts. The measurements agrees well with the `powheg-pythia8` Monte Carlo predictions.

The results are combined with two electron channel measurements. The combination of the channels produces a single result with a reduced overall uncertainty, in many bins reduced by a factor of ~ 2. A high precision of $< 0.3\%$ is achieved in the central measurement bins on the Z-peak. The uncertainty reduction is due to increased data statistics and profiled systematic sources. The impact of the data upon PDF distributions and the effective weak mixing angle was studied through the combined profiling method. Significant improvements are observed in the valence, strange and gluon PDF distributions. The reduction in PDF uncertainties is entwined with an effective weak mixing angle sensitivity, which is shown to reduce the uncertainty in comparison to the ATLAS $\sqrt{s} = 7\,\text{TeV}$ measurement. The total uncertainty of $\sin^2\theta_W^{\text{eff}\cdot}$ is the smallest yet reported at the LHC.

A future, more rigorous analysis of the impact on the PDFs and $\sin^2\theta_W^{\text{eff}\cdot}$ with improved theoretical predictions should result in improved sensitivities beyond that reported in this thesis. Future ATLAS data sets should further improve on this result due to increased statistical yield in the peripheral binning regions and an improved muon momentum scale modelling in the ATLAS detector.

17. APPENDIX

1. ATLAS Coordinates Diagram

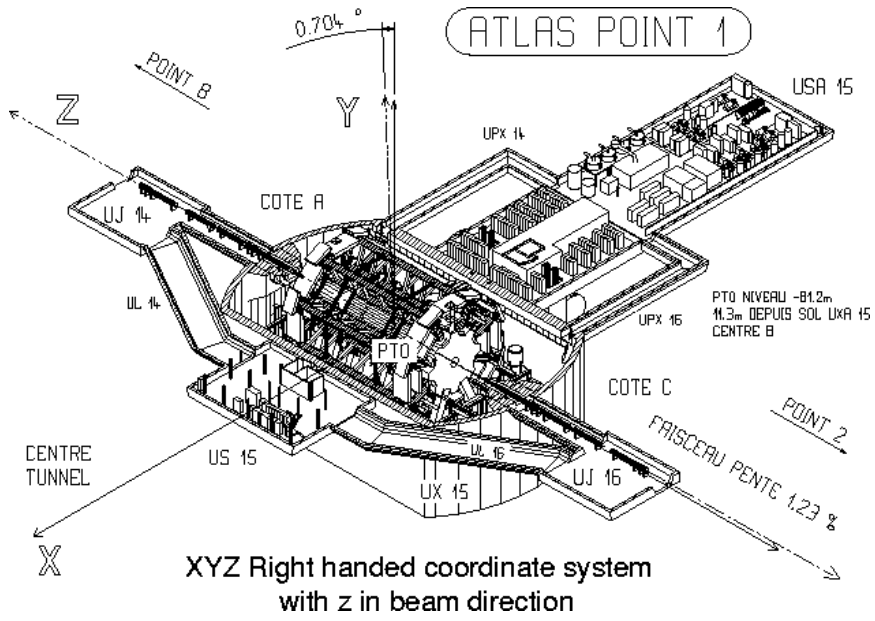

FIG. 92: Detailed view of the ATLAS detector in the interaction point (IP) 1 cavern, indicating the underground storage areas and the coordinate system employed by ATLAS. Note that due to the tilt of the LHC ring due to construction parameters the coordinate axis also has a tilt[149].

2. ATLAS Software Packages

Table 38 details the software packages used in the thesis measurement. All the packages listed were not written by the thesis author except for the "Muon ID Sagitta Corrections" package which was original work by the thesis author.

Name of Correction	Treatment	Name of Package & Version
Lineshape Reweighting	Generator-level	LineShapeTool-00-00-04
Vertex Reweighting	Generator-level	PrimaryVertexReweighting-00-09-30
Pile-up Corrections	Generator-level	PileupReweighting-00-02-12
Muon Momentum Corrections	Reconstruction-level	MuonMomentumCorrections-00-09-30
Muon Efficiency Corrections	Reconstruction-level	MuonEfficiencyCorrections-02-01-20
Muon Trigger Efficiencies	Reconstruction-level	TrigMuonEfficiency-00-02-54
Muon ID Sagitta Corrections	Reconstruction-level	SagittaCorrections-00-00-01
`svn+sh://svn.cern.ch/reps/atlasoff/`		
`svn+sh://svn.cern.ch/reps/atlasinst/Institutes/QMUL/`		

TABLE 38: Table of external packages used in this analysis. The name of the correction to MC is given along with the level at which the correction is applied and the official name of the package and its software version. The Apache-Subversion (SVN) repositories where the packages can be found are also listed for completeness.

3. Dressed & Bare C-factors and Uncertainties

In the uncertainties section (Section 11), uncertainty frequency plots were shown quantifying the precision of Born-results across the 504 measurement bins (Figure 68). Equivalent figures are shown for dressed- and bare-results in Figures 94 and 95.

Scaling cross-section values using C-factors may introduce a scaling bias to the results. Figure 93 shows the C-factor accuracy. The Born- and dressed-results are scaled with C-factors to get effective-bare-results. These are then compared to directly-unfolded bare-results. The figure shows 92% of bins have $< 0.1\%$ level accuracy using the C-factor method, however the remaining 8% of bins show deviations above this. The less-accurately described bins typically occur in the edges of the measurement phase space (high value $|\cos\theta^*|$). This could potentially influence future fits to the data if C-factor scaled cross-sections are used. For this reason, although dressed-results show smaller total uncertainties, Born-results are reported in the main body of the text.

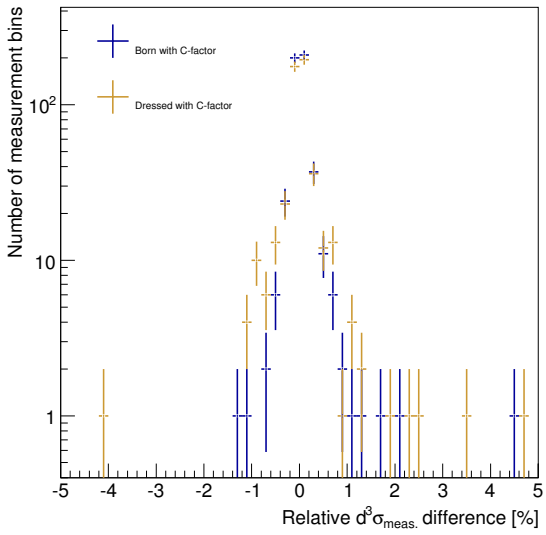

FIG. 93: Comparison of directly unfolded to the bare truth-level cross-section values with Born and dressed cross-section values with applied C-factors.

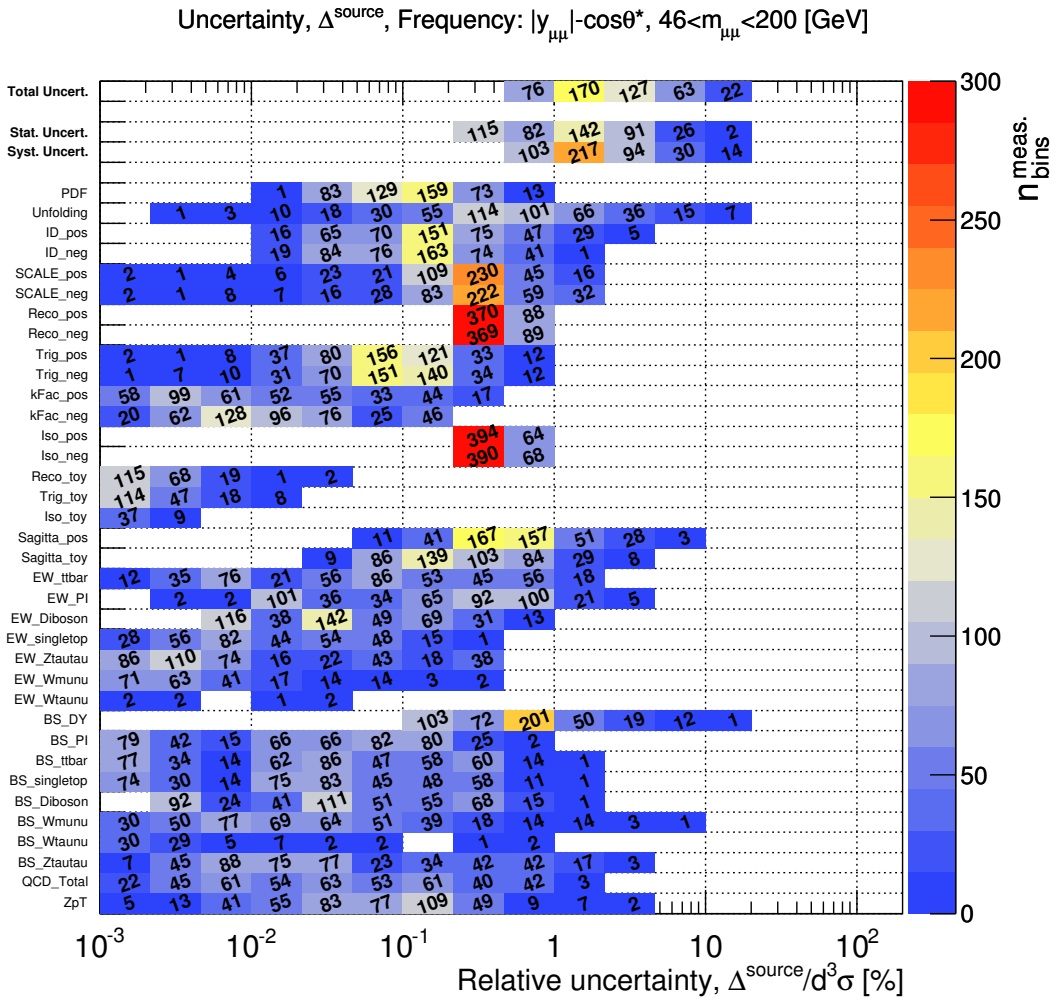

FIG. 94: Systematic and statistical uncertainty frequency distributions for the dressed cross-sections. The first row is the total uncertainty, which is composed of the two rows directly below named "Stat. Uncert." and "Syst. Uncert." in quadrature sum. The "Syst. Uncert." row is composed of all of the remaining rows below in quadratic sum. Table 21 summarises the y-axis aliases of the uncertainty sources. The phase space includes 504 measurement bins, 46 of which are vetoed because of low expected statistical precision.

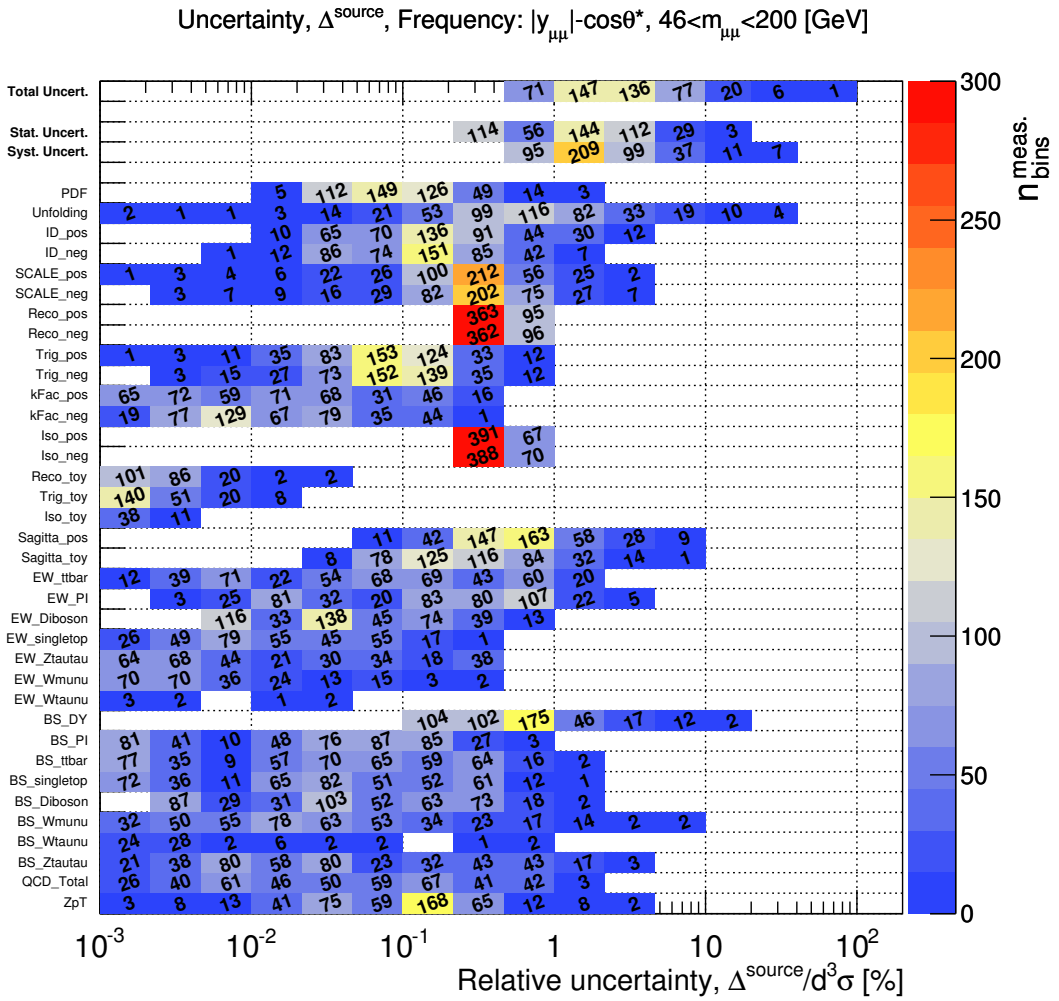

FIG. 95: Systematic and statistical uncertainty frequency distributions for the bare cross-sections. The first row is the total uncertainty, which is composed of the two rows directly below named "Stat. Uncert." and "Syst. Uncert." in quadrature sum. The "Syst. Uncert." row is composed of all of the remaining rows below in quadratic sum. Table 21 summarises the y-axis aliases of the uncertainty sources. The phase space includes 504 measurement bins, 46 of which are vetoed because of low expected statistical precision.

4. Dressed-results and Bare-results tables

The non-decomposed Born-, dressed- and bare-results are presented in Tables 39-45. The first four columns provide the measurement bin information, the next three general columns summarise the Born-, dressed- and bare-results respectively. In each general column the first two sub-columns give the measured unfolded cross-section and the total uncertainty (excluding luminosity uncertainty); the subsequent two columns give the MC truth-level predictions and prediction's statistical uncertainty; the last two columns provide the C-factors for scaling the cross-sections or predictions to different MC truth-level definitions.

				Born						Dressed						Bare					
$\mathcal{B}$	$m_{\mu\mu}$ [GeV]	$\lvert y_{\mu\mu}\rvert$	$\cos\theta^*$	$d^3\sigma_{\text{meas.}}$ [pb/GeV]	$\Delta^{\text{total}}_{\text{meas.}}$ [%]	$d^3\sigma_{\text{truth}}$ [pb/GeV]	$\Delta^{\text{Stat.}}_{\text{truth}}$ [%]	$C_{\text{Dres.}}$	C_{Bare}	$d^3\sigma_{\text{meas.}}$ [pb/GeV]	$\Delta^{\text{total}}_{\text{meas.}}$ [%]	$d^3\sigma_{\text{truth}}$ [pb/GeV]	$\Delta^{\text{Stat.}}_{\text{truth}}$ [%]	C_{Born}	C_{Bare}	$d^3\sigma_{\text{meas.}}$ [pb/GeV]	$\Delta^{\text{total}}_{\text{meas.}}$ [%]	$d^3\sigma_{\text{truth}}$ [pb/GeV]	$\Delta^{\text{Stat.}}_{\text{truth}}$ [%]	C_{Born}	$C_{\text{Dres.}}$
1	46 – 66	0.0 – 0.2	-1.0 – -0.7	0.0143	± 4.76	0.0139	± 2.06	1.17	1.25	0.0166	± 4.63	0.0162	± 1.92	0.86	1.07	0.0178	± 4.57	0.0173	± 1.86	0.80	0.93
2	46 – 66	0.0 – 0.2	-0.7 – -0.4	0.1042	± 2.30	0.1065	± 0.79	1.08	1.12	0.1124	± 2.14	0.1148	± 0.72	0.93	1.04	0.1169	± 2.10	0.1194	± 0.69	0.89	0.96
3	46 – 66	0.0 – 0.2	-0.4 – 0.0	0.1439	± 2.07	0.1462	± 0.56	1.10	1.16	0.1578	± 1.88	0.1602	± 0.52	0.91	1.05	0.1664	± 1.82	0.1690	± 0.50	0.87	0.95
4	46 – 66	0.0 – 0.2	0.0 – 0.4	0.1423	± 2.05	0.1440	± 0.57	1.10	1.16	0.1567	± 1.89	0.1585	± 0.52	0.91	1.06	0.1654	± 1.85	0.1673	± 0.50	0.86	0.95
5	46 – 66	0.0 – 0.2	0.4 – 0.7	0.1006	± 2.37	0.1030	± 0.75	1.08	1.13	0.1083	± 2.23	0.1109	± 0.72	0.93	1.05	0.1138	± 2.20	0.1165	± 0.70	0.88	0.95
6	46 – 66	0.0 – 0.2	0.7 – 1.0	0.0140	± 5.76	0.0143	± 2.03	1.14	1.20	0.0159	± 5.62	0.0162	± 1.90	0.88	1.05	0.0167	± 5.58	0.0171	± 1.86	0.83	0.95
7	46 – 66	0.2 – 0.4	-1.0 – -0.7	0.0146	± 4.80	0.0141	± 2.27	1.15	1.21	0.0168	± 4.54	0.0162	± 1.91	0.87	1.06	0.0177	± 4.52	0.0171	± 1.86	0.83	0.95
8	46 – 66	0.2 – 0.4	-0.7 – -0.4	0.1032	± 2.47	0.1071	± 0.74	1.08	1.12	0.1114	± 2.35	0.1157	± 0.72	0.93	1.04	0.1158	± 2.33	0.1202	± 0.69	0.89	0.96
9	46 – 66	0.2 – 0.4	-0.4 – 0.0	0.1447	± 2.03	0.1468	± 0.57	1.09	1.15	0.1577	± 1.86	0.1599	± 0.52	0.92	1.05	0.1660	± 1.83	0.1683	± 0.50	0.87	0.95
10	46 – 66	0.2 – 0.4	0.0 – 0.4	0.1438	± 2.21	0.1437	± 0.56	1.09	1.16	0.1567	± 2.03	0.1565	± 0.52	0.92	1.06	0.1662	± 1.96	0.1659	± 0.50	0.87	0.94
11	46 – 66	0.2 – 0.4	0.4 – 0.7	0.1000	± 2.42	0.1031	± 0.79	1.08	1.12	0.1078	± 2.32	0.1112	± 0.73	0.93	1.04	0.1121	± 2.27	0.1156	± 0.71	0.89	0.96
12	46 – 66	0.2 – 0.4	0.7 – 1.0	0.0140	± 4.80	0.0131	± 2.11	1.20	1.27	0.0167	± 4.56	0.0157	± 1.94	0.84	1.06	0.0178	± 4.52	0.0166	± 1.89	0.79	0.94
13	46 – 66	0.4 – 0.6	-1.0 – -0.7	0.0140	± 5.22	0.0141	± 2.04	1.15	1.22	0.0161	± 5.14	0.0163	± 1.91	0.87	1.06	0.0171	± 5.11	0.0172	± 1.86	0.82	0.94
14	46 – 66	0.4 – 0.6	-0.7 – -0.4	0.1077	± 2.34	0.1097	± 0.78	1.07	1.12	0.1158	± 2.24	0.1178	± 0.72	0.93	1.04	0.1205	± 2.20	0.1226	± 0.69	0.89	0.96
15	46 – 66	0.4 – 0.6	-0.4 – 0.0	0.1458	± 2.04	0.1478	± 0.55	1.10	1.16	0.1597	± 1.82	0.1619	± 0.52	0.91	1.06	0.1689	± 1.73	0.1712	± 0.50	0.86	0.95
16	46 – 66	0.4 – 0.6	0.0 – 0.4	0.1416	± 2.05	0.1440	± 0.56	1.10	1.16	0.1552	± 1.87	0.1577	± 0.52	0.91	1.06	0.1641	± 1.75	0.1667	± 0.50	0.86	0.95
17	46 – 66	0.4 – 0.6	0.4 – 0.7	0.0962	± 2.68	0.0992	± 0.80	1.08	1.13	0.1040	± 2.58	0.1072	± 0.74	0.92	1.05	0.1088	± 2.56	0.1121	± 0.72	0.88	0.96
18	46 – 66	0.4 – 0.6	0.7 – 1.0	0.0144	± 5.00	0.0134	± 2.24	1.14	1.21	0.0163	± 4.79	0.0152	± 1.97	0.88	1.06	0.0173	± 4.78	0.0161	± 1.92	0.83	0.94
19	46 – 66	0.6 – 0.8	-1.0 – -0.7	0.0153	± 4.77	0.0150	± 2.06	1.13	1.20	0.0173	± 4.65	0.0170	± 1.87	0.88	1.05	0.0183	± 4.61	0.0179	± 1.83	0.84	0.95
20	46 – 66	0.6 – 0.8	-0.7 – -0.4	0.1085	± 2.26	0.1100	± 0.76	1.07	1.11	0.1163	± 2.10	0.1180	± 0.71	0.93	1.04	0.1207	± 2.05	0.1224	± 0.69	0.90	0.96
21	46 – 66	0.6 – 0.8	-0.4 – 0.0	0.1483	± 1.84	0.1483	± 0.57	1.09	1.15	0.1619	± 1.59	0.1619	± 0.53	0.92	1.05	0.1708	± 1.52	0.1707	± 0.50	0.87	0.95
22	46 – 66	0.6 – 0.8	0.0 – 0.4	0.1433	± 1.68	0.1422	± 0.56	1.10	1.16	0.1572	± 1.56	0.1559	± 0.53	0.91	1.05	0.1657	± 1.54	0.1644	± 0.51	0.87	0.95
23	46 – 66	0.6 – 0.8	0.4 – 0.7	0.0982	± 2.42	0.0980	± 0.80	1.08	1.13	0.1061	± 2.27	0.1059	± 0.74	0.93	1.05	0.1110	± 2.23	0.1107	± 0.72	0.88	0.96
24	46 – 66	0.6 – 0.8	0.7 – 1.0	0.0139	± 5.32	0.0132	± 2.23	1.13	1.20	0.0157	± 5.19	0.0149	± 2.00	0.89	1.06	0.0167	± 5.12	0.0158	± 1.94	0.84	0.94
25	46 – 66	0.8 – 1.0	-1.0 – -0.7	0.0150	± 5.13	0.0146	± 2.08	1.13	1.18	0.0169	± 4.99	0.0164	± 1.90	0.89	1.05	0.0176	± 4.98	0.0172	± 1.86	0.85	0.95
26	46 – 66	0.8 – 1.0	-0.7 – -0.4	0.1088	± 2.15	0.1127	± 0.75	1.07	1.12	0.1167	± 2.07	0.1209	± 0.70	0.93	1.04	0.1215	± 2.05	0.1258	± 0.68	0.90	0.96
27	46 – 66	0.8 – 1.0	-0.4 – 0.0	0.1475	± 1.70	0.1491	± 0.56	1.08	1.15	0.1600	± 1.57	0.1617	± 0.51	0.92	1.06	0.1690	± 1.54	0.1708	± 0.50	0.87	0.95
28	46 – 66	0.8 – 1.0	0.0 – 0.4	0.1400	± 1.69	0.1406	± 0.57	1.09	1.16	0.1533	± 1.57	0.1540	± 0.53	0.91	1.06	0.1625	± 1.53	0.1631	± 0.51	0.86	0.94
29	46 – 66	0.8 – 1.0	0.4 – 0.7	0.0976	± 2.23	0.0961	± 0.80	1.09	1.14	0.1065	± 2.13	0.1049	± 0.75	0.92	1.05	0.1114	± 2.11	0.1097	± 0.72	0.88	0.96
30	46 – 66	0.8 – 1.0	0.7 – 1.0	0.0132	± 5.70	0.0126	± 2.40	1.14	1.21	0.0150	± 5.57	0.0143	± 2.03	0.88	1.07	0.0160	± 5.56	0.0153	± 1.97	0.83	0.94
31	46 – 66	1.0 – 1.2	-1.0 – -0.7	0.0169	± 5.52	0.0140	± 2.05	1.13	1.17	0.0190	± 5.64	0.0157	± 1.96	0.89	1.04	0.0197	± 6.21	0.0164	± 1.91	0.85	0.96
32	46 – 66	1.0 – 1.2	-0.7 – -0.4	0.1139	± 1.99	0.1128	± 0.76	1.06	1.10	0.1208	± 1.91	0.1196	± 0.70	0.94	1.04	0.1257	± 1.88	0.1245	± 0.68	0.91	0.96
33	46 – 66	1.0 – 1.2	-0.4 – 0.0	0.1481	± 1.81	0.1498	± 0.55	1.09	1.14	0.1609	± 1.66	0.1628	± 0.52	0.92	1.05	0.1694	± 1.61	0.1714	± 0.50	0.87	0.95
34	46 – 66	1.0 – 1.2	0.0 – 0.4	0.1382	± 1.74	0.1381	± 0.58	1.09	1.16	0.1511	± 1.58	0.1510	± 0.53	0.91	1.06	0.1598	± 1.52	0.1597	± 0.52	0.86	0.95
35	46 – 66	1.0 – 1.2	0.4 – 0.7	0.0956	± 2.32	0.0929	± 0.80	1.09	1.14	0.1044	± 2.27	0.1015	± 0.76	0.92	1.04	0.1086	± 2.26	0.1056	± 0.74	0.88	0.96
36	46 – 66	1.0 – 1.2	0.7 – 1.0	0.0125	± 4.88	0.0116	± 2.27	1.19	1.27	0.0149	± 4.73	0.0137	± 2.07	0.84	1.07	0.0159	± 4.75	0.0147	± 2.01	0.79	0.94
37	46 – 66	1.2 – 1.4	-1.0 – -0.7	0.0158	± 4.33	0.0145	± 2.12	1.13	1.18	0.0178	± 4.17	0.0164	± 1.91	0.89	1.05	0.0186	± 4.16	0.0171	± 1.87	0.85	0.95
38	46 – 66	1.2 – 1.4	-0.7 – -0.4	0.1177	± 1.99	0.1151	± 0.76	1.06	1.10	0.1252	± 1.90	0.1224	± 0.71	0.94	1.03	0.1294	± 1.86	0.1264	± 0.67	0.91	0.97
39	46 – 66	1.2 – 1.4	-0.4 – 0.0	0.1518	± 1.65	0.1492	± 0.55	1.09	1.14	0.1651	± 1.49	0.1624	± 0.52	0.92	1.05	0.1737	± 1.44	0.1708	± 0.50	0.87	0.95
40	46 – 66	1.2 – 1.4	0.0 – 0.4	0.1391	± 1.72	0.1346	± 0.57	1.10	1.16	0.1525	± 1.58	0.1475	± 0.54	0.91	1.05	0.1608	± 1.54	0.1556	± 0.52	0.87	0.95
41	46 – 66	1.2 – 1.4	0.4 – 0.7	0.0863	± 2.73	0.0906	± 0.83	1.08	1.13	0.0931	± 2.74	0.0977	± 0.77	0.93	1.05	0.0975	± 2.85	0.1023	± 0.75	0.89	0.96
42	46 – 66	1.2 – 1.4	0.7 – 1.0	0.0114	± 5.38	0.0110	± 2.44	1.18	1.26	0.0135	± 5.08	0.0130	± 2.20	0.85	1.07	0.0144	± 4.96	0.0139	± 2.07	0.79	0.94
43	46 – 66	1.4 – 1.6	-1.0 – -0.7	0.0099	± 5.21	0.0091	± 2.52	1.16	1.21	0.0115	± 4.97	0.0106	± 2.35	0.86	1.04	0.0120	± 4.95	0.0110	± 2.31	0.83	0.96
44	46 – 66	1.4 – 1.6	-0.7 – -0.4	0.1162	± 1.95	0.1142	± 0.74	1.06	1.09	0.1233	± 1.83	0.1211	± 0.69	0.94	1.03	0.1272	± 1.80	0.1250	± 0.68	0.91	0.97
45	46 – 66	1.4 – 1.6	-0.4 – 0.0	0.1547	± 1.54	0.1511	± 0.56	1.08	1.13	0.1670	± 1.45	0.1631	± 0.52	0.93	1.05	0.1751	± 1.42	0.1710	± 0.50	0.88	0.95
46	46 – 66	1.4 – 1.6	0.0 – 0.4	0.1352	± 1.69	0.1349	± 0.59	1.09	1.15	0.1478	± 1.62	0.1474	± 0.56	0.92	1.05	0.1555	± 1.60	0.1550	± 0.52	0.87	0.95
47	46 – 66	1.4 – 1.6	0.4 – 0.7	0.0868	± 2.49	0.0876	± 0.85	1.09	1.13	0.0947	± 2.43	0.0955	± 0.80	0.92	1.04	0.0985	± 2.40	0.0993	± 0.76	0.88	0.96
48	46 – 66	1.4 – 1.6	0.7 – 1.0	0.0084	± 6.16	0.0075	± 2.82	1.17	1.23	0.0098	± 6.06	0.0087	± 2.62	0.86	1.05	0.0103	± 6.09	0.0092	± 2.53	0.81	0.95
49	46 – 66	1.6 – 1.8	-1.0 – -0.7	0.0044	± 7.81	0.0040	± 3.75	1.10	1.12	0.0048	± 7.62	0.0044	± 3.59	0.91	1.02	0.0049	± 7.51	0.0044	± 3.58	0.90	0.98
50	46 – 66	1.6 – 1.8	-0.7 – -0.4	0.0946	± 2.20	0.0941	± 0.82	1.06	1.08	0.1000	± 2.12	0.0995	± 0.78	0.95	1.03	0.1025	± 2.10	0.1020	± 0.75	0.92	0.98
51	46 – 66	1.6 – 1.8	-0.4 – 0.0	0.1509	± 1.57	0.1504	± 0.56	1.07	1.13	0.1618	± 1.50	0.1612	± 0.52	0.93	1.05	0.1700	± 1.48	0.1694	± 0.50	0.89	0.95
52	46 – 66	1.6 – 1.8	0.0 – 0.4	0.1324	± 1.72	0.1314	± 0.59	1.09	1.16	0.1447	± 1.62	0.1436	± 0.55	0.92	1.06	0.1530	± 1.60	0.1518	± 0.53	0.87	0.95
53	46 – 66	1.6 – 1.8	0.4 – 0.7	0.0716	± 2.53	0.0692	± 0.97	1.08	1.12	0.0776	± 2.47	0.0750	± 0.88	0.92	1.04	0.0804	± 2.49	0.0777	± 0.86	0.89	0.97
54	46 – 66	1.6 – 1.8	0.7 – 1.0	0.0036	± 8.17	0.0029	± 4.36	1.19	1.22	0.0042	± 7.91	0.0035	± 4.02	0.84	1.03	0.0044	± 8.12	0.0036	± 3.97	0.82	0.97
55	46 – 66	1.8 – 2.0	-1.0 – -0.7	0.0018	± 11.74	0.0013	± 6.53	1.10	1.15	0.0020	± 11.85	0.0014	± 6.28	0.91	1.04	0.0021	± 12.62	0.0015	± 6.18	0.87	0.96
56	46 – 66	1.8 – 2.0	-0.7 – -0.4	0.0396	± 2.79	0.0376	± 1.26	1.07	1.10	0.0422	± 2.75	0.0401	± 1.20	0.94	1.04	0.0437	± 2.79	0.0415	± 1.17	0.91	0.97
57	46 – 66	1.8 – 2.0	-0.4 – 0.0	0.1520	± 1.64	0.1519	± 0.57	1.07	1.12	0.1629	± 1.55	0.1628	± 0.52	0.93	1.04	0.1697	± 1.54	0.1696	± 0.50	0.90	0.96
58	46 – 66	1.8 – 2.0	0.0 – 0.4	0.1313	± 1.64	0.1291	± 0.59	1.09	1.15	0.1434	± 1.57	0.1410	± 0.55	0.92	1.05	0.1509	± 1.55	0.1483	± 0.53	0.87	0.95
59	46 – 66	1.8 – 2.0	0.4 – 0.7	0.0274	± 3.31	0.0274	± 1.46	1.13	1.17	0.0309	± 3.20	0.0308	± 1.38	0.89	1.04	0.0321	± 3.16	0.0321	± 1.33	0.85	0.96
60	46 – 66	1.8 – 2.0	0.7 – 1.0	0.0014	± 12.97	0.0011	± 7.41	1.15	1.15	0.0016	± 12.53	0.0013	± 6.56	0.87	1.00	0.0016	± 13.13	0.0013	± 6.64	0.87	1.00
61	46 – 66	2.0 – 2.2	-1.0 – -0.7	–	–	–	–	–	–	–	–	–	–	–	–	–	–	–	–	–	–
62	46 – 66	2.0 – 2.2	-0.7 – -0.4	0.0024	± 10.26	0.0021	± 5.12	1.17	1.23	0.0027	± 9.87	0.0025	± 4.82	0.86	1.05	0.0029	± 9.62	0.0026	± 4.72	0.82	0.95
63	46 – 66	2.0 – 2.2	-0.4 – 0.0	0.1155	± 1.69	0.1119	± 0.65	1.07	1.12	0.1239	± 1.63	0.1201	± 0.60	0.93	1.04	0.1294	± 1.63	0.1254	± 0.58	0.89	0.96
64	46 – 66	2.0 – 2.2	0.0 – 0.4	0.0967	± 1.94	0.0943	± 0.68	1.10	1.16	0.1064	± 1.87	0.1037	± 0.66	0.91	1.05	0.1120	± 1.86	0.1092	± 0.62	0.86	0.95
65	46 – 66	2.0 – 2.2	0.4 – 0.7	0.0016	± 11.26	0.0014	± 6.32	1.27	1.40	0.0021	± 10.72	0.0018	± 5.59	0.79	1.10	0.0023	± 10.98	0.0020	± 5.40	0.72	0.91
66	46 – 66	2.0 – 2.2	0.7 – 1.0	–	–	–	–	–	–	–	–	–	–	–	–	–	–	–	–	–	–
67	46 – 66	2.2 – 2.4	-1.0 – -0.7	–	–	–	–	–	–	–	–	–	–	–	–	–	–	–	–	–	–
68	46 – 66	2.2 – 2.4	-0.7 – -0.4	–	–	–	–	–	–	–	–	–	–	–	–	–	–	–	–	–	–
69	46 – 66	2.2 – 2.4	-0.4 – 0.0	0.0386	± 2.66	0.0377	± 1.09	1.08	1.14	0.0417	± 2.61	0.0408	± 1.03	0.92	1.05	0.0439	± 2.59	0.0430	± 0.99	0.88	0.95
70	46 – 66	2.2 – 2.4	0.0 – 0.4	0.0350	± 2.69	0.0342	± 1.14	1.09	1.15	0.0382	± 2.60	0.0373	± 1.09	0.92	1.06	0.0404	± 2.56	0.0394	± 1.04	0.87	0.95
71	46 – 66	2.2 – 2.4	0.4 – 0.7	–	–	–	–	–	–	–	–	–	–	–	–	–	–	–	–	–	–
72	46 – 66	2.2 – 2.4	0.7 – 1.0	–	–	–	–	–	–	–	–	–	–	–	–	–	–	–	–	–	–

TABLE 39: Measured cross-section values unfolded to the Born, dressed and bare truth-levels in the 1$^{\text{st}}$ mass window of the measurement. The luminosity uncertainty of 1.9% is not included.

				Born						Dressed						Bare					
$\mathcal{B}$	$m_{\mu\mu}$ [GeV]	$\lvert y_{\mu\mu}\rvert$	$\cos\theta^*$	$d^3\sigma_{\text{meas.}}$ [pb/GeV]	$\Delta^{\text{total}}_{\text{meas.}}$ [%]	$d^3\sigma_{\text{truth}}$ [pb/GeV]	$\Delta^{\text{Stat.}}_{\text{truth}}$ [%]	$C_{\text{Dres.}}$	C_{Bare}	$d^3\sigma_{\text{meas.}}$ [pb/GeV]	$\Delta^{\text{total}}_{\text{meas.}}$ [%]	$d^3\sigma_{\text{truth}}$ [pb/GeV]	$\Delta^{\text{Stat.}}_{\text{truth}}$ [%]	C_{Born}	C_{Bare}	$d^3\sigma_{\text{meas.}}$ [pb/GeV]	$\Delta^{\text{total}}_{\text{meas.}}$ [%]	$d^3\sigma_{\text{truth}}$ [pb/GeV]	$\Delta^{\text{Stat.}}_{\text{truth}}$ [%]	C_{Born}	$C_{\text{Dres.}}$
73	66 – 80	0.0 – 0.2	-1.0 – -0.7	0.0784	± 2.11	0.0777	± 1.10	1.35	1.66	0.1059	± 1.91	0.1050	± 0.94	0.74	1.23	0.1298	± 1.85	0.1288	± 0.84	0.60	0.82
74	66 – 80	0.0 – 0.2	-0.7 – -0.4	0.1952	± 1.41	0.1911	± 0.70	1.40	1.79	0.2739	± 1.20	0.2679	± 0.59	0.71	1.28	0.3496	± 1.14	0.3417	± 0.52	0.56	0.78
75	66 – 80	0.0 – 0.2	-0.4 – 0.0	0.1702	± 1.49	0.1686	± 0.64	1.44	1.88	0.2453	± 1.33	0.2429	± 0.53	0.69	1.30	0.3199	± 1.31	0.3166	± 0.47	0.53	0.77
76	66 – 80	0.0 – 0.2	0.0 – 0.4	0.1765	± 1.52	0.1688	± 0.64	1.44	1.87	0.2539	± 1.38	0.2425	± 0.53	0.70	1.30	0.3301	± 1.39	0.3148	± 0.47	0.54	0.77
77	66 – 80	0.0 – 0.2	0.4 – 0.7	0.1936	± 1.37	0.1894	± 0.70	1.42	1.81	0.2745	± 1.17	0.2684	± 0.59	0.71	1.28	0.3507	± 1.15	0.3425	± 0.52	0.55	0.78
78	66 – 80	0.0 – 0.2	0.7 – 1.0	0.0762	± 2.08	0.0748	± 1.12	1.36	1.68	0.1036	± 1.92	0.1018	± 0.95	0.73	1.24	0.1282	± 1.86	0.1260	± 0.85	0.59	0.81
79	66 – 80	0.2 – 0.4	-1.0 – -0.7	0.0812	± 2.14	0.0793	± 1.09	1.33	1.63	0.1078	± 2.00	0.1053	± 0.94	0.75	1.23	0.1326	± 1.98	0.1295	± 0.84	0.61	0.81
80	66 – 80	0.2 – 0.4	-0.7 – -0.4	0.1977	± 1.33	0.1955	± 0.69	1.41	1.79	0.2782	± 1.15	0.2749	± 0.58	0.71	1.27	0.3537	± 1.12	0.3493	± 0.51	0.56	0.79
81	66 – 80	0.2 – 0.4	-0.4 – 0.0	0.1725	± 1.47	0.1724	± 0.64	1.43	1.86	0.2461	± 1.24	0.2459	± 0.53	0.70	1.30	0.3206	± 1.22	0.3202	± 0.46	0.54	0.77
82	66 – 80	0.2 – 0.4	0.0 – 0.4	0.1718	± 1.40	0.1658	± 0.65	1.44	1.88	0.2483	± 1.24	0.2395	± 0.54	0.69	1.30	0.3242	± 1.22	0.3125	± 0.47	0.53	0.77
83	66 – 80	0.2 – 0.4	0.4 – 0.7	0.1852	± 1.40	0.1852	± 0.71	1.44	1.85	0.2662	± 1.26	0.2661	± 0.59	0.70	1.29	0.3425	± 1.23	0.3421	± 0.52	0.54	0.78
84	66 – 80	0.2 – 0.4	0.7 – 1.0	0.0745	± 2.02	0.0728	± 1.13	1.36	1.67	0.1016	± 1.91	0.0993	± 0.96	0.73	1.23	0.1244	± 1.87	0.1216	± 0.87	0.60	0.82
85	66 – 80	0.4 – 0.6	-1.0 – -0.7	0.0785	± 2.07	0.0796	± 1.08	1.35	1.64	0.1061	± 1.97	0.1075	± 0.93	0.74	1.21	0.1287	± 1.95	0.1305	± 0.84	0.61	0.82
86	66 – 80	0.4 – 0.6	-0.7 – -0.4	0.1980	± 1.54	0.1968	± 0.69	1.39	1.76	0.2762	± 1.29	0.2744	± 0.58	0.72	1.27	0.3497	± 1.26	0.3473	± 0.51	0.57	0.79
87	66 – 80	0.4 – 0.6	-0.4 – 0.0	0.1780	± 1.28	0.1730	± 0.63	1.42	1.84	0.2528	± 1.11	0.2456	± 0.53	0.70	1.29	0.3277	± 1.09	0.3180	± 0.46	0.54	0.77
88	66 – 80	0.4 – 0.6	0.0 – 0.4	0.1700	± 1.30	0.1649	± 0.65	1.45	1.90	0.2460	± 1.14	0.2384	± 0.54	0.69	1.31	0.3233	± 1.12	0.3130	± 0.47	0.53	0.76
89	66 – 80	0.4 – 0.6	0.4 – 0.7	0.1808	± 1.48	0.1766	± 0.73	1.45	1.88	0.2632	± 1.38	0.2568	± 0.60	0.69	1.29	0.3401	± 1.38	0.3316	± 0.53	0.53	0.77
90	66 – 80	0.4 – 0.6	0.7 – 1.0	0.0736	± 2.11	0.0739	± 1.13	1.37	1.67	0.1009	± 1.99	0.1013	± 0.96	0.73	1.22	0.1228	± 2.00	0.1234	± 0.86	0.60	0.82
91	66 – 80	0.6 – 0.8	-1.0 – -0.7	0.0836	± 2.16	0.0822	± 1.07	1.32	1.59	0.1103	± 2.00	0.1085	± 0.92	0.76	1.21	0.1332	± 1.98	0.1311	± 0.84	0.63	0.83
92	66 – 80	0.6 – 0.8	-0.7 – -0.4	0.2012	± 1.50	0.1983	± 0.69	1.39	1.76	0.2798	± 1.29	0.2756	± 0.58	0.72	1.27	0.3550	± 1.25	0.3493	± 0.51	0.57	0.79
93	66 – 80	0.6 – 0.8	-0.4 – 0.0	0.1751	± 1.39	0.1728	± 0.64	1.41	1.83	0.2477	± 1.11	0.2444	± 0.53	0.71	1.29	0.3202	± 1.04	0.3158	± 0.47	0.55	0.77
94	66 – 80	0.6 – 0.8	0.0 – 0.4	0.1671	± 1.18	0.1628	± 0.65	1.45	1.90	0.2418	± 1.07	0.2354	± 0.54	0.69	1.32	0.3184	± 1.05	0.3097	± 0.47	0.53	0.76
95	66 – 80	0.6 – 0.8	0.4 – 0.7	0.1765	± 1.50	0.1728	± 0.73	1.46	1.88	0.2572	± 1.39	0.2517	± 0.61	0.69	1.29	0.3316	± 1.37	0.3244	± 0.53	0.53	0.78
96	66 – 80	0.6 – 0.8	0.7 – 1.0	0.0716	± 2.21	0.0696	± 1.16	1.39	1.72	0.0997	± 2.08	0.0970	± 0.98	0.72	1.24	0.1231	± 2.03	0.1198	± 0.87	0.58	0.81
97	66 – 80	0.8 – 1.0	-1.0 – -0.7	0.0830	± 2.22	0.0836	± 1.06	1.32	1.59	0.1099	± 2.06	0.1107	± 0.92	0.76	1.20	0.1323	± 2.04	0.1332	± 0.83	0.63	0.83
98	66 – 80	0.8 – 1.0	-0.7 – -0.4	0.2068	± 1.44	0.2061	± 0.67	1.36	1.72	0.2814	± 1.17	0.2803	± 0.57	0.74	1.26	0.3560	± 1.12	0.3543	± 0.51	0.58	0.79
99	66 – 80	0.8 – 1.0	-0.4 – 0.0	0.1756	± 1.24	0.1724	± 0.64	1.40	1.83	0.2469	± 1.03	0.2422	± 0.54	0.71	1.30	0.3213	± 0.98	0.3149	± 0.47	0.55	0.77
100	66 – 80	0.8 – 1.0	0.0 – 0.4	0.1630	± 1.18	0.1599	± 0.66	1.44	1.90	0.2354	± 1.07	0.2309	± 0.55	0.69	1.31	0.3097	± 1.04	0.3036	± 0.48	0.53	0.76
101	66 – 80	0.8 – 1.0	0.4 – 0.7	0.1716	± 1.38	0.1695	± 0.74	1.47	1.91	0.2528	± 1.23	0.2497	± 0.61	0.68	1.30	0.3285	± 1.19	0.3245	± 0.53	0.52	0.77
102	66 – 80	0.8 – 1.0	0.7 – 1.0	0.0672	± 2.59	0.0683	± 1.18	1.39	1.73	0.0932	± 2.55	0.0947	± 0.99	0.72	1.25	0.1162	± 2.66	0.1181	± 0.88	0.58	0.80
103	66 – 80	1.0 – 1.2	-1.0 – -0.7	0.0835	± 2.31	0.0831	± 1.06	1.30	1.55	0.1080	± 2.21	0.1077	± 0.93	0.77	1.20	0.1294	± 2.26	0.1292	± 0.84	0.64	0.83
104	66 – 80	1.0 – 1.2	-0.7 – -0.4	0.2053	± 1.55	0.2046	± 0.67	1.37	1.71	0.2807	± 1.23	0.2797	± 0.58	0.73	1.25	0.3520	± 1.18	0.3507	± 0.51	0.58	0.80
105	66 – 80	1.0 – 1.2	-0.4 – 0.0	0.1756	± 1.26	0.1712	± 0.64	1.40	1.82	0.2453	± 1.06	0.2391	± 0.54	0.72	1.30	0.3197	± 1.02	0.3113	± 0.47	0.55	0.77
106	66 – 80	1.0 – 1.2	0.0 – 0.4	0.1591	± 1.19	0.1563	± 0.67	1.45	1.92	0.2315	± 1.08	0.2273	± 0.55	0.69	1.32	0.3061	± 1.05	0.3003	± 0.48	0.52	0.76
107	66 – 80	1.0 – 1.2	0.4 – 0.7	0.1631	± 1.53	0.1626	± 0.76	1.49	1.94	0.2424	± 1.36	0.2419	± 0.62	0.67	1.31	0.3168	± 1.34	0.3162	± 0.54	0.51	0.76
108	66 – 80	1.0 – 1.2	0.7 – 1.0	0.0666	± 2.72	0.0642	± 1.20	1.42	1.76	0.0947	± 2.63	0.0914	± 1.00	0.70	1.23	0.1168	± 2.61	0.1128	± 0.90	0.57	0.81
109	66 – 80	1.2 – 1.4	-1.0 – -0.7	0.0695	± 2.35	0.0681	± 1.17	1.26	1.53	0.0877	± 2.16	0.0861	± 1.03	0.79	1.21	0.1059	± 2.11	0.1040	± 0.94	0.65	0.83
110	66 – 80	1.2 – 1.4	-0.7 – -0.4	0.2115	± 1.48	0.2057	± 0.67	1.35	1.69	0.2854	± 1.20	0.2775	± 0.58	0.74	1.25	0.3580	± 1.17	0.3481	± 0.51	0.59	0.80
111	66 – 80	1.2 – 1.4	-0.4 – 0.0	0.1764	± 1.27	0.1715	± 0.64	1.39	1.81	0.2457	± 1.06	0.2387	± 0.54	0.72	1.30	0.3196	± 1.01	0.3104	± 0.47	0.55	0.77
112	66 – 80	1.2 – 1.4	0.0 – 0.4	0.1550	± 1.38	0.1529	± 0.67	1.45	1.94	0.2249	± 1.29	0.2219	± 0.56	0.69	1.33	0.3001	± 1.29	0.2962	± 0.48	0.52	0.75
113	66 – 80	1.2 – 1.4	0.4 – 0.7	0.1584	± 1.67	0.1553	± 0.78	1.51	1.97	0.2394	± 1.45	0.2345	± 0.63	0.66	1.30	0.3126	± 1.46	0.3057	± 0.55	0.51	0.77
114	66 – 80	1.2 – 1.4	0.7 – 1.0	0.0490	± 2.75	0.0491	± 1.38	1.42	1.77	0.0698	± 2.54	0.0699	± 1.15	0.70	1.25	0.0868	± 2.56	0.0871	± 1.02	0.56	0.80
115	66 – 80	1.4 – 1.6	-1.0 – -0.7	0.0277	± 3.49	0.0270	± 1.87	1.30	1.57	0.0360	± 3.26	0.0351	± 1.62	0.77	1.20	0.0433	± 3.22	0.0423	± 1.48	0.64	0.83
116	66 – 80	1.4 – 1.6	-0.7 – -0.4	0.2058	± 1.55	0.2025	± 0.68	1.32	1.64	0.2722	± 1.30	0.2679	± 0.59	0.76	1.24	0.3383	± 1.26	0.3328	± 0.53	0.61	0.80
117	66 – 80	1.4 – 1.6	-0.4 – 0.0	0.1786	± 1.23	0.1741	± 0.63	1.37	1.78	0.2451	± 1.05	0.2390	± 0.54	0.73	1.30	0.3178	± 1.02	0.3097	± 0.47	0.56	0.77
118	66 – 80	1.4 – 1.6	0.0 – 0.4	0.1550	± 1.31	0.1484	± 0.68	1.45	1.94	0.2254	± 1.20	0.2158	± 0.57	0.69	1.33	0.3008	± 1.23	0.2877	± 0.49	0.52	0.75
119	66 – 80	1.4 – 1.6	0.4 – 0.7	0.1435	± 1.70	0.1418	± 0.81	1.50	1.98	0.2159	± 1.39	0.2131	± 0.66	0.67	1.32	0.2843	± 1.34	0.2807	± 0.57	0.51	0.76
120	66 – 80	1.4 – 1.6	0.7 – 1.0	0.0198	± 4.07	0.0187	± 2.24	1.45	1.86	0.0288	± 3.80	0.0271	± 1.84	0.69	1.28	0.0369	± 3.75	0.0348	± 1.62	0.54	0.78
121	66 – 80	1.6 – 1.8	-1.0 – -0.7	0.0058	± 10.70	0.0047	± 4.45	1.27	1.65	0.0073	± 11.24	0.0059	± 3.91	0.79	1.30	0.0095	± 11.84	0.0077	± 3.44	0.61	0.77
122	66 – 80	1.6 – 1.8	-0.7 – -0.4	0.1461	± 1.86	0.1448	± 0.80	1.32	1.64	0.1926	± 1.67	0.1909	± 0.69	0.76	1.24	0.2397	± 1.64	0.2375	± 0.62	0.61	0.80
123	66 – 80	1.6 – 1.8	-0.4 – 0.0	0.1746	± 1.30	0.1695	± 0.64	1.37	1.78	0.2398	± 1.10	0.2327	± 0.55	0.73	1.30	0.3108	± 1.06	0.3014	± 0.48	0.56	0.77
124	66 – 80	1.6 – 1.8	0.0 – 0.4	0.1479	± 1.33	0.1425	± 0.70	1.47	1.96	0.2177	± 1.21	0.2096	± 0.57	0.68	1.34	0.2909	± 1.22	0.2799	± 0.50	0.51	0.75
125	66 – 80	1.6 – 1.8	0.4 – 0.7	0.0973	± 2.19	0.0970	± 0.98	1.53	2.03	0.1492	± 1.89	0.1488	± 0.79	0.65	1.32	0.1973	± 1.85	0.1969	± 0.68	0.49	0.76
126	66 – 80	1.6 – 1.8	0.7 – 1.0	0.0040	± 7.17	0.0035	± 5.15	1.49	1.96	0.0060	± 6.59	0.0053	± 4.21	0.67	1.31	0.0078	± 6.35	0.0069	± 3.65	0.51	0.76
127	66 – 80	1.8 – 2.0	-1.0 – -0.7	0.0020	± 11.17	0.0016	± 7.75	1.09	1.36	0.0022	± 11.16	0.0017	± 7.35	0.91	1.24	0.0028	± 10.95	0.0021	± 6.57	0.73	0.80
128	66 – 80	1.8 – 2.0	-0.7 – -0.4	0.0540	± 2.53	0.0528	± 1.33	1.34	1.69	0.0726	± 2.38	0.0709	± 1.14	0.74	1.26	0.0913	± 2.39	0.0892	± 1.02	0.59	0.79
129	66 – 80	1.8 – 2.0	-0.4 – 0.0	0.1727	± 1.44	0.1682	± 0.64	1.36	1.74	0.2347	± 1.29	0.2284	± 0.55	0.74	1.28	0.3011	± 1.25	0.2928	± 0.48	0.57	0.78
130	66 – 80	1.8 – 2.0	0.0 – 0.4	0.1404	± 1.50	0.1365	± 0.71	1.46	1.93	0.2050	± 1.37	0.1992	± 0.59	0.69	1.33	0.2718	± 1.35	0.2641	± 0.51	0.52	0.75
131	66 – 80	1.8 – 2.0	0.4 – 0.7	0.0340	± 3.33	0.0344	± 1.64	1.60	2.17	0.0543	± 3.07	0.0549	± 1.29	0.63	1.36	0.0739	± 3.14	0.0749	± 1.11	0.46	0.73
132	66 – 80	1.8 – 2.0	0.7 – 1.0	0.0009	± 13.78	0.0007	± 10.99	1.40	1.82	0.0012	± 12.58	0.0010	± 9.38	0.71	1.30	0.0016	± 12.16	0.0014	± 8.24	0.55	0.77
133	66 – 80	2.0 – 2.2	-1.0 – -0.7	–	–	–	–	–	–	–	–	–	–	–	–	–	–	–	–	–	–
134	66 – 80	2.0 – 2.2	-0.7 – -0.4	0.0035	± 10.81	0.0030	± 5.53	1.45	1.95	0.0050	± 10.50	0.0044	± 4.56	0.69	1.34	0.0067	± 10.76	0.0059	± 3.95	0.51	0.74
135	66 – 80	2.0 – 2.2	-0.4 – 0.0	0.1254	± 1.66	0.1218	± 0.76	1.36	1.75	0.1701	± 1.56	0.1651	± 0.65	0.74	1.29	0.2191	± 1.54	0.2127	± 0.57	0.57	0.78
136	66 – 80	2.0 – 2.2	0.0 – 0.4	0.1000	± 1.88	0.0981	± 0.84	1.47	1.95	0.1470	± 1.77	0.1443	± 0.69	0.68	1.33	0.1949	± 1.75	0.1913	± 0.60	0.51	0.75
137	66 – 80	2.0 – 2.2	0.4 – 0.7	0.0024	± 8.99	0.0022	± 6.43	1.63	2.32	0.0040	± 8.17	0.0036	± 5.04	0.61	1.42	0.0056	± 7.84	0.0051	± 4.20	0.43	0.70
138	66 – 80	2.0 – 2.2	0.7 – 1.0	–	–	–	–	–	–	–	–	–	–	–	–	–	–	–	–	–	–
139	66 – 80	2.2 – 2.4	-1.0 – -0.7	–	–	–	–	–	–	–	–	–	–	–	–	–	–	–	–	–	–
140	66 – 80	2.2 – 2.4	-0.7 – -0.4	–	–	–	–	–	–	–	–	–	–	–	–	–	–	–	–	–	–
141	66 – 80	2.2 – 2.4	-0.4 – 0.0	0.0394	± 3.33	0.0390	± 1.34	1.39	1.77	0.0548	± 3.27	0.0543	± 1.13	0.72	1.28	0.0699	± 3.32	0.0693	± 1.00	0.56	0.78
142	66 – 80	2.2 – 2.4	0.0 – 0.4	0.0363	± 2.89	0.0345	± 1.42	1.42	1.89	0.0516	± 2.82	0.0490	± 1.18	0.70	1.33	0.0688	± 2.83	0.0652	± 1.03	0.53	0.75
143	66 – 80	2.2 – 2.4	0.4 – 0.7	–	–	–	–	–	–	–	–	–	–	–	–	–	–	–	–	–	–
144	66 – 80	2.2 – 2.4	0.7 – 1.0	–	–	–	–	–	–	–	–	–	–	–	–	–	–	–	–	–	–

TABLE 40: Measured cross-section values unfolded to the Born, dressed and bare truth-levels in the 2$^{\text{nd}}$ mass window of the measurement. The luminosity uncertainty of 1.9% is not included.

$\mathcal{B}$	$m_{\mu\mu}$ [GeV]	$\lvert y_{\mu\mu}\rvert$	$\cos\theta^*$	Born						Dressed						Bare					
				$d^3\sigma_{\text{meas.}}$ [pb/GeV]	$\Delta^{\text{total}}_{\text{meas.}}$ [%]	$d^3\sigma_{\text{truth}}$ [pb/GeV]	$\Delta^{\text{Stat.}}_{\text{truth}}$ [%]	$C_{\text{Dres.}}$	C_{Bare}	$d^3\sigma_{\text{meas.}}$ [pb/GeV]	$\Delta^{\text{total}}_{\text{meas.}}$ [%]	$d^3\sigma_{\text{truth}}$ [pb/GeV]	$\Delta^{\text{Stat.}}_{\text{truth}}$ [%]	C_{Born}	C_{Bare}	$d^3\sigma_{\text{meas.}}$ [pb/GeV]	$\Delta^{\text{total}}_{\text{meas.}}$ [%]	$d^3\sigma_{\text{truth}}$ [pb/GeV]	$\Delta^{\text{Stat.}}_{\text{truth}}$ [%]	C_{Born}	$C_{\text{Dres.}}$
145	80 – 91	0.0 – 0.2	-1.0 – -0.7	2.2379	± 0.70	2.2410	± 0.23	0.96	1.06	2.1436	± 0.73	2.1472	± 0.24	1.04	1.11	2.3686	± 0.73	2.3728	± 0.22	0.94	0.90
146	80 – 91	0.0 – 0.2	-0.7 – -0.4	3.5689	± 0.61	3.5231	± 0.18	0.98	1.07	3.4800	± 0.61	3.4354	± 0.19	1.03	1.10	3.8312	± 0.60	3.7823	± 0.18	0.93	0.91
147	80 – 91	0.0 – 0.2	-0.4 – 0.0	3.0719	± 0.78	3.0121	± 0.17	0.98	1.07	3.0153	± 0.79	2.9559	± 0.17	1.02	1.09	3.2978	± 0.78	3.2322	± 0.17	0.93	0.91
148	80 – 91	0.0 – 0.2	0.0 – 0.4	3.0748	± 0.83	3.0075	± 0.17	0.98	1.07	3.0160	± 0.83	2.9503	± 0.17	1.02	1.09	3.2964	± 0.83	3.2256	± 0.17	0.93	0.91
149	80 – 91	0.0 – 0.2	0.4 – 0.7	3.5641	± 0.70	3.5033	± 0.19	0.98	1.07	3.4801	± 0.70	3.4208	± 0.19	1.02	1.10	3.8273	± 0.69	3.7619	± 0.18	0.93	0.91
150	80 – 91	0.0 – 0.2	0.7 – 1.0	2.2575	± 0.73	2.2397	± 0.23	0.96	1.06	2.1628	± 0.72	2.1457	± 0.24	1.04	1.11	2.3904	± 0.71	2.3718	± 0.22	0.94	0.90
151	80 – 91	0.2 – 0.4	-1.0 – -0.7	2.2473	± 0.70	2.2413	± 0.23	0.96	1.06	2.1556	± 0.72	2.1502	± 0.24	1.04	1.10	2.3736	± 0.72	2.3677	± 0.22	0.95	0.91
152	80 – 91	0.2 – 0.4	-0.7 – -0.4	3.5357	± 0.63	3.5034	± 0.19	0.97	1.07	3.4384	± 0.65	3.4068	± 0.19	1.03	1.10	3.7896	± 0.65	3.7550	± 0.18	0.93	0.91
153	80 – 91	0.2 – 0.4	-0.4 – 0.0	3.0562	± 1.04	3.0026	± 0.17	0.98	1.07	2.9927	± 1.03	2.9399	± 0.17	1.02	1.10	3.2786	± 1.03	3.2193	± 0.17	0.93	0.91
154	80 – 91	0.2 – 0.4	0.0 – 0.4	3.0770	± 0.75	3.0058	± 0.17	0.98	1.07	3.0158	± 0.76	2.9459	± 0.17	1.02	1.10	3.3058	± 0.75	3.2298	± 0.17	0.93	0.91
155	80 – 91	0.2 – 0.4	0.4 – 0.7	3.5745	± 0.71	3.5120	± 0.18	0.97	1.07	3.4807	± 0.73	3.4190	± 0.19	1.03	1.10	3.8360	± 0.75	3.7677	± 0.18	0.93	0.91
156	80 – 91	0.2 – 0.4	0.7 – 1.0	2.2615	± 0.89	2.2403	± 0.23	0.96	1.06	2.1747	± 0.89	2.1541	± 0.23	1.04	1.10	2.4000	± 0.89	2.3775	± 0.22	0.94	0.91
157	80 – 91	0.4 – 0.6	-1.0 – -0.7	2.2311	± 0.64	2.2186	± 0.23	0.96	1.06	2.1468	± 0.65	2.1348	± 0.24	1.04	1.10	2.3552	± 0.64	2.3418	± 0.22	0.95	0.91
158	80 – 91	0.4 – 0.6	-0.7 – -0.4	3.5180	± 0.76	3.4973	± 0.19	0.97	1.07	3.4154	± 0.76	3.3956	± 0.19	1.03	1.10	3.7637	± 0.76	3.7420	± 0.18	0.93	0.91
159	80 – 91	0.4 – 0.6	-0.4 – 0.0	3.0479	± 0.76	2.9914	± 0.17	0.98	1.07	2.9721	± 0.76	2.9172	± 0.17	1.03	1.10	3.2685	± 0.76	3.2081	± 0.17	0.93	0.91
160	80 – 91	0.4 – 0.6	0.0 – 0.4	3.0647	± 0.65	2.9909	± 0.17	0.98	1.07	2.9908	± 0.66	2.9187	± 0.17	1.02	1.10	3.2870	± 0.65	3.2079	± 0.17	0.93	0.91
161	80 – 91	0.4 – 0.6	0.4 – 0.7	3.5473	± 0.78	3.4942	± 0.19	0.97	1.07	3.4449	± 0.79	3.3930	± 0.19	1.03	1.11	3.8111	± 0.79	3.7542	± 0.18	0.93	0.90
162	80 – 91	0.4 – 0.6	0.7 – 1.0	2.2428	± 0.66	2.2313	± 0.23	0.96	1.06	2.1635	± 0.65	2.1526	± 0.23	1.04	1.10	2.3788	± 0.64	2.3671	± 0.22	0.94	0.91
163	80 – 91	0.6 – 0.8	-1.0 – -0.7	2.2134	± 0.79	2.2213	± 0.23	0.96	1.05	2.1320	± 0.83	2.1400	± 0.24	1.04	1.09	2.3340	± 0.86	2.3430	± 0.22	0.95	0.91
164	80 – 91	0.6 – 0.8	-0.7 – -0.4	3.5049	± 0.90	3.4663	± 0.19	0.97	1.07	3.3950	± 0.90	3.3578	± 0.19	1.03	1.10	3.7477	± 0.90	3.7062	± 0.18	0.94	0.91
165	80 – 91	0.6 – 0.8	-0.4 – 0.0	3.0424	± 0.56	2.9579	± 0.17	0.97	1.07	2.9471	± 0.58	2.8642	± 0.18	1.03	1.11	3.2627	± 0.58	3.1700	± 0.17	0.93	0.90
166	80 – 91	0.6 – 0.8	0.0 – 0.4	3.0453	± 0.57	2.9668	± 0.17	0.97	1.07	2.9536	± 0.58	2.8770	± 0.18	1.03	1.11	3.2729	± 0.58	3.1880	± 0.17	0.93	0.90
167	80 – 91	0.6 – 0.8	0.4 – 0.7	3.5218	± 0.85	3.4585	± 0.19	0.97	1.08	3.4150	± 0.87	3.3531	± 0.19	1.03	1.11	3.7869	± 0.87	3.7186	± 0.18	0.93	0.90
168	80 – 91	0.6 – 0.8	0.7 – 1.0	2.2279	± 0.68	2.2074	± 0.23	0.97	1.06	2.1554	± 0.67	2.1355	± 0.24	1.03	1.10	2.3672	± 0.66	2.3455	± 0.22	0.94	0.91
169	80 – 91	0.8 – 1.0	-1.0 – -0.7	2.1907	± 0.90	2.1792	± 0.24	0.96	1.05	2.1117	± 0.89	2.1004	± 0.24	1.04	1.09	2.3078	± 0.88	2.2955	± 0.23	0.95	0.92
170	80 – 91	0.8 – 1.0	-0.7 – -0.4	3.4648	± 0.97	3.4321	± 0.19	0.97	1.07	3.3627	± 0.98	3.3313	± 0.19	1.03	1.10	3.7059	± 0.99	3.6708	± 0.18	0.93	0.91
171	80 – 91	0.8 – 1.0	-0.4 – 0.0	3.0237	± 0.64	2.9316	± 0.18	0.96	1.07	2.9081	± 0.68	2.8180	± 0.18	1.04	1.12	3.2466	± 0.69	3.1454	± 0.17	0.93	0.90
172	80 – 91	0.8 – 1.0	0.0 – 0.4	3.0125	± 0.59	2.9283	± 0.18	0.96	1.08	2.8962	± 0.59	2.8143	± 0.18	1.04	1.12	3.2414	± 0.59	3.1492	± 0.17	0.93	0.89
173	80 – 91	0.8 – 1.0	0.4 – 0.7	3.4956	± 0.99	3.4312	± 0.19	0.97	1.08	3.3994	± 1.03	3.3359	± 0.19	1.03	1.11	3.7604	± 1.05	3.6900	± 0.18	0.93	0.90
174	80 – 91	0.8 – 1.0	0.7 – 1.0	2.2070	± 0.81	2.1827	± 0.24	0.97	1.06	2.1347	± 0.81	2.1112	± 0.24	1.03	1.10	2.3441	± 0.79	2.3183	± 0.23	0.94	0.91
175	80 – 91	1.0 – 1.2	-1.0 – -0.7	1.9416	± 0.90	1.9298	± 0.25	0.97	1.06	1.8778	± 0.91	1.8664	± 0.25	1.03	1.09	2.0533	± 0.89	2.0410	± 0.24	0.95	0.91
176	80 – 91	1.0 – 1.2	-0.7 – -0.4	3.4388	± 0.65	3.3782	± 0.19	0.97	1.07	3.3270	± 0.65	3.2680	± 0.19	1.03	1.10	3.6762	± 0.64	3.6103	± 0.18	0.94	0.91
177	80 – 91	1.0 – 1.2	-0.4 – 0.0	2.9757	± 0.61	2.8869	± 0.18	0.96	1.07	2.8461	± 0.62	2.7604	± 0.18	1.05	1.12	3.1891	± 0.61	3.0927	± 0.17	0.93	0.89
178	80 – 91	1.0 – 1.2	0.0 – 0.4	2.9896	± 0.76	2.8912	± 0.18	0.96	1.07	2.8599	± 0.82	2.7640	± 0.18	1.05	1.12	3.2147	± 0.84	3.1064	± 0.17	0.93	0.89
179	80 – 91	1.0 – 1.2	0.4 – 0.7	3.4426	± 0.64	3.3858	± 0.19	0.97	1.08	3.3398	± 0.63	3.2845	± 0.19	1.03	1.11	3.7063	± 0.62	3.6444	± 0.18	0.93	0.90
180	80 – 91	1.0 – 1.2	0.7 – 1.0	1.9292	± 1.00	1.9186	± 0.25	0.97	1.07	1.8697	± 1.02	1.8597	± 0.25	1.03	1.10	2.0596	± 1.03	2.0487	± 0.24	0.94	0.91
181	80 – 91	1.2 – 1.4	-1.0 – -0.7	1.2781	± 0.96	1.2601	± 0.31	0.97	1.06	1.2357	± 0.95	1.2183	± 0.31	1.03	1.10	1.3537	± 0.94	1.3347	± 0.30	0.94	0.91
182	80 – 91	1.2 – 1.4	-0.7 – -0.4	3.3831	± 0.67	3.3172	± 0.19	0.96	1.07	3.2559	± 0.67	3.1924	± 0.19	1.04	1.11	3.6068	± 0.67	3.5366	± 0.18	0.94	0.90
183	80 – 91	1.2 – 1.4	-0.4 – 0.0	2.9439	± 0.62	2.8505	± 0.18	0.95	1.07	2.8077	± 0.63	2.7181	± 0.18	1.05	1.12	3.1536	± 0.62	3.0526	± 0.17	0.93	0.89
184	80 – 91	1.2 – 1.4	0.0 – 0.4	2.9419	± 0.77	2.8411	± 0.18	0.95	1.08	2.8101	± 0.83	2.7122	± 0.18	1.05	1.13	3.1682	± 0.85	3.0573	± 0.17	0.93	0.89
185	80 – 91	1.2 – 1.4	0.4 – 0.7	3.3634	± 0.75	3.3198	± 0.19	0.97	1.08	3.2516	± 0.75	3.2097	± 0.19	1.03	1.11	3.6242	± 0.74	3.5777	± 0.18	0.93	0.90
186	80 – 91	1.2 – 1.4	0.7 – 1.0	1.2716	± 1.18	1.2682	± 0.31	0.97	1.07	1.2322	± 1.28	1.2295	± 0.31	1.03	1.10	1.3589	± 1.33	1.3561	± 0.30	0.94	0.91
187	80 – 91	1.4 – 1.6	-1.0 – -0.7	0.4838	± 1.42	0.4711	± 0.51	0.96	1.06	0.4660	± 1.39	0.4537	± 0.51	1.04	1.10	0.5122	± 1.36	0.4988	± 0.49	0.94	0.91
188	80 – 91	1.4 – 1.6	-0.7 – -0.4	3.1512	± 1.05	3.0923	± 0.20	0.96	1.07	3.0247	± 1.08	2.9678	± 0.20	1.04	1.11	3.3594	± 1.10	3.2963	± 0.19	0.94	0.90
189	80 – 91	1.4 – 1.6	-0.4 – 0.0	2.8767	± 0.62	2.7929	± 0.18	0.95	1.07	2.7399	± 0.64	2.6597	± 0.18	1.05	1.12	3.0798	± 0.64	2.9896	± 0.17	0.93	0.89
190	80 – 91	1.4 – 1.6	0.0 – 0.4	2.8817	± 0.64	2.7895	± 0.18	0.95	1.08	2.7477	± 0.65	2.6596	± 0.18	1.05	1.13	3.1000	± 0.65	3.0009	± 0.17	0.93	0.89
191	80 – 91	1.4 – 1.6	0.4 – 0.7	3.1030	± 1.18	3.0707	± 0.20	0.96	1.08	2.9895	± 1.22	2.9592	± 0.20	1.04	1.12	3.3457	± 1.23	3.3117	± 0.19	0.93	0.89
192	80 – 91	1.4 – 1.6	0.7 – 1.0	0.4749	± 1.12	0.4677	± 0.51	0.97	1.07	0.4601	± 1.09	0.4531	± 0.51	1.03	1.11	0.5102	± 1.06	0.5026	± 0.48	0.93	0.90
193	80 – 91	1.6 – 1.8	-1.0 – -0.7	0.0900	± 2.62	0.0827	± 1.21	0.96	1.06	0.0863	± 2.60	0.0792	± 1.22	1.04	1.11	0.0955	± 2.48	0.0878	± 1.16	0.94	0.90
194	80 – 91	1.6 – 1.8	-0.7 – -0.4	2.2120	± 0.99	2.1655	± 0.24	0.95	1.06	2.1123	± 1.02	2.0675	± 0.24	1.05	1.11	2.3514	± 1.02	2.3014	± 0.23	0.94	0.90
195	80 – 91	1.6 – 1.8	-0.4 – 0.0	2.8230	± 0.67	2.7246	± 0.18	0.95	1.07	2.6946	± 0.70	2.5999	± 0.18	1.05	1.12	3.0208	± 0.70	2.9144	± 0.17	0.93	0.89
196	80 – 91	1.6 – 1.8	0.0 – 0.4	2.8078	± 0.88	2.7209	± 0.18	0.96	1.08	2.6827	± 0.88	2.5998	± 0.18	1.05	1.13	3.0249	± 0.88	2.9314	± 0.17	0.93	0.89
197	80 – 91	1.6 – 1.8	0.4 – 0.7	2.1911	± 1.29	2.1600	± 0.24	0.96	1.08	2.0997	± 1.30	2.0701	± 0.24	1.04	1.13	2.3655	± 1.29	2.3316	± 0.23	0.93	0.89
198	80 – 91	1.6 – 1.8	0.7 – 1.0	0.0892	± 1.93	0.0831	± 1.21	0.96	1.08	0.0855	± 1.93	0.0798	± 1.22	1.04	1.12	0.0960	± 1.89	0.0895	± 1.15	0.93	0.89
199	80 – 91	1.8 – 2.0	-1.0 – -0.7	0.0209	± 6.35	0.0174	± 2.62	0.95	1.04	0.0198	± 6.53	0.0165	± 2.68	1.05	1.10	0.0218	± 6.59	0.0182	± 2.55	0.96	0.91
200	80 – 91	1.8 – 2.0	-0.7 – -0.4	0.8019	± 1.69	0.7739	± 0.39	0.95	1.06	0.7627	± 1.75	0.7359	± 0.40	1.05	1.12	0.8523	± 1.80	0.8223	± 0.38	0.94	0.89
201	80 – 91	1.8 – 2.0	-0.4 – 0.0	2.7056	± 1.52	2.6084	± 0.19	0.95	1.07	2.5792	± 1.62	2.4852	± 0.19	1.05	1.12	2.8905	± 1.66	2.7851	± 0.18	0.94	0.89
202	80 – 91	1.8 – 2.0	0.0 – 0.4	2.6807	± 1.55	2.6055	± 0.19	0.95	1.08	2.5597	± 1.57	2.4883	± 0.19	1.05	1.13	2.8859	± 1.59	2.8052	± 0.18	0.93	0.89
203	80 – 91	1.8 – 2.0	0.4 – 0.7	0.7840	± 1.37	0.7670	± 0.40	0.96	1.08	0.7489	± 1.39	0.7326	± 0.40	1.05	1.13	0.8470	± 1.38	0.8284	± 0.38	0.93	0.88
204	80 – 91	1.8 – 2.0	0.7 – 1.0	0.0192	± 5.62	0.0170	± 2.66	0.92	1.06	0.0178	± 5.82	0.0156	± 2.75	1.08	1.15	0.0205	± 5.88	0.0181	± 2.55	0.94	0.87
205	80 – 91	2.0 – 2.2	-1.0 – -0.7	0.0025	± 10.57	0.0022	± 7.39	0.89	1.01	0.0023	± 11.02	0.0020	± 7.69	1.13	1.14	0.0025	± 10.81	0.0022	± 7.25	0.99	0.88
206	80 – 91	2.0 – 2.2	-0.7 – -0.4	0.0487	± 3.57	0.0475	± 1.59	0.96	1.08	0.0468	± 3.55	0.0456	± 1.61	1.04	1.12	0.0524	± 3.51	0.0512	± 1.52	0.93	0.89
207	80 – 91	2.0 – 2.2	-0.4 – 0.0	1.9323	± 0.92	1.8673	± 0.22	0.95	1.07	1.8409	± 0.96	1.7785	± 0.22	1.05	1.12	2.0679	± 0.96	1.9978	± 0.21	0.93	0.89
208	80 – 91	2.0 – 2.2	0.0 – 0.4	1.9236	± 1.25	1.8647	± 0.22	0.95	1.08	1.8348	± 1.26	1.7786	± 0.22	1.05	1.13	2.0710	± 1.26	2.0072	± 0.21	0.93	0.89
209	80 – 91	2.0 – 2.2	0.4 – 0.7	0.0490	± 3.55	0.0465	± 1.61	0.95	1.09	0.0467	± 3.61	0.0444	± 1.64	1.05	1.14	0.0533	± 3.62	0.0506	± 1.53	0.92	0.88
210	80 – 91	2.0 – 2.2	0.7 – 1.0	0.0026	± 17.28	0.0021	± 7.45	0.93	1.03	0.0025	± 18.70	0.0020	± 7.70	1.07	1.11	0.0028	± 19.10	0.0022	± 7.28	0.97	0.90
211	80 – 91	2.2 – 2.4	-1.0 – -0.7	–	–	–	–	–	–	–	–	–	–	–	–	–	–	–	–	–	–
212	80 – 91	2.2 – 2.4	-0.7 – -0.4	–	–	–	–	–	–	–	–	–	–	–	–	–	–	–	–	–	–
213	80 – 91	2.2 – 2.4	-0.4 – 0.0	0.6426	± 1.19	0.6196	± 0.38	0.95	1.07	0.6103	± 1.16	0.5884	± 0.39	1.05	1.13	0.6896	± 1.14	0.6646	± 0.37	0.93	0.89
214	80 – 91	2.2 – 2.4	0.0 – 0.4	0.6441	± 1.08	0.6144	± 0.38	0.95	1.07	0.6141	± 1.11	0.5855	± 0.39	1.05	1.13	0.6920	± 1.10	0.6598	± 0.37	0.93	0.89
215	80 – 91	2.2 – 2.4	0.4 – 0.7	–	–	–	–	–	–	–	–	–	–	–	–	–	–	–	–	–	–
216	80 – 91	2.2 – 2.4	0.7 – 1.0	–	–	–	–	–	–	–	–	–	–	–	–	–	–	–	–	–	–

TABLE 41: Measured cross-section values unfolded to the Born, dressed and bare truth-levels in the 3$^{\text{rd}}$ mass window of the measurement. The luminosity uncertainty of 1.9% is not included.

$\mathcal{B}$	$m_{\mu\mu}$ [GeV]	$\lvert y_{\mu\mu}\rvert$	$\cos\theta^*$	Born						Dressed						Bare					
				$d^3\sigma_{\text{meas.}}$ [pb/GeV]	$\Delta^{\text{total}}_{\text{meas.}}$ [%]	$d^3\sigma_{\text{truth}}$ [pb/GeV]	$\Delta^{\text{Stat.}}_{\text{truth}}$ [%]	$C_{\text{Dres.}}$	C_{Bare}	$d^3\sigma_{\text{meas.}}$ [pb/GeV]	$\Delta^{\text{total}}_{\text{meas.}}$ [%]	$d^3\sigma_{\text{truth}}$ [pb/GeV]	$\Delta^{\text{Stat.}}_{\text{truth}}$ [%]	C_{Born}	C_{Bare}	$d^3\sigma_{\text{meas.}}$ [pb/GeV]	$\Delta^{\text{total}}_{\text{meas.}}$ [%]	$d^3\sigma_{\text{truth}}$ [pb/GeV]	$\Delta^{\text{Stat.}}_{\text{truth}}$ [%]	C_{Born}	$C_{\text{Dres.}}$
217	91 – 102	0.0 – 0.2	-1.0 – -0.7	2.7900	± 0.65	2.7863	± 0.20	0.95	0.84	2.6378	± 0.66	2.6344	± 0.21	1.06	0.89	2.3405	± 0.73	2.3372	± 0.22	1.19	1.13
218	91 – 102	0.0 – 0.2	-0.7 – -0.4	4.1437	± 0.56	4.0842	± 0.17	0.95	0.84	3.9188	± 0.58	3.8623	± 0.17	1.06	0.89	3.4751	± 0.66	3.4245	± 0.18	1.19	1.13
219	91 – 102	0.0 – 0.2	-0.4 – 0.0	3.5585	± 0.74	3.4837	± 0.16	0.95	0.84	3.3681	± 0.76	3.2965	± 0.16	1.06	0.89	2.9870	± 0.81	2.9226	± 0.17	1.19	1.13
220	91 – 102	0.0 – 0.2	0.0 – 0.4	3.5763	± 0.77	3.4874	± 0.16	0.95	0.84	3.3868	± 0.79	3.3024	± 0.16	1.06	0.89	3.0027	± 0.86	2.9272	± 0.17	1.19	1.13
221	91 – 102	0.0 – 0.2	0.4 – 0.7	4.1856	± 0.63	4.0935	± 0.17	0.94	0.84	3.9552	± 0.67	3.8672	± 0.17	1.06	0.89	3.5127	± 0.79	3.4322	± 0.18	1.19	1.13
222	91 – 102	0.0 – 0.2	0.7 – 1.0	2.8131	± 0.63	2.8012	± 0.20	0.95	0.84	2.6600	± 0.65	2.6492	± 0.21	1.06	0.89	2.3581	± 0.74	2.3495	± 0.22	1.19	1.13
223	91 – 102	0.2 – 0.4	-1.0 – -0.7	2.7689	± 0.69	2.7497	± 0.21	0.95	0.84	2.6211	± 0.70	2.6027	± 0.21	1.06	0.89	2.3234	± 0.81	2.3060	± 0.22	1.19	1.13
224	91 – 102	0.2 – 0.4	-0.7 – -0.4	4.0894	± 0.65	4.0619	± 0.17	0.95	0.84	3.8699	± 0.66	3.8442	± 0.17	1.06	0.89	3.4285	± 0.73	3.4069	± 0.18	1.19	1.13
225	91 – 102	0.2 – 0.4	-0.4 – 0.0	3.5570	± 0.89	3.4535	± 0.16	0.95	0.84	3.3722	± 0.95	3.2716	± 0.16	1.06	0.88	2.9891	± 1.14	2.8951	± 0.17	1.19	1.13
226	91 – 102	0.2 – 0.4	0.0 – 0.4	3.5707	± 0.72	3.4930	± 0.16	0.95	0.84	3.3797	± 0.73	3.3063	± 0.16	1.06	0.89	2.9924	± 0.79	2.9283	± 0.17	1.19	1.13
227	91 – 102	0.2 – 0.4	0.4 – 0.7	4.1693	± 0.70	4.1155	± 0.17	0.95	0.84	3.9432	± 0.71	3.8926	± 0.17	1.06	0.89	3.4924	± 0.79	3.4494	± 0.18	1.19	1.13
228	91 – 102	0.2 – 0.4	0.7 – 1.0	2.8272	± 0.76	2.8240	± 0.20	0.94	0.84	2.6646	± 0.81	2.6625	± 0.21	1.06	0.89	2.3662	± 0.96	2.3664	± 0.22	1.19	1.13
229	91 – 102	0.4 – 0.6	-1.0 – -0.7	2.7406	± 0.62	2.7238	± 0.21	0.95	0.84	2.5903	± 0.63	2.5743	± 0.21	1.06	0.89	2.2998	± 0.69	2.2855	± 0.22	1.19	1.13
230	91 – 102	0.4 – 0.6	-0.7 – -0.4	4.0419	± 0.70	4.0089	± 0.17	0.95	0.84	3.8316	± 0.72	3.8000	± 0.17	1.05	0.88	3.3913	± 0.79	3.3627	± 0.18	1.19	1.13
231	91 – 102	0.4 – 0.6	-0.4 – 0.0	3.5178	± 0.64	3.4331	± 0.16	0.95	0.84	3.3433	± 0.67	3.2619	± 0.16	1.05	0.88	2.9547	± 0.77	2.8807	± 0.17	1.19	1.13
232	91 – 102	0.4 – 0.6	0.0 – 0.4	3.5697	± 0.60	3.4789	± 0.16	0.95	0.84	3.3858	± 0.62	3.2994	± 0.16	1.05	0.88	2.9960	± 0.69	2.9190	± 0.17	1.19	1.13
233	91 – 102	0.4 – 0.6	0.4 – 0.7	4.1720	± 0.76	4.1287	± 0.17	0.95	0.84	3.9503	± 0.77	3.9101	± 0.17	1.06	0.89	3.4966	± 0.86	3.4632	± 0.18	1.19	1.13
234	91 – 102	0.4 – 0.6	0.7 – 1.0	2.8291	± 0.61	2.8210	± 0.20	0.94	0.84	2.6695	± 0.63	2.6623	± 0.21	1.06	0.89	2.3728	± 0.70	2.3673	± 0.22	1.19	1.12
235	91 – 102	0.6 – 0.8	-1.0 – -0.7	2.6847	± 0.73	2.6812	± 0.21	0.94	0.84	2.5317	± 0.73	2.5283	± 0.21	1.06	0.89	2.2534	± 0.79	2.2494	± 0.23	1.19	1.12
236	91 – 102	0.6 – 0.8	-0.7 – -0.4	4.0262	± 0.84	3.9540	± 0.17	0.95	0.84	3.8176	± 0.88	3.7480	± 0.18	1.05	0.88	3.3784	± 1.02	3.3135	± 0.19	1.19	1.13
237	91 – 102	0.6 – 0.8	-0.4 – 0.0	3.4967	± 0.54	3.4019	± 0.16	0.95	0.84	3.3281	± 0.55	3.2370	± 0.16	1.05	0.88	2.9319	± 0.61	2.8513	± 0.17	1.19	1.14
238	91 – 102	0.6 – 0.8	0.0 – 0.4	3.5509	± 0.54	3.4650	± 0.16	0.95	0.84	3.3785	± 0.55	3.2966	± 0.16	1.05	0.88	2.9769	± 0.61	2.9053	± 0.17	1.19	1.13
239	91 – 102	0.6 – 0.8	0.4 – 0.7	4.1673	± 0.79	4.1177	± 0.17	0.95	0.84	3.9512	± 0.80	3.9051	± 0.17	1.05	0.89	3.4965	± 0.89	3.4585	± 0.18	1.19	1.13
240	91 – 102	0.6 – 0.8	0.7 – 1.0	2.8455	± 0.66	2.8225	± 0.20	0.94	0.84	2.6781	± 0.66	2.6567	± 0.21	1.06	0.89	2.3885	± 0.70	2.3695	± 0.22	1.19	1.12
241	91 – 102	0.8 – 1.0	-1.0 – -0.7	2.6156	± 0.82	2.6115	± 0.21	0.94	0.84	2.4669	± 0.84	2.4635	± 0.22	1.06	0.89	2.1913	± 0.93	2.1890	± 0.23	1.19	1.13
242	91 – 102	0.8 – 1.0	-0.7 – -0.4	3.9560	± 0.83	3.8838	± 0.17	0.95	0.84	3.7490	± 0.86	3.6791	± 0.18	1.06	0.88	3.3169	± 1.02	3.2515	± 0.19	1.19	1.13
243	91 – 102	0.8 – 1.0	-0.4 – 0.0	3.4496	± 0.66	3.3572	± 0.16	0.96	0.84	3.2957	± 0.66	3.2069	± 0.16	1.05	0.88	2.8917	± 0.75	2.8147	± 0.17	1.19	1.14
244	91 – 102	0.8 – 1.0	0.0 – 0.4	3.5368	± 0.55	3.4389	± 0.16	0.95	0.84	3.3773	± 0.56	3.2833	± 0.16	1.05	0.88	2.9651	± 0.63	2.8822	± 0.17	1.19	1.14
245	91 – 102	0.8 – 1.0	0.4 – 0.7	4.1417	± 0.98	4.1060	± 0.17	0.95	0.84	3.9158	± 1.01	3.8833	± 0.17	1.06	0.89	3.4716	± 1.20	3.4467	± 0.18	1.19	1.13
246	91 – 102	0.8 – 1.0	0.7 – 1.0	2.8144	± 0.78	2.7851	± 0.20	0.94	0.84	2.6475	± 0.78	2.6201	± 0.21	1.06	0.89	2.3631	± 0.82	2.3389	± 0.22	1.19	1.12
247	91 – 102	1.0 – 1.2	-1.0 – -0.7	2.2094	± 0.91	2.2022	± 0.23	0.94	0.84	2.0798	± 0.94	2.0735	± 0.24	1.06	0.89	1.8498	± 1.02	1.8447	± 0.25	1.19	1.12
248	91 – 102	1.0 – 1.2	-0.7 – -0.4	3.8914	± 0.64	3.8115	± 0.17	0.95	0.84	3.6908	± 0.65	3.6143	± 0.18	1.05	0.88	3.2592	± 0.71	3.1901	± 0.19	1.19	1.13
249	91 – 102	1.0 – 1.2	-0.4 – 0.0	3.3978	± 0.60	3.2975	± 0.16	0.96	0.84	3.2524	± 0.61	3.1558	± 0.17	1.04	0.88	2.8499	± 0.67	2.7652	± 0.18	1.19	1.14
250	91 – 102	1.0 – 1.2	0.0 – 0.4	3.4979	± 0.74	3.4040	± 0.16	0.96	0.84	3.3460	± 0.73	3.2559	± 0.16	1.05	0.88	2.9348	± 0.87	2.8577	± 0.17	1.19	1.14
251	91 – 102	1.0 – 1.2	0.4 – 0.7	4.1530	± 0.60	4.0761	± 0.17	0.95	0.84	3.9331	± 0.61	3.8596	± 0.17	1.06	0.89	3.4876	± 0.67	3.4213	± 0.18	1.19	1.13
252	91 – 102	1.0 – 1.2	0.7 – 1.0	2.4072	± 0.88	2.3858	± 0.22	0.94	0.84	2.2654	± 0.90	2.2451	± 0.23	1.06	0.89	2.0233	± 0.97	2.0045	± 0.24	1.19	1.12
253	91 – 102	1.2 – 1.4	-1.0 – -0.7	1.4392	± 0.94	1.4234	± 0.29	0.95	0.84	1.3600	± 0.96	1.3454	± 0.29	1.06	0.89	1.2043	± 1.06	1.1918	± 0.31	1.19	1.13
254	91 – 102	1.2 – 1.4	-0.7 – -0.4	3.7577	± 0.66	3.6892	± 0.18	0.95	0.84	3.5729	± 0.65	3.5080	± 0.18	1.05	0.88	3.1481	± 0.71	3.0913	± 0.19	1.19	1.13
255	91 – 102	1.2 – 1.4	-0.4 – 0.0	3.3348	± 0.61	3.2284	± 0.16	0.96	0.84	3.1934	± 0.62	3.0910	± 0.17	1.04	0.87	2.7937	± 0.69	2.7038	± 0.18	1.19	1.14
256	91 – 102	1.2 – 1.4	0.0 – 0.4	3.4547	± 0.74	3.3531	± 0.16	0.96	0.84	3.3018	± 0.74	3.2044	± 0.16	1.05	0.88	2.8943	± 0.87	2.8102	± 0.17	1.19	1.14
257	91 – 102	1.2 – 1.4	0.4 – 0.7	4.0877	± 0.62	4.0208	± 0.17	0.95	0.84	3.8758	± 0.63	3.8119	± 0.17	1.05	0.89	3.4367	± 0.70	3.3786	± 0.18	1.19	1.13
258	91 – 102	1.2 – 1.4	0.7 – 1.0	1.5982	± 1.24	1.5835	± 0.27	0.94	0.84	1.5069	± 1.24	1.4930	± 0.28	1.06	0.89	1.3426	± 1.38	1.3295	± 0.29	1.19	1.12
259	91 – 102	1.4 – 1.6	-1.0 – -0.7	0.5311	± 1.25	0.5220	± 0.47	0.95	0.83	0.5069	± 1.30	0.4984	± 0.48	1.05	0.87	0.4423	± 1.53	0.4355	± 0.51	1.20	1.14
260	91 – 102	1.4 – 1.6	-0.7 – -0.4	3.4349	± 1.09	3.3953	± 0.18	0.95	0.84	3.2726	± 1.12	3.2359	± 0.19	1.05	0.88	2.8719	± 1.36	2.8425	± 0.20	1.19	1.14
261	91 – 102	1.4 – 1.6	-0.4 – 0.0	3.2494	± 0.63	3.1610	± 0.17	0.96	0.84	3.1066	± 0.63	3.0220	± 0.17	1.05	0.88	2.7215	± 0.69	2.6481	± 0.18	1.19	1.14
262	91 – 102	1.4 – 1.6	0.0 – 0.4	3.4032	± 0.64	3.3020	± 0.16	0.96	0.84	3.2523	± 0.64	3.1556	± 0.17	1.05	0.88	2.8548	± 0.72	2.7710	± 0.18	1.19	1.14
263	91 – 102	1.4 – 1.6	0.4 – 0.7	3.8184	± 0.94	3.7517	± 0.18	0.95	0.84	3.6208	± 0.98	3.5568	± 0.18	1.05	0.89	3.2096	± 1.19	3.1502	± 0.19	1.19	1.13
264	91 – 102	1.4 – 1.6	0.7 – 1.0	0.5968	± 1.19	0.5901	± 0.44	0.95	0.85	0.5670	± 1.24	0.5609	± 0.45	1.05	0.89	0.5040	± 1.41	0.4988	± 0.48	1.18	1.12
265	91 – 102	1.6 – 1.8	-1.0 – -0.7	0.0979	± 1.97	0.0918	± 1.12	0.96	0.83	0.0944	± 1.96	0.0886	± 1.14	1.04	0.86	0.0813	± 2.05	0.0765	± 1.22	1.20	1.16
266	91 – 102	1.6 – 1.8	-0.7 – -0.4	2.3828	± 1.02	2.3463	± 0.22	0.95	0.84	2.2720	± 1.04	2.2375	± 0.23	1.05	0.88	1.9944	± 1.23	1.9658	± 0.24	1.19	1.14
267	91 – 102	1.6 – 1.8	-0.4 – 0.0	3.1739	± 0.64	3.0715	± 0.17	0.96	0.84	3.0340	± 0.64	2.9359	± 0.17	1.05	0.88	2.6600	± 0.68	2.5748	± 0.18	1.19	1.14
268	91 – 102	1.6 – 1.8	0.0 – 0.4	3.3587	± 0.71	3.2387	± 0.16	0.95	0.84	3.2034	± 0.74	3.0883	± 0.17	1.05	0.88	2.8214	± 0.86	2.7182	± 0.18	1.19	1.14
269	91 – 102	1.6 – 1.8	0.4 – 0.7	2.7083	± 1.05	2.6491	± 0.21	0.95	0.84	2.5756	± 1.09	2.5186	± 0.21	1.05	0.88	2.2797	± 1.34	2.2266	± 0.23	1.19	1.13
270	91 – 102	1.6 – 1.8	0.7 – 1.0	0.1134	± 2.54	0.1060	± 1.05	0.96	0.84	0.1089	± 2.56	0.1019	± 1.06	1.04	0.87	0.0949	± 2.87	0.0888	± 1.14	1.19	1.15
271	91 – 102	1.8 – 2.0	-1.0 – -0.7	0.0216	± 3.42	0.0185	± 2.51	0.95	0.83	0.0204	± 3.48	0.0175	± 2.57	1.06	0.88	0.0178	± 3.74	0.0153	± 2.74	1.21	1.14
272	91 – 102	1.8 – 2.0	-0.7 – -0.4	0.8529	± 1.26	0.8298	± 0.37	0.96	0.84	0.8178	± 1.29	0.7958	± 0.38	1.04	0.87	0.7134	± 1.56	0.6949	± 0.41	1.19	1.15
273	91 – 102	1.8 – 2.0	-0.4 – 0.0	2.9905	± 1.46	2.9135	± 0.17	0.95	0.84	2.8551	± 1.48	2.7822	± 0.18	1.05	0.88	2.5011	± 1.86	2.4405	± 0.19	1.19	1.14
274	91 – 102	1.8 – 2.0	0.0 – 0.4	3.2230	± 1.16	3.0981	± 0.17	0.95	0.84	3.0735	± 1.21	2.9532	± 0.17	1.05	0.88	2.7114	± 1.53	2.6011	± 0.18	1.19	1.14
275	91 – 102	1.8 – 2.0	0.4 – 0.7	0.9773	± 1.58	0.9495	± 0.35	0.96	0.84	0.9339	± 1.62	0.9071	± 0.36	1.05	0.88	0.8241	± 1.95	0.7997	± 0.38	1.19	1.13
276	91 – 102	1.8 – 2.0	0.7 – 1.0	0.0231	± 4.31	0.0206	± 2.35	0.99	0.85	0.0228	± 4.22	0.0204	± 2.36	1.01	0.86	0.0195	± 4.99	0.0175	± 2.54	1.18	1.17
277	91 – 102	2.0 – 2.2	-1.0 – -0.7	0.0022	± 15.86	0.0020	± 7.52	1.02	0.83	0.0023	± 14.67	0.0020	± 7.55	0.98	0.81	0.0019	± 18.22	0.0016	± 8.26	1.20	1.23
278	91 – 102	2.0 – 2.2	-0.7 – -0.4	0.0509	± 5.40	0.0510	± 1.50	0.98	0.84	0.0496	± 5.45	0.0498	± 1.52	1.03	0.86	0.0426	± 6.88	0.0429	± 1.63	1.19	1.16
279	91 – 102	2.0 – 2.2	-0.4 – 0.0	2.1576	± 0.95	2.0915	± 0.20	0.96	0.84	2.0618	± 0.95	1.9986	± 0.21	1.05	0.87	1.8032	± 1.06	1.7486	± 0.22	1.20	1.14
280	91 – 102	2.0 – 2.2	0.0 – 0.4	2.3021	± 1.07	2.2167	± 0.20	0.95	0.84	2.1975	± 1.11	2.1154	± 0.20	1.05	0.88	1.9357	± 1.34	1.8615	± 0.21	1.19	1.14
281	91 – 102	2.0 – 2.2	0.4 – 0.7	0.0626	± 2.80	0.0600	± 1.39	0.97	0.84	0.0605	± 2.88	0.0580	± 1.41	1.03	0.87	0.0526	± 3.35	0.0504	± 1.51	1.19	1.15
282	91 – 102	2.0 – 2.2	0.7 – 1.0	0.0034	± 9.77	0.0029	± 6.39	0.95	0.85	0.0032	± 9.88	0.0027	± 6.53	1.06	0.90	0.0029	± 10.45	0.0024	± 6.85	1.17	1.11
283	91 – 102	2.2 – 2.4	-1.0 – -0.7	–	–	–	–	–	–	–	–	–	–	–	–	–	–	–	–	–	–
284	91 – 102	2.2 – 2.4	-0.7 – -0.4	–	–	–	–	–	–	–	–	–	–	–	–	–	–	–	–	–	–
285	91 – 102	2.2 – 2.4	-0.4 – 0.0	0.7239	± 1.24	0.6957	± 0.35	0.96	0.84	0.6937	± 1.29	0.6664	± 0.36	1.04	0.87	0.6065	± 1.49	0.5822	± 0.38	1.19	1.14
286	91 – 102	2.2 – 2.4	0.0 – 0.4	0.7517	± 1.08	0.7204	± 0.35	0.96	0.84	0.7195	± 1.10	0.6894	± 0.35	1.04	0.88	0.6318	± 1.18	0.6059	± 0.38	1.19	1.14
287	91 – 102	2.2 – 2.4	0.4 – 0.7	–	–	–	–	–	–	–	–	–	–	–	–	–	–	–	–	–	–
288	91 – 102	2.2 – 2.4	0.7 – 1.0	–	–	–	–	–	–	–	–	–	–	–	–	–	–	–	–	–	–

TABLE 42: Measured cross-section values unfolded to the Born, dressed and bare truth-levels in the 4$^{\text{th}}$ mass window of the measurement. The luminosity uncertainty of 1.9% is not included.

				Born						Dressed						Bare					
$\mathcal{B}$	$m_{\mu\mu}$ [GeV]	$\lvert y_{\mu\mu}\rvert$	$\cos\theta^*$	$d^3\sigma_{\text{meas.}}$ [pb/GeV]	$\Delta^{\text{total}}_{\text{meas.}}$ [%]	$d^3\sigma_{\text{truth}}$ [pb/GeV]	$\Delta^{\text{Stat.}}_{\text{truth}}$ [%]	$C_{\text{Dres.}}$	C_{Bare}	$d^3\sigma_{\text{meas.}}$ [pb/GeV]	$\Delta^{\text{total}}_{\text{meas.}}$ [%]	$d^3\sigma_{\text{truth}}$ [pb/GeV]	$\Delta^{\text{Stat.}}_{\text{truth}}$ [%]	C_{Born}	C_{Bare}	$d^3\sigma_{\text{meas.}}$ [pb/GeV]	$\Delta^{\text{total}}_{\text{meas.}}$ [%]	$d^3\sigma_{\text{truth}}$ [pb/GeV]	$\Delta^{\text{Stat.}}_{\text{truth}}$ [%]	C_{Born}	$C_{\text{Dres.}}$
289	102 – 116	0.0 – 0.2	-1.0 – -0.7	0.1079	± 1.94	0.1062	± 0.93	1.35	0.90	0.1454	± 1.67	0.1434	± 0.82	0.74	0.67	0.0976	± 2.10	0.0959	± 0.97	1.11	1.49
290	102 – 116	0.0 – 0.2	-0.7 – -0.4	0.1297	± 1.64	0.1300	± 0.84	1.30	0.91	0.1696	± 1.41	0.1695	± 0.74	0.77	0.70	0.1179	± 1.78	0.1184	± 0.87	1.10	1.43
291	102 – 116	0.0 – 0.2	-0.4 – 0.0	0.1117	± 1.77	0.1104	± 0.79	1.26	0.90	0.1406	± 1.56	0.1387	± 0.70	0.80	0.72	0.1009	± 1.91	0.0997	± 0.82	1.11	1.39
292	102 – 116	0.0 – 0.2	0.0 – 0.4	0.1151	± 1.77	0.1120	± 0.78	1.25	0.91	0.1439	± 1.55	0.1400	± 0.70	0.80	0.73	0.1048	± 1.90	0.1019	± 0.81	1.10	1.37
293	102 – 116	0.0 – 0.2	0.4 – 0.7	0.1392	± 1.64	0.1350	± 0.82	1.28	0.91	0.1783	± 1.39	0.1732	± 0.73	0.78	0.71	0.1266	± 1.79	0.1226	± 0.86	1.10	1.41
294	102 – 116	0.0 – 0.2	0.7 – 1.0	0.1082	± 1.78	0.1089	± 0.92	1.34	0.91	0.1446	± 1.55	0.1453	± 0.81	0.75	0.68	0.0978	± 1.91	0.0985	± 0.95	1.10	1.48
295	102 – 116	0.2 – 0.4	-1.0 – -0.7	0.1045	± 1.76	0.1042	± 0.94	1.35	0.91	0.1407	± 1.57	0.1402	± 0.82	0.74	0.67	0.0946	± 1.85	0.0944	± 0.98	1.10	1.49
296	102 – 116	0.2 – 0.4	-0.7 – -0.4	0.1339	± 2.10	0.1290	± 0.84	1.32	0.90	0.1760	± 1.61	0.1704	± 0.74	0.76	0.68	0.1214	± 2.39	0.1167	± 0.88	1.11	1.46
297	102 – 116	0.2 – 0.4	-0.4 – 0.0	0.1138	± 1.66	0.1104	± 0.79	1.26	0.90	0.1438	± 1.47	0.1396	± 0.70	0.79	0.71	0.1029	± 1.78	0.0998	± 0.82	1.11	1.40
298	102 – 116	0.2 – 0.4	0.0 – 0.4	0.1151	± 1.69	0.1142	± 0.78	1.26	0.90	0.1452	± 1.46	0.1438	± 0.69	0.79	0.72	0.1038	± 1.81	0.1032	± 0.81	1.11	1.39
299	102 – 116	0.2 – 0.4	0.4 – 0.7	0.1414	± 1.59	0.1386	± 0.81	1.30	0.91	0.1843	± 1.37	0.1808	± 0.72	0.77	0.70	0.1292	± 1.70	0.1265	± 0.84	1.10	1.43
300	102 – 116	0.2 – 0.4	0.7 – 1.0	0.1130	± 1.71	0.1137	± 0.90	1.32	0.90	0.1490	± 1.56	0.1497	± 0.80	0.76	0.69	0.1021	± 1.79	0.1028	± 0.94	1.11	1.46
301	102 – 116	0.4 – 0.6	-1.0 – -0.7	0.1022	± 1.90	0.0998	± 0.96	1.36	0.91	0.1384	± 1.61	0.1355	± 0.84	0.74	0.67	0.0929	± 2.06	0.0906	± 1.00	1.10	1.50
302	102 – 116	0.4 – 0.6	-0.7 – -0.4	0.1244	± 1.93	0.1250	± 0.86	1.37	0.91	0.1707	± 1.59	0.1711	± 0.74	0.73	0.66	0.1125	± 2.11	0.1132	± 0.89	1.10	1.51
303	102 – 116	0.4 – 0.6	-0.4 – 0.0	0.1141	± 1.82	0.1084	± 0.80	1.32	0.90	0.1493	± 1.42	0.1425	± 0.69	0.76	0.69	0.1031	± 2.06	0.0977	± 0.83	1.11	1.46
304	102 – 116	0.4 – 0.6	0.0 – 0.4	0.1142	± 1.54	0.1110	± 0.79	1.31	0.92	0.1497	± 1.32	0.1457	± 0.69	0.76	0.70	0.1046	± 1.66	0.1016	± 0.81	1.09	1.43
305	102 – 116	0.4 – 0.6	0.4 – 0.7	0.1396	± 1.67	0.1389	± 0.81	1.33	0.91	0.1852	± 1.43	0.1840	± 0.71	0.75	0.69	0.1270	± 1.77	0.1264	± 0.84	1.10	1.46
306	102 – 116	0.4 – 0.6	0.7 – 1.0	0.1156	± 1.72	0.1172	± 0.89	1.29	0.91	0.1493	± 1.49	0.1510	± 0.79	0.78	0.70	0.1048	± 1.86	0.1064	± 0.92	1.10	1.42
307	102 – 116	0.6 – 0.8	-1.0 – -0.7	0.1006	± 1.90	0.0981	± 0.97	1.32	0.90	0.1325	± 1.63	0.1296	± 0.85	0.76	0.68	0.0904	± 2.04	0.0880	± 1.01	1.11	1.47
308	102 – 116	0.6 – 0.8	-0.7 – -0.4	0.1211	± 1.92	0.1198	± 0.87	1.40	0.90	0.1698	± 1.60	0.1679	± 0.74	0.71	0.65	0.1095	± 2.07	0.1084	± 0.91	1.11	1.55
309	102 – 116	0.6 – 0.8	-0.4 – 0.0	0.1098	± 1.44	0.1063	± 0.80	1.38	0.91	0.1517	± 1.21	0.1470	± 0.69	0.72	0.66	0.1000	± 1.53	0.0968	± 0.83	1.10	1.52
310	102 – 116	0.6 – 0.8	0.0 – 0.4	0.1168	± 1.50	0.1146	± 0.77	1.37	0.91	0.1596	± 1.26	0.1564	± 0.66	0.73	0.67	0.1066	± 1.60	0.1047	± 0.80	1.09	1.49
311	102 – 116	0.6 – 0.8	0.4 – 0.7	0.1406	± 1.82	0.1414	± 0.81	1.35	0.91	0.1911	± 1.52	0.1914	± 0.70	0.74	0.67	0.1275	± 1.98	0.1284	± 0.84	1.10	1.49
312	102 – 116	0.6 – 0.8	0.7 – 1.0	0.1153	± 1.73	0.1166	± 0.89	1.28	0.91	0.1477	± 1.54	0.1490	± 0.80	0.78	0.71	0.1045	± 1.85	0.1058	± 0.92	1.10	1.41
313	102 – 116	0.8 – 1.0	-1.0 – -0.7	0.0880	± 2.09	0.0869	± 1.03	1.35	0.90	0.1190	± 1.78	0.1177	± 0.89	0.74	0.67	0.0796	± 2.21	0.0786	± 1.07	1.11	1.50
314	102 – 116	0.8 – 1.0	-0.7 – -0.4	0.1200	± 1.81	0.1150	± 0.89	1.43	0.91	0.1700	± 1.40	0.1639	± 0.75	0.70	0.64	0.1098	± 1.97	0.1050	± 0.92	1.09	1.56
315	102 – 116	0.8 – 1.0	-0.4 – 0.0	0.1088	± 1.70	0.1038	± 0.81	1.48	0.90	0.1604	± 1.23	0.1538	± 0.67	0.67	0.61	0.0984	± 1.91	0.0936	± 0.85	1.11	1.64
316	102 – 116	0.8 – 1.0	0.0 – 0.4	0.1188	± 1.51	0.1143	± 0.77	1.43	0.91	0.1700	± 1.20	0.1640	± 0.65	0.70	0.63	0.1083	± 1.63	0.1041	± 0.80	1.10	1.58
317	102 – 116	0.8 – 1.0	0.4 – 0.7	0.1469	± 1.54	0.1440	± 0.80	1.34	0.91	0.1964	± 1.28	0.1929	± 0.69	0.75	0.68	0.1332	± 1.69	0.1305	± 0.83	1.10	1.48
318	102 – 116	0.8 – 1.0	0.7 – 1.0	0.1101	± 2.15	0.1123	± 0.91	1.28	0.91	0.1412	± 1.73	0.1434	± 0.81	0.78	0.71	0.0998	± 2.40	0.1020	± 0.94	1.10	1.41
319	102 – 116	1.0 – 1.2	-1.0 – -0.7	0.0666	± 2.45	0.0659	± 1.19	1.38	0.89	0.0918	± 2.06	0.0909	± 1.01	0.72	0.64	0.0592	± 2.60	0.0586	± 1.24	1.12	1.55
320	102 – 116	1.0 – 1.2	-0.7 – -0.4	0.1144	± 1.80	0.1096	± 0.91	1.48	0.91	0.1684	± 1.36	0.1623	± 0.76	0.68	0.61	0.1039	± 1.98	0.0993	± 0.95	1.10	1.63
321	102 – 116	1.0 – 1.2	-0.4 – 0.0	0.1061	± 1.51	0.1026	± 0.82	1.54	0.91	0.1633	± 1.23	0.1582	± 0.66	0.65	0.59	0.0964	± 1.60	0.0932	± 0.85	1.10	1.70
322	102 – 116	1.0 – 1.2	0.0 – 0.4	0.1177	± 1.54	0.1157	± 0.77	1.50	0.91	0.1776	± 1.23	0.1741	± 0.63	0.66	0.60	0.1070	± 1.64	0.1053	± 0.80	1.10	1.65
323	102 – 116	1.0 – 1.2	0.4 – 0.7	0.1492	± 1.49	0.1455	± 0.79	1.36	0.91	0.2018	± 1.24	0.1972	± 0.69	0.74	0.67	0.1358	± 1.59	0.1324	± 0.82	1.10	1.49
324	102 – 116	1.0 – 1.2	0.7 – 1.0	0.0927	± 2.65	0.0911	± 1.01	1.30	0.90	0.1203	± 2.28	0.1184	± 0.89	0.77	0.70	0.0838	± 2.90	0.0823	± 1.04	1.11	1.44
325	102 – 116	1.2 – 1.4	-1.0 – -0.7	0.0422	± 2.94	0.0412	± 1.49	1.48	0.91	0.0624	± 2.38	0.0611	± 1.24	0.67	0.61	0.0382	± 3.10	0.0373	± 1.56	1.10	1.64
326	102 – 116	1.2 – 1.4	-0.7 – -0.4	0.1083	± 2.46	0.1033	± 0.94	1.53	0.90	0.1642	± 1.60	0.1579	± 0.77	0.65	0.59	0.0981	± 2.79	0.0934	± 0.98	1.11	1.69
327	102 – 116	1.2 – 1.4	-0.4 – 0.0	0.1023	± 1.90	0.0975	± 0.84	1.60	0.90	0.1632	± 1.31	0.1563	± 0.67	0.62	0.56	0.0926	± 2.12	0.0881	± 0.87	1.11	1.77
328	102 – 116	1.2 – 1.4	0.0 – 0.4	0.1191	± 1.57	0.1145	± 0.77	1.52	0.91	0.1799	± 1.19	0.1735	± 0.63	0.66	0.60	0.1085	± 1.70	0.1042	± 0.80	1.10	1.66
329	102 – 116	1.2 – 1.4	0.4 – 0.7	0.1503	± 1.53	0.1467	± 0.79	1.39	0.91	0.2083	± 1.25	0.2037	± 0.68	0.72	0.65	0.1366	± 1.61	0.1332	± 0.82	1.10	1.53
330	102 – 116	1.2 – 1.4	0.7 – 1.0	0.0598	± 3.23	0.0606	± 1.23	1.32	0.91	0.0795	± 2.52	0.0803	± 1.08	0.75	0.69	0.0545	± 3.62	0.0555	± 1.27	1.09	1.45
331	102 – 116	1.4 – 1.6	-1.0 – -0.7	0.0138	± 6.05	0.0144	± 2.52	1.67	0.90	0.0235	± 3.73	0.0242	± 1.96	0.60	0.54	0.0123	± 6.94	0.0130	± 2.62	1.11	1.86
332	102 – 116	1.4 – 1.6	-0.7 – -0.4	0.0955	± 2.41	0.0930	± 0.99	1.58	0.90	0.1507	± 1.72	0.1473	± 0.80	0.63	0.57	0.0865	± 2.63	0.0841	± 1.04	1.11	1.75
333	102 – 116	1.4 – 1.6	-0.4 – 0.0	0.0977	± 1.62	0.0952	± 0.85	1.63	0.91	0.1592	± 1.24	0.1551	± 0.67	0.61	0.56	0.0885	± 1.72	0.0862	± 0.88	1.10	1.80
334	102 – 116	1.4 – 1.6	0.0 – 0.4	0.1170	± 1.82	0.1117	± 0.78	1.53	0.91	0.1787	± 1.30	0.1714	± 0.64	0.65	0.59	0.1065	± 2.02	0.1016	± 0.81	1.10	1.69
335	102 – 116	1.4 – 1.6	0.4 – 0.7	0.1408	± 2.16	0.1400	± 0.81	1.40	0.91	0.1976	± 1.67	0.1961	± 0.69	0.71	0.65	0.1281	± 2.38	0.1276	± 0.84	1.10	1.54
336	102 – 116	1.4 – 1.6	0.7 – 1.0	0.0231	± 4.57	0.0228	± 2.02	1.46	0.91	0.0337	± 3.60	0.0333	± 1.68	0.68	0.62	0.0209	± 4.84	0.0206	± 2.09	1.10	1.62
337	102 – 116	1.6 – 1.8	-1.0 – -0.7	0.0024	± 19.11	0.0027	± 5.88	1.88	0.93	0.0047	± 9.54	0.0051	± 4.32	0.53	0.49	0.0022	± 22.03	0.0025	± 5.99	1.08	2.03
338	102 – 116	1.6 – 1.8	-0.7 – -0.4	0.0630	± 3.60	0.0632	± 1.21	1.65	0.90	0.1045	± 2.43	0.1042	± 0.95	0.61	0.55	0.0565	± 3.97	0.0568	± 1.26	1.11	1.83
339	102 – 116	1.6 – 1.8	-0.4 – 0.0	0.0926	± 2.69	0.0924	± 0.86	1.60	0.91	0.1492	± 1.85	0.1476	± 0.69	0.63	0.57	0.0840	± 3.01	0.0841	± 0.90	1.10	1.76
340	102 – 116	1.6 – 1.8	0.0 – 0.4	0.1178	± 1.98	0.1117	± 0.78	1.52	0.91	0.1783	± 1.37	0.1699	± 0.64	0.66	0.60	0.1071	± 2.19	0.1014	± 0.81	1.10	1.68
341	102 – 116	1.6 – 1.8	0.4 – 0.7	0.1031	± 2.77	0.0990	± 0.96	1.45	0.91	0.1488	± 2.13	0.1436	± 0.80	0.69	0.63	0.0942	± 2.95	0.0903	± 1.00	1.10	1.59
342	102 – 116	1.6 – 1.8	0.7 – 1.0	0.0043	± 7.15	0.0044	± 4.64	1.60	0.90	0.0070	± 5.26	0.0070	± 3.66	0.63	0.57	0.0039	± 7.78	0.0039	± 4.77	1.11	1.77
343	102 – 116	1.8 – 2.0	-1.0 – -0.7	0.0004	± 17.53	0.0004	± 14.74	2.46	0.77	0.0011	± 11.22	0.0010	± 9.99	0.41	0.31	0.0003	± 20.21	0.0003	± 16.18	1.29	3.18
344	102 – 116	1.8 – 2.0	-0.7 – -0.4	0.0213	± 4.76	0.0213	± 2.09	1.80	0.90	0.0386	± 3.05	0.0382	± 1.56	0.56	0.50	0.0190	± 5.12	0.0191	± 2.17	1.11	2.00
345	102 – 116	1.8 – 2.0	-0.4 – 0.0	0.0879	± 2.23	0.0857	± 0.89	1.62	0.90	0.1426	± 1.65	0.1389	± 0.71	0.62	0.56	0.0794	± 2.36	0.0773	± 0.93	1.11	1.80
346	102 – 116	1.8 – 2.0	0.0 – 0.4	0.1175	± 3.30	0.1085	± 0.80	1.50	0.91	0.1747	± 2.15	0.1632	± 0.65	0.66	0.61	0.1074	± 3.69	0.0989	± 0.83	1.10	1.65
347	102 – 116	1.8 – 2.0	0.4 – 0.7	0.0365	± 5.62	0.0364	± 1.59	1.50	0.91	0.0549	± 3.90	0.0545	± 1.30	0.67	0.60	0.0329	± 6.36	0.0330	± 1.65	1.10	1.65
348	102 – 116	1.8 – 2.0	0.7 – 1.0	0.0008	± 18.18	0.0007	± 11.24	1.69	0.93	0.0014	± 12.22	0.0012	± 8.71	0.59	0.55	0.0008	± 19.18	0.0007	± 11.51	1.07	1.80
349	102 – 116	2.0 – 2.2	-1.0 – -0.7	–	–	–	–	–	–	–	–	–	–	–	–	–	–	–	–	–	–
350	102 – 116	2.0 – 2.2	-0.7 – -0.4	0.0013	± 12.94	0.0014	± 8.13	2.34	0.92	0.0032	± 7.13	0.0032	± 5.39	0.43	0.39	0.0012	± 13.90	0.0013	± 8.40	1.09	2.56
351	102 – 116	2.0 – 2.2	-0.4 – 0.0	0.0627	± 3.34	0.0611	± 1.06	1.66	0.91	0.1041	± 2.37	0.1012	± 0.83	0.60	0.55	0.0570	± 3.55	0.0555	± 1.10	1.10	1.82
352	102 – 116	2.0 – 2.2	0.0 – 0.4	0.0798	± 3.08	0.0757	± 0.95	1.55	0.91	0.1230	± 2.26	0.1172	± 0.77	0.65	0.59	0.0728	± 3.24	0.0689	± 0.99	1.10	1.70
353	102 – 116	2.0 – 2.2	0.4 – 0.7	0.0023	± 9.43	0.0021	± 6.68	1.98	0.92	0.0045	± 6.17	0.0042	± 4.72	0.51	0.46	0.0021	± 10.08	0.0020	± 6.69	1.09	2.16
354	102 – 116	2.0 – 2.2	0.7 – 1.0	–	–	–	–	–	–	–	–	–	–	–	–	–	–	–	–	–	–
355	102 – 116	2.2 – 2.4	-1.0 – -0.7	–	–	–	–	–	–	–	–	–	–	–	–	–	–	–	–	–	–
356	102 – 116	2.2 – 2.4	-0.7 – -0.4	–	–	–	–	–	–	–	–	–	–	–	–	–	–	–	–	–	–
357	102 – 116	2.2 – 2.4	-0.4 – 0.0	0.0223	± 4.82	0.0216	± 1.78	1.64	0.90	0.0365	± 3.39	0.0354	± 1.40	0.61	0.55	0.0201	± 5.17	0.0195	± 1.86	1.11	1.81
358	102 – 116	2.2 – 2.4	0.0 – 0.4	0.0241	± 6.49	0.0241	± 1.69	1.55	0.91	0.0378	± 4.30	0.0373	± 1.36	0.65	0.59	0.0218	± 7.21	0.0219	± 1.76	1.10	1.71
359	102 – 116	2.2 – 2.4	0.4 – 0.7	–	–	–	–	–	–	–	–	–	–	–	–	–	–	–	–	–	–
360	102 – 116	2.2 – 2.4	0.7 – 1.0	–	–	–	–	–	–	–	–	–	–	–	–	–	–	–	–	–	–

TABLE 43: Measured cross-section values unfolded to the Born, dressed and bare truth-levels in the 5$^{\text{th}}$ mass window of the measurement. The luminosity uncertainty of 1.9% is not included.

				Born						Dressed						Bare					
$\mathcal{B}$	$m_{\mu\mu}$ [GeV]	$\lvert y_{\mu\mu}\rvert$	$\cos\theta^*$	$d^3\sigma_{\text{meas.}}$ [pb/GeV]	$\Delta^{\text{total}}_{\text{meas.}}$ [%]	$d^3\sigma_{\text{truth}}$ [pb/GeV]	$\Delta^{\text{Stat.}}_{\text{truth}}$ [%]	$C_{\text{Dres.}}$	C_{Bare}	$d^3\sigma_{\text{meas.}}$ [pb/GeV]	$\Delta^{\text{total}}_{\text{meas.}}$ [%]	$d^3\sigma_{\text{truth}}$ [pb/GeV]	$\Delta^{\text{Stat.}}_{\text{truth}}$ [%]	C_{Born}	C_{Bare}	$d^3\sigma_{\text{meas.}}$ [pb/GeV]	$\Delta^{\text{total}}_{\text{meas.}}$ [%]	$d^3\sigma_{\text{truth}}$ [pb/GeV]	$\Delta^{\text{Stat.}}_{\text{truth}}$ [%]	C_{Born}	$C_{\text{Dres.}}$
361	116 – 150	0.0 – 0.2	-1.0 – -0.7	0.0237	± 2.98	0.0243	± 0.75	1.15	0.93	0.0272	± 2.82	0.0279	± 0.82	0.87	0.81	0.0219	± 3.23	0.0225	± 0.75	1.08	1.24
362	116 – 150	0.0 – 0.2	-0.7 – -0.4	0.0250	± 2.40	0.0255	± 0.72	1.17	0.93	0.0292	± 2.31	0.0298	± 0.78	0.86	0.80	0.0233	± 2.55	0.0238	± 0.73	1.07	1.25
363	116 – 150	0.0 – 0.2	-0.4 – 0.0	0.0222	± 2.46	0.0214	± 0.68	1.16	0.93	0.0257	± 2.38	0.0248	± 0.72	0.86	0.81	0.0208	± 2.63	0.0200	± 0.68	1.07	1.24
364	116 – 150	0.0 – 0.2	0.0 – 0.4	0.0218	± 2.53	0.0221	± 0.68	1.16	0.93	0.0252	± 2.40	0.0255	± 0.72	0.87	0.80	0.0202	± 2.73	0.0205	± 0.68	1.08	1.24
365	116 – 150	0.0 – 0.2	0.4 – 0.7	0.0265	± 2.31	0.0266	± 0.71	1.16	0.93	0.0308	± 2.24	0.0309	± 0.75	0.86	0.80	0.0246	± 2.47	0.0247	± 0.71	1.07	1.25
366	116 – 150	0.0 – 0.2	0.7 – 1.0	0.0256	± 2.68	0.0251	± 0.72	1.15	0.93	0.0295	± 2.63	0.0289	± 0.79	0.87	0.81	0.0238	± 2.85	0.0233	± 0.73	1.08	1.24
367	116 – 150	0.2 – 0.4	-1.0 – -0.7	0.0226	± 2.77	0.0228	± 0.75	1.16	0.94	0.0263	± 2.78	0.0265	± 0.82	0.86	0.81	0.0211	± 2.90	0.0214	± 0.75	1.07	1.24
368	116 – 150	0.2 – 0.4	-0.7 – -0.4	0.0244	± 2.71	0.0246	± 0.74	1.19	0.93	0.0291	± 2.58	0.0294	± 0.79	0.84	0.78	0.0227	± 2.92	0.0230	± 0.74	1.07	1.28
369	116 – 150	0.2 – 0.4	-0.4 – 0.0	0.0214	± 2.54	0.0212	± 0.69	1.17	0.93	0.0252	± 2.43	0.0248	± 0.73	0.85	0.79	0.0200	± 2.71	0.0197	± 0.69	1.07	1.26
370	116 – 150	0.2 – 0.4	0.0 – 0.4	0.0218	± 2.46	0.0219	± 0.67	1.17	0.93	0.0256	± 2.37	0.0257	± 0.72	0.85	0.80	0.0203	± 2.62	0.0204	± 0.67	1.07	1.26
371	116 – 150	0.2 – 0.4	0.4 – 0.7	0.0274	± 2.32	0.0274	± 0.70	1.16	0.93	0.0319	± 2.28	0.0318	± 0.75	0.86	0.80	0.0256	± 2.48	0.0256	± 0.70	1.07	1.24
372	116 – 150	0.2 – 0.4	0.7 – 1.0	0.0251	± 2.90	0.0259	± 0.70	1.14	0.93	0.0287	± 2.75	0.0297	± 0.78	0.87	0.82	0.0233	± 3.13	0.0242	± 0.71	1.07	1.22
373	116 – 150	0.4 – 0.6	-1.0 – -0.7	0.0216	± 2.76	0.0217	± 0.77	1.17	0.93	0.0253	± 2.74	0.0255	± 0.85	0.85	0.79	0.0200	± 2.92	0.0202	± 0.77	1.07	1.26
374	116 – 150	0.4 – 0.6	-0.7 – -0.4	0.0240	± 2.60	0.0234	± 0.76	1.22	0.93	0.0294	± 2.50	0.0287	± 0.82	0.82	0.76	0.0224	± 2.76	0.0218	± 0.76	1.08	1.32
375	116 – 150	0.4 – 0.6	-0.4 – 0.0	0.0204	± 2.64	0.0207	± 0.70	1.20	0.94	0.0245	± 2.40	0.0248	± 0.74	0.83	0.78	0.0191	± 2.87	0.0194	± 0.70	1.07	1.28
376	116 – 150	0.4 – 0.6	0.0 – 0.4	0.0221	± 2.31	0.0226	± 0.67	1.20	0.94	0.0266	± 2.08	0.0270	± 0.72	0.84	0.78	0.0207	± 2.51	0.0211	± 0.67	1.07	1.28
377	116 – 150	0.4 – 0.6	0.4 – 0.7	0.0272	± 2.54	0.0281	± 0.69	1.18	0.93	0.0322	± 2.38	0.0331	± 0.74	0.85	0.79	0.0252	± 2.75	0.0260	± 0.69	1.08	1.27
378	116 – 150	0.4 – 0.6	0.7 – 1.0	0.0267	± 2.42	0.0269	± 0.69	1.13	0.93	0.0301	± 2.41	0.0303	± 0.76	0.89	0.83	0.0249	± 2.53	0.0250	± 0.69	1.07	1.21
379	116 – 150	0.6 – 0.8	-1.0 – -0.7	0.0203	± 2.85	0.0198	± 0.82	1.17	0.93	0.0237	± 2.82	0.0231	± 0.90	0.86	0.79	0.0188	± 3.00	0.0183	± 0.83	1.08	1.26
380	116 – 150	0.6 – 0.8	-0.7 – -0.4	0.0234	± 2.63	0.0224	± 0.77	1.25	0.93	0.0292	± 2.48	0.0281	± 0.84	0.80	0.74	0.0217	± 2.82	0.0208	± 0.77	1.08	1.35
381	116 – 150	0.6 – 0.8	-0.4 – 0.0	0.0204	± 2.28	0.0200	± 0.70	1.25	0.93	0.0255	± 2.20	0.0249	± 0.77	0.80	0.75	0.0190	± 2.43	0.0186	± 0.71	1.07	1.34
382	116 – 150	0.6 – 0.8	0.0 – 0.4	0.0238	± 2.18	0.0227	± 0.66	1.21	0.93	0.0288	± 2.04	0.0274	± 0.72	0.83	0.77	0.0222	± 2.35	0.0211	± 0.67	1.07	1.30
383	116 – 150	0.6 – 0.8	0.4 – 0.7	0.0289	± 2.33	0.0287	± 0.68	1.20	0.94	0.0348	± 2.25	0.0346	± 0.74	0.83	0.78	0.0270	± 2.47	0.0269	± 0.68	1.07	1.29
384	116 – 150	0.6 – 0.8	0.7 – 1.0	0.0265	± 2.35	0.0268	± 0.69	1.13	0.93	0.0299	± 2.35	0.0303	± 0.76	0.88	0.83	0.0247	± 2.45	0.0250	± 0.69	1.07	1.21
385	116 – 150	0.8 – 1.0	-1.0 – -0.7	0.0163	± 3.25	0.0164	± 0.91	1.20	0.92	0.0195	± 3.19	0.0197	± 0.99	0.84	0.77	0.0150	± 3.47	0.0151	± 0.90	1.08	1.30
386	116 – 150	0.8 – 1.0	-0.7 – -0.4	0.0220	± 2.55	0.0212	± 0.81	1.28	0.92	0.0282	± 2.49	0.0272	± 0.87	0.78	0.72	0.0203	± 2.71	0.0196	± 0.81	1.08	1.39
387	116 – 150	0.8 – 1.0	-0.4 – 0.0	0.0203	± 2.26	0.0196	± 0.72	1.30	0.93	0.0263	± 2.17	0.0255	± 0.78	0.77	0.72	0.0189	± 2.40	0.0183	± 0.71	1.07	1.39
388	116 – 150	0.8 – 1.0	0.0 – 0.4	0.0236	± 2.00	0.0229	± 0.66	1.26	0.93	0.0298	± 1.95	0.0288	± 0.72	0.79	0.74	0.0220	± 2.12	0.0213	± 0.66	1.07	1.35
389	116 – 150	0.8 – 1.0	0.4 – 0.7	0.0305	± 2.11	0.0300	± 0.67	1.20	0.93	0.0366	± 2.03	0.0360	± 0.73	0.83	0.78	0.0284	± 2.23	0.0280	± 0.67	1.07	1.29
390	116 – 150	0.8 – 1.0	0.7 – 1.0	0.0233	± 2.47	0.0242	± 0.73	1.14	0.94	0.0265	± 2.46	0.0275	± 0.80	0.88	0.82	0.0218	± 2.60	0.0226	± 0.73	1.07	1.21
391	116 – 150	1.0 – 1.2	-1.0 – -0.7	0.0121	± 3.76	0.0122	± 1.06	1.23	0.93	0.0148	± 3.53	0.0150	± 1.14	0.82	0.76	0.0112	± 4.06	0.0113	± 1.07	1.08	1.32
392	116 – 150	1.0 – 1.2	-0.7 – -0.4	0.0202	± 2.58	0.0195	± 0.83	1.32	0.93	0.0266	± 2.51	0.0257	± 0.91	0.76	0.71	0.0189	± 2.73	0.0182	± 0.83	1.07	1.41
393	116 – 150	1.0 – 1.2	-0.4 – 0.0	0.0201	± 2.18	0.0193	± 0.73	1.36	0.93	0.0274	± 2.01	0.0263	± 0.79	0.73	0.68	0.0187	± 2.32	0.0179	± 0.73	1.08	1.47
394	116 – 150	1.0 – 1.2	0.0 – 0.4	0.0237	± 1.96	0.0230	± 0.66	1.32	0.94	0.0312	± 1.84	0.0303	± 0.73	0.76	0.71	0.0223	± 2.08	0.0215	± 0.66	1.07	1.41
395	116 – 150	1.0 – 1.2	0.4 – 0.7	0.0306	± 2.08	0.0306	± 0.66	1.22	0.93	0.0374	± 2.00	0.0374	± 0.73	0.82	0.76	0.0285	± 2.22	0.0285	± 0.66	1.07	1.31
396	116 – 150	1.0 – 1.2	0.7 – 1.0	0.0194	± 3.31	0.0203	± 0.81	1.14	0.93	0.0221	± 2.91	0.0232	± 0.87	0.88	0.82	0.0180	± 3.74	0.0190	± 0.81	1.07	1.22
397	116 – 150	1.2 – 1.4	-1.0 – -0.7	0.0080	± 6.89	0.0073	± 1.35	1.34	0.93	0.0107	± 4.97	0.0099	± 1.47	0.74	0.69	0.0075	± 7.70	0.0068	± 1.36	1.07	1.44
398	116 – 150	1.2 – 1.4	-0.7 – -0.4	0.0185	± 2.78	0.0182	± 0.86	1.39	0.93	0.0256	± 2.63	0.0252	± 0.95	0.72	0.67	0.0172	± 2.99	0.0169	± 0.87	1.07	1.49
399	116 – 150	1.2 – 1.4	-0.4 – 0.0	0.0187	± 2.49	0.0186	± 0.75	1.40	0.93	0.0263	± 2.15	0.0261	± 0.82	0.72	0.66	0.0174	± 2.72	0.0173	± 0.75	1.08	1.51
400	116 – 150	1.2 – 1.4	0.0 – 0.4	0.0239	± 1.98	0.0231	± 0.66	1.34	0.93	0.0319	± 1.89	0.0309	± 0.73	0.75	0.70	0.0223	± 2.09	0.0216	± 0.66	1.07	1.43
401	116 – 150	1.2 – 1.4	0.4 – 0.7	0.0315	± 1.98	0.0306	± 0.65	1.23	0.94	0.0388	± 1.86	0.0376	± 0.72	0.81	0.76	0.0296	± 2.11	0.0287	± 0.65	1.07	1.31
402	116 – 150	1.2 – 1.4	0.7 – 1.0	0.0133	± 2.98	0.0136	± 0.99	1.18	0.93	0.0157	± 3.03	0.0160	± 1.07	0.85	0.79	0.0124	± 3.13	0.0127	± 1.00	1.07	1.26
403	116 – 150	1.4 – 1.6	-1.0 – -0.7	0.0023	± 9.89	0.0026	± 2.36	1.60	0.93	0.0037	± 6.40	0.0041	± 2.48	0.63	0.58	0.0021	± 11.05	0.0024	± 2.34	1.08	1.72
404	116 – 150	1.4 – 1.6	-0.7 – -0.4	0.0164	± 2.60	0.0161	± 0.92	1.38	0.93	0.0226	± 2.47	0.0222	± 1.00	0.72	0.67	0.0152	± 2.73	0.0150	± 0.93	1.07	1.49
405	116 – 150	1.4 – 1.6	-0.4 – 0.0	0.0178	± 2.26	0.0175	± 0.76	1.44	0.93	0.0257	± 2.05	0.0251	± 0.84	0.69	0.65	0.0166	± 2.39	0.0163	± 0.76	1.07	1.55
406	116 – 150	1.4 – 1.6	0.0 – 0.4	0.0234	± 2.12	0.0229	± 0.66	1.36	0.93	0.0318	± 1.93	0.0311	± 0.73	0.74	0.69	0.0218	± 2.27	0.0213	± 0.65	1.07	1.46
407	116 – 150	1.4 – 1.6	0.4 – 0.7	0.0299	± 2.06	0.0298	± 0.66	1.22	0.93	0.0365	± 1.93	0.0364	± 0.72	0.82	0.76	0.0278	± 2.17	0.0278	± 0.66	1.07	1.31
408	116 – 150	1.4 – 1.6	0.7 – 1.0	0.0048	± 5.52	0.0051	± 1.56	1.34	0.94	0.0064	± 4.55	0.0068	± 1.73	0.75	0.70	0.0045	± 6.04	0.0048	± 1.56	1.06	1.42
409	116 – 150	1.6 – 1.8	-1.0 – -0.7	0.0003	± 33.23	0.0004	± 5.90	2.13	0.92	0.0007	± 13.43	0.0009	± 5.52	0.47	0.43	0.0003	± 37.61	0.0004	± 5.90	1.09	2.32
410	116 – 150	1.6 – 1.8	-0.7 – -0.4	0.0109	± 3.96	0.0105	± 1.14	1.51	0.92	0.0163	± 3.25	0.0158	± 1.23	0.66	0.61	0.0101	± 4.30	0.0097	± 1.15	1.08	1.63
411	116 – 150	1.6 – 1.8	-0.4 – 0.0	0.0175	± 2.25	0.0172	± 0.79	1.46	0.92	0.0257	± 2.04	0.0251	± 0.85	0.68	0.63	0.0162	± 2.37	0.0159	± 0.79	1.08	1.58
412	116 – 150	1.6 – 1.8	0.0 – 0.4	0.0235	± 2.27	0.0231	± 0.66	1.35	0.93	0.0317	± 2.05	0.0311	± 0.73	0.74	0.69	0.0219	± 2.46	0.0216	± 0.66	1.07	1.44
413	116 – 150	1.6 – 1.8	0.4 – 0.7	0.0231	± 3.14	0.0215	± 0.79	1.26	0.94	0.0290	± 2.52	0.0271	± 0.86	0.79	0.74	0.0217	± 3.42	0.0201	± 0.79	1.07	1.35
414	116 – 150	1.6 – 1.8	0.7 – 1.0	0.0008	± 22.67	0.0010	± 3.91	1.47	0.93	0.0012	± 14.68	0.0014	± 4.02	0.68	0.63	0.0007	± 26.32	0.0009	± 3.79	1.08	1.58
415	116 – 150	1.8 – 2.0	-1.0 – -0.7	–	–	–	–	–	–	–	–	–	–	–	–	–	–	–	–	–	–
416	116 – 150	1.8 – 2.0	-0.7 – -0.4	0.0035	± 5.15	0.0035	± 2.01	1.68	0.90	0.0059	± 4.39	0.0059	± 2.07	0.60	0.54	0.0031	± 5.40	0.0032	± 2.01	1.11	1.85
417	116 – 150	1.8 – 2.0	-0.4 – 0.0	0.0164	± 2.77	0.0154	± 0.81	1.45	0.93	0.0236	± 2.17	0.0223	± 0.89	0.69	0.64	0.0153	± 3.02	0.0144	± 0.81	1.08	1.56
418	116 – 150	1.8 – 2.0	0.0 – 0.4	0.0238	± 1.99	0.0222	± 0.67	1.34	0.93	0.0319	± 1.89	0.0299	± 0.73	0.74	0.69	0.0222	± 2.05	0.0207	± 0.67	1.07	1.44
419	116 – 150	1.8 – 2.0	0.4 – 0.7	0.0079	± 3.66	0.0078	± 1.31	1.35	0.95	0.0107	± 3.41	0.0105	± 1.43	0.74	0.70	0.0075	± 3.77	0.0073	± 1.30	1.06	1.43
420	116 – 150	1.8 – 2.0	0.7 – 1.0	–	–	–	–	–	–	–	–	–	–	–	–	–	–	–	–	–	–
421	116 – 150	2.0 – 2.2	-1.0 – -0.7	–	–	–	–	–	–	–	–	–	–	–	–	–	–	–	–	–	–
422	116 – 150	2.0 – 2.2	-0.7 – -0.4	0.0002	± 15.87	0.0002	± 10.04	2.78	0.84	0.0006	± 9.80	0.0006	± 7.82	0.36	0.30	0.0002	± 17.88	0.0002	± 9.61	1.19	3.30
423	116 – 150	2.0 – 2.2	-0.4 – 0.0	0.0118	± 3.06	0.0112	± 0.96	1.49	0.93	0.0175	± 2.68	0.0168	± 1.03	0.67	0.62	0.0109	± 3.16	0.0104	± 0.97	1.08	1.61
424	116 – 150	2.0 – 2.2	0.0 – 0.4	0.0167	± 2.83	0.0155	± 0.80	1.38	0.93	0.0229	± 2.46	0.0213	± 0.88	0.73	0.68	0.0156	± 2.92	0.0144	± 0.81	1.07	1.48
425	116 – 150	2.0 – 2.2	0.4 – 0.7	0.0005	± 11.69	0.0004	± 5.64	1.92	0.97	0.0009	± 9.64	0.0008	± 5.77	0.52	0.50	0.0004	± 12.31	0.0004	± 5.49	1.03	1.99
426	116 – 150	2.0 – 2.2	0.7 – 1.0	–	–	–	–	–	–	–	–	–	–	–	–	–	–	–	–	–	–
427	116 – 150	2.2 – 2.4	-1.0 – -0.7	–	–	–	–	–	–	–	–	–	–	–	–	–	–	–	–	–	–
428	116 – 150	2.2 – 2.4	-0.7 – -0.4	–	–	–	–	–	–	–	–	–	–	–	–	–	–	–	–	–	–
429	116 – 150	2.2 – 2.4	-0.4 – 0.0	0.0040	± 4.27	0.0038	± 1.59	1.51	0.93	0.0061	± 3.85	0.0057	± 1.73	0.66	0.62	0.0038	± 4.42	0.0036	± 1.60	1.07	1.62
430	116 – 150	2.2 – 2.4	0.0 – 0.4	0.0047	± 5.18	0.0046	± 1.47	1.44	0.94	0.0067	± 4.37	0.0066	± 1.60	0.69	0.65	0.0044	± 5.31	0.0043	± 1.48	1.07	1.54
431	116 – 150	2.2 – 2.4	0.4 – 0.7	–	–	–	–	–	–	–	–	–	–	–	–	–	–	–	–	–	–
432	116 – 150	2.2 – 2.4	0.7 – 1.0	–	–	–	–	–	–	–	–	–	–	–	–	–	–	–	–	–	–

TABLE 44: Measured cross-section values unfolded to the Born, dressed and bare truth-levels in the 6$^{\text{th}}$ mass window of the measurement. The luminosity uncertainty of 1.9% is not included.

$\mathcal{B}$	$m_{\mu\mu}$ [GeV]	$\lvert y_{\mu\mu}\rvert$	$\cos\theta^*$	Born						Dressed						Bare					
				$d^3\sigma_{\text{meas.}}$ [pb/GeV]	$\Delta^{\text{total}}_{\text{meas.}}$ [%]	$d^3\sigma_{\text{truth}}$ [pb/GeV]	$\Delta^{\text{Stat.}}_{\text{truth}}$ [%]	$C_{\text{Dres.}}$	C_{Bare}	$d^3\sigma_{\text{meas.}}$ [pb/GeV]	$\Delta^{\text{total}}_{\text{meas.}}$ [%]	$d^3\sigma_{\text{truth}}$ [pb/GeV]	$\Delta^{\text{Stat.}}_{\text{truth}}$ [%]	C_{Born}	C_{Bare}	$d^3\sigma_{\text{meas.}}$ [pb/GeV]	$\Delta^{\text{total}}_{\text{meas.}}$ [%]	$d^3\sigma_{\text{truth}}$ [pb/GeV]	$\Delta^{\text{Stat.}}_{\text{truth}}$ [%]	C_{Born}	$C_{\text{Dres.}}$
433	150 – 200	0.0 – 0.2	-1.0 – -0.7	0.0061	± 4.91	0.0060	± 0.80	0.99	0.94	0.0060	± 4.95	0.0059	± 0.80	1.01	0.95	0.0057	± 5.17	0.0056	± 0.82	1.07	1.05
434	150 – 200	0.0 – 0.2	-0.7 – -0.4	0.0053	± 4.57	0.0054	± 0.83	0.99	0.94	0.0053	± 4.64	0.0054	± 0.86	1.01	0.95	0.0050	± 4.91	0.0051	± 0.86	1.06	1.06
435	150 – 200	0.0 – 0.2	-0.4 – 0.0	0.0047	± 4.43	0.0046	± 0.78	0.99	0.94	0.0046	± 4.50	0.0046	± 0.81	1.01	0.95	0.0044	± 4.73	0.0043	± 0.81	1.06	1.06
436	150 – 200	0.0 – 0.2	0.0 – 0.4	0.0047	± 4.44	0.0047	± 0.77	0.99	0.94	0.0047	± 4.53	0.0047	± 0.79	1.01	0.95	0.0044	± 4.76	0.0045	± 0.79	1.06	1.05
437	150 – 200	0.0 – 0.2	0.4 – 0.7	0.0057	± 4.31	0.0058	± 0.80	0.99	0.94	0.0057	± 4.38	0.0058	± 0.83	1.01	0.95	0.0054	± 4.61	0.0055	± 0.83	1.06	1.05
438	150 – 200	0.0 – 0.2	0.7 – 1.0	0.0068	± 4.90	0.0063	± 0.77	0.99	0.94	0.0068	± 4.94	0.0063	± 0.79	1.01	0.95	0.0065	± 5.26	0.0060	± 0.79	1.06	1.05
439	150 – 200	0.2 – 0.4	-1.0 – -0.7	0.0056	± 5.35	0.0056	± 0.82	0.99	0.94	0.0056	± 5.42	0.0055	± 0.85	1.01	0.95	0.0053	± 5.67	0.0053	± 0.84	1.07	1.06
440	150 – 200	0.2 – 0.4	-0.7 – -0.4	0.0052	± 4.67	0.0052	± 0.85	1.00	0.94	0.0051	± 4.73	0.0052	± 0.88	1.00	0.95	0.0048	± 4.99	0.0049	± 0.87	1.06	1.06
441	150 – 200	0.2 – 0.4	-0.4 – 0.0	0.0048	± 4.46	0.0045	± 0.79	0.99	0.94	0.0048	± 4.53	0.0045	± 0.81	1.01	0.95	0.0046	± 4.82	0.0043	± 0.81	1.06	1.05
442	150 – 200	0.2 – 0.4	0.0 – 0.4	0.0048	± 4.35	0.0048	± 0.77	1.00	0.94	0.0048	± 4.41	0.0048	± 0.80	1.00	0.94	0.0045	± 4.64	0.0045	± 0.79	1.06	1.06
443	150 – 200	0.2 – 0.4	0.4 – 0.7	0.0060	± 4.40	0.0060	± 0.79	1.00	0.94	0.0060	± 4.46	0.0060	± 0.81	1.00	0.95	0.0057	± 4.71	0.0057	± 0.81	1.06	1.06
444	150 – 200	0.2 – 0.4	0.7 – 1.0	0.0065	± 5.17	0.0066	± 0.76	1.00	0.94	0.0064	± 5.21	0.0065	± 0.79	1.00	0.94	0.0061	± 5.55	0.0062	± 0.78	1.07	1.06
445	150 – 200	0.4 – 0.6	-1.0 – -0.7	0.0045	± 6.81	0.0050	± 0.87	1.00	0.94	0.0045	± 6.86	0.0050	± 0.89	1.00	0.95	0.0042	± 7.61	0.0047	± 0.89	1.06	1.06
446	150 – 200	0.4 – 0.6	-0.7 – -0.4	0.0056	± 5.38	0.0050	± 0.87	1.00	0.94	0.0055	± 5.41	0.0050	± 0.89	1.00	0.95	0.0053	± 5.87	0.0047	± 0.89	1.06	1.06
447	150 – 200	0.4 – 0.6	-0.4 – 0.0	0.0043	± 4.12	0.0044	± 0.80	1.00	0.94	0.0043	± 4.19	0.0044	± 0.82	1.00	0.94	0.0041	± 4.42	0.0042	± 0.82	1.06	1.06
448	150 – 200	0.4 – 0.6	0.0 – 0.4	0.0049	± 4.49	0.0049	± 0.76	1.00	0.94	0.0049	± 4.54	0.0049	± 0.78	1.00	0.94	0.0047	± 4.79	0.0046	± 0.78	1.06	1.06
449	150 – 200	0.4 – 0.6	0.4 – 0.7	0.0060	± 4.43	0.0063	± 0.77	1.00	0.95	0.0060	± 4.48	0.0063	± 0.79	1.00	0.95	0.0057	± 4.77	0.0060	± 0.79	1.06	1.06
450	150 – 200	0.4 – 0.6	0.7 – 1.0	0.0072	± 4.84	0.0067	± 0.75	0.98	0.94	0.0071	± 4.91	0.0066	± 0.77	1.02	0.96	0.0068	± 5.35	0.0063	± 0.77	1.06	1.05
451	150 – 200	0.6 – 0.8	-1.0 – -0.7	0.0045	± 5.89	0.0043	± 0.93	0.99	0.94	0.0045	± 5.99	0.0043	± 0.95	1.01	0.95	0.0043	± 6.39	0.0041	± 0.96	1.07	1.05
452	150 – 200	0.6 – 0.8	-0.7 – -0.4	0.0050	± 4.63	0.0047	± 0.90	1.01	0.94	0.0051	± 4.66	0.0047	± 0.94	0.99	0.94	0.0048	± 4.94	0.0044	± 0.92	1.06	1.07
453	150 – 200	0.6 – 0.8	-0.4 – 0.0	0.0041	± 4.58	0.0042	± 0.82	1.01	0.95	0.0041	± 4.61	0.0043	± 0.84	0.99	0.94	0.0038	± 4.94	0.0040	± 0.84	1.06	1.06
454	150 – 200	0.6 – 0.8	0.0 – 0.4	0.0052	± 3.74	0.0050	± 0.75	1.00	0.94	0.0053	± 3.79	0.0050	± 0.77	1.00	0.94	0.0050	± 3.98	0.0047	± 0.77	1.06	1.06
455	150 – 200	0.6 – 0.8	0.4 – 0.7	0.0066	± 3.93	0.0066	± 0.76	1.00	0.94	0.0066	± 3.97	0.0066	± 0.78	1.00	0.94	0.0062	± 4.20	0.0062	± 0.78	1.06	1.06
456	150 – 200	0.6 – 0.8	0.7 – 1.0	0.0063	± 4.26	0.0063	± 0.77	0.99	0.94	0.0062	± 4.31	0.0063	± 0.80	1.01	0.95	0.0059	± 4.53	0.0060	± 0.79	1.06	1.06
457	150 – 200	0.8 – 1.0	-1.0 – -0.7	0.0034	± 6.11	0.0034	± 1.05	0.99	0.93	0.0033	± 6.19	0.0034	± 1.06	1.01	0.94	0.0031	± 6.52	0.0032	± 1.08	1.08	1.06
458	150 – 200	0.8 – 1.0	-0.7 – -0.4	0.0049	± 4.81	0.0044	± 0.93	0.99	0.94	0.0048	± 4.85	0.0044	± 0.95	1.01	0.94	0.0046	± 5.25	0.0041	± 0.96	1.06	1.06
459	150 – 200	0.8 – 1.0	-0.4 – 0.0	0.0043	± 4.04	0.0042	± 0.83	1.02	0.94	0.0044	± 4.05	0.0042	± 0.85	0.98	0.92	0.0040	± 4.31	0.0039	± 0.85	1.06	1.08
460	150 – 200	0.8 – 1.0	0.0 – 0.4	0.0051	± 3.67	0.0050	± 0.75	1.01	0.95	0.0051	± 3.69	0.0050	± 0.78	0.99	0.93	0.0048	± 3.92	0.0047	± 0.77	1.06	1.07
461	150 – 200	0.8 – 1.0	0.4 – 0.7	0.0065	± 4.08	0.0069	± 0.74	1.00	0.95	0.0065	± 4.10	0.0069	± 0.76	1.00	0.95	0.0061	± 4.45	0.0065	± 0.76	1.06	1.06
462	150 – 200	0.8 – 1.0	0.7 – 1.0	0.0056	± 4.48	0.0060	± 0.80	0.99	0.94	0.0056	± 4.53	0.0059	± 0.81	1.01	0.95	0.0053	± 4.80	0.0056	± 0.82	1.06	1.05
463	150 – 200	1.0 – 1.2	-1.0 – -0.7	0.0024	± 6.82	0.0025	± 1.23	1.01	0.95	0.0024	± 6.85	0.0025	± 1.26	0.99	0.94	0.0023	± 7.19	0.0024	± 1.26	1.05	1.06
464	150 – 200	1.0 – 1.2	-0.7 – -0.4	0.0040	± 4.76	0.0039	± 0.98	1.01	0.94	0.0041	± 4.77	0.0040	± 1.02	0.99	0.93	0.0038	± 5.08	0.0037	± 1.01	1.06	1.08
465	150 – 200	1.0 – 1.2	-0.4 – 0.0	0.0042	± 3.94	0.0040	± 0.84	1.02	0.94	0.0043	± 3.97	0.0041	± 0.88	0.98	0.92	0.0039	± 4.20	0.0038	± 0.86	1.06	1.08
466	150 – 200	1.0 – 1.2	0.0 – 0.4	0.0053	± 3.30	0.0051	± 0.74	1.02	0.94	0.0054	± 3.31	0.0052	± 0.77	0.98	0.93	0.0050	± 3.50	0.0049	± 0.76	1.06	1.08
467	150 – 200	1.0 – 1.2	0.4 – 0.7	0.0067	± 3.64	0.0070	± 0.73	1.00	0.94	0.0067	± 3.66	0.0070	± 0.76	1.00	0.94	0.0063	± 3.94	0.0066	± 0.75	1.06	1.06
468	150 – 200	1.0 – 1.2	0.7 – 1.0	0.0048	± 4.70	0.0049	± 0.88	0.99	0.94	0.0047	± 4.76	0.0048	± 0.90	1.01	0.94	0.0045	± 5.01	0.0046	± 0.91	1.07	1.06
469	150 – 200	1.2 – 1.4	-1.0 – -0.7	0.0013	± 10.91	0.0014	± 1.62	1.00	0.93	0.0013	± 11.07	0.0014	± 1.73	1.00	0.93	0.0012	± 12.19	0.0013	± 1.67	1.08	1.07
470	150 – 200	1.2 – 1.4	-0.7 – -0.4	0.0038	± 4.81	0.0036	± 1.02	1.01	0.94	0.0039	± 4.81	0.0037	± 1.04	0.99	0.93	0.0036	± 5.20	0.0034	± 1.05	1.07	1.08
471	150 – 200	1.2 – 1.4	-0.4 – 0.0	0.0040	± 3.88	0.0039	± 0.85	1.03	0.95	0.0041	± 3.88	0.0040	± 0.90	0.97	0.92	0.0038	± 4.12	0.0037	± 0.87	1.06	1.09
472	150 – 200	1.2 – 1.4	0.0 – 0.4	0.0053	± 3.41	0.0052	± 0.74	1.01	0.94	0.0054	± 3.42	0.0052	± 0.77	0.99	0.93	0.0050	± 3.63	0.0049	± 0.76	1.06	1.07
473	150 – 200	1.2 – 1.4	0.4 – 0.7	0.0072	± 3.29	0.0072	± 0.72	1.00	0.94	0.0073	± 3.32	0.0072	± 0.75	1.00	0.94	0.0068	± 3.52	0.0068	± 0.74	1.06	1.07
474	150 – 200	1.2 – 1.4	0.7 – 1.0	0.0031	± 5.50	0.0033	± 1.08	1.00	0.94	0.0031	± 5.59	0.0032	± 1.09	1.00	0.94	0.0029	± 5.86	0.0031	± 1.11	1.06	1.06
475	150 – 200	1.4 – 1.6	-1.0 – -0.7	0.0004	± 13.77	0.0005	± 2.91	1.04	0.94	0.0004	± 13.49	0.0005	± 2.91	0.96	0.91	0.0004	± 14.79	0.0004	± 2.97	1.06	1.10
476	150 – 200	1.4 – 1.6	-0.7 – -0.4	0.0031	± 4.85	0.0031	± 1.11	1.02	0.94	0.0032	± 4.83	0.0031	± 1.16	0.98	0.92	0.0029	± 5.14	0.0029	± 1.14	1.06	1.08
477	150 – 200	1.4 – 1.6	-0.4 – 0.0	0.0038	± 3.77	0.0037	± 0.88	1.02	0.94	0.0039	± 3.77	0.0038	± 0.92	0.98	0.92	0.0036	± 4.00	0.0035	± 0.90	1.07	1.09
478	150 – 200	1.4 – 1.6	0.0 – 0.4	0.0055	± 3.41	0.0051	± 0.74	1.01	0.94	0.0056	± 3.40	0.0052	± 0.77	0.99	0.93	0.0052	± 3.70	0.0048	± 0.76	1.07	1.08
479	150 – 200	1.4 – 1.6	0.4 – 0.7	0.0068	± 3.66	0.0070	± 0.73	1.00	0.94	0.0069	± 3.65	0.0070	± 0.75	1.00	0.94	0.0064	± 3.98	0.0066	± 0.75	1.06	1.06
480	150 – 200	1.4 – 1.6	0.7 – 1.0	0.0011	± 9.11	0.0012	± 1.79	1.00	0.95	0.0011	± 9.17	0.0012	± 1.81	1.00	0.95	0.0010	± 9.68	0.0011	± 1.83	1.05	1.06
481	150 – 200	1.6 – 1.8	-1.0 – -0.7	–	–	–	–	–	–	–	–	–	–	–	–	–	–	–	–	–	–
482	150 – 200	1.6 – 1.8	-0.7 – -0.4	0.0020	± 5.88	0.0020	± 1.37	1.04	0.94	0.0020	± 5.80	0.0021	± 1.44	0.96	0.91	0.0018	± 6.29	0.0019	± 1.41	1.06	1.10
483	150 – 200	1.6 – 1.8	-0.4 – 0.0	0.0037	± 4.20	0.0035	± 0.90	1.02	0.94	0.0037	± 4.15	0.0035	± 0.93	0.98	0.93	0.0035	± 4.48	0.0033	± 0.93	1.06	1.08
484	150 – 200	1.6 – 1.8	0.0 – 0.4	0.0052	± 3.27	0.0052	± 0.74	1.02	0.95	0.0054	± 3.26	0.0053	± 0.78	0.98	0.92	0.0050	± 3.45	0.0049	± 0.76	1.06	1.08
485	150 – 200	1.6 – 1.8	0.4 – 0.7	0.0054	± 4.71	0.0050	± 0.87	1.00	0.94	0.0054	± 4.66	0.0050	± 0.90	1.00	0.94	0.0051	± 5.16	0.0047	± 0.89	1.06	1.07
486	150 – 200	1.6 – 1.8	0.7 – 1.0	–	–	–	–	–	–	–	–	–	–	–	–	–	–	–	–	–	–
487	150 – 200	1.8 – 2.0	-1.0 – -0.7	–	–	–	–	–	–	–	–	–	–	–	–	–	–	–	–	–	–
488	150 – 200	1.8 – 2.0	-0.7 – -0.4	0.0006	± 13.60	0.0006	± 2.44	1.03	0.94	0.0006	± 13.28	0.0007	± 2.47	0.97	0.92	0.0005	± 14.93	0.0006	± 2.50	1.06	1.09
489	150 – 200	1.8 – 2.0	-0.4 – 0.0	0.0033	± 4.29	0.0032	± 0.93	1.02	0.94	0.0033	± 4.24	0.0033	± 0.98	0.98	0.92	0.0031	± 4.66	0.0030	± 0.96	1.07	1.09
490	150 – 200	1.8 – 2.0	0.0 – 0.4	0.0051	± 3.14	0.0050	± 0.75	1.01	0.94	0.0052	± 3.15	0.0051	± 0.79	0.99	0.93	0.0048	± 3.36	0.0047	± 0.77	1.07	1.08
491	150 – 200	1.8 – 2.0	0.4 – 0.7	0.0017	± 6.53	0.0017	± 1.50	1.04	0.95	0.0017	± 6.37	0.0017	± 1.54	0.97	0.92	0.0016	± 7.15	0.0016	± 1.53	1.05	1.09
492	150 – 200	1.8 – 2.0	0.7 – 1.0	–	–	–	–	–	–	–	–	–	–	–	–	–	–	–	–	–	–
493	150 – 200	2.0 – 2.2	-1.0 – -0.7	–	–	–	–	–	–	–	–	–	–	–	–	–	–	–	–	–	–
494	150 – 200	2.0 – 2.2	-0.7 – -0.4	–	–	–	–	–	–	–	–	–	–	–	–	–	–	–	–	–	–
495	150 – 200	2.0 – 2.2	-0.4 – 0.0	0.0024	± 4.46	0.0023	± 1.11	1.02	0.93	0.0025	± 4.46	0.0023	± 1.16	0.98	0.91	0.0023	± 4.67	0.0021	± 1.15	1.07	1.09
496	150 – 200	2.0 – 2.2	0.0 – 0.4	0.0038	± 3.84	0.0034	± 0.91	1.01	0.94	0.0038	± 3.81	0.0035	± 0.95	0.99	0.93	0.0035	± 4.07	0.0032	± 0.93	1.06	1.08
497	150 – 200	2.0 – 2.2	0.4 – 0.7	–	–	–	–	–	–	–	–	–	–	–	–	–	–	–	–	–	–
498	150 – 200	2.0 – 2.2	0.7 – 1.0	–	–	–	–	–	–	–	–	–	–	–	–	–	–	–	–	–	–
499	150 – 200	2.2 – 2.4	-1.0 – -0.7	–	–	–	–	–	–	–	–	–	–	–	–	–	–	–	–	–	–
500	150 – 200	2.2 – 2.4	-0.7 – -0.4	–	–	–	–	–	–	–	–	–	–	–	–	–	–	–	–	–	–
501	150 – 200	2.2 – 2.4	-0.4 – 0.0	0.0009	± 8.18	0.0008	± 1.89	1.01	0.94	0.0009	± 8.11	0.0008	± 1.94	0.99	0.93	0.0009	± 8.79	0.0007	± 1.94	1.06	1.08
502	150 – 200	2.2 – 2.4	0.0 – 0.4	0.0011	± 7.28	0.0010	± 1.70	1.03	0.94	0.0012	± 7.11	0.0010	± 1.80	0.97	0.92	0.0011	± 7.87	0.0009	± 1.75	1.06	1.09
503	150 – 200	2.2 – 2.4	0.4 – 0.7	–	–	–	–	–	–	–	–	–	–	–	–	–	–	–	–	–	–
504	150 – 200	2.2 – 2.4	0.7 – 1.0	–	–	–	–	–	–	–	–	–	–	–	–	–	–	–	–	–	–

TABLE 45: Measured cross-section values unfolded to the Born, dressed and bare truth-levels in the 7$^{\text{th}}$ mass window of the measurement. The luminosity uncertainty of 1.9% is not included.

[1] ATLAS Collaboration. Measurement of the double-differential high-mass drell–yan cross section in pp collisions at $\sqrt{s} = 8\,\text{tev}$ with the atlas detector. *Journal of High Energy Physics*, 2016(8):1–61, 2016. 10, 59, 62, 174

[2] Lewis James Armitage, Frank Ellinghaus, Robert Hickling, Uta Klein, Mykhailo Lisovyi, Eram Rizvi, and Markus Zinser. Double-differential high-mass Drell-Yan cross-section measurement in *pp* collisions at $\sqrt{8}$ TeV with the ATLAS detector. Technical Report ATL-COM-PHYS-2015-1381, CERN, Geneva, Nov 2015. 10, 113

[3] Eram Rizvi, Alexandre Glazov, Lewis James Armitage, Tony Kwan, Richard Keeler, Elena Yatsenko, and Andrey Sapronov. Measurement of the Drell-Yan triple-differential cross-section in pp collisions at $\sqrt{s} = 8$ TeV. Technical Report ATL-COM-PHYS-2015-1575, CERN, Geneva, Dec 2015. 10, 170, 172, 183

[4] OPAL Collaboration. Tests of the standard model and constraints on new physics from measurements of fermion pair production at 189 GeV to 209 GeV at LEP. *Eur. Phys. J.*, C33:173–212, 2004. 11

[5] DONUT Collaboration. Observation of tau neutrino interactions. *Physics Letters B*, 504(3):218 – 224, 2001.

[6] CDF Collaboration. Observation of top quark production in $\overline{p}p$ collisions with the collider detector at fermilab. *Phys. Rev. Lett.*, 74:2626–2631, Apr 1995.

[7] CMS Collaboration. Observation of a new boson at a mass of 125 GeV with the CMS experiment at the LHC. *Phys. Lett.*, B716:30, 2012.

[8] ATLAS Collaboration. Observation of a new particle in the search for the Standard Model Higgs boson with the ATLAS detector at the LHC. *Phys. Lett.*, B716:1, 2012. 11

[9] CERN. The Standard Model: https://home.cern/about/physics/standard-model. 12 02.12.2015. 11

[10] LHCb Collaboration. Observation of $j/\psi p$ resonances consistent with pentaquark states in $\Lambda_b^0 \to j/\psi K^- p$ decays. *Phys. Rev. Lett.*, 115:072001, Aug 2015. 12

[11] Nima Arkani-Hamed, Savas Dimopoulos, and Gia Dvali. Phenomenology, astrophysics, and cosmology of theories with submillimeter dimensions and tev scale quantum gravity. *Phys. Rev. D*, 59:086004, Mar 1999. 12

[12] Nima Arkani-Hamed, Savas Dimopoulos, and G.R. Dvali. The Hierarchy problem and new dimensions at a millimeter. *Phys. Lett.*, B429:263, 1998. 12

[13] Sheldon L. Glashow. Partial-symmetries of weak interactions. *Nuclear Physics*, 22(4):579 – 588, 1961. 12

[14] A. Salam. Renormalizability of gauge theories. *Phy. Rev*, 127(331), 1962.

[15] Steven Weinberg. A Model of Leptons. *Physical Review Letters*, 19:1264–1266, 1967. 12

[16] F. Englert and R. Brout. Broken symmetry and the mass of gauge vector mesons. *Phys. Rev. Lett.*, 13:321–323, 1964. 12

[17] Peter W. Higgs. Broken symmetries and the masses of gauge bosons. *Phys. Rev. Lett.*, 13:508–509, 1964.

[18] G.S. Guralnik, C.R. Hagen, and T.W.B. Kibble. Global conservation laws and massless particles. *Phys. Rev. Lett.*, 13:585–587, 1964. 12

[19] Bruno R. Stella and Hans-Jurgen Meyer. Y(9.46 GeV) and the gluon discovery (a critical recollection of PLUTO results). *Eur. Phys. J.*, H36:203–243, 2011. 12

[20] CERN Archive. Gargamelle: first neutral current. En juillet 1973, une grande découverte est annoncée dans le grand amphithéâtre du CERN : le groupe Gargamelle a détecté les courants neutres faibles ! Cette observation confirme la théorie électrofaible, qui prédit que la force faible et la force électromagnétique doivent former une unique interaction. http://cds.cern.ch/record/39468, 1973. 12

[21] UA1 Collaboration. Experimental observation of isolated large transverse energy electrons with associated missing energy at s=540 gev. *Physics Letters B*, 122(1):103 – 116, 1983. 12

[22] M. Banner et al. Observation of single isolated electrons of high transverse momentum in events with missing transverse energy at the {CERN} pp collider. *Physics Letters B*, 122(5–6):476 – 485, 1983.

[23] P. Bagnaia et al. Evidence for $Z^0 \to e^+e^-$ at the CERN $p\bar{p}$ collider. *Physics Letters B*, 129:130–140, September 1983.

[24] UA1 Collaboration. Experimental observation of lepton pairs of invariant mass around 95 GeV/c^2 at the CERN SPS collider. *Physics Letters B*, 126:398–410, July 1983. 12

[25] H1 and ZEUS Collaborations. Combined Measurement and QCD Analysis of the Inclusive e+- p Scattering Cross Sections at HERA. *JHEP*, 01:109, 2010. 16

[26] L. A. Harland-Lang, A. D. Martin, P. Motylinski, and R. S. Thorne. Parton distributions in the LHC era: MMHT 2014 PDFs. *Eur. Phys. J.*, C75(5):204, 2015. 17, 18, 210

[27] V. N. Gribov and L. N. Lipatov. e+ e- pair annihilation and deep inelastic e p scattering in perturbation theory. *Sov. J. Nucl. Phys.*, 15:675–684, 1972. [Yad. Fiz.15,1218(1972)]. 17

[28] V. N. Gribov and L. N. Lipatov. Deep inelastic e p scattering in perturbation theory. *Sov. J. Nucl. Phys.*, 15:438–450, 1972. [Yad. Fiz.15,781(1972)]. 17

[29] Guido Altarelli and G. Parisi. Asymptotic Freedom in Parton Language. *Nucl. Phys.*, B126:298, 1977. 17

[30] John C. Collins, Davison E. Soper, and George F. Sterman. Factorization of Hard Processes in QCD. *Adv. Ser. Direct. High Energy Phys.*, 5:1–91, 1989. 18

[31] S. D. Drell and T.-M. Yan. Massive Lepton-Pair Production in Hadron-Hadron Collisions at High Energies. *Physical Review Letters*, 25:316–320, August 1970. 18, 19

[32] ATLAS Collaboration. Measurement of the inclusive $W^{\pm}$ and Z/gamma cross sections in the electron and muon decay channels in pp collisions at $\sqrt{s} = 7$ TeV with the ATLAS detector. *Phys. Rev.*, D85:072004, 2012. 19, 62

[33] ATLAS Collaboration. Measurement of the high-mass Drell–Yan differential cross-section in pp collisions at sqrt(s)=7 TeV with the ATLAS detector. *Phys. Lett.*, B725:223–242, 2013. 87, 88

[34] ATLAS Collaboration. Measurement of the low-mass Drell-Yan differential cross section at $\sqrt{s} = 7$ TeV using the ATLAS detector. *JHEP*, 06:112, 2014. 19

[35] CMS Collaboration. Measurement of the Inclusive W and Z Production Cross Sections in pp Collisions at $\sqrt{s} = 7$ TeV. *JHEP*, 10:132, 2011. 19

[36] CMS Collaboration. Measurement of the Drell-Yan Cross Section in pp Collisions at $\sqrt{s} = 7$ TeV. *JHEP*, 10:007, 2011.

[37] CMS Collaboration. Measurement of the differential and double-differential Drell-Yan cross sections in proton-proton collisions at $\sqrt{s} = 7$ TeV. *JHEP*, 12:030, 2013.

[38] CMS Collaboration. Measurements of differential and double-differential Drell-Yan cross sections in proton-proton collisions at 8 TeV. *Eur. Phys. J.*, C75(4):147, 2015. 19, 167

[39] LHCb Collaboration. Inclusive W and Z production in the forward region at $\sqrt{s} = 7$ TeV. *JHEP*, 06:058, 2012. 19

[40] LHCb Collaboration. Measurement of the cross-section for $Z \to e^+e^-$ production in pp collisions at $\sqrt{s} = 7$ TeV. *JHEP*, 02:106, 2013.

[41] LHCb Collaboration. Measurement of forward Z $\to$ e$^+$e$^-$ production at $\sqrt{s} = 8$ TeV. *JHEP*, 05:109, 2015.

[42] LHCb Collaboration. Measurement of the forward Z boson production cross-section in pp collisions at $\sqrt{s} = 7$ TeV. *JHEP*, 08:039, 2015.

[43] LHCb Collaboration. Measurement of forward W and Z boson production in pp collisions at $\sqrt{s} = 8$ TeV. *JHEP*, 01:155, 2016. 19

[44] M Bellomo, A Cooper-Sarkar, S Glazov, M Klein, U Klein, J Kretzschmar, V Radescu, A Sapronov, and S Whitehead. QCD analysis of the ATLAS W,Z inclusive cross-section measurements and determination of the strange sea density. Technical Report ATL-COM-PHYS-2011-1430. STDM-2011-43, CERN, Geneva, Oct 2011. Supporting document for the analysis. 19

[45] Elena Yatsenko. *Measurement of Neutral Current Drell-Yan production using ATLAS data collected at $\sqrt{s} = 8$ TeV*. PhD thesis, U. Hamburg, Dept. Phys., 2015. 19, 24, 210

[46] K.A. Olive and Particle Data Group. Review of particle physics. *Chinese Physics C*, 38(9):090001, 2014. 19, 87, 89

[47] Jack Robert Goddard and Eram Rizvi. *A Measurement of the Low Mass Drell-Yan Differential Cross Section in the Di-Muon Channel with $\sqrt{s} = 7$ TeV Proton-Proton Collisions at the ATLAS Experiment*. PhD thesis, Queen Mary, U. of London (main), 2014. Presented 21 11 2013. 20, 21, 210

[48] John C. Collins and Davison E. Soper. Angular distribution of dileptons in high-energy hadron collisions. *Phys. Rev. D*, 16:2219–2225, 1977. 21

[49] A. Bodek. J. Han, A. Khukhunaishvili, and W. Sakumoto. Using Drell-Yan forward-backward asymmetry to reduce PDF errors in the measurement of electroweak parameters. *Eur. Phys. J.*, C76(3):115, 2016. 24

[50] CERN. https://public-archive.web.cern.ch/public-archive/en/About/Global-en.html. 11:35, 03.02.16. 25

[51] Cinzia De Melis. The CERN accelerator complex. Complexe des accélérateurs du CERN. Jan 2016. General Photo. 25, 210

[52] CERN. https://cds.cern.ch/record/1165534/files/CERN-Brochure-2009-003-Eng.pdf. 16:42, 03.02.16. 26, 28, 221

[53] CERN. TheLHC:https://home.cern/topics/large-hadron-collider. 16:58, 03.02.16. 28

[54] CERN. https://cerncourier.com/cws/article/cern/54381. 20.33, 16.01.2017. 28, 221

[55] P. Grafström and W. Kozanecki. Luminosity determination at proton colliders. *Progress in Particle and Nuclear Physics*, 81:97 – 148, 2015. 28, 29, 30, 221

[56] Samuel Nathan Webb and Terry Wyatt. *Factorisation of beams in van der Meer scans and measurements of the ϕ^*_η distribution of $Z \to e^+e^-$ events in pp collisions at $\sqrt{s} = 8$ TeV with the ATLAS detector*. PhD thesis, Manchester U., Jun 2015. Presented 19 May 2015. 30

[57] S. van der Meer. Calibration of the Effective Beam Height in the ISR. 1968. 30

[58] C. Rubbia. Measurement of the Luminosity of p anti-p Collider with a (Generalized) Van Der Meer Method. 1977. 30

[59] ATLAS Collaboration. https://twiki.cern.ch/twiki/bin/view/AtlasPublic/LuminosityPublicResults. 15.04, 08.03.2016. 32, 210

[60] Joao Pequenao and Paul Schaffner. An computer generated image representing how ATLAS detects particles. Jan 2013. 33, 210

[61] Joao Pequenao. Computer generated image of the whole ATLAS detector. Mar 2008. 34, 210

[62] ATLAS Collaboration. The atlas experiment at the cern large hadron collider. *Journal of Instrumentation*, 3(08):S08003, 2008. 33, 34, 37, 40, 44, 45, 46, 210, 211

[63] Joao Pequenao. Computer generated image of the ATLAS inner detector. Mar 2008. 35, 210

[64] Joao Pequenao. Computer Generated image of the ATLAS calorimeter. Mar 2008. 36, 210

[65] Christian W. Fabjan and Fabiola Gianotti. Calorimetry for particle physics. *Rev. Mod. Phys.*, 75:1243–1286, Oct 2003. 36

[66] M Aleksa, F Bergsma, P A Giudici, A Kehrli, M Losasso, X Pons, H Sandaker, P S Miyagawa, S W Snow, J C Hart, and L Chevalier. Measurement of the atlas solenoid magnetic field. *Journal of Instrumentation*, 3(04):P04003, 2008. 38

[67] ATLAS Collaboration. Commissioning of the ATLAS Muon Spectrometer with Cosmic Rays. *Eur. Phys. J.*, C70:875–916, 2010. 39, 210

[68] ATLAS Collaboration. Measurement of the muon reconstruction performance of the ATLAS detector using 2011 and 2012 LHC proton–proton collision data. *Eur. Phys. J.*, C74(11):3130, 2014. 42, 58, 84, 87

[69] Torbjorn Sjostrand, Stephen Mrenna, and Peter Z. Skands. A Brief Introduction to PYTHIA 8.1. *Comput.Phys.Commun.*, 178:852–867, 2008. 48

[70] B. Andersson, G. Gustafson, G. Ingelman, and T. Sjöstrand. Parton fragmentation and string dynamics. *Physics Reports*, 97(2):31 – 145, 1983. 48

[71] Stefano Frixione and Bryan R. Webber. Matching NLO QCD computations and parton shower simulations. *JHEP*, 0206:029, 2002. 48

[72] Paolo Nason. A New method for combining NLO QCD with shower Monte Carlo algorithms. *JHEP*, 0411:040, 2004. 48

[73] Stefano Frixione, Paolo Nason, and Carlo Oleari. Matching NLO QCD computations with Parton Shower simulations: the POWHEG method. *JHEP*, 0711:070, 2007.

[74] Simone Alioli, Paolo Nason, Carlo Oleari, and Emanuele Re. A general framework for implementing NLO calculations in shower Monte Carlo programs: the POWHEG BOX. *JHEP*, 1006:043, 2010. 48

[75] J. A. M. Vermaseren. Two Photon Processes at Very High-Energies. *Nucl. Phys.*, B229:347, 1983. 48

[76] S. P. Baranov et al. Lpair - a generator for lepton pair production. In Proceedings of the Workshop, editor, *Physics at HERA*, number pp. 1478 1482. HERA, October 1991. 48

[77] Stefano Frixione, Fabian Stoeckli, Paolo Torrielli, and Bryan R. Webber. NLO QCD corrections in Herwig++ with MC@NLO. *JHEP*, 1101:053, 2011. 48

[78] G. Corcella, I.G. Knowles, G. Marchesini, S. Moretti, K. Odagiri, et al. HERWIG 6: An Event generator for hadron emission reactions with interfering gluons (including supersymmetric processes). *JHEP*, 0101:010, 2001.

[79] J. M. Butterworth and M. H. Seymour. Multi-parton interactions in Herwig for the LHC. *http://projects.hepforge.org/jimmy*, 2009.

[80] B.R. Webber. A qcd model for jet fragmentation including soft gluon interference. *Nuclear Physics B*, 238(3):492 – 528, 1984. 48

[81] Piotr Golonka and Zbigniew Was. PHOTOS Monte Carlo: A Precision tool for QED corrections in Z and W decays. *Eur.Phys.J.*, C45:97–107, 2006. 48, 81, 183

[82] ATLAS Collaboration. Summary of atlas pythia 8 tunes. ATLAS-CONF-2012-003, http://cdsweb.cern.ch/record/1474107/. 49

[83] GEANT4 Collaboration (S. Agostinelli and others). GEANT4: A simulation toolkit. *Nucl. Instrum. Meth.*, A506:250, 2003. 49

[84] CERN ROOT. ROOT: `https://root.cern.ch/root/htmldoc/guides/users-guide/ROOTUsersGuide.html`. April 13.04.2016. 49

[85] H.-L. Lai, M. Guzzi, J. Huston, Z. Li, et al. New parton distributions for collider physics. *Phys. Rev.*, D82:074024, 2010. 51, 122, 183

[86] ATLAS Collaboration. Measurement of the Z to tau tau Cross Section with the ATLAS Detector. *Phys. Rev.*, D84:112006, 2011. 54, 221

[87] D. Bardin, S. Bondarenko, P. Christova, L. Kalinovskaya, et al. SANC integrator in the progress: QCD and EW contributions. *JETP Lett.*, 96:285–289, 2012. 55, 81, 222

[88] Sergey G. Bondarenko and Andrey A. Sapronov. NLO EW and QCD proton-proton cross section calculations with mcsanc-v1.01. *Comput.Phys.Commun.*, 184:2343–2350, 2013. 55, 81, 222

[89] ATLAS Collaboration. Observation and measurement of Higgs boson decays to WW^* with the ATLAS detector. *Phys. Rev. D*, 92(arXiv:1412.2641. CERN-PH-EP-2014-270):012006. 73 p, Dec 2014. Comments: 73 pages plus author list + cover pages (86 pages total), 47 figures, 30 tables, submitted to Physical Review D, All figures including auxiliary figures are available at http://atlas.web.cern.ch/Atlas/GROUPS/PHYSICS/PAPERS/HIGG-2013-13/. 53, 55, 222

[90] J. M. Campbell and R. K. Ellis. An update on vector boson pair production at hadron colliders. *Phys. Rev.*, D60:113006, 1999. 55, 81, 183, 222

[91] John M. Campbell, R. Keith Ellis, and Ciaran Williams. Vector boson pair production at the LHC. *JHEP*, 07:018, 2011. 81

[92] ATLAS Collaboration. Measurement of total and differential W^+W^- production cross sections in proton-proton collisions at $\sqrt{s} = 8$ TeV with the ATLAS detector and limits on anomalous triple-gauge-boson couplings. *JHEP*, 09:029, 2016. 55, 222

[93] M Cacciari, M Czakon, M. L. Mangano, and A Mitov. Top-pair production at hadron colliders with next-to-next-to-leading logarithmic soft-gluon resummation. *Phys. Lett.*, B710:612, 2012. 56, 81, 222

[94] Peter Baernreuther, Michal Czakon, and Alexander Mitov. Percent Level Precision Physics at the Tevatron: First Genuine NNLO QCD Corrections to $q\bar{q} \to t\bar{t} + X$. *Phys. Rev. Lett.*, 109:132001, 2012.

[95] Michal Czakon and Alexander Mitov. NNLO corrections to top-pair production at hadron colliders: the all-fermionic scattering channels. *JHEP*, 1212:054, 2012.

[96] Michal Czakon and Alexander Mitov. NNLO corrections to top pair production at hadron colliders: the quark-gluon reaction. *JHEP*, 1301:080, 2013.

[97] Michal Czakon, Paul Fiedler, and Alexander Mitov. The total top quark pair production cross-section at hadron colliders through $O(\alpha_S^4)$. *Phys. Rev. Lett.*, 110:252004, 2013.

[98] Michal Czakon and Alexander Mitov. Top++: A Program for the Calculation of the Top-Pair Cross-Section at Hadron Colliders. 2011. 81

[99] Nikolaos Kidonakis. Two-loop soft anomalous dimensions for single top quark associated production with a W- or H-. *Phys. Rev.*, D82:054018, 2010. 56, 81, 222

[100] ATLAS Collaboration. Measurement of the $W \to \ell\nu$ and $Z/\gamma^* \to \ell\ell$ production cross sections in proton-proton collisions at $\sqrt{s} = 7$ TeV with the ATLAS detector. *JHEP*, 12:060, 2010. 56, 222

[101] ATLAS Collaboration. Measurement of the $W \to \tau\nu_\tau$ cross section in pp collisions at $\sqrt{s}$ =7 TeV with the ATLAS experiment. *Phys. Lett.*, B706:276–294, 2012. 56, 222

[102] ATLAS Collaboration. Measurement of the low-mass Drell-Yan differential cross section at $\sqrt{s} = 7$ TeV using the ATLAS detector. *JHEP*, 1406:112, 2014. 62

[103] G. Cowan. *Statistical Data Analysis*. Oxford science publications. Clarendon Press, 1998. 69, 71

[104] ATLAS Collaboration. Proposal for truth particle observable definitions in physics measurements. Technical Report ATL-PHYS-PUB-2015-013, CERN, Geneva, Jun 2015. 69

[105] D. Sivia and J. Skilling. *Data Analysis: A Bayesian Tutorial*. Oxford science publications. OUP Oxford, 2006. 71

[106] G. D'Agostini. Improved iterative Bayesian unfolding. *Universita "La Sapienza" and INFN*, http://www.roma1.infn.it/~dagos/unf2.pdf, 2010. 71

[107] B. Laforge and L. Schoeffel. Elements of statistical methods in high-energy physics analyses. *Nucl.Instrum.Meth.*, A394:115–120, 1997. 72

[108] Ye Li and Frank Petriello. Combining QCD and electroweak corrections to dilepton production in FEWZ. *Phys. Rev. D*, 86:094034, 2012. 81

[109] Kirill Melnikov and Frank Petriello. Electroweak gauge boson production at hadron colliders through $\mathcal{O}(\alpha_s^2)$. *Phys. Rev. D*, 74:114017, 2006.

[110] Ryan Gavin et al. FEWZ 2.0: A code for hadronic Z production at next-to-next-to-leading order. *Comput. Phys. Commun.*, 182:2388, 2011. 81

[111] A.D. Martin, W.J. Stirling, R.S. Thorne, and G. Watt. Parton distributions for the LHC. *Eur. Phys. J.*, C63:189, 2009. 81

[112] Gerard 't Hooft and M. J. G. Veltman. Regularization and Renormalization of Gauge Fields. *Nucl. Phys.*, B44:189–213, 1972. 81

[113] Gerardus 't Hooft. Dimensional regularization and the renormalization group. *Nucl. Phys. B*, 61(CERN-TH-1666):455–68, 1973.

[114] William A. Bardeen, A. J. Buras, D. W. Duke, and T. Muta. Deep Inelastic Scattering Beyond the Leading Order in Asymptotically Free Gauge Theories. *Phys. Rev.*, D18:3998, 1978. 81

[115] Reinhard Alkofer and Lorenz von Smekal. The Infrared behavior of QCD Green's functions: Confinement dynamical symmetry breaking, and hadrons as relativistic bound states. *Phys. Rept.*, 353:281, 2001. 81

[116] Ikaros I. Y. Bigi, Mikhail A. Shifman, N. G. Uraltsev, and A. I. Vainshtein. The Pole mass of the heavy quark. Perturbation theory and beyond. *Phys. Rev.*, D50:2234–2246, 1994.

[117] Matthew Dowling and Sven Moch. Top-quark Pair Production in a Running Mass Scheme. *PoS*, EPS-HEP2013:214, 2013. 81

[118] ATLAS Collaboration. Performance of the ATLAS muon trigger in pp collisions at $\sqrt{s} = 8$ TeV. *Eur. Phys. J.*, C75:120, 2015. 87, 88

[119] Robert Scot Hickling and Eram Rizvi. *Measuring the Drell-Yan Cross Section at High Mass in the Dimuon Channel*. PhD thesis, Queen Mary, U. of London, Sep 2014. Presented 12 Nov 2014. 87, 88, 108

[120] O Arnaez, N Besson, M Boonekamp, F Ellinghaus, G Gaycken, S Glazov, C Goeringer, L Han, S Hou, M Karnevskiy, F Kiss, U Klein, H Liu, J Liu, M Liu, K Mueller, T Nunnemann, F Pfeiffer, J Qian, K Schmieden, M Schott, J Strandberg, J Therhaag, E von Torne, H Wang, N Wermes, K Yamamoto, B Zhou, and J Zhu. A first measurement of the transverse momentum distribution of Drell-Yan lepton pairs at sqrt(s)=7 TeV with ATLAS. Technical Report ATL-PHYS-INT-2012-033, CERN, Geneva, Apr 2012. 96

[121] Nenad Vranjes, Troels Petersen, and Mikhail Karnevskiy. Measurement of m_W at 7 TeV: Muon momentum corrections and uncertainties. Technical Report ATL-COM-PHYS-2014-1433, CERN, Geneva, Nov 2014. 96, 100

[122] M Karnevskiy, T-H Lin, M Schott, C Zimmermann, L Tomlinson, S Webb, and Mykhailo Lisovyi. Measurement of the transverse momentum and azimuthal decorrelation of leptons in DrellYan events at sqrts = 8 TeV with ATLAS. Technical Report ATL-COM-PHYS-2014-281, CERN, Geneva, Apr 2014. 113

[123] Michal Bartlomiej Balcerak, Bartlomiej Ryniec, Alexey Ezhilov, Kristof Schmieden, Aaron James Armbruster, Oleg Fedin, Daniel Froidevaux, Mykhailo Lisovyi, Elzbieta Richter-Was, and Manuella Vincter. Probing QCD dynamics with measurement of polarisation angular coefficients in $Z \to ll$ process with ATLAS detector. Technical Report ATL-COM-PHYS-2014-583, CERN, Geneva, Jun 2014. 113

[124] ATLAS Collaboration. Luminosity determination in pp collisions at $\sqrt{s} = 8$ tev using the atlas detector at the lhc. *The European Physical Journal C*, 76(12):653, 2016. 121

[125] J. Gao, M. Guzzi, J. Huston, H.-L. Lai, et al. The CT10 NNLO Global Analysis of QCD. 2013. 122, 183

[126] Unfolding in the Standard Model and Top groups. https://twiki.cern.ch/twiki/bin/view/AtlasProtected/StandardModelUnfolding. Accessed: 2016-05-20. 122

[127] ATLAS Collaboration. ATLAS recomendations: https://twiki.cern.ch/twiki/bin/view/AtlasProtected/WZElectroweakCommonTopics2013. 16.08.2016. 123

[128] ATLAS Collaboration. Measurement of the angular coefficients in Z-boson events using electron and muon pairs from data taken at $\sqrt{s} = 8$ TeV with the ATLAS detector. *J. High Energy Phys.*, 08(CERN-EP-2016-087. arXiv:1606.00689):159. 84 p, Jun 2016. Comments: 84 pages plus author list + cover pages (101 pages total), 33 figures, 27 tables. Submitted to JHEP. All figures including auxiliary figures are available at https://atlas.web.cern.ch/Atlas/GROUPS/PHYSICS/PAPERS/STDM-2014-10/. 148, 174

[129] A. Glazov. Averaging of DIS cross section data. *AIP Conf.Proc.*, 792:237–240, 2005. 172

[130] H1 and ZEUS Collaborations. Measurement of the inclusive ep scattering cross section at low q^2 and x at hera. *Eur. Phys. J.*, C63:625–678, 2009. 172

[131] K Bachas, M Bellomo, F Bührer, S Camarda, A Cooper-Sarkar, J Dassoulas, R S Hickling, F Ellinghaus, C Issever, C T Jeske, D Froidevaux, L Iconomidou-Fayard, A Glazov, T Guillemin, A Kapliy, M Karnevskiy, M Klein, U Klein, J Kretzschmar, T Kono, A Lewis, K Lohwasser, M Lisovyi, T Matsushita, J Maurer, P Onyisi, E Richter-Was, E Rizvi, V Radescu, P Sommer, G Sedov, T Serre, A Schaffer, S Schmitt, J Sendler, M Shochet, J Tseng, M Vincter, M Wielers, and E Yatsenko. Measurement and QCD Analysis of Differential Inclusive $W^+ \to l\nu$ and $Z/gamma^* \to ll$ Production and Leptonic Decay Cross Sections with ATLAS: Analysis STDM-2012-20: W and Z inclusive cross section with 2011 data. Technical Report ATL-COM-PHYS-2013-217, CERN, Geneva, Feb 2012. 172

[132] ATLAS Collaboration. Measurement of the transverse momentum and ϕ^*_η distributions of Drell–Yan lepton pairs in proton–proton collisions at $\sqrt{s} = 8$ TeV with the ATLAS detector. *Eur. Phys. J. C*, 76(arXiv:1512.02192. CERN-PH-EP-2015-275):291. 59 p, Dec 2015. 174

[133] J. Blümlein, S. Moch, T. Riemann, John M. Campbell, and R.K. Ellis. Loops and legs in quantum field theory mcfm for the tevatron and the lhc. *Nuclear Physics B - Proceedings Supplements*, 205:10 – 15, 2010. 183

[134] Tancredi Carli, Dan Clements, Amanda Cooper-Sarkar, Claire Gwenlan, Gavin P. Salam, Frank Siegert, Pavel Starovoitov, and Mark Sutton. A posteriori inclusion of parton density functions in nlo qcd final-state calculations at hadron colliders: the applgrid project. *The European Physical Journal C*, 66(3):503–524, 2010. 183

[135] W.F.L. Hollik. Radiative Corrections in the Standard Model and their Role for Precision Tests of the Electroweak Theory. *Fortsch. Phys.*, 38:165, 1990. 183

[136] K. Nakamura et al. Review of particle physics. *J. Phys.*, G37:075021, 2010. 183, 186, 220

[137] Ryan Gavin, Ye Li, Frank Petriello, and Seth Quackenbush. FEWZ 2.0: A code for hadronic Z production at next-to-next-to-leading order. 2010. 183

[138] Stefan Dittmaier and Max Huber. Radiative corrections to the neutral-current Drell-Yan process in the Standard Model and its minimal supersymmetric extension. *JHEP*, 1001:060, 2010. 183

[139] A. D. Martin, R. G. Roberts, W. J. Stirling, and R. S. Thorne. Parton distributions incorporating QED contributions. *Eur. Phys. J.*, C39:155, 2005. 183

[140] S. Alekhin et al. HERAFitter. *Eur. Phys. J.*, C75(7):304, 2015. 184

[141] XFitter Collaboration. XFitter https://www.xfitter.org/xFitter/. 12.09.2016. 184

[142] S. Schael et al. Precision electroweak measurements on the Z resonance. *Phys. Rept.*, 427:257–454, 2006. 186, 220

[143] Kenji Abe et al. A High precision measurement of the left-right Z boson cross-section asymmetry. *Phys. Rev. Lett.*, 84:5945–5949, 2000.

[144] D0 Collaboration. Measurement of the effective weak mixing angle in $p\overline{p} \to z/\gamma^* \to e^+e^-$ events. *Phys. Rev. Lett.*, 115:041801, Jul 2015.

[145] CDF Collaboration. Indirect measurement of $\sin^2\theta_W$ (or M_W) using $\mu^+\mu^-$ pairs from γ^*/Z bosons produced in $p\bar{p}$ collisions at a center-of-momentum energy of 1.96 TeV. *Phys. Rev.*, D89(7):072005, 2014.

[146] ATLAS Collaboration. Measurement of the forward-backward asymmetry of electron and muon pair-production in pp collisions at $\sqrt{s} = 7$ TeV with the ATLAS detector. *JHEP - Submitted*, 2015.

[147] CMS Collaboration. Forward-backward asymmetry of Drell-Yan lepton pairs in pp collisions at $\sqrt{s} = 7$ TeV. *Phys. Lett.*, B718:752–772, 2013.

[148] LHCb Collaboration. Measurement of the forward-backward asymmetry in $z/\gamma^* \to \mu\mu$ decays and determination of the effective weak mixing angle. *Journal of High Energy Physics*, 2015(11):1–19, 2015. 186, 220

[149] ATLAS Collaboration. https://atlas.fis.utfsm.cl/atlas/hlt/ATLAS_coord.gif. 11.03.2016. 188, 220

LIST OF FIGURES

LIST OF TABLES